1. REPORT DATE (DD-MM-YYYY)	2. REPORT TYPE	3. DATES COVERED (From - To)
31-03-2014	Final Report	10-Mar-2009 - 31-Dec-2013

4. TITLE AND SUBTITLE	5a. CONTRACT NUMBER
Reactive Material Structures	
	5b. GRANT NUMBER
	W911NF-09-C-0014
	5c. PROGRAM ELEMENT NUMBER
	8620AR

6. AUTHORS	5d. PROJECT NUMBER
M.E. Grudza, W.J. Flis, H.L. Lam, D.C. Jann, R.D. Ciccarelli	
	5e. TASK NUMBER
	5f. WORK UNIT NUMBER

7. PERFORMING ORGANIZATION NAMES AND ADDRESSES	8. PERFORMING ORGANIZATION REPORT NUMBER
DE Technologies Inc. 100 Queens Drive King of Prussia, PA 19406 -3562	

9. SPONSORING/MONITORING AGENCY NAME(S) AND ADDRESS (ES)	10. SPONSOR/MONITOR'S ACRONYM(S) ARO
U.S. Army Research Office P.O. Box 12211 Research Triangle Park, NC 27709-2211	11. SPONSOR/MONITOR'S REPORT NUMBER(S) 55354-EG-DRP.1

12. DISTRIBUTION AVAILIBILITY STATEMENT

Approved for Public Release; Distribution Unlimited

13. SUPPLEMENTARY NOTES
The views, opinions and/or findings contained in this report are those of the author(s) and should not contrued as an official Department of the Army position, policy or decision, unless so designated by other documentation.

14. ABSTRACT
We have developed a Reactive Material Structure (RMS), a reactive, blast-enhancing material with sufficient strength and mass density to be suitable as a casing material for a penetrating munition. The material is a composite laminate of braided, woven, and wound wire in a polymeric matrix that is loaded with a combustible metal powder. We progressively improved and scaled up the fabrication process, from small coupon test specimens to structures weighing 10 kilograms. We successfully demonstrated that the RMS can enhance explosive blast by a factor of four or more over a conventional steel casing and can survive penetration into concrete in a representative munition at

15. SUBJECT TERMS
reactive materials, penetrating weapons, enhanced blast

16. SECURITY CLASSIFICATION OF:			17. LIMITATION OF ABSTRACT	15. NUMBER OF PAGES	19a. NAME OF RESPONSIBLE PERSON William Flis
a. REPORT	b. ABSTRACT	c. THIS PAGE	UU		19b. TELEPHONE NUMBER 610-337-2800
UU	UU	UU			

Report Title

Reactive Material Structures

ABSTRACT

We have developed a Reactive Material Structure (RMS), a reactive, blast-enhancing material with sufficient strength and mass density to be suitable as a casing material for a penetrating munition. The material is a composite laminate of braided, woven, and wound wire in a polymeric matrix that is loaded with a combustible metal powder. We progressively improved and scaled up the fabrication process, from small coupon test specimens to structures weighing 10 kilograms. We successfully demonstrated that the RMS can enhance explosive blast by a factor of four or more over a conventional steel casing and can survive penetration into concrete in a representative munition at typical bomb-delivery velocities.

Enter List of papers submitted or published that acknowledge ARO support from the start of the project to the date of this printing. List the papers, including journal references, in the following categories:

(a) Papers published in peer-reviewed journals (N/A for none)

Received   Paper

TOTAL:

Number of Papers published in peer-reviewed journals:

(b) Papers published in non-peer-reviewed journals (N/A for none)

Received   Paper

TOTAL:

Number of Papers published in non peer-reviewed journals:

(c) Presentations

Number of Presentations:

Non Peer-Reviewed Conference Proceeding publications (other than abstracts):

<u>Received</u>   <u>Paper</u>

TOTAL:

Number of Non Peer-Reviewed Conference Proceeding publications (other than abstracts):

Peer-Reviewed Conference Proceeding publications (other than abstracts):

<u>Received</u>   <u>Paper</u>

TOTAL:

Number of Peer-Reviewed Conference Proceeding publications (other than abstracts):

(d) Manuscripts

<u>Received</u>   <u>Paper</u>

TOTAL:

Number of Manuscripts:

Books

<u>Received</u>   <u>Paper</u>

TOTAL:

Patents Submitted

Patents Awarded

Awards

None.

Graduate Students

NAME	PERCENT_SUPPORTED
FTE Equivalent:	
Total Number:	

Names of Post Doctorates

NAME	PERCENT_SUPPORTED
FTE Equivalent:	
Total Number:	

Names of Faculty Supported

NAME	PERCENT_SUPPORTED
FTE Equivalent:	
Total Number:	

Names of Under Graduate students supported

NAME	PERCENT_SUPPORTED
FTE Equivalent:	
Total Number:	

Student Metrics

This section only applies to graduating undergraduates supported by this agreement in this reporting period

The number of undergraduates funded by this agreement who graduated during this period: 0.00

The number of undergraduates funded by this agreement who graduated during this period with a degree in science, mathematics, engineering, or technology fields:------ 0.00

The number of undergraduates funded by your agreement who graduated during this period and will continue to pursue a graduate or Ph.D. degree in science, mathematics, engineering, or technology fields:------ 0.00

Number of graduating undergraduates who achieved a 3.5 GPA to 4.0 (4.0 max scale):....... 0.00

Number of graduating undergraduates funded by a DoD funded Center of Excellence grant for Education, Research and Engineering:...... 0.00

The number of undergraduates funded by your agreement who graduated during this period and intend to work for the Department of Defense 0.00

The number of undergraduates funded by your agreement who graduated during this period and will receive scholarships or fellowships for further studies in science, mathematics, engineering or technology fields: 0.00

Names of Personnel receiving masters degrees

NAME
Total Number:

Names of personnel receiving PHDs

NAME
Total Number:

Names of other research staff

NAME	PERCENT_SUPPORTED
FTE Equivalent:	
Total Number:	

Sub Contractors (DD882)

1 a. Energetic Materials Research and Testing Center   **1 b.**

00000

Sub Contractor Numbers (c):

Patent Clause Number (d-1):

Patent Date (d-2):

Work Description (e): Ballistic testing services.

Sub Contract Award Date (f-1):

Sub Contract Est Completion Date(f-2):

---

1 a. Colorado School of Mines   **1 b.** Research Administration

1500 Illinois St

Golden   CO   804011911

Sub Contractor Numbers (c):

Patent Clause Number (d-1):

Patent Date (d-2):

Work Description (e): Investigate Spark Plasma Sintering process for producing reactive materials.

Sub Contract Award Date (f-1):

Sub Contract Est Completion Date(f-2):

---

1 a. Colorado School of Mines   **1 b.** Office of Research Services

1500 Illinois Street

Golden   CO   804011911

Sub Contractor Numbers (c):

Patent Clause Number (d-1):

Patent Date (d-2):

Work Description (e): Investigate Spark Plasma Sintering process for producing reactive materials.

Sub Contract Award Date (f-1):

Sub Contract Est Completion Date(f-2):

---

1 a. Materials Research & Design, Inc.   **1 b.** 300 E. Swedesford Rd.

Wayne   PA   19087

Sub Contractor Numbers (c):

Patent Clause Number (d-1):

Patent Date (d-2):

Work Description (e): Compute properties of wire-reinforced composite materials; provide design input on techn

Sub Contract Award Date (f-1):

Sub Contract Est Completion Date(f-2):

1 a. Exponent, Inc.   **1 b.** 16450 Via Esprillo

San Diego   CA   92127

Sub Contractor Numbers (c):
Patent Clause Number (d-1):
Patent Date (d-2):
Work Description (e): Test various reactive materials and components for possible hazards in their handling, ass
Sub Contract Award Date (f-1):
Sub Contract Est Completion Date(f-2):

---

1 a. Exponent, Inc.   **1 b.** 16450 Via Esprillo

San Diego   CA   921271828

Sub Contractor Numbers (c):
Patent Clause Number (d-1):
Patent Date (d-2):
Work Description (e): Test various reactive materials and components for possible hazards in their handling, ass
Sub Contract Award Date (f-1):
Sub Contract Est Completion Date(f-2):

---

1 a. SRI International   **1 b.** 333 Ravenswood Ave

Menlo Park   CA   94025

Sub Contractor Numbers (c):
Patent Clause Number (d-1):
Patent Date (d-2):
Work Description (e): Develop fluorinated polymers for incorporation in reactive materials.
Sub Contract Award Date (f-1):
Sub Contract Est Completion Date(f-2):

---

1 a. MATSYS, Inc.   **1 b.** 504 Shaw Road Suite 215

Sterling   VA   201669436

Sub Contractor Numbers (c):
Patent Clause Number (d-1):
Patent Date (d-2):
Work Description (e): Provide reactive materials manufactured by Hot Isostatic Pressing.
Sub Contract Award Date (f-1):
Sub Contract Est Completion Date(f-2):

---

1 a. MATSYS, Inc.   **1 b.** 504 Shaw Road Suite 215

Sterling   VA   201669436

Sub Contractor Numbers (c):
Patent Clause Number (d-1):
Patent Date (d-2):
Work Description (e): Provide reactive materials manufactured by Hot Isostatic Pressing.
Sub Contract Award Date (f-1):
Sub Contract Est Completion Date(f-2):

1 a. University of Illinois - Urbana - Champaign

1 b. c/o OSPRA

1901 S. First Street, Suite A

Champaign IL 618207406

Sub Contractor Numbers (c):

Patent Clause Number (d-1):

Patent Date (d-2):

Work Description (e): Testing of reactive materials.

Sub Contract Award Date (f-1):

Sub Contract Est Completion Date(f-2):

---

1 a. University of Illinois - Urbana - Champaign

1 b. 1901 S. First Street, Suita A, MC-68

Champaign IL 618207406

Sub Contractor Numbers (c):

Patent Clause Number (d-1):

Patent Date (d-2):

Work Description (e): Testing of reactive materials.

Sub Contract Award Date (f-1):

Sub Contract Est Completion Date(f-2):

---

1 a. Alliant Techsystems, Inc. - Launch Systems Division

1 b. PO Box 707

Brigham City UT 84302-0707

Sub Contractor Numbers (c):

Patent Clause Number (d-1): NA

Patent Date (d-2):

Work Description (e): Testing of reactive materials

Sub Contract Award Date (f-1): 10/9/09 12:00AM

Sub Contract Est Completion Date(f-2): 12/31/13 12:00AM

Inventions (DD882)

Scientific Progress

Technology Transfer

Table of Contents

Abstract

We have developed a Reactive Material Structure (RMS), a reactive, blast-enhancing material with sufficient strength and mass density to be suitable as a casing material for a penetrating munition. The material is a composite laminate of braided, woven, and wound wire in a polymeric matrix that is loaded with a combustible metal powder. We progressively improved and scaled up the fabrication process, from small coupon test specimens to structures weighing 10 kilograms. We successfully demonstrated that the RMS can enhance explosive blast by a factor of four or more over a conventional steel casing and can survive penetration into concrete in a representative munition at typical bomb-delivery velocities.

List of Figures

List of Tables

Section I

Introduction

This is DE Technologies, Inc.'s (DET) Final Progress Report (FPR) for the Defense Research Projects Agency (DARPA) Reactive Material Structures (RMS) Program, contract number W911NF-09-C-0014, awarded March 10, 2009. This report summarizes work by DET and its subcontractors during the period March 10, 2009 through January 31, 2014.

At the direction of DARPA, the program was organized into two phases, with DARPA-defined goals for demonstrated material performance in each phase. The objectives of Phases I and II were to produce a reactive material structure with the following properties:

1. Density of 7.8 g/cc
2. Internal energy of 1,500 cal/g
3. Demonstrated strength of 50 ksi in Phase I and 100 ksi in Phase II
4. Increase in blast impulse by a factor of 2 in Phase I and a factor of 4 in Phase II over a comparable steel-cased warhead when used as a casing material in a warhead and/or bomb with a ratio of metal mass to explosive charge mass of 3.0.

1.1 Phase I

The DET Phase I RMS program was a two-year material development effort investigating two approaches: Fiber-Reinforced Polymer-Based Reactive Composite Materials and Metallic Composite Materials based on metal powder systems. Each concept had two variations resulting in four different material formulations.

The Phase I program was organized into four technological thrusts, three of which were material development efforts, and fourth dealing with the ultimate application of the materials as an explosive-warhead blast enhancer. The program was structured such that each of the three material development thrusts began as a standalone effort; however, as the program progressed, there were decision points for down-selection and integration of efforts where beneficial.

Thrust A focused on the Fiber-Reinforced Polymer-Based Reactive Composite Materials, based on metallic fibers and conventional composite-materials technology. Matrix materials included commercial epoxies loaded with reactive metal powders. The constituent elements of epoxies, including carbon, oxygen, nitrogen, and hydrogen, are all potential reactants with the metal fill. To supplement this effort, high-strength energetic polymers were developed by SRI International in Thrust C. These incorporated fluorine, which, as a strong oxidizer, offered a potential for greater reactivity. The intent was to synthesize energetic polymers to replace the commercial polymers used in Thrust A. In testing, however, the energetic polymers showed no advantages in enhancing blast over commercial epoxies, and in June 2010 this effort was terminated.

Thrust B focused on Metallic Composite Materials assembled via powder-metallurgy techniques. Two different processes were investigated. Team member MATSYS Corporation utilized Hot Isostatic Pressing (HIP) to fully consolidate Cold Isostatic Pressed (CIPed) green bodies of mixed metal powders. The composites are mixtures of two or more metals, with the metals themselves capable of reacting exothermically with each other (intermetallic reaction). In MATSYS's HIP process, the parameters may be varied in order to control the amount of diffusion bonding along the interfaces between the metal particles. The degree of diffusion bonding affects the material's strength and reactivity.

The second process considered in Thrust B was Spark Plasma Sintering (SPS), investigated by the Colorado School of Mines (CSM). In this process an electrical current generates heat to bond the particles of

CIPed green bodies of mixed metal powders. The metal mixtures examined were similar to those under consideration for the HIP process. The degree of intermetallic formation at the particle boundaries can be controlled via various process parameters (e.g., current, pressure). As with the HIP process, this has a direct effect on material strength and reactivity.

In Thrust D, DET investigated explosive-driven mechanisms for fracturing a reactive-material casing, depositing thermal energy to ignite it, and dispersing it into the air to promote its combustion. Approaches considered included material parameters like porosity and inclusions to facilitate coupling the explosive shock energy to the material system. Sub-scale blast tests of these concepts were performed by the University of Illinois at Urbana-Champaign (UIUC). Other approaches examined included grooving the casing and explosive wave-shaping. Larger-scale blast testing was performed by Alliant Techsystems (ATK) in a warhead-type explosive device.

1.2 Phase II

In Phase II, DET furthered the development of our RMS for application in penetrating munitions. We reviewed and implemented analytical and computational models of concrete penetration. We exercised these models to design notional full-scale penetrators that exploit RMS blast enhancement to achieve performance comparable to existing conventional bomb penetrators but in significantly smaller sizes. With our team member ATK, we conducted blast chamber testing to determine the effect of RMS casing to explosive mass ratio, in the range of 1 to 12, on blast enhancement. We fabricated specimens for independent blast chamber testing at Applied Research Associates, Inc. (ARA). In concert with team member Materials Research & Design, Inc. (MR&D), we conducted an iterative effort to improve the strength of our RMS, particularly the compressive strength. We scaled up our fabrication process to produce specimens as large as 10 kg on existing equipment. Test specimens representative of penetrating munitions were designed, fabricated, and ballistically tested to demonstrate survivability against concrete targets.

1.3 Report Organization

The following sections discuss the technical approach and describe the major accomplishments of each phase. In this report, Sections II through VI presents the results of Phase I. Section II describes the Phase I Thrust A effort investigating fiber-reinforced polymer-based reactive composite materials. Section III presents the results of the Hot Isostatic Pressing effort as part of Phase I Thrust B. Section IV presents the results of the Spark Plasma Sintering effort at Colorado School of Mines, also part of Thrust B. Section V presents the Phase I Thrust C effort on energetic binders performed by SRI International. Section VI presents the Phase I Thrust D effort on warhead mechanisms, including the small-scale testing at University of Illinois at Urbana-Champaign and large-scale blast testing at ATK.

Sections VII through XIV present the Phase II results. Section VII describes the analytical and computational methodology for predicting penetration performance and structural survivability of penetrating bombs. Section VIII discusses application of this methodology in trade studies for the application of RMS in notional bomb designs. Section IX describes efforts at improving mechanical properties of the RMS, by modifying the braid layup to increase the tensile, compressive, and flexural strengths and moduli, as demonstrated by testing. Section X describes the first iteration of blast tests, to investigate the effect of the ratio of casing mass to explosive mass on blast enhancement by RMS. Section XI discusses scaling up the fabrication, with attention to safety, of RMS specimens that were used in the blast tests (1-kg nominal mass) and later ballistic tests (10-kg nominal mass). Section XII reports trade studies for the application of RMS in notional bomb designs, addressing the issues of penetration ability and survivability. Section XIII presents detailed designs of scaled bomb penetrators incorporating RMS in a nominal 10-kg size

for ballistic testing. Section XIV reports the setup and results of the ballistic survivability tests. Project accomplishments for both program phases are summarized in Section XV.

Section II

Phase I Thrust A: Fiber-Reinforced Polymer-Based Reactive Composite Materials

This section summarizes the development of polymer-based reactive composite materials. The first part describes ternary plots, also known as triangle plots, and their application in formulating material combinations for Reactive Material Structures. The second part of this section describes the composite materials developed and their corresponding density and strength.

2.1 Ternary Plots

A ternary plot consists of an equilateral triangle within which mixtures of three materials are represented. Each point within the triangle represents a unique combination of proportions of the three components. For the present program, it was most useful to define material proportions in terms of volume fractions. Each apex of the triangle represents 100% volume fraction of one of the component. For any point within the triangle, the value of the volume fraction of each component is proportional to the distance from the point to the side opposite that component's apex. For example, in Fig. 2-1, the volume fraction of tungsten (for which the top apex represents 100%) is proportional to the distance from the point to the bottom side of the triangle.
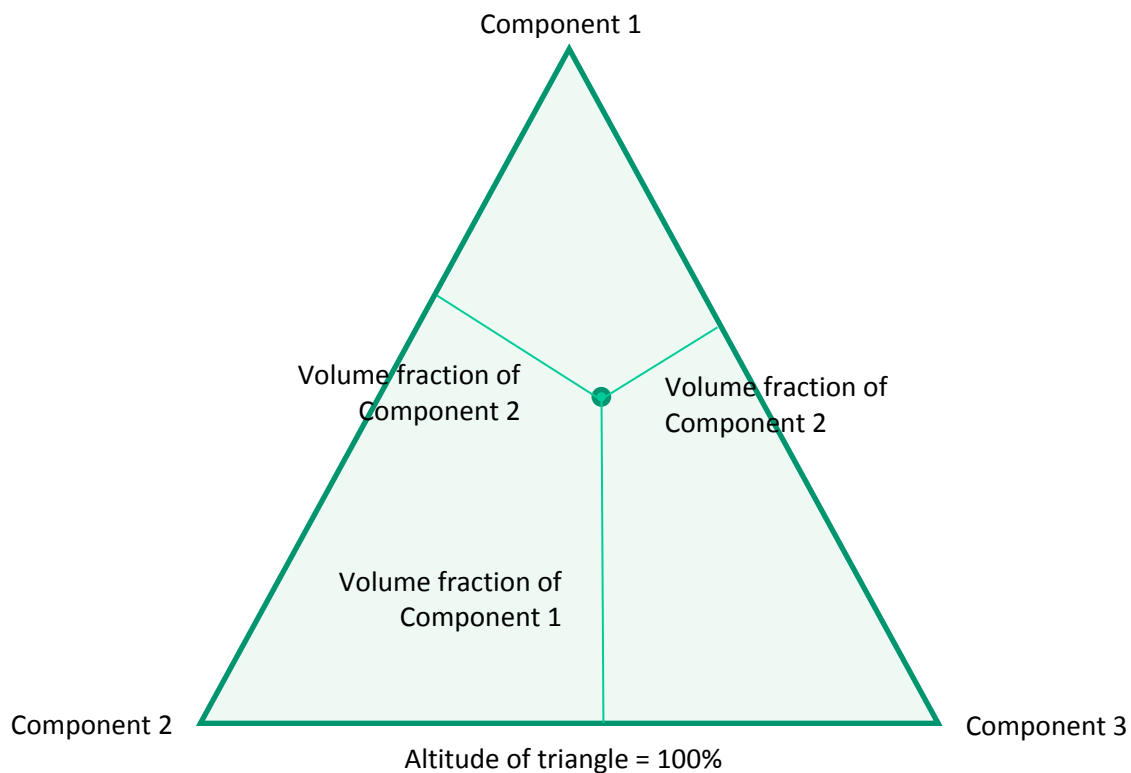
Fig. 2-1. Ternary plot for a three-component system.

Another interpretation of the diagram is shown in Fig. 2-2, in which the volume fractions are seen to be proportional to the areas of triangles formed by connecting the point with the apexes of the triangle plot. The volume fractions corresponding to a given point are thus the *barycentric coordinates* of the point within the triangle.
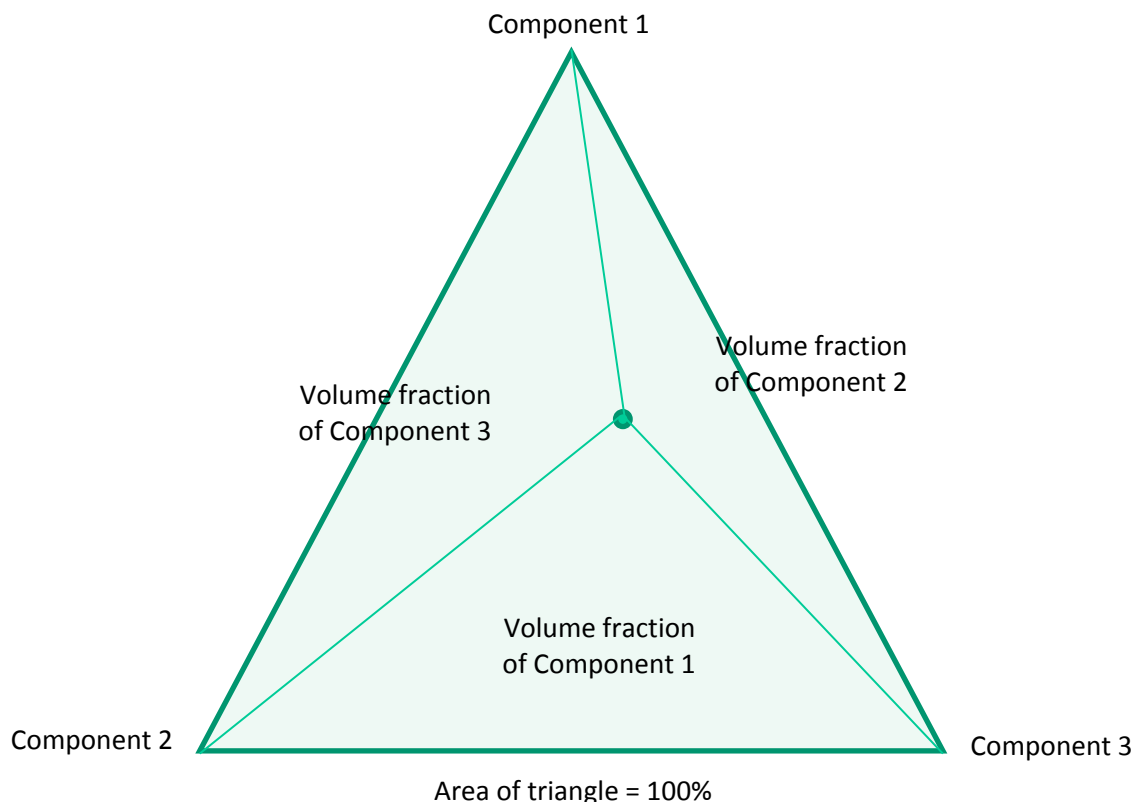
Fig. 2-2. Alternate interpretation of ternary plot.

2.1.1 Computer Code

A computer code for creating ternary plots was programmed in VisualBasic^{TM}. The program divides the triangular plot into small triangles, at the apexes of which material properties are determined by the appropriate rule of mixture. Around the perimeter of each small triangle, material properties are then interpolated linearly, in order to construct contours of those properties.

After exercising the program, it was noticed that all of the contours of interest (strength, mass density, and combustion energy) appeared to be straight lines. A mathematical theorem was found that states that straight lines in such barycentric coordinates are described by linear homogeneous equations, in which form the rules of mixture for strength, density, and energy are easily cast.

2.2 Tungsten-Aluminum-Epoxy System

Figure 2-3 is a ternary plot for the tungsten-aluminum-epoxy material system. The dotted gray lines represent constant values of volume fraction of each component in increments of 10% (e.g., the horizontal lines are contours of equal volume fraction of tungsten). The red and blue lines are contours of constant mass density and theoretical combustion energy, respectively.

Highlighted are the program-required goals of 7.8 g/cc density and 1500 cal/g energy. To satisfy these, a point must lie above the highlighted red density line and below the highlighted blue energy line; note that only materials of this system having very low volume fractions (less than about 18%) of epoxy can simultaneously meet both requirements. In our experience, decreasing the epoxy's volume fraction below about 75% of the aluminum's so greatly increases the viscosity of the epoxy-aluminum mixture so that it becomes unworkable. Also highlighted are two material formulations with their respective properties.
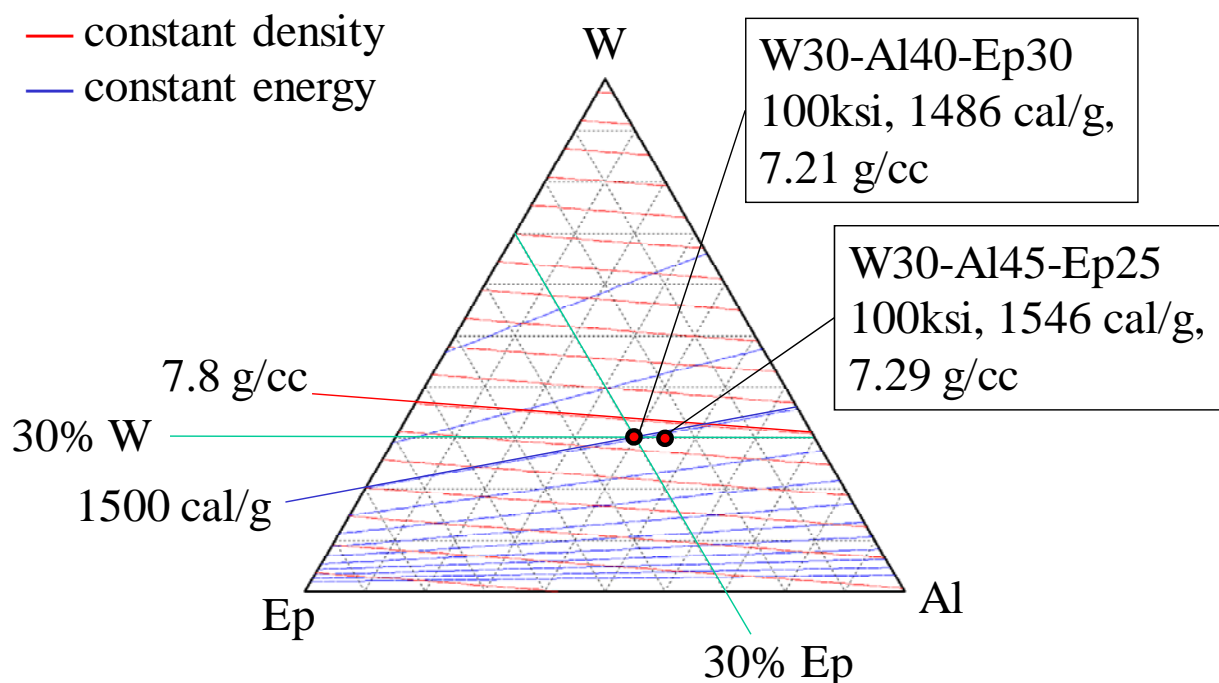
Fig. 2-3. Ternary plot for the tungsten-aluminum-epoxy material system.

2.3 Material Properties

Material properties used to design materials were gleaned from several references. It was discovered that there were significant errors in the properties of zirconium reported in the two references by Fischer and Grubelich (1996, 1998). In Table 2-1, values in **boldface** were selected for use in the program.

Table 2-1. Component material properties.

Material	Density (g/cc)	Energy (cal/g)
Tungsten, W	19.25 (wi) **19.3** (f&g, CRC)	**0** (assumed)
Aluminum, Al	**2.70** (f&g) 2.6989 (CRC)	**7422** (f&g, wi) 7424 (g&k)
Zirconium, Zr	6.52 (wi) 5.68 (f&g) 6.505 (Kohn) **6.506** (CRC, Steinberg)	2830 (wi) 2135 (f&g) **2878** (g&k)
Epoxy, Ep	1.14	7900
Boron, B	2.50 (f&g) 2.34x/2.37a (CRC) **2.34** (gk)	**14050** (f&g) 14039 (g&k)
Hafnium, Hf	11.4 (f&g) **13.3** (CRC, Steinberg) 13.31 (Kohn, wi)	**1491** (f&g)

References: (wi) = Wikipedia; (f&g) = Fischer & Grubelich; (g&k) = Gotzmer & Kim; (CRC) = CRC Handbook of Chem. and Physics; (Kohn) = AFWL EOS handbook; (Steinberg) = LLNL EOS handbook.

Energies per unit volume of the various candidate component materials are listed in Table 2-2. Note that epoxy, while highly energetic on a mass basis, is, with its low density, a poor performer on a volume basis. This indicates that both density and energy are increased by decreasing the amount of epoxy.

Table 2-2. Component material properties.

Material	Density (g/cc)	Energy (cal/g)	Energy (cal/cc)
Tungsten, W	19.3	0	0
Aluminum, Al	2.70	7422	20039
Zirconium, Zr	6.506	2878	18724
Epoxy, Ep	1.14	7900	9006
Boron, B	2.34	14050	32877
Hafnium, Hf	13.3	1491	19830
Program goals	7.8	1500	(11700)

This table also reveals an opportunity for a possible trade-off between aluminum and zirconium. Neither metal is clearly superior. Using a greater volume fraction of aluminum slightly increases the energy, while using more zirconium increases the density.

The computer code discussed above and a Mathcad™ document were used to compute the strength, density, and energy of various formulations, listed in Table 2-3. Testing showed that a 30% volume of tungsten can achieve 100-ksi strength. Previous formulations used a minimum of 30% volume of epoxy, which is the generally accepted minimum matrix content for fiber-reinforced composites.

Table 2-3. Summary of Strength, Density, and Energy of Selected Composite Materials.

Material	Strength (ksi)	Density (g/cc)	Energy (cal/g)
W30-Al40-Ep30	100	7.21	1486
W30-Al45-Ep25	100	7.29	1546
W30-Zr40-Ep30	100	8.74	1168
W23-Zr47-Ep30	76.8	7.85	1469
W30-Zr45-Ep25	100	9.01	1187
W23-Zr52-Ep25	76.8	8.11	1480
W30-Zr15.5-Al24.5-Ep30	100	7.80	1348
W30-Zr13.5-Al31.5-Ep25	100	7.80	1421
W30-Hf5.5-Al34.5-Ep30	100	7.80	1372
W30-Hf4.8-Al40.2-Ep25	100	7.80	1444
W34-B36-Ep30	113	7.80	1852
W30-B45-Ep25	100	7.13	2391

Boron was also considered as a substitute for aluminum. Formulations with 36 vol% and 45 vol% of boron have energies of 1,852 and 2,391 cal/g, respectively. However, boron may be incompatible with the resin hardeners, and safety tests would need to be performed before specimens could be prepared.

2.4 Four-Component Materials

For composites with four components, the corresponding plot is a three-dimensional regular tetrahedron, as represented in Fig. 2-4. Again, each apex of the figure represents 100% of a component, and for each point within the tetrahedron the fraction of each component is proportional to its distance from the face opposite its 100% apex. Material fraction is also proportional to the volume of the irregular tetrahedron formed by connecting the point to the three opposite apices.
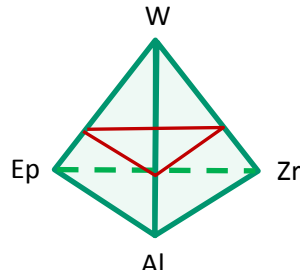
Fig. 2-4. Tetrahedral plot for the tungsten-epoxy-aluminum-zirconium system.

If, however, one of the material fractions is fixed at some value, then the three remaining fractions may be varied over a slice through the tetrahedron parallel to one of its faces, which is an equilateral triangle. Within this slice (highlighted in red in Fig. 2-4), the three other materials vary up to a value equal to 100% minus the fixed fraction of the fourth component. An example plot for the tungsten-epoxy-aluminum-zirconium material with the tungsten volume fraction fixed at 30% is shown in Fig. 2-5.
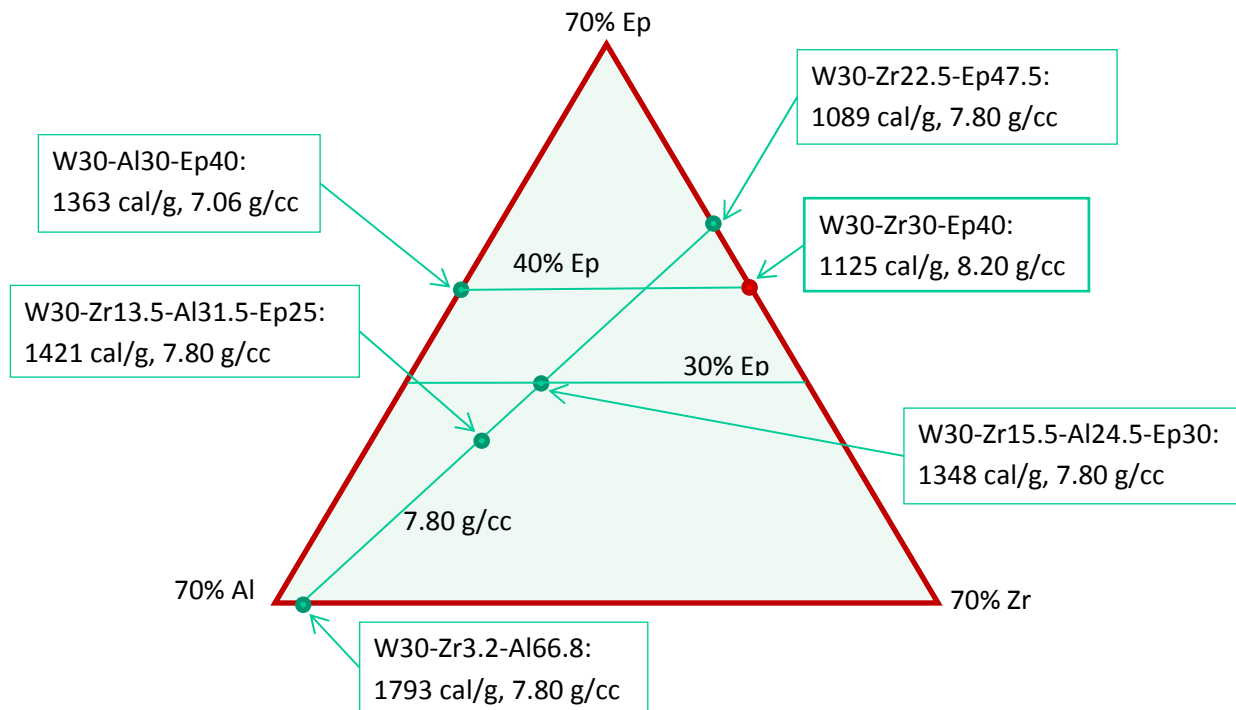
Fig. 2-5. Triangular slice of tetrahedral plot for the tungsten-epoxy-aluminum-zirconium system, with a fixed volume fraction of tungsten of 30%.

2.5 Tungsten-Boron-Epoxy System

We also investigated systems combining tungsten wire, boron wire or powder, and epoxy (see Fig. 2-6). With boron's high combustion energy, this system is able to exceed the required density and energy over a range of compositions that include a large enough fraction of epoxy as to be workable (green region in the figure). In particular, a system of 34% tungsten wire, 30% boron powder, and 30% epoxy is predicted to have a strength of 113 ksi, a combustion energy of 1852 cal/g, and a density of 7.8 g/cc.
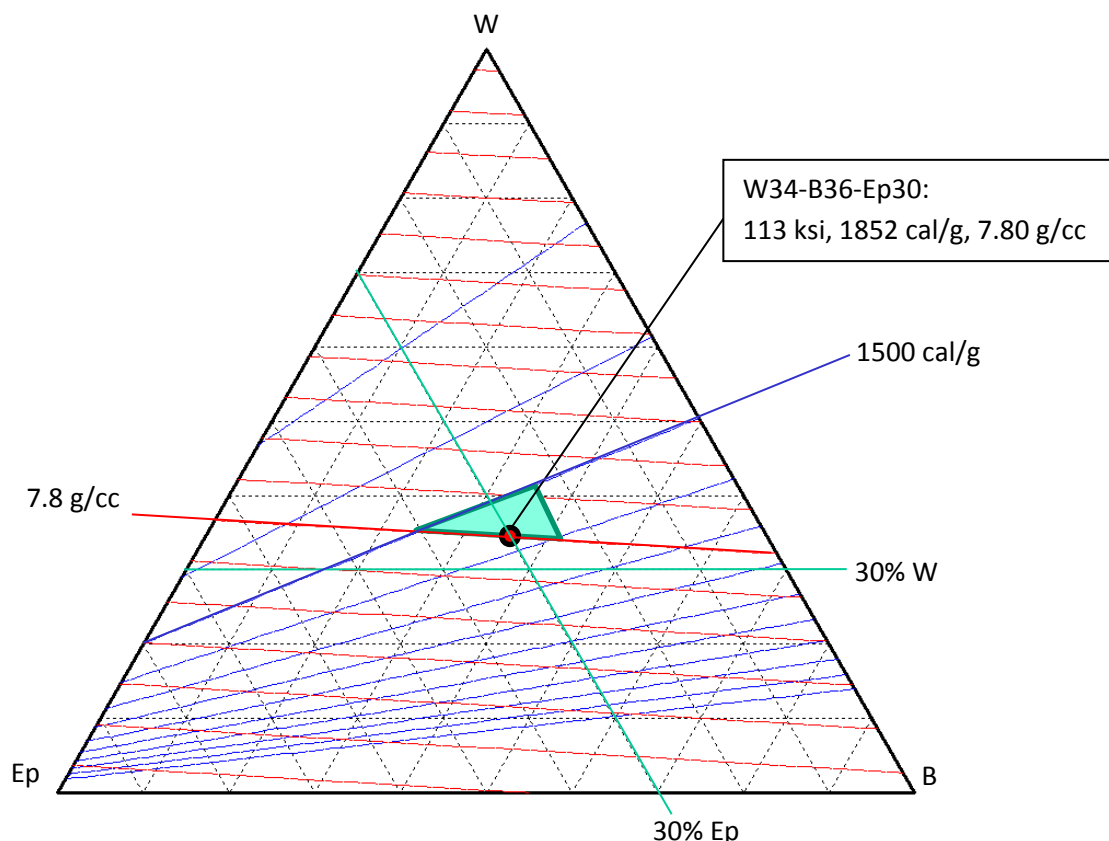
Fig. 2-6. Ternary plot for the tungsten-boron-epoxy material system.

2.6 Reactive Composites

This subsection discusses the development of the reactive composites to meet the Phase I property goals, which was done in two phases. The first phase used a flat dog-bone geometry for the tensile test specimens. This simple geometry allowed development of the layup techniques necessary to achieve the required material strengths of 25 ksi and 50 ksi defined in program milestones 2 and 3. The second phase focused on demonstrating structural tensile strengths of 25 ksi and 50 ksi in a nominally one-inch-diameter hollow tube.

2.6.1 Material Tensile Properties Assessment

The materials selected based on the mechanical properties evaluation of various tungsten-wire-reinforced epoxy systems (Epon 826/Epikure 3223 and Araldite 8615/Aradur 8615) were prepared with the incorporation of metal powders (Al and Zr, –325 mesh). Tungsten-wire-reinforced, metal-powder-filled dog-bone specimens were prepared in a similar fashion as the tungsten-wire-reinforced unfilled epoxy, except for the consolidation method. Because of the high viscosity of the powder-epoxy mixtures, resin transfer molding (RTM) could not be used to infiltrate the preform. Therefore, the braided preforms were impregnated with metal-filled epoxy mixture and compression-molded.

In all formulations the metal-powder volume content was kept at 30%, while the tungsten wire content was adjusted to meet the density requirement, with the balance epoxy. Theoretically, these formulations have densities of at least 7.8 g/cc and tensile strengths of 100 ksi or higher; however, the energy values fell slightly below the 1,500-cal/g goal. These formulations were used to develop processing techniques for handling high reinforcement content and for properties evaluations.

Six to eight specimens of each of the four types of materials were fabricated and tested (Table 2-4 and Fig. 2-7). Tensile testing was performed on an Instron Model 4206 equipped with a universal joint to ensure proper alignment during testing. Crosshead speed was 0.004 in/min (1 mm/min). Because of frequent jaw fractures when the specimens were tested as fabricated, half-penny (~0.06" dia.) shaped grooves were introduced on both edges, at mid-section of the gage length. Gage-length failures within 5% variation were consistently obtained once the grooves were added.

Table 2-4. Theoretical properties of two formulations of W-wire-reinforced metal-powder-filled epoxy.

RMS formulation	Energy (cal/g)	Density (g/cc)	UTS (ksi)	Weight (%)	Volume (%)
W-Al-Epoxy	1,324	7.96	144	86/11/3	35/30/35
W-Zr-Epoxy	1,322	8.20	100	72/24/4	30/30/40
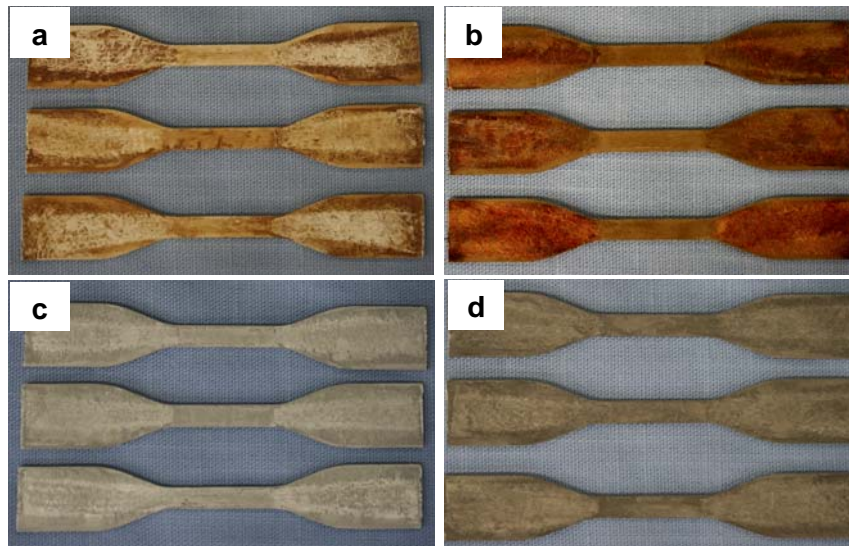
Fig. 2-7. Tungsten-wire-reinforced metal-powder-filled epoxy tensile specimens: a) Al-powder-filled Araldite 8615/Aradur 8615; b) Zr-powder-filled Araldite 8615/Aradur 8615; c) Al-powder-filled Epon 826/Epicure 3223; and d) Zr-powder-filled Epon 826/Epikure 3223.

Table 2-5 and Fig. 2-8 show the measured tensile properties. The higher wire content of 35% by volume in Al-filled epoxy systems yielded ultimate tensile strengths of 101 ksi to 111 ksi, while the lower wire content of 30% vol. in a Zr-filled matrix yielded nearly 80 ksi. The experimental values are close to the theoretical values and exceed the Phase I goal.

The actual densities fell short of the theoretical values. This discrepancy was attributed to the design of the mold, which was difficult to close tightly, resulting in greater-than-intended thicknesses of the dog-bone specimens. The extra thickness altered the proportions of the matrix material and the wires, resulting in a lower density. The mold design was modified for the second set of specimens.

Also, the theoretical energies of the materials fell below the required 1,500 cal/g. To increase energy, the aluminum powder content was increased. This required that the content of tungsten wires and epoxy resin be reduced to accommodate more aluminum. Based on the combustion energies of the constituents, assuming no contribution from the tungsten, energy release of nearly 1,500 cal/g can be obtained with an aluminum volume fraction of 40% to 45%.

Table 2-5. Average tensile properties of W-wire-reinforced metal-powder-filled epoxy material systems.

| Specimen ID | Description | Composition (% vol.) | Yield | | Ultimate | | Density (g/cc) |
			Strain (%)	Stress (psi)	Strain (%)	Stress (psi)	
ALWEP	W-wire-reinforced Al-powder-filled Epon 826/Epikure 3223	30Al-35W-35Epon	0.97	19,664	14.51	111,580	7.61
ALWARD	W-wire-reinforced Al-powder-filled Araldite 8615/Aradur 8615	30Al-35W-35Araldite	1.27	31,981	10.11	101,836	6.76
ZRWEP	W-wire-reinforced Zr-powder-filled Epon 826/Epikure 3223	30Zr-30W-40Epon	1.16	22,578	10.06	79,818	6.68
ZRWARD	W-wire-reinforced Zr-powder-filled Araldite 8615/Aradur 8615	30Zr-30W-40Araldite	1.43	30,204	10.52	78,476	6.58
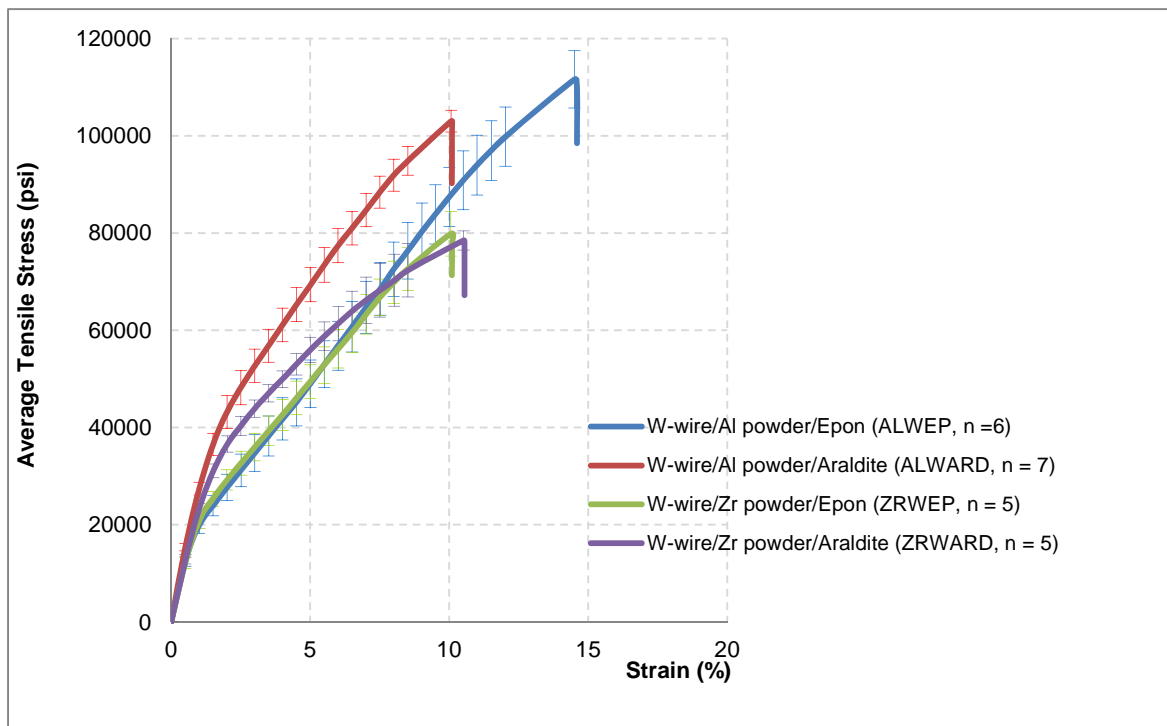
Fig. 2-8. Average tensile properties of tungsten-wire-reinforced metal-powder-filled epoxy material systems (*n* = number of specimens).

Two new formulations were developed, each containing 30% wire by volume, which yields a 100 ksi strength and a 7.8 g/cc density. For more energy, they had 40% and 45% Al by volume, with the balance epoxy. Figure 2-9 shows both types. The 45% Al/25% epoxy had a doughy consistency that made it difficult to infiltrate the wires. Adding a little acetone reduced its viscosity, allowing it to penetrate the wire preform. Aside from non-uniform flow, 25% epoxy was insufficient to fully wet the wire preform and left dry spots on the specimen surfaces, as shown in Fig. 2-9(b). The 40% Al/30% epoxy mixture also displayed high viscosity but flowed better than the 45% Al/25% epoxy, which obviated the need for acetone, and the specimens were more uniform and free of voids.
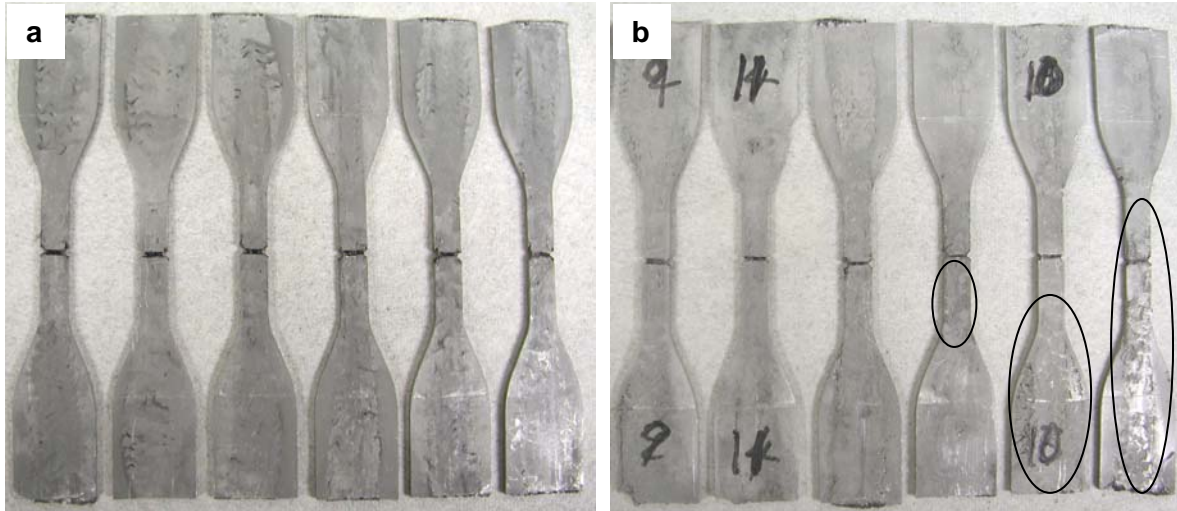
Fig. 2-9. Notched tensile specimens: a) 30% vol. W-wire/40% Al powder/30% epoxy; b) 30% vol. W-wire/45% Al powder/25% epoxy.

Reducing the wire content from 35% to 30% lowered the density to ~7.1 g/cc for 40% Al/30% epoxy and 7.2 g/cc for 45% Al/25% epoxy. Ultimate tensile strength also dropped by 15% to 17% (Fig. 2-10 and Table 2-6). No significant differences in ultimate tensile strength were seen between the 40% Al/30% epoxy and 45% Al/25% epoxy. A rightward and downward shift in the stress-strain curve of 30% W/45% Al/25% epoxy and a greater deformation to failure were attributed to insufficient bonding between wire and matrix. Debonding, matrix fracture, and wires re-aligning prior to fracturing were the observed mechanisms for the shifting the curve (Fig. 2-11(a)). A clean wire-matrix fracture indicates adequate bonding, as seen for the 30% W/40% Al/35% epoxy formulation in Fig. 2-11(b).
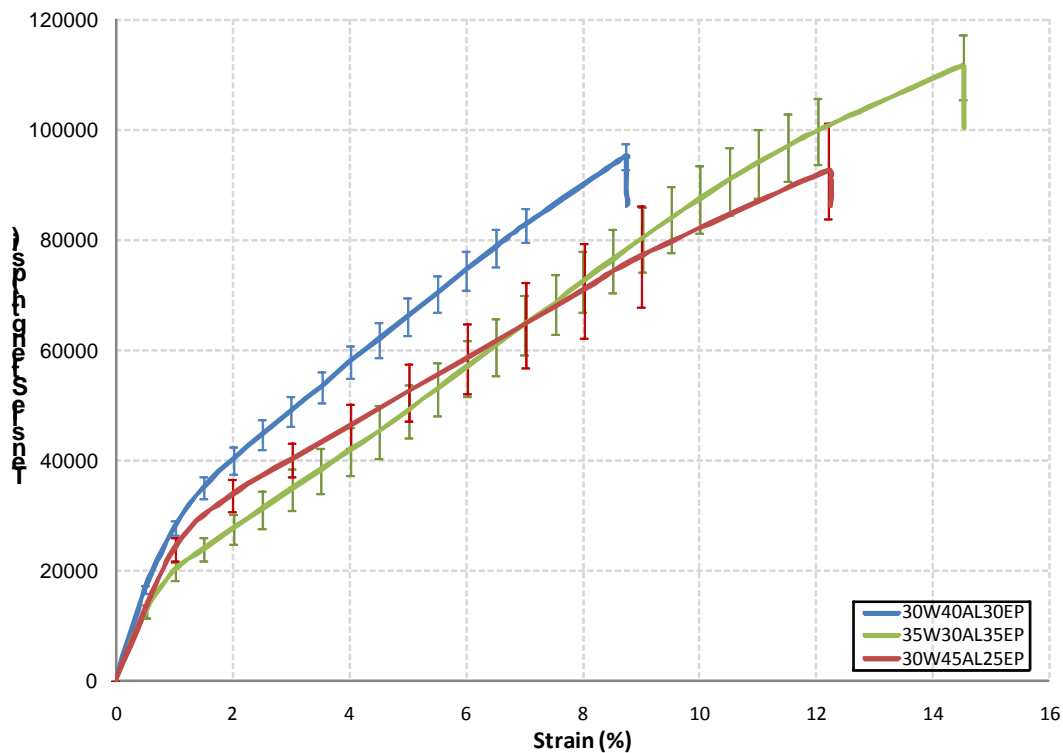
Fig. 2-10. Stress-strain properties of W-wire-reinforced Al-powder-filled epoxy materials.

- 12 -

Table 2-6. Tensile properties of W-wire-reinforced Al-powder-filled epoxy RMS.

Specimen ID (number *n* of specimens tested)	Formulation volume % [wt. %]			Estimated energy (cal/g)	Density (g/cc)	Yield		Ultimate	
	W	Al	Epoxy			Strain (%)	Stress (psi)	Strain (%)	Stress (psi)
35W30AL35EP (*n* = 6)	35 [86.3]	30 [10.6]	35 [3.1]	1,324	7.2	0.97	19,664	14.51	111,580
30W40AL30EP (*n* = 6)	30 [81.7]	40 [15.7]	30 [2.6]	1,486	7.2	1.05	28,801	8.74	95,245
30W45AL25EP (*n* = 8)	30 [80.8]	45 [17.5]	25 [1.7]	1,546	7.1	1.05	24,690	12.21	92,682
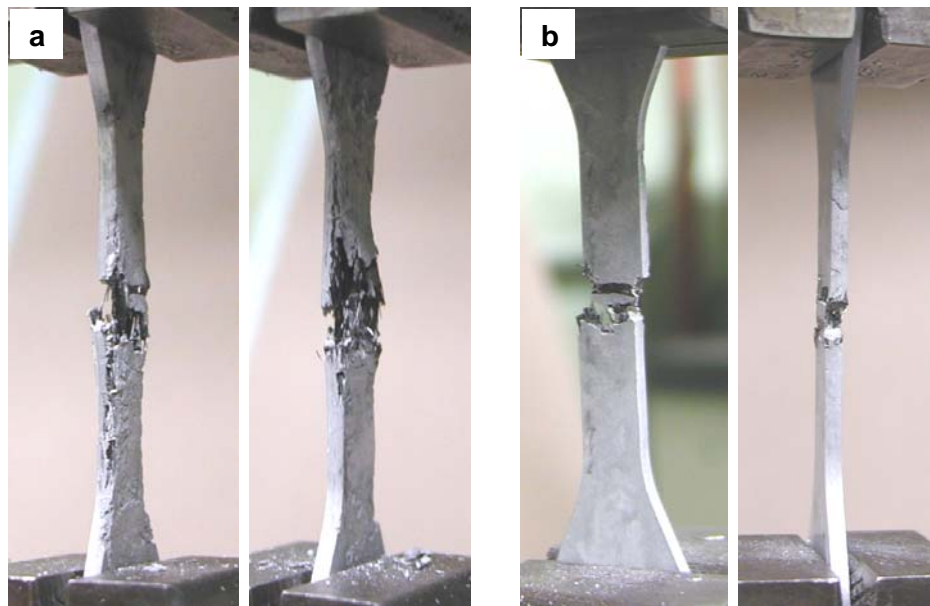
Fig. 2-11. Fracture of dog bone specimens. a) 30% vol. W-wire/45% Al powder/25% epoxy, poor wire-matrix bonding due to insufficient epoxy content; b) 30% vol. W-wire/40% Al powder/30% epoxy.

Among the formulations listed above in Table 2-6, the 30% vol. W-wire/40% Al-powder/30% epoxy has a theoretical energy within 1% of the goal, while its density is 92% of required. This material has better processability and an ultimate strength of 95 ksi, almost fulfilling the Phase II goal of 100 ksi. Based on these observations, this formulation was selected as the baseline for the structural strength assessment in a hollow tube geometry with dimensions of 1" ID x 1.3" OD x 10" length.

2.6.2 Structural Tensile Strength Assessment

Materials for structural strength testing were down-selected based on the blast tests of small cylinders described below and tensile strength tests described above. As discussed above, the W-wire-reinforced Al-powder-filled epoxy composite fell just short of meeting the energy and density requirements, but achieved a strength nearly double that required. This material was selected as the baseline for the structural strength assessment. A second material was also determined, in order to approach a balance among the three requirements; the volume content of W wire was reduced to 15%, lowering the strength, but allowing the addition of hafnium powder, which increased both density and energy. This material, 15% W, 19% Al, 30% Hf, and 36% epoxy by volume, meets the required energy and density, while its lower strength of 50 ksi still satisfies the Phase I requirement. Properties are listed in Table 2-7.

Table 2-7. Computed properties of the down-selected RMS formulations.

Material	Volume % (Wt. %)	Strength (ksi)	Density (g/cc)	Energy (cal/g)
Al-W-Ep	40–30–30 (14.96 – 80.22 – 4.82)	100	7.21	1486
Al-Hf-W-Ep	19–30–15–36 (6.56 – 51.09 – 37.04 – 6.56)	50	7.82	1665

Cylindrical specimens were made by triaxially braiding multiple layers of W wire over a cylindrical mandrel. Metal-powder-filled epoxy was applied between layers, and the assembly was consolidated in a clamshell mold. The 12" tube was then cut to appropriate lengths for various tests.

Cylinders for the small chamber tests, shown in Fig. 2-12, had a 1.012" inner diameter (to accommodate a 1" explosive pellet) and a 1.327" outer diameter. The latter was dictated by the actual density and specimen mass requirement for a specific length. The first batch of specimens for the UIUC and ATK tests had densities less than expected due to pinching of the wire braid on closing the mold, which prevented the mold from fully closing and resulted in an asymmetric cross section and larger OD. To correct this, the wire braid construction and mold design were modified, which significantly improved the density, and the densities of subsequent batches approached the theoretical values.
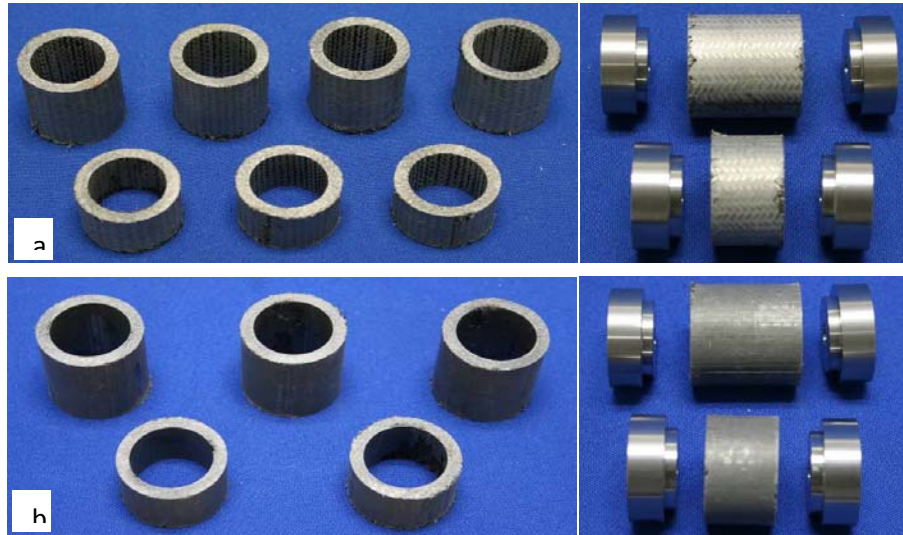
Fig. 2-12. Blast test specimens: a) Al-W-EP, and b) Al-Hf-W-Ep. Specimen length for small chamber tests: ATK: 1.25"; UIUC: 0.75" and 1.25"; and ARA: 1" (fragmentation test) and 3" (fully closed chamber test).

Tension and compression cylinders were made in the same fashion as the blast cylinders except for diameter. To keep the breaking load within the testing machine's capacity (30,000 lb), the ID and OD were reduced to 1.006" and 1.215", respectively. Specimens were cut to 10" lengths for tensile testing and 3.5" for compression. End fixtures were attached using structural adhesive, as shown in Fig. 2-13.
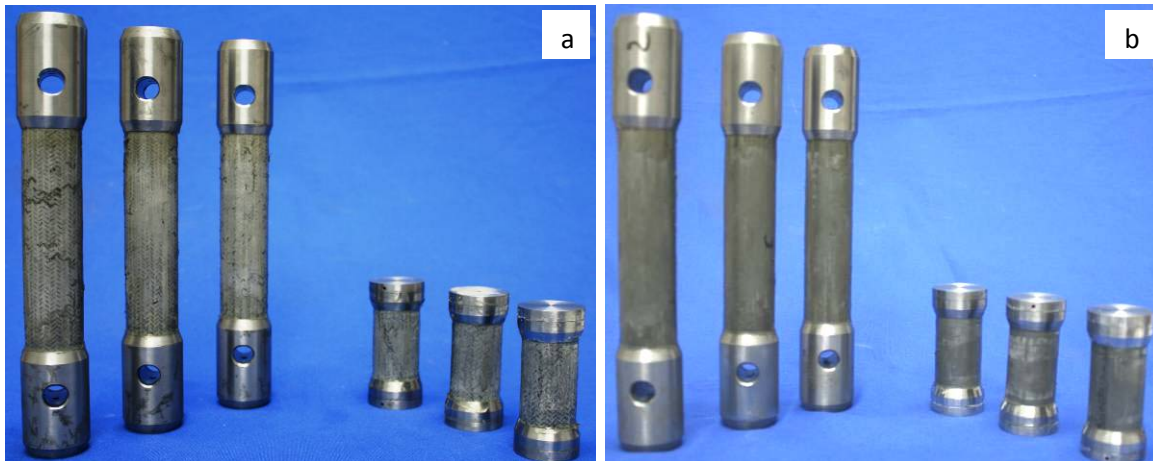
Fig. 2-13. Tension (10" long) and compression (3.5" long) specimens with end fixtures attached: a) Al-W-Ep; b) Al-Hf-W-Ep.
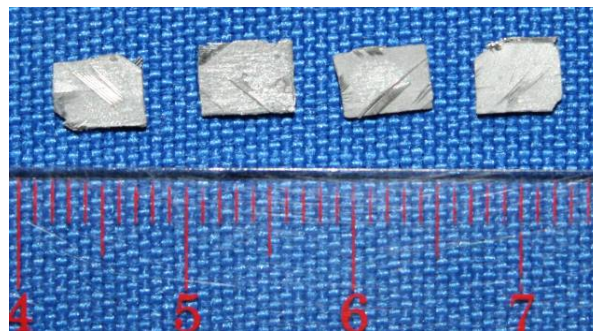
Fig. 2-14. Impact sensitivity test specimens.

Table 2-8. Specimen properties from actual measurements (nominal values).

Material	Specimen type (no. of specimens)	ID (in)	OD (in)	Length (in)	Density (g/cc)	Mass (g)
Al-W-Ep	UIUC blast test (3)	1.012	1.335	0.75, 1.25	6.78	50, 85
Al-W-Ep	ATK blast test (3)	1.012	1.335	1.25	6.78	85
Al-W-Ep	ARA fragmentation test (3)	1.012	1.335	1.0	7.27	???
Al-W-Ep	ARA fully closed test	1.012	1.335	3.628	7.16	256
Al-W-Ep	DET tension	1.006	1.215	10	7.51	451
Al-W-Ep	DET compression	1.006	1.215	3.5	7.51	158
Al-W-Ep	Impact sensitivity	5 mm (L) $\times$ 4 mm (W) $\times$ 0.4 mm (t)			6.37	35 mg
Al-Hf-W-Ep 19-30-15-36	UIUC blast test (3)	1.012	1.335	0.75, 1.25	6.79	50, 85
Al-Hf-W-Ep	ATK blast test (3)	1.012	1.335	1.25	6.79	83
Al-Hf-W-Ep	ARA fragmentation test (3)	1.012	1.335	1.0	7.19	85
Al-Hf-W-Ep	DET tension (3)	1.006	1.215	10	7.81	474
Al-Hf-W-Ep	DET compression (3)	1.006	1.215	3.5	7.81	166
Al-Hf-W-Ep	Impact sensitivity	5 mm (L) $\times$ 4 mm (W) $\times$ 0.4 mm (t)			6.37	35 mg

2.6.3 Tensile Tests

Al-W-Ep Cylinders

Mechanical testing was conducted at the University of Pennsylvania, on an Instron Model 4620 at a crosshead speed of 0.004 in/min (1 mm/min). Initially, a 0.10"-radius groove was machined around the circumference of each cylinder, in the middle of the gage region, to induce fracture there. Gage-region fracture did occur, but failure was not complete at the maximum loading. The discontinuity in the outer tungsten layers due to cutting the groove caused delamination of the inner layers, with the wires remaining intact, as shown in Fig. 2-15. This occurred at about 67 ksi and 37 ksi for Al-W-Ep and Al-Hf-W-Ep, respectively, about 30% lower than theoretical prediction and the values in previous tests with dog-bone specimens. A gradual reduction in cross-sectional area in the gage region is preferred to minimize stress concentration, but due to the high reinforcement content and poor metal/epoxy bonding, such reduction could not be introduced without damaging the cylinder. Therefore, a small-radius groove was cut around the circumference to induce gage fracture.

Fig. 2-15. Fracture of tensile specimen with groove in gage region showing the tungsten wires in the inner layers remained intact. Al-W-Ep (top) and Al-Hf-W-Ep (bottom).

In the second iteration, the groove was omitted (Fig. 2-16) to avoid the stress concentration that promoted delamination. Three specimens of each formulation were tested. For the Al-W-Ep, complete fracture occurred in the region of the hole through which a 0.5"-diameter pin was inserted to secure the specimen to the Instron (Fig. 2-17). All three specimens failed in the same manner, at ultimate tensile strengths of 69 ksi to 76 ksi (Fig. 2-18).
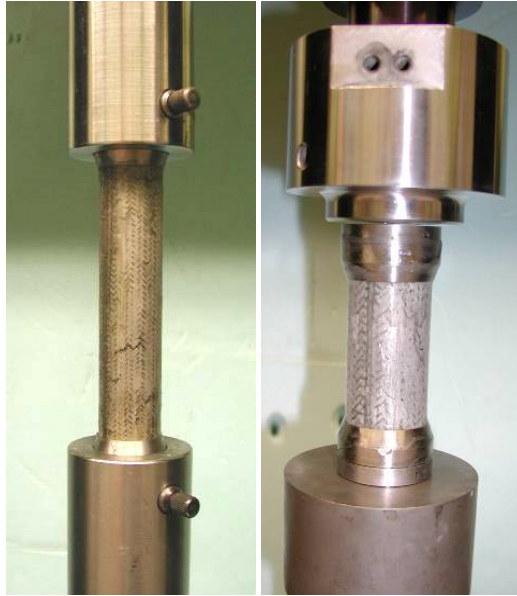
Fig. 2-16. Testing in tension (left) and compression (right).

Fig. 2-17. Fracture of tensile-test cylinders of Al-Hf-W-Ep (top) and Al-W-Ep (bottom).

Al-Hf-W-Ep Cylinders

All three Al-Hf-W-Ep specimens failed in the gage region, at ultimate tensile strengths of 35 ksi to 37 ksi (Fig. 2-15 above). These specimens (Fig. 2-17 above) did not undergo complete failure, as the fracture region exhibited only matrix failure, with all W wires remaining intact. The premature failure was attributed to loss of structural integrity as the matrix failed, which allowed re-alignment of the bias-braided wires toward the loading direction; this is evident in the intact braid structure. Perhaps better bonding between wire and matrix and braid construction can improve the strength of the composite.
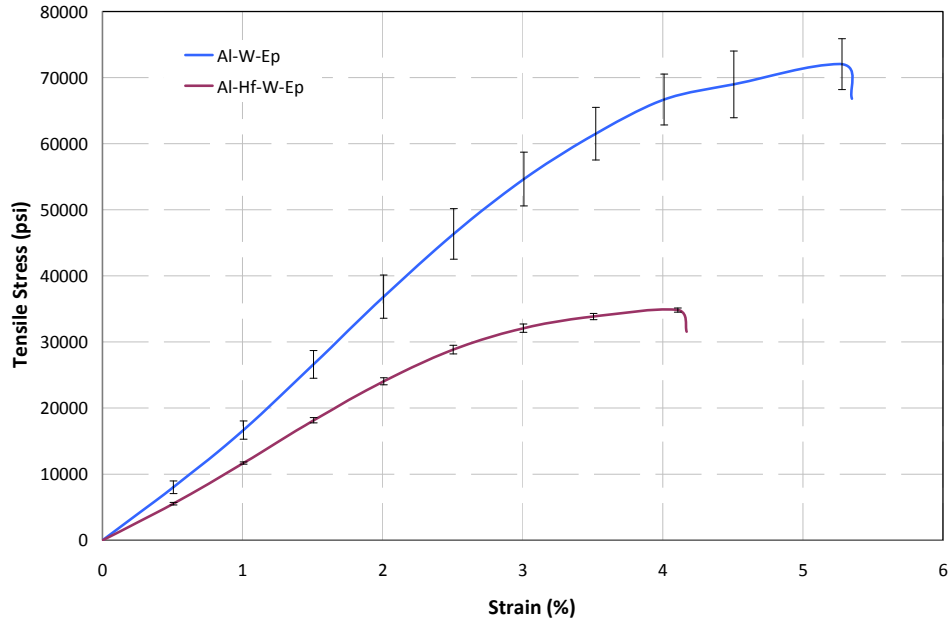
Fig. 2-18. Average tensile behavior of RMS composites.

Both materials exhibited ultimate tensile strengths about 30% less than theoretical prediction and the values obtained from the dog-bone specimens. The Al-W-Ep contained 30% W wire by volume and the Al-Hf-W-Ep system contained 15% W wire. Tensile strengths are expected to be 100 ksi for the former and 50 ksi for the latter, which values were previously achieved in the dog-bone specimens. This discrepancy was attributed to distortion of the wire braid due to the incorporated holes and to insufficient bonding between two dissimilar materials (steel end fixtures and RMS).

2.6.4 Compression Tests

To prevent the ends of the specimens from mushrooming during compression, end caps were attached. Testing was performed at 0.004 in/min (1 mm/min). Both materials failed in similar fashion, buckling of the wire braid in the gage region (Fig. 2-19). The epoxy matrix failed at a low load, giving way to buckling of the wire braid at ~10 ksi for the Al-Hf-W-Ep system and ~34 ksi for the Al-W-Ep system (Fig. 2-20). Mechanical properties are summarized in Table 2-9.

Table 2-9. Mechanical Properties of the RMS composites.

Material	Tensile strength (ksi)	Compressive strength (ksi)	Density (g/cc)
Al-W-Ep	73.3 ± 4.5	34.4 ± 0.3	7.51
Al-Hf-W-Ep	34.8 ± 0.4	10.3 ± 1.4	7.81
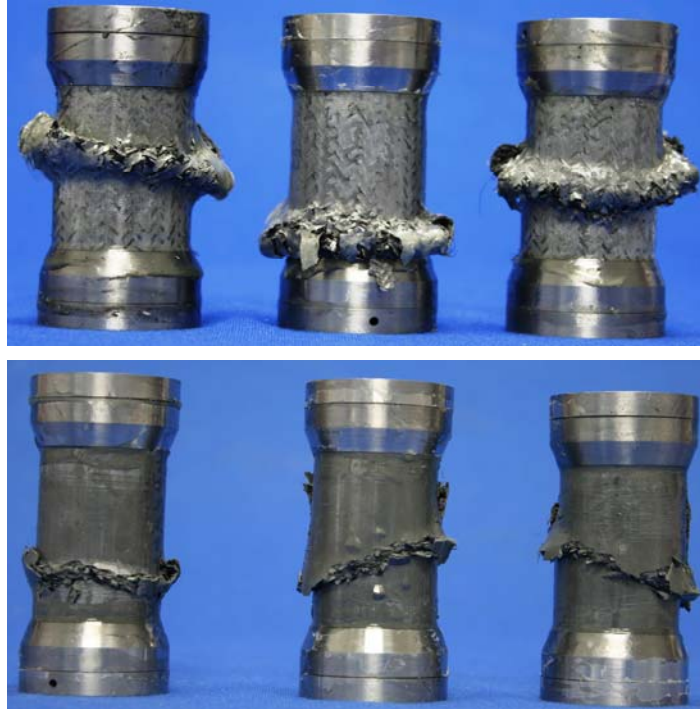
Fig. 2-19. Fracture of compression specimens.
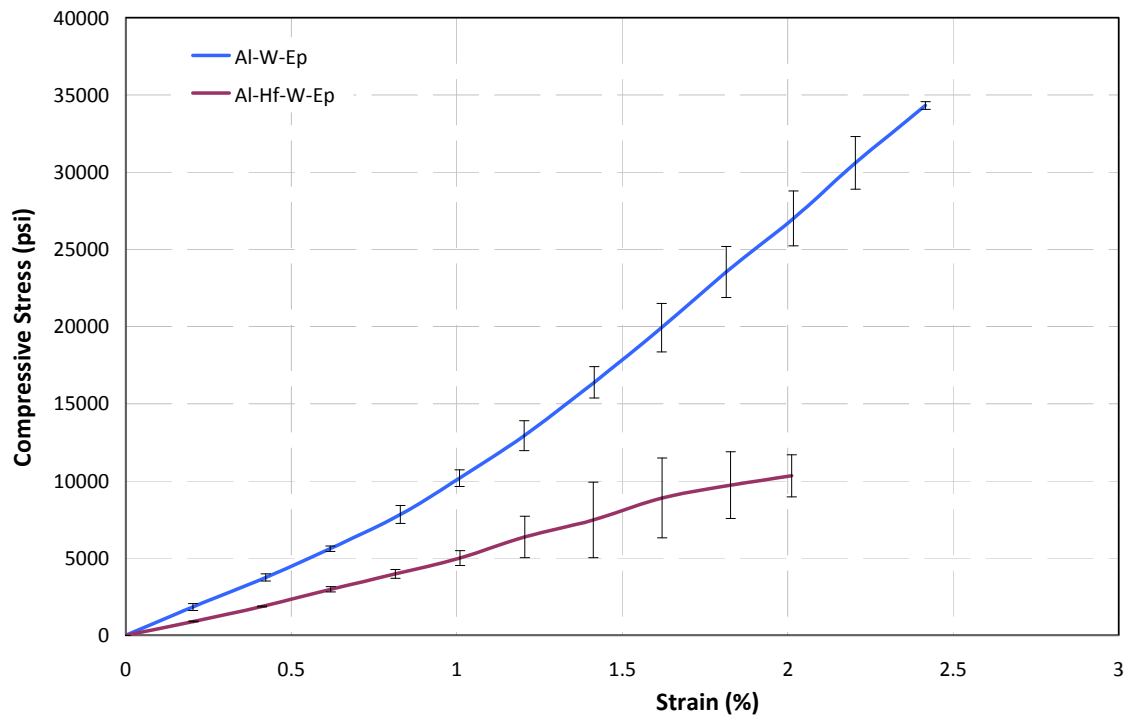
Fig. 2-20. Average compressive behavior of RMS composites.

Section III

Phase I Thrust B: Powder Metallurgy Processes, Hot Isostatic Pressing

3.1 Objective

The overall objective of the metallic composite materials task, performed by Matsys Corporation, was to demonstrate a powder-based manufacturing technology for processing high-density, high-strength metallic composites using a conventional powder-based processing approach. The specific objectives were:

1. Design high-density reactive material powder blend;
2. Design consolidation process to achieve the desired density; and
3. Characterize the material mechanical properties.

3.2 Accomplishments

The Hf/Al powder blend with a density of 7.89 g/cc developed previously was chosen to evaluate increased energy output through a thermite reaction. Bismuth trioxide was added in two ratios, 15% or 10% by volume. Test specimens for energy release were prepared and delivered. Results for these materials are summarized below. Additional specimens of aluminum and Al/Ti/B_4C were produced for energy release testing.

Mechanical characterization results were as follows:
- The Hf/Al composite has an average compressive strength of 75.7 ksi (522 MPa) and an average tensile strength of 57.6 ksi (397 MPa);
- The Hf/Al/Bi_2O_3 composite with 15 vol% Bi_2O_3 has an average compressive strength of 50.3 ksi (347 MPa) and an average tensile strength of 10.8 ksi (74 MPa); and
- The Hf/Al/Bi_2O_3 composite with 10 vol% Bi_2O_3 has an average compressive strength of 56.8 ksi (392 MPa).

Cylinders for testing at the University of Illinois with 1.006" ID $\times$ 0.75" L from:
- Aluminum – Valimet H2 via CIP process;
- Al/Ti/B_4C;
- Hf/Al; and
- Hf/Al/Bi_2O_3 composite with 15 vol% Bi_2O_3.

Cylinders for testing at ATK with 1.006" ID $\times$ 1.25" L from:
- Aluminum – Valimet H2 via CIP process;
- Al/Ti/B_4C;
- Hf/Al; and
- Hf/Al/Bi_2O_3 composite with 15 vol% Bi_2O_3.

Cylinders for testing at NSWC Indian Head with 1.01" ID $\times$ 1.0" L of Hf/Al/Bi_2O_3 composite with 15 vol% Bi_2O_3, and cylinders for testing at ARA with 1.01" ID $\times$ 3.617" L of the same formulation were produced.

3.3 Technical Approach

The proposed material systems will use a blend of elemental powders, consisting of highly reactive materials interspersed with a reactive binder. The powder blend will be consolidated to full density to maximize its load-carrying capability, including strength and ductility. Consolidation will occur below the reaction initiation temperature to prevent energy release during compaction, thereby preserving energy

for release upon demand. The use of different powder materials allows tailoring of the mechanical and reactive properties by varying the volume fraction of each element and adjusting its particle size.

This effort includes three main tasks:

Task I - High-Density Reactive Powder Blend Design

The design of a powder blend for structural reactive materials is governed by four factors: theoretical density of the powder blend, consolidation of the reactive powder blend below the reaction initiation temperature, mechanical strength of the composite, and energetic release upon demand.

Task II - Powder Consolidation

The objective of this task is to identify the temperature-pressure-time regime to reach the desired densification below the reaction initiation temperature.

Task III - Material Characterization

The objective of this task is to characterize the mechanical properties of the fully dense material, including ultimate tensile and compressive strengths and failure strains. Matsys provided specimens for other team members for characterization of the reactive properties.

Task IV - Parts Fabrication

The objective of this task is to fabricate parts and provide them for testing and characterization of the reactive properties.

3.4 Technical Work

The technical work completed under each task is as follows:

Task I - High-Density Reactive Powder Blend Design

Based on earlier work by DET and Matsys, three powder formulations were identified as of interest: Hf/Al, Ta/Al, and W/Al. Each formulation was to be designed so that the fully dense material would have a density of 7.86 g/cc. In addition, the Hf/Al formulation included two powder blends: one with a theoretical density of 8.78 g/cc and the other with a theoretical density of 7.86 g/cc. We initiated our effort with the Hf/Al blend and we have selected the following two powder blend formulations:

Powder	Weight %	Volume %
Hf	83	49
Al	17	51

with a theoretical density of 7.86 g/cc.

We then added an oxidizer, Bi_2O_3, to the Hf/Al blend, and we have selected the following two powder blend formulations:

Powder	Weight %	Volume %
Hf	72	42
Al	16	48
Bi_2O_3	12	10

with a theoretical density of 7.83 g/cc; and

Powder	Weight %	Volume %
Hf	67	39
Al	16	46
Bi_2O_3	17	15

with a theoretical density of 7.76 g/cc.

In addition to the blend formulation, a critical parameter is the particle size for each constituent. A small particle size will enhance reaction kinetics, by increasing the reaction rate and sustaining the reaction to full completion. If the particle size for the soft material is smaller than that of the hard material it enables full densification at the lowest temperature. We selected Valimet H2 Al with an average particle size of 3.2 μm. All hard materials were selected with a particle size less than 45 μm (–325 mesh).

Task II - Powder Consolidation. The objective of this task is to identify the temperature-pressure-time regime to reach the desired densification below the reaction initiation temperature.

Hf/Al Powder Blend Consolidation

Initially Hf/Al was HIPed to a maximum temperature of 550 °C. The material was fully dense but some intermetallics were formed. It was extremely strong under compression but very brittle in tension. To improve the tensile behavior, maximum HIP temperature was reduced to 525 °C. This material had average strengths of 75.7 ksi (522 MPa) in compression and 57.6 ksi (397 MPa) in tension.

Hf/Al/Bi₂O₃ Powder Blend Consolidation with 10 vol% Bi₂O₃

A HIP canister of 1½-in diameter and 4½-in height was fabricated of aluminum. The canister was filled with the Hf/Al/Bi₂O₃ (10 vol% Bi₂O₃) powder blend, degassed at temperature, and sealed under vacuum. The canister was then consolidated in Matsys's instrumented HIP. Its High Temperature Eddy Current Sensor (HiTECS) enables monitoring the change in diameter of the compact during densification and identifying the temperature, pressure and time at which full densification has occurred.

HIP schedules and diameter measurements for the experiment are shown in Fig. 3-1. Initially, temperature was increased to 150 °C while pressure was increased to 4.5 ksi (31 MPa). Next, temperature was raised to 400 °C and pressure to 28 ksi (193 MPa). Significant densification was observed during each pressurization. Subsequently, pressure was held constant while temperature was raised to 475 °C, which was maintained for 5 minutes. Finally, the HIP was cooled to room temperature.

Examination of the compact after HIP showed that the canister deformed uniformly. Its density was measured to be 99% of TMD.

A second experiment was repeated to achieve full density. The same HIP schedules were used, except that the maximum temperature was increased from 475 °C to 500 °C. The HIP schedules and diameter measurements for this second experiment are shown in Fig. 3-2.
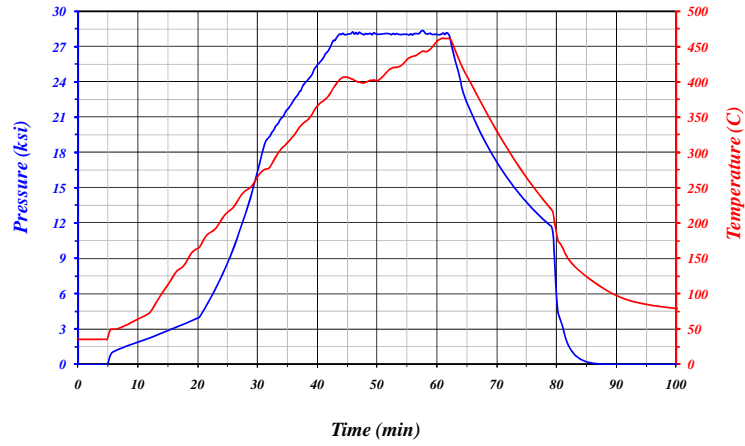
(a) HIP schedules
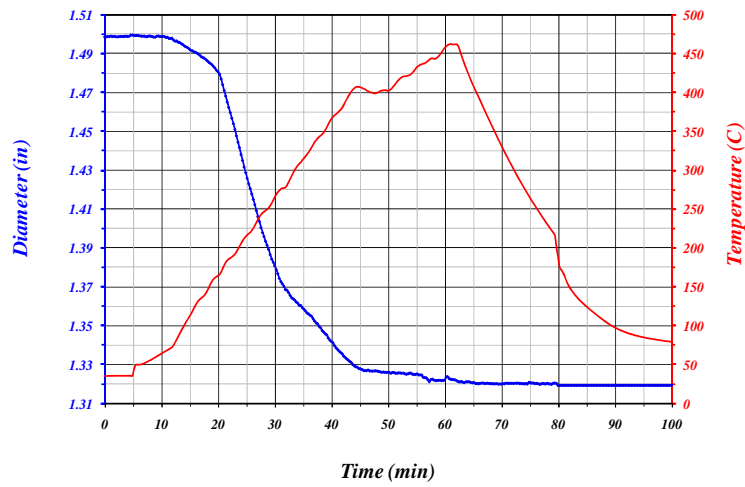
(b) Specimen diameter measurements
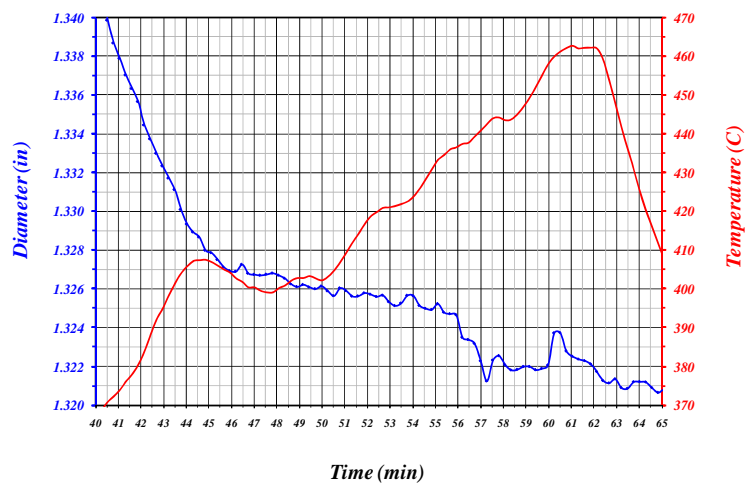
(c) Diameter measurements near maximum temperature

Fig. 3-1. Instrumented-HIP data for the canister with a blend of Hf/Al/Bi$_2$O$_3$ (10 vol% Bi$_2$O$_3$).
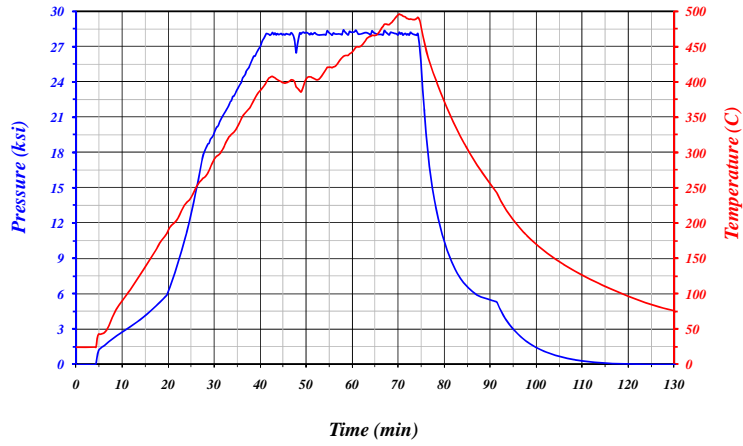
(a) HIP schedules
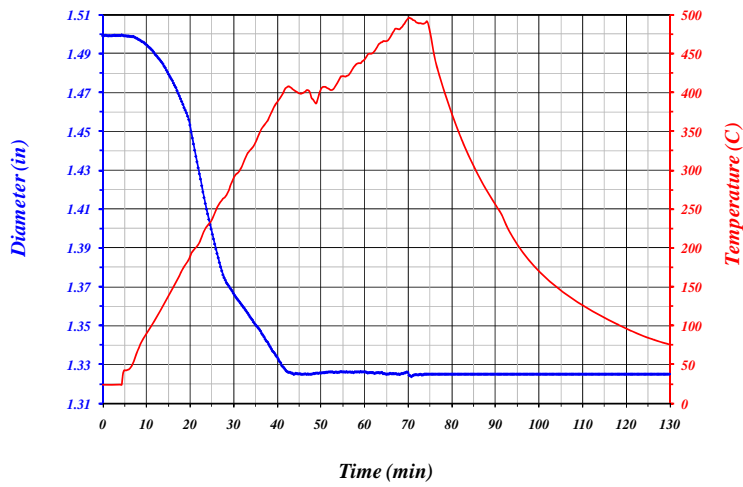
(b) Specimen diameter measurements
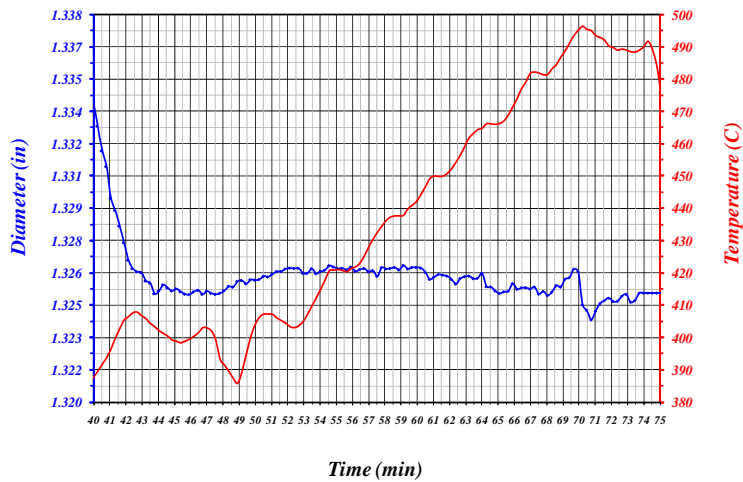
(c) Diameter measurements near maximum temperature

Fig. 3-2. Instrumented-HIP data for the canister with a blend of Hf/Al/Bi$_2$O$_3$ (10 vol% Bi$_2$O$_3$).

Again, examination of the compact after HIP showed that the canister deformed uniformly. A density measurement indicated that the material is 99.93% of TMD.

Hf/Al/Bi$_2$O$_3$ Powder Blend Consolidation with 15 vol% Bi$_2$O$_3$

A HIP canister of 1½-in diameter and 4½-in height was fabricated of aluminum. The canister was filled with the Hf/Al/Bi$_2$O$_3$ (15 vol% Bi$_2$O$_3$) powder blend, de-gassed at temperature and sealed under vacuum. The canister was then consolidated in Matsys's instrumented HIP.

HIP schedules and diameter measurements for the experiment are shown in Fig. 3-3. Initially, the temperature was increased to 225 ^{o}C while pressure was increased to 15 ksi (103 MPa). Next, the temperature was increased to 400 ^{o}C while the pressure was increased to 28 ksi (193 MPa). Significant densification was observed during each pressurization. Subsequently, the pressure was held constant while the temperature was raised to 500 ^{o}C. This temperature was maintained for 10 minutes, and the HIP was cooled to room temperature.
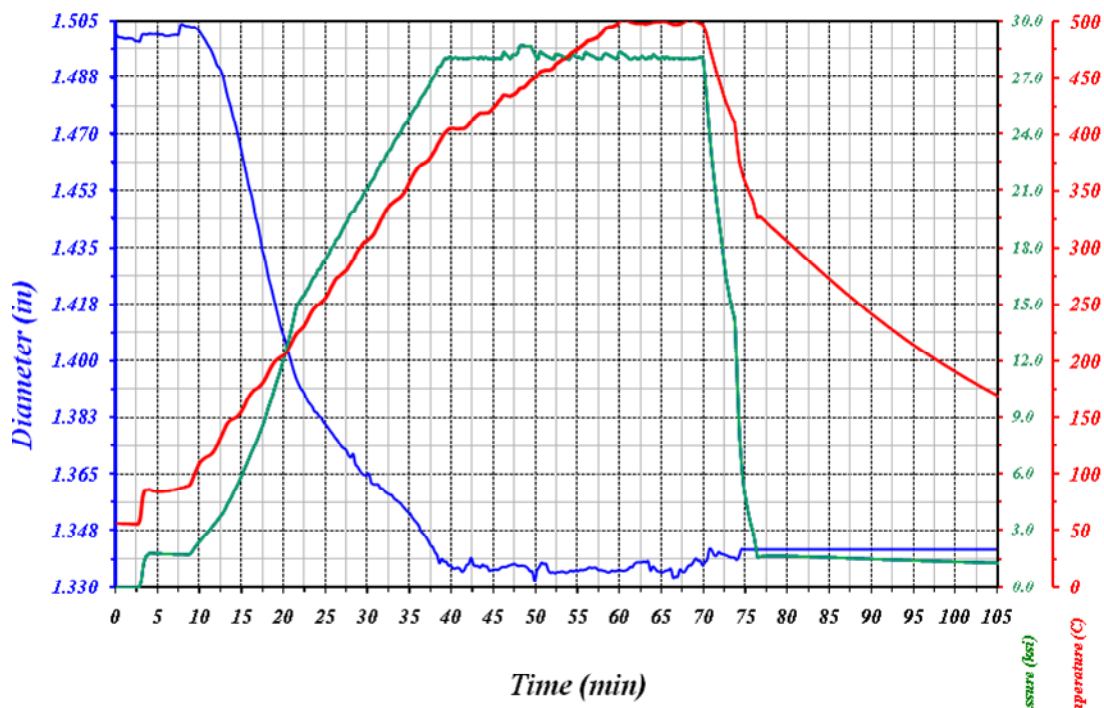
Fig. 3-3. Instrumented-HIP data for the canister with a blend of Hf/Al/Bi$_2$O$_3$ (15 vol% Bi$_2$O$_3$). The actual measurements of HIP temperature, pressure and the diameter measurements are shown.

Once more, examination of the compact after HIP showed that the canister deformed uniformly. A measurement indicated that the material density is 99.3% of TMD.

Task III - Material Characterization. The objective of this task is to characterize the mechanical properties of the fully dense material, including ultimate tensile and compressive strengths and failure strains.

Compressive and tensile specimens were machined from fully dense compacts using EDM to characterize the compressive and tensile strength of the fully dense material. Test data obtained to date are summarized in Tables 3-1 and 3-2.

Table 3-1. Summary of Material Formulations, Processing Conditions, and Density Measurements.

Material formulation	HIP conditions max. temp. (°C)	Theoretical density (g/cc)	Measured density (g/cc)	Relative density (%)
Al/Hf	525	7.890	7.913	100.00
Al/Hf/Bi$_2$O$_3$ (10 vol%)	475	7.825	7.748	99.02
Al/Hf/Bi$_2$O$_3$ (10 vol%)	500	7.825	7.8195	99.93
Al/Hf/Bi$_2$O$_3$ (15 vol%)	500	7.763		99.28

Table 3-2. Summary of Material Formulations and Mechanical Properties.

Material formulation	Compressive strength (ksi)	Compressive failure strain (%)	Tensile strength (ksi)	Tensile failure strain (%)
Al/Hf	75.7	3.5 - 5.2	57.6	1.2 - 1.5
Al/Hf/Bi$_2$O$_3$ (10 vol%)	58.7	2.7 - 3.2		
Al/Hf/Bi$_2$O$_3$ (10 vol%)	54.8	5.10		
Al/Hf/Bi$_2$O$_3$ (15 vol%)	50.3	2.7 - 5	10.8	

The Hf/Al composite has an average compressive strength of 75.7 ksi (522 MPa) and an average tensile strength of 57.6 ksi (397 MPa) with a failure strain ranging between 1.2 and 1.5%.

The Hf/Al/Bi$_2$O$_3$ composite with 10 vol% Bi$_2$O$_3$ had an average compressive strength of 58.7 ksi (405 MPa) for material processed at 475 °C. Average compressive strength dropped to 54.8 ksi (378 MPa) when processed at 500 °C; however, failure strain increased from about 3% to over 5%. The drop in strength is unexpected but the increase in failure strain is due to increased bonding as a result of the higher processing temperature. Further work is being performed to fully characterize this formulation.

The Hf/Al/Bi$_2$O$_3$ composite with 15 vol% Bi$_2$O$_3$ has an average compressive strength of 50.3 ksi (347 MPa) and an average tensile strength of 10.8 ksi (74 MPa).

Task IV - Parts Fabrication. The objective of this task is to fabricate parts and provide them for testing and characterization of the reactive properties. The following parts have been fabricated:

We made 3 cylinders from each material for testing at the University of Illinois. The cylinders had 1.006" ID $\times$ 0.75" L, and the materials were as follows:
- Aluminum – Valimet H2 via CIP process;
- Al/Ti/B$_4$C;
- Hf/Al; and
- Hf/Al/Bi$_2$O$_3$ composite with 15 vol% Bi$_2$O$_3$.

We made 3 cylinders from each material for blast-chamber testing at ATK. The cylinders had 1.006" ID $\times$ 1.25" L, and the materials were as follows:
- Aluminum – Valimet H2 via CIP process;
- Al/Ti/B$_4$C;
- Hf/Al; and
- Hf/Al/Bi$_2$O$_3$ composite with 15 vol% Bi$_2$O$_3$.

Three cylinders were prepared for testing at Indian Head with 1.01" ID $\times$ 1.0" L from Hf/Al/Bi$_2$O$_3$ composite with 15 vol% Bi$_2$O$_3$.

Six cylinders were prepared for blast-chamber testing at ARA with 1.01" ID $\times$ 3.617" L from Hf/Al/Bi$_2$O$_3$ composite with 15 vol% Bi$_2$O$_3$.

Section IV

Phase I Thrust B: Powder Metallurgy Processes, Spark Plasma Sintering

Colorado School of Mines (CSM) selected the hafnium-aluminum material system for initial processing by Spark Plasma Sintering (SPS) using the Gleeble 1500. Given the density goal of 7.8 g/cc, CSM focused on Hf-Al formulations with hafnium content of 80% (by mass) or greater. Seven compositions were developed for compression testing, as summarized in Table 4-1. Specimens were machined using EDM to create 3-mm-diameter by 4-mm-long compression specimens, which were tested using a custom fixture.

Table 4-1. Representative compression-sample chemistry and process parameters.

Sample	Composition (wt% Al/wt% Hf)	Process temperature (°C)	Process time (seconds)
13.2	20/80	600	60
15.2	16/84	600	60
16.1	8/92	600	180
18.1	16/84	600	180
20.2	16/84	555	300
22.1	20/80	575	300
22.2	20/80	575	300

Compression data, shown in Fig. 4-1, indicate the potential range of material/mechanical properties that SPS can produce. Measured strengths range from 27 to 37 ksi, somewhat below the 50 ksi goal. However, these data are not fully indicative of the potential of SPS since the specimens were measured to have 30% porosity. It was expected that strength would increase with the amount of intermetallic (Hf_2Al, $HfAl$, Hf_3Al_2) present and hence the Phase I goal of 50 ksi could be achieved.
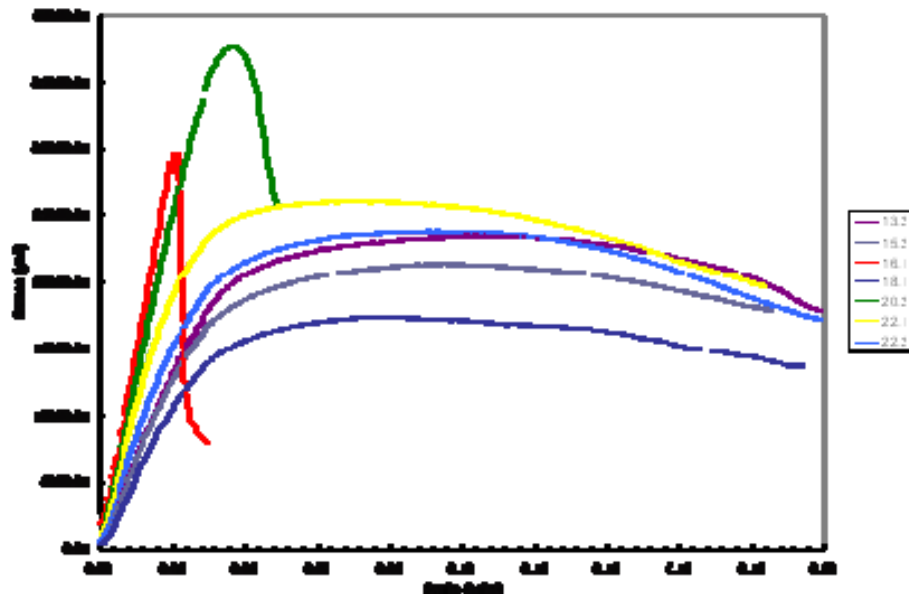
Fig. 4-1. Compression test results.

The only process parameter that appeared to affect the mechanical properties of the product is time of processing. This suggested that the key to tailoring the mechanical/material properties of this system is the amount of intermetallic formed at the interface between the Hf and Al powders.

The following figures show the relative amount of intermetallic formed. Figure 4-2 is roughly equivalent to specimen 22.1. A large degree of porosity is apparent (black) while aluminum (dark grey) and hafnium (white) are present. The intermetallic (light grey) can be seen between the particles. The porosity, inter-metallic, Al powder, and Hf powder are more evident in Fig. 4-3.
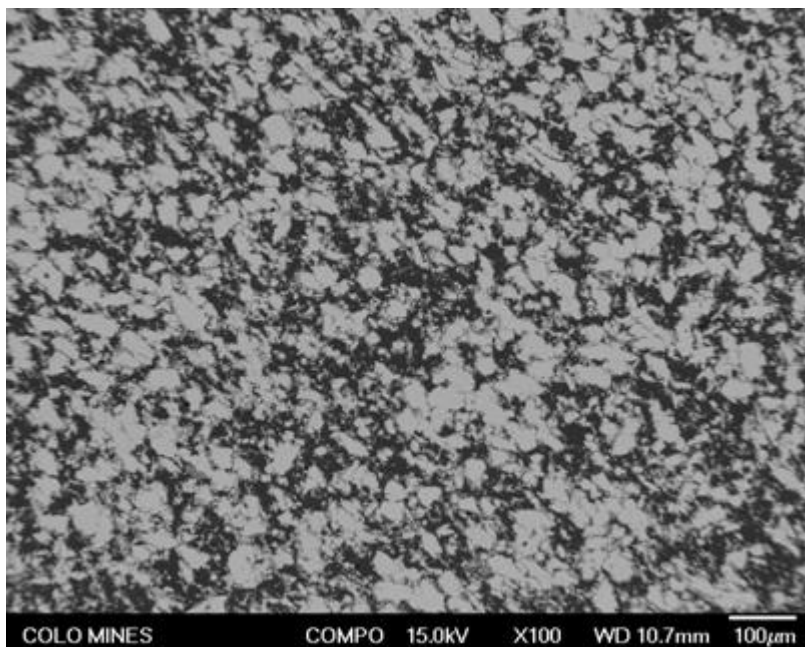
Fig. 4-2. Backscatter SEM image of a specimen of 20/80 wt% Al/Hf processed at 600 °C for 180 seconds at 100× magnification.
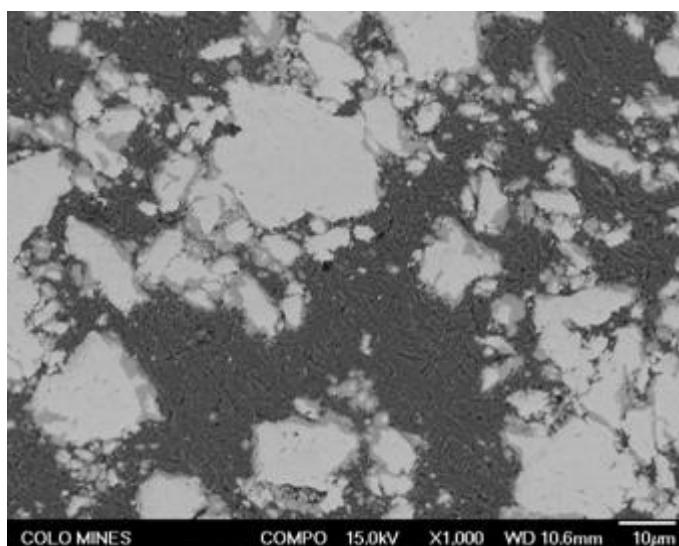
Fig. 4-3. BSEM image at 1000× magnification of the same specimen in Fig. 4-2.

This microstructure is apparent in all of the strongest specimens. Small pores can be seen in the alumi-num. However, pores are not readily obvious in the starting powder (Fig. 4-4). It should be noted that it

appears that all of the aluminum has consolidated and no individual particles remain after processing. The hafnium does not appear to change from the original powder (Fig. 4-5).
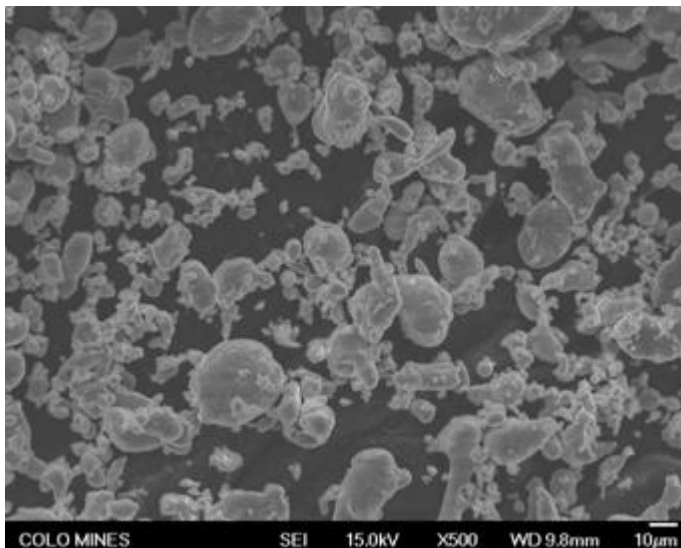
Fig. 4-4. Secondary electron image of raw aluminum powder on carbon tape.
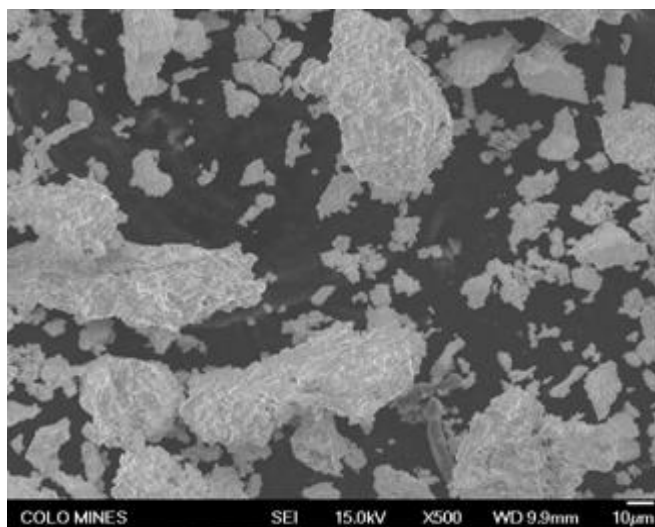
Fig. 4-5. As-received hafnium powder.

After the initial processing studies were finished, CSM focused on a more production-oriented process for the synthesis of specimens for blast testing. CSM worked with Coors Ceramics for making net-shape green constructs using their CIP facilities. These green bodies were then to be consolidated using the CSM SPS process. The compositions of the CIPed powders were as follows:

	Wt%	Vol%
Hf/Al	82/18	48.03/51.97
Hf/Al/W	50/20/30	29.54/58.24/12.22
Hf/Al/Ta	60/20/20	28.98/57.13/13.89

An example of a CIP Hf/Al hollow cylinder is shown in Fig. 4-6.

Fig. 4-6. CIP Hf/Al green construct approximately 1.5" OD x 1.0" ID x 6" L.

All chemistries can be CIPed to greater than 93% TMD based on Archimedes measurements on compacts post-CIP. Because of this, no compression is applied during SPS so final density of the SPS samples is approximately 93% of TMD. SPS reactions were conducted in a forming-gas atmosphere (argon with 5% hydrogen to reduce any oxides present on the Al particle surface).

During processing of the hollow cylinders, the apparatus for performing the SPS process failed. The failure was significant and could not be easily remedied in time to provide specimens for either the UIUC or ATK chamber tests. As a result of this delay, it was decided to discontinue the SPS investigation.

Section V

Phase I Thrust C: Energetic Binders

In this section, the efforts of SRI International in developing energetic binders for polymer-matrix-based composite materials are described. These binders are energetic in that they contain some fluorine, which it was hoped would increase reactive material energy output by possibly reacting with some of the composite's inert ingredients, such as tungsten. However, the epoxy formulations developed in this effort showed no superiority in blast testing over commercial epoxy products. As a result, this effort was terminated in June 2010.

5.1 Initial Objectives

SRI's effort initially focused on developing fiber-reinforced composites containing a matrix composed of highly fluorinated thermoset resin and reactive-metal particulates. The fabricated fibers will provide the main strength aspect of the overall composite, but preferably they will consist, at least partially, of a reactive material itself. The reaction between the fluoro-resin/air and the particulates/fibers will result in higher energetic output than achievable by comparable non-fluorinated composites.

5.2 Synthesis

SRI successfully scaled up synthesis of their leading epoxy compound, PA4, to 20-gram batches. Plans to increase to 50-gram batches are in place ready for the stage, when large composite specimens will be prepared.

Literature search and consideration of methods to synthesize epoxy components with higher fluorine content were begun as well as for the synthesis of crosslinkers that possess fluorine content. Currently, we are using a non-fluorinated crosslinker to rigidize the cured resins.

More of the PA4 component was synthesized since it is our standard Part A component at this stage. One fluoro crosslinker containing four linking groups was completed and analyzed for its chemical structure as shown in the scheme below. The synthesized material shows the expected structure according to NMR analysis.

The first synthesized fluoro crosslinker is designated "PA6" in our epoxy series since it contains epoxy sites and can serve as a fluoro reagent by itself. In fact, its F-factor is 2.70, which is 17% higher than our standard Part A component, PA4. The synthesis of PA6 is illustrated in Fig. 5-1. We will assess its potential as both crosslinker and a sole Part A.
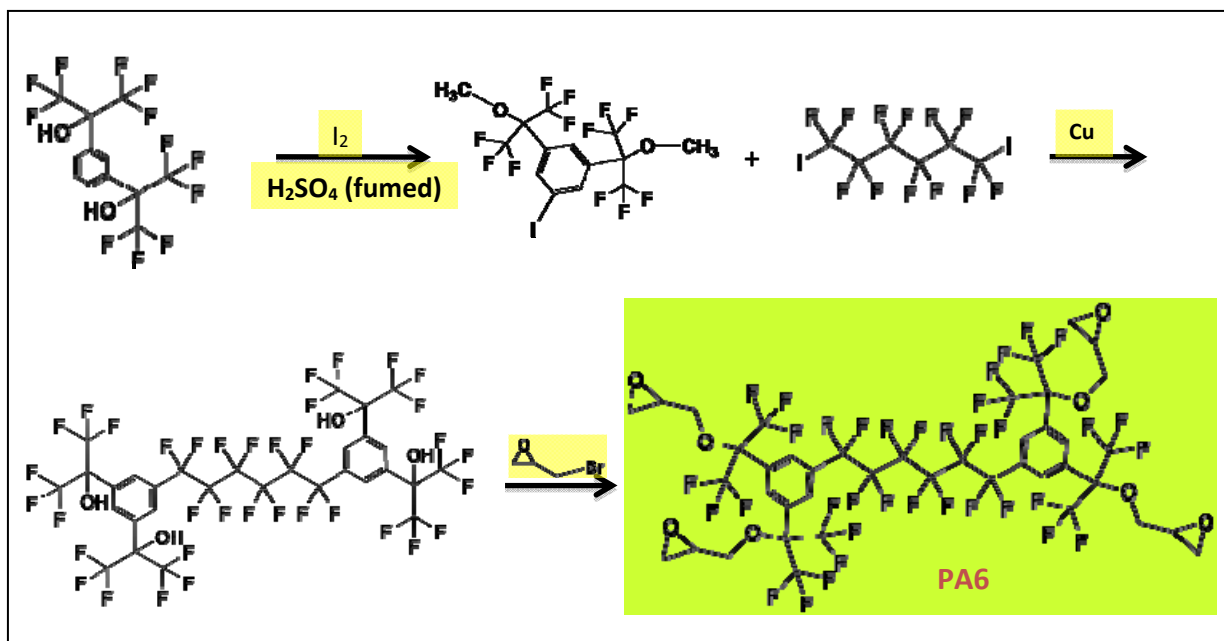
Fig. 5-1. Synthesis of Part A component PA6.

Work with this thermoset polymer involves in-situ reaction in the presence of metal powder. Due to potential reactivities between the powders and the reagents as well as the final polymeric products, SRI are first conducted a series DSC and TGA analyses to assess potential interactions between the organic reagents, derived polymer and metal powders.

5.2.1 Evaluation of Polytriazole

In October, SRI began evaluating a thermoset polytriazole as a potential self-propelling polymer candidate (Fig. 5-2). This polymer was first experimented with several years ago at SRI, and several of its monomers have been synthesized. Due to its energetic sensitivity SRI first had to evaluate if incorporating Zr and Al powders would destabilize the polymer during the processing temperature regime. A series of DSC and TGA analyses did not reveal any special reactivity beyond the self-behavior of the polymer.
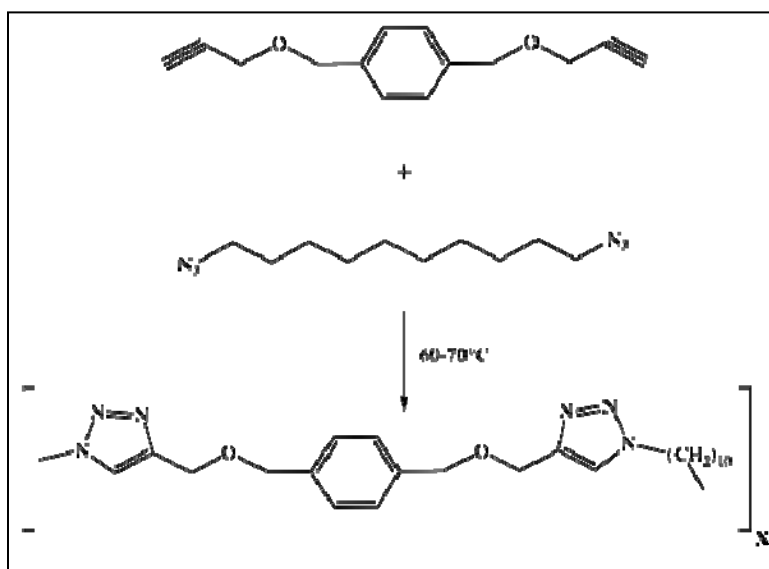
Fig. 5-2. Polytriazole synthesis and structure.

However, once SRI started to formulate it with powders as a curable resin following procedures developed several years ago, it did not cure. SRI tried to assess whether decomposition of the reagents or impurities due to storing the reagents (in a freezer) for several years has degraded its curability.

In December, it was found that the curing of the polytriazole is not as efficient as reported. SRI determined that the reagents had not degraded during their long storage in a freezer, and it was assumed that it is an issue of managing the fraction of crosslinker.

5.2.2 Part A/Part B formulations and curing study

Additional Part A/Part B combinations were evaluated. The trend of higher aromatic content yielding greater stiffness continued to manifest itself. Addition of crosslinkers to linear (aliphatic) fluoro reagent couples has started and will be completed in August.

A problem associated with the volatilization of the most promising Part A/Part B combinations has been solved by changing the curing heating schedule via a gradual heating of the mixture.

Formulations with powders

SRI continued formulating various Part A/Part B combinations with fine Zr micron-size powders (1 to 4 µm in diameter). Stoichiometric levels of these powders are still low in their volume fractions and therefore the resultant slurries maintain low viscosities, suitable for fabric infiltration.

Composite Fabrication

SRI demonstrated the capability to infiltrate such slurries into glass-fiber weaves (tapes and braids) and obtained stiffened composites. The fiber density in these composites is as high as 45% and the slurry can be easily infiltrated between the single fibers of the woven yarns without segregation of the metal particles. Since the glass fibers are much finer than the tungsten wires, we do not anticipate any problems in infiltrating even larger Zr powder (−325 mesh). The cured formulations bond very well to glass.

Test Specimen Preparation

From August through October, SRI prepared sets of coupons with reactive material formulations based on one epoxy formulation and various metal powders. Powders included 2- to 5-µm and −325 mesh Zr and Al added at 30 vol% and an additional higher loading for each of these powders. SRI prepared a total of twelve sets of test specimens, listed in Table 5-1.

Table 5-1. Metal-powder-loaded fluorinated-epoxy-based specimens.

ID #	Description
PAB33	100% fluoro epoxy (PA4/PB6)/2wt% tricarballylic acid (TCA)
M20	30%vol-zirconium, -325 mesh/70%vol-fluoro epoxy (PA4/PB6)/2wt% TCA
M19	30%vol-zirconium, 2-5µm/70%vol-fluoro epoxy (PA4/PB6)/2wt% TCA
PAB34	100% fluoro epoxy (PA3/PB6)/5wt% TCA
M21	30%vol-zirconium, -325 mesh/70%vol-fluoro epoxy (PA3/PB6)/5wt% TCA
M22	30%vol-zirconium, 2-5µm/70%vol-fluoro epoxy (PA3/PB6)/5wt% TCA
M23	30%vol-aluminum, -325 mesh/70%vol-fluoro epoxy (PA4/PB6)/2wt% TCA
M24	30%vol-aluminum, Valimet H-2 (spherical 2 µm)/70%vol-fluoro epoxy (PA4/PB6)/2wt% TCA
M25	60%vol-zirconium, -325 mesh/40%vol-fluoro epoxy (PA4/PB6)/2wt% TCA
M27	60%vol- aluminum, Valimet H-2 /40%vol-fluoro epoxy (PA4/PB6)/2wt% TCA
M28	60%vol-zirconium, 2-5µm /40%vol-fluoro epoxy (PA4/PB6)/2wt% TCA
M30	20%vol-Zr, 2-5µm /20%vol-Al, Valimet H-2/60%vol-fluoro epoxy (PA4/PB6)/2wt% TCA

SRI's focus then turned from preparing coupons for the blast tests at UIUC to preparing dog-bone test bars for tensile testing. After selecting the smallest dimension provided by the ASTM methods, a mold (Fig. 5-3) was prepared to fabricate one dog-bone at a time using the solvent-containing process. The advantage of this process is the capability to load matrix materials with high loadings of metal particulates (Zr and Al), followed by removal of the solvent prior to curing under pressure. This process imitates lay-up and vacuum-infiltration processes. A disadvantage of this process is that it needs to incorporate a step for efficiently evaporating the solvent at mild temperature before the heat-curing step in which the composite specimen is pressed at about 500 psi.
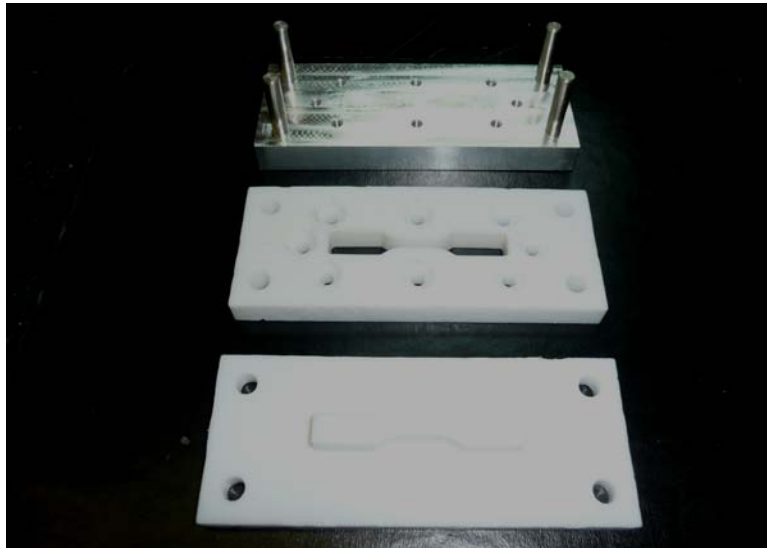
Fig. 5-3. Mold for preparing dog-bone specimens.

The irregular configuration and the stiffness of the W braids made this process more difficult. It took several iterations of mold operation and slurry processing to develop an adequate process for a matrix consisting of 30 vol% Zr fine particles (2-5 µm) and 70 vol% fluoroepoxy (PA4/PB6/2% TCA crosslinker). Figure 5-4 shows W/Zr/Fluoroepoxy composite specimens.

Fig. 5-4. Dog-bone specimens.

SRI switched to matrices of 57 vol% fine Al (4 µm) and 43 vol% epoxy, which matches the overall composition of 30% W, 40% Al, and 30% epoxy that provides the required strength and density. Since this almost doubles the powder loading, SRI had to adjust the solvent quantities (acetone) and practice several processing procedures to obtain relatively good specimens as shown in Fig. 5-5. The specimens still have grooves that seem to be hairline shallow cracks. The specimens can be readily sanded and polished and provide a very metallic (aluminum) appearance. The process improvement is still in progress.

In mechanical tests, it was found that the specimens were found to break at the large gripping end tabs. This is due to the lesser reinforcement by the wire braid in the end tabs. SRI continued to work on by-

passing this deficiency. After testing the specimens SRI planned to perform density and SEM analyses of the high-density area of the dog bones.
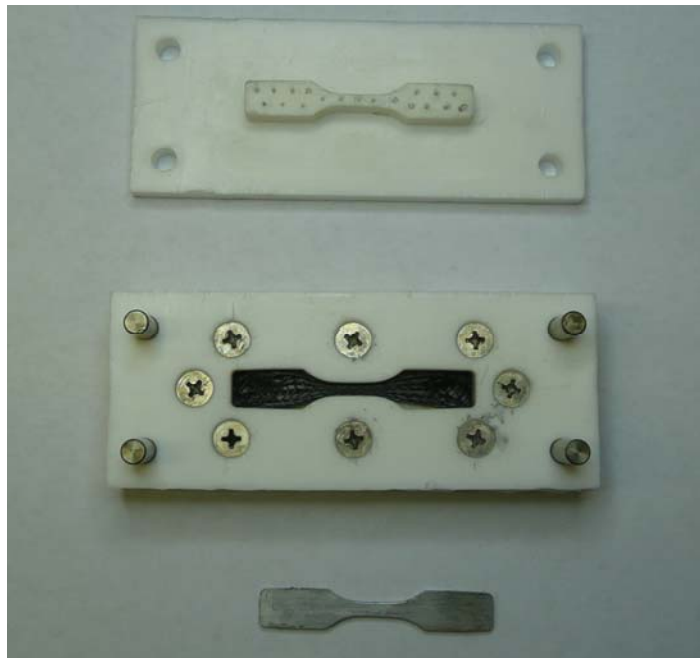
Fig. 5-5. Partially assembled dog-bone mold and dog-bone specimen.

5.3 Fabrication of Cylinder Specimens for ATK Scaled-Up Tests

Lab activity focus then shifted toward producing specimens for blast testing at ATK. SRI scaled up the synthesis of our epoxy reagents in order to have sufficient excess amount of formulations to practice and generate adequate specimens as required for the test. In parallel, SRI developed an alternative pro-cedure to the one used by DET, in which a braiding machine is used as a part of the process. In order to avoid the need to ship formulations cross-country, SRI developed an alternative route, in which much of the processing can be done under inert or vacuum conditions. This made it easy to deal with the micron-size particles SRI planned to use.

SRI obtained 2"-diameter tubular tungsten-wire braids from DET. A 1"-diameter Teflon rod is covered with slurry and the braid is mounted on top, as shown in Fig. 5-6. In winding the braid, the rod is rotated by the gear motor on the left. The hand crank at the bottom maintains tension in the braid during wind-ing. The braid is infiltrated with the slurry of epoxy and metal powder, which is applied with a brush, as shown in Fig. 5-7. The excess of the material is folded around the rod, as shown in Fig. 5-8. The infiltrat-ed and wound specimen is first wrapped with low-surface-tension glass mesh, as shown in Fig. 5-9, then tied with a tungsten wire, as shown in Fig. 5-10. After incorporation of the slurry into the first layer, the next layer is then put on top. Subsequent braid tubes, if any, are folded in a staggered manner to obtain a uniform thickness. The completed specimen is dismounted from the fixture, Fig. 5-11, and then bagged for vacuum curing, Fig. 5-12.

Fig. 5-6. Mounting of braid in fixture.

Fig. 5-7. Infiltration of braid with the epoxy-metal-powder slurry.

Fig. 5-8. Specimen after infiltration with slurry.

Fig. 5-9. Wrapping specimen with glass mesh.

Fig. 5-10. Specimen after wrapping and binding with tungsten wire.

Fig. 5-11. Specimen after dismounting from fixture.
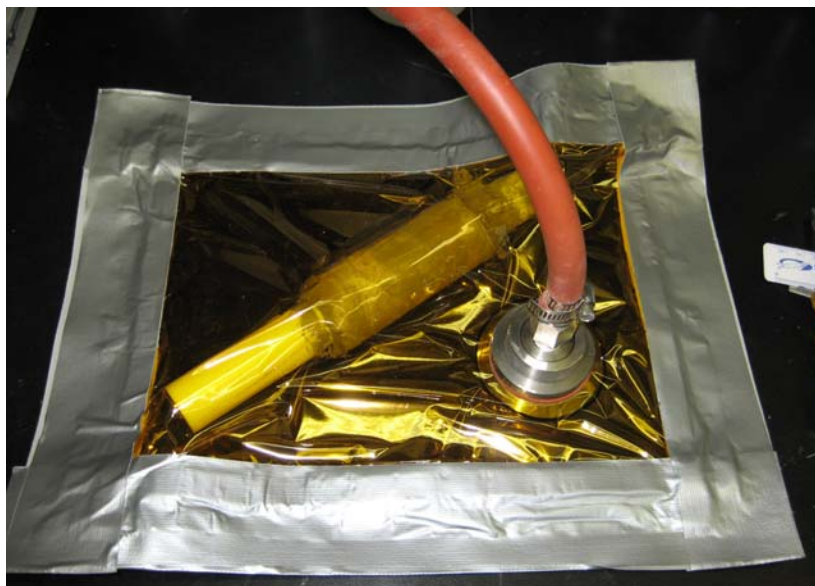
Fig. 5-12. Specimen during vacuum curing.

5.4 Further Development of Specimens for Tensile Testing

In December we focused on preparing dog-bone specimens for mechanical tensile testing. We have selected the smallest dimension provided by the ASTM methods and prepared a mold to allow the formation of one dog-bone at a time using our solvent containing process. The advantage of this process is the capability to load matrix materials with high loadings of metal particulates, followed by removal of the solvent prior to curing under press. This process imitates lay-up and vacuum-infiltration processes.

One disadvantage of this process is that the method needs to incorporate a step for efficiently evaporating the solvent at mild temperature prior to heat-curing at which the composite specimen is pressed at around 500 psi. We have been able to overcome this problem by drilling small holes in the Teflon lid used to press the specimens.

However, once SRI started the tensile strength measurements it was realized that the breaking of the specimens occurs in the end tab region of the dog-bone rather than the test region due to the much lower reinforcement by W wires in this area. We also observe that the wires in the narrow area are not evenly distributed due to the narrow configuration they are forced into. We are changing our test specimen configuration in order to have an even distribution of wires throughout each specimen and yet not consume much slurry material. The new specimens will be rectangular in shape.

5.5 Modeling of Formulation Energy Output

We are in the middle of modeling both our and DET's formulations for their energetic output LLNL's Cheetah code (version 5.0). This code takes into account all the potential species that can be generated by the reaction of the reagents in an energetic mixture. The code requires that the assumed species exist in its database, and some may be missing when it comes to metal fluorides. Cheetah estimates both the mechanical and thermal contribution to the total detonation energy. The mechanical contribution is the work done by the expanding gases. The initial calculations were done in anaerobic conditions, i.e., in the absence of oxygen (all fuel and oxidizer elements are provided by the metal and polymer). Various mixtures of the metals Zr, Al, and W were combined with the non-fluorinated epoxy (PA0/PB0) and two fluorinated epoxies (PA4/PB6) and (PA3/PB6). Mixtures of the metals and Teflon were included for comparison as Teflon is the polymeric material with the greatest F-factor (moles of fluorine per mass of polymer multiplied by 100). Metals and polymers were combined in a proportion of 30/70 by volume. Several fluorinated products of the metals were included in the calculations shown in Table 5-2.

Table 5-2. Material systems incorporating fluoridated epoxies.

Formul.	Zr % vol	Al % vol	W % vol	Teflon % vol	PA0/PB0 % vol	PA4/PB6 % vol	PA3/PB6 % vol	Mechanical Energy (kJ/cc)	Thermal Energy (kJ/cc)	Total Det. Energy (kJ/cc)	Total Det. Energy (kJ/g)
Zr-1	30			70				-5.207	-12.717	-17.924	-5.089
Zr-2	30				70			-4.860	-2.462	-7.322	-2.563
Zr-3	30					70		-5.648	-8.163	-13.811	-4.403
Zr-4	30						70	-6.119	-8.261	-14.380	-4.584
Zr-1*	24			76				-5.391	-12.748	-18.139	-5.416
Zr-2*	51				49			-5.424	-4.651	-10.074	-2.552
Zr-3*	45					55		-5.051	-9.103	-14.154	-3.671
Zr-4*	43						57	-5.648	-8.923	-14.571	-3.876
Al-1*		23		77				-8.1126	-11.971	-20.097	-8.539
Al-2		30			70			-3.112	-2.478	-5.590	-3.250
Al-3		30				70		-4.859	-8.067	-12.925	-6.463
Al-4		30					70	-5.460	-8.235	-13.695	-6.848
Al-2*		15		85				-4.383	-2.258	-6.641	-4.398
Al-3*		20				80		-6.169	-8.603	-14.772	-7.775
Al-4*		21					79	-6.700	-8.757	-15.456	-8.092
W-1			30	70				-1.270	-3.446	-4.716	-0.642
W-2			30		70			-1.353	-0.357	-1.710	-0.256
W-3			30			70		-1.296	-1.570	-2.866	-0.411
W-4			30				70	-1.464	-1.647	-3.112	-0.447
W-2*			5	95				-1.994	-0.258	-2.252	-1.025
W-3*			13			87		-1.896	-1.305	-3.201	-0.804
W-4*			13				87	-2.238	-1.069	-3.307	-0.831

* Optimized Total Detonation Energy

Formulation	Zr %vol	Al %vol	W %vol	Teflon % vol	PA0/PB0 % vol	PA4/PB6 % vol	PA3/PB6 % vol	Mechanical Energy (kJ/cc)	Thermal Energy (kJ/cc)	Total Det. Energy (kJ/cc)	Total Det. Energy (kJ/g)	Total Comb. Energy **(kJ/g)
Zr-1	30			70				-5.207	-12.717	-17.924	-5.089	-10.19
Zr-2	30				70			-4.860	-2.462	-7.322	-2.563	-17.94
Zr-3	30					70		-5.648	-8.163	-13.811	-4.403	-11.69
Zr-4	30						70	-6.119	-8.261	-14.380	-4.584	-11.39
Zr-5	60				40			-4.658	-4.266	-8.923	-2.022	-14.23
Zr-6	60					40		-2.753	-7.987	-10.739	-2.348	-11.91
Zr-7	60						40	-2.966	-7.835	-10.801	-2.361	-11.79
Al-1		23		77				-8.1126	-11.971	-20.097	-8.539	-14.62
Al-2		30			70			-3.112	-2.478	-5.590	-3.250	-30.79
Al-3		30				70		-4.859	-8.067	-12.925	-6.463	-19.53
Al-4		30					70	-5.460	-8.235	-13.695	-6.848	-19.06
Al-5		60			40			-1.233	-2.108	-3.341	-1.561	-30.96
Al-6		60				40		-1.436	-3.662	-5.098	-2.217	-25.34
Al-7		60					40	-1.728	-3.575	-5.303	-2.306	-25.11
W-1			30	70				-1.270	-3.446	-4.716	-0.642	-4.10
W-2			30		70			-1.353	-0.357	-1.710	-0.256	-6.94
W-3			30			70		-1.296	-1.570	-2.866	-0.411	-4.50
W-4			30				70	-1.464	-1.647	-3.112	-0.447	-4.37
Zr/Al	20	20				60		-5.182	-8.979	-14.161	-4.955	-15.52
W/Al-1		40	30		30			-0.812	-1.732	-2.544	-0.351	-6.28
W/Al-2		40	30			30		-0.635	-4.020	-4.655	-0.632	-5.36
W/Zr-1	40		30		30			-2.897	-3.796	-6.692	-0.764	-4.94
W/Zr-2	40		30			30		-1.541	-6.513	-8.054	-0.907	-4.16
W/Zr/Al-1	20	20	30		30			-1.742	-3.408	-5.150	-0.644	-5.52
W/Zr/Al-2	20	20	30			30		-1.783	-6.626	-8.409	-1.035	-4.74
Al-8		40			60			-2.260	-2.530	-4.790	-2.575	-30.09
Al-9		40				60		-3.614	-7.466	-11.079	-5.276	-21.17
Z-8	40				60			-5.104	-2.668	-7.772	-2.302	-16.33
Zr-9	40					60		-5.604	-8.436	-14.039	-3.883	-11.79

The obvious observations are:

- The total detonation energies (kJ/g) rank by metal with aluminum > zirconium >> tungsten.
- The fluorine polymers give substantially higher mechanical and thermal contributions to the total detonation energies than the non-fluorinated PA0/PB0 that are used by DET.

- The total detonation energies of mixtures that include fluorine rank according to % fluorine with Teflon > PA3/PB6 > PA4/PB6.
- The thermal energy from detonation of the fluorinated mixtures is greater than the mechanical energy. The opposite is true for the non-fluorinated polymer. This is due to the large energy release on forming metal-fluorine bonds.
- Allowing the program to optimize the total detonation energy (kJ/cc) by varying composition gave slightly higher detonation energies for aluminum and zirconium metals while the tungsten metal mixtures gave low overall energy release that was fairly insensitive to composition.

We are currently calculating the energetic output for the same series in the actual cases when oxygen is present.

We continued our modeling effort with the Cheetah program. More formulations were evaluated after receiving the data accumulated at UIUC. We also extended the analysis to the energy evolved during combustion of these compositions in air. The calculations in air are currently limited to overall combustion energy and they cannot estimate the mechanical and thermal components of the energy like in the case of anaerobic detonation.

SRI discussed with LLNL extending the modeling capability to air. Dr. Sorin Bastea of LLNL recommended requesting another software package offered by LLNL, which links the Cheetah program with Hydrocode. He agreed to help define the problem in Hydrocode and instruct how to run the program, but warned that this process is time-consuming and requires a fair amount of processing time. Alternatively, he recommended considering some notes in the Cheetah manual about the effect of post-detonation combustion and what type of estimates may be useful. According to Bastea, Cheetah also provides TNT equivalence for both detonation and combustion, the average of which may also be a simple estimate of performance.

The table on the next page summarizes more of the Cheetah calculations including the combustion calculations. All the combinations show that in the absence of air, the fluoroepoxy yields significantly greater detonation energy, while the combustion in air significantly favors the hydrocarbon epoxy as expected. Since the UIUC tests were performed in air, the epoxy samples should have given significantly better results relative to the parallel fluoroepoxy formulations. The fact that they provide similar pressure output suggests that the fluoroepoxy has a positive effect due to limited accessibility of oxygen. We therefore predict that in the absence of air the fluorine content will have a significant effect.

The best UIUC results were obtained with M30 formulation, which was a mixture of 20vol% Zr/20%vol Al/60%vol fluoroepoxy. Detonation energy calculations indicated that this combination provides more energy than the average of separate formulations containing 40vol% Zr or 40vol% Al. This finding merits further consideration.

More formulations were evaluated using Cheetah prior to the meeting in Seattle and after the meeting per internal discussions and discussions with DET about incorporating Zr and Hf as density enhancers. At this stage our program database does not include Hf species and we make the assumption that the energy values are similar to or better than Zr on a mole basis, as we found in an unrelated previous project (see Scheme below). By volume the value for a mole of Hf is very similar to Zr (95.4%).
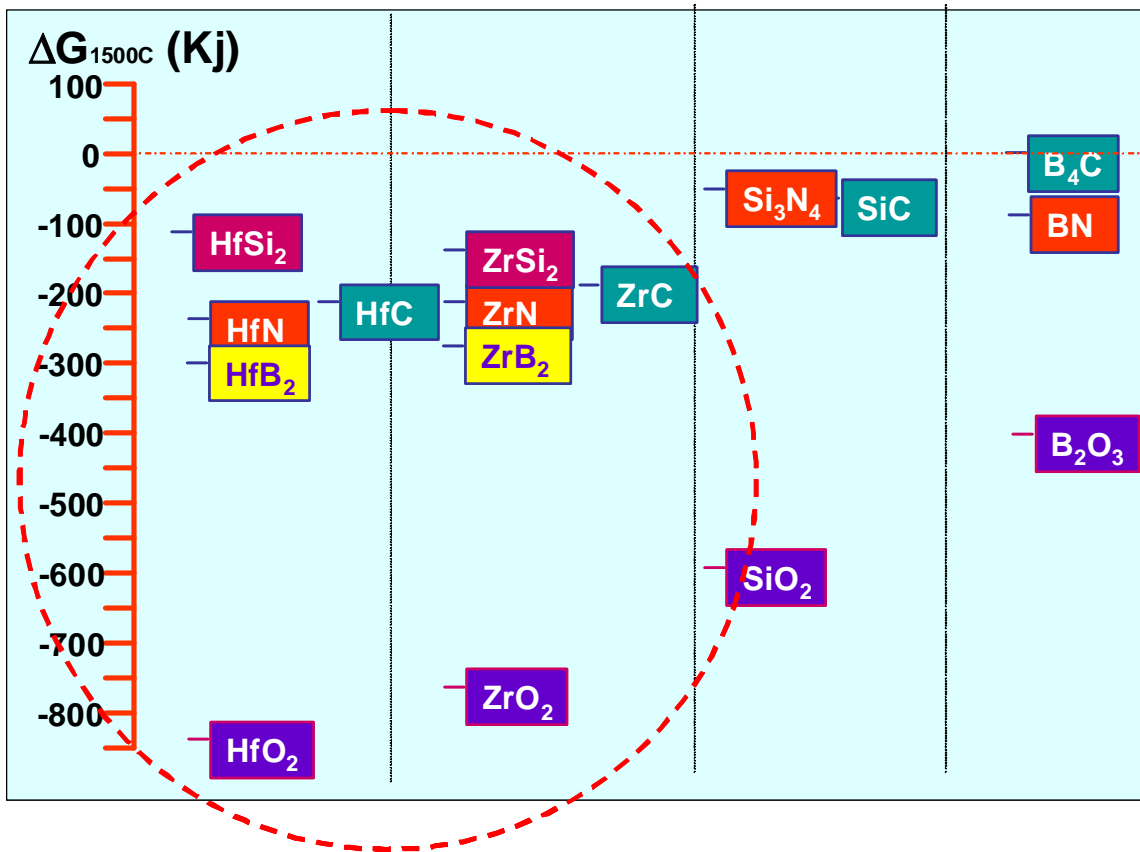
Fig. 5-13. Energies of various component materials.

Section VI

Phase I Thrust D: Warhead Mechanisms

The focus of Thrust D was to investigate means of facilitating the release of the reactive material's energy. Mechanisms investigated include macro-scale features to promote case fracture and breakup, thereby inducing mixing of the reactants with the ambient air and detonation products. Meso-scale material features to promote thermal ignition and fracture were also investigated.

The ultimate goal of the program was to have the RMS release its energy in such a way as to increase blast impulse in a warhead application. The Phase I demonstration warhead, shown in Fig. 6-1, was designed to have a ratio of case mass to explosive mass of 3.0. The mass of the explosive was nominally 1/6 lb (75.6 g) and the case mass nominally ½ lb (227 g).

0.780-in ID

0.994-in OD

6.00-in.
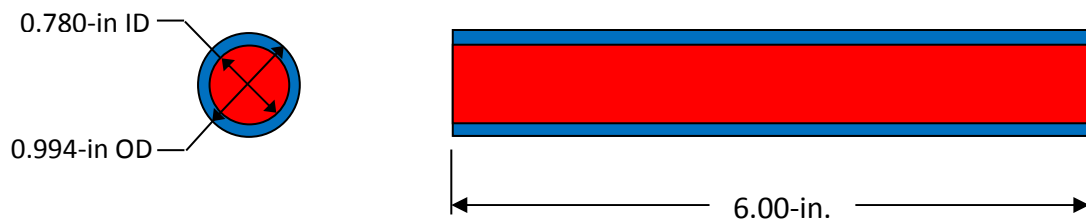
Fig. 6-1. Phase I demonstration warhead.

6.1 First Iteration of Subscale Tests

Subscale tests were conducted by the University of Illinois at Urbana-Champaign (UIUC) in September and October 2009. A Reynolds RP-1 Exploding-Bridgewire (EBW) detonator was used to explosively shock a pellet of reactive material, as shown in Fig. 6-2. Tests were conducted in an enclosed chamber instrumented to record pressure histories, from which blast impulse was calculated.

Output Pellet
RDX
PETN   RP1 Case

Heavy steel confinement
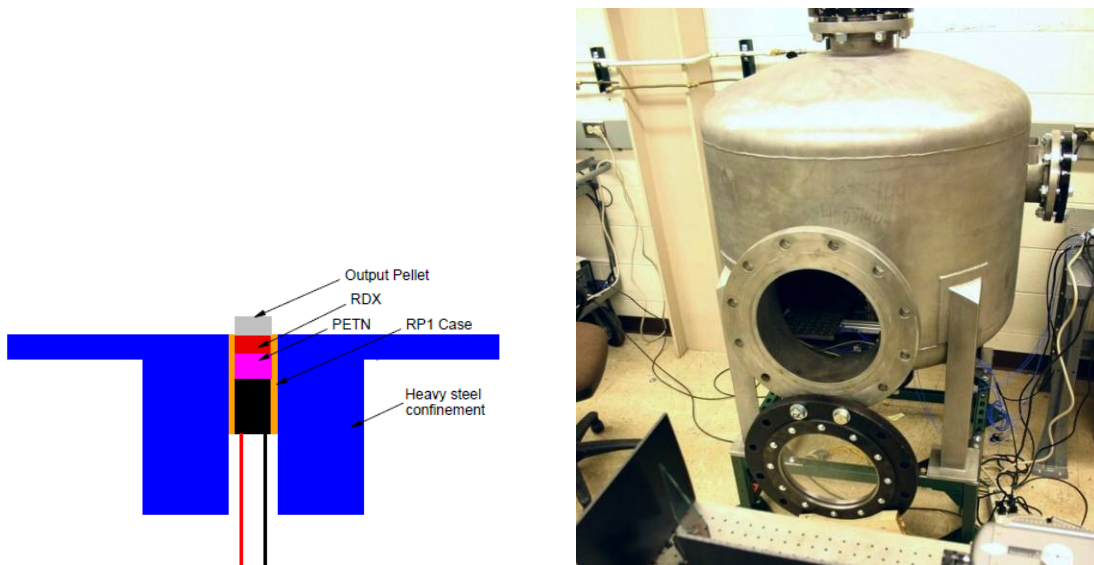
Fig. 6-2. UIUC's test setup.

Material specimens from Thrusts A, B, and C were provided in powder form, as pressed compacts with nominal 10% porosity, and as fully dense materials. The primary metric measured in the tests was total impulse as compared to bare and steel-covered detonators. Data were grouped by material type: epoxy-

based, metal-metal mixtures, and metal-metal-oxide mixtures. The experimental impulse data are summarized for the three material types in Figs. 6-3, 6-4, and 6-5.
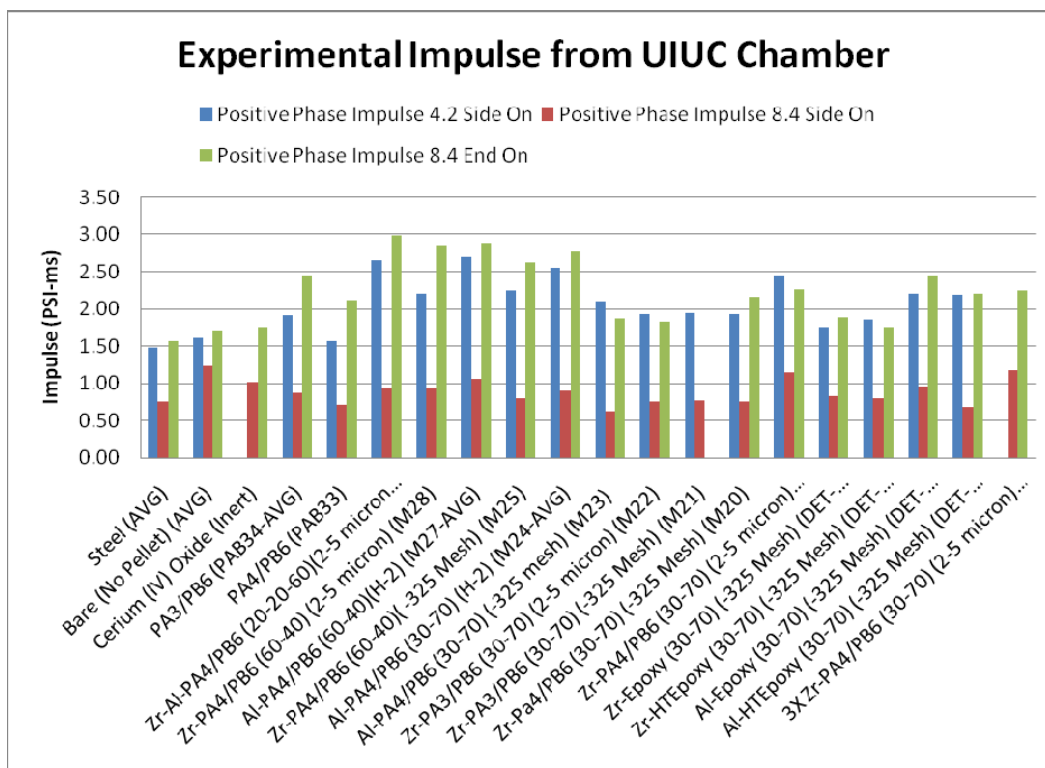
Fig. 6-3. Measured impulse of epoxy-based reactive materials.
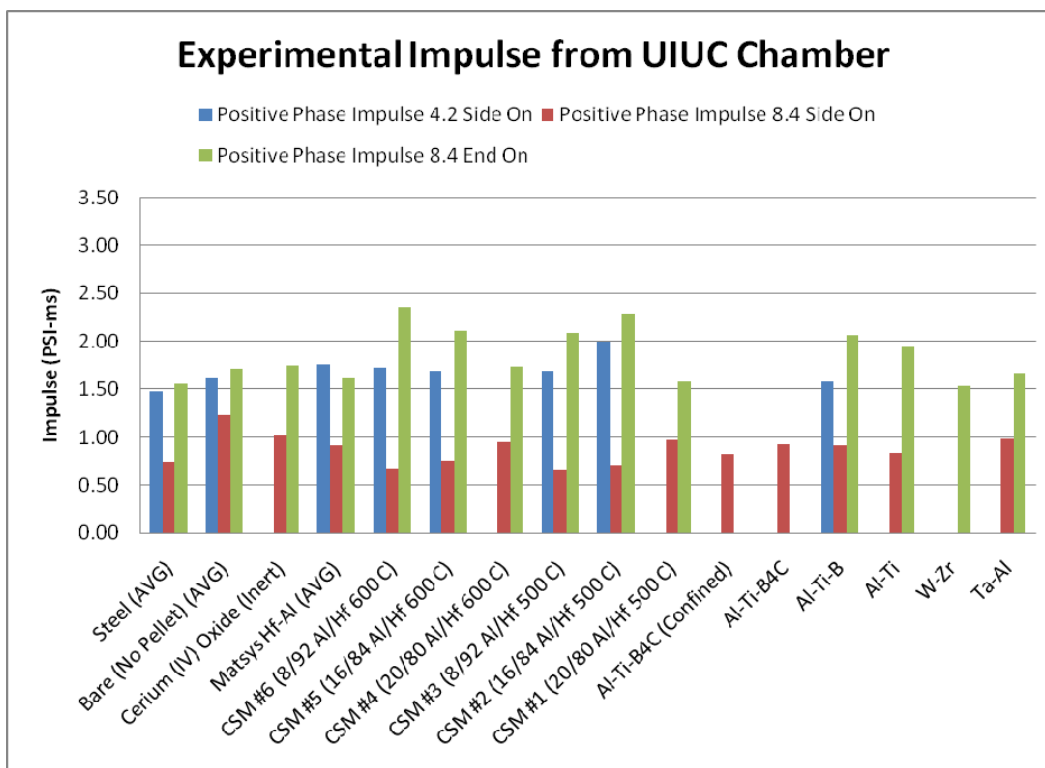
Fig. 6-4. Measured impulse of metal-metal reactive materials.
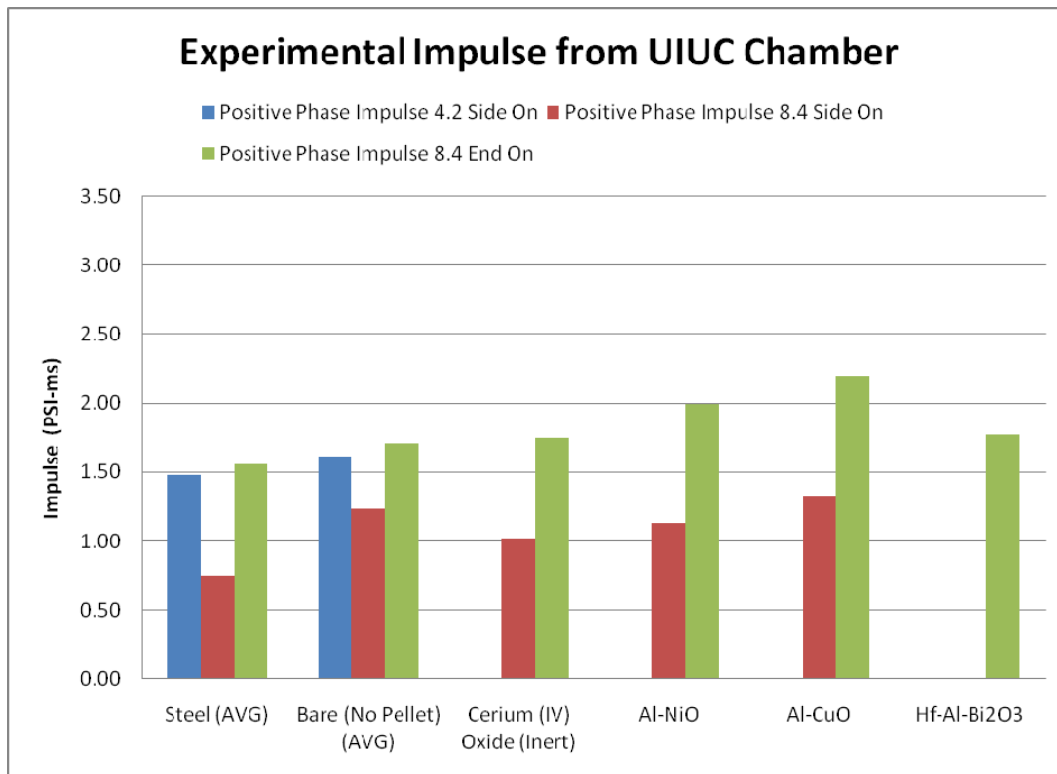
Fig. 6-5. Measured impulse of metal–metal-oxide reactive materials.

The epoxy-based materials achieved the greatest impulse, by a factor of two over the baseline bare and steel-covered detonators. While impulse levels of the metal-metal mixtures were generally lower than the epoxy-based, a few of them also performed well, particularly CSM's Hf-Al (with 50% porosity). The metal–metal-oxide group had the lowest impulse, but only a few materials were in this group.

However, the results cannot be considered definitive for several reasons. The material sample was a solid cylinder end-loaded by the small amount of explosive in a detonator. This load does not promote fracture as effectively as an explosive-filled tube, as in the ultimate application. Therefore, the weaker, softer epoxy-based materials and the higher-porosity CSM specimens would experience more fracture and greater reactivity as compared to the stronger Matsys metal-metal mixtures with only 10% porosity.

In addition, the reactive material specimens ranged in mass from about 1 to 1.8 grams. Of course it is unlikely that 100% of the reactive material was combusted in any test. The actual amount combusted and contributing to the impulse is likely small, which means the resulting increase in impulse could be too small to measure given the low fidelity of the subscale test.

6.2 Second Iteration of Subscale Tests

This subsection summarizes a second series of explosive chamber tests conducted by UIUC in April 2010. The objective of these tests was to measure the increase in quasi-static chamber pressure produced from an explosive charge surrounded by a reactive material casing as compared to a bare explosive charge and a similar charge within an inert steel casing.

6.2.1 Test Setup

The explosive charge in this test series was a PBXN-9 cylinder with a 1.0-inch diameter and a nominal ½-inch length. Its mass was nominally 10 g, with actual masses ranging from 9.61 to 10.41 g. The mass var-

iation arose from UIUC's cutting the charges from 1.0-inch-long charges, which was done in a safe but imprecise manner. This test series was conducted with some urgency, and there was insufficient time to procure charges with a precise ½-inch length.

The test assembly, shown in Fig. 6-6, consisted of the explosive, steel end plates, and casing. The ratio of the casing mass to explosive charge mass was fixed at 3. The CTH computer code predicted the explosive detonation would project the case fragments at an average velocity of 949 m/s. A ¾-inch-diameter hole in the bottom end plate allowed the charge to be supported endwise on a vertical wooden dowel. A hole in the opposite end plate accommodated a Reynolds RP-80 EBW detonator.
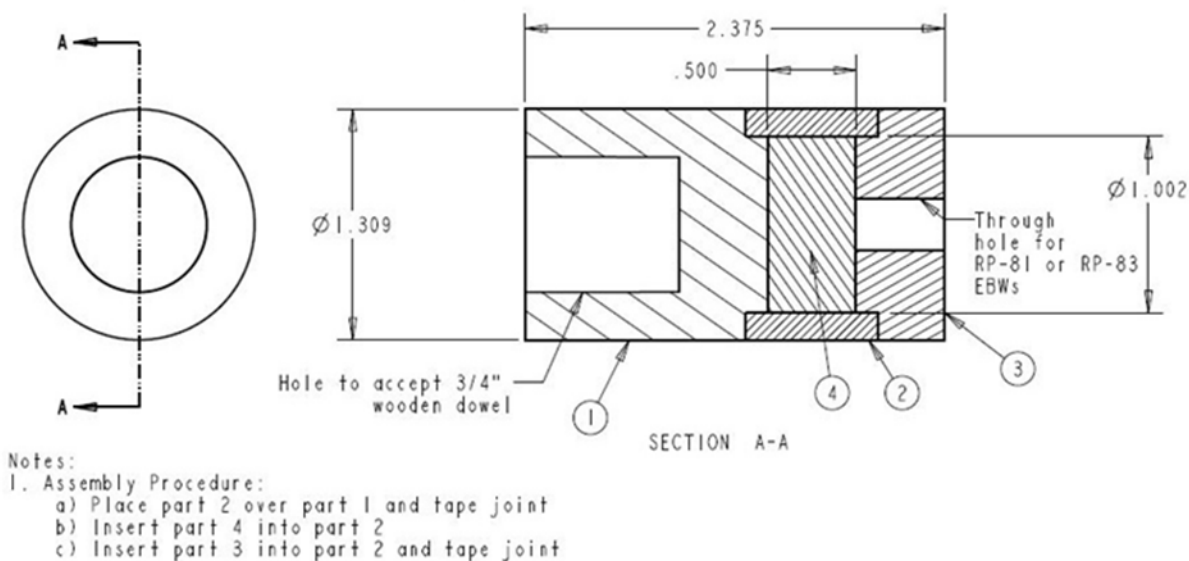
Fig. 6-6. UIUC explosive pellet test assembly.

The reactive materials tested in this series are listed in Table 6-1. Materials were supplied by DE Technologies, Matsys Corporation, and SRI International, all in the form of hollow tubes, having inside diameter of 1.002 inches and length of 0.75 inch. Casing thickness was varied with material density to provide the desired case-to-explosive mass ratio of 3. The nominal charge mass of 10 g would dictate a case mass of 30 g; however, the length of the case was ¾ inch to accommodate the end plates, ¼ inch longer than the explosive charge. Therefore the nominal casing mass was 45 g, 30 g of it over the explosive charge, and 15 g interfaced with the end plates.

Table 6-1. Materials Tested by UIUC.

Material Designation	Supplier	Desription	Strength (ksi)	Theoretical Bulk Density (g/cc)	Bulk Density (g/cc)	Components	Volume (%)	Mass (%)	Particle Size
CIP'd Aluminum	MATSYS	CIP'd Aluminum	---	2.70	2.63	Aluminum Powder	100	100	H-2 Aluminum
30W-40Al-30Epoxy	DET	Tungsten Wire Composite	95.25	7.22	6.78	Tungsten Wire	30.00	80.18	Wire, 0.004-in Dia.
						Aluminum Powder	40.00	14.96	< 44 $\perp$m, average of 7-15 $\perp$m
						Epoxy	30.00	4.86	---
30W-20Al-20B-30Epoxy	DET	Tungsten Wire Composite	95.25*	7.15	6.15	Tungsten Wire	30.00	80.99	Wire, 0.004-in Dia.
						Aluminum Powder	20.00	7.55	< 44 $\perp$m, average of 7-15 $\perp$m
						Boron Powder	20.00	6.55	< 5 $\perp$m
						Epoxy	30.00	4.91	---
15W-Al19-Hf30-36Epoxy	DET	Tungsten Wire Composite	50*	7.82	6.79	Tungsten Wire	15.00	37.02	Wire, 0.004-in Dia.
						Aluminum Powder	19.00	6.56	< 44 $\perp$m, average of 7-15 $\perp$m
						Hafnium Powder	30.00	51.03	< 44 $\perp$m
						Epoxy	36.00	5.39	---
Hf-Al	MATSYS	HIP'd Powder	57.6	7.88	7.77	Hafnium Powder	48.90	82.50	< 44 $\perp$m
						Aluminum Powder	51.10	17.50	3.2 $\perp$m
HF-Al-Bi$_2$O$_3$	MATSYS	HIP'd Powder	In Process	7.84	7.74	Hafnium Powder	39.51	67.00	< 45 $\perp$m
						Aluminum Powder	46.48	16.00	3.2 $\perp$m
						Bismuth Trioxide	14.01	16.00	< 4 $\perp$m
Ti-Al-B$_4$C	MATSYS	HIP-d Powder	77.2	3.31	3.26	Titanium Powder	34.34	47.00	< 20 $\perp$m
						Aluminum Powder	55.15	45.00	3.2 $\perp$m
						Boron Carbide	10.51	8.00	< 8 $\perp$m
W-Al-Fl_Epoxy	SRI	Tungsten Wire Composite	---	---	6.62	Tungsten Wire	30.00	---	Wire, 0.004-in Dia.
						Aluminum Powder	40.00	---	< 44 $\perp$m, average of 7-15 $\perp$m
						Fl-Epoxy	30.00	---	---
W-Hf-Al-Fl_Epoxy	SRI	Tungsten Wire Compiste	---	---	7.83/8.48+	Tungsten Wire	19.89/24.2+	---	Wire, 0.004-in Dia.
						Hafnium Powder	20.68/19.34+	---	< 44 μm, average of 22.23 μm
						Aluminum Powder	24.65/23.06+	---	< 44 μm, average of 13.91 μm
						Fl-Epoxy	22.54/31.37+	---	---
*Estimated Tensile Strength									
+Values are for two supplied specimens									

Tests were conducted in UIUC's explosive chamber, nominally a 4-foot cube with a volume of 1.812 m^3, shown in Fig. 6-7. The test assembly was supported in the center of the chamber by a wooden dowel.

(a) Exterior.   (b) Interior.

Fig. 6-7. UIUC explosive test chamber.

Instrumentation consisted of five pressure gauges of three different types. Three gauges, intended for transient pressure measurements, were lollypop-mounted inside the chamber, as shown in Fig. 6-7(b). The gauges were oriented transverse to the shock and therefore were measuring side-on pressure. Fig-

ure 6-8 shows their placement relative to the explosive charge. Two of the gauges were piezoresistive types from Kulite, model XTEL-190-200A, with a 200-psi maximum pressure. The third gauge, a piezoe-lectric type from Kistler, model 603B1, has a 15,000-psi maximum pressure and a 1-μs rise time.
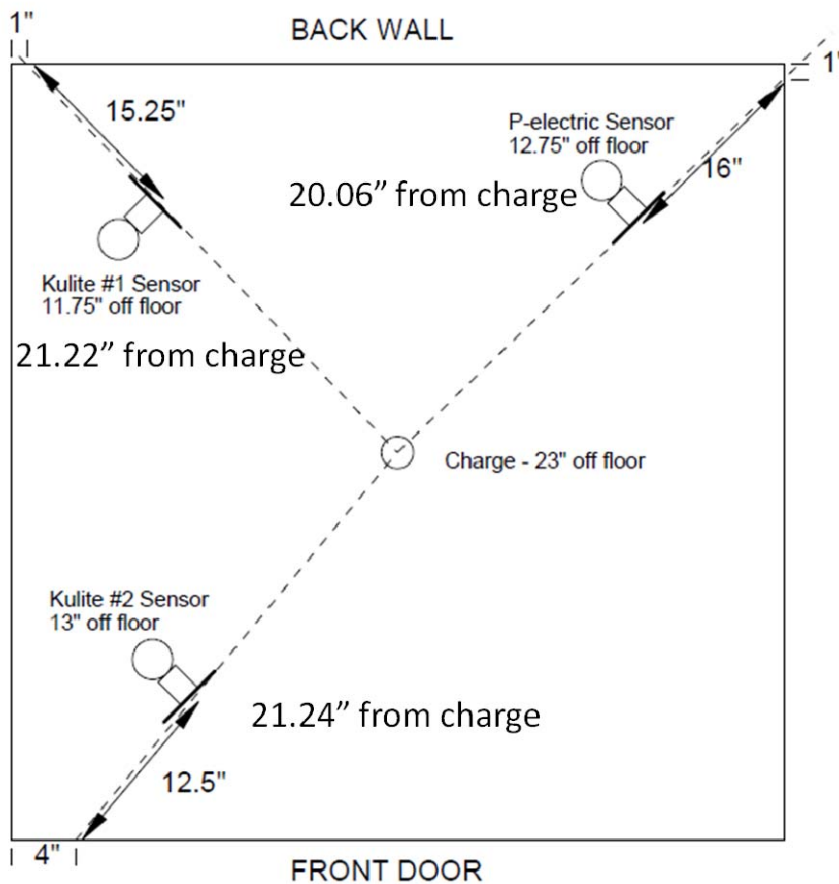
Fig. 6-8. Locations of pressure transducers on test chamber floor.

Quasi Static Pressure (QSP) was measured using Gem pressure gauges mounted on a tap from the rear wall of the chamber. Figure 6-9 shows the placement of the tap on the chamber. The GEM1 gauge was mounted with its face oriented normal to the flow within the tap, while the GEM2 gauge was mounted transverse to the flow. The Gem model 1200 gauge has a 6,000-psi maximum pressure rating.

A total of fifteen tests were conducted in this series. Table 6-2 lists the charge and casing masses. At the time of the tests, the number of explosive charges was limited. The plan was to test every reactive ma-terial type at least once. Repeat tests were then to be performed for tests in which any anomaly oc-curred and for materials that exhibited significant pressures. As discussed above, there were significant test-to-test variations in explosive charge mass; in analyzing the results, this variation was accounted for, as discussed in the *Summary and Conclusions* Section.
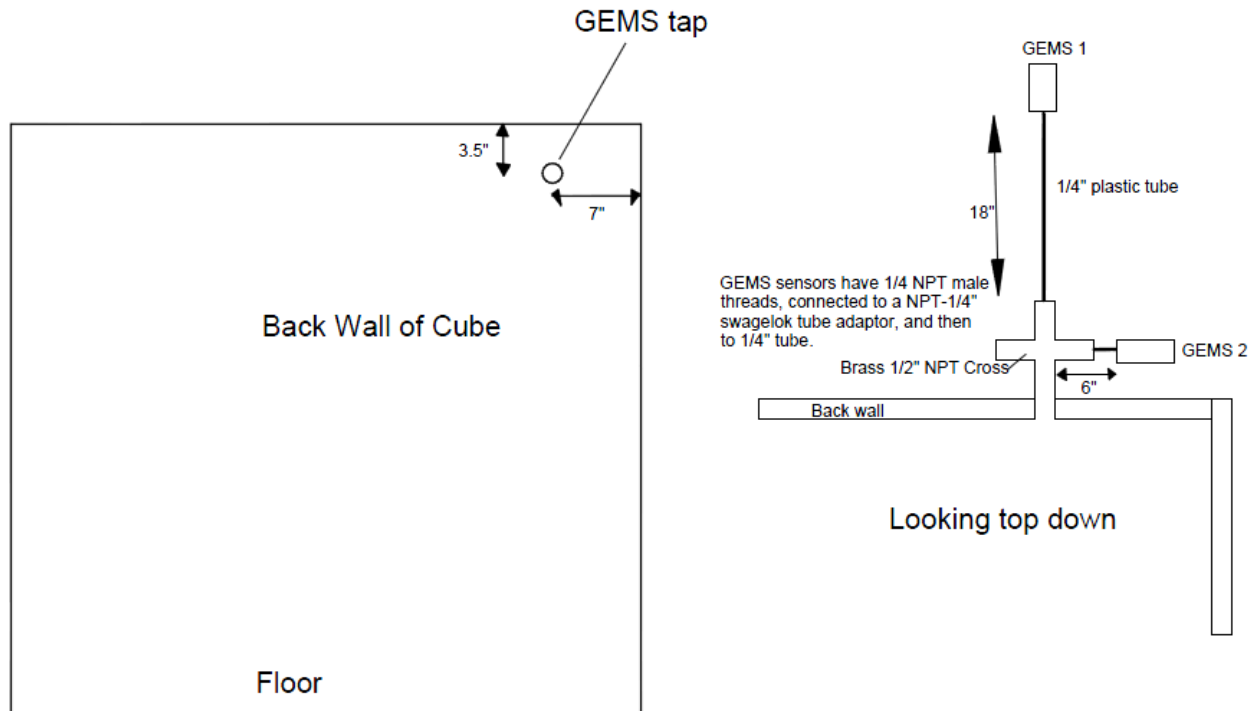
Fig. 6-9. Pressure tap and gauge location for the Quasi Static Pressure measurements.

Table 6-2. Chamber Tests Conducted by UIUC.

Test Number	Date	Description	Charge Mass (g)	Case Mass (g)
0	4/5/2010	Bare Explosive	9.70	0
1	4/14/2010	Steel Casing	10.28	52.00
2	4/14/2010	DET W-Al-Ep #6	10.11	50.96
3	4/14/2010	MATSYS Hf-Al #1	9.75	54.80
4	4/14/2010	SRI W-Al-FEp CS-11	9.75	51.0
5	4/14/2010	DET W-Al-B-Ep #1	10.03	48.67
6	4/14/2010	MATSYS Hf-Al-Bi$_2$O$_3$ #1	10.20	54.82
7	4/14/2010	SRI W-Al-Hf-FEp CS-13	9.61	54.14
8	4/14/2010	DET W-Hf-Al-Ep #5	10.05	50.04
9	4/14/2010	MATSYS Hf-Al-B$_4$C #1	9.74	23.69
10	4/14/2010	MATSYS CIP'd AL #1	9.74	25.98
11	4/14/2010	Steel Casing	10.00	52.00
12	4/15/2010	MATSYS Hf-Al-Bi$_2$O$_3$ #2	9.85	54.81
13	4/15/2010	DET W-Hf-Al-Ep	9.99	49.23
14	4/15/2010	SRI W-Al-Hf-FEp CS-12	10.41	50.70

6.2.2 Quasi-Static Pressure

Test "0" was of the bare explosive charge. The quasi-static pressure (QSP) in the chamber is plotted versus time in Fig. 6-10 for both Gem gauges. The data show that pressure oscillates with deceasing amplitude. A linear fit was done to the pressure data between 40 ms and 190 ms. The y intercept of the fit is taken as the QSP value indicated in the figure. For Test "0", the QSPs from Gem1 and Gem 2 were 2.92 and 2.94 psi, respectively. The linear-fit process was used to determine the QSP for all of the tests.
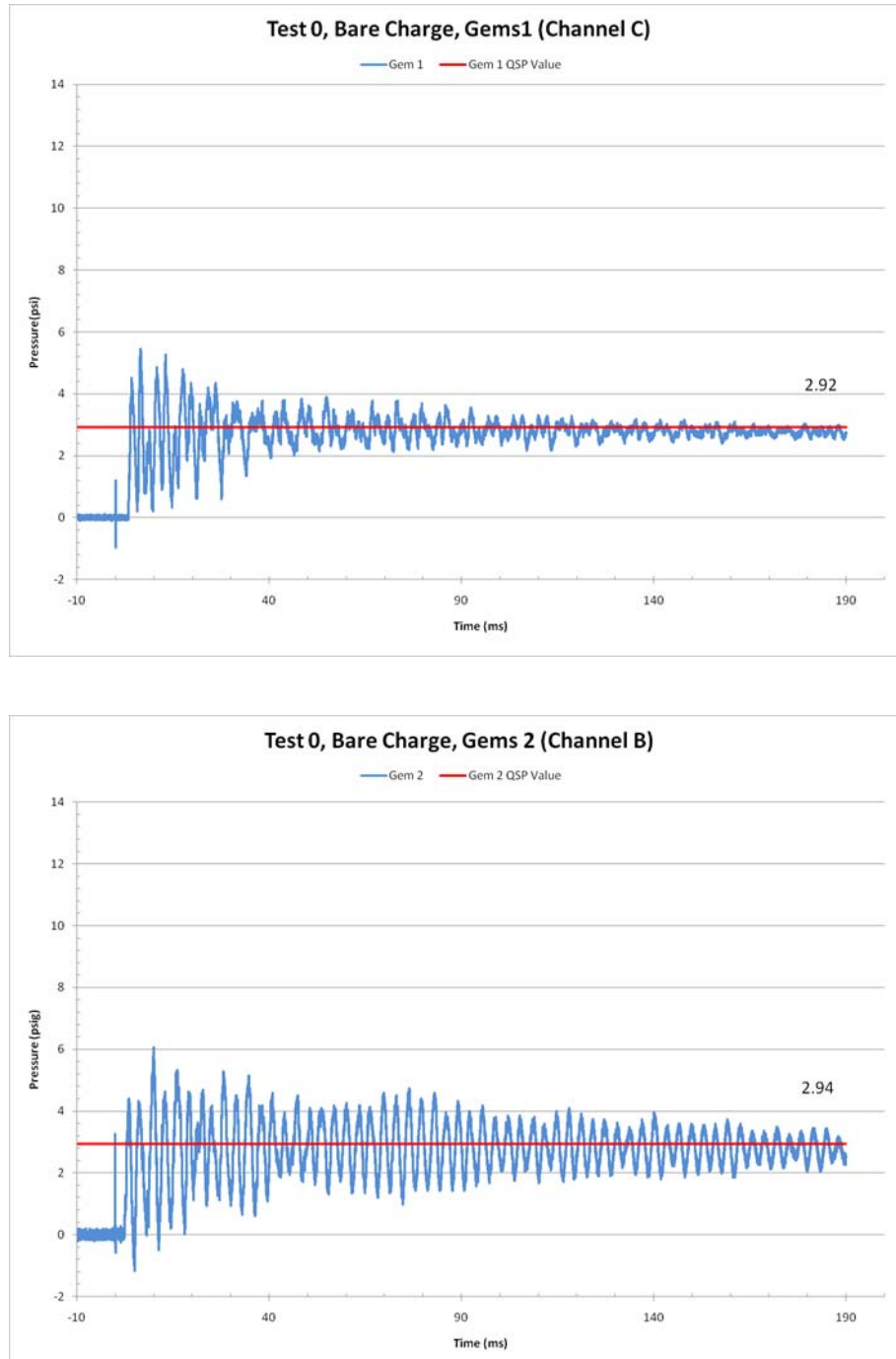
Fig. 6-10. Quasi-static pressure histories from Test 0, bare explosive charge.

Figures 6-11 and 6-12 show the QSP histories from the two tests of the steel-encased charge, Tests "1" and "11". As expected, the steel casing yielded QSP values lower than those of the bare charge.
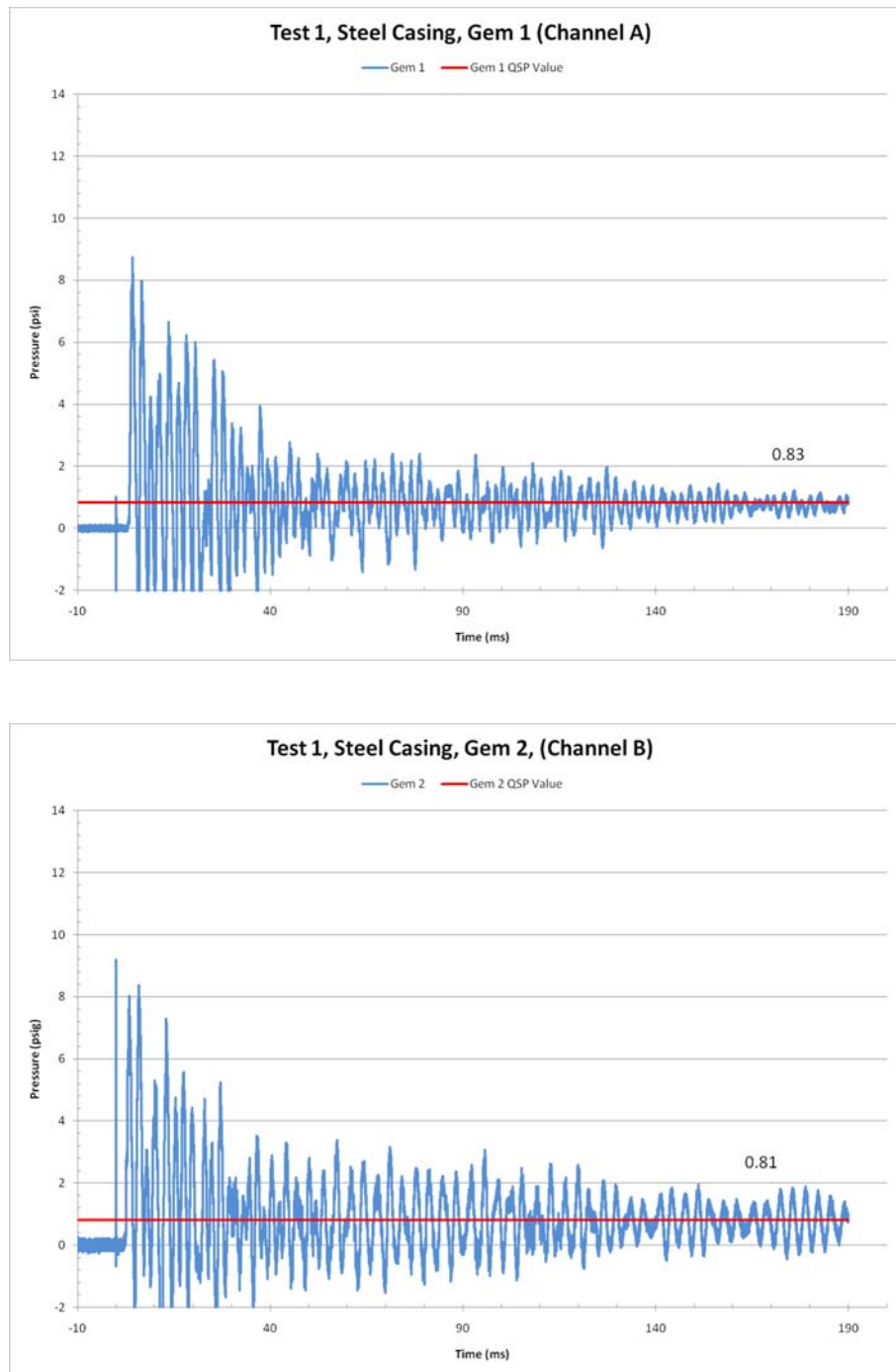
Fig. 6-11. Quasi-static pressure histories from Test 1, steel casing.
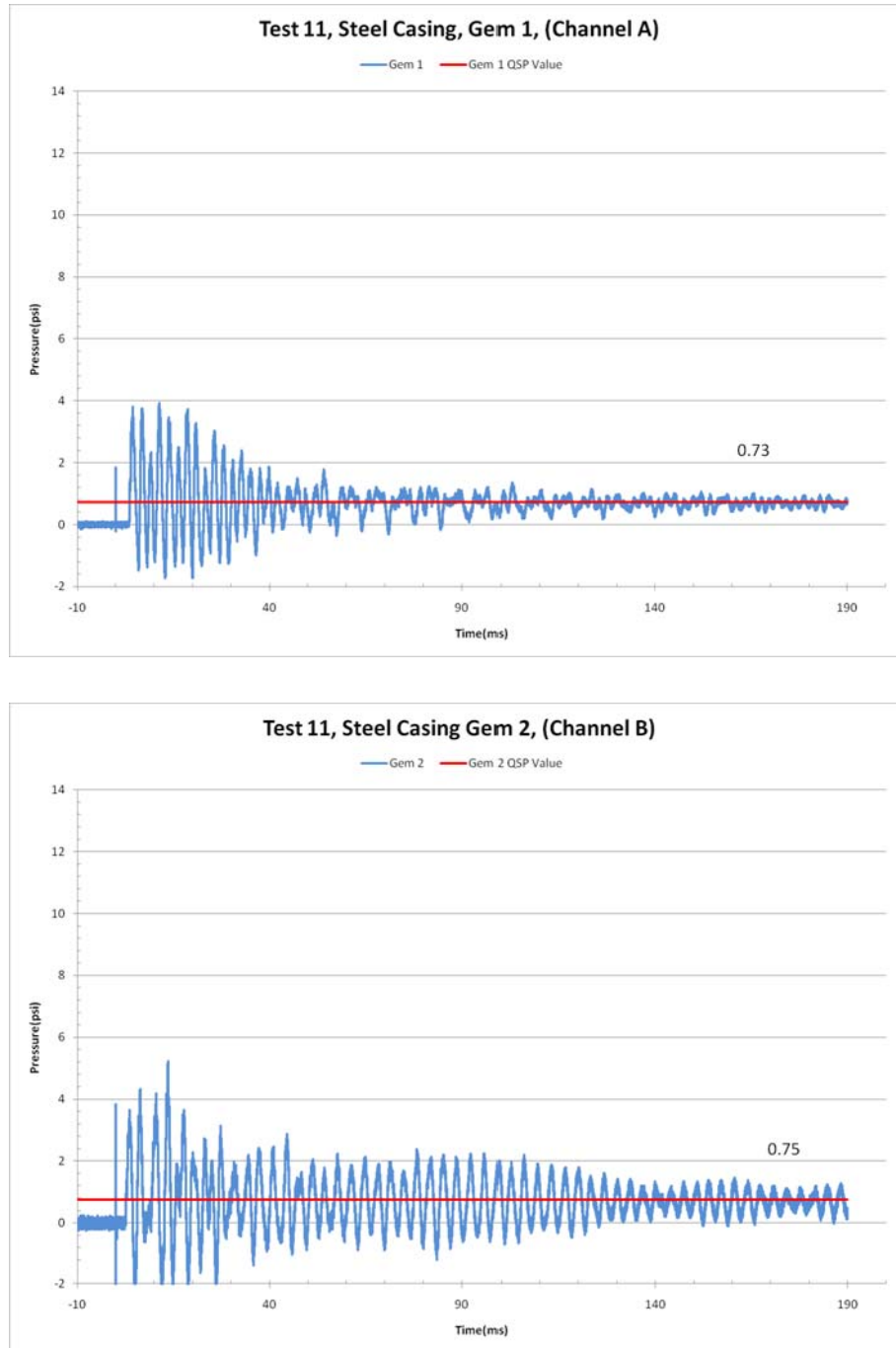
Fig. 6-12. Quasi-static pressure histories from Test 11, steel casing.

Figures 6-13 through 6-24 show the QSP histories in sequential order for the reactive material casings. One test of each reactive material was performed. All of the reactive material casings produced pressures greater than the bare and steel-encased charges. QSPs for the reactive materials ranged from 4.13 to 8.49 psi.

The materials that yielded the three highest QSPs were tested again. The material with the highest QSP was the Matsys Hf-Al-Bi$_2$O$_3$ formulation, with values of 8.17 and 8.16 psi. The QSP histories from this test

are shown in Fig. 6-17. The retest of this material was Test 12, for which the QSP versus time data are shown in Fig. 6-22; the QSP values for both gauges were 8.49 psi.
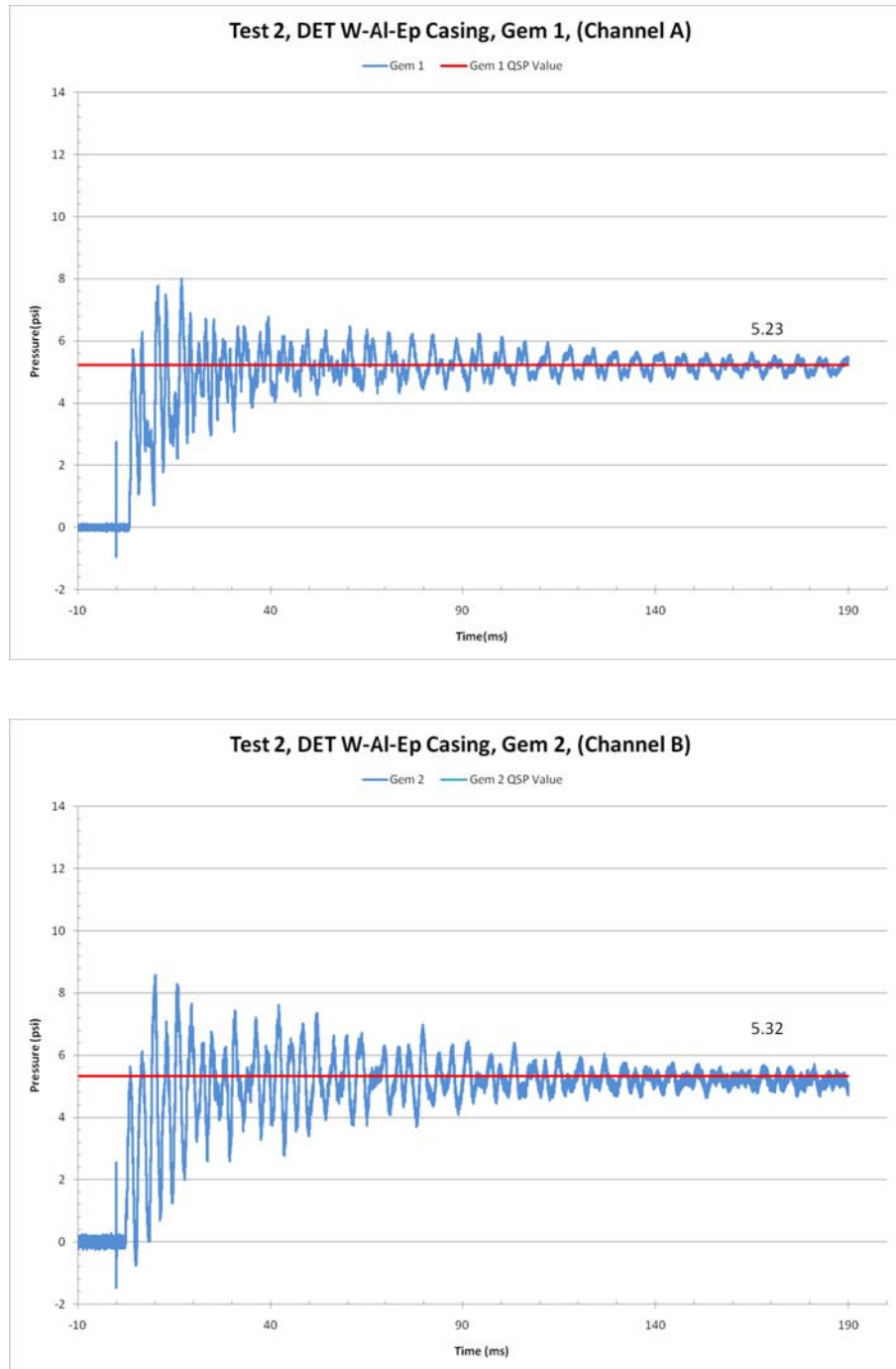
Fig. 6-13. Quasi-static pressure histories from Test 2, DET W-Al-Epoxy casing.

The material that produced the second highest chamber pressure was the DET W-Al-Hf-Epoxy in Test 8, with QSP values of 6.20 and 6.44 psi; the QSP histories from this test are shown in Fig. 6-19. For the second test of this material, Test 13, the QSP versus time data are shown in Fig. 6-23; the QSP values were 5.88 and 6.08 psi.

The material that yielded the third highest chamber pressure was SRI's W-Al-Hf-Ep system, data of which are shown in Fig. 6-18; the QSPs were 6.01 and 6.10 psi. For the repeat of this test, Test 14, the data are shown in Fig. 6-24; the QSPs were 5.76 and 5.82 psi.
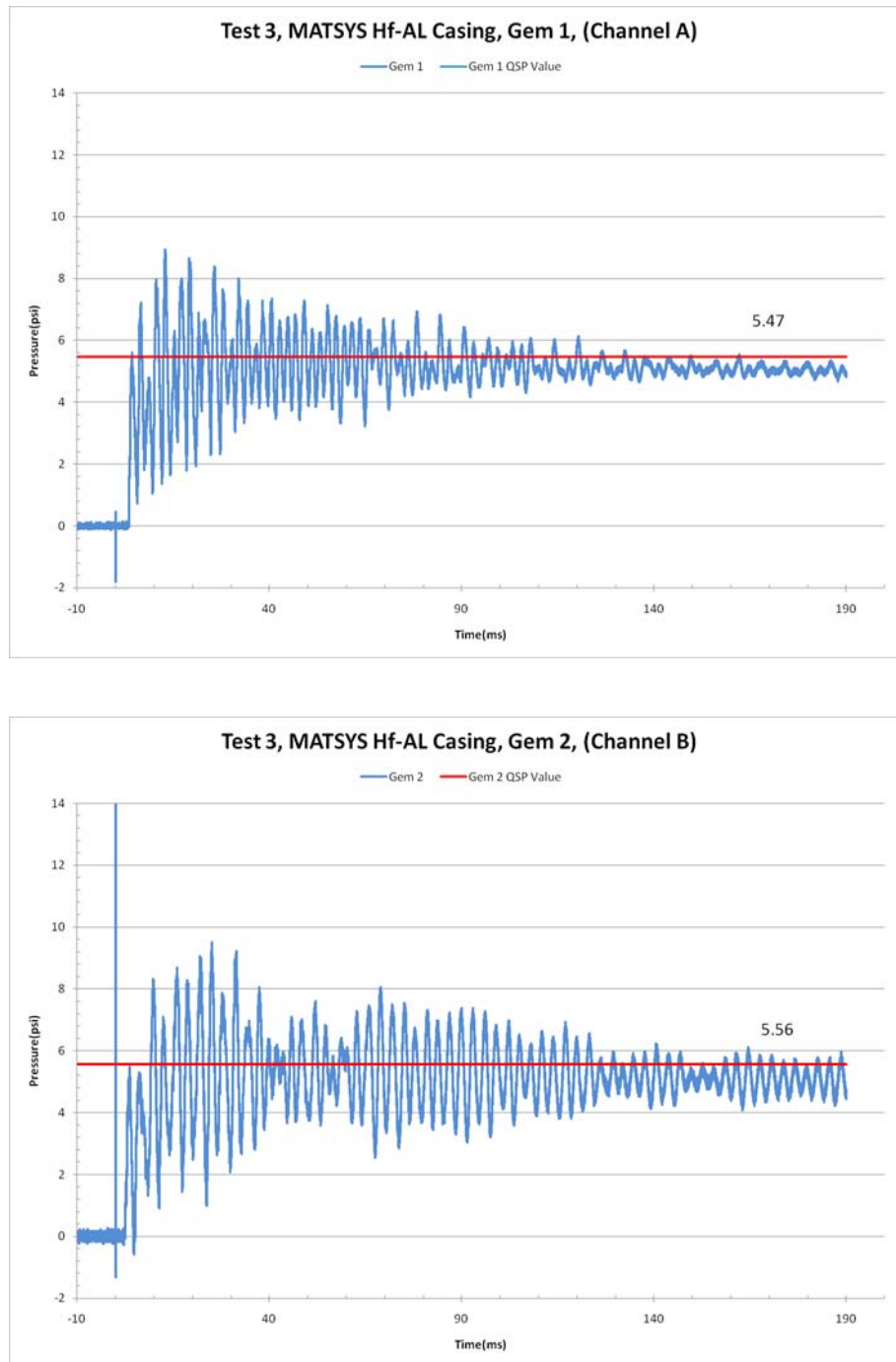
Fig. 6-14. Quasi-static pressure histories from Test 3, Matsys Hf-Al casing.
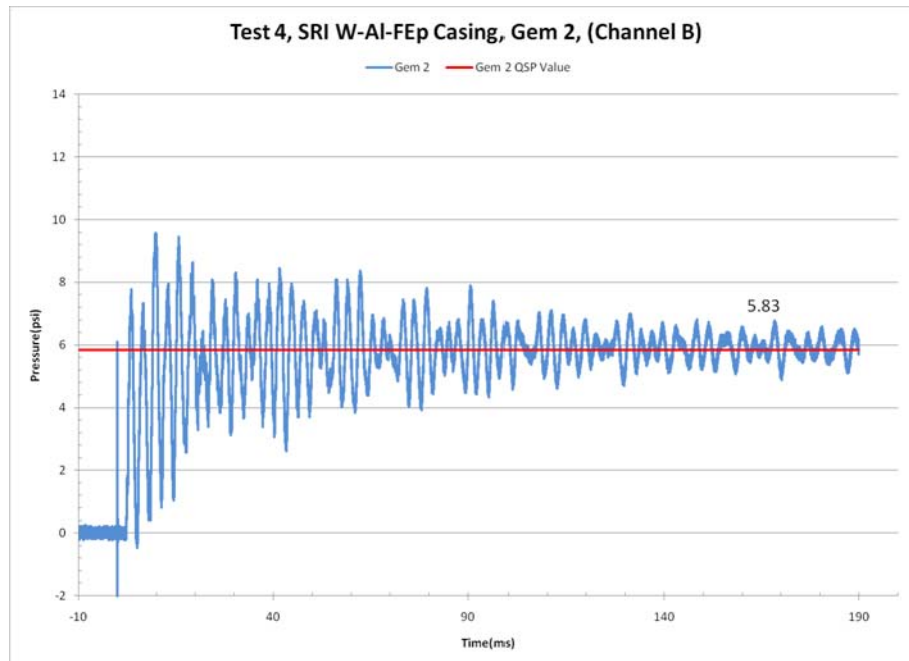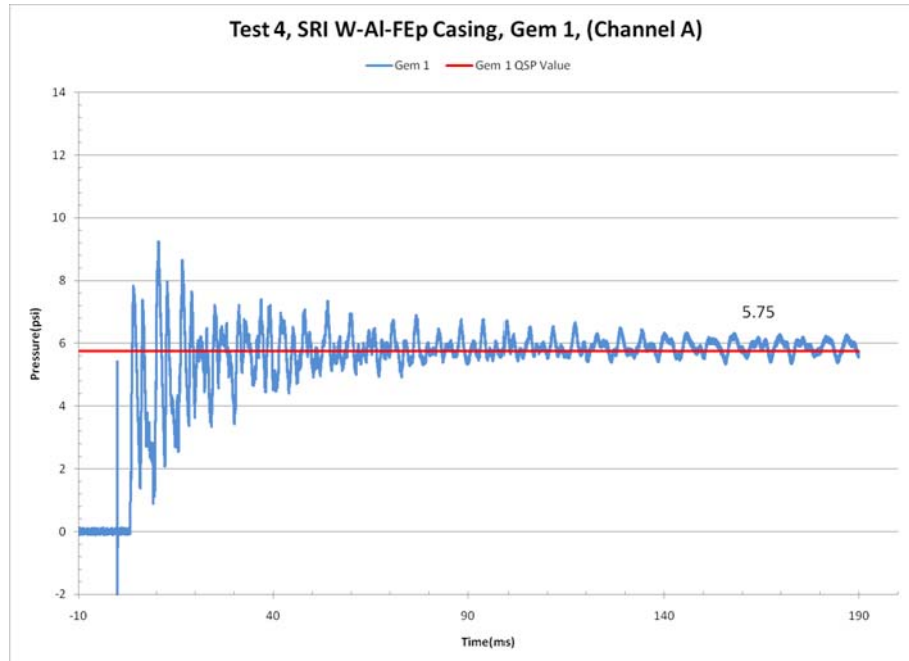
Fig. 6-15. Quasi-static pressure histories from Test 4, SRI W-Al-FlEp casing.
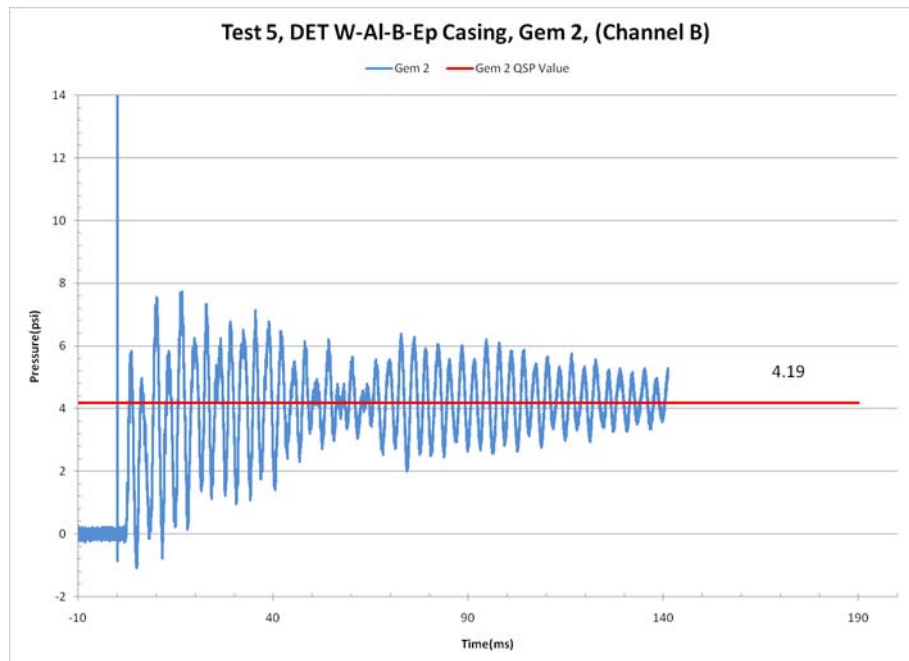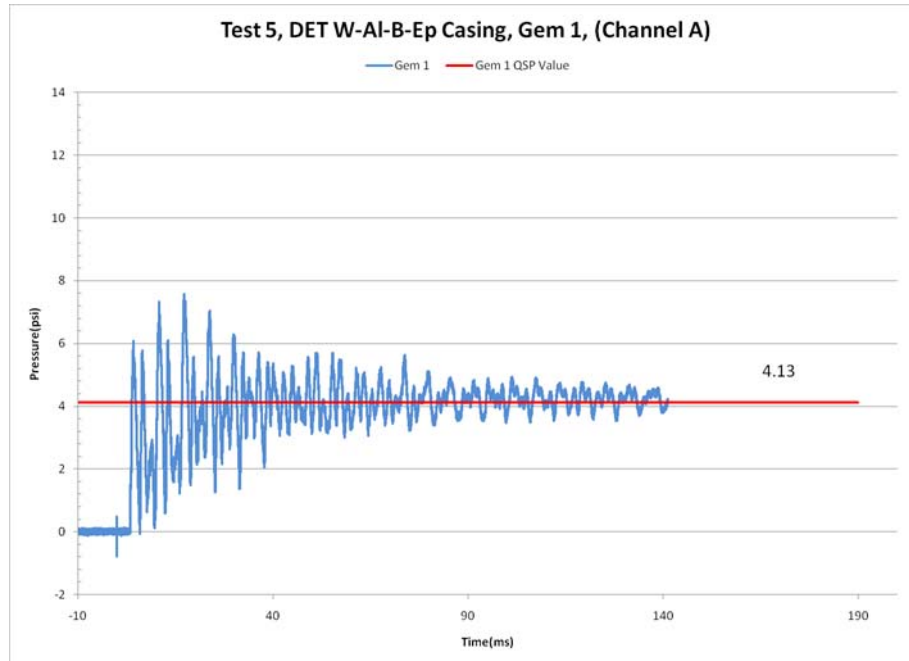
Fig. 6-16. Quasi-static pressure histories from Test 5, DET W-Al-B-Ep casing.
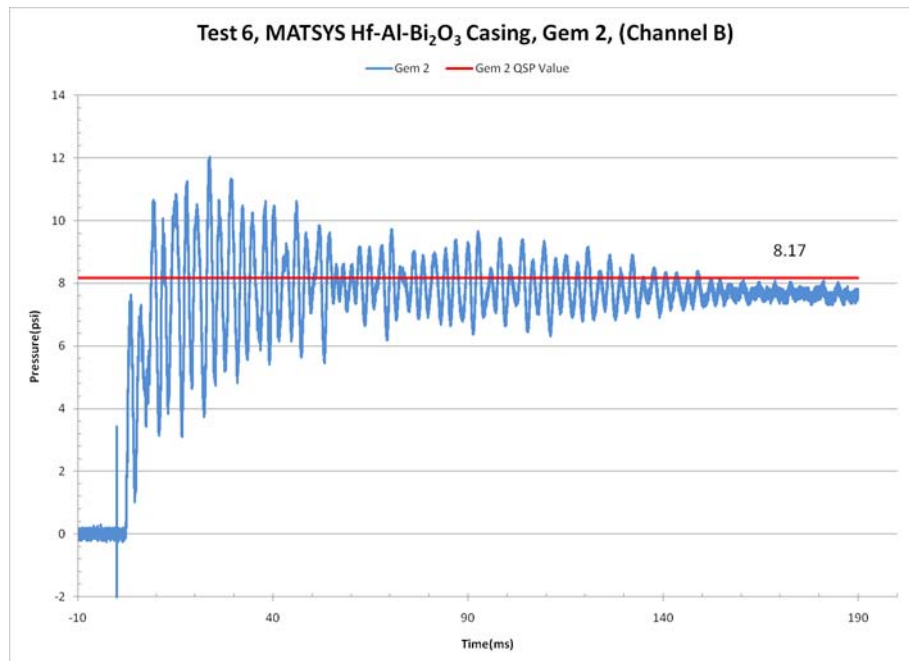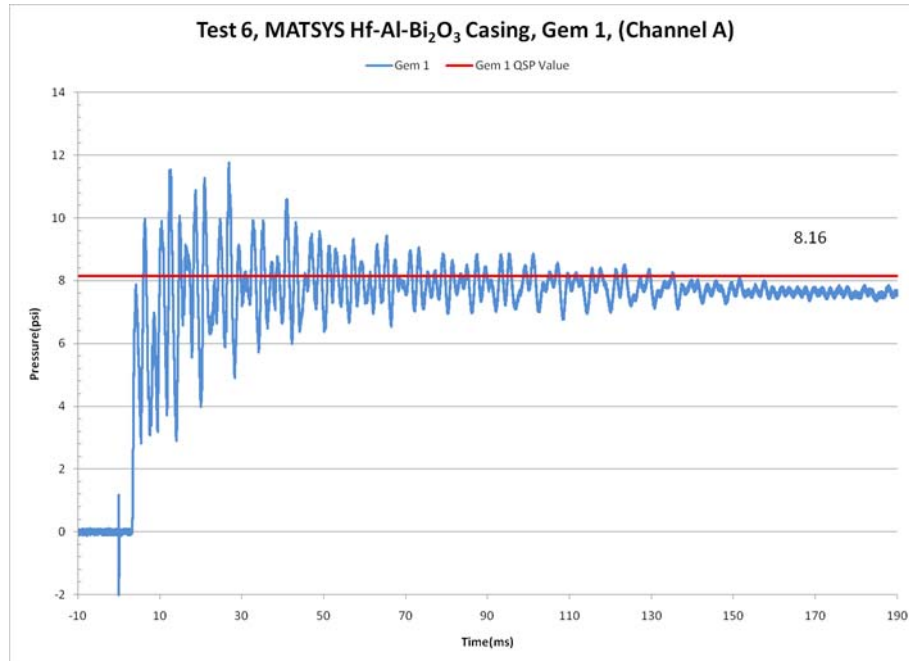
Fig. 6-17. Quasi-static pressure histories from Test 6, Matsys Hf-Al-Bi$_2$O$_3$ casing.
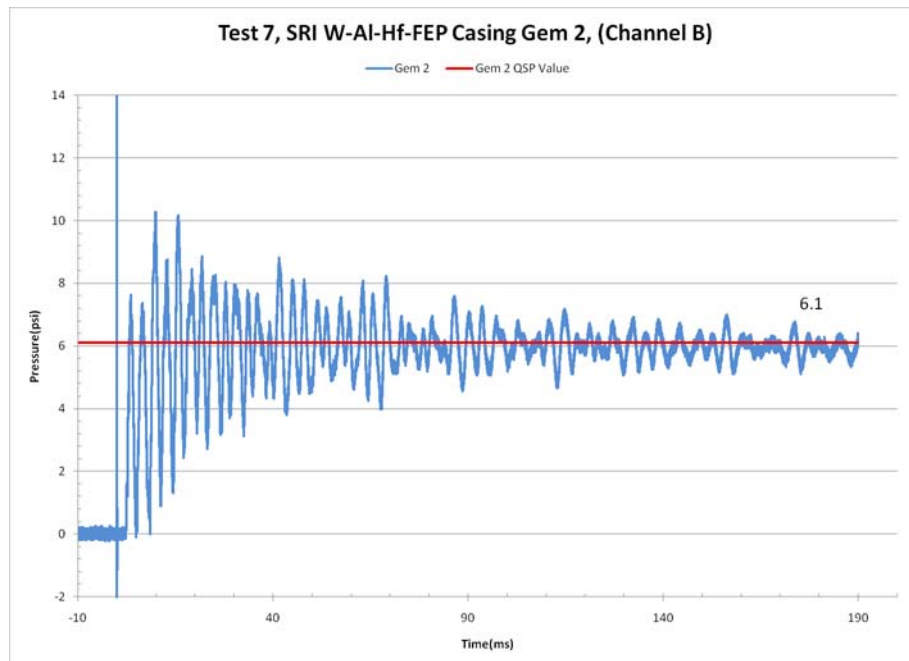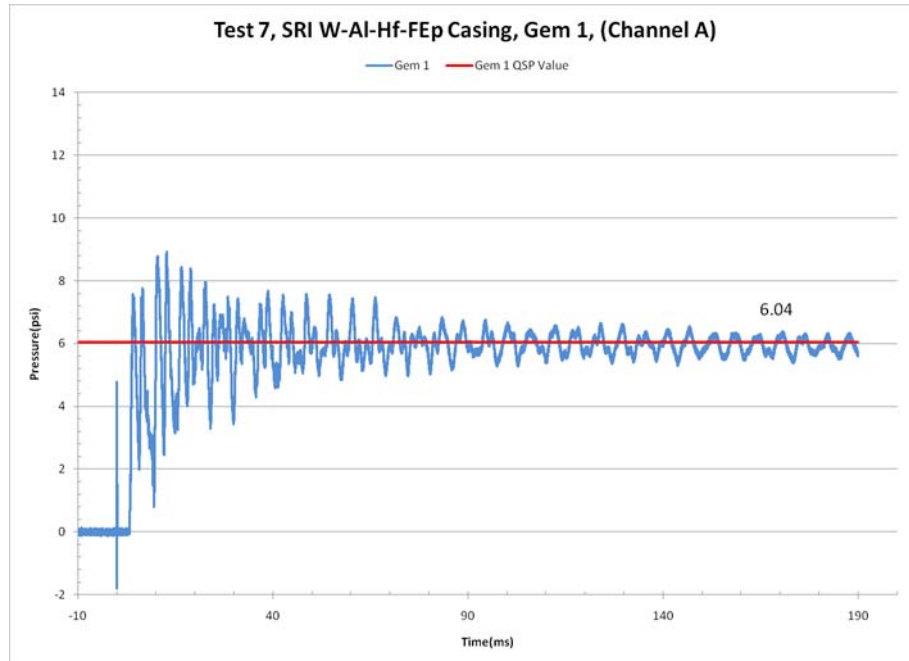
Fig. 6-18. Quasi-static pressure histories from Test 7, SRI W-Al-Hf-FlEp casing.
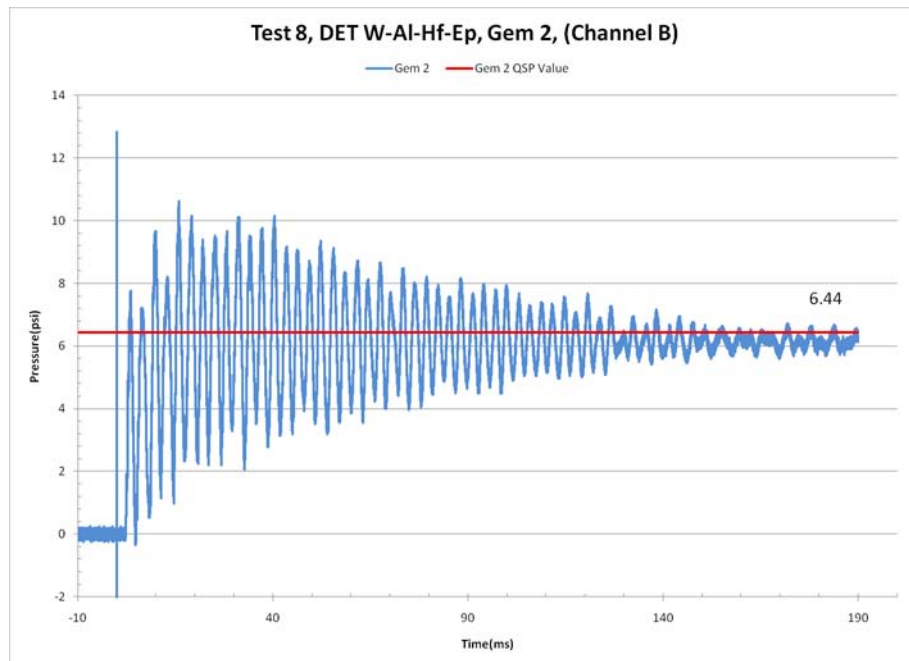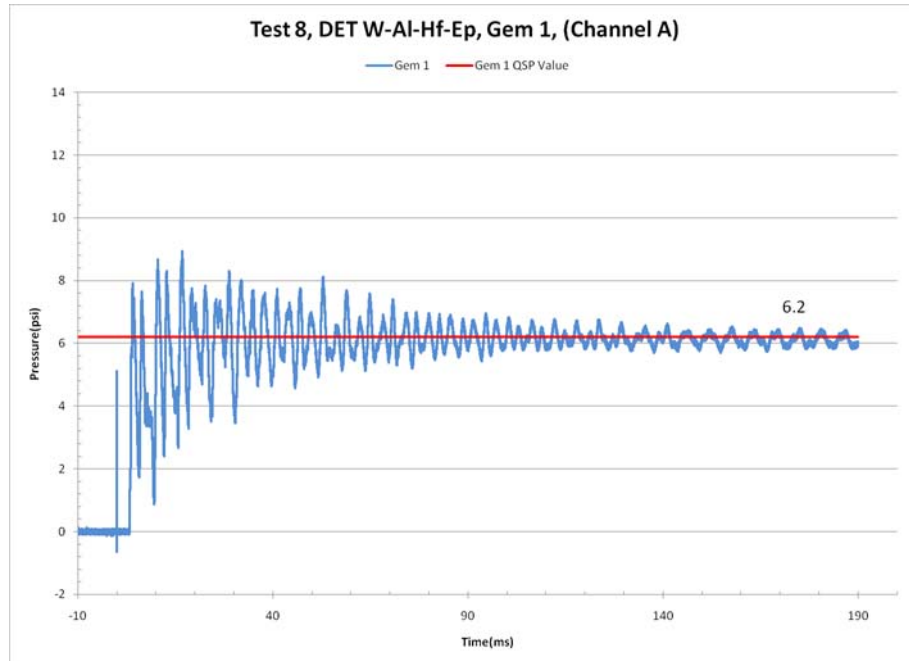
Fig. 6-19. Quasi-static pressure histories from Test 8, DET W-Al-Hf-Ep casing.
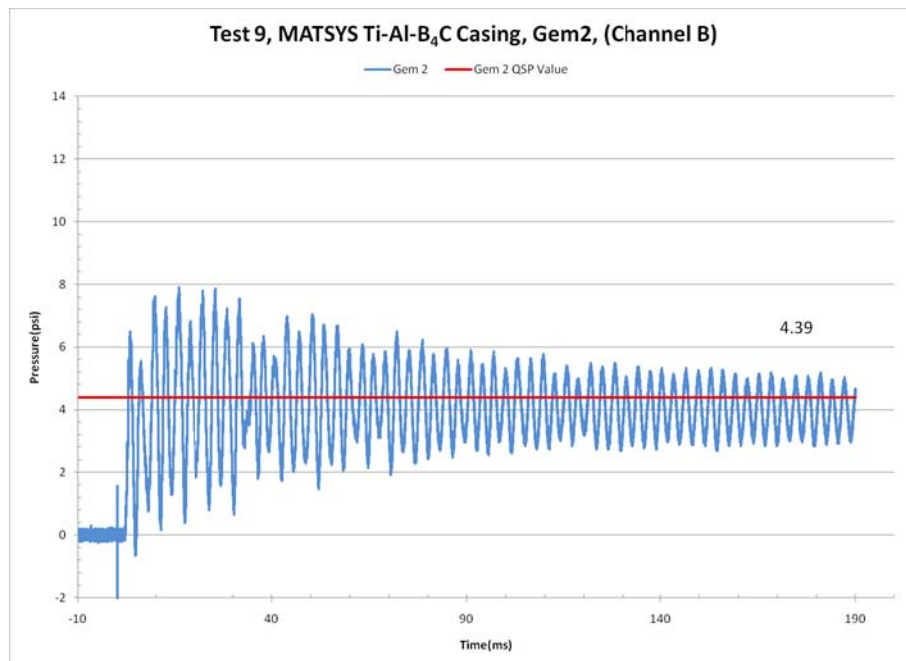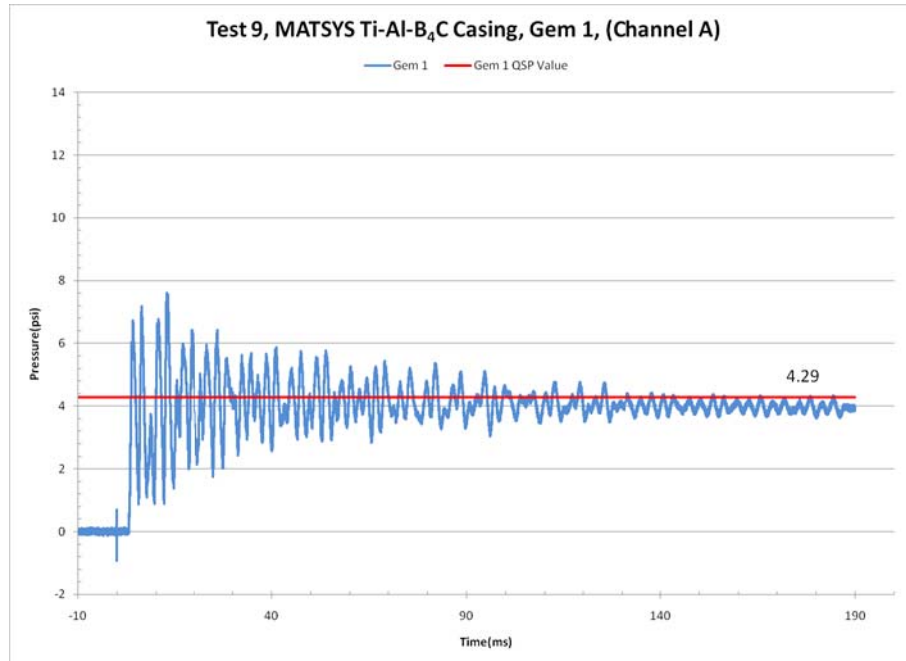
Fig. 6-20. Quasi-static pressure histories from Test 9, Matsys Ti-Al-B$_4$C casing.
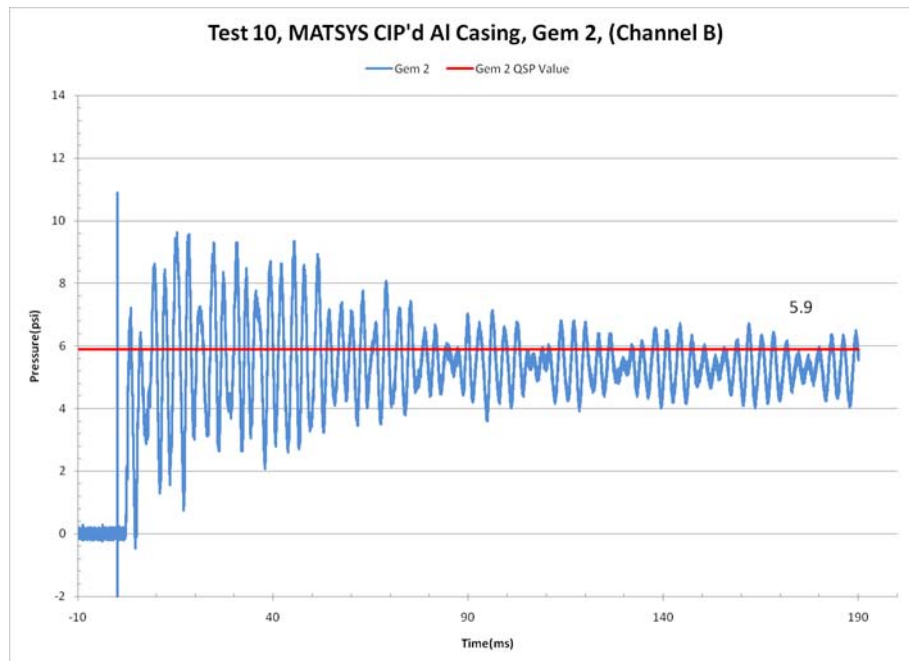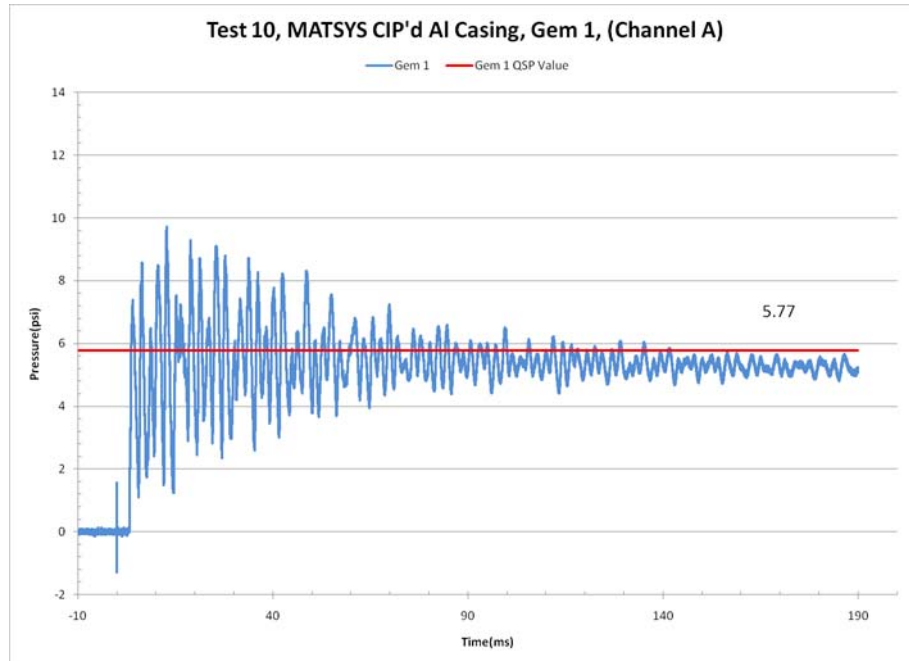
Fig. 6-21. Quasi-static pressure histories from Test 10, Matsys CIPed Al casing.
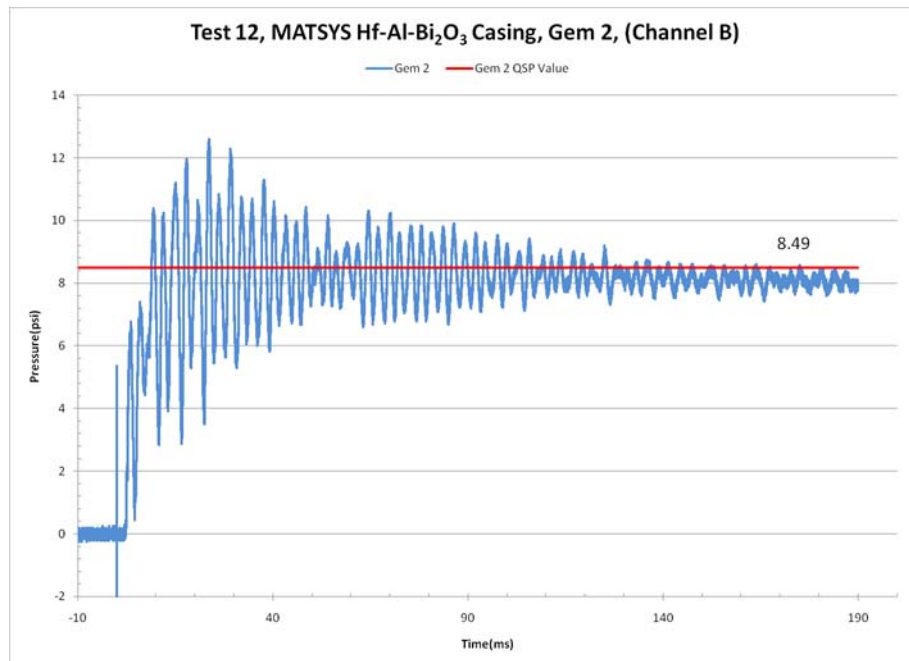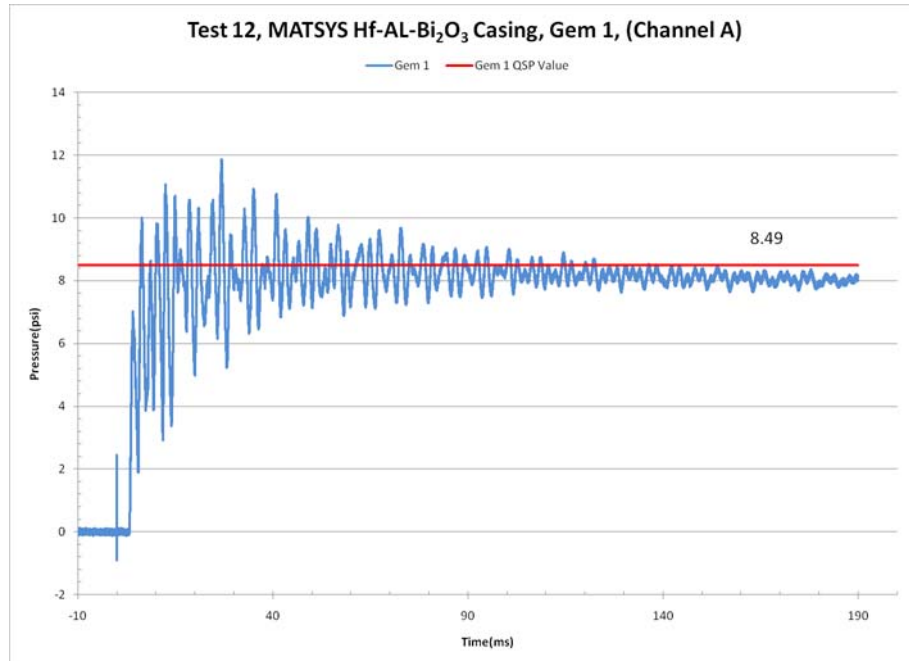
Fig. 6-22. Quasi-static pressure histories from Test 12, Matsys Hf-Al-Bi$_2$O$_3$ casing.
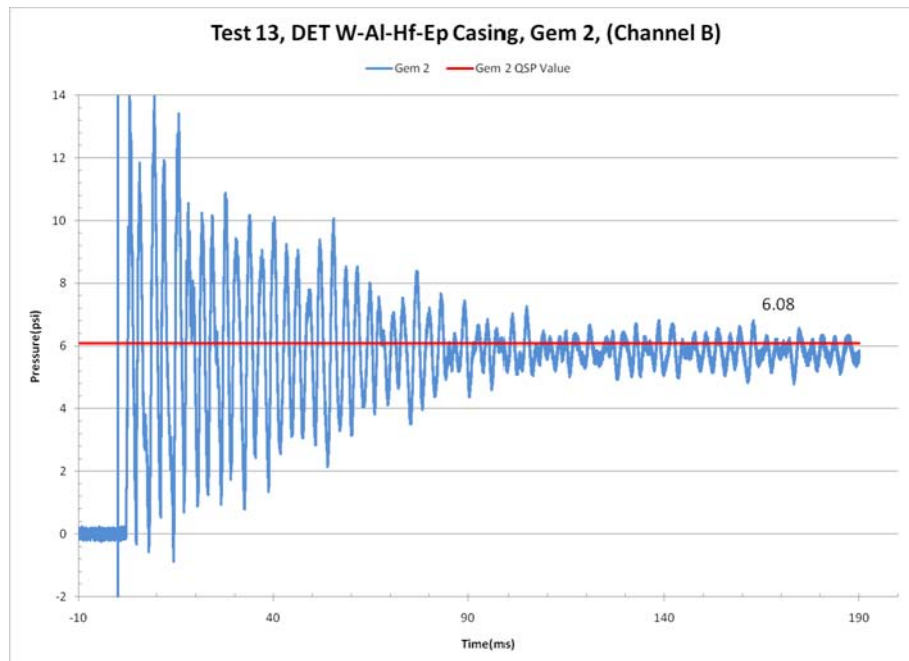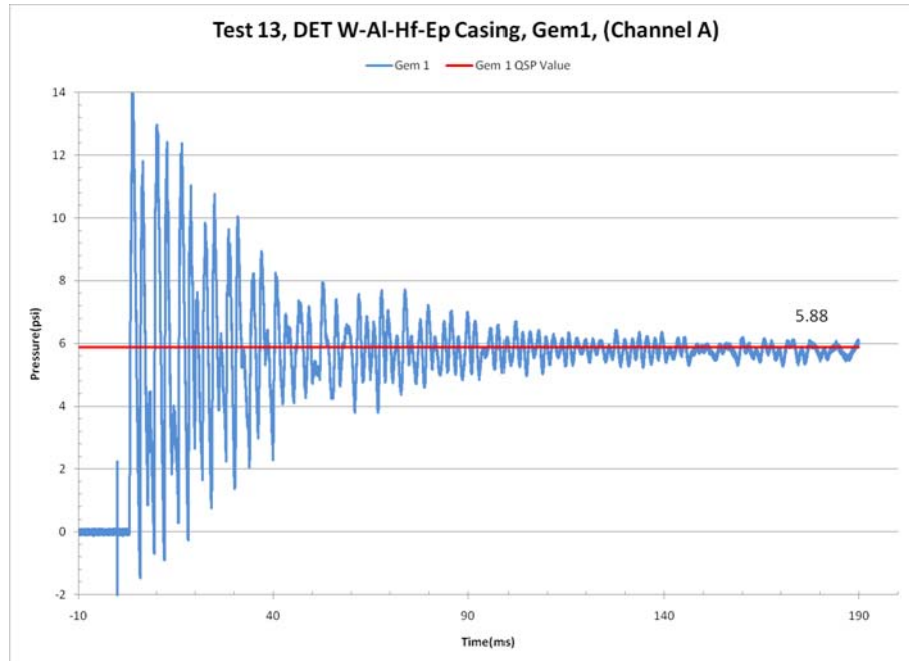
Fig. 6-23. Quasi-static pressure histories from Test 13, DET W-Al-Hf-EP casing.
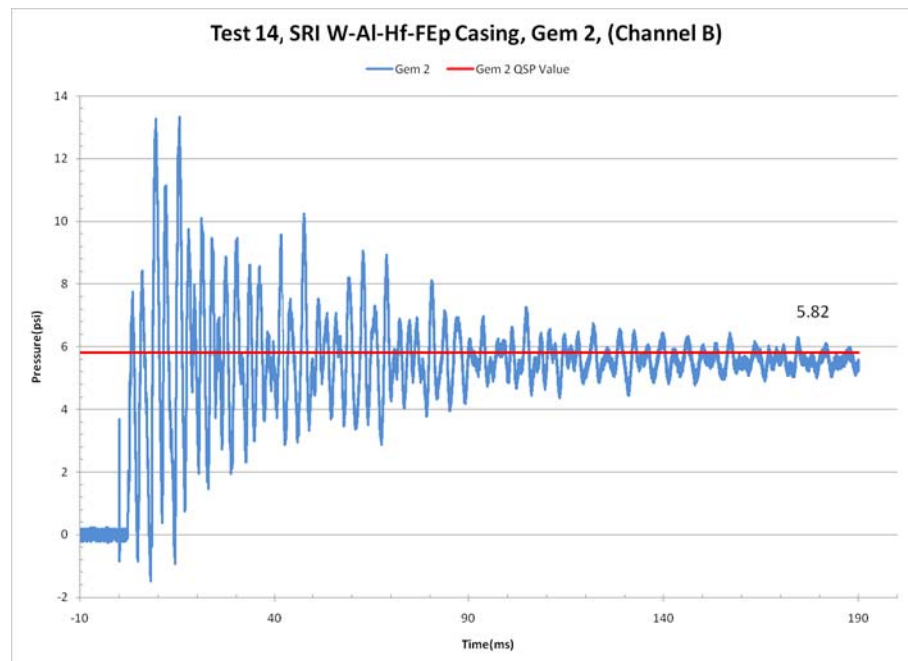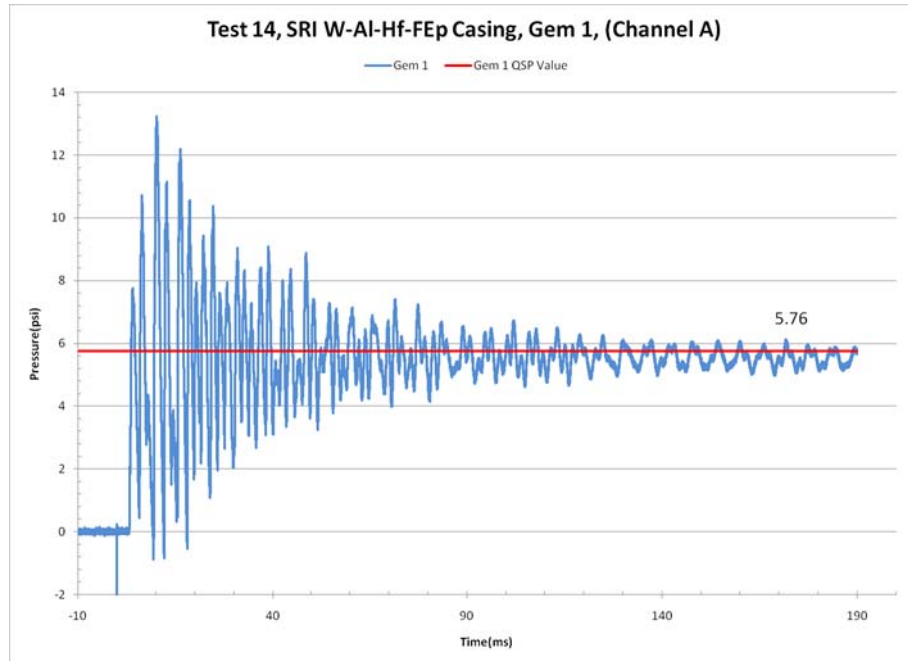
Fig. 6-24. Quasi-static pressure histories from Test 14, SRI W-Al-Hf-FlEP casing.

The QSP values for all the tests are listed in Table 6-3.

Table 6-3. Summary of Quasi-Static Pressures in UIUC Chamber Tests.

Test #	N-9 Explosive Mass (g)	Case Mass (g)	Casing Material	Quasi-Static Pressure (psi)	
				Gems 1	Gems 2
0	9.70		Bare N9 Explosive	2.92	2.94
1	10.28	52.00	Steel #1	0.83	0.81
2	10.11	50.96	DET#6 W-Al-Ep	5.23	5.32
3	9.74	54.80	Matsys#1 Hf-Al	5.47	5.56
4	9.75	51.00	CS11 W-Al-FlEp	5.75	5.83
5	10.03	48.67	DET#1 W-Al-B-Ep	4.13	4.19
6	10.20	54.82	Matsys Hf-Al-Bi$_2$O$_3$	8.16	8.17
7	9.61	54.14	SRI Cs13 W-Al-Hf-FlEp	6.04	6.10
8	10.05	50.04	DET#5 W-Al-Hf-Ep	6.20	6.44
9	9.74	23.69	Matsys Al-Ti-B$_4$C	4.29	4.39
10	9.74	25.98	Matsys CIP'd Al	5.77	5.90
11	10.00	52.00	Steel #2	0.73	0.75
12	9.85	54.81	Matsys#2 Hf-Al-Bi$_2$O$_3$	8.49	8.49
13	9.99	49.23	DET#4 W-Al-Hf-Ep #4	5.88	6.08
14	10.41	50.70	SRI CS12 W-Al-Hf-FlEp	5.76	5.82

6.2.3 Transient Pressure

The fast-acting Kulite pressure gauges were used to record the side-on pressure to a time of 12 ms after explosive initiation. The pressure versus time plots for Test "0" of the bare charge are shown in Fig. 6-25, in which Gauges "A" and "B" correspond to Kulite #1 and #2 in Fig. 6-8, located 21.22 and 21.24 inches from the charge. The peak pressures recorded by the two gauges were 16.27 and 16.99 psi. The corresponding arrival times were 617.0 and 571.4 μs.

The pressure histories from the Tests 1 and 11 with the steel casing are shown in Figs. 6-26 and 6-27. The peak pressures recorded by the A and B gauges in Test 1 were 8.46 and 8.02 psi, and in Test 11 are 9.26 and 8.4 psi. These values are nearly half the peak values produced by the bare charge.

The pressure histories for the reactive materials are shown in Figs. 6-28 to 6-39. The peak pressures and arrival times for all the tests are listed in Table 6-4. In general, the reactive materials produced peak pressures significantly higher than that of steel and on the order of the pressure produced by the bare charge. Further, it can be seen that the pressure traces produced by the reactive materials are steadily rising over the recorded time period; this rise is attributable to the QSP discussed above.
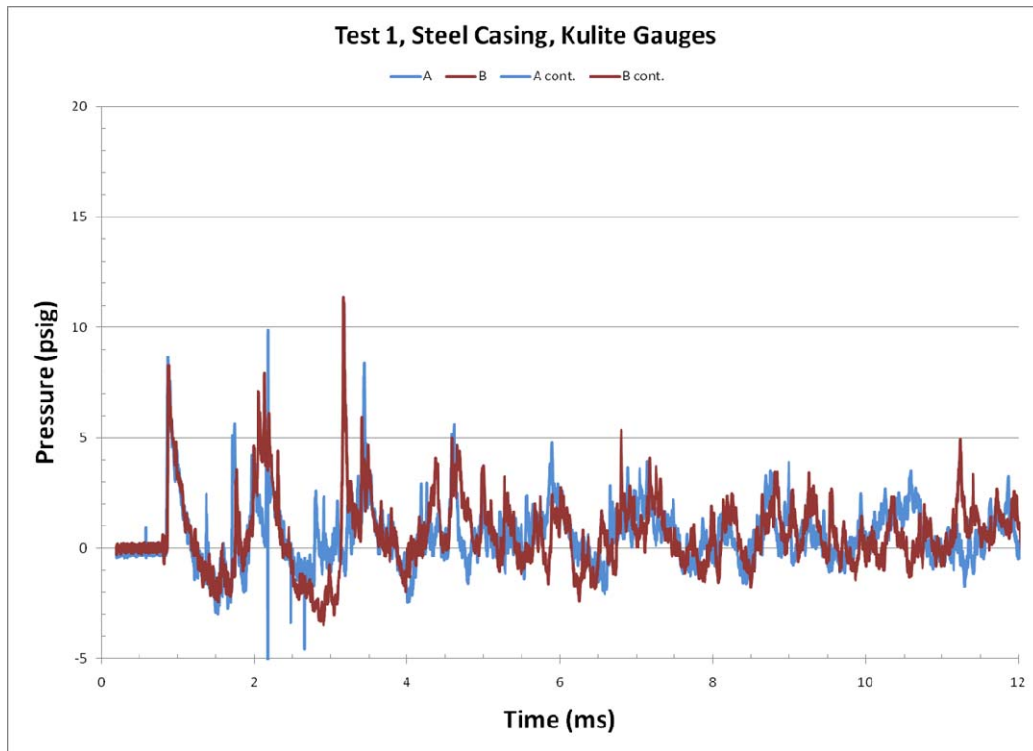
Fig. 6-25. Early-time pressure histories from Test 0, bare explosive charge.
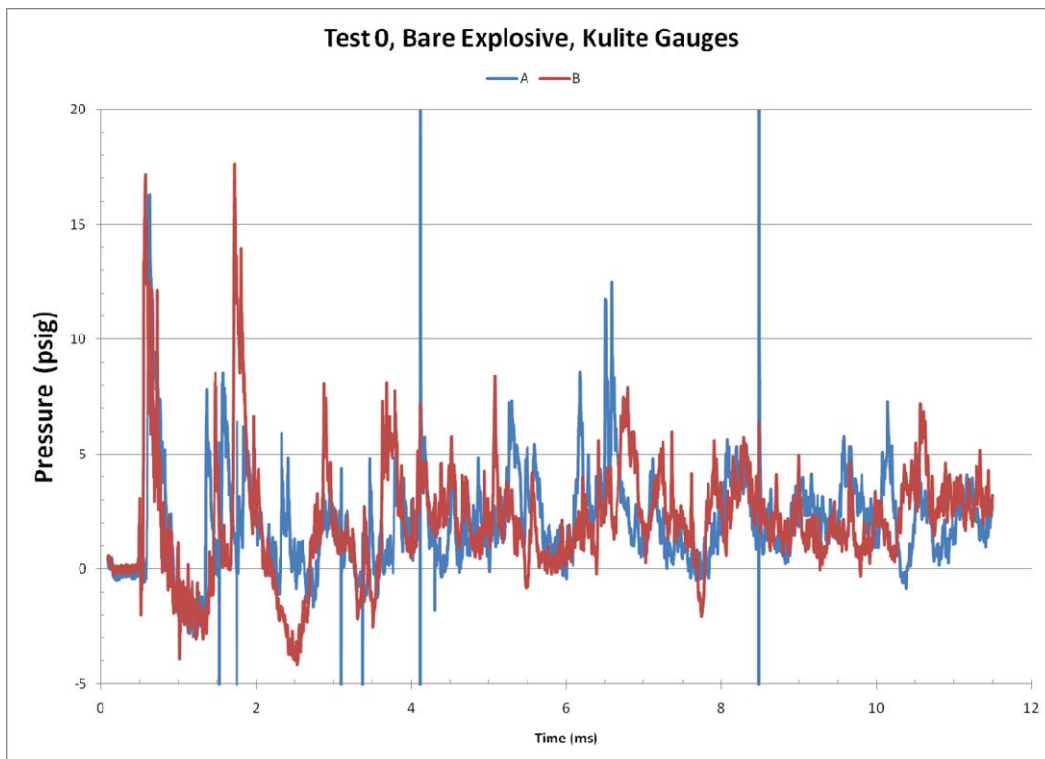
Fig. 6-26. Early-time pressure histories from Test 1, steel casing.
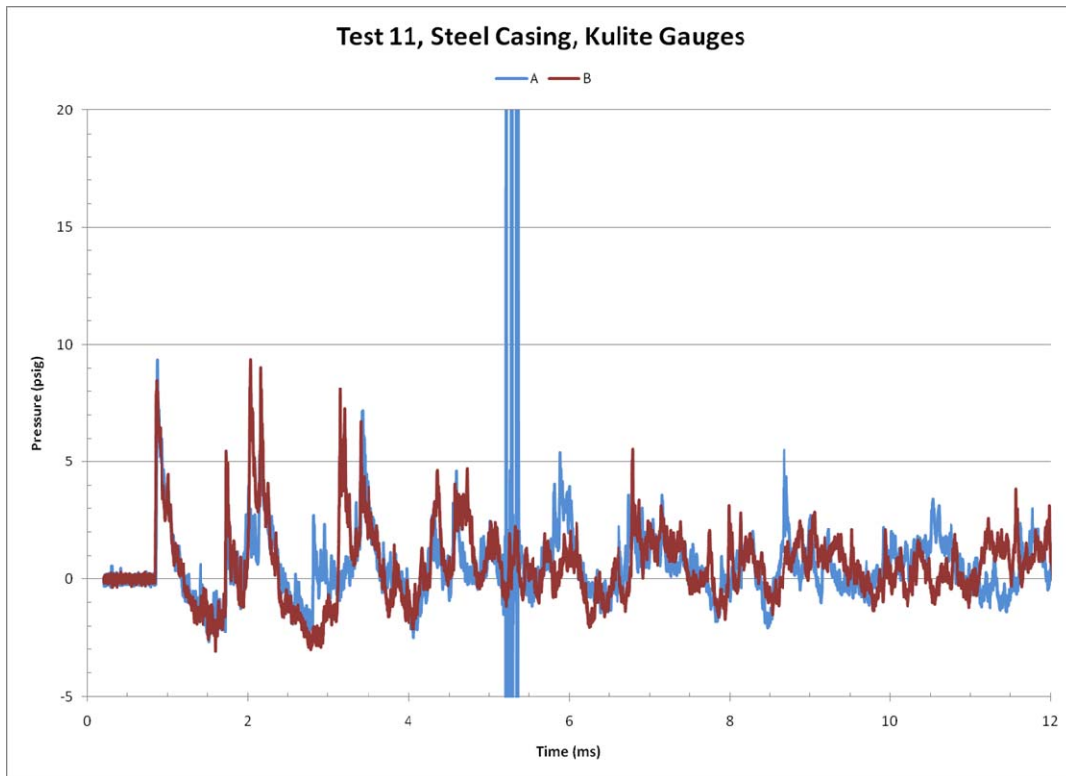
Fig. 6-27. Early-time pressure histories from Test 11, steel casing.
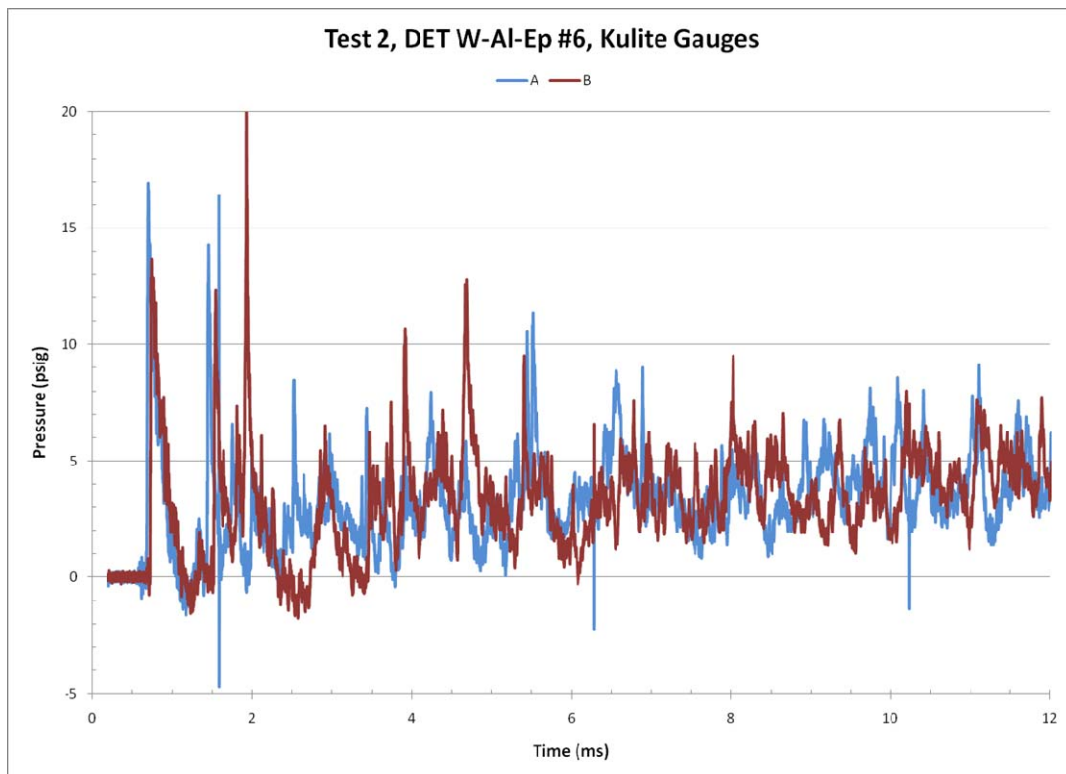
Fig. 6-28. Early-time pressure histories from Test 2, DET W-Al-Epoxy casing.
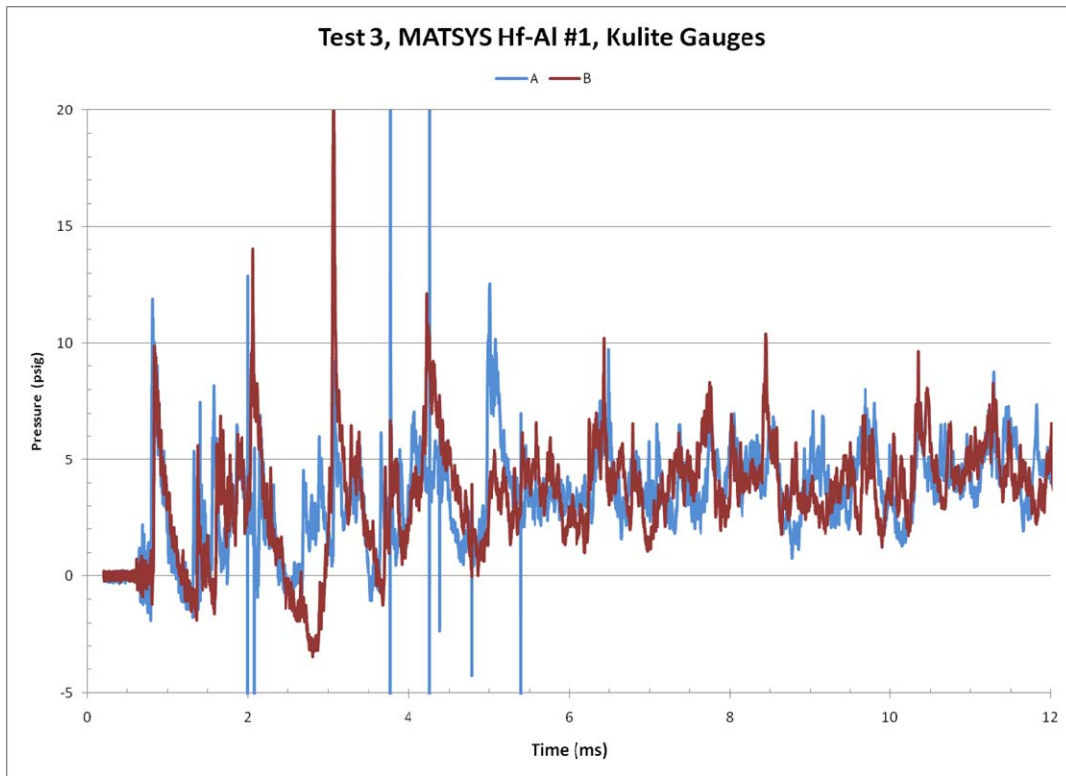
Fig. 6-29. Early-time pressure histories from Test 3, Matsys Hf-Al casing.
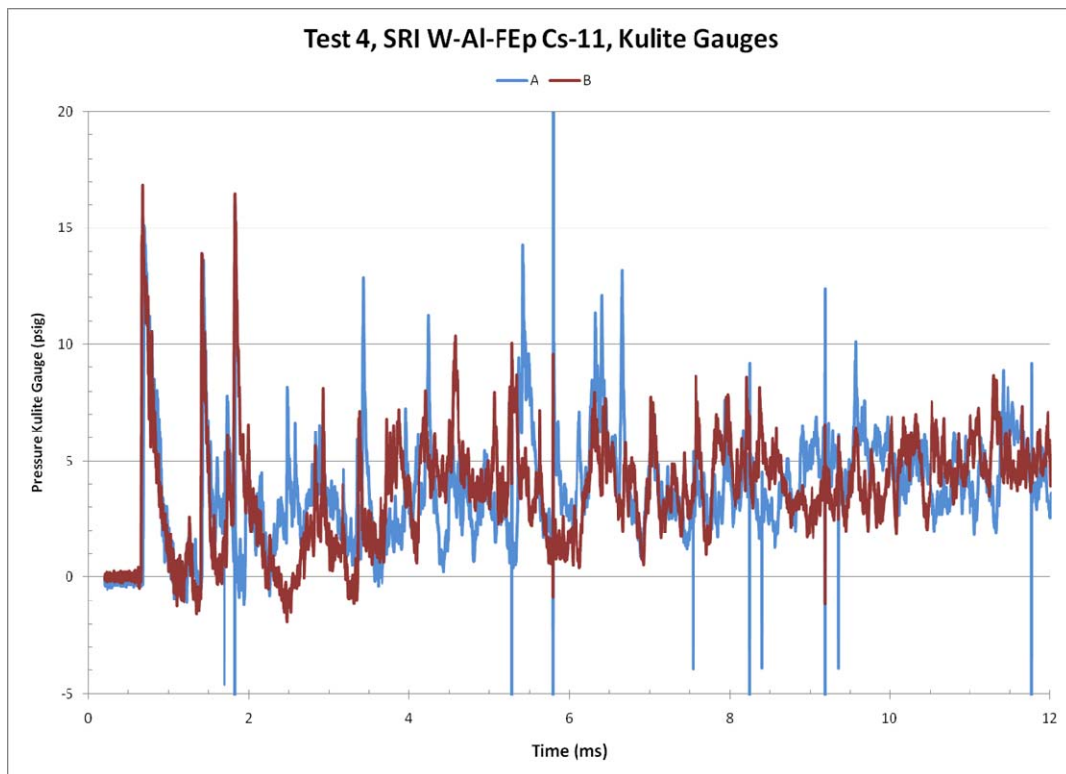
Fig. 6-30. Early-time pressure versus histories from Test 4, SRI W-Al-FlEp casing.
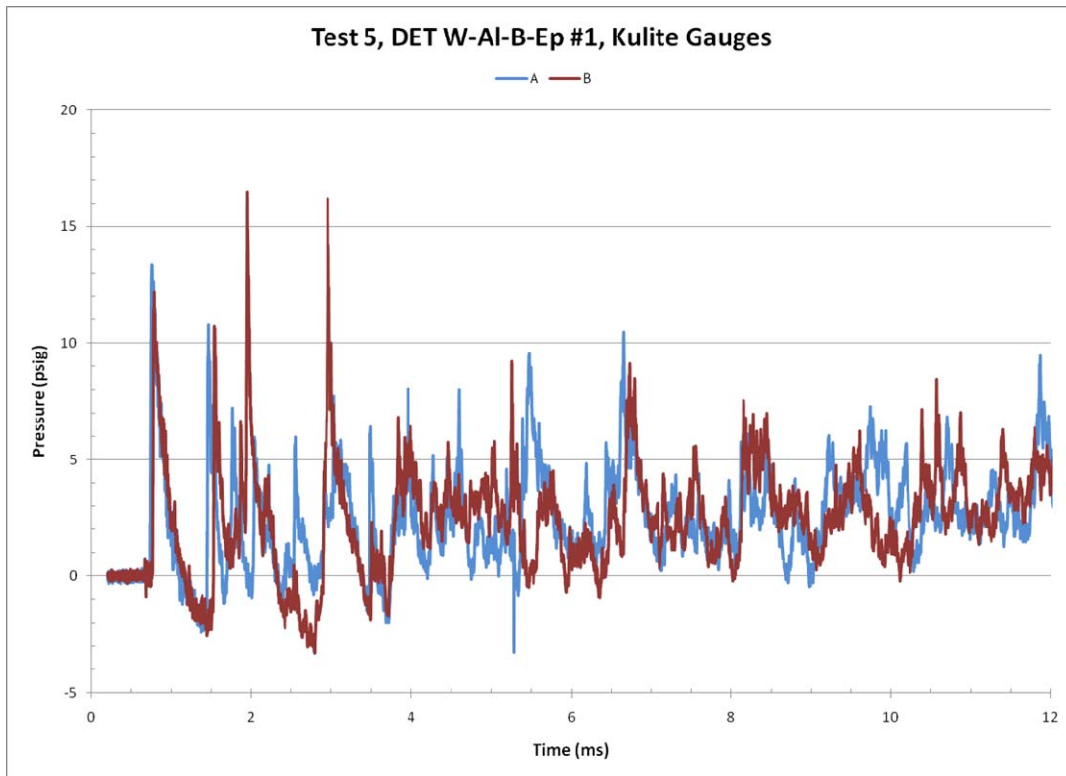
Fig. 6-31. Early-time pressure histories from Test 5, DET W-Al-B-Ep casing.
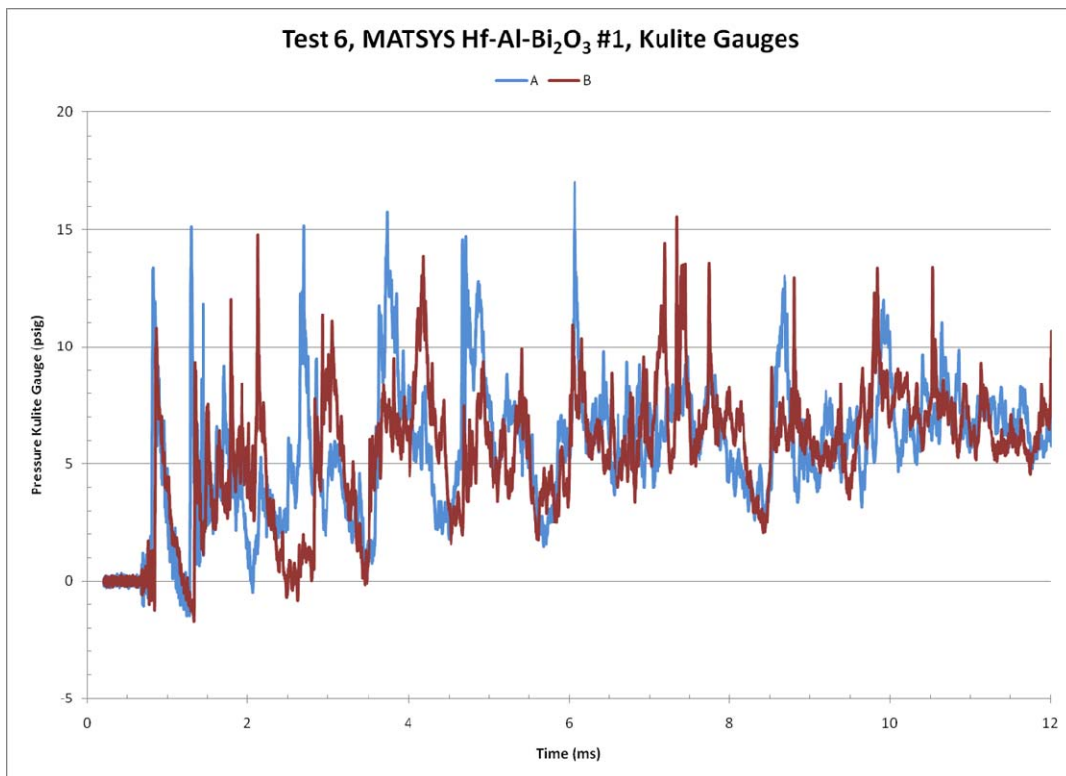
Fig. 6-32. Early-time pressure histories from Test 6, Matsys Hf-Al-Bi$_2$O$_3$ casing.
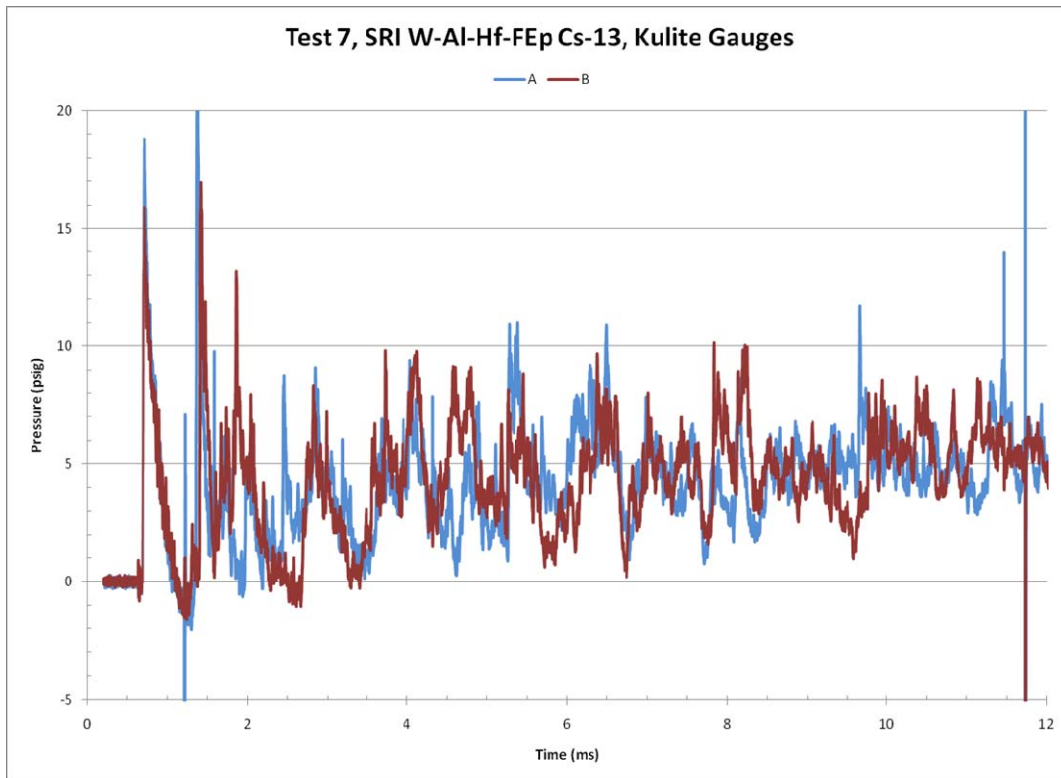
Fig. 6-33. Early-time pressure histories from Test 7, SRI W-Al-Hf-FlEp casing.
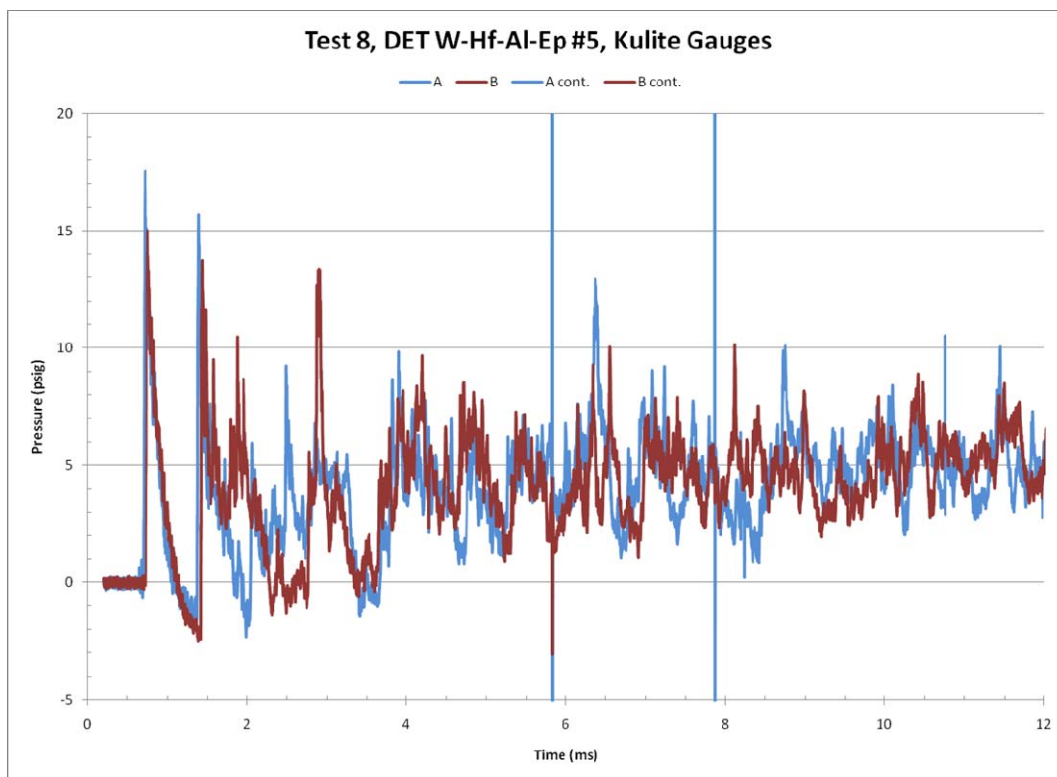
Fig. 6-34. Early-time pressure histories from Test 8, DET W-Al-Hf-Ep casing.
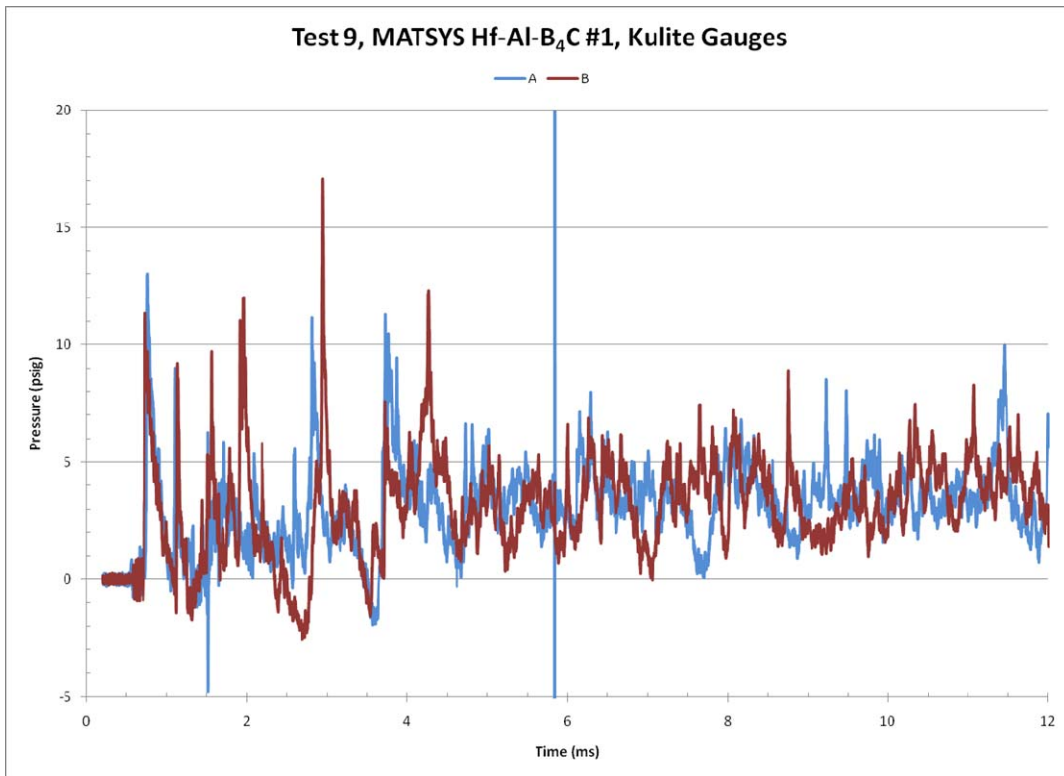
Fig. 6-35. Early-time pressure histories from Test 9, Matsys Ti-Al-B₄C casing.
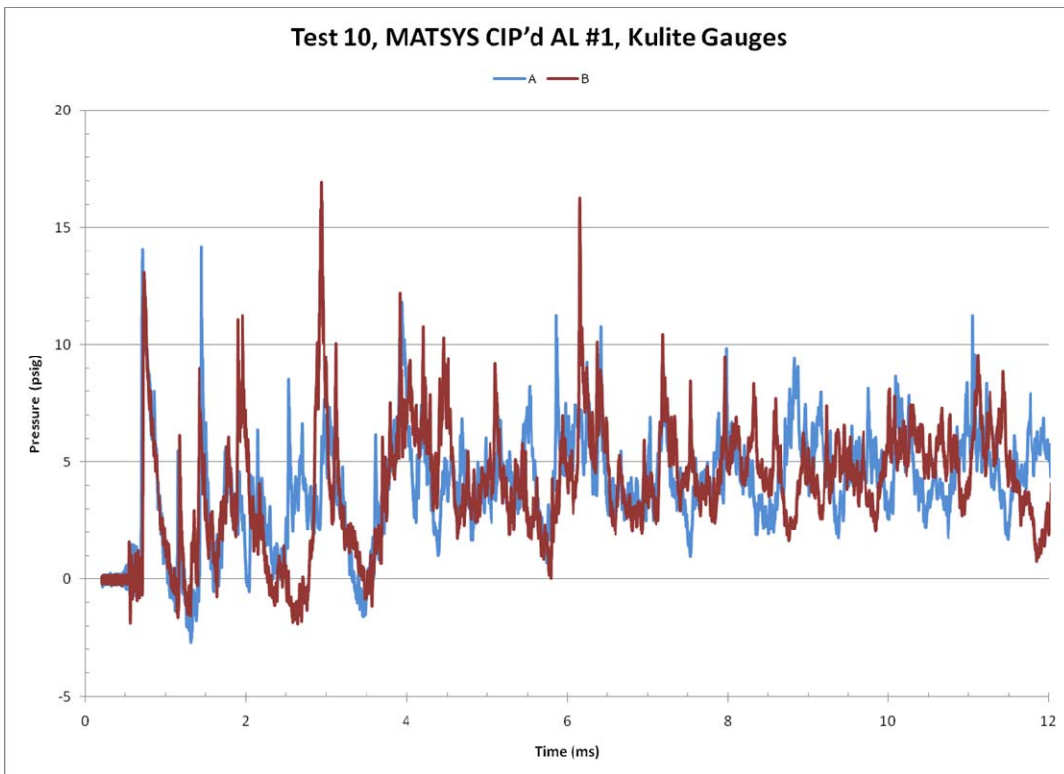
Fig. 6-36. Early-time pressure histories from Test 10, Matsys CIPed Al casing.
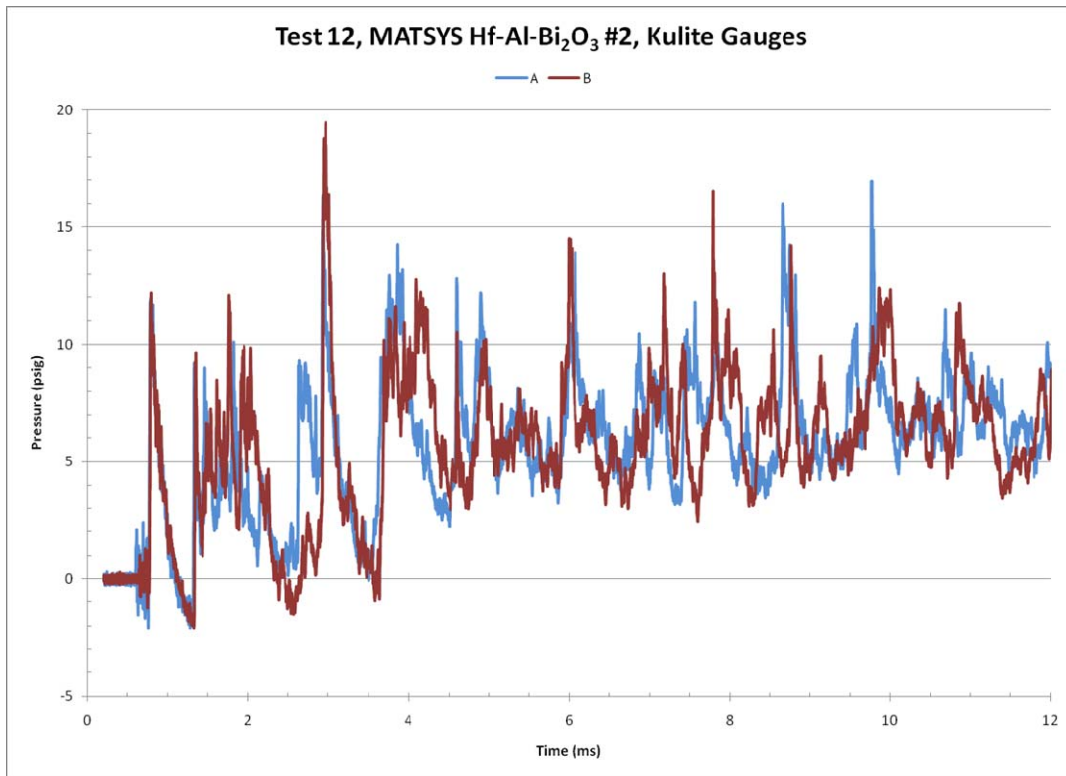
Fig. 6-37. Early-time pressure histories from Test 12, Matsys Hf-Al-Bi$_2$O$_3$ casing.
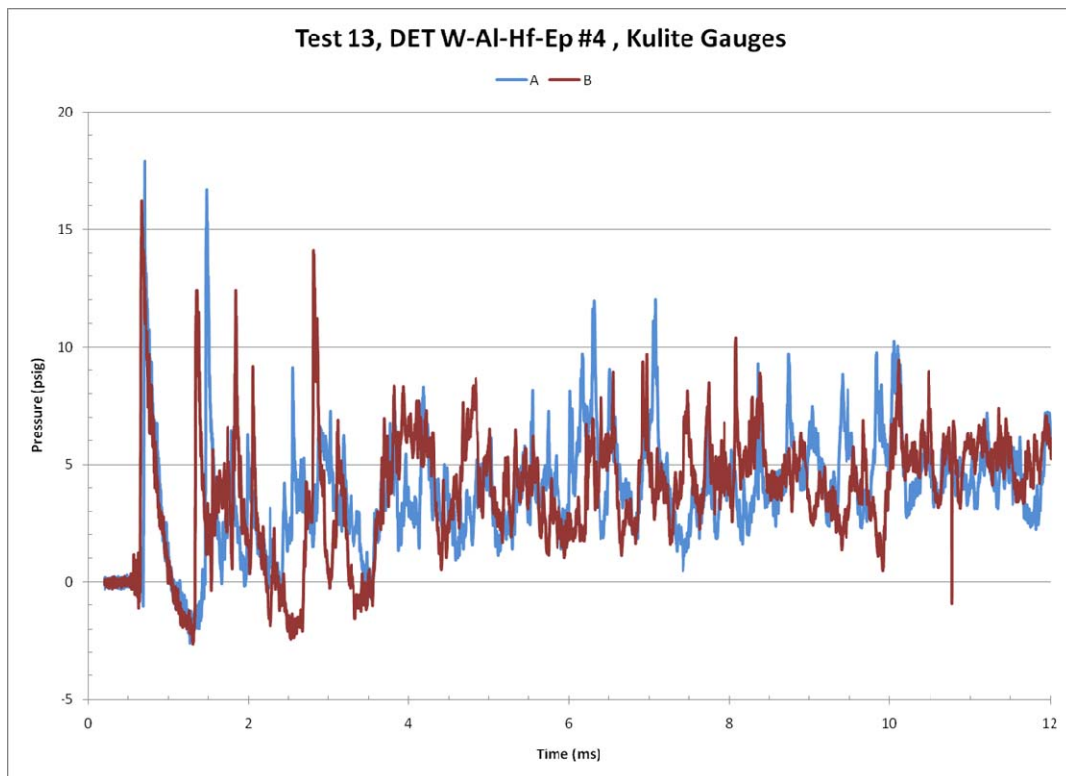
Fig. 6-38. Early-time pressure histories from Test 13, DET W-Al-Hf-EP casing.
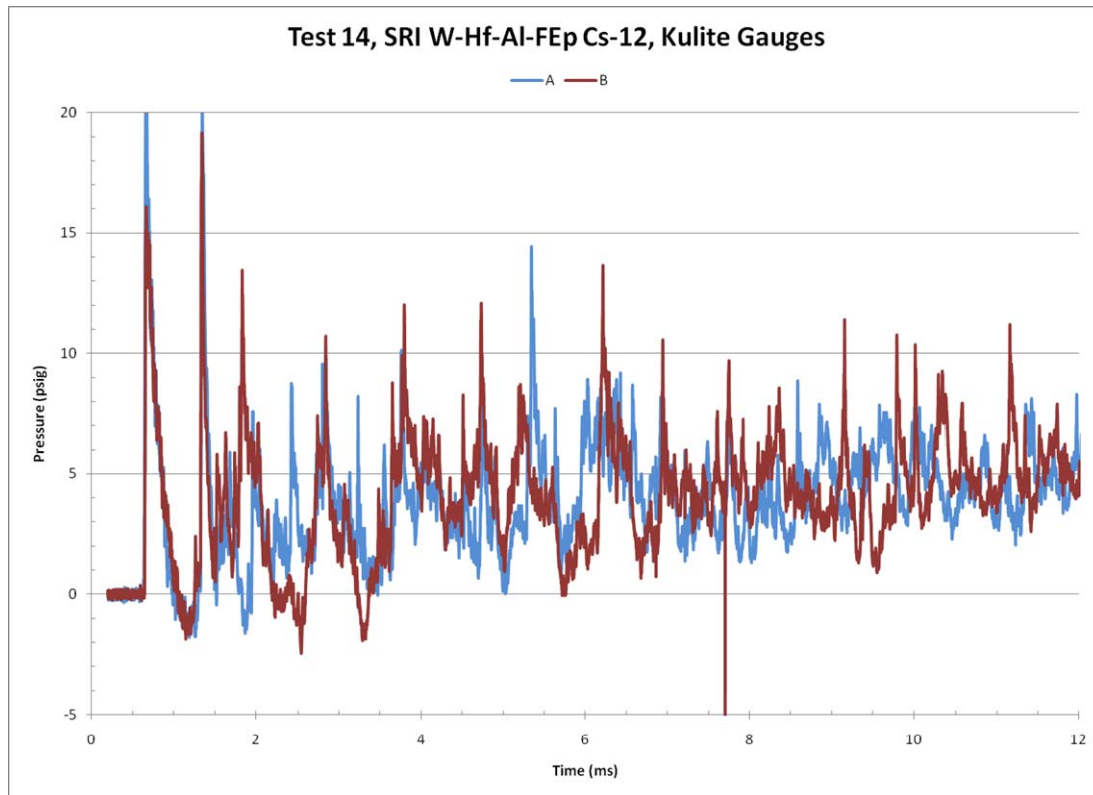
Fig. 6-39. Early-time pressure histories from Test 14, SRI W-Al-Hf-FlEP casing.

Table 6-4. Peak Pressures and Arrival Times in UIUC Chamber Tests.

Test #	N-9 Explosive Mass (g)	Case Mass (g)	Casing Material	Peak Transient Pressure (psi)		Time of Peak Pressure (δs)	
				Kulite 1 (A)	Kulite 2 (B)	Kulite 1 (A)	Kulite 2 (B)
0	9.70	0.00	Bare N9 Explosive	16.27	16.99	617.0	571.4
1	10.28	52.00	Steel #1	8.46	8.02	869.6	873.8
2	10.11	50.96	DET#6 W-Al-Ep	16.80	13.44	706.2	748.9
3	9.74	54.80	Matsys#1 Hf-Al	11.75	9.71	802.6	825.6
4	9.75	51.00	CS11 W-Al-FlEp	15.38	16.79	872.8	671.1
5	10.03	48.67	DET#1 W-Al-B-Ep	13.33	12.16	749.4	779.4
6	10.20	54.82	Matsys Hf-Al-Bi$_2$O$_3$	13.35	10.79	813.2	851.0
7	9.61	54.14	SRI Cs13 W-Al-Hf-FlEp	18.76	15.92	715.2	711.6
8	10.05	50.04	DET#5 W-Al-Hf-Ep	17.52	15.00	717.2	749.6
9	9.74	23.69	Matsys Al-Ti-B$_4$C	12.96	11.32	762.8	733.0
10	9.74	25.98	Matsys CIP'd Al	14.08	13.10	707.6	724.2
11	10.00	52.00	Steel #2	9.26	8.40	863.0	857.0
12	9.85	54.81	Matsys#2 Hf-Al-Bi$_2$O$_3$	11.97	12.20	782.2	788.6
13	9.99	49.23	DET#4 W-Al-Hf-Ep #4	17.78	16.19	701.0	661.8
14	10.41	50.70	SRI CS12 W-Al-Hf-FlEp	22.67	15.98	666.4	666.8

6.2.4 Impulse

Impulse was calculated by numerically integrating the transient pressure histories given above. Figure 6-40 shows impulse versus time for the bare explosive charge, Test 0. This shows an initial ramp-up in impulse at about 1 ms, followed by another ramp-up just before 2 ms. After 2 ms, impulse increases

nearly linearly with time, reaching a value of about 24 psi-ms at about 11 ms. The early-time impulse before 2 ms is a result of the dynamic pressure waves from the blast event. The later steady increase is most likely attributable to a temperature rise within the chamber due to the explosive event. This is analagous to heating a closed vessel, which results in increasing the internal pressure, hence "impulse," over time. Integrating the pressure history would yield an impulse value, but obviously this is not the dynamic impulse produced by a blast wave. Therefore, only the early part of the impulse curve should be considered true impulse, with the subsequent increase being related to thermal effects.
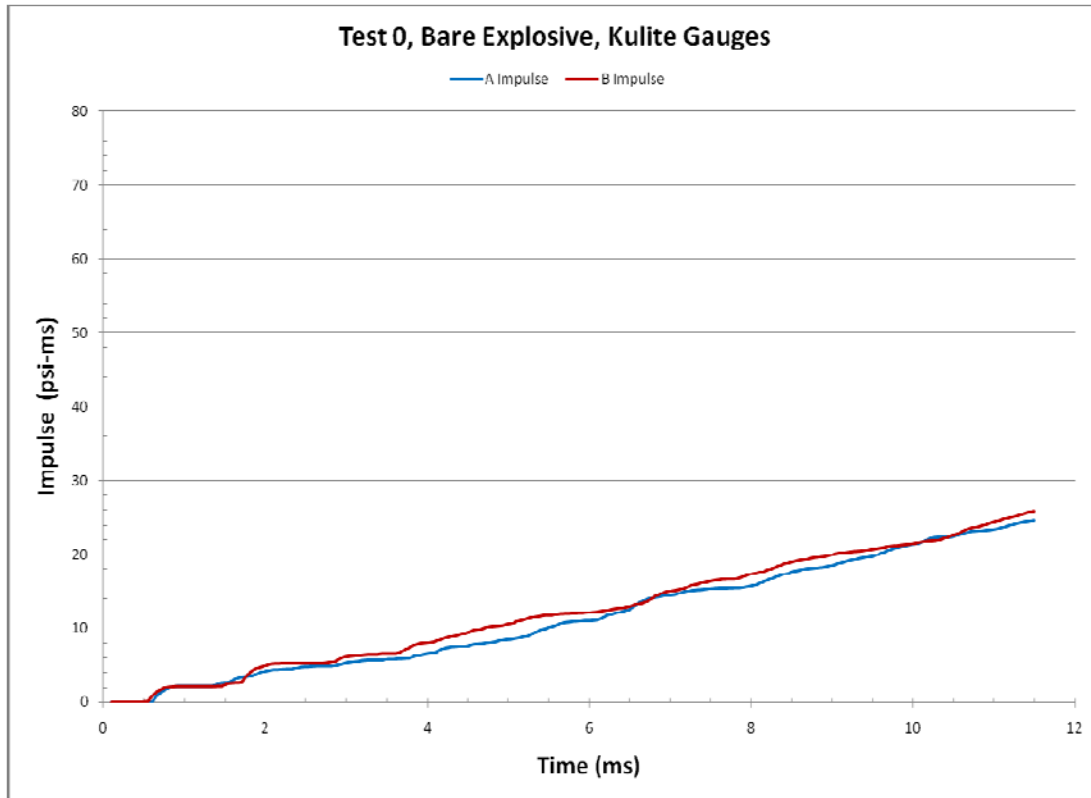
Fig. 6-40. Impulse versus time from Test 0, bare explosive charge.

The impulse histories from the tests with the steel casings are shown in Figs. 6-41 and 6-42. The total impulse is much less than that of the bare charge, reaching values of only 10 to 11 psi-ms at late time. The early-time impulse, which includes the first positive pressure pulse, is 1.06 psi-ms, about half that of the bare charge. Figures 6-43 to 6-54 show the impulse histories for the remaining tests. The general characteristics of the impulse curves for the reactive material casings are essentially the same. The first ramp-up in impulse occurs at about 1 ms, with values ranging from 1 to 2 psi-ms. Some time after 2 ms, the impulse curves become fairly linear, reaching values of 30 to 65 psi-ms at 12 ms.
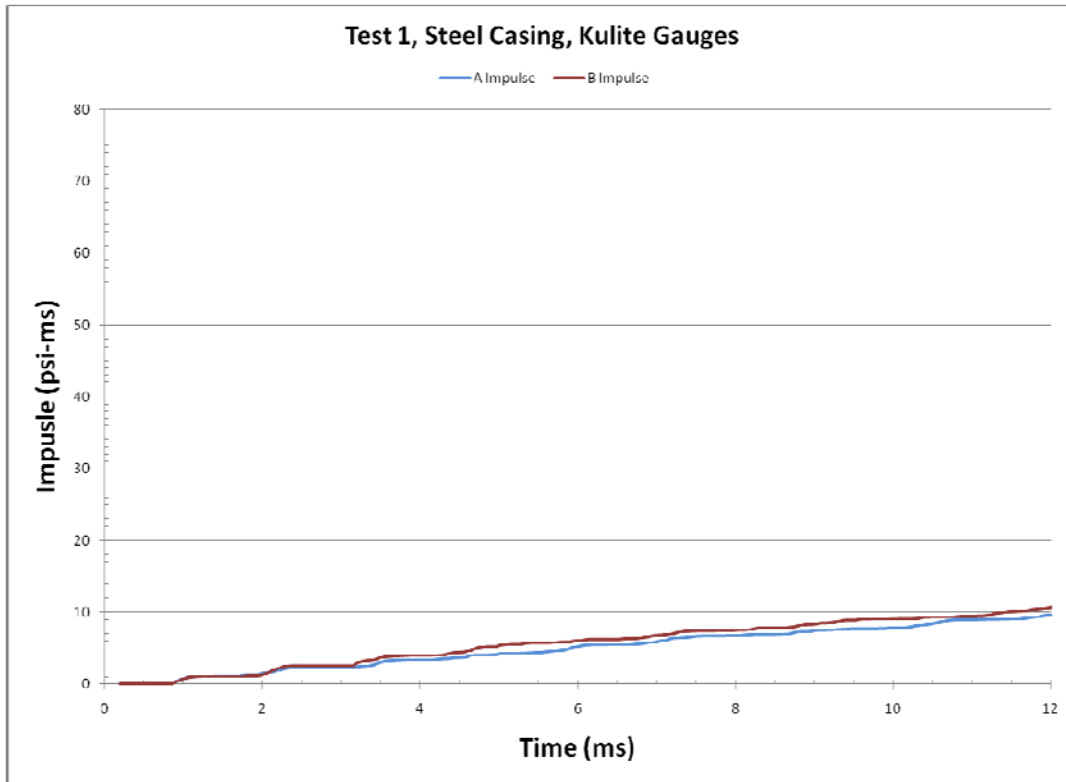
Fig. 6-41. Impulse versus time from Test 1, steel casing.
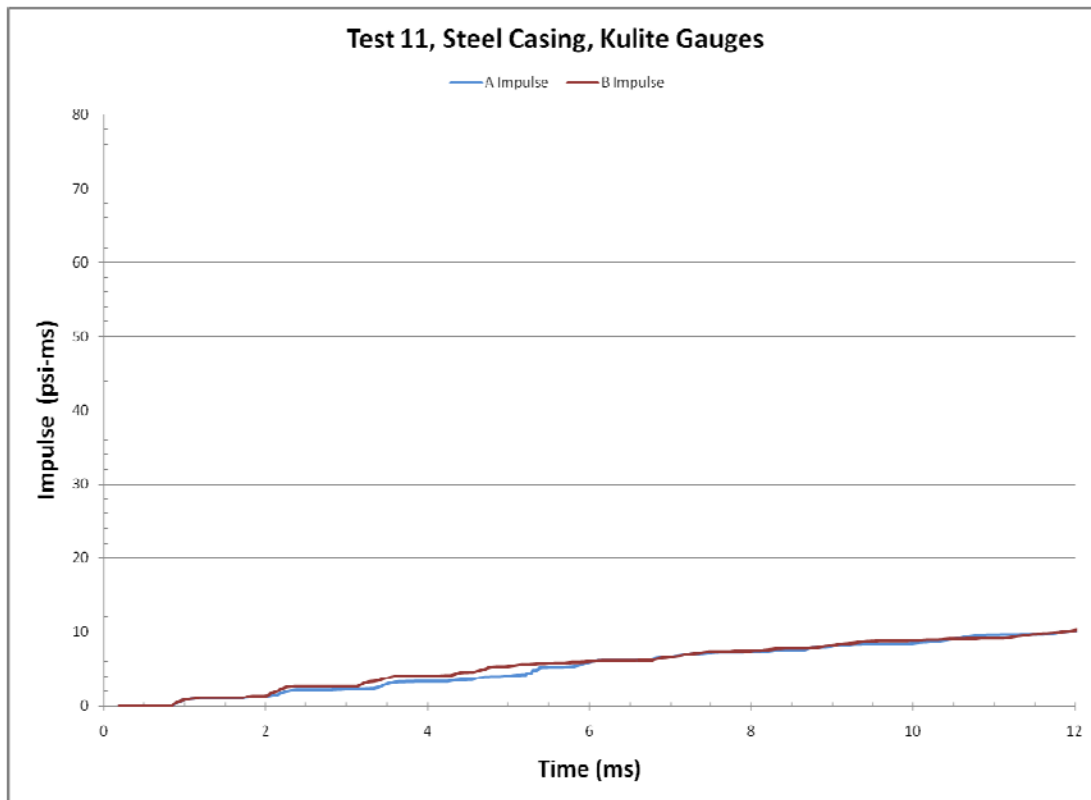
Fig. 6-42. Impulse versus time from Test 11, steel casing.
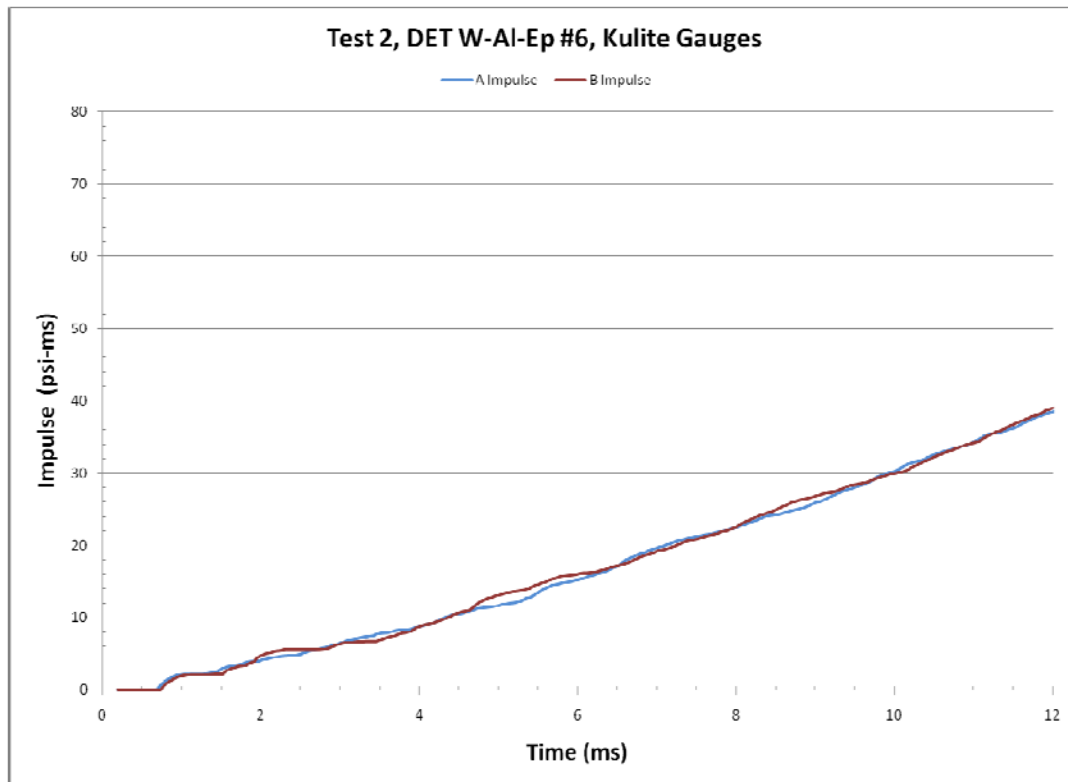
Fig. 6-43. Impulse versus time from Test 2, DET W-Al-Epoxy casing.
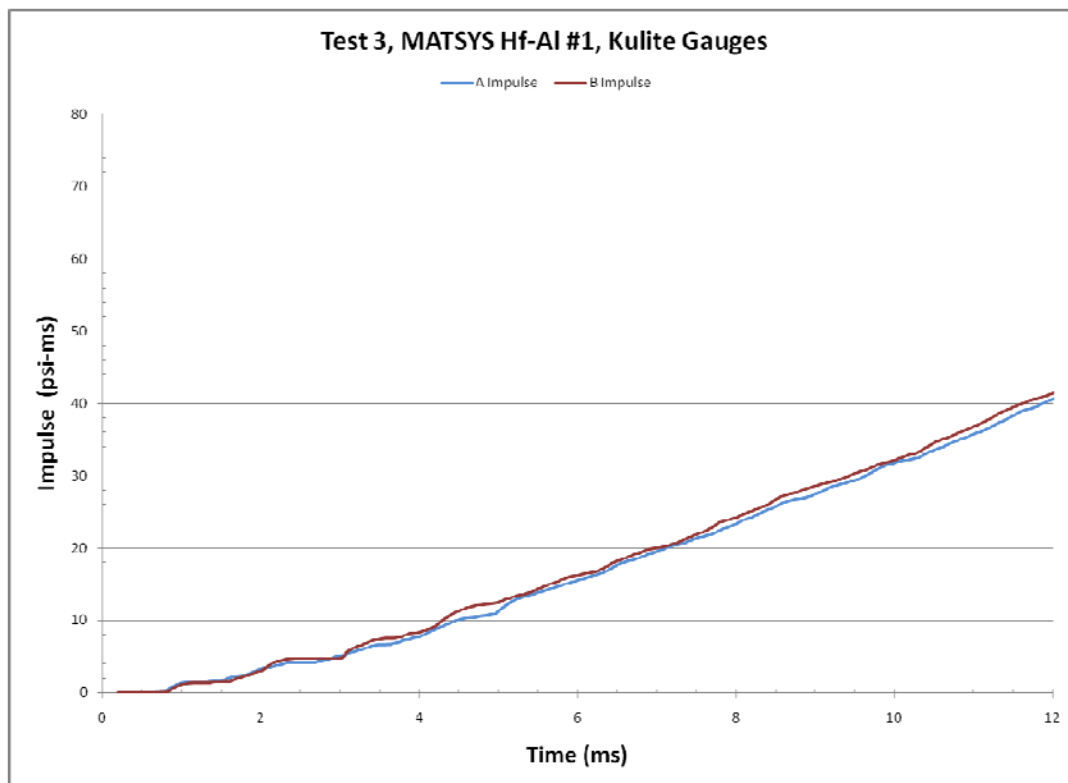
Fig. 6-44. Impulse versus time from Test 3, Matsys Hf-Al casing.
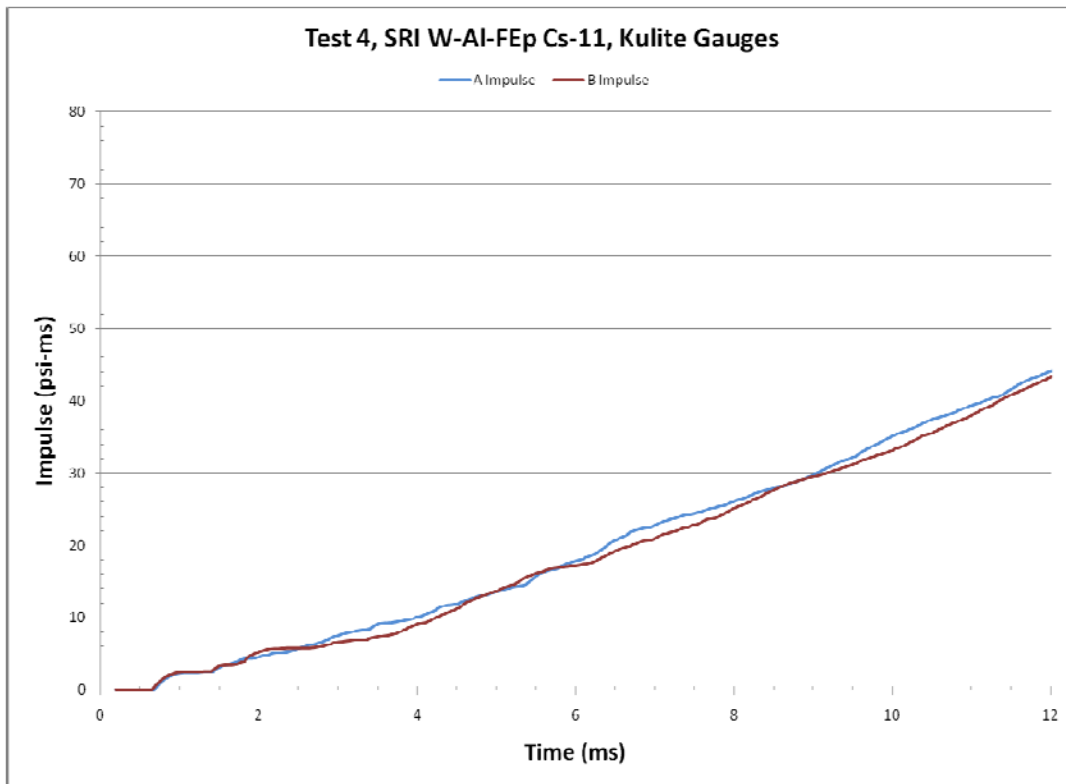
Fig. 6-45. Impulse versus time from Test 4, SRI W-Al-FlEp casing.
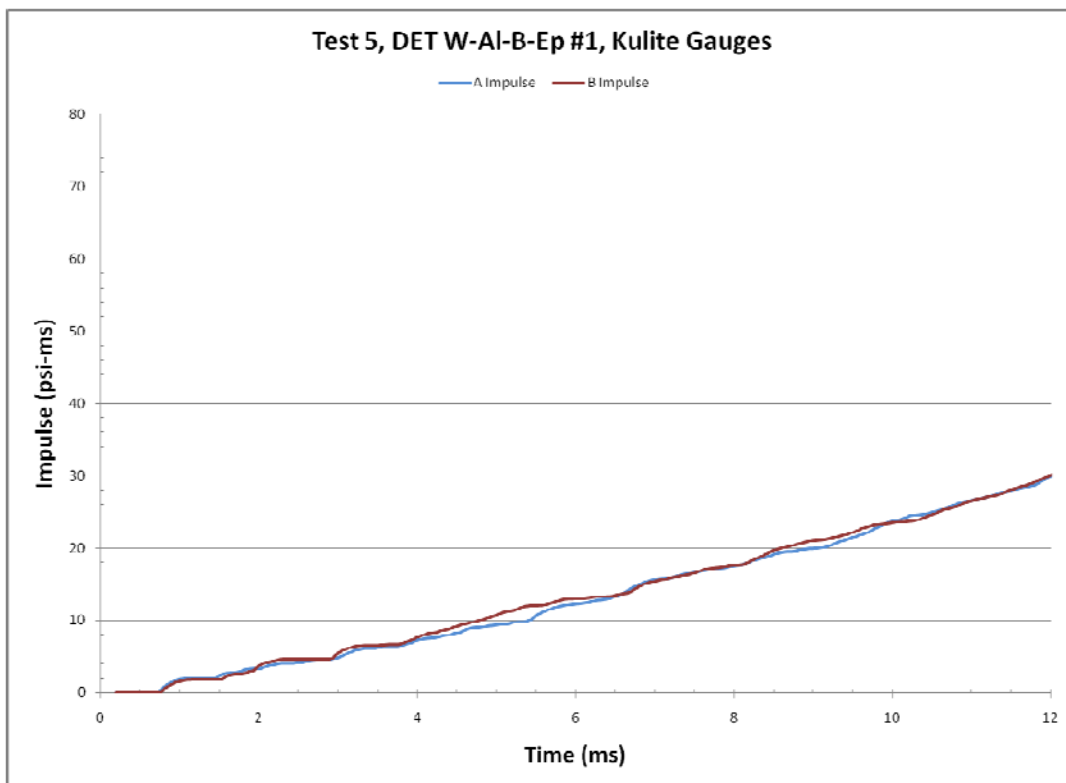
Fig. 6-46. Impulse versus time from Test 5, DET W-Al-B-Ep casing.
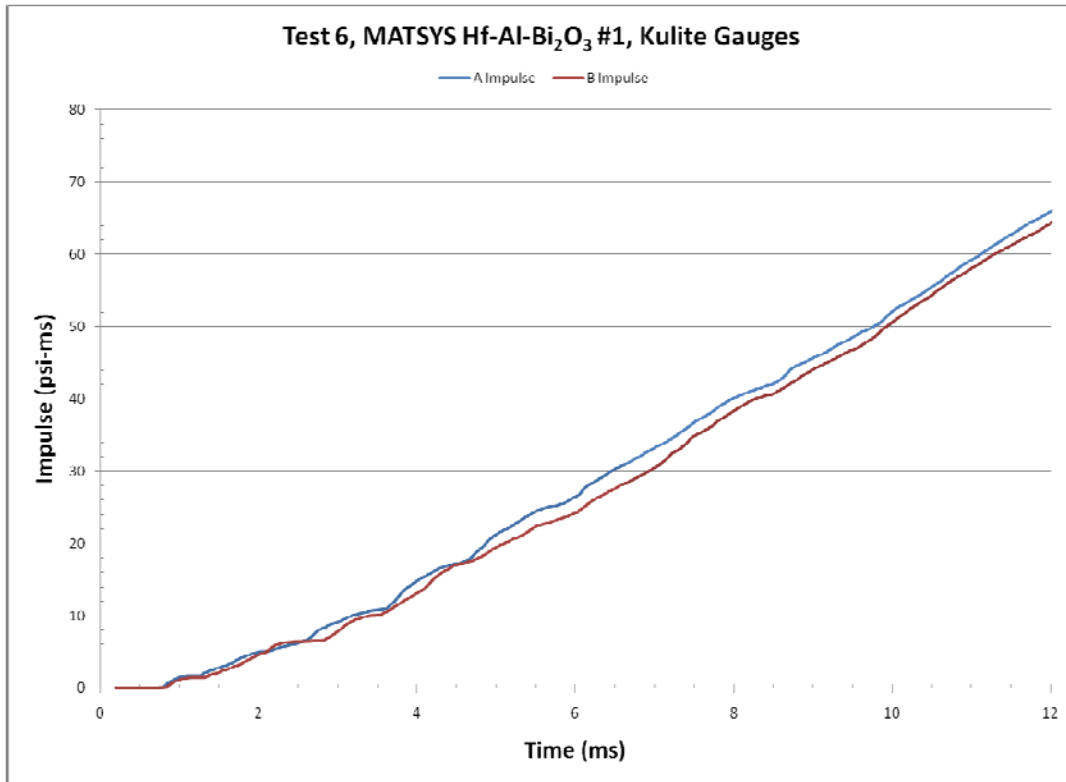
Fig. 6-47. Impulse versus time from Test 6, Matsys Hf-Al-Bi$_2$O$_3$ casing.
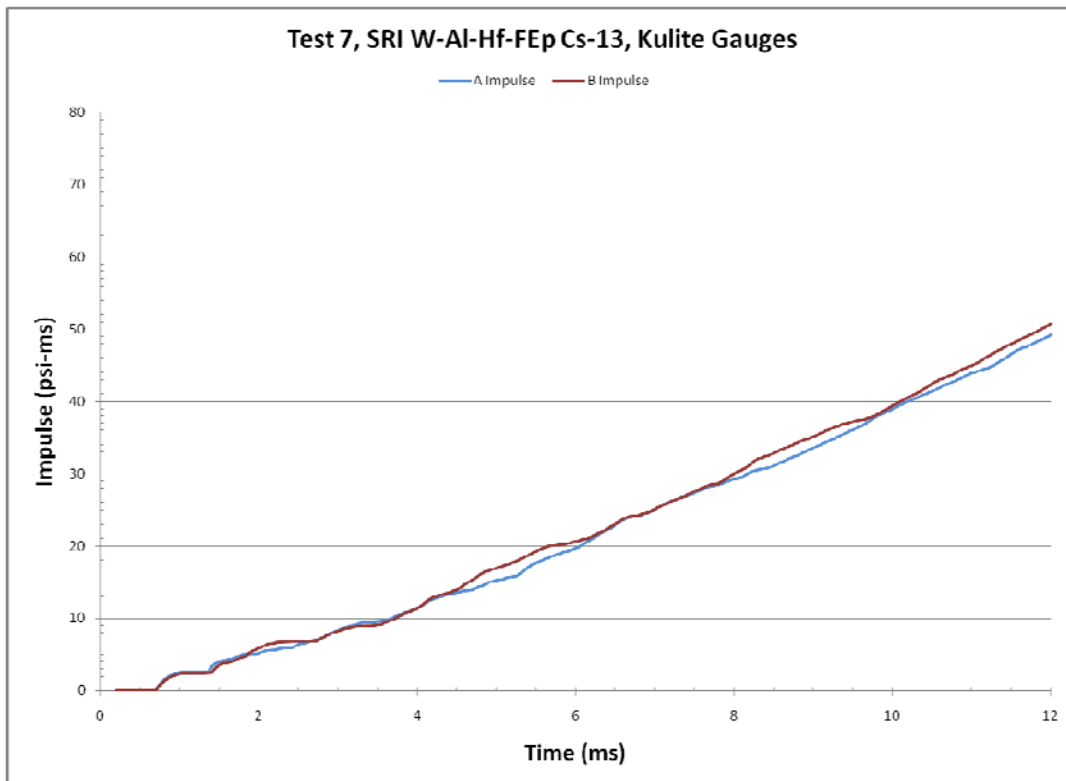
Fig. 6-48. Impulse versus time from Test 7, SRI W-Al-Hf-FlEp casing.
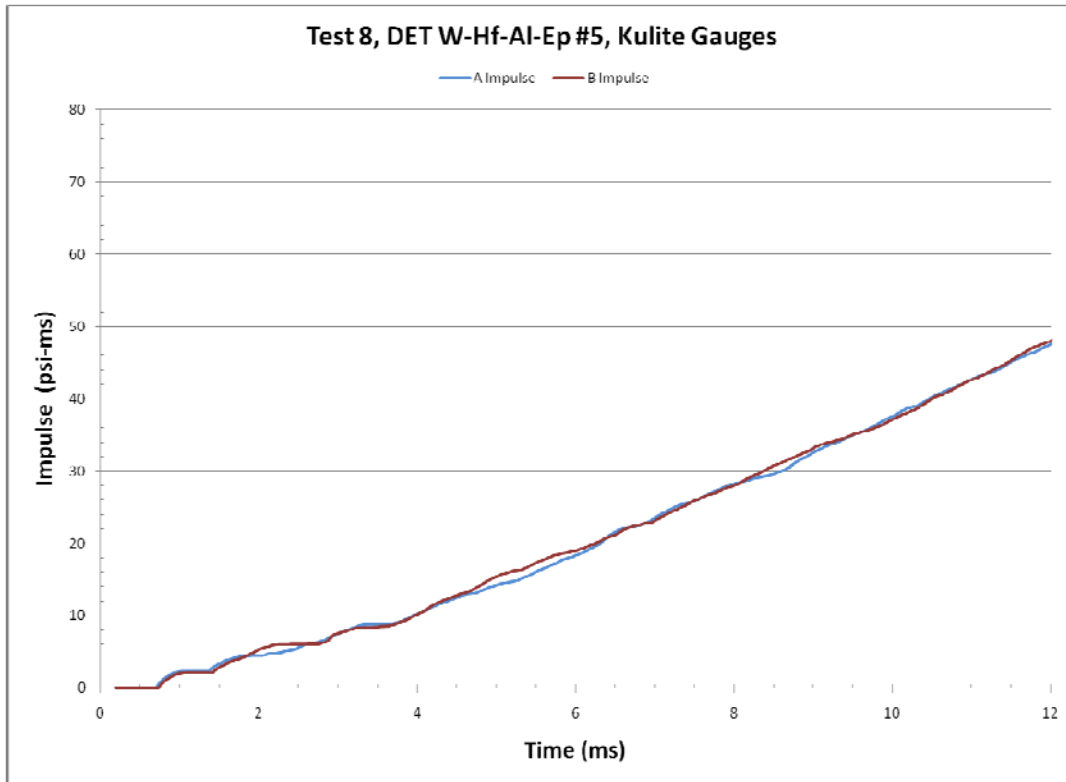
Fig. 6-49. Impulse versus time from Test 8, DET W-Al-Hf-Ep casing.
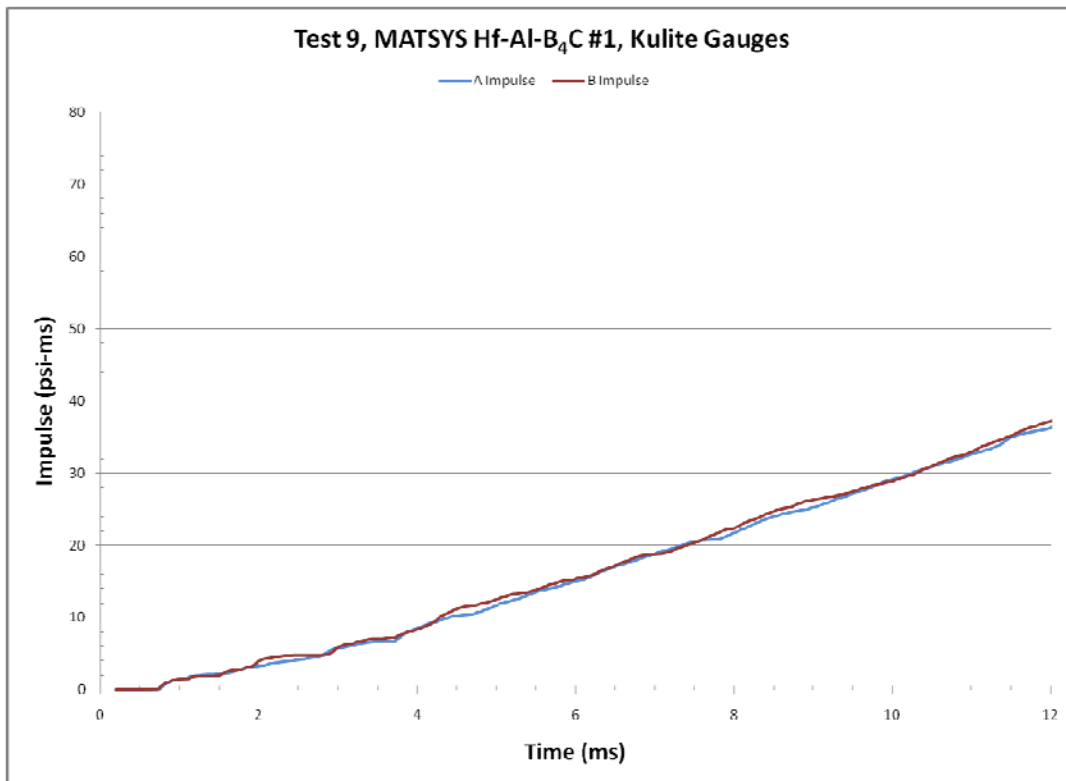
Fig. 6-50. Impulse versus time from Test 9, Matsys Ti-Al-B$_4$C casing.
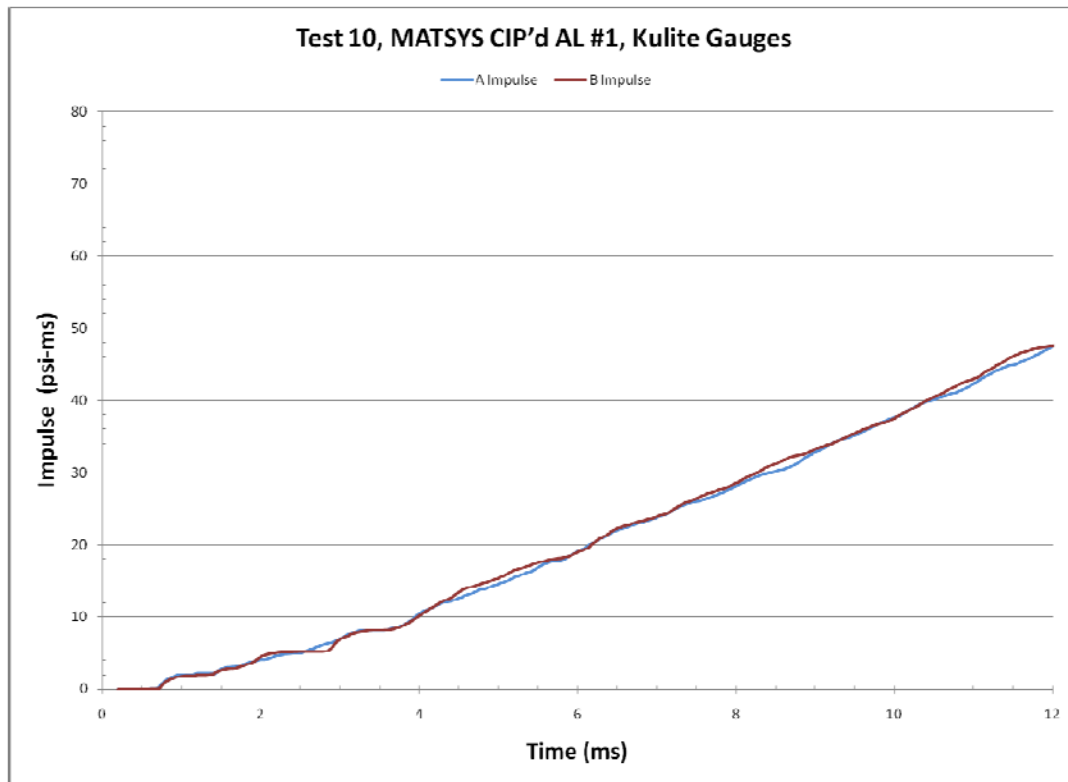
Fig. 6-51. Impulse versus time from Test 10, Matsys CIPed Al casing.
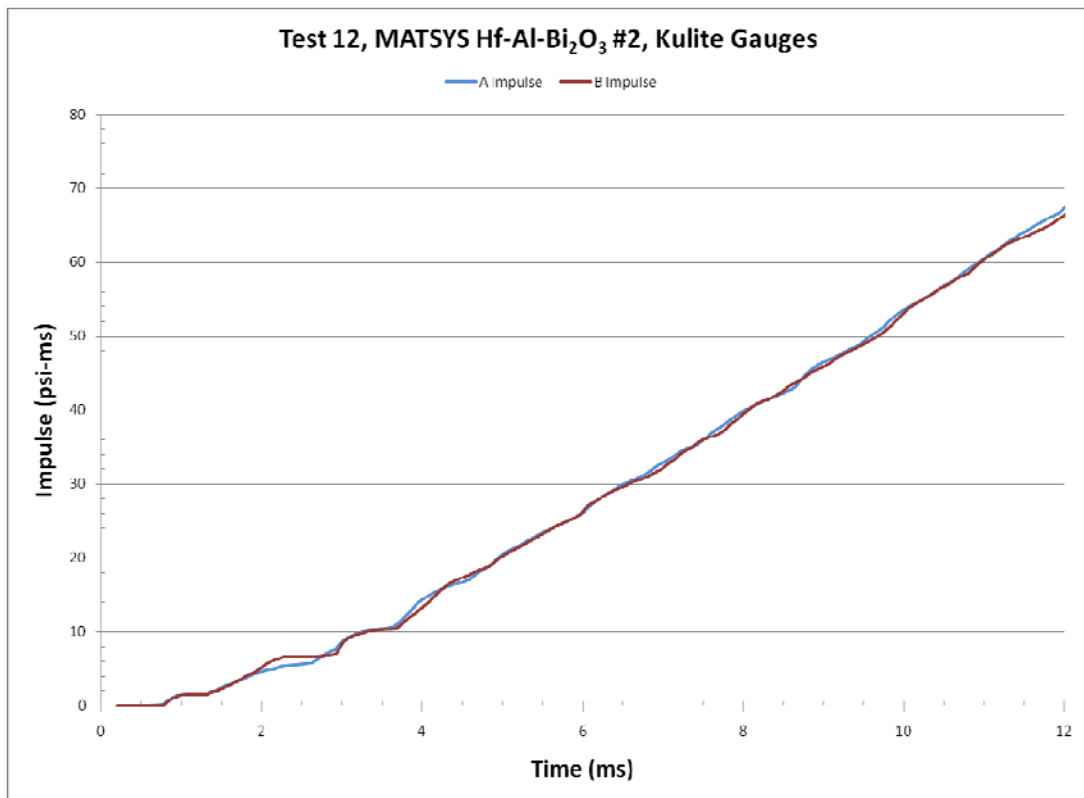
Fig. 6-52. Impulse versus time from Test 12, Matsys Hf-Al-Bi$_2$O$_3$ casing.
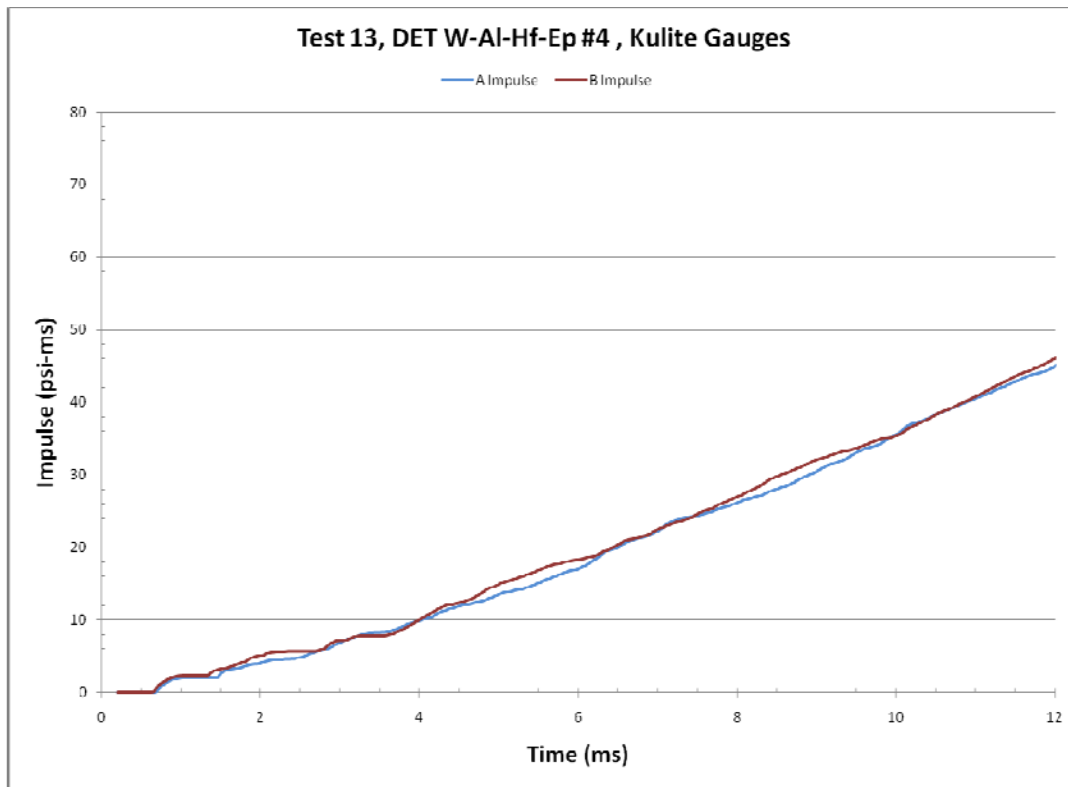
Fig. 6-53. Impulse versus time from Test 13, DET W-Al-Hf-EP casing.
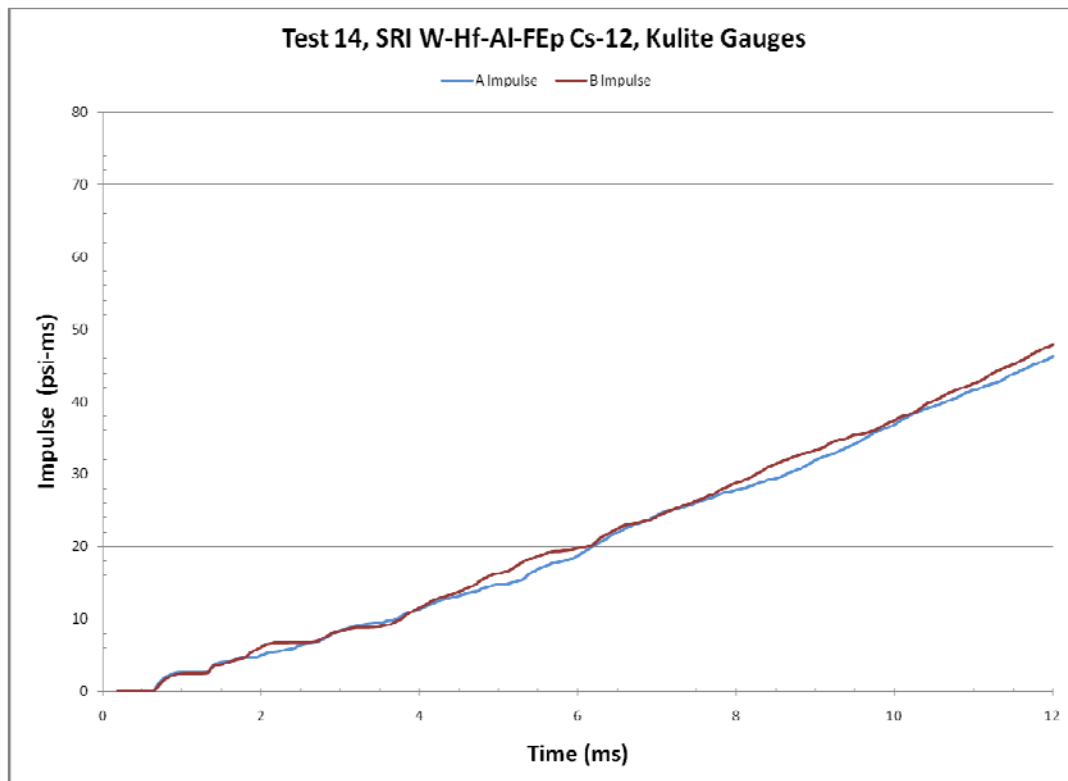
Fig. 6-54. Impulse versus time from Test 14, SRI W-Al-Hf-FlEP casing.

6.2.5 Analysis

The QSP was analyzed in order to estimate the amount of energy released by the various reactive materials. This calculation was based on the ideal-gas law,

$$\Delta E_{air} = \frac{V \Delta P}{\gamma - 1}$$

where ΔP is the measured QSP, γ is the ratio of specific heats for air, taken as 1.4, V is the volume of the chamber, and ΔE_{air} is the energy imparted to the air from the test item.

The above equation yields the total energy, including contributions from the explosive and RMS casing. To determine the energy released by the casing, an energy balance was applied. The input energy includes the detonation energy E_{Expl} of explosive and the energy E_{Expl} released by the casing, while the output energy includes the kinetic energies KE of the casing and end caps, plastic work PE done on the casing and end caps, and the energy ΔE_{air} of the air, so that

$$E_{Expl} + E_{RM} = KE + PE + \Delta E_{air}$$

Solving for E_{RM} yields

$$E_{RM} = KE + PE + \Delta E_{air} - E_{Expl}$$

Therefore, given the change in energy of the chamber air that is derived from the measured QSP, we can calculate the energy released by the reactive material given the kinetic energy and plastic work imparted to the casing and end confinement, and the energy released by the explosive.

The heat of detonation of PBXN-9 is listed as 5.878 kJ/g. However, the explosive products are not fully oxidized through detonation. If full oxidation occurs, the heat of combustion of PBXN-9 is 9.390 kJ/g. In order to determine which value to use in the energy equation, we consider the test of the bare charge, Test 0. In this test there was no casing or end confinement, so the energy imparted to the air equals the energy from released by the explosive, ignoring any losses of the chamber.

The average QSP for Test 0 was 2.93 psi (19.93 kPa). Applying the above equation with the chamber volume of 1.812 m^3, the change in energy is 90.3 kJ. The mass of explosive includes the PBXN-9 charge of 9.7 g and the detonator mass of 0.53 g, totaling 10.23 g. The specific energy of the explosive and detonator is 8.83 kJ/g, within 6% of the handbook value for PBXN-9's heat of detonation. If the mass of the detonator is ignored, the specific energy becomes 9.31 kJ/g, within 1% of the handbook value.

The two tests with the steel casing can be used to assess the energy absorbed by the casing and end confinement. The average QSP from the steel-casing Tests 1 and 11 were 0.82 and 0.74 psi (5.58 kPa and 5.03 kPa), which correspond to energies of 25.3 kJ and 22.8 kJ, with an average of 24.05 kJ. Comparing this value to that from the test of the bare charge indicates the steel casing and end confinement result in an energy decrease of 66.25 kJ. In other words, the steel casing and end confinement absorbed 66.25 kJ in the form of kinetic energy, plastic work, and fracture energy.

In calculating the energy released by the reactive materials, the amount of energy absorbed by the casing and end confinement need to be known. It was assumed that the RM casings absorbed the same amount of energy as the steel casing; the specific energy output of each formulation was then determined based on the measured QSPs. Table 6-5 lists the specific energies, the four highest of which were obtained by Matsys CIPed aluminum, Matsys Ti-Al-B$_4$C, Matsys Al-Hf-Bi$_2$O$_3$, and DET W-Al-Hf-Epoxy. The top two materials, the CIPed Al and the Ti-Al-B$_4$C, have densities that are too low for consideration as RMS materials but were tested here only to compare to previous work.

Table 6-5. Calculated Specific Energies Based on Measured QSP.

Test #	Casing Material	RM Energy (J)	RM Energy Expl. Heat of Combustion (cal/g)
2	DET#6 Al-Ep-W	138,746	651
3	Matsys#1 Hf-Al	149,172	651
4	CS11 W-Al-Fep	157,623	739
5	DET#1 B-Al-Ep-W	105,018	516
6	Matsys Hf-Al-Bi2O3	226,934	989
7	CS13 W-Al-FEP-Hf	167,346	739
8	DET#5 Hf-Al-Ep-W	171,442	819
9	Matsys Al-Ti-B4C	112,916	1139
10	Matsys Al	159,171	1464
12	Matsys Hf-Al-Bi2O3 #2	239,948	1046
13	DET Hf/Al/Ep/W #4	161,366	761
14	CS12 W-Al-Fep-Hf	151,903	737

6.2.6 Summary and Conclusions

A total of 15 chamber tests were conducted by UIUC. Collected data included the dynamic side-on pressure versus time, measured by fast-acting gauges placed within the chamber. In addition, the QSP chamber pressure was recorded by two gauges from a pressure tap off the back of the chamber.

The transient data exhibit no noticeable trends. Measured peak pressures for the reactive materials and bare charge ranged from 12 to 22 psi, with noticeable scatter among the duplicate tests and gauges. The two tests of the steel-cased charges resulted in significantly lower peak pressures about 8 to 9 psi.

Impulse calculations were difficult to reduce since the rise in QSP was being recorded by the transient gauges. As discussed above there was a late-time drift upwards of the transient pressure, which was most likely due to the rise in QSP within the chamber. Therefore large impulse values were calculated, but these values included the QSP rise and hence cannot be considered as dynamic impulse.

The measured QSP values indicated significant reactivity for several of the reactive materials. Table 6-6 summarizes the measure QSP values normalized by the average QSP for the steel casing tests. A factor greater than 10 was achieved by the MATSYS Hf-Al-Bi$_2$O$_3$ material.

Table 6-6. Relative Blast Performance of Best-Performing RMS Candidates.

Material	Class	Relative QSP*
Steel (baseline)	Inert	1.0
None (bare explosive)	None	3.77
Hf-Al-Bi$_2$O$_3$	Intermetallic/thermite	10.7
Hf-Al-Epoxy-W	Polymer-based	8.02
Hf-Al	Intermetallic	7.13
Al-Epoxy-W	Polymer-based	6.82

 * normalized to the inert steel casing

Calculations of the released energy based on measured QSP values showed specific energies ranging from 516 to 1464 cal/g. The 1464 cal/g was achieved by the HIPed aluminum casing fabricated by MATSYS. The MATSYS Hf-Al-Bi$_2$O$_3$ achieved the highest specific energy of the reactive materials, with values of 989 and 1046 cal/g in two tests; this material also had the highest recorded QSP values.

6.3 ATK Blast Tests

This subsection summarizes a series of explosive chamber tests conducted by Alliant Techsystems (ATK) Launch Systems Group, Corinne, Utah, in May 2010. These tests differ in three ways from those performed at UIUC: 1) the explosive charge used at ATK was about twice the mass at 23.4 g; 2) the explosive type was LX-14; and 3) chamber volume was nominally half at 31 ft^3.

ATK performed some considerable preparation to transform an existing horizontal cylindrical chamber to a vertical chamber, which greatly simplified placement of the charge and expedited test throughput. Chamber modifications included: 1) fabricating a heavy-duty stand and base-plate; 2) fabricating side mounting plates for pressure transducer and thermocouple mounts; and 3) fabricating a swing bracket for opening the access panel. The chamber and instrumentation were characterized in a series of pre-tests using multiple-size bare charges, steel encased charge, and RM encased charge.

6.3.1 Objective

The objective of the test series was to measure the increase in quasi-static chamber pressure produced from an explosive charge surrounded by a reactive material casing as compared to a bare explosive charge and a baseline charge with a steel casing (inert). A secondary objective was to compare the initial pressure-impulse for the bare, steel baseline, and reactive materials. Temperature measurement of the gas products was considered a low-effort, high-risk secondary objective.

6.3.2 Test Article

The charges used in this test series were cylinders of LX-14 explosive, nominally 1.0 inch in diameter by 1.0 inch in length, with a nominal mass of 23.4 g. The press density was measured as 98.1% TMD.

Figure 6-55 is a drawing of the test device, which consists of an explosive charge (part 4), steel end caps (parts 1 and 3), and casing (part 2). Tests of the bare charge were performed without the end plates and casing. The ratio of case mass to explosive charge mass was held constant at 3. A hole in the bottom steel end plate accommodates placement of the charge on top of a vertical ¾-inch-diameter wooden dowel. A hole in the opposite end plate accommodates an RP-81 EBW detonator. This configuration facilitated placement of the charge and shortened set-up times between tests.
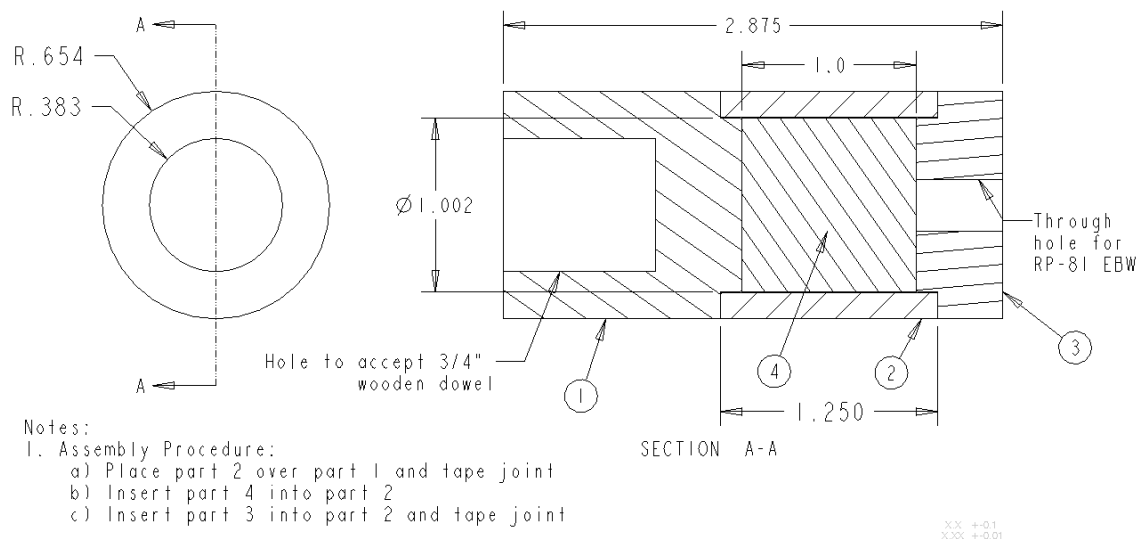
Fig. 6-55. ATK blast test charge with confinement.

The CTH computer code predicted the average velocity of the case (assumed steel) from the explosive detonation to be 1107 m/s (3631 ft/s). The results are shown in Fig. 6-56.
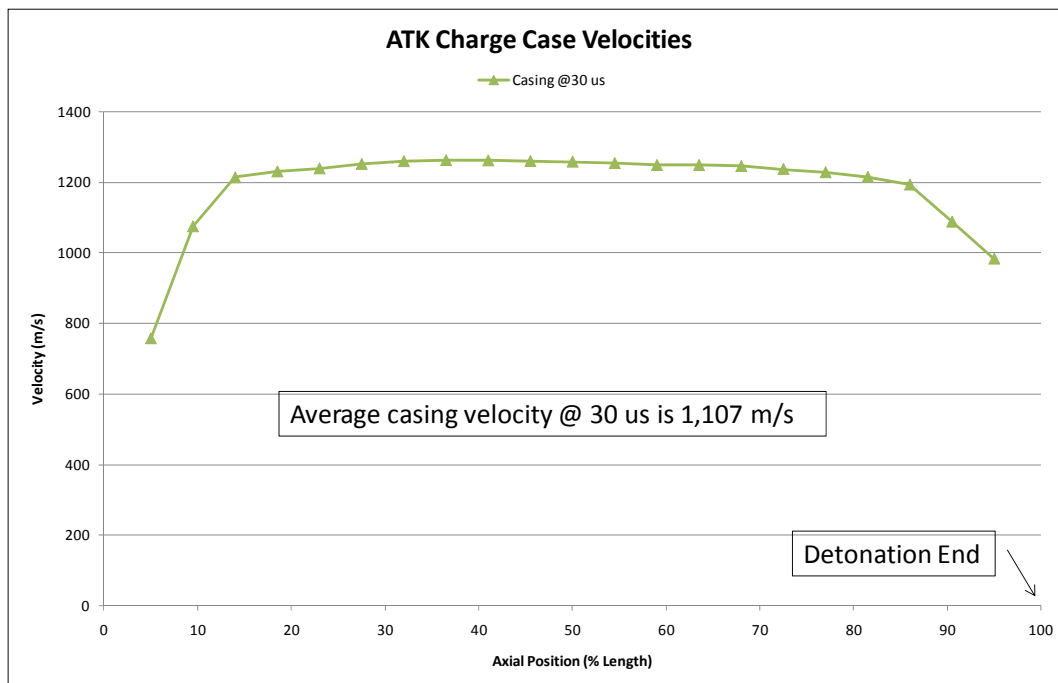
Fig. 6-56. CTH-calculated steel casing velocities for 1"-long ATK charge.

The LX-14 explosive charges were pressed at ATK's explosive facility in Corinne, Utah. The 1.0-inch-diameter charges were pressed in two heights, 1 inch and 0.5 inch, as shown in Fig. 6-57. The 0.5-inch charges were used in the pre-test chamber calibration tests. As listed in Table 6-7, the mass density among the charges is very consistent. The average calculated mass density is 1.811 g/cc, 98.13% of TMD. There was no significant change in charge size after 24 hours, as shown in Table 6-8.

Fig. 6-57. Pressed LX-14 charges with L/D=1 and L/D=0.5.

Table 6-7. LX-14 charge measurements and press density.

Pellet #	Weight (g)	Diameter (in)	Length (in)	Calculated Density (g/cc)	Immersion Density (g/cc)	% TMD
1	11.66	1.0000	0.5010	1.808	1.8135	98.03
2	11.65	1.0010	0.4995	1.808	1.8156	98.14
3	11.64	1.0005	0.5005	1.805	1.8114	97.91
4	23.28	1.0000	0.9960	1.816	1.8171	98.22
5	23.40	1.0005	1.0000	1.816	1.8186	98.30
6	23.40	1.0005	1.0005	1.815	1.8158	98.15

Table 6-8. LX-14 charge measurements after 24 hours.

Pellet #	Weight (g)	Diameter (in)	Height (in)
1	11.66	1.0000	0.5010
2	11.65	1.0010	0.4990
3	11.64	1.0000	0.5005
4	23.29	1.0000	0.9960
5	23.40	1.0005	0.9995
6	23.40	1.0005	1.0010

6.3.3 Materials Tested

The reactive materials tested in this series are listed in Table 6-9. Materials were supplied by DE Technologies, Matsys Corporation, and SRI International in the form of hollow tubes, with internal diameters of nominally 1.006 inches and lengths of 1.25 inches. The casing thicknesses were varied with the material density to bring the case-to-explosive mass ratio to the desired value of 3. For the nominal charge mass of 23.4 g, case mass would then be 70.2 g; however, the case was extended 1/8 inch on each end for attachment to end plates. This yields a nominal casing mass of 87.75 g, of which 70.2 g is located over the explosive charge, with the other 17.55 g hanging over the end plates.

6.3.4 Test Setup

The tests were conducted in ATK's explosive chamber, shown in Figs. 6-58 and 6-59. This cylindrical chamber is nominally 32 inches in diameter by 60 inches long, with an interior volume of 31 ft^3, which includes the bump-outs for the side panels and a well cavity in the bottom. The explosive charge was supported in the chamber's center on a wooden dowel. The two gauges positioned directly across from the charge were protected from fragments by a circular steel plate that stood off from the panel by about ½". The access door has a swing hinge to support its weight for quick opening and closing.

Table 6-9. Materials tested at ATK.

Material Designation	Supplier	Desription	Strength (ksi)	Theoretical Bulk Density (g/cc)	Bulk Density (g/cc)	Components	Volume (%)	Mass (%)	Particle Size
CIP'd Aluminum	MATSYS	CIP'd Aluminum	---	2.70	2.63	Aluminum Powder	100	100	H-2 Aluminum
30W-40Al-30Epoxy	DET	Tungsten Wire Composite	95.25	7.22	6.78	Tungsten Wire	30.00	80.18	Wire, 0.004-in Dia.
						Aluminum Powder	40.00	14.96	< 44 μm, average of 7-15 μm
						Epoxy	30.00	4.86	---
30W-20Al-20B-30Epoxy	DET	Tungsten Wire Composite	95.25*	7.15	6.15	Tungsten Wire	30.00	80.99	Wire, 0.004-in Dia.
						Aluminum Powder	20.00	7.55	< 44 μm, average of 7-15 μm
						Boron Powder	20.00	6.55	< 5 μm
						Epoxy	30.00	4.91	---
15W-Al19-Hf30-36Epoxy	DET	Tungsten Wire Composite	50*	7.82	6.79	Tungsten Wire	15.00	37.02	Wire, 0.004-in Dia.
						Aluminum Powder	19.00	6.56	< 44 μm, average of 7-15 μm
						Hafnium Powder	30.00	51.03	< 44 μm
						Epoxy	36.00	5.39	---
Hf-Al	MATSYS	HIP'd Powder	57.6	7.88	7.77	Hafnium Powder	48.90	82.50	< 44 μm
						Aluminum Powder	51.10	17.50	3.2 μm
HF-Al-Bi$_2$O$_3$	MATSYS	HIP'd Powder	12	7.84	7.74	Hafnium Powder	39.51	67.00	< 45 μm
						Aluminum Powder	46.48	16.00	3.2 μm
						Bismuth Trioxide	14.01	16.00	< 4 μm
Ti-Al-B$_4$C	MATSYS	HIP-d Powder	77.2	3.31	3.26	Titanium Powder	34.34	47.00	< 20 μm
						Aluminum Powder	55.15	45.00	3.2 μm
						Boron Carbide	10.51	8.00	< 8 μm
W-Al-Fl_Epoxy	SRI	Tungsten Wire Composite	---	---	6.62	Tungsten Wire	30.00	---	Wire, 0.004-in Dia.
						Aluminum Powder	40.00	---	< 44 μm, average of 7-15 μm
						Fl-Epoxy	30.00	---	---
W-Hf-Al-Fl_Epoxy	SRI	Tungsten Wire Compiste	---	---	7.83/8.48+	Tungsten Wire	19.89/24.2+	---	Wire, 0.004-in Dia.
						Hafnium Powder	20.68/19.34+	---	< 44 μm, average of 22.23 μm
						Aluminum Powder	24.65/23.06+	---	< 44 μm, average of 13.91 μm
						Fl-Epoxy	22.54/31.37+	---	---
*Estimated Tensile Strength									
+Values are for two supplied specimens									

Fig. 6-58. Exterior of ATK's explosive chamber showing the front access door and the side panels.
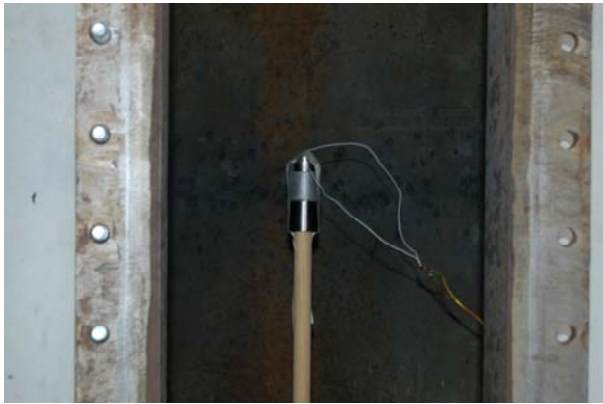
Fig. 6-59. Interior of ATK's explosive chamber showing the test article set on wooden dowel (left) and the gauge shield (right) for the mid-height gage position.

Instrumentation consisted of seven pressure transducers of two different types, shown in Fig. 6-60. Four of the transducers were piezoresistive types from Kulite, model ETS-IA-375-500SG, with a 500-psi maximum pressure. The second was a piezoresistive type from Endevco, model 8530B-500, with a 500-psi maximum pressure. Both types are designed for a blast environment with high shock resistance, high natural frequency, and high stability during temperature transients. The operating temperature range for the Endevco is 0 °F to 200 °F while the Kulite is -65 °F to 250 °F. Both gauges were recommended for recording both the early-time impulse and the late-time Quasi-Static-Pressure (QSP).

Fig. 6-60. Pressure gauges from Endevco 8530B-500 (left) and Kulite ETS-IA-375-500SG (right).

Three Nanmac (Model E12) eroding thermocouples were used to measure the dynamic temperature of the gas products. These thermocouples, shown in Fig. 6-61, are typically used for temperature measurement of rocket nozzle blast and propellant burning, and have microsecond response times and maximum temperatures of 2300 °C. Each features an erodible junction that allows it to be refurbished between tests, via grinding or sanding as shown in Fig. 6-62.

Fig. 6-61. Nanmac high-temperature fast-response thermocouples.

Fig. 6-62. Photographs of a new Nanmac thermocouple (left) and a resurfaced end (right).

Figure 6-63 indicates the qualitative position of each pressure and thermocouple port with respect to the charge. Three pressure gauges were mounted on each side panel and one on the bottom.
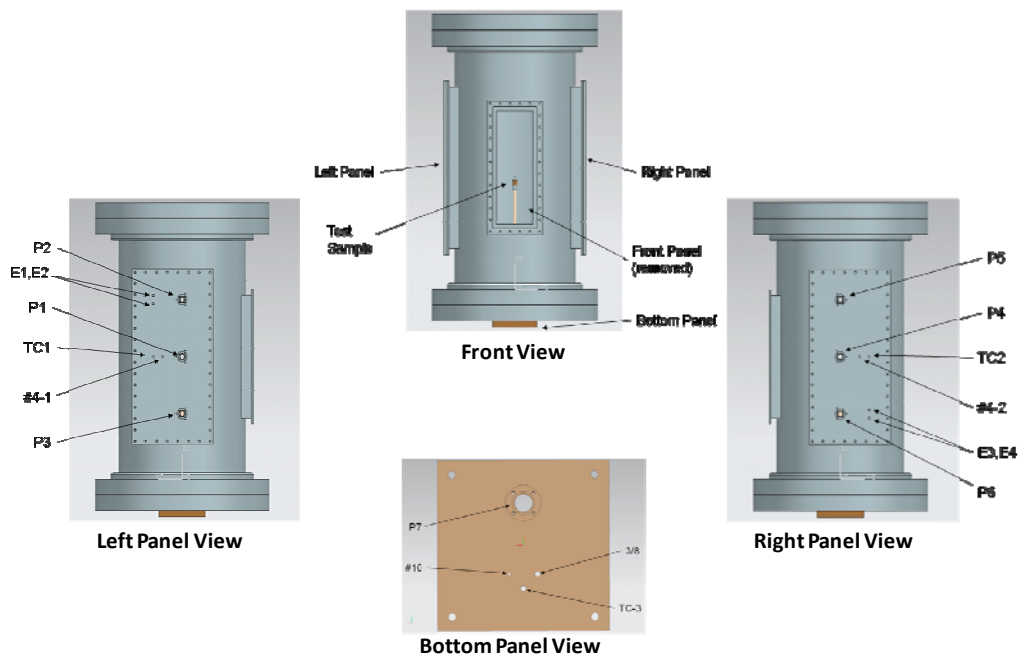
Fig. 6-63. Schematic of pressure and temperature port locations. The Endevco transducers were located at ports P1, P2, and P3. The Kulite transducers were located at ports P4, P5, P6, and P7.

Figure 6-64 shows a reference frame for the chamber setup. The origin of the frame is located at the center of the test article. The distances to each port used for the tests are listed in Table 6-10.
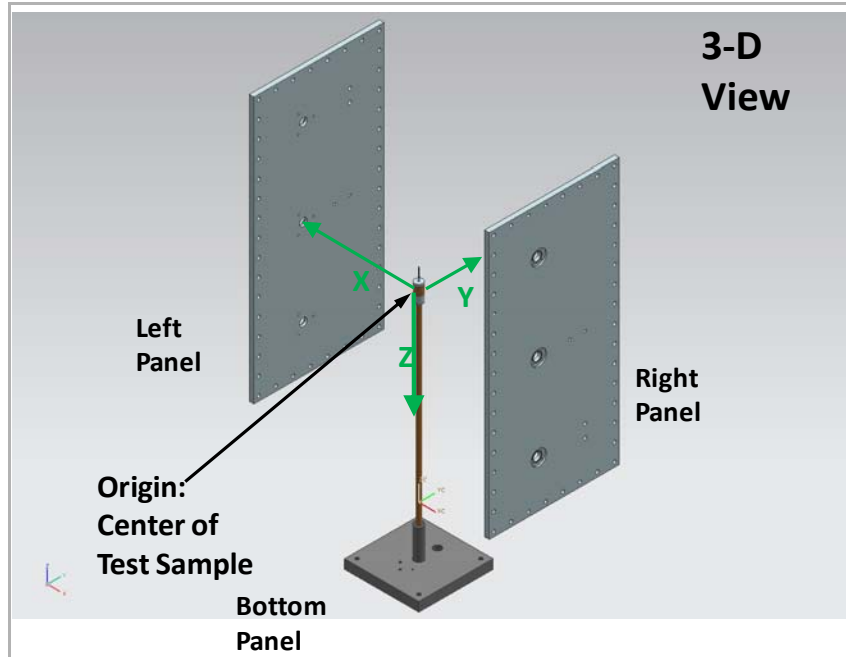
Fig. 6-64. Reference frame for port positions with respect to test article.

Table 6-10. Distances in inches for pressure ports (P1 through P7) and thermocouple ports (TC1 through TC3). TD is total distance.

	Port P1	Port P2	Port P3	Port P4	Port P5	Port P6	Port P7	Port # 4-1	Port # 4-2	Port # 10	Port 3/8	TC1	TC2	TC3
X AXIS	18.7	18.7	18.7	18.7	18.7	18.7	0	19.5	19.5	1.0	1.0	18.5	18.5	0
Y AXIS	0	0	0	0	0	0	3.0	5.0	5.0	2.0	2.0	7.5	7.5	3.0
Z AXIS	0	14.0	14.0	0	14.0	14.0	35.0	0	0	35.0	35.0	0	0	34.0
TD	18.7	23.4	23.4	18.7	23.4	23.4	35.1	20.1	20.1	35.1	35.1	20.0	20.0	34.1

The pressure transducers were mounted flush with the chamber walls using a mounting fixture consisting of a steel hold-down plate and Delrin/Sorbothane isolator as shown in Fig. 6-65. The gauge is threaded into a Delrin spacer that is isolated from the tank wall using ¼"-thick Sorbothane gaskets, which act as pressure seals as well as shock isolators.
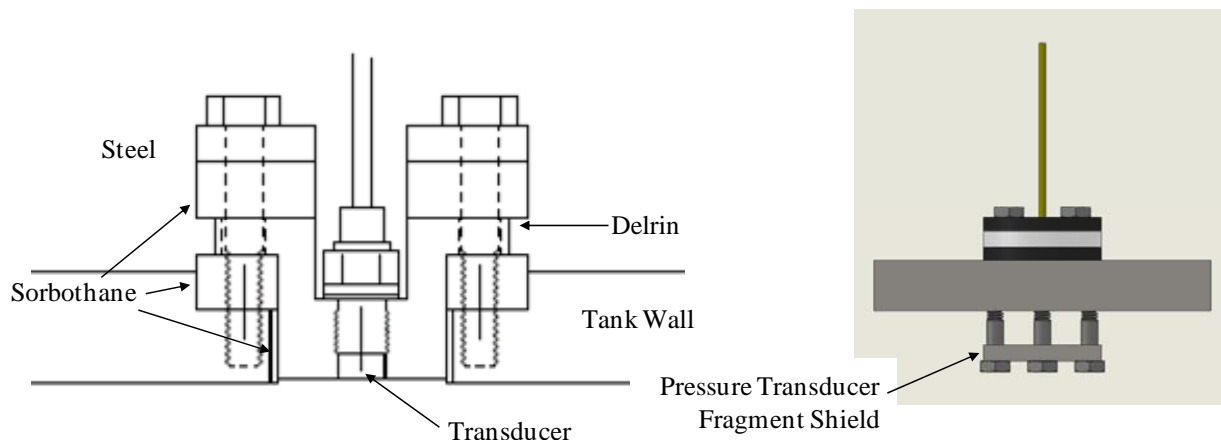
Fig. 6-65. Diagrams showing the pressure transducer shock isolator (left) and fragment shield (right).

6.3.5 Predictions - Estimated QSP for Bare and Encased Charges

As for the UIUC tests, estimates of the chamber QSP were predicted, given the larger size of the ATK test article and smaller volume of the chamber. Table 6-11 summarizes the calculated energy and QSP values for the bare and cased charges tested. The anticipated QSP for a reactive-material-encased charge was 42 to 48 psi (nominal).

Table 6-11. Calculated energy and QSP values for bare, steel-encased, and RMS-cased charges.

Charge Mass (g)	Case Material	Case Mass (g)	Explosive Detonation Energy (J)	Explosive Combustion Energy (J)	Reactive Casing Energy (J)	Casing and End Plate KE and PW Energy (J)	Net Energy (Expl. Det.) (J)	Net Energy (Expl. Combustion) (J)	Quasi Static Pressure Detonation (psig)	Quasi Static Pressure Combustion (psig)
12.2	None	0.0	71,712	114,558	0	0	71,712	114,558	4.80	7.67
23.4	None	0.0	137,545	219,726	0	0	137,545	219,726	9.20	14.70
23.4	Steel	88.0	137,545	219,726	0	94,039	43,506	125,687	2.91	8.41
23.4	RM	88.0	137,545	219,726	552,288	52,400	637,433	719,614	42.66	48.16

6.3.6 Test Results

A total of fifteen tests were conducted for this series over a period of several days. Several weeks prior to this, pre-tests were performed with bare, steel-encased, and reactive-encased charges for chamber and instrumentation characterization. As a result of the pre-tests, the final types of pressure transducers and their mount positions were decided.

The tests are summarized in Table 6-12. The plan was to test every reactive material configuration at least once and then repeat those materials that yielded significant pressures or where an anomaly occurred. Results of the pre-tests showed significant damage to the unshielded transducers and thermocouples could occur from steel fragments. Therefore, the steel-encased charge was held until the end.

Table 6-12. Chamber tests conducted by ATK.

Test No.	Date	Material Supplier	Description	Charge Mass (g)	Case Mass (g)
T-0	5/24/2010	ATK	Bare	23.40	NA
T-1	5/24/2010	DET	30W-40Al-30Epoxy	23.40	85.36
T-2	5/25/2010	DET	15W-19Al-30Hf-36Epoxy	23.40	82.55
T-3	5/25/2010	DET	30W-20Al-20B-30Epoxy	23.40	81.52
T-4	5/25/2010	Matsys	Hf+Al	23.40	87.67
T-5	5/25/2010	Matsys	Hf+Al+Bi2O3	23.41	87.95
T-6	5/25/2010	Matsys	Al+Ti+B2C	23.41	43.83
T-7	5/25/2010	SRI/DET	W/Al/Fl-Epoxy	23.40	89.28
T-8	5/25/2010	SRI/DET	W/Al/Hf/Fl-Epoxy	23.40	94.52
T-9	5/26/2010	Matsys	Al (H2)	23.40	45.21
T-10	5/26/2010	Matsys	Hf+Al+Bi2O3	23.40	87.55
T-11	5/26/2010	DET	15W-19Al-30Hf-36Epoxy	23.40	81.72
T-12	5/26/2010	SRI/DET	W/Al/Hf/Fl-Epoxy	23.40	87.5
T-13	5/26/2010	Matsys	Al (H2)	23.40	45.29
T-14	5/26/2010	DET	Steel	23.40	87.49

The LX-14 charge masses were consistent at 23.4 g. Most of the casings weighed from 81 to 89 g. The Al+Ti+B2C and Al(H2), with their low densities, had about half the mass. Al+Ti+B2C was considered a legacy material (good performer in previous tests), while the Al(H2) was considered a reactive material baseline. Wall thickness of these materials was kept the same as the others to maintain similar casing breakup. Using thicker casings to make up for the mass shortfall would have too great effect on the shock physics, i.e., greater rarefactions and less shock-heating for the outermost material.

Typical unassembled hardware and capped charge are shown in Figs. 6-66 and 6-67.

Fig. 6-66. Test article prior to assembly. From left to right: the detonator housing confinement, LX-14 explosive charge, RMS case, and end confinement.
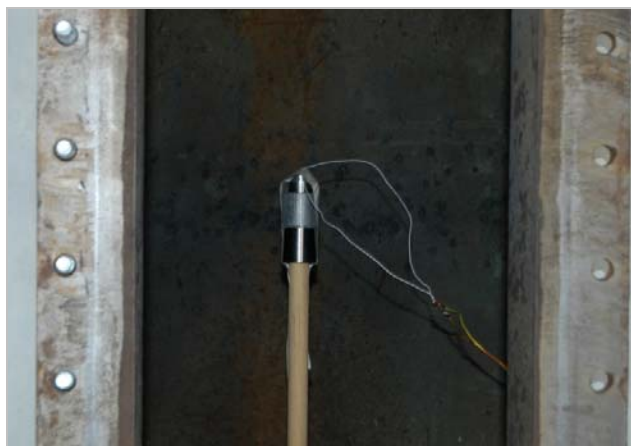
Fig. 6-67. Test article on wooden dowel with the detonator connected.

Both the Kulite and Endevco pressure transducers worked well in recording time-resolved pressures as well as QSPs. This subsection focuses on the quasi-static pressure. The pressure records were analyzed using HBM software product Perception Free Viewer, version 6.12. QSP values for each pressure transducer are listed in Table 6-13. An "x" indicates that no data were recorded. Average pressures for all transducers are listed in the rightmost column. The QSP was calculated using a linear regression for the range of data between about 20 and 100 ms. The *y*-intercept of this line was taken as the QSP.

Table 6-13. Summary of Quasi-Static Chamber Pressures.

Test	Recording	Casing	Case	LX-14 Explosive	Quasi-Static Pressure (psi)							
No.	No.	Material	Mass (g)	Mass (g)	P1	P2	P3	P4	P5	P6	P7	Ave
T-0	075	Bare	NA	23.4	18.43	17.99	18.18	18.26	18.29	18.77	18.22	18.31
T-1	076	30W-40Al-30Epoxy	85.36	23.4	34.85	34.65	34.83	34.79	34.98	34.78	34.66	34.79
T-2	078	15W-19Al-30Hf-36Epoxy	82.55	23.4	34.81	34.69	34.72	34.83	34.92	35.26	34.81	34.86
T-3	079	30W-20Al-20B-30Epoxy	81.52	23.4	26.10	25.31	25.55	25.95	25.91	23.82	26.47	25.59
T-4	080	Hf+Al	87.67	23.4	30.69	31.01	30.45	30.52	30.01	30.48	29.23	30.34
T-5	081	Hf+Al+Bi2O3	87.95	23.41	34.15	33.73	33.76	34.07	33.84	33.17	33.72	33.78
T-6	082	Al+Ti+B2C	43.83	23.41	32.60	31.36	31.90	32.40	x	32.97	32.64	32.31
T-7	086	W/Al/Fl-Epoxy	89.28	23.4	31.80	31.56	31.55	32.00	32.11	x	31.77	31.80
T-8	087	W/Al/Hf/Fl-Epoxy	94.52	23.4	33.40	33.14	32.91	33.50	33.58	x	33.41	33.32
T-9	094	Al (H2)	45.21	23.4	36.00	35.18	35.99	36.30	36.37	x	37.93	36.30
T-10	088	Hf+Al+Bi2O3	87.55	23.4	33.20	32.35	32.38	33.40	x	x	32.32	32.73
T-11	089	15W-19Al-30Hf-36Epoxy	81.72	23.4	31.80	31.10	31.26	31.90	x	x	32.41	31.69
T-12	090	W/Al/Hf/Fl-Epoxy	87.5	23.4	29.90	x	29.62	30.00	x	30.25	29.44	29.84
T-13	091	Al (H2)	45.29	23.4	35.40	32.51	34.94	35.80	x	x	35.36	34.80
T-14	092	Steel	87.49	23.4	4.67	4.09	4.52	4.60	x	x	4.36	4.45

As expected, the average QSP for the steel-cased charge, 4.45 psi, was much less than the bare charge's 18.31 psi. Average QSP for the reactive-cased charges ranged from 25.59 to 34.86 psi. The CIPed aluminum had the highest QSP, 36.30 psi (T-9); this material was very weak in tension, so this is understandable from a break-up standpoint; also, it contains much more aluminum (45 g) than the other materials (at most 13 g), among which the best was 15W-19Al-30Hf-36Epoxy at 34.86 psi, and second-best was Matsys's Hf+Al+Bi2O3 at 33.78 psi; these results may be considered similar, within test-to-test variation.

For example, between T-9 and T-13 (Al-H2 the purest form and easiest to break up), the difference in QSP is 5%, whereas case masses differ by only 0.18%. Similarly, the QSP for T-2 and T-11 (15W-19Al-30Hf-36Epoxy) differ by 10%, where case masses differ by 1%. The weakest performer was 30W-20Al-20B-30Epoxy at 25.59 psi; this result is not unexpected since boron is known to be difficult to ignite.

Residual powder found in the chamber is shown in Fig. 6-68. Typical QSP plots for a bare charge, steel-encased, and reactive-material-cased are shown in Figs. 6-69 through 6-71.

Fig. 6-68. Post-test debris and fine powder.
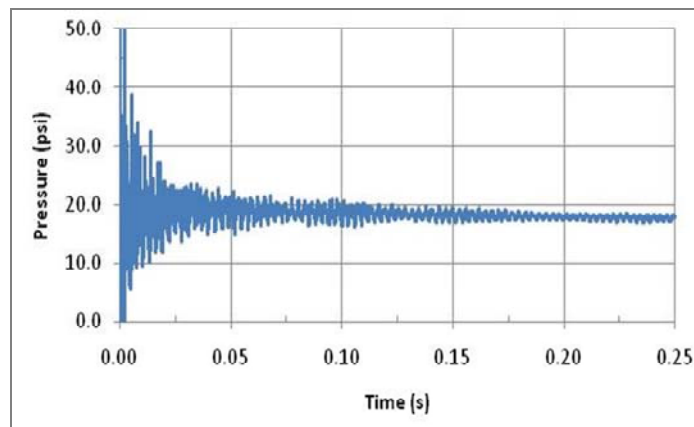
Fig. 6-69. QSP plot for bare charge (LX-14).
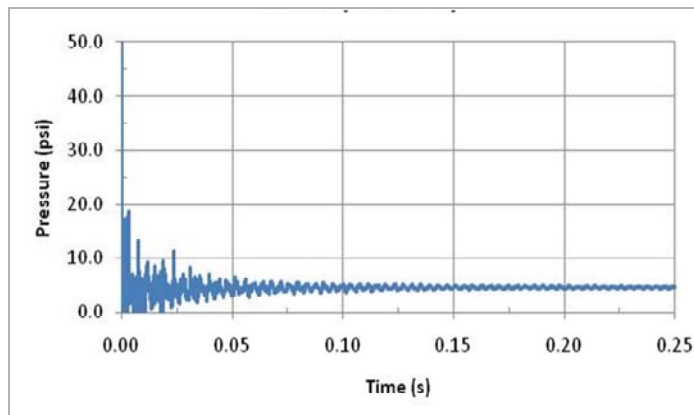
Fig. 6-70. QSP plot for steel-encased charge.
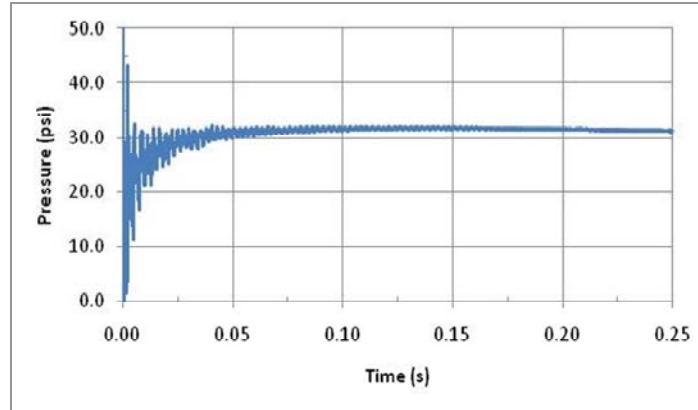
Fig. 6-71. QSP plot for 15W-19Al-30Hf-36Epoxy-encased charge.

The QSP plots for each test including all the transducer ports are shown below in Figs. 6-72 through 6-86. In each case, the pressure is plotted out to 250 ms. The title above each plot indicates the material followed by the recording number and port number separated by a dash.
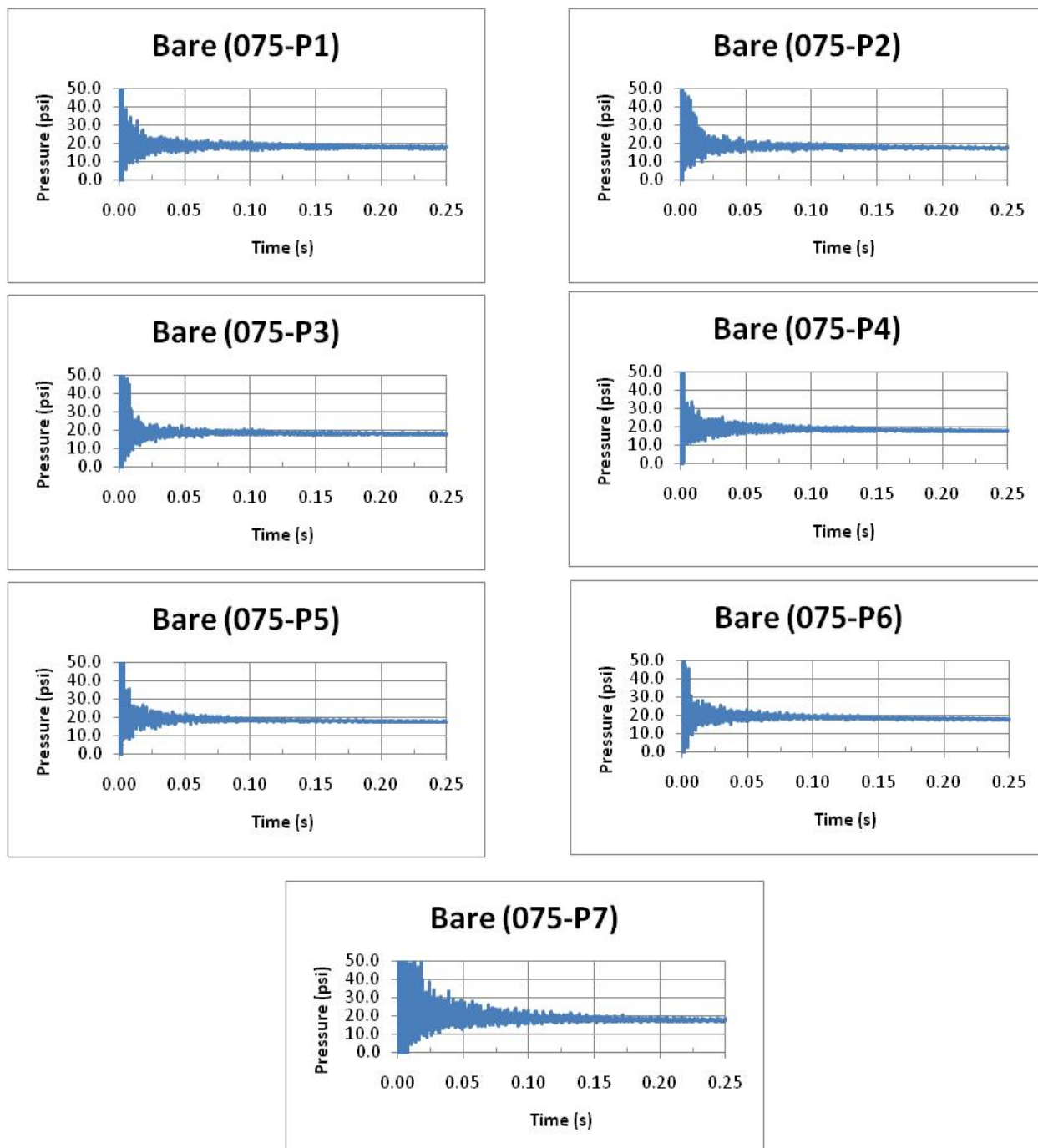
Fig. 6-72. QSP plots for bare charge (Test T-0).
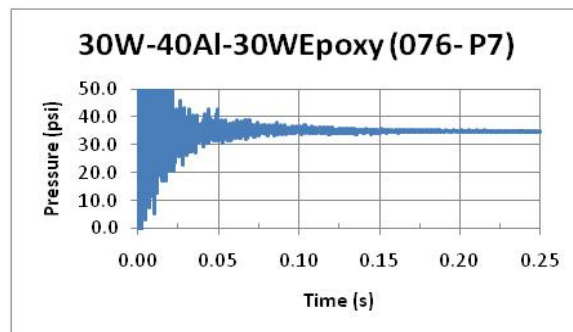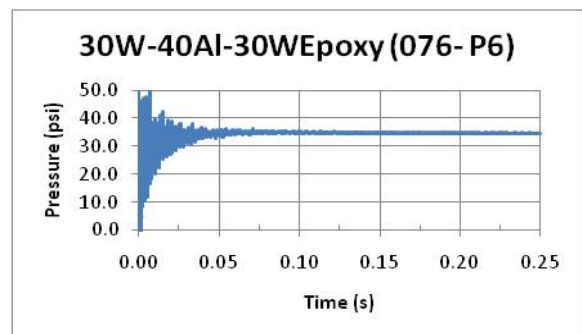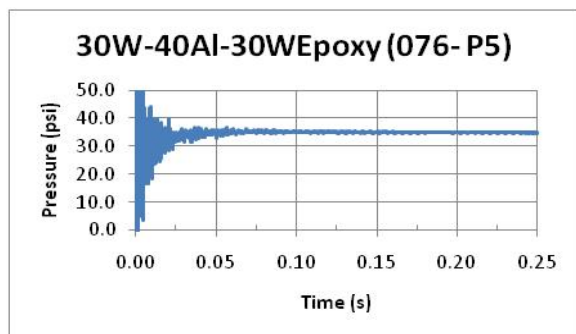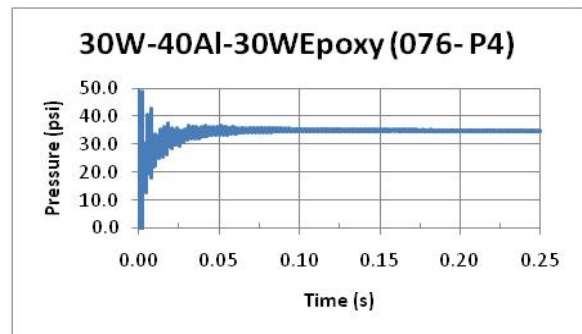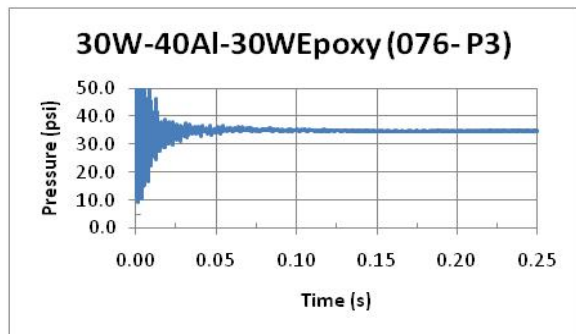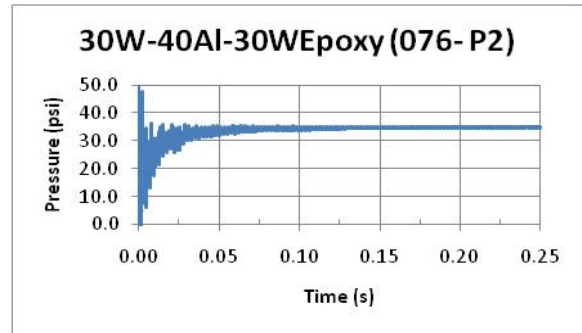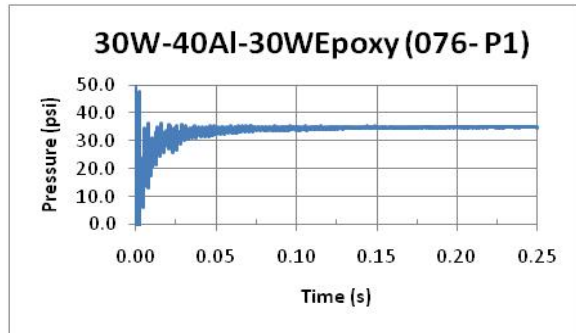
Fig. 6-73. QSP plots for 30W-40Al-30Epoxy (Test T-1).
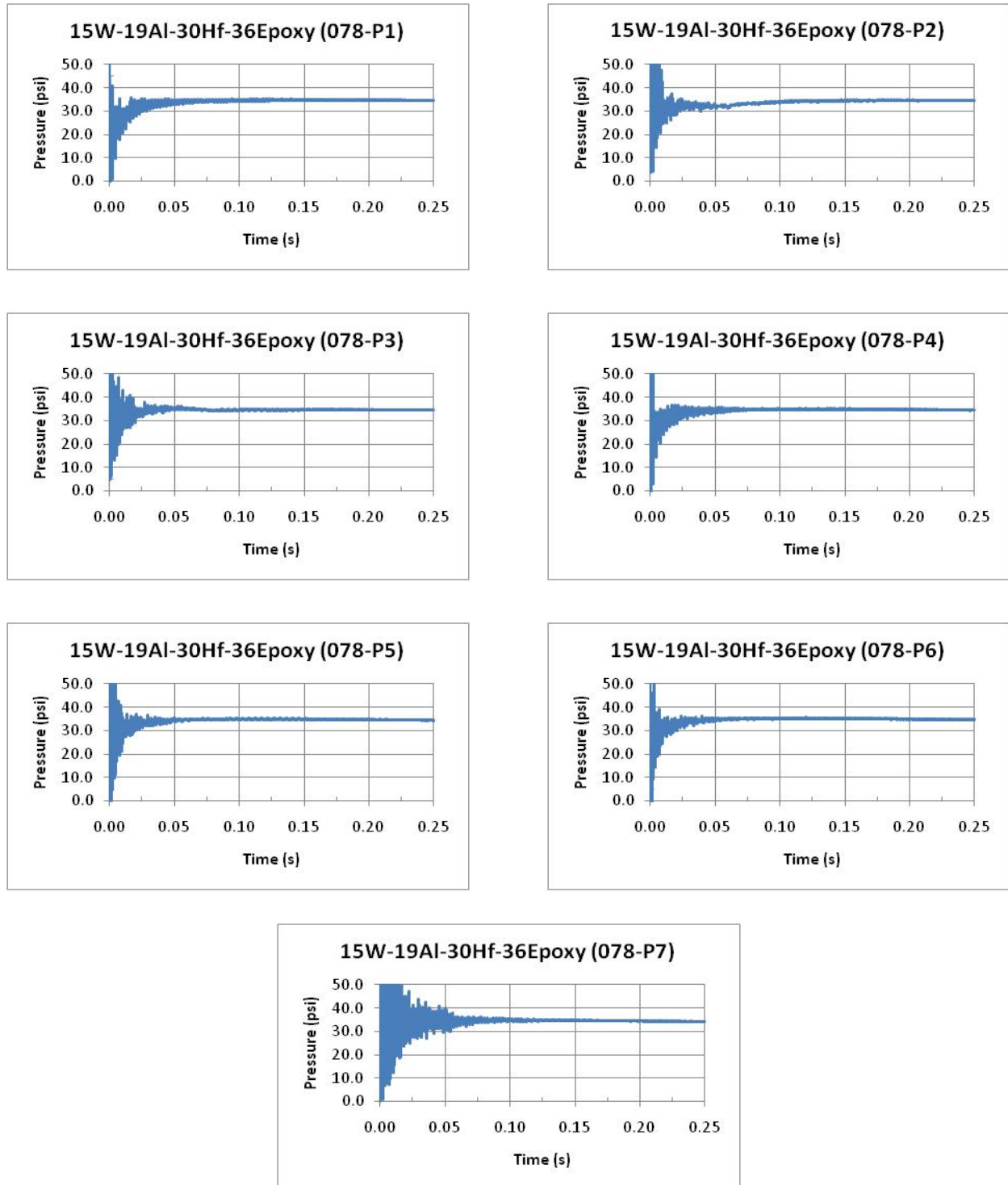
Fig. 6-74. QSP plots for 15W-19Al-30Hf-36Epoxy (Test T-2).
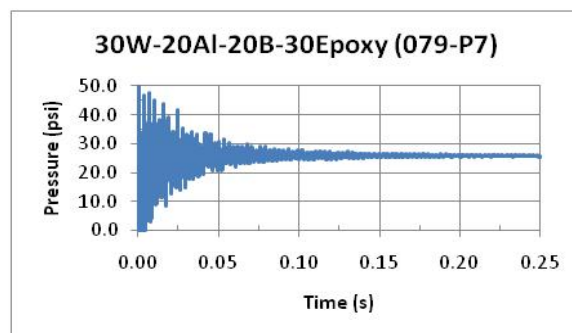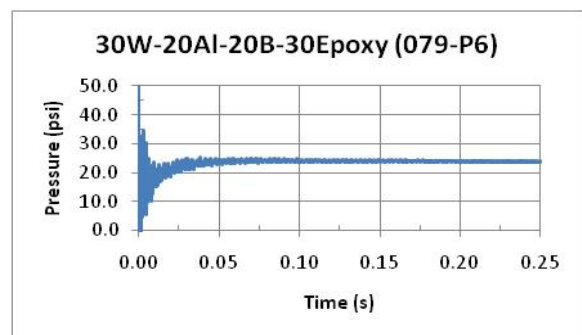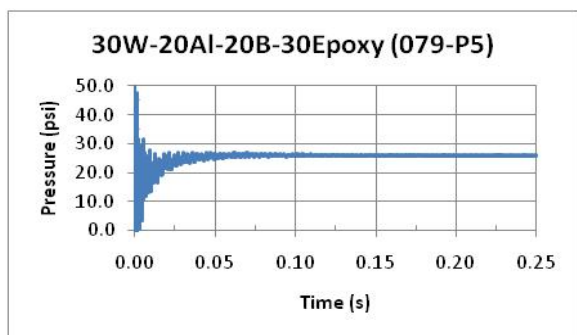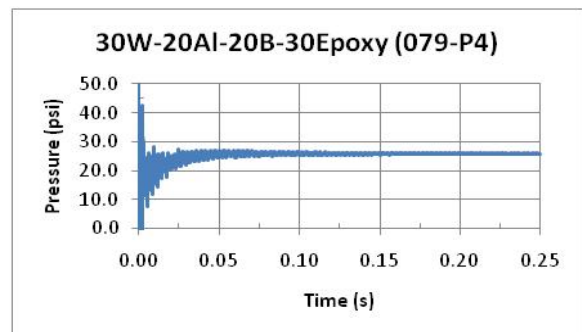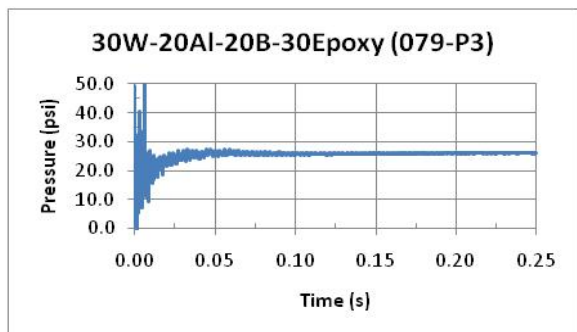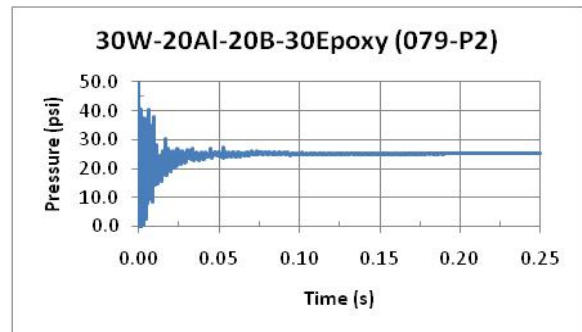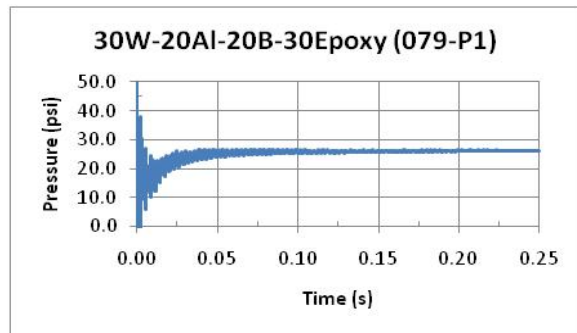
Fig. 6-75. QSP plots for 30W-20Al-20B-30Epoxy (Test T-3).
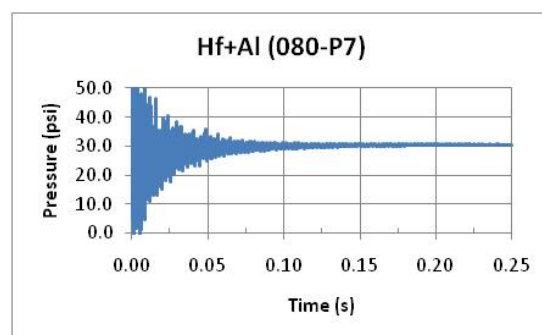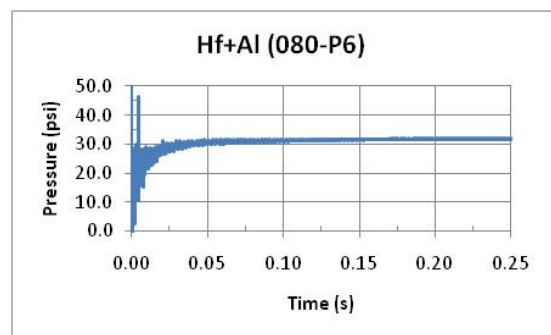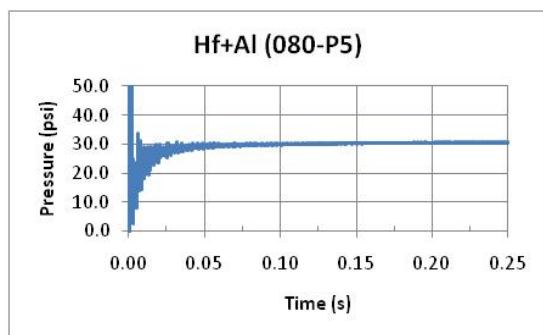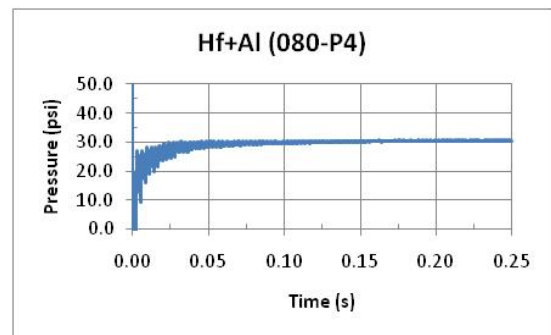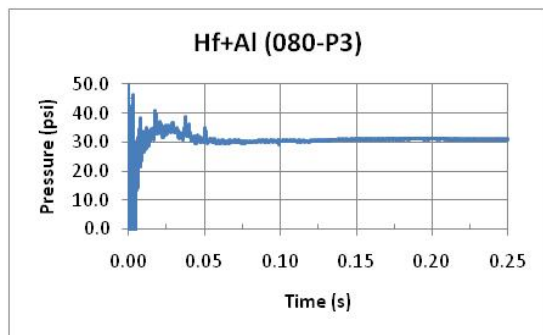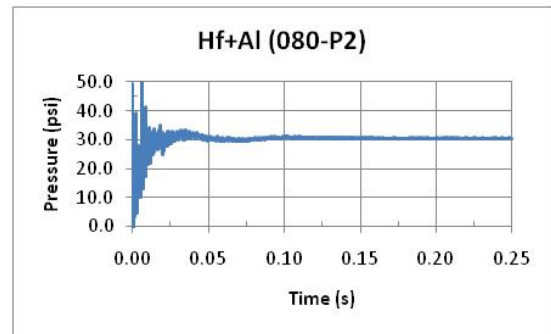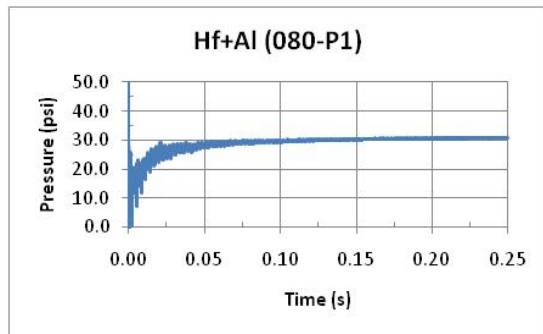
Fig. 6-76. QSP plots for Hf + Al (Test T-4).
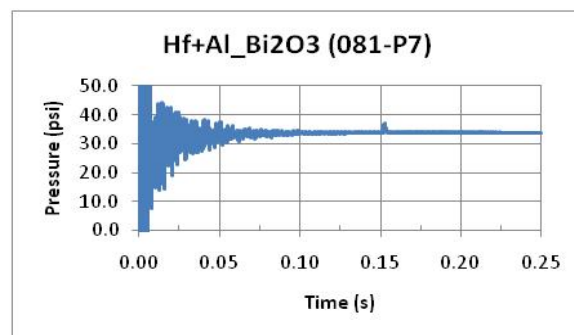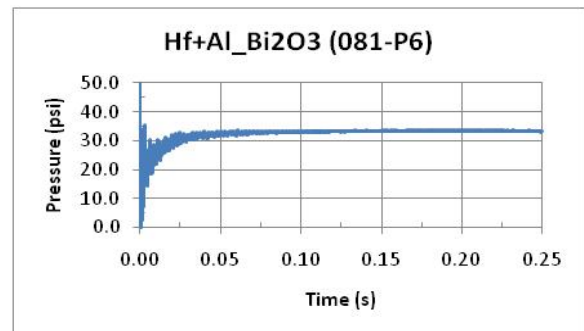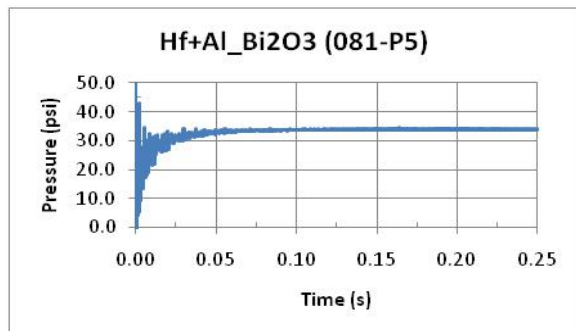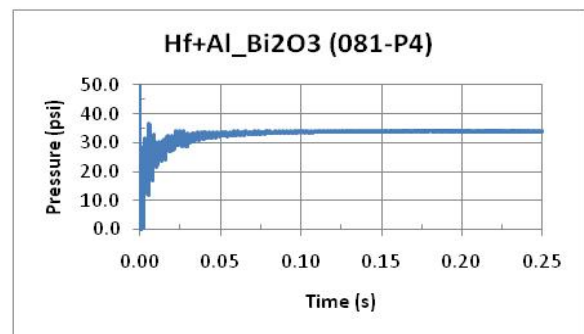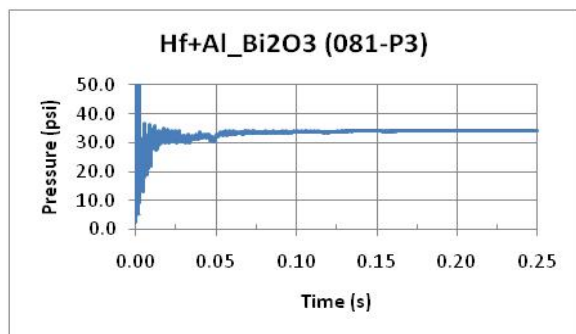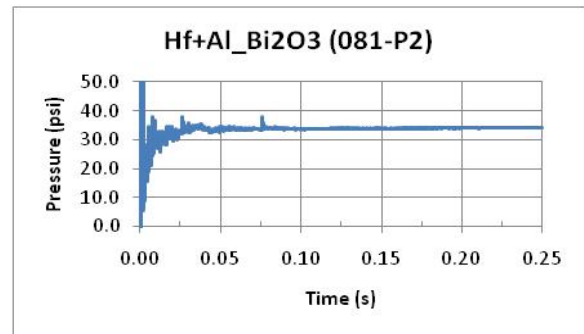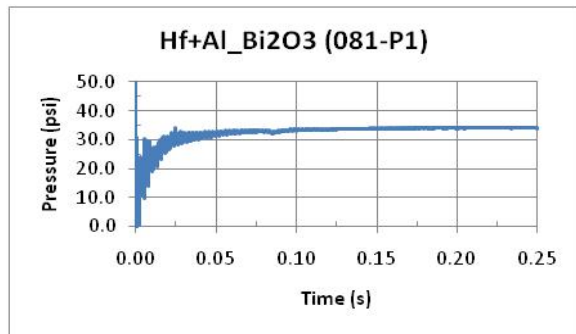
Fig. 6-77. QSP plots for Hf + Al + Bi2O3 (Test T-5).
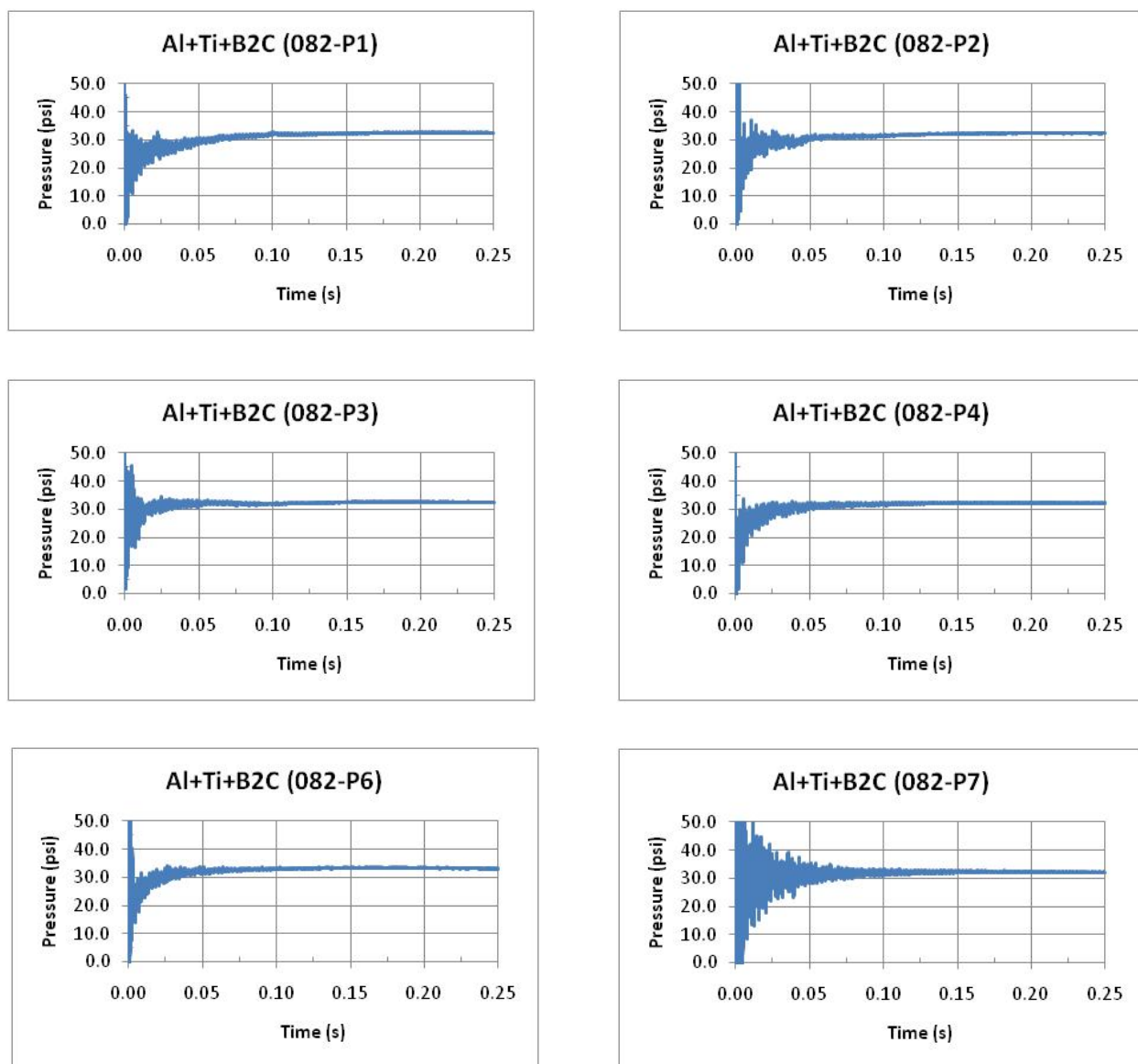
Fig. 6-78. QSP plots for Al/Ti/B2C (Test T-6).
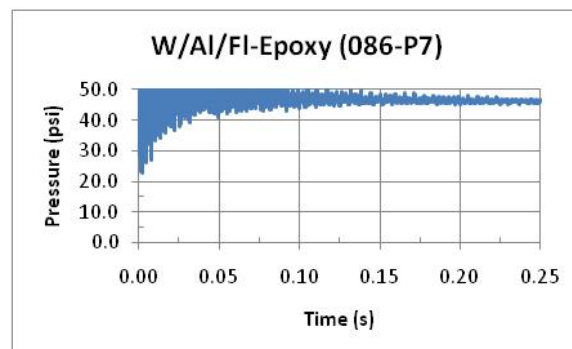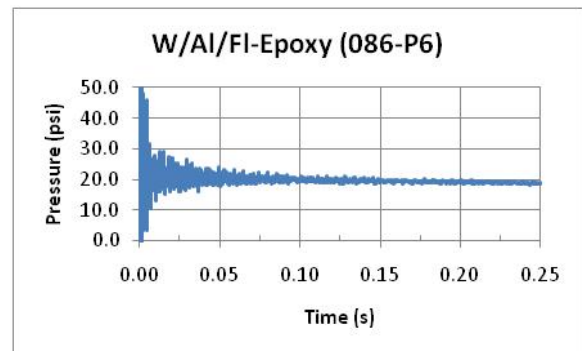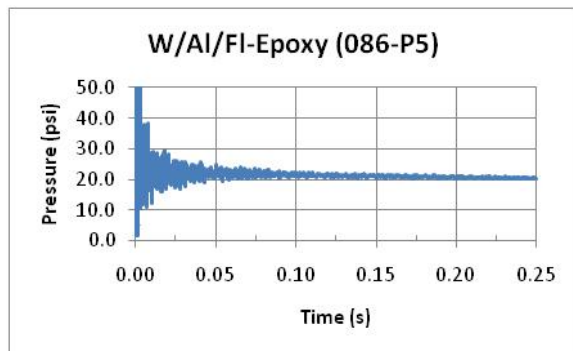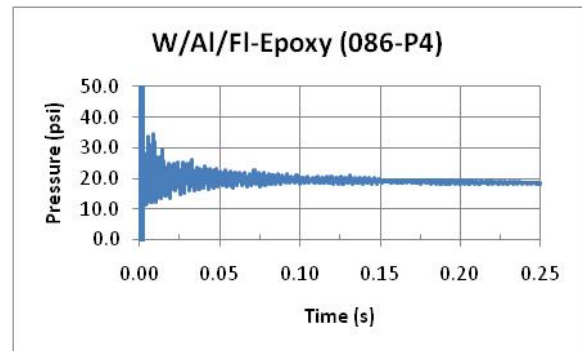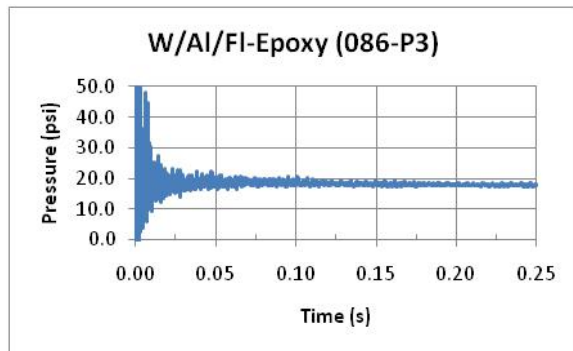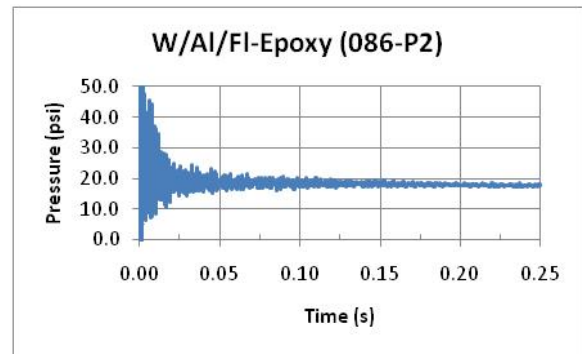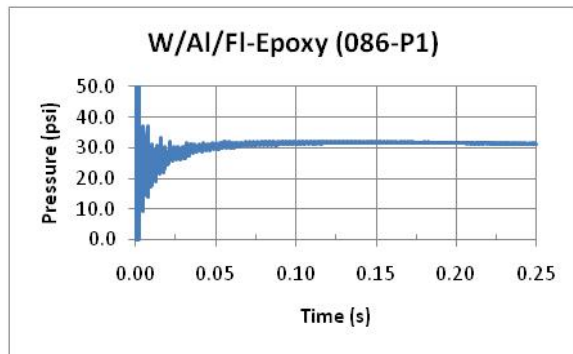
Fig. 6-79. QSP plots for W/Al/Fl-Epoxy (Test T-7).
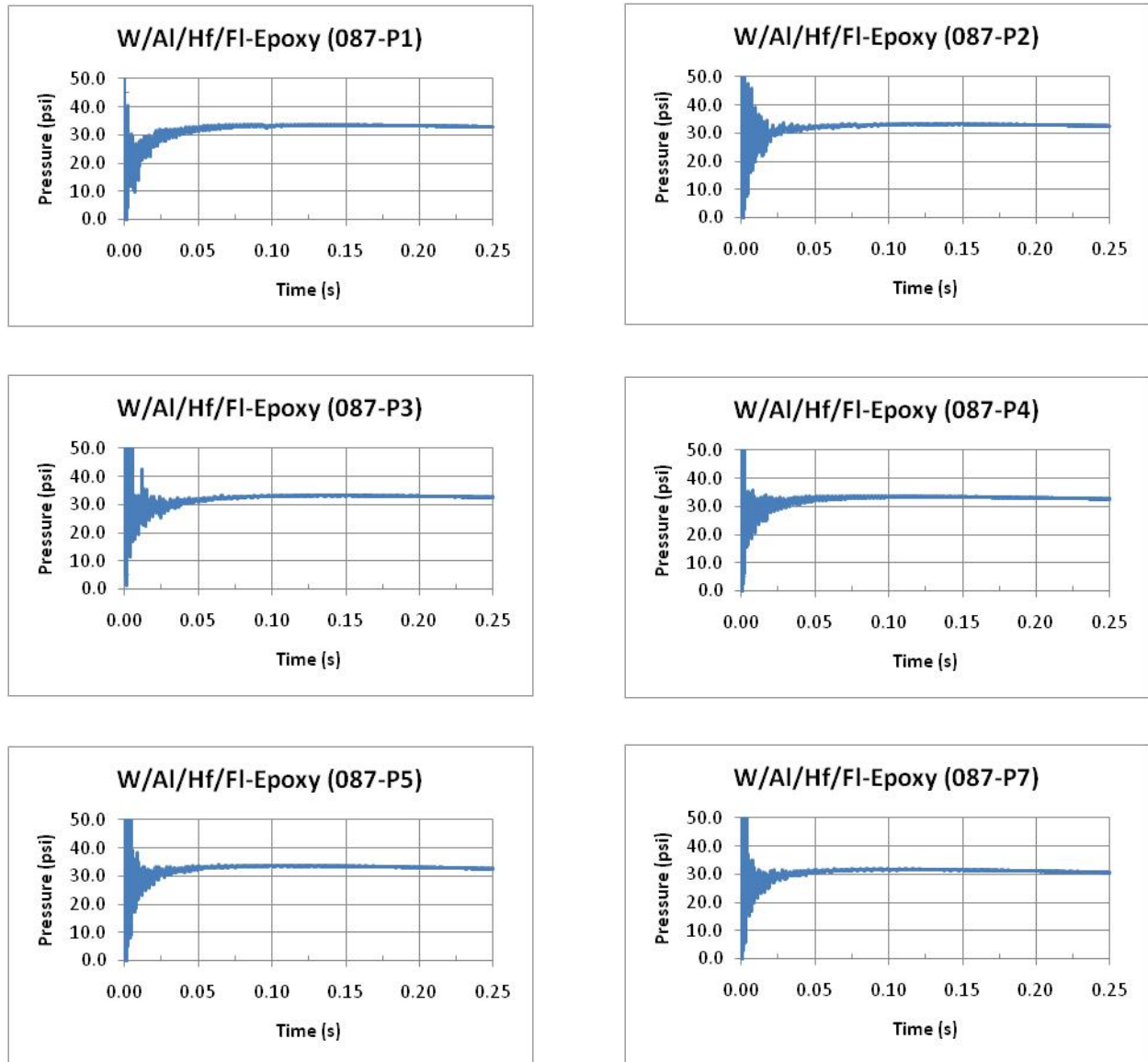
Fig. 6-80. QSP plots for W/Al/Hf/Fl-Epoxy (Test T-8).
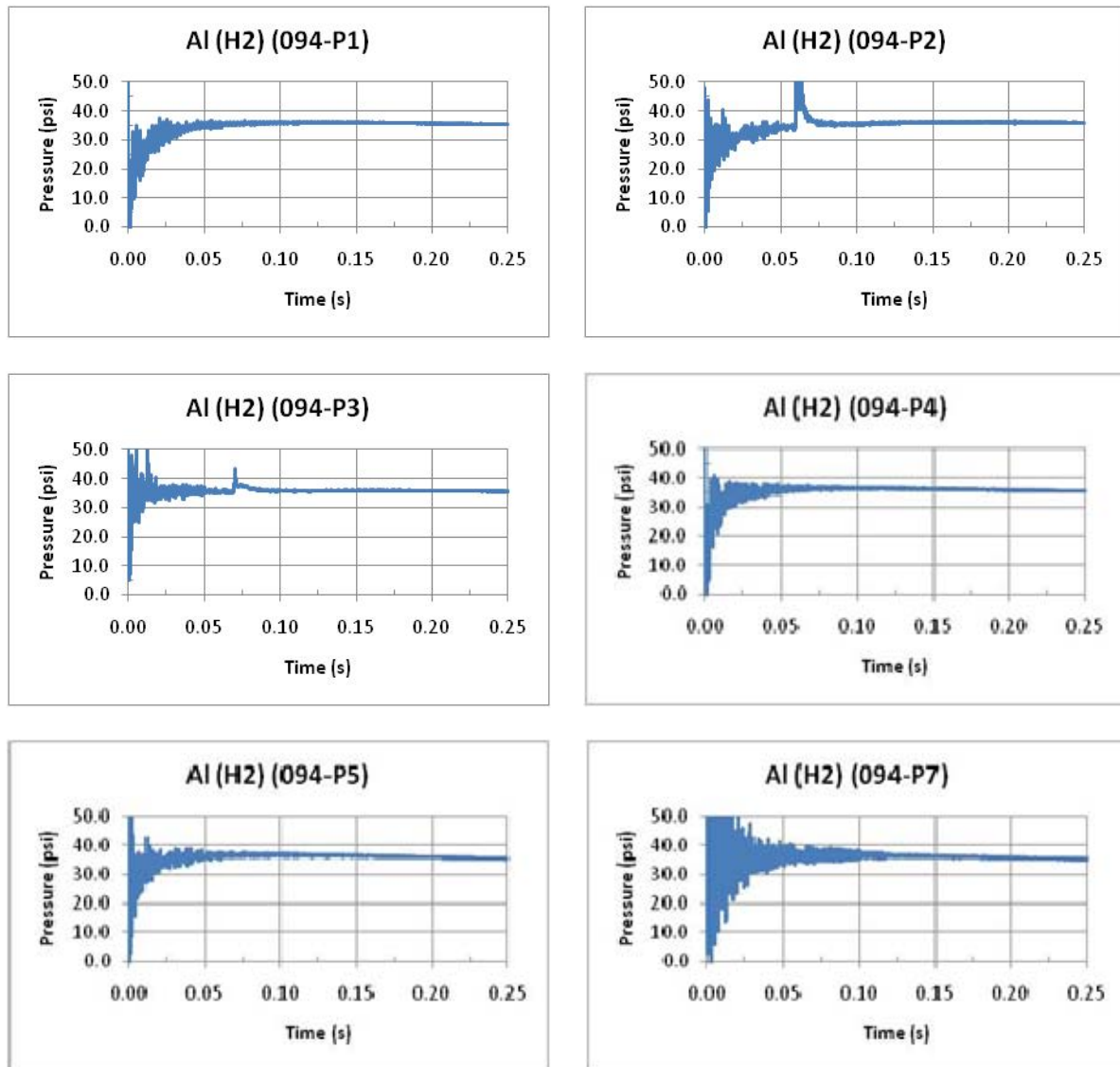
Fig. 6-81. QSP plots for Al-H2 (Test T-9).
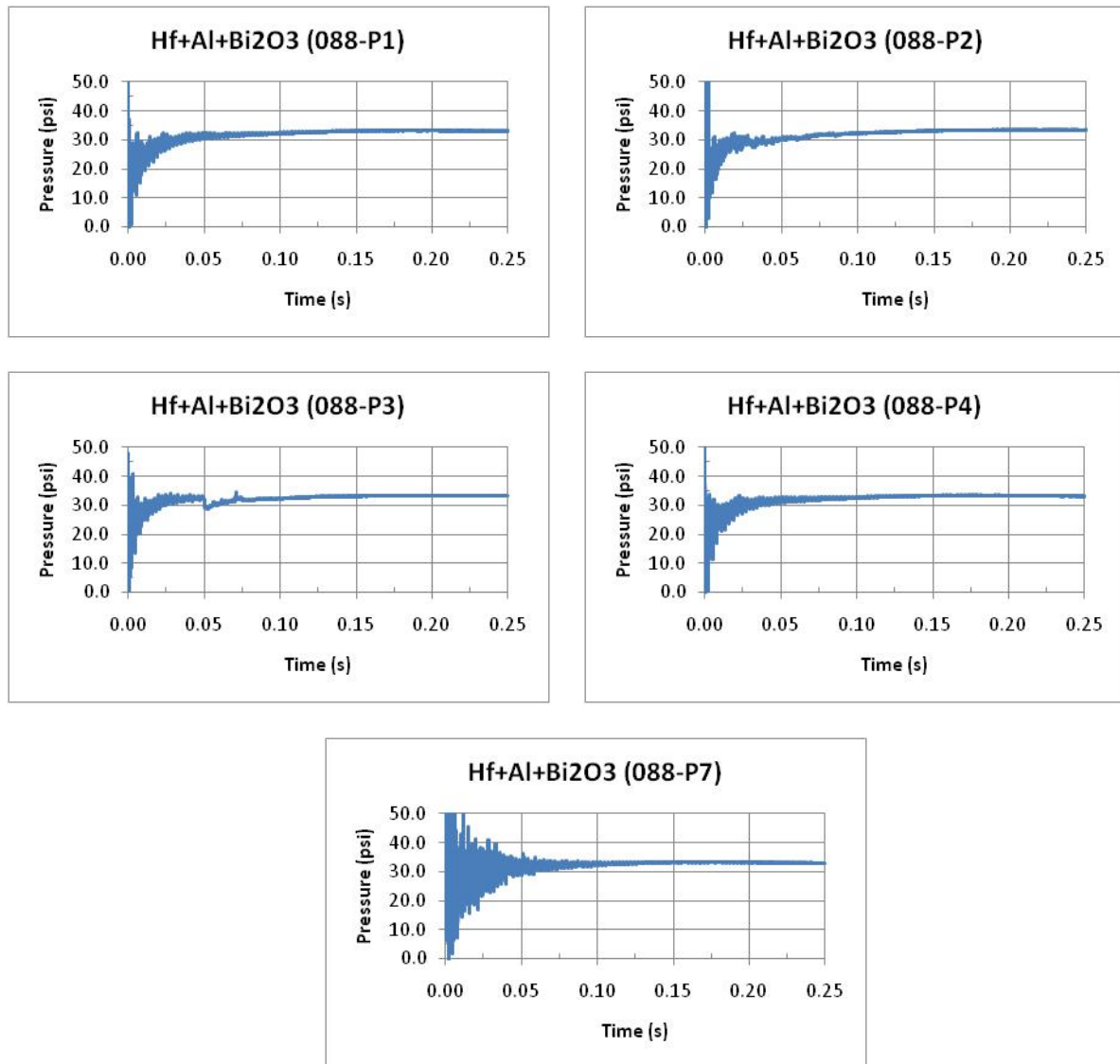
Fig. 6-82. QSP plots for Hf-Al-Bi2O3 (Test T-10).
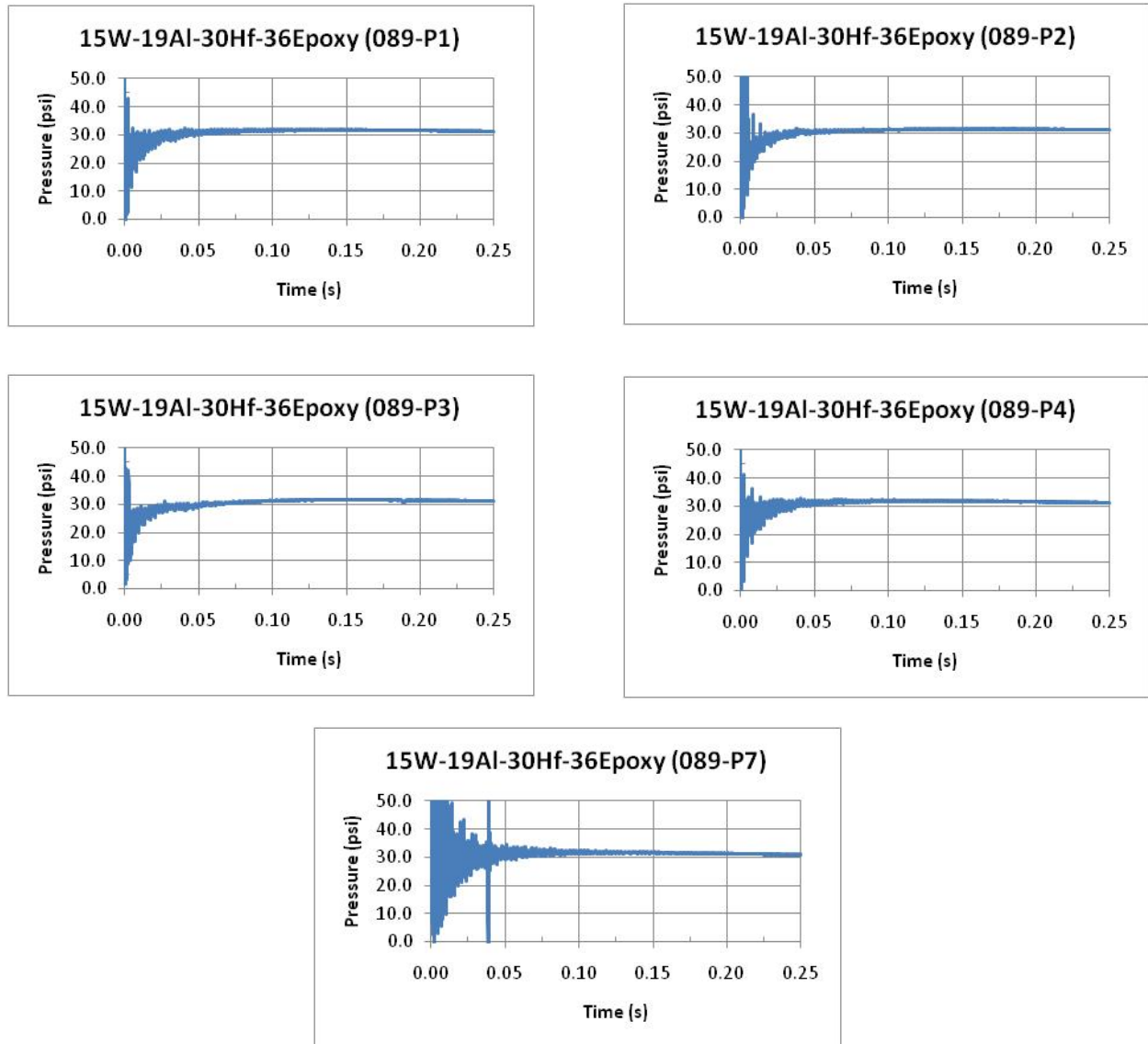
Fig. 6-83. QSP plots for 15W/19Al/30Hf/36Epoxy (Test T-11).
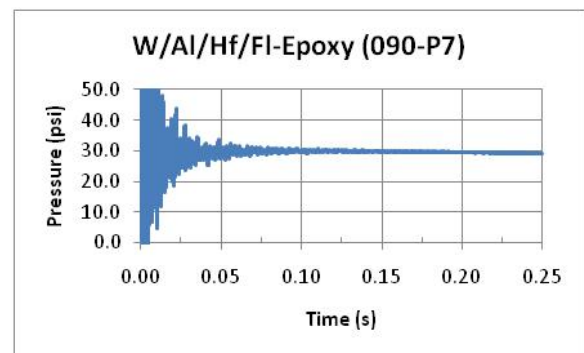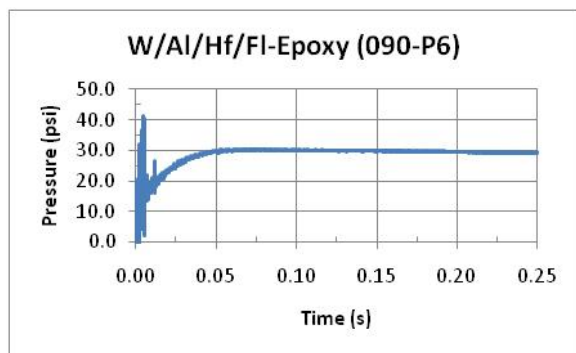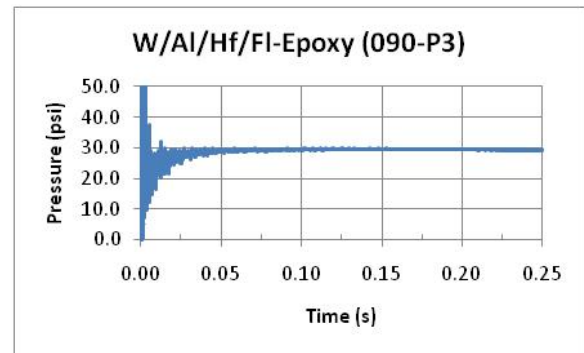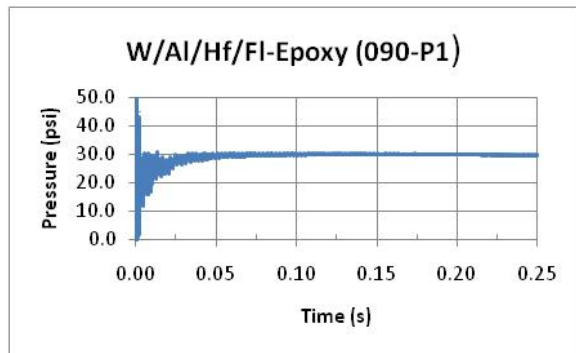
Fig. 6-84. QSP plots for W/Al/Hf/Fl-Epoxy (Test T-12).
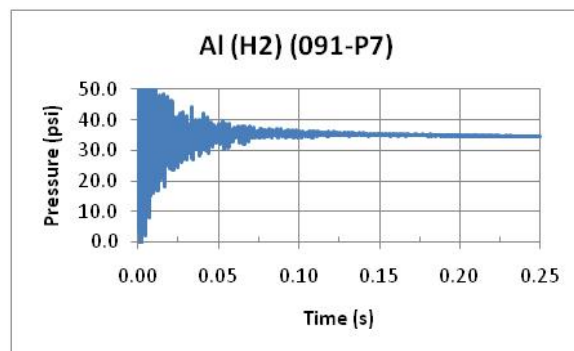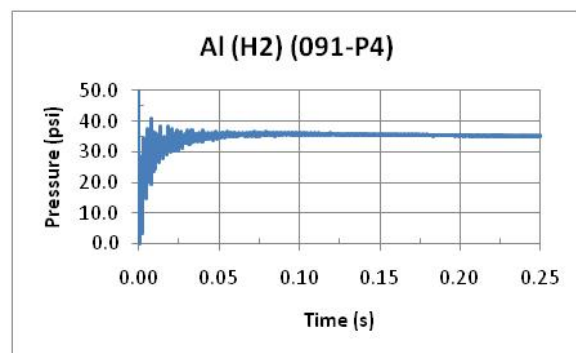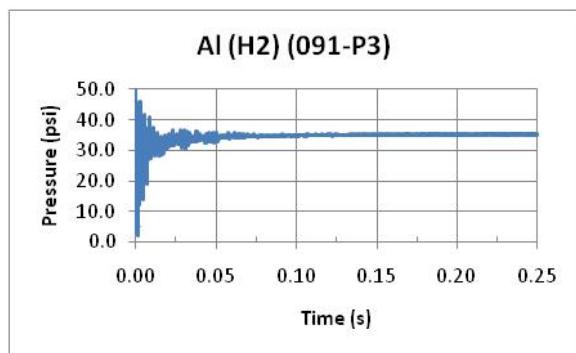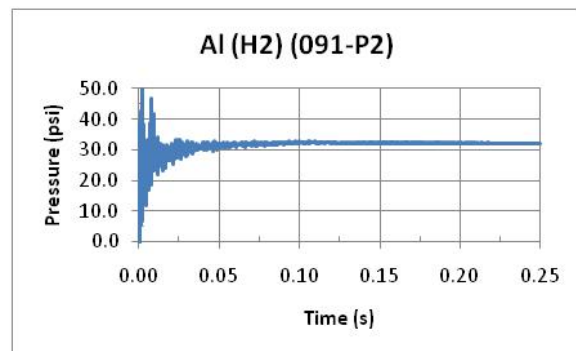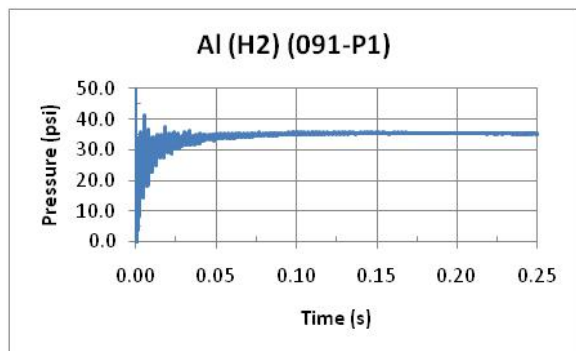
Fig. 6-85. QSP plots for Al(H2) (Test T-13).
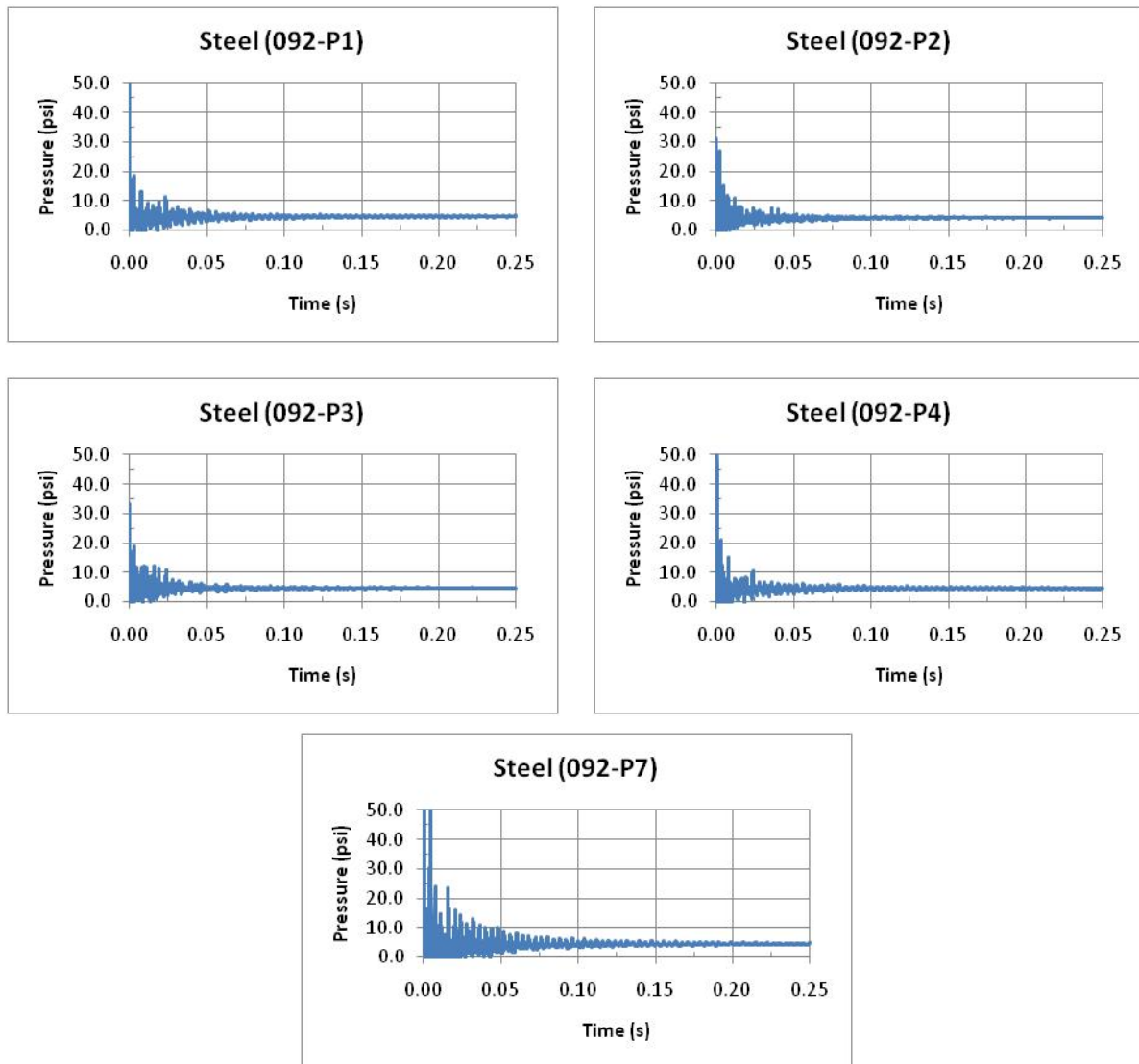
Fig. 6-86. QSP plots for steel (Test T-14).

Transient Pressure and Impulse

Fast-acting Endevco and Kulite pressure transducers were used to record pressures at the chamber walls. Pressure ports P1 and P4 may be considered at normal incidence to the blast wave while all others are at angles other than 90°. Furthermore, ports P1 and P4 were shielded from fragment impact by a stand-off plate; all other ports were left open to the blast wave. For each port, the following data were extracted: TOA, time of arrival; P_{max}, maximum pressure; and t_w, pulse width. Pulse width is measured from the first rise to the first crossing of the abscissa. Impulse was calculated by numerically integrating the pressure history up to the end of the first pulse, thereby eliminating the contribution or superposition of the quasi-static pressure build-up. These data are summarized in Tables 6-8 through 6-10. The green and red highlighting represents the minimum and maximum values in each column. The pressure histories and impulse of the initial pulse are shown in Figs. 6-87 through 6-101. Ports P1 through P6 are plotted out to 0.6 ms, while port P7 is plotted out to 1.2 ms. It is surmised that the pulse durations recorded at P7 tended to be longer because of the confinement effect of its location in a well cavity at the bottom of the chamber.

Table 6-14. Time-of-arrival, maximum pressure, pulse width, and impulse data for pressure ports P1, P2, and P3.

Test No.	Case Material Designation	P1				P2				P3			
		TOA (µs)	Pmax (psi)	tw (µs)	Impulse (psi-s)	TOA (µs)	Pmax (psi)	tw (µs)	Impulse (psi-s)	TOA (µs)	Pmax (psi)	tw (µs)	Impulse (psi-s)
T-0	Bare	356	181.7	391	0.0204	507	92.8	445	0.0124	503	134.8	387	0.0139
T-1	30W-40Al-30Epoxy	428	402.4	364	0.0269	588	59.8	478	0.0154	644	78.7	415	0.0165
T-2	15W-19Al-30Hf-36Epoxy	388	191.4	500	0.0241	631	74.7	451	0.0150	638	62.2	448	0.0134
T-3	30W-20Al-20B-30Epoxy	421	127.7	413	0.0196	592	58.6	426	0.0096	672	50.3	351	0.0089
T-4	Hf+Al	471	174.5	326	0.0160	710	49.3	438	0.0110	686	82.0	441	0.0160
T-5	Hf+Al+Bi2O3	445	193.3	663	0.0224	662	59.9	403	0.0121	749	55.6	435	0.0092
T-6	Al+Ti+B2C	363	286.2	366	0.0199	588	59.9	403	0.0106	664	65.1	429	0.0107
T-7	W/Al/Fl-Epoxy	422	282.3	427	0.0254	588	62.9	998	0.0102	601	62.2	412	0.0126
T-8	W/Al/Hf/Fl-Epoxy	407	291.2	335	0.0252	588	76.7	332	0.0134	594	71.5	434	0.0116
T-9	Al (H2)	373	187.1	301	0.0218	576	51.0	333	0.0098	586	76.7	400	0.0134
T-10	Hf+Al+Bi2O3	424	163.4	384	0.0181	659	60.5	421	0.0106	697	48.0	402	0.0093
T-11	15W-19Al-30Hf-36Epoxy	385	276.5	349	0.0280	591	66.7	452	0.0126	596	73.1	291	0.0094
T-12	W/Al/Hf/Fl-Epoxy	325	158.9	482	0.0218	x	x	x	x	325	0.9	480	0.0091
T-13	Al (H2)	356	166.5	617	0.0220	x	x	x	x	585	59.1	377	0.0102
T-14	Steel	543	61.2	334	0.0083	705	31.3	483	0.0051	864	34.4	389	0.0044

Table 6-15. Time-of-arrival, maximum pressure, pulse width, and impulse data for pressure ports P4, P5, and P6.

Test No.	Case Material Designation	P4				P5				P6			
		TOA (µs)	Pmax (psi)	tw (µs)	Impulse (psi-s)	TOA (µs)	Pmax (psi)	tw (µs)	Impulse (psi-s)	TOA (µs)	Pmax (psi)	tw (µs)	Impulse (psi-s)
T-0	Bare	309	170.0	340	0.0194	490	96.9	409	0.0118	443	211.0	394	0.0148
T-1	30W-40Al-30Epoxy	431	248.0	385	0.0225	621	83.8	326	0.0124	648	67.4	286	0.0101
T-2	15W-19Al-30Hf-36Epoxy	387	219.8	357	0.0247	617	99.2	442	0.0160	621	85.8	454	0.0129
T-3	30W-20Al-20B-30Epoxy	420	219.8	437	0.0210	615	77.4	431	0.0114	643	93.0	240	0.0083
T-4	Hf+Al	479	208.9	610	0.0198	685	61.8	442	0.0105	770	64.2	434	0.0092
T-5	Hf+Al+Bi2O3	448	225.3	325	0.0215	664	88.7	380	0.0120	693	63.7	403	0.0093
T-6	Al+Ti+B2C	376	227.0	293	0.0209	x	x	x	x	617	62.5	416	0.0100
T-7	W/Al/Fl-Epoxy	397	346.6	362	0.0277	561	128.4	361	0.0146	x	x	x	x
T-8	W/Al/Hf/Fl-Epoxy	399	286.9	328	0.0275	568	153.5	336	0.0153	x	x	x	x
T-9	Al (H2)	373	289.4	280	0.0226	x	x	x	x	x	x	x	x
T-10	Hf+Al+Bi2O3	455	166.4	421	0.0215	x	x	x	x	x	x	x	x
T-11	15W-19Al-30Hf-36Epoxy	375	223.6	390	0.0252	x	x	x	x	x	x	x	x
T-12	W/Al/Hf/Fl-Epoxy	384	234.2	358	0.0252	x	x	x	x	x	x	x	x
T-13	Al (H2)	358	173.7	347	0.0203	x	x	x	x	x	x	x	x
T-14	Steel	376	95.0	471	0.0102	x	x	x	x	x	x	x	x

Table 6-16. Time-of-arrival, maximum pressure, pulse width, and impulse data for pressure port P7.

Test No.	Case Material Designation	P7			
		TOA (µs)	Pmax (psi)	tw (µs)	Impulse (psi-s)
T-0	Bare	1137	163.8	1220	0.0641
T-1	30W-40Al-30Epoxy	1547	204.7	1561	0.0741
T-2	15W-19Al-30Hf-36Epoxy	1532	321.1	1583	0.0898
T-3	30W-20Al-20B-30Epoxy	1571	147.0	1131	0.0539
T-4	Hf+Al	1902	186.7	1135	0.0507
T-5	Hf+Al+Bi2O3	1744	227.7	924	0.0604
T-6	Al+Ti+B2C	1668	325.2	1164	0.0656
T-7	W/Al/Fl-Epoxy	1454	238.4	1564	0.0762
T-8	W/Al/Hf/Fl-Epoxy	1451	180.0	1163	0.0738
T-9	Al (H2)	1638	441.8	1398	0.0795
T-10	Hf+Al+Bi2O3	1772	258.2	1046	0.0637
T-11	15W-19Al-30Hf-36Epoxy	1532	248.7	1128	0.0720
T-12	W/Al/Hf/Fl-Epoxy	1470	162.3	1208	0.0712
T-13	Al (H2)	1578	230.0	1186	0.0674
T-14	Steel	2.011	94.4	1.116	0.0201
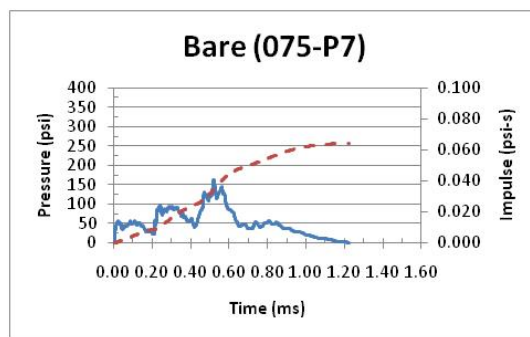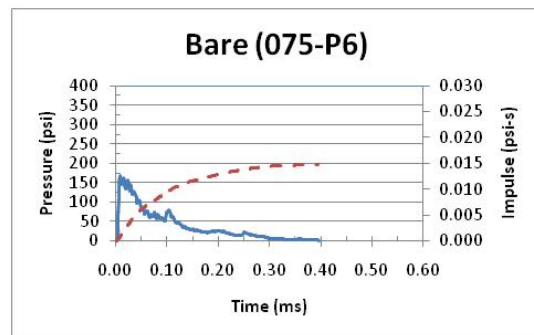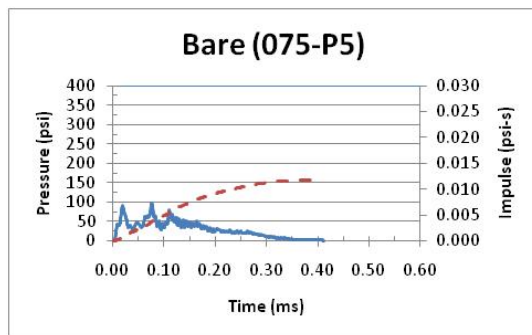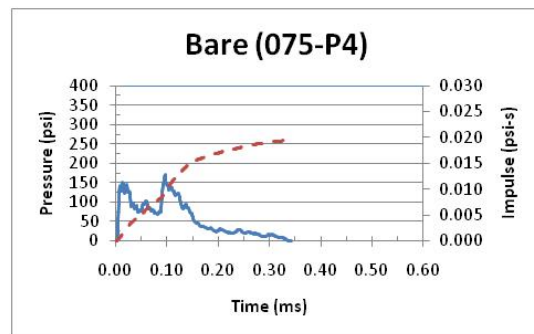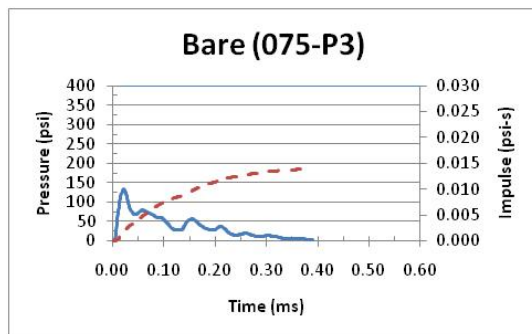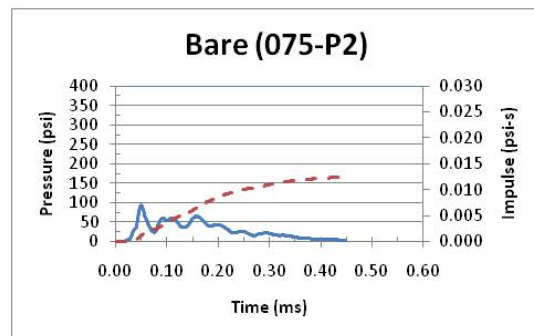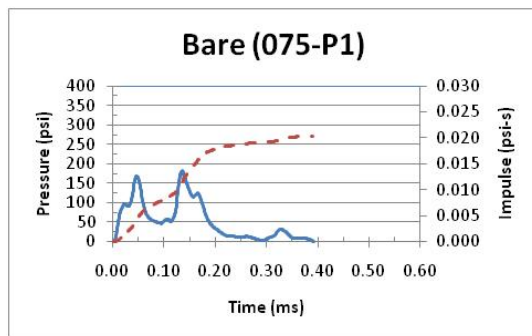
Fig. 6-87. Pressure history and impulse for bare charge (Test T-0).
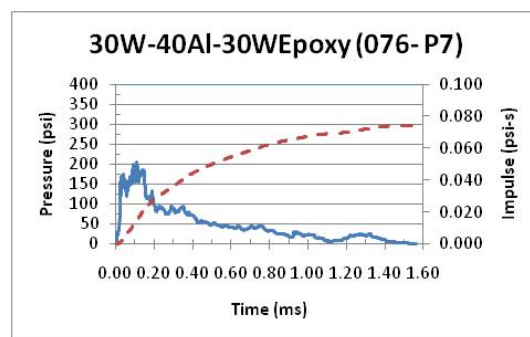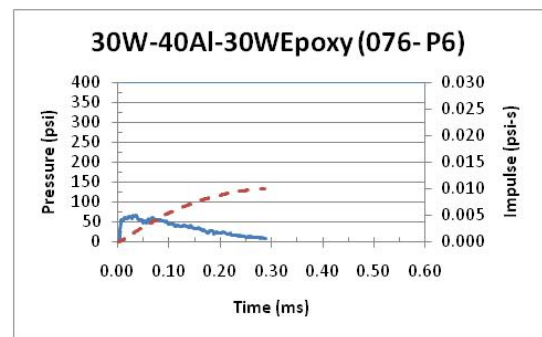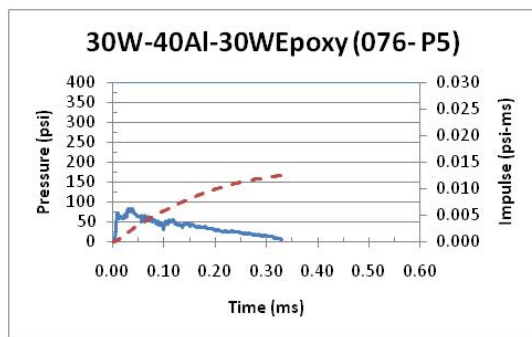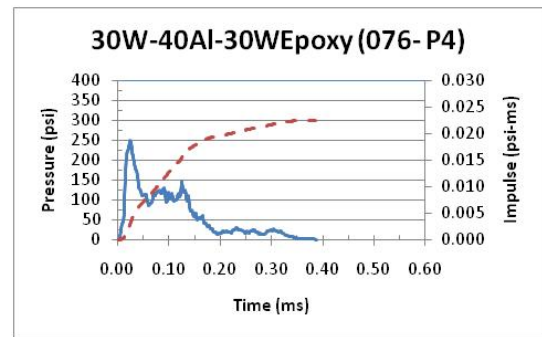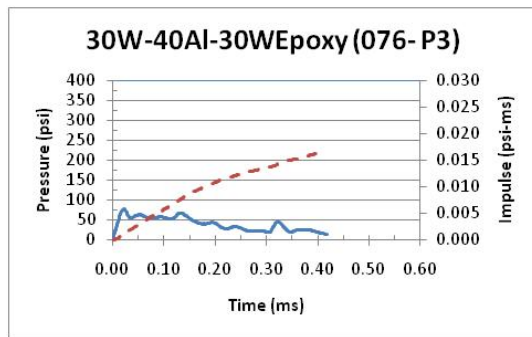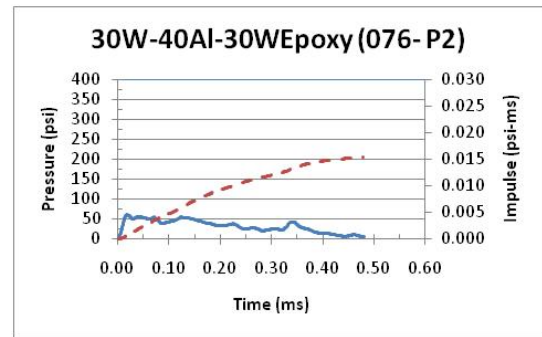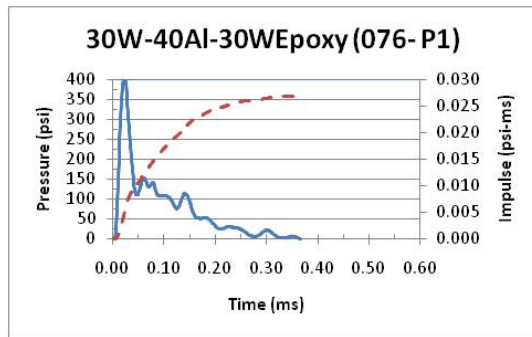
Fig. 6-88. Pressure history and impulse for 30W-40Al-30Epoxy (Test T-1).
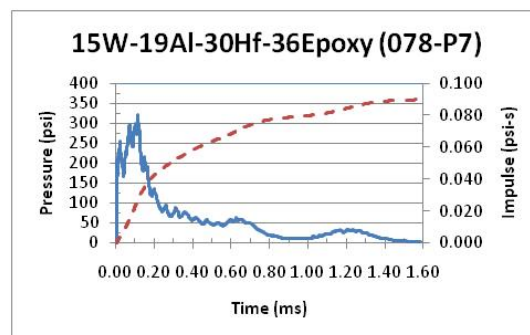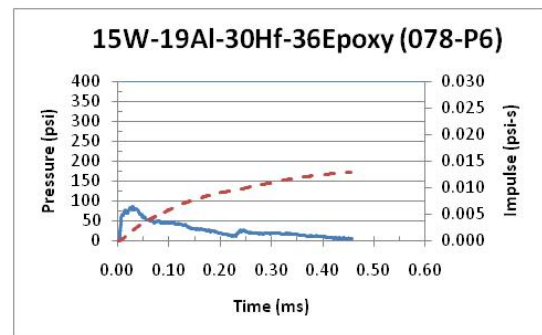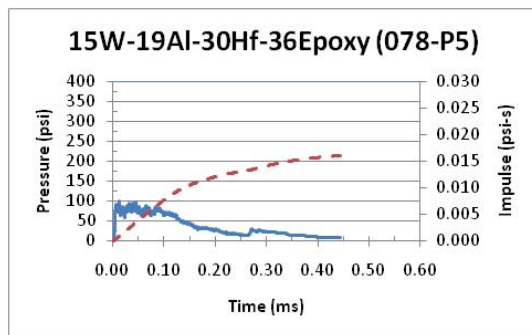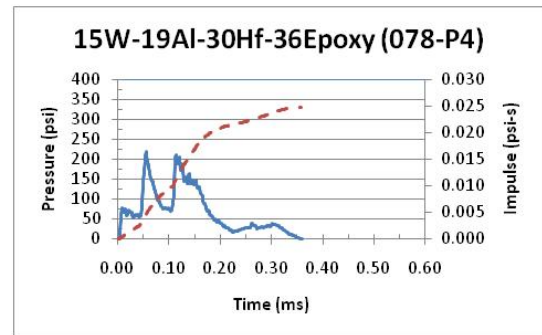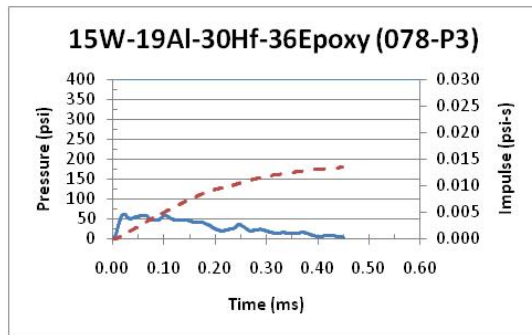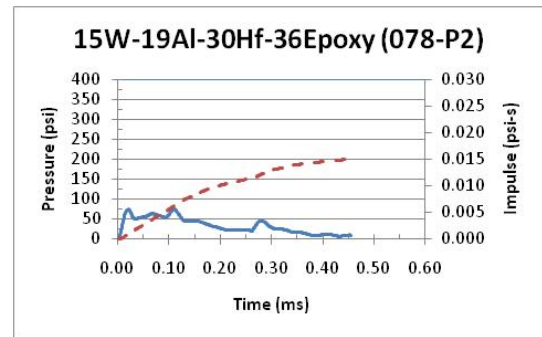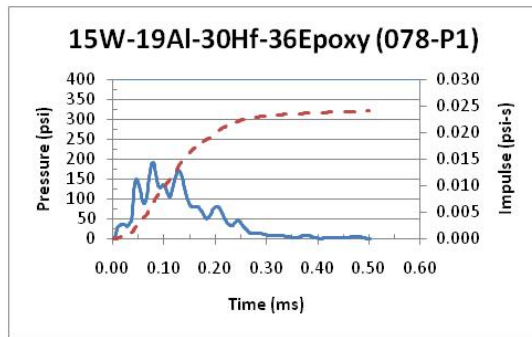
Fig. 6-89. Pressure history and impulse for 15W-19Al-30Hf-36Epoxy (Test T-2).
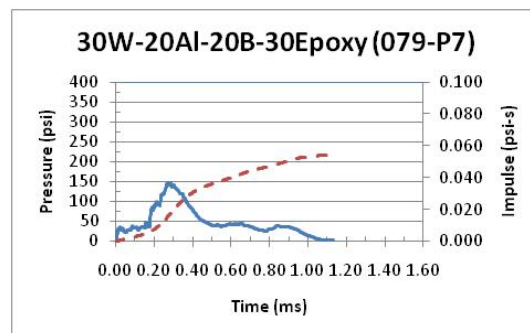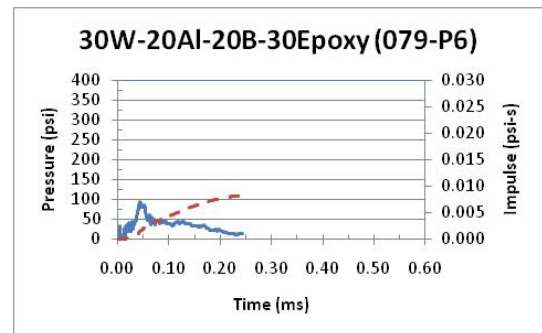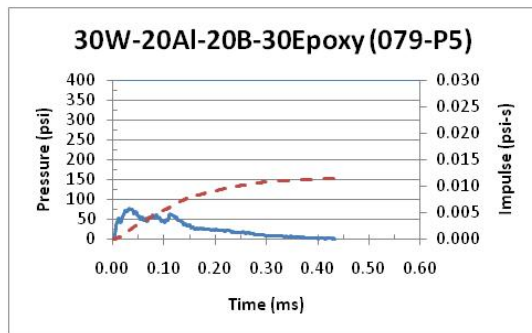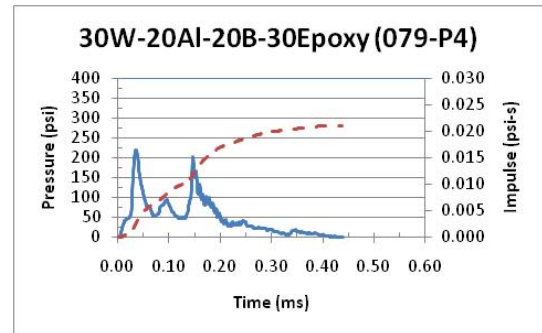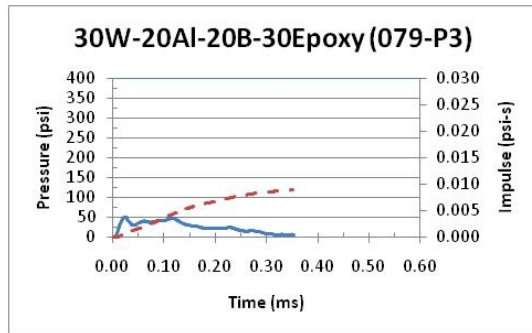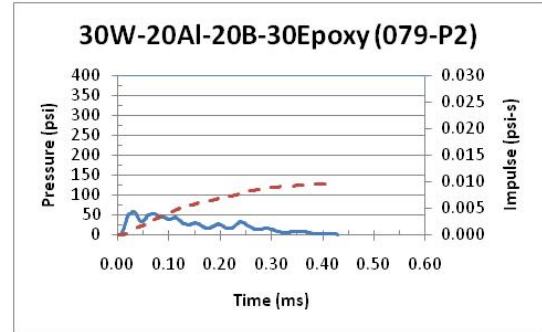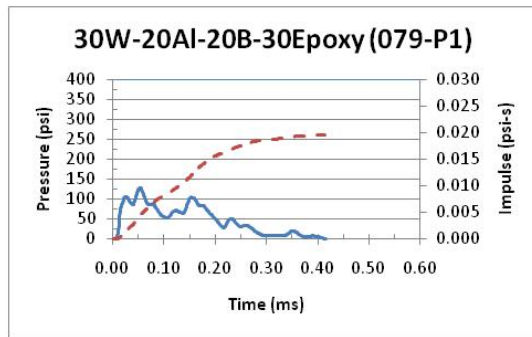
Fig. 6-90. Pressure history and impulse for 30W-20Al-20B-30Epoxy (Test T-3).
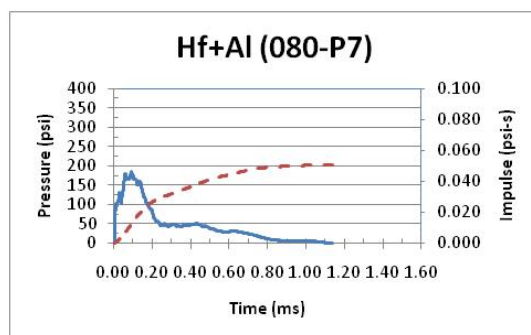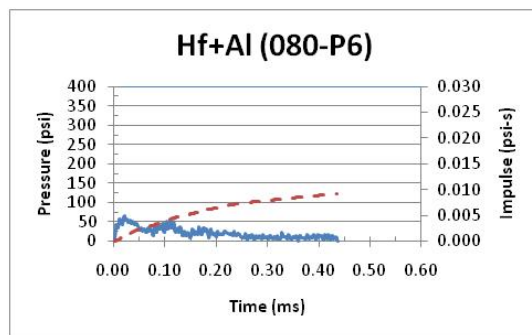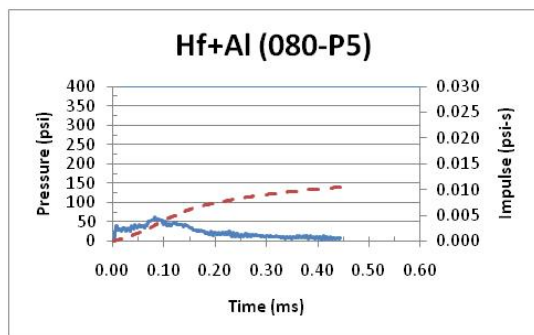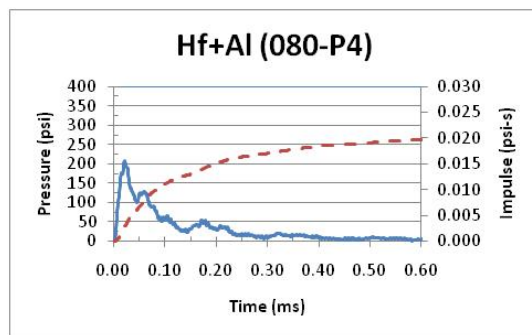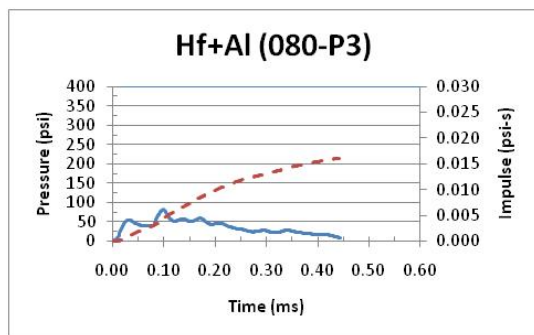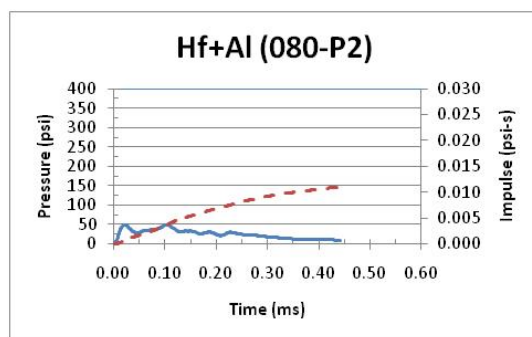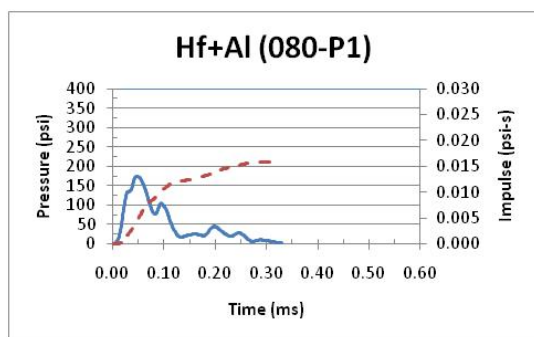
Fig. 6-91. Pressure history and impulse for Hf + Al (Test T-4).
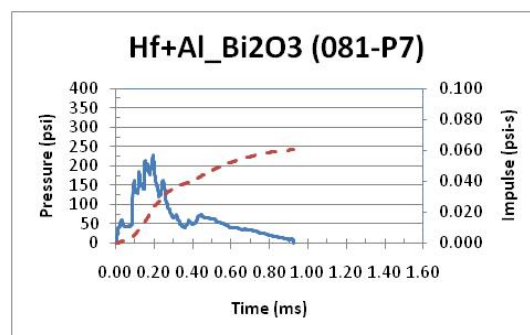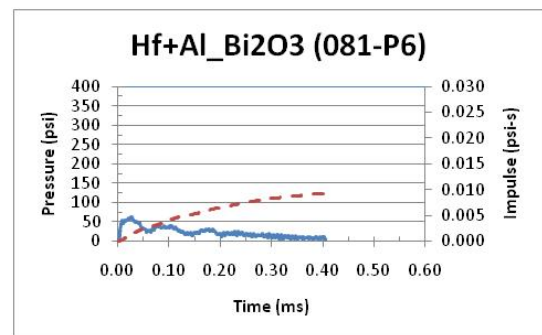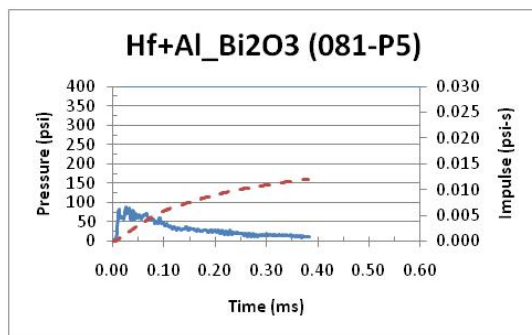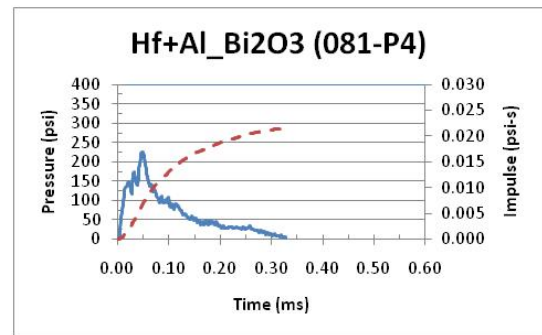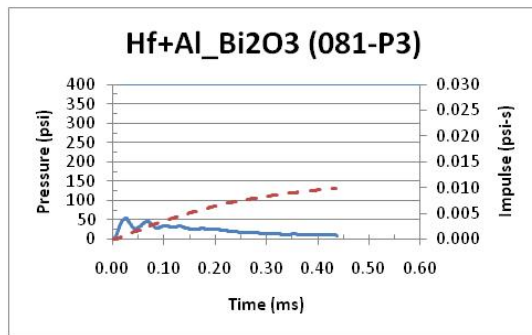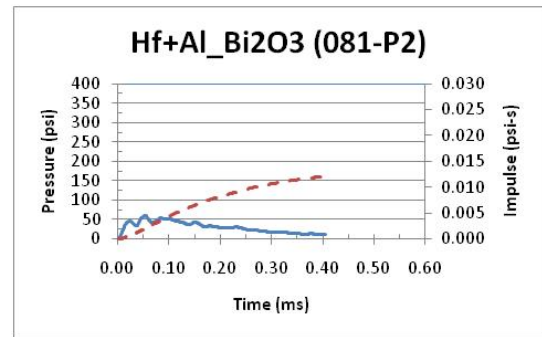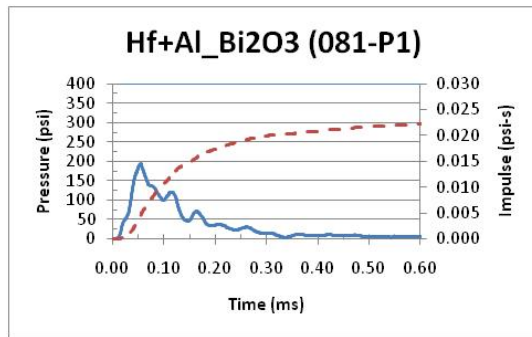
Fig. 6-92. Pressure history and impulse for Hf + Al + Bi$_2$O$_3$ (Test T-5).
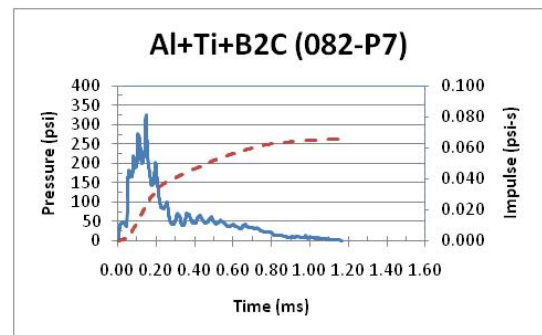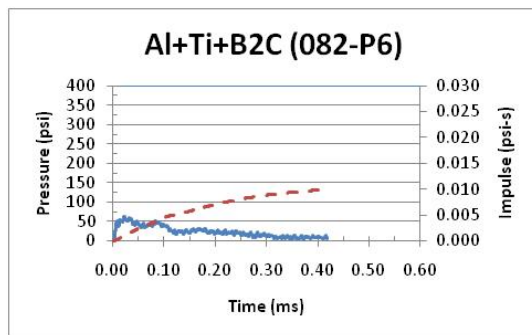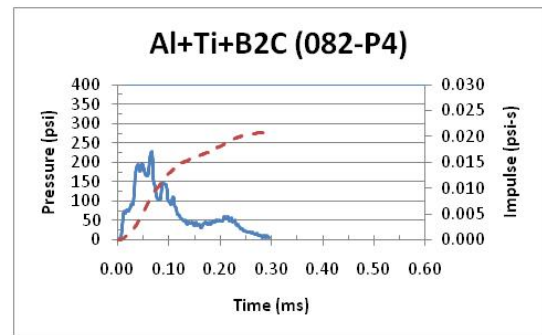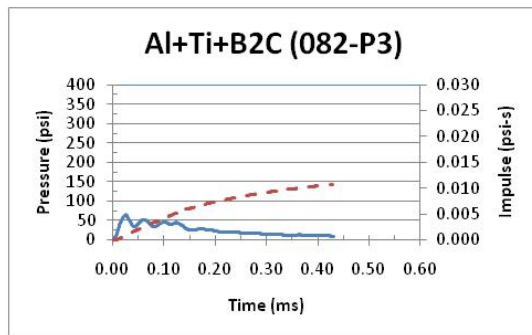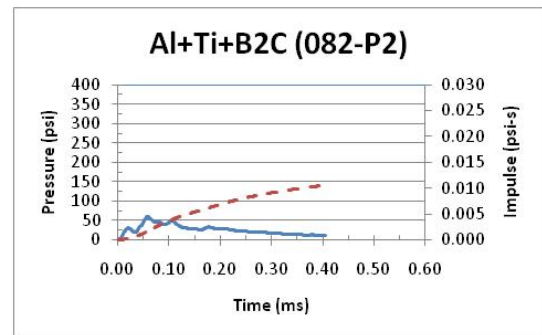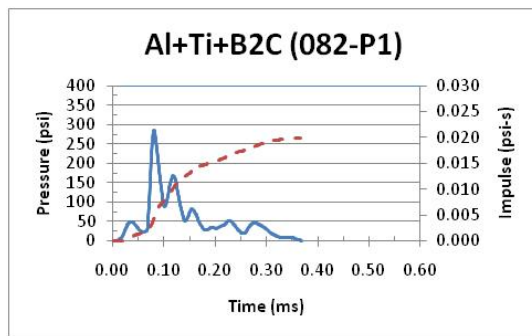
Fig. 6-93. Pressure history and impulse for Al + Ti + B$_2$C (Test T-6).
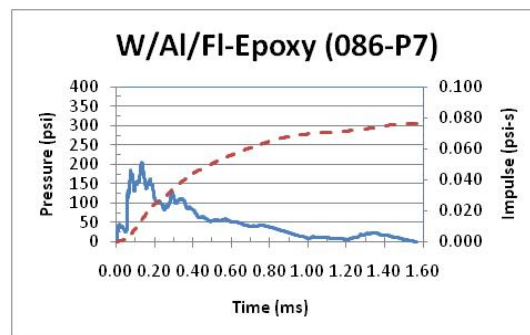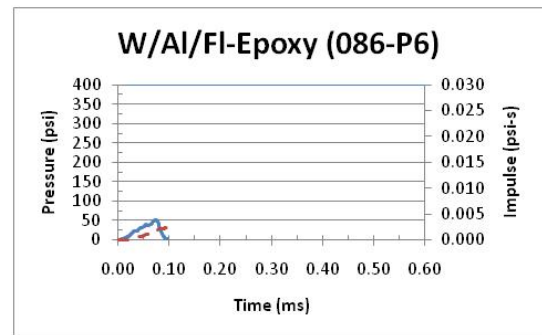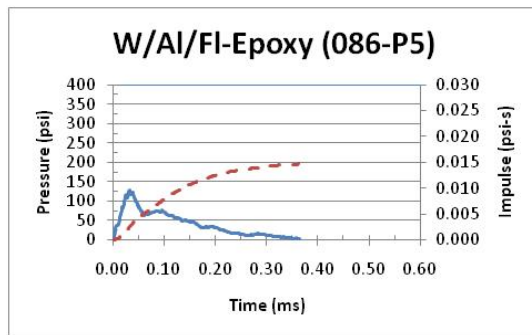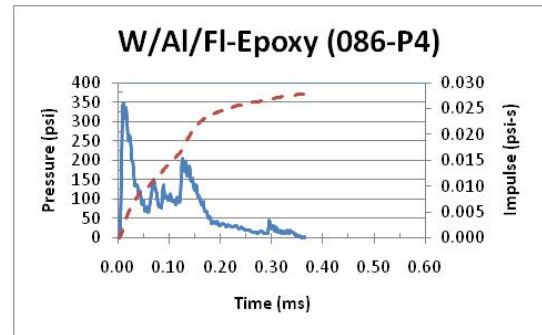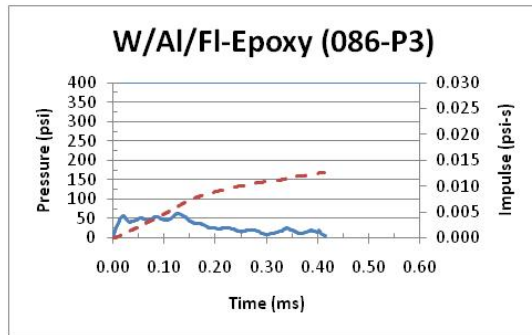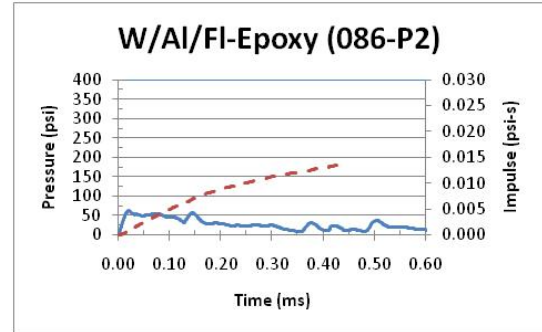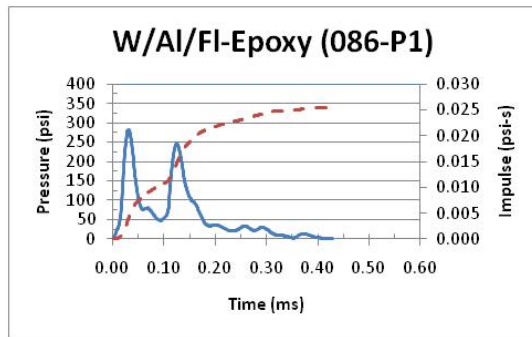
Fig. 6-94. Pressure history and impulse for W/Al/Fl-Epoxy (Test T-7).
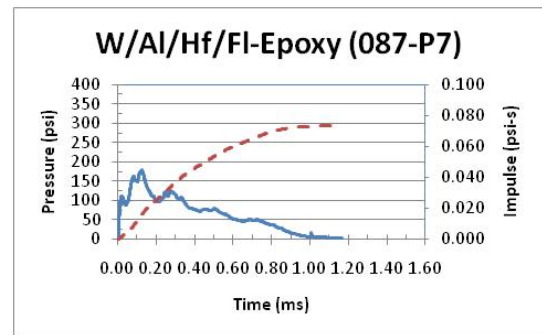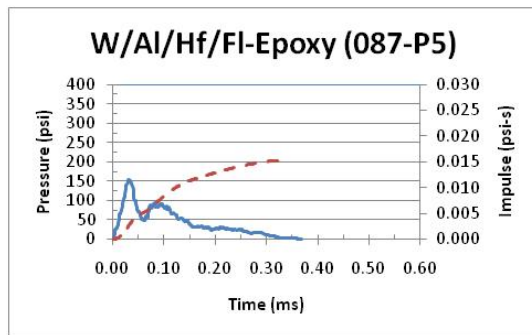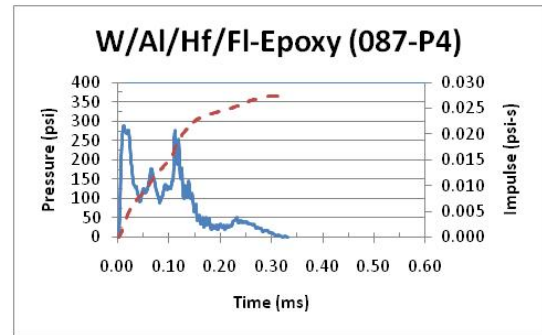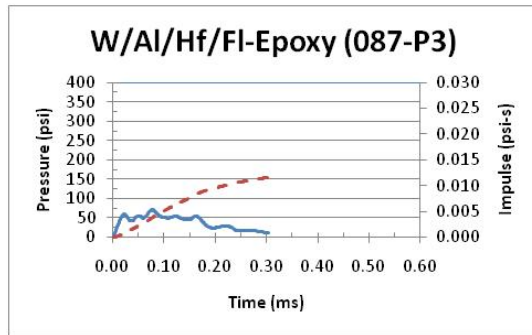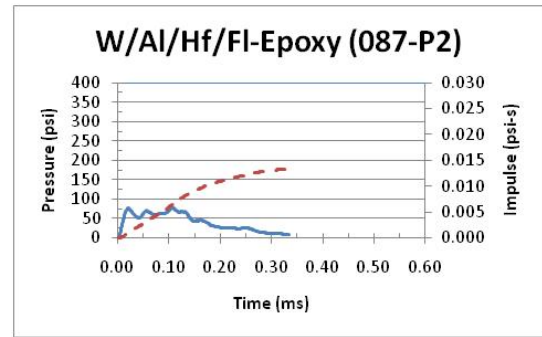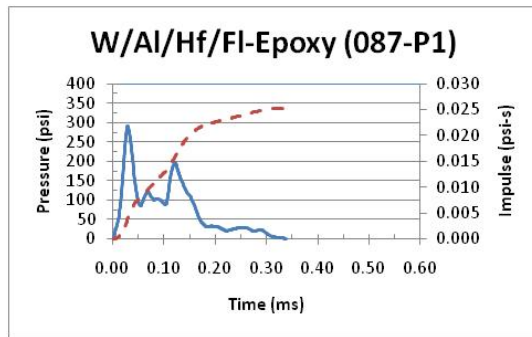
Fig. 6-95. Pressure history and impulse for W/Al/Hf/Fl-Epoxy (Test T-8).
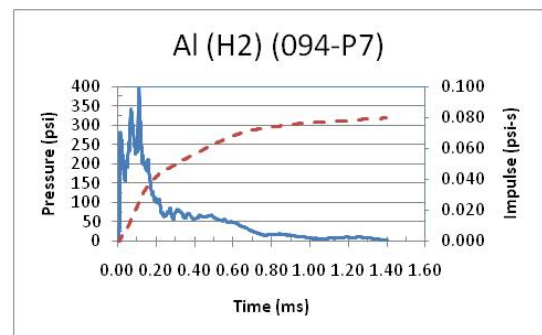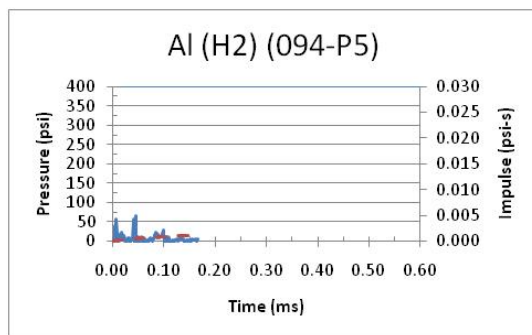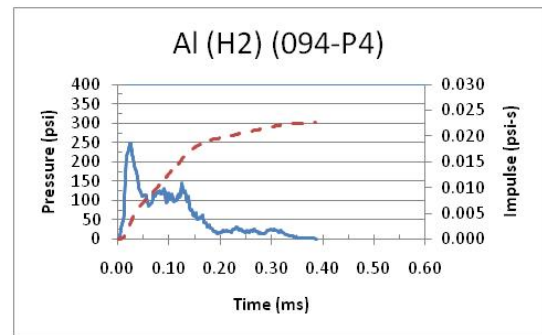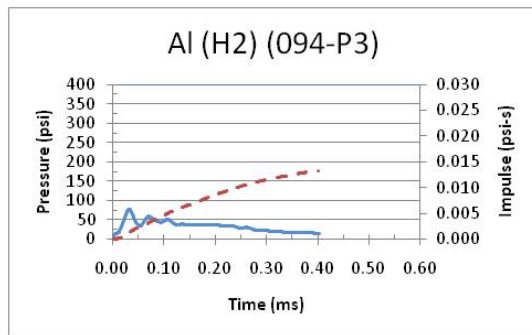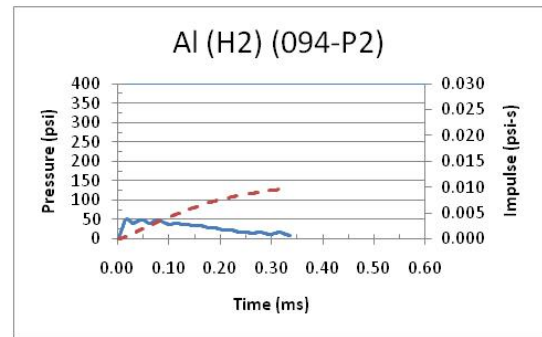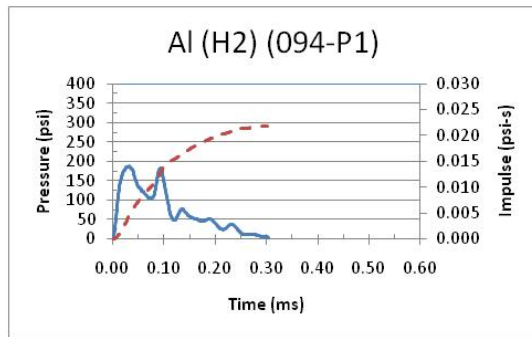
Fig. 6-96. Pressure history and impulse for Al-H2 (Test T-9).
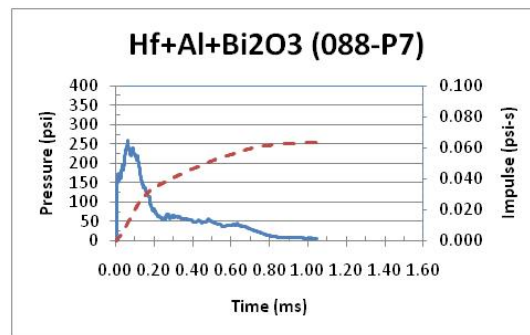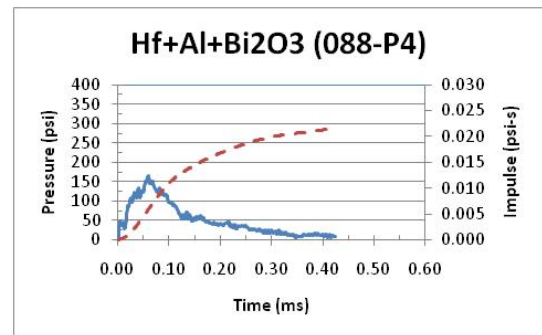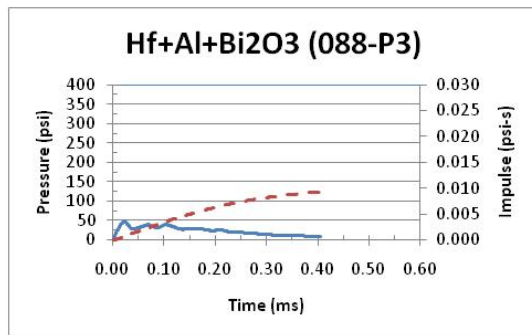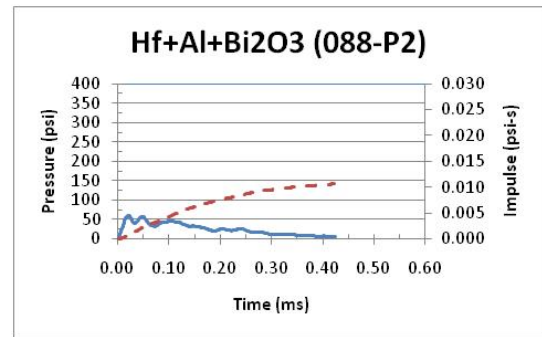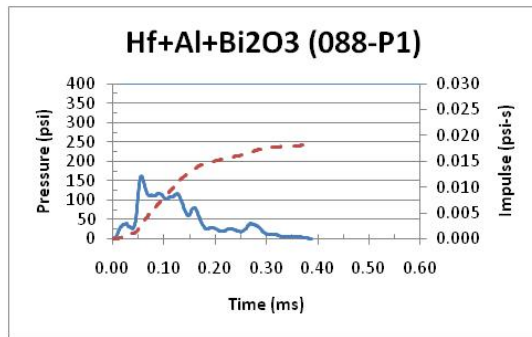
Fig. 6-97. Pressure history and impulse for Hf + Al +Bi$_2$O$_3$ (Test T-10).
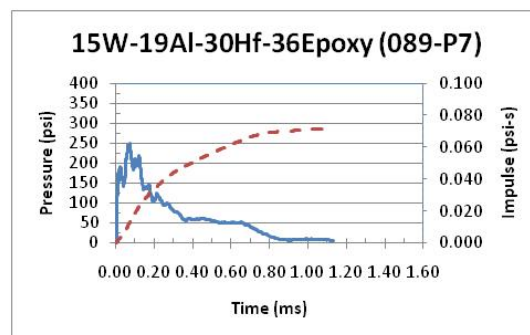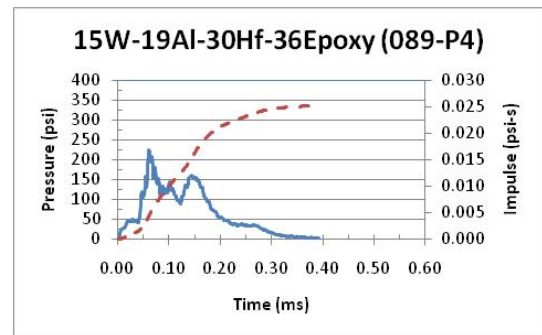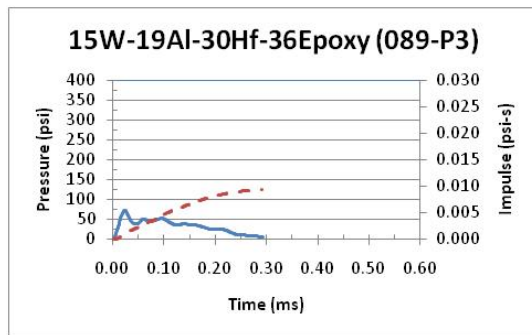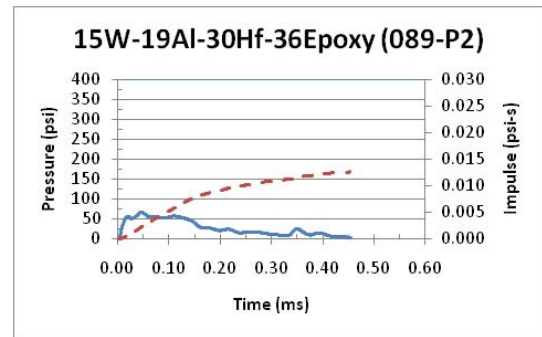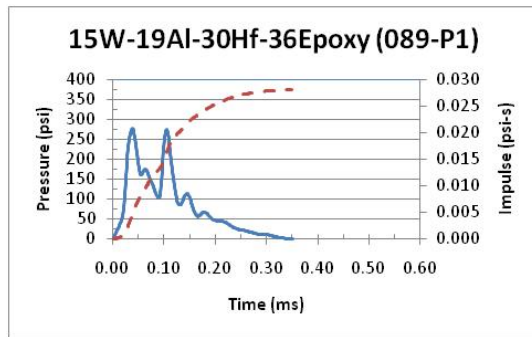
Fig. 6-98. Pressure history and impulse for 15W-19Al-30Hf-36Epoxy (Test T-11).
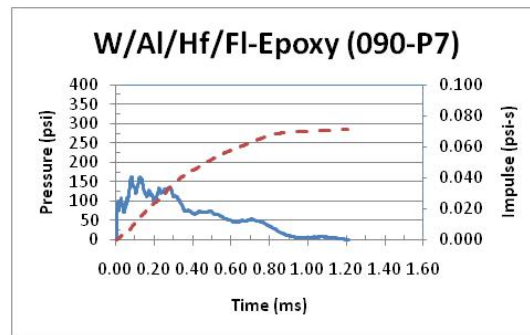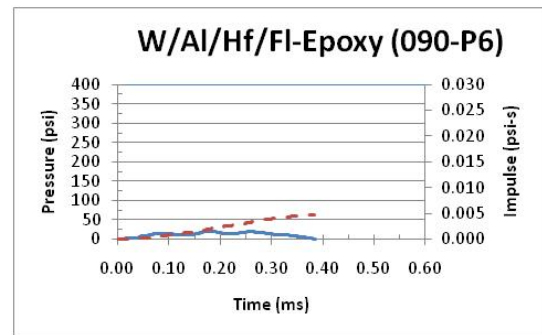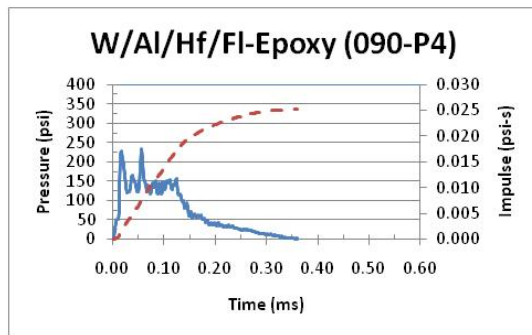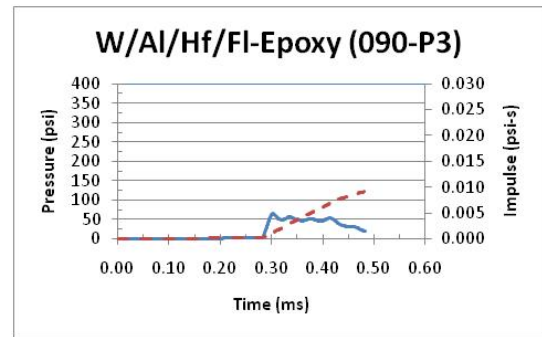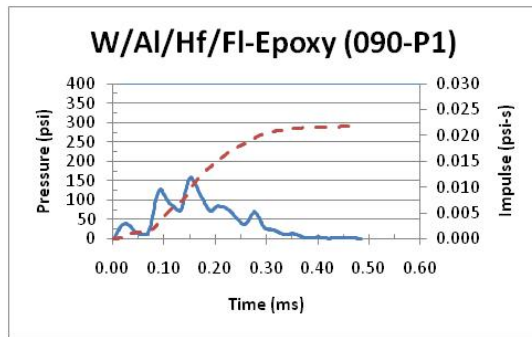
Fig. 6-99. Pressure history and impulse for W/Al/Hf/Fl-Epoxy (Test T-12).
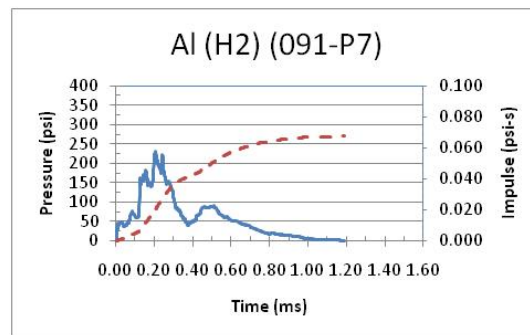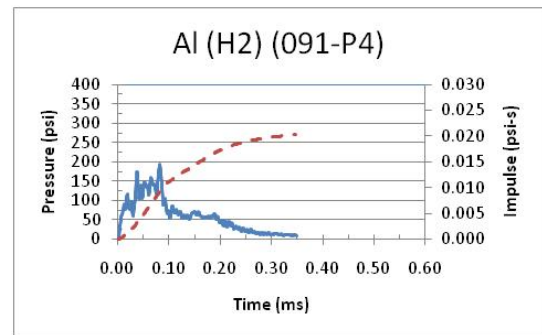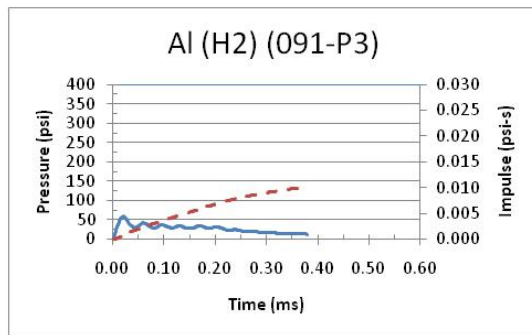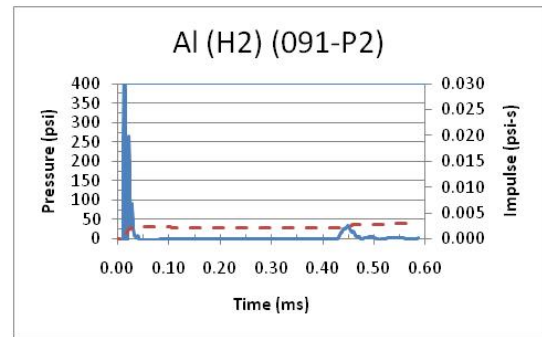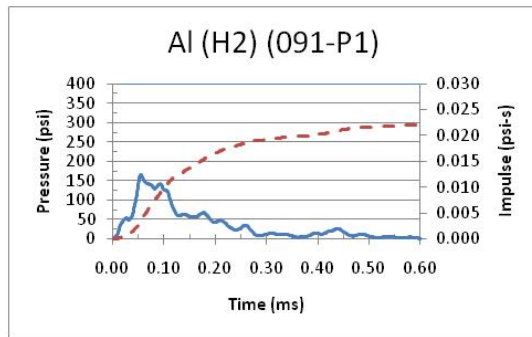
Fig. 6-100. Pressure history and impulse for Al-H2 (Test T-13).
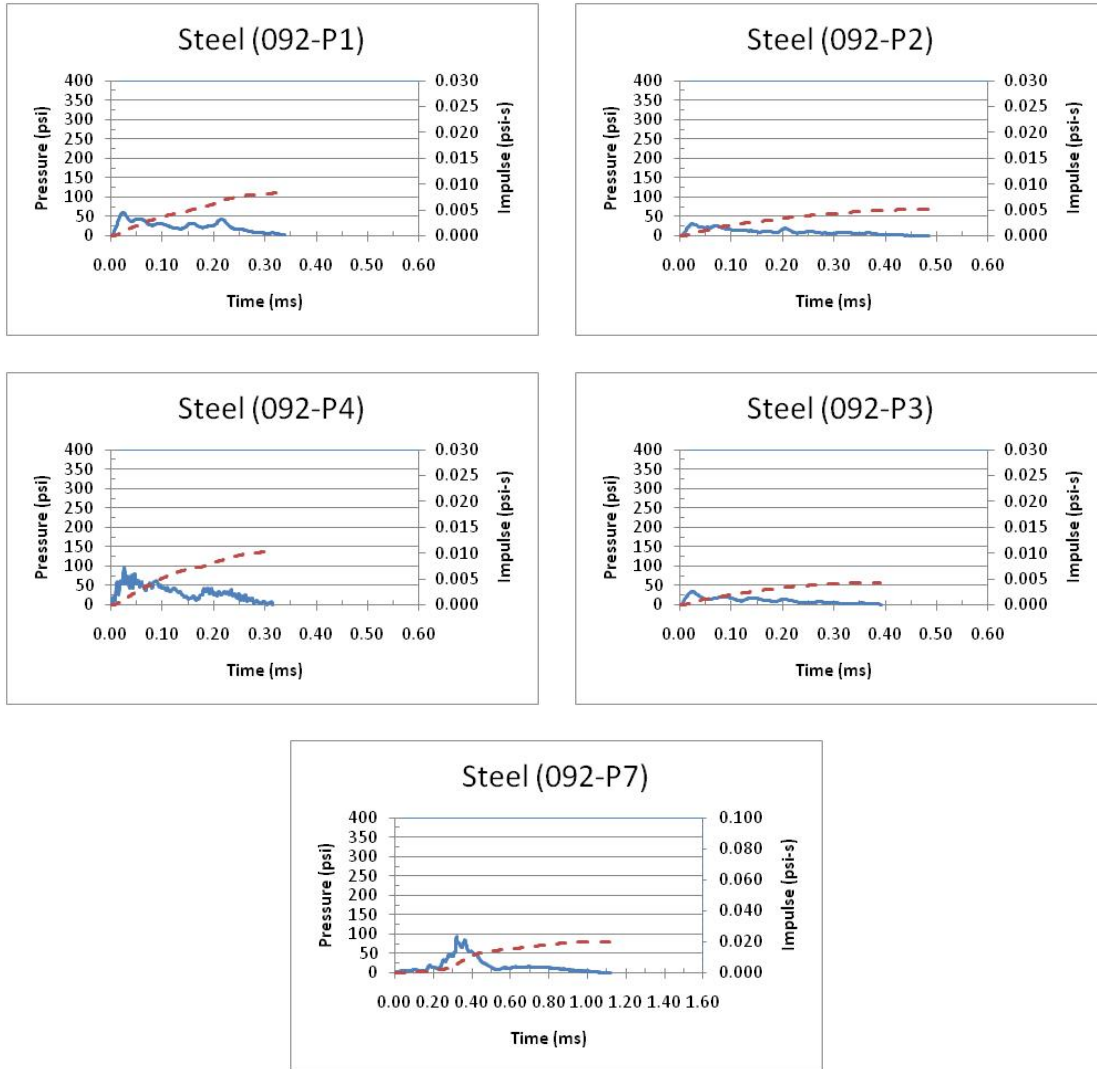
Fig. 6-101. Pressure history and impulse for steel (Test T-14).

Impulse Analysis

In analyzing the pressure data we found it beneficial to divide the pressure histories into three (3) groups: 1) ports P1 and P4; 2) ports P2, P3, P5, and P6; and 3) port P7. The rationale for these groupings is based on Figs. 6-102 and 6-103. Ports P1 and P4 are shielded, level with and equidistant from the charge, and have a similar pulse shape. Ports P2, P3, P5, and P6 are equidistant from the charge and share a similar pulse shape. Ports P1 and P4 tend to have higher peak pressures and more distinct peaks. Ports P2, P3, P5, and P6 tend to have a lower peak pressures. Port P7 has higher peak pressures and longer pulse duration due to an apparent confinement effect of the cavity well.
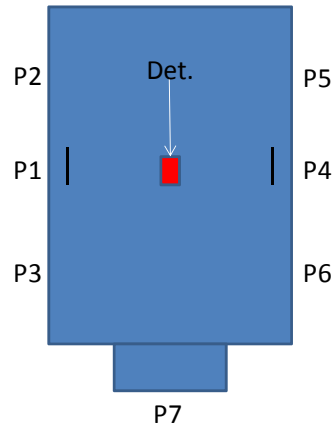
Fig. 6-102. Schematic of pressure transducer positions relative to the charge.
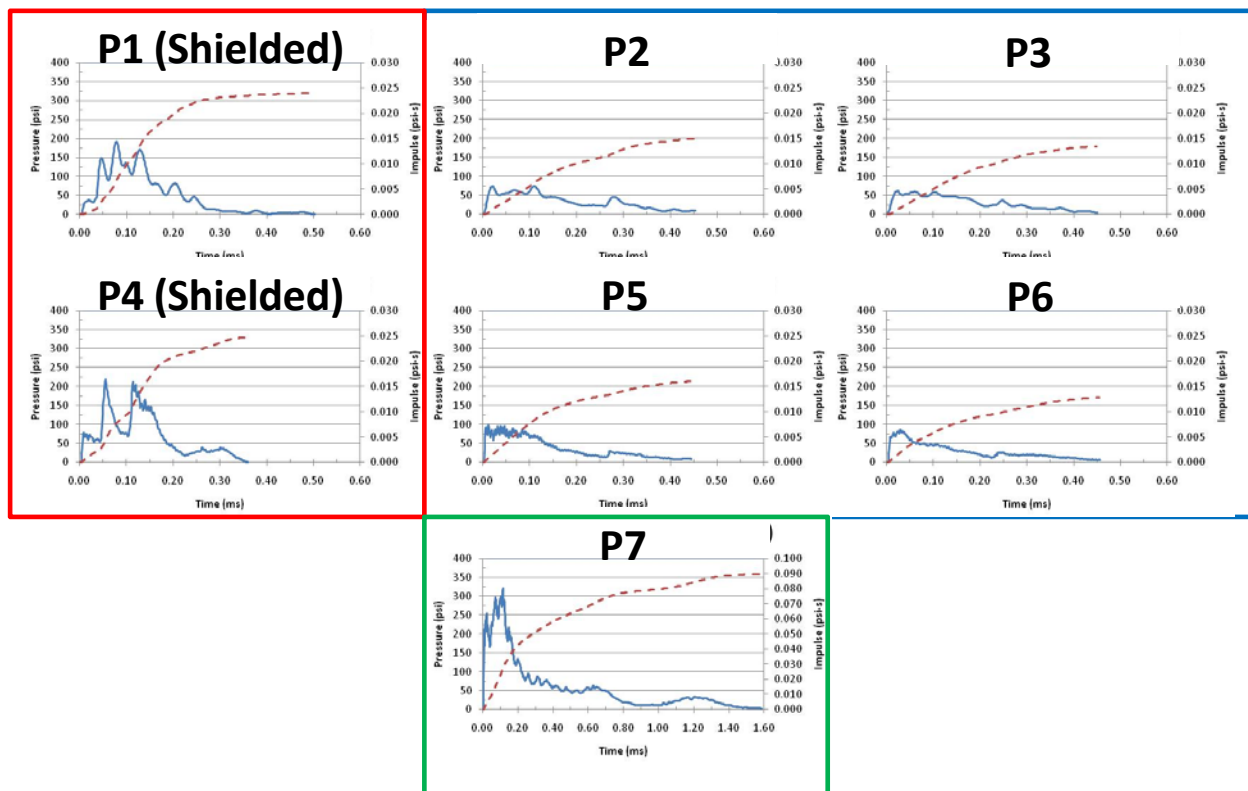
Fig. 6-103. Example pressure and impulse traces for RM case (15W-19Al-30Hf-36Epoxy, Test T-2).

For each group of data, average impulse and impulse ratio were calculated. The ratio is the average impulse of the RM over the average impulse of the baseline steel. The data were then sorted based on this ratio, as summarized in Tables 6-17 through 6-19. As seen in the tables, the reactive materials' relative performance based on impulse was 2.86 to 4.46 times that of the baseline steel depending on the position within the chamber. In each case the best performer is 15W-19Al-30Hf-36Epoxy. Note that the Al(H2) has a high impulse ratio (3.95) for the well cavity (P7) but only moderately high for the side-wall ports; perhaps this is a late-time burning or mixing effect that occurs in the well cavity.

Table 6-17. Sorted Impulse Data for Ports P1 and P4.

Test No.	Recording No.	Case Material Designation	P001 Impulse (psi-s)	P004 Impulse (psi-s)	Iave (psi-s)	Ratio I_{ave}/I_{steel}
T-14	92	Steel	0.0083	0.0102	0.0093	1.00
T-4	80	Hf+Al	0.0160	0.0198	0.0179	1.93
T-10	88	Hf+Al+Bi2O3	0.0181	0.0215	0.0198	2.13
T-0	75	Bare	0.0204	0.0194	0.0199	2.14
T-3	79	30W-20Al-20B-30Epoxy	0.0196	0.0210	0.0203	2.19
T-6	82	Al+Ti+B2C	0.0199	0.0209	0.0204	2.20
T-13	91	Al (H2)	0.0220	0.0203	0.0212	2.28
T-5	81	Hf+Al+Bi2O3	0.0224	0.0215	0.0220	2.36
T-9	94	Al (H2)	0.0218	0.0226	0.0222	2.39
T-12	90	W/Al/Hf/Fl-Epoxy	0.0218	0.0252	0.0235	2.53
T-2	78	15W-19Al-30Hf-36Epoxy	0.0241	0.0247	0.0244	2.63
T-1	76	30W-40Al-30Epoxy	0.0269	0.0225	0.0247	2.66
T-8	87	W/Al/Hf/Fl-Epoxy	0.0252	0.0275	0.0264	2.84
T-7	86	W/Al/Fl-Epoxy	0.0254	0.0277	0.0266	2.86
T-11	89	15W-19Al-30Hf-36Epoxy	0.0280	0.0252	0.0266	2.86

Table 6-18. Sorted Impulse Data for Ports P2, P3, P5, and P6.

Test No.	Recording No.	Case Material Designation	P002 Impulse (psi-s)	P003 Impulse (psi-s)	P005 Impulse (psi-s)	P006 Impulse (psi-s)	Iave (psi-s)	Ratio I_{ave}/I_{steel}
T-14	92	Steel	0.0051	0.0044	x	x	0.0047	1.00
T-12	90	W/Al/Hf/Fl-Epoxy	x	0.0091	x	x	0.0091	1.93
T-3	79	30W-20Al-20B-30Epoxy	0.0096	0.0089	0.0114	0.0083	0.0096	2.02
T-10	88	Hf+Al+Bi2O3	0.0106	0.0093	x	x	0.0100	2.10
T-13	91	Al (H2)	x	0.0102	x	x	0.0102	2.15
T-6	82	Al+Ti+B2C	0.0106	0.0107	x	0.0100	0.0104	2.21
T-5	81	Hf+Al+Bi2O3	0.0121	0.0092	0.0120	0.0093	0.0107	2.25
T-11	89	15W-19Al-30Hf-36Epoxy	0.0126	0.0094	x	x	0.0110	2.32
T-9	94	Al (H2)	0.0098	0.0134	x	x	0.0116	2.45
T-4	80	Hf+Al	0.0110	0.0160	0.0105	0.0092	0.0117	2.47
T-7	86	W/Al/Fl-Epoxy	0.0102	0.0126	0.0146	x	0.0125	2.64
T-0	75	Bare	0.0124	0.0139	0.0118	0.0148	0.0132	2.80
T-8	87	W/Al/Hf/Fl-Epoxy	0.0134	0.0116	0.0153	x	0.0134	2.84
T-1	76	30W-40Al-30Epoxy	0.0154	0.0165	0.0124	0.0101	0.0136	2.88
T-2	78	15W-19Al-30Hf-36Epoxy	0.0150	0.0134	0.0160	0.0129	0.0143	3.03

Table 6-19. Sorted Impulse Data for Port P7.

Test No.	Recording No.	Case Material Designation	P007 Impulse (psi-s)	Ratio I_{P7}/I_{steel}
T-14	92	Steel	0.0201	1.00
T-4	80	Hf+Al	0.0507	2.52
T-3	79	30W-20Al-20B-30Epoxy	0.0539	2.68
T-5	81	Hf+Al+Bi2O3	0.0604	3.00
T-10	88	Hf+Al+Bi2O3	0.0637	3.16
T-0	75	Bare	0.0641	3.18
T-6	82	Al+Ti+B2C	0.0656	3.26
T-13	91	Al (H2)	0.0674	3.35
T-12	90	W/Al/Hf/Fl-Epoxy	0.0712	3.53
T-11	89	15W-19Al-30Hf-36Epoxy	0.0720	3.58
T-8	87	W/Al/Hf/Fl-Epoxy	0.0738	3.66
T-1	76	30W-40Al-30Epoxy	0.0741	3.68
T-7	86	W/Al/Fl-Epoxy	0.0762	3.78
T-9	94	Al (H2)	0.0795	3.95
T-2	78	15W-19Al-30Hf-36Epoxy	0.0898	4.46

Material Ranking

In this subsection, materials are ranked based on impulse and QSP. For ranking based on impulse, we chose to use the side-wall ports P2, P3, P5, and P6. The rationale behind this is the following: 1) similar distance to the charge, and 2) the port is unobscured by shielding or the well cavity. For the QSP, all ports were used in the calculations assuming that all port positions reached the same equilibrium pressure. The impulse ranking is based on the average impulses of the four gauges. The QSP ranking is based on the average QSP of all seven gauges. As shown in Table 6-20, the W/Al and W/Al/Hf Epoxy composites rank high for both impulse and QSP. The high impulse may be attributed to the W fibers impacting the face of the transducer.

Table 6-20. Comparison of Material Ranking for Impulse and QSP.

Ranking	Impulse (P2,P3,P5,P6)	QSP (All Ports)
1	15W-19Al-30Hf-36Epoxy	Al (H2)
2	30W-40Al-30Epoxy	15W-19Al-30Hf-36Epoxy
3	W/Al/Hf/Fl-Epoxy	30W-40Al-30Epoxy
4	Bare	Hf+Al+Bi2O3
5	W/Al/Fl-Epoxy	W/Al/Hf/Fl-Epoxy
6	Hf+Al	Al+Ti+B2C
7	Al (H2)	W/Al/Fl-Epoxy
8	Hf+Al+Bi2O3	Hf+Al
9	Al+Ti+B2C	30W-20Al-20B-30Epoxy
10	30W-20Al-20B-30Epoxy	Bare
11	Steel	Steel

Section VII

Models of Concrete Penetration

We performed a literature review on analytical and computational modeling of penetration by non-deforming projectiles into concrete. We later based our designs for concrete penetrators on an analytical model of concrete penetration by Forrestal et al. (1994) and subsequent work by Jones and Rule and others, as well as on computational modeling, using EPIC and other codes.

7.1 Forrestal's Model of Concrete Penetration

Previously, Flis et al. (2008) reviewed the concrete-penetration model of Forrestal et al. The model was validated to some degree by comparing its predicted results with several sets of available concrete penetration data (Forrestal et al. (1994); Moxley and Cummins (2008); Unosson (2000)). An analysis was performed on sets of penetration data for a particular armor-piercing projectile against three types of concrete: conventional concrete, high-strength concrete, and very high-strength concrete.

In this subsection, the concrete penetration model of Forrestal et al. is first reviewed. Recently, Chen (2008) applied the dimensionless penetration parameters developed by Li and Chen (2003) to Forrestal's model, whereby the dependence of the final penetration depth is reduced to two parameters, which Chen calls an impact function I and a geometric function, denoted here as G. The impact function I depends on the penetrator's initial kinetic energy per unit cross-sectional area and the strength of the target. The geometric function G depends only on the penetrator's mass per unit cross-sectional area, its nose shape, and the density of the concrete target. It is shown here, first, that for a given general class of penetrators the dimensionless penetration (penetration depth divided by penetrator diameter) depends on G rather weakly. Second, it is shown that, with properly selected values of the concrete strength terms that appear in the model, all three sets of data can be fitted along a single curve, which is given by Forrestal's model. This indicates that all three types of concrete undergo penetration in a manner consistent with Forrestal's model.

7.1.1 Model Equations

Forrestal et al. (1994) proposed a semi-empirical model of penetration by non-deforming ogival nose rods into concrete. The model consists of the equation

$$m\frac{dV}{dt} = \begin{cases} -cz, & z < 4a \\ -\pi a^2\left(Sf_c' + N\rho V^2\right) & 4a < z < P \end{cases} \tag{7-1}$$

where:
m = penetrator mass
V = penetrator velocity
z = current penetration depth (i.e., $dz/dt = V$)
P = final penetration depth
a = penetrator radius
f_c' = compressive quasi-static strength of concrete
ρ = mass density of concrete
S = empirical strength factor
N = empirical drag coefficient, which accounts for penetrator's (ogival) nose shape,

$$N = \frac{8\psi - 1}{24\psi^2} \tag{7-2}$$

in which ψ = CRH (caliber radius head) of the ogival nose.

Forrestal's integration of this model yielded an expression for the final penetration depth,

$$Z_{final} = \frac{m}{2\pi a^2 \rho N} \ln\left(1 + \frac{N\rho V_1^2}{Sf_c'}\right) + 4a \tag{7-3}$$

where V_1 is the penetrator velocity after an initial start-up phase during which the ogival nose becomes fully engaged with the target (during which the penetrator reaches a depth of $4a$), given by

$$V_1^2 = \frac{mV_0^2 - 4\pi a^3 Sf'}{m + 4\pi a^3 \rho N} \tag{7-4}$$

where V_0 is the penetrator striking velocity.

7.1.2 Dimensionless Penetration Parameters

Through a dimensional analysis of Forrestal's model, Li and Chen (2003) showed that the dimensionless final depth of penetration Z_{final}/d, where $d = 2a$ is the penetrator diameter, depends on the dimensionless parameters

$$I* = \frac{mV_0^2}{d^3 f'} \tag{7-5}$$

and

$$\lambda = \frac{m}{\rho d^3} \tag{7-6}$$

as well as the nose shape factor, N.[1]

Li and Chen combined these three parameters, $I*$, λ, and N into two new dimensionless parameters, the *impact function*,

$$I = \frac{mV_0^2}{d^3 Sf_c'} \tag{7-7}$$

and the *geometric function*,

$$G = \frac{m}{\rho d^3 N} \tag{7-8}$$

Note that I varies with impact velocity and target strength, whereas G is fixed for a given penetrator and target density. Larger values of G correspond to lower-drag (smaller N), more slender (smaller d), or more massive (larger m) projectiles.

Li and Chen showed that Forrestal's solution for the final penetration depth can be expressed in terms of these parameters as

$$\frac{Z_{final}}{d} = \begin{cases} \sqrt{\dfrac{1+k\pi/4G}{1+I/G}\dfrac{4k}{\pi}I} & \text{for } Z_{final}/d < k \\[3mm] \dfrac{2}{\pi}G\ln\left(\dfrac{1+I/G}{1+k\pi/4G}\right) + k & \text{for } Z_{final}/d \geq k \end{cases} \tag{7-9}$$

where Forrestal's model uses the value k = 2.

---

[1] These are similar to dimensionless parameters developed by Sjøl and Teland (2000), which differ in that a dimensionless velocity, equal to the square-root of Li and Chen's $I*$, is used instead of $I*$.
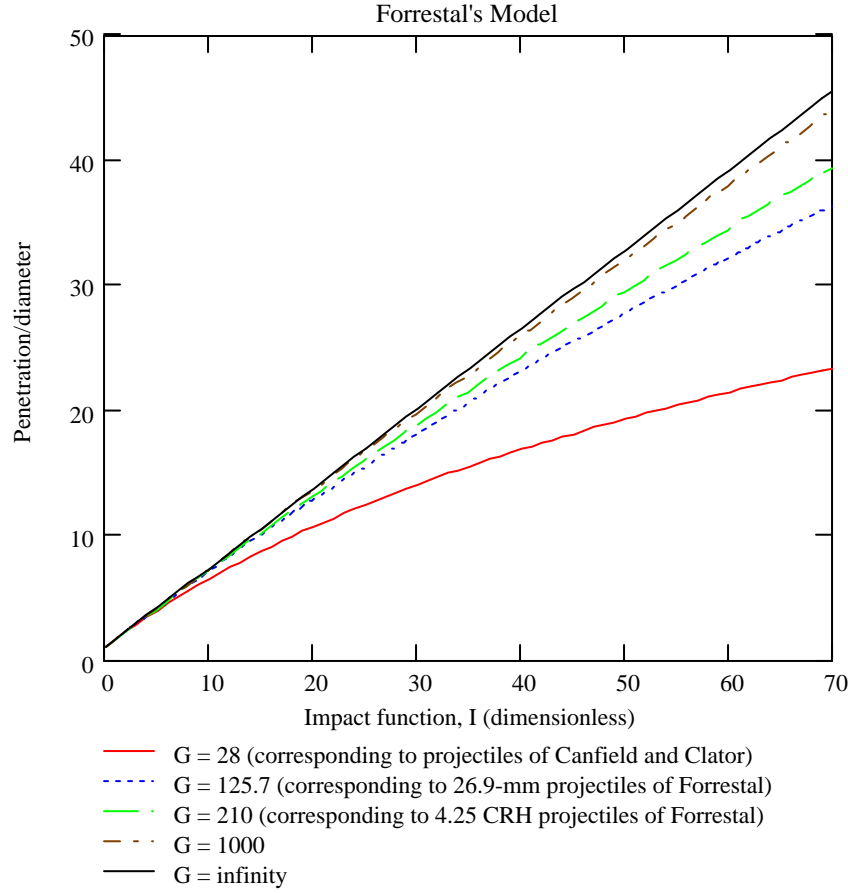
Fig. 7-1. Plot of dimensionless form of Forrestal's model, Eq. (7-9),
for several values of the geometric function *G*.

7.2.1 General Formula for Nose Coefficient *N*

Forrestal et al. limited their model to ogival-nosed penetrators, for which the drag coefficient *N* has a simple formula, Eq. (7-2). From the same spherical-cavity-expansion theory used by Forrestal et al. in their model, Jones et al. (1998) derived a general expression for *N* that can be applied to any nose shape,

$$N = \frac{8}{d^2} \int_0^h \frac{yy'^3}{1+y'^2} dx \tag{7-10}$$

where *x* and *y* are the axial and radial coordinates, *y* = *y*(*x*) is the nose shape function, and the prime denotes differentiation. For ogival noses, this formula reduces, of course, to Eq. (7-2). Interestingly, this formula is identical to the theoretical formula for the drag coefficient of a body in hypersonic flow; consequently, shapes that are theoretically optimal for hypersonic flow are theoretically optimal for concrete penetration.

7.2.2 Optimal Nose Shape

Based on Eq. (7-10), Jones et al. showed that the optimal (minimum-drag) shape for a penetrator nose of given length, which is given parametrically as

$$\begin{aligned} x(t) &= r_{opt} A(t) \\ y(t) &= r_{opt} B(t) \end{aligned} \quad t_0 \le t \le 1 \tag{7-11}$$

- 133 -

where

$$A(t) = \frac{1}{4}\left(\frac{1}{t^2} + \frac{3}{4t^4} + \ln t - \frac{7}{4}\right); \ B(t) = \frac{\left(t^2+1\right)^2}{4t^3}; \ r_{opt} = \frac{L_n}{A(t_0)} \qquad (7\text{-}12)$$

where L_n is the length of the nose and in which t_0 is given by the condition

$$B(t_0) - \frac{R}{L_n} A(t_0) = 0 \qquad (7\text{-}13)$$

where R is the penetrator radius. This optimal shape is identical to a theoretical optimal shape (for the minimum drag coefficient) in hypersonic flow (see, e.g., Eggers et al., 1955), which shape was first described by Newton (1687). The drag coefficient for this shape is

$$N = 1 - \frac{C(t_0)}{8B^2(t_0)} \qquad (7\text{-}14)$$

where

$$C(t) = \frac{1}{2t^2} + \frac{5}{4t^4} + \frac{1}{2t^6} + \ln t - \frac{9}{4} \qquad (7\text{-}15)$$

This shape is slightly flat-ended with a radius r_{opt} at the tip; longer noses have smaller flat ends. The shape is nearly conical but slightly convex, as shown in Fig. 7-2 and compared with an ogive in Fig. 7-3; it is not tangent with the penetrator body at the shoulder. The parameter t in the above is equal at every point along the lateral surface to the local slope $y' = dy/dx$, which decreases from a value of unity (thus making an angle of 45°) at the tip to a value of t_0 at the shoulder.
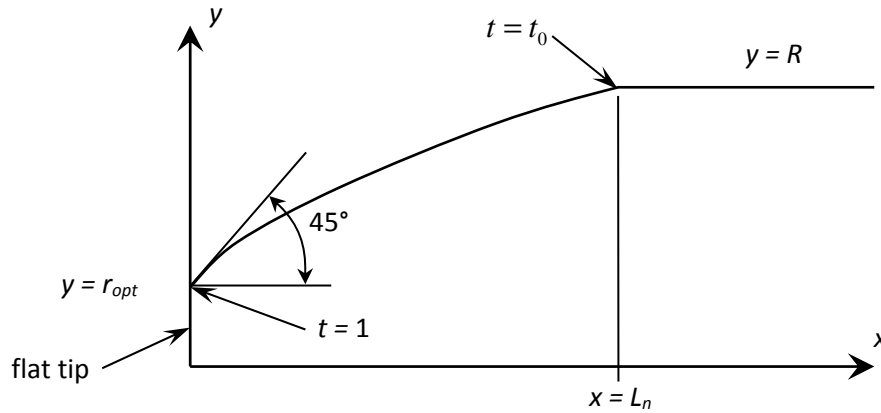
Fig. 7-2. Optimal nose shape for minimum drag in penetrating concrete.
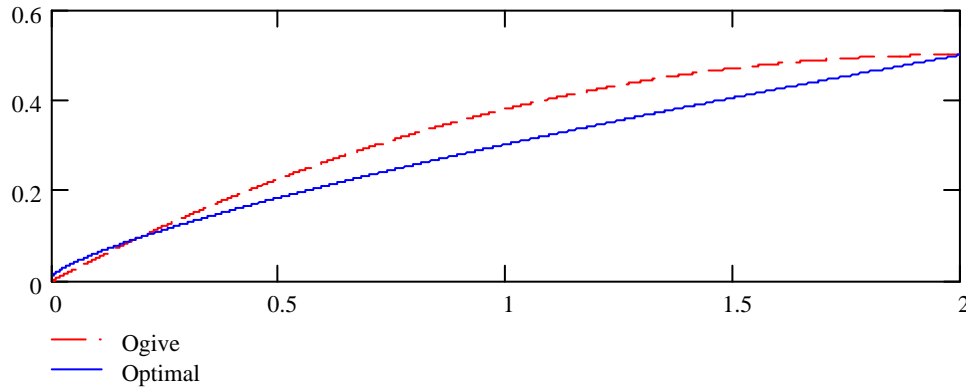
Fig. 7-3. Optimal nose shape for minimum drag (solid blue curve) compared with an ogive (dashed red curve) of equal length.

This is the theoretical optimal shape for a nose of given length. Optimal shapes for noses constrained to be truncated conic, spherical-conic, or truncated ogival were derived by Ben-Dor et al. (2003), who also showed that the optimal truncated-conic penetrator is close in performance to the absolute optimal shape. Jones and Rule (2000) showed that, if the penetrator experiences also pressure-dependent friction, the optimal shape depends also on the penetrator velocity.

7.2.3 Other Nose Shapes

Jones et al. (1998) gave formulas for the drag coefficient for other shapes as well, including cones,

$$N = \sin^2 \psi \tag{7-16}$$

where ψ is the apex half-angle, and hemispheres,

$$N = 1/2 \tag{7-17}$$

For flat noses, $N = 1$, which is also the theoretical value for stepped noses. According to these formulas, for a given nose length, a conical nose has a lower value of N, and hence yields greater penetration according to the model, than an ogival nose; this general trend agrees with that implied by the empirical penetration equations of Young (1997) for concrete and geological materials.

For complicated nose shapes, closed-form formulas for N can possibly be derived, but often it is easier to compute N numerically, which can be done with the formula

$$N \approx \frac{4}{d^2} \sum_i \frac{(y_i + y_{i-1})(y_i - y_{i-1})^3}{(x_i - x_{i-1})^2 + (y_i - y_{i-1})^2} \tag{7-18}$$

We have found that using 1000 points with this formula gives agreement with the exact formulas for ogives and cones to better than five significant figures.

7.3 Young's Penetration Equations

Young's equation for penetration depth D for striking velocities V of at least 100 ft/s is

$$D = 0.00178 S N_{Young} \left(\frac{W}{A}\right)^{0.7} (V - 100) \tag{7-19}$$

where S is the target strength factor, N_{Young} is Young's nose-shape factor, W is the mass of the penetrator, and A is its cross-sectional area. For ogival noses,

$$N_{Young} = 0.18 \left(\frac{L_n}{D}\right) + 0.56 \tag{7-20}$$

and for conical noses,

$$N_{Young} = 0.25 \left(\frac{L_n}{D}\right) + 0.56 \tag{7-21}$$

where L_n is the nose length and D is the penetrator diameter. These are the only available formulas for N_{Young}, for ogives and cones; thus, Young's equation cannot be directly applied to other nose shapes. Young and Forrestal are in agreement in that conical noses penetrate better than ogives of equal length.

Forrestal's model predicts only a small effect of nose shape for robust penetrators, high-strength concrete, and low impact velocities. On the contrary, EPIC, EPIC-PENCRV, and Young's equation all predict a much stronger effect of nose shape, even at relatively low (transonic) velocities.

7.4 EPIC Code

EPIC is a general-purpose finite-element computer code useful for analyzing dynamic events such as impact, penetration, and explosive-metal interactions. To compute deep penetrations into concrete, we made use of two of EPIC's special capabilities, the particle-conversion technique and the PENCRV link.

7.4.1 Particle-Conversion Technique

In EPIC's particle-conversion technique, finite elements are converted with particles when the effective plastic strain reaches some specified value, usually 40% to 50%. This allows the target to fail in various modes, including particulation or rubblization and large-scale cracking, while avoiding the excessive distortion of elements, which lead to computational difficulties (very small time-step, artificial stiffness). For present purposes, it was sufficient to restrict particle replacement to the target (a penetrator that survives impact experiences only a few percent strain).

The result of a typical computation is shown in Fig. 7-4. Note the separated particles at the top, the coalescence of particles into large-scale cracks near the target surface, and particulation developing at the crater bottom. The development of the large-scale crack in this manner is rather realistic, as concrete targets typically develop conical craters that are 1.5 to 2 penetrator diameters deep.

7.4.2 EPIC Link to PENCRV

EPIC includes a link to PENCRV, an analytical model of the target response, dependent on the current (deformed) shape of the penetrator, which is modeled by finite elements. In this model, the target has only two properties, density and compressive strength. This model, which is available for both 2-D and 3-D computations, runs very fast, requiring only about 1 minute for a sufficiently fine mesh on a modern single processor in 2-D, and about one-half hour for 3-D.

Fig. 7-4. Result of an EPIC computation using the particle-conversion technique.

7.5 CTH Code

7.5.1 Code Description

CTH is a large-deformation, strong shock wave, solid-fluid mechanics code developed at Sandia National Laboratories. It has models for multi-phase, elastic, viscoplastic, porous and explosive materials. Several meshes are available: 3-D rectilinear, 2-D rectilinear and cylindrical, and 1-D rectilinear, cylindrical, and spherical meshes. The overall solution sequence of CTH is a Lagrangian step followed by an Eulerian remap and then a data base modification step where materials may be discarded, or the mesh may be adapted, or velocity transformations applied. Adaptive mesh refinement is available for maximizing resolution in regions of interest. While CTH is superior at handling large deformations, it is not suitable for predicting structural response.

7.5.2 CTH Calculations

CTH was used to analyze the penetration depth into concrete of an existing 2000-lb penetrating bomb. Several concrete strength models were employed (with and without a special boundary layer interface routine invoked) to determine the effect on penetration depth. The two available concrete strength models are Brittle Fracture Kinetics (BFK) and Holmquist-Johnson-Cook (HJC). The impact conditions for all simulations were 0° obliquity and 0° angle of attack. The computational mesh was set up in 2-D ax-isymmetry with a 0.6-mm cell size. The impact velocity was 1200 ft/s. The results are listed in Table 7-1.

Table 7-1. CTH baseline results for a 2000-lb penetrating bomb.

Concrete model	Concrete compressive strength (psi)	Penetration depth (in)	Penetration depth (penetrator lengths)
BFK (default)	5000	98.6	1.04
BFK with BLINT	5000	112.1	1.18
HJC (default)	7000	40.3	0.42
HJC with BLINT	7000	64.4	0.68

7.5.3 Material Models

The EOS input to CTH for the penetrator fill, penetrator case, and concrete target are listed in order below. PTFE was used as a surrogate for the explosive fill with density adjusted to match the explosive. The Mie-Gruneisen EOS was used for the PTFE fill and steel case. The constants for the case are for 4130 steel. For the target, the default parameters for SAC5 concrete were used. The COTAU parameter used in the BFK model was adjusted according to the size of the target as described in the model's reference manual. CTH uses the cm-g-s system of units with temperature in electron-volts.

BFK calculations:
- Mat1 mgrun PTFE ro=1.72 (explosive fill surrogate)
- Mat2 mgrun user r0=7.86 cs=4.529e5 s=1.5 g0=1.84 cv=5.18e10 (steel case)
- Mat3 conc=SAC5 cosfac=0.833 cotau=4.83 (concrete target)

HJC calculations:
- Mat1 mgrun PTFE ro=1.72 (explosive fill surrogate)
- Mat2 mgrun user r0=7.86 cs=4.529e5 s=1.5 g0=1.84 cv=5.18e10 (steel case)
- Mat3 hjc r0=2.28 cs=2.0e5 cv=6.54e6 (concrete target)

The strength model input (constitutive) for the penetrator fill, penetrator case, and concrete target are listed in order below. For PTFE, an elastic/perfectly plastic model was used with a yield strength of 1.38e8 dyn/cm^2 (2000 psi). For the steel case, the default parameters for the Johnson-Cook model were

used for 4340 steel with a yield strength of approximately 305 ksi. The BFK model was used for SAC-5 concrete with its scaling factor (see COSFAC above) adjusted for an unconfined compressive strength of 5000 psi. The default compressive strength for the HJC model is 7000 psi.

BFK Calculations:

- Matep 1 yield=1.38e8 poissons=0.46 (explosive fill surrogate)
- Matep 2 J0 '4340_Temp_Mart' (steel case)
- Matep 3 conc=SAC5 poissons=0.2 (concrete target)

HJC Calculations:

- Matep 1 yield=1.38e8 poissons=0.46 (explosive fill surrogate)
- Matep 2 J0 '4340_Temp_Mart' (steel case)
- Matep 3 HJC Concrete1 den=2.28

For calculations involving the Boundary Layer Interface (BLINT) algorithm, the CTH input is listed below. The BLINT algorithm allows a sliding interface between two materials.

- Blint 1 hard 2 soft 3

The "hard" identifies the harder of two materials (penetrator) and the "soft" identifies the softer of two materials (target). This algorithm allows definition of the thickness of the hard and soft boundary layers. In this case the code defaults were used.

7.5.4 Example Calculation

Figure 7-5 is the final material plot (2D-CTH) for a generic 2000-lb bomb penetrating 5000-psi concrete at an initial impact velocity of 1200 ft/s. In this case CTH predicts a penetration depth equal to a little over one penetrator length.
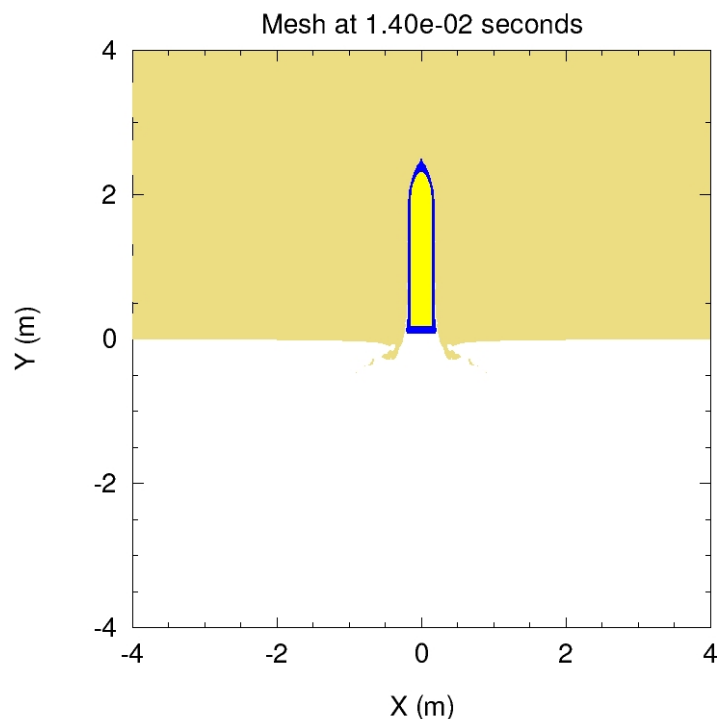
Fig. 7-5. Final material plot for 2000-lb bomb penetrating-5000 psi concrete (BFK).

7.5.5 Summary

For this penetrator Forrestal's model predicts approximately 62 inches into concrete. In comparing the penetration results, the BFK and BFK-w/BLINT models overpredict Forrestal's model by 60% and 81%, respectively. On the other hand, the default HJC model underpredicts by 35%. The HJC model with BLINT invoked is in best agreement, overpredicting Forrestal by less than 1%.

7.6 ALE-3D Code

The ALE-3D computer code was investigated as an analysis tool. ALE-3D code provides some unique capabilities compared to the EPIC and CTH codes. The basic computational scheme of ALE-3D consists of a Lagrangian step followed by an advection step. In the advection step, nodes in selected materials can be relaxed either to relieve distortion or to improve accuracy and efficiency. ALE-3D thus has the option of treating structural members in a Lagrangian mode and treating materials which undergo large distortions in an Arbitrary Lagrangian-Eulerian (ALE) mode, all within the same mesh/problem configuration. The Lagrangian mesh is most appropriate for the penetrator since in a successful bomb design the penetrator experiences only small strains and little deformation. The ALE mode is most appropriate for the target given the large strains and deformation it experiences during penetration.

ALE-3D was used to simulate a 2000-lb bomb penetrating concrete. In this simulation the DTRA concrete model was used; this model has a baseline concrete strength of 2.5 ksi. The strength constants were scaled to a strength value of 5 ksi for this simulation. The initial mesh plot is shown in Fig. 7-6. A plot at the time penetration ceases is presented in Fig. 7-7. ALE-3D predicted an accurate penetration depth for the given velocity and penetrator type.
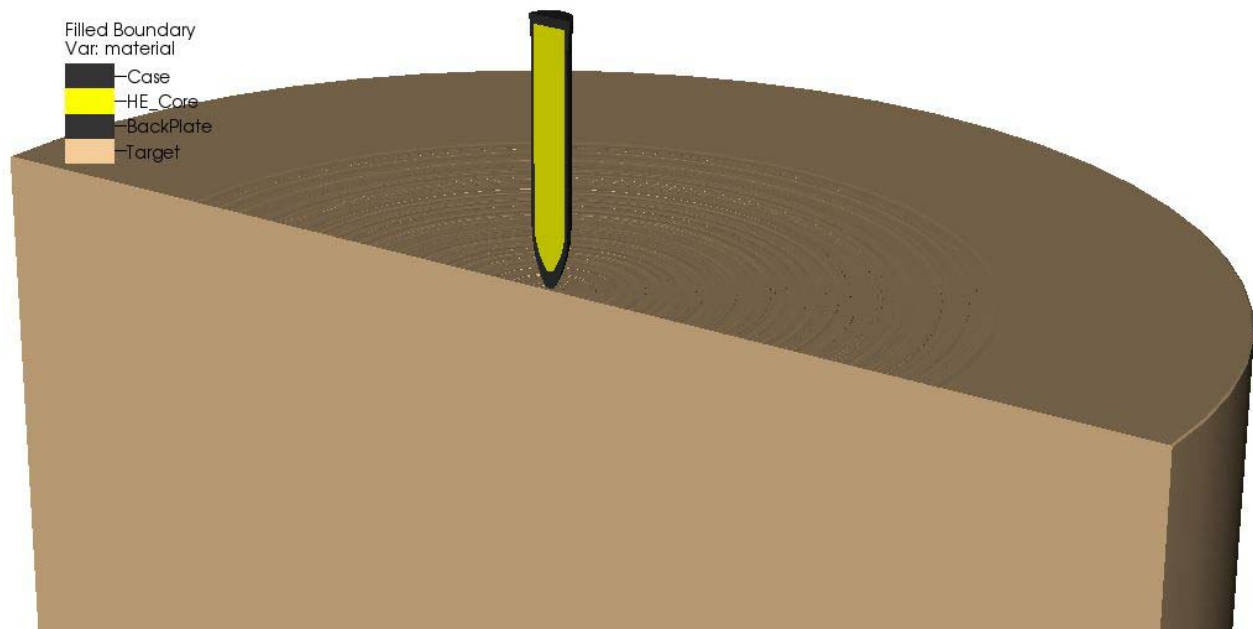
Fig. 7-6. Initial plot from an ALE-3D simulation of a 2,000-lb bomb impacting concrete.
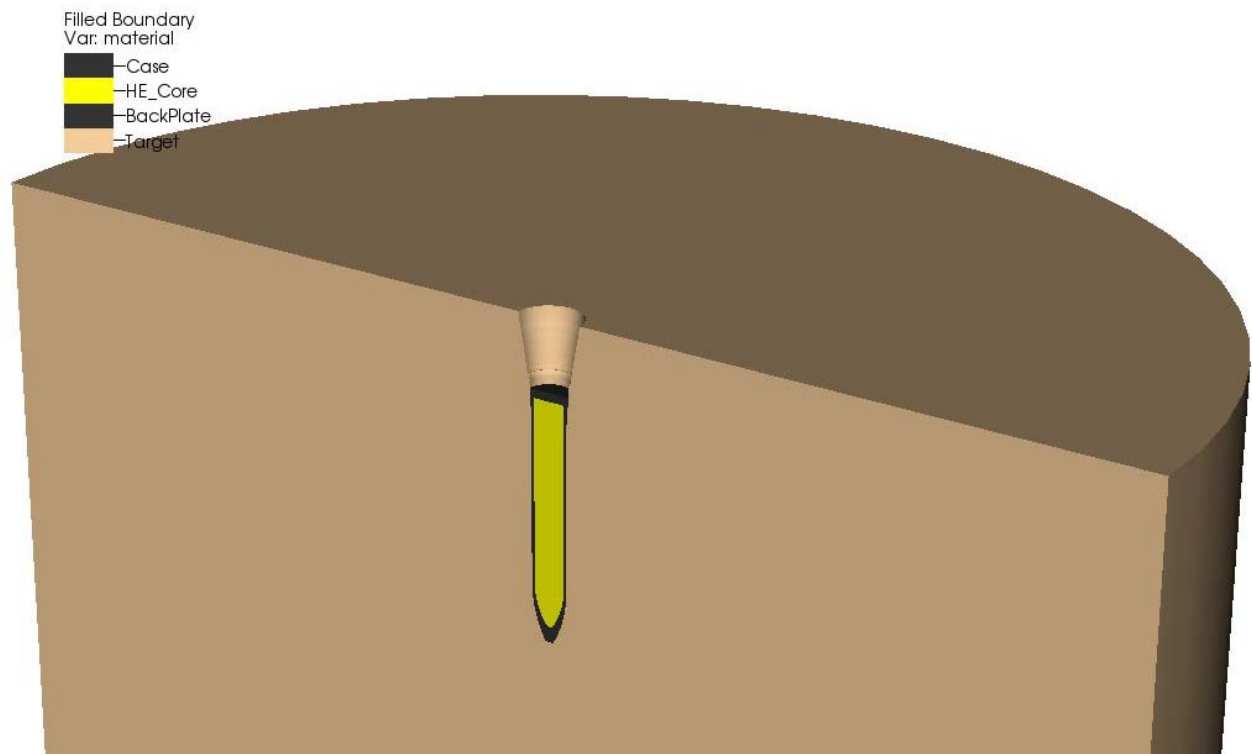
Fig. 7-7. Final plot from an ALE-3D simulation of a 2,000-lb bomb impacting concrete.

Based on this simulation and some additional check-out runs, the ALE-3D code is considered a suitable tool for assessing penetrator survivability. ALE-3D runs fairly slowly compared to EPIC, and therefore EPIC is more suitable for conducting trade studies. However, the ALE formulation provides greater fidelity in terms of the loading on the casing. Therefore ALE-3D will be applied in the final stages of bomb design.

Section VIII

Computational Analysis of Concrete Penetration

Several computational tools are available for predicting penetration into concrete. In the present design study, we limited our use to the EPIC finite-element code, mainly for convenience and ease of use. We have not attempted to validate or calibrate its predictions against any experimental data, but have compared selected computations with predictions of Forrestal's model of concrete penetration; agreement is very good, in terms of final penetration depth and deceleration history.

8.1 Modeling using the EPIC Code

EPIC's built-in material properties library features several established models for various types of concrete, of which we made use of the following three with the particle-conversion method:

- Holmquist-Johnson-Cook (HJC) model for SAC-5 concrete, with a compressive strength of 5.9 ksi
- HJC model for 7-ksi concrete
- Modified HULL model for 5-ksi concrete

In addition, several models are available for various grades of steel, of which the following were used:

- Johnson-Cook (JC) model for 4340 steel, hardness Rc 30
- Steinberg-Guinan model of 4340 steel, hardness Rc 38
- JC model of 1006 (mild) steel, hardness Rf 94

Isothermal plastic stress-strain curves for these models are plotted in Fig. 8-1.
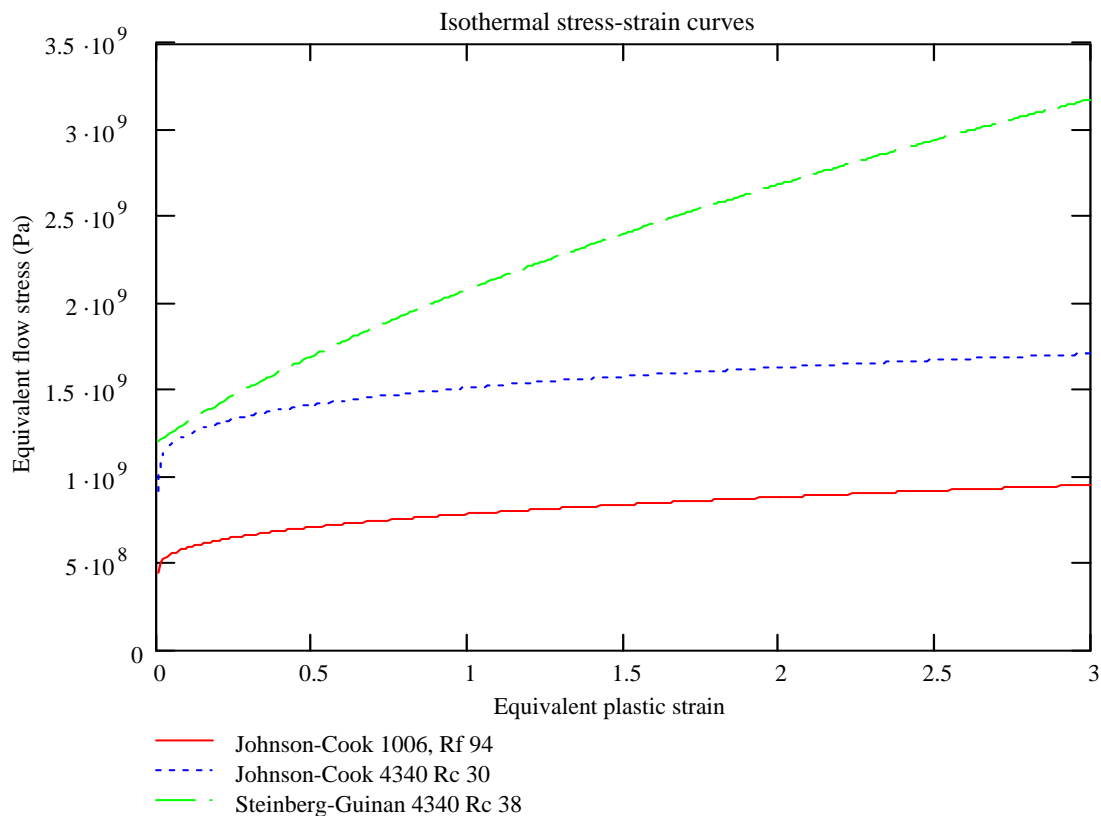
Fig. 8-1. Isothermal stress-strain curves for Johnson-Cook models of various grades of steel.

In all cases, the explosive fill was modeled as "INERT EXPLOSIVE (GENERIC)", which is EPIC's default for bomb penetrators.

8.2 Penetrator Survivability and Failure Modes

A common bomb failure criterion is the predicted final effective plastic strain in the casing. Depending on the type of steel, a few per cent is considered tolerable, above which there is easily visible overall deformation of the bomb.

In unyawed impacts at low obliquities, the usual failure mode (the result of too weak a casing material or too great an impact velocity) is lateral bulging of the fore part of the casing, as shown in Fig. 8-2. The underlying mechanism is forward shifting of the explosive fill, as evidenced by the void visible in the figure at the rear of the bomb's explosive cavity. In this computation, final effective plastic strain exceeded 20%. When the explosive fill is omitted from the computation, strains run less than 2%; this supports the hypothesis that shifting of the explosive is the underlying mechanism, rather than, say, simple buckling.
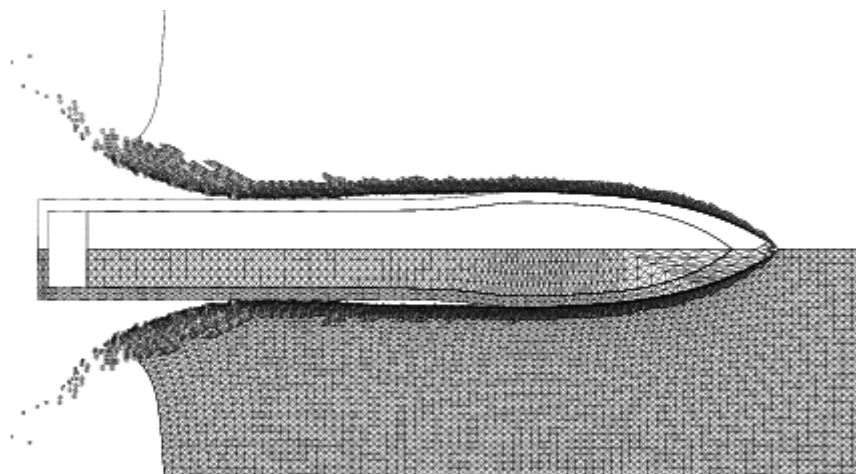
Fig. 8-2. EPIC computation of a bomb at high velocity shows the incipient failure mode of lateral bulging caused by forward shifting of the explosive fill (note void at rear of internal cavity).

8.3 Penetrator Design Studies

The EPIC code and Forrestal's model were exercised to determine how a dense, medium-strength reactive material, which has been demonstrated to enhance blast, can be incorporated into effective bomb penetrators without sacrificing penetration or blast performance, but in a significantly smaller size. Considered were penetrators in the weight classes of 2,000 lb (comparable to the BLU-109/B bomb) to be replaced by a 500-lb bomb containing RMS, and 30,000 lb (comparable to the Massive Ordnance Penetrator, MOP) to be replaced by a 7,000-lb bomb with RMS.

The reactive material was assumed to have the material characteristics of a mild steel, 1006 grade, which has a yield strength of about 500 MPa (75 ksi). Since this is significantly softer than the hardened steels typically used in bomb penetrators, substantially thicker casings of reactive material were used to prevent their deformation.

8.3.1 A 500-lb-class Bomb to Replace BLU-109/B

A notional 500-lb-class bomb penetrator was conceived based on the characteristics of the 2,000-lb-class BLU-109/B, as summarized in Table 8-1. First, a "Scaled BLU-109" design was created by simple geometric scaling of the BLU-109 down to a 500-lb size. Based on a gross mass of the BLU-109 of 2,000 lb, the scale factor is equal to the cube-root of (500/2000), or 0.630. All bomb dimensions and the penetra-

tion depth are scaled by this factor. Penetrations listed in the table are predicted by Forrestal's model for an impact at 1000 ft/s into 5-ksi concrete.

In a second step, a 500-lb RMS-cased bomb design was developed from the Scaled BLU-109 by reducing the diameter and increasing the casing thickness (but maintaining the same length) so that it would have a greater cross-sectional density, thereby increasing penetration performance, while replacing the inert steel casing with RMS at the density of steel (7.8 g/cc) in order to enhance blast. As a rough measure of density, an Effective M/C (ratio of casing mass to explosive charge mass) is computed. This is the M/C ratio that would be used, for example, to compute casing projection velocity by a Gurney formula; that is, it applies to a typical cross-section of the bomb over the explosive, and it does not include casing material in the nose or tail. For the BLU-109 and Scaled BLU-109, the Effective M/C is 1.73. For the RMS-cased penetrator, it was arbitrarily decided to increase the Effective M/C to 6.

Table 8-1. Development of a notional 500-lb-class RMS-cased bomb penetrator.

	BLU-109	Scaled BLU-109	RMS
Total mass (lb)	2000	500	500
Diameter	37 cm (14.56")	23.3 cm (9.18")	19.1 cm (7.52")
Effective M/C	1.73	1.73	6.0
Penetration into 5-ksi concrete	1.66 m (65.3")	1.05 m (41.4")	1.63 m (64.0")
Explosive mass (lb)	535	134	60 (+ 423 RMS)
Theoretical energy (GJ)	1.45	0.37	1.36
Effective energy (GJ)	0.79	0.199	1.04

This results in a casing with a smaller diameter (7.5 in.) and greater thickness (1.325 in., vs. 0.713 in. for the Scaled BLU-109), as shown in Fig. 8-3. The increase in cross-sectional density increases the predicted penetration to very nearly the same as the actual BLU-109. The RMS-cased bomb's theoretical total energy of its 60 lb of explosive (at 1430 cal/g) and 423 lb of RMS (at 1494 cal/g) is 1.36 GJ, almost equal to the 1.45 GJ of the BLU-109's 535 lb of explosive. Total theoretical energy is computed from the formula

$$E = \left(M_{expl} \cdot 1430 \frac{cal}{g} + M_{RMS} \cdot 1494 \frac{cal}{g} \right)\left(4.184 \frac{J}{cal} \right)\left(454 \frac{g}{lb} \right)$$
(8-1)

where M_{expl} is the mass of the explosive and M_{RMS} is the mass of the RMS. Moreover, in terms of *effective* energy in generating blast, the 500-lb RMS-cased design significantly exceeds that of the 2,000-lb BLU-109. Effective energy is estimated from the formula

$$E_{effective} = \left(\eta_{expl} \cdot M_{expl} \cdot 1430 \frac{cal}{g} + \eta_{RMS} \cdot M_{RMS} \cdot 1494 \frac{cal}{g} \right)\left(4.184 \frac{J}{cal} \right)\left(454 \frac{g}{lb} \right)$$
(8-2)

where the η's are efficiencies calibrated to Quasi-Static Overpressures measured in the ARA Blast Chamber Tests of RMS casings and inert steel casings (with M/C = 3). Equation (8-2) is fitted to effective energies determined from the measured overpressures using the ideal gas law,

$$E_{effective} = \frac{P_{measured}V_{chamber}}{\gamma - 1}$$
(8-3)

where $P_{measured}$ is the recorded quasi-static overpressure, $V_{chamber}$ is the (enclosed) chamber volume, and γ is the ratio of specific heats, taken as 1.4, the value for air. The calibrated efficiency values are $\eta_{expl} = 0.56; \eta_{RMS} = 0.795$. Using Eq. (8-2), then, the effective energy of the small RMS-cased bomb is 1.04 GJ, compared to 0.79 GJ for the much larger BLU-109.

60.2

4.9"

1.33"   7.5"
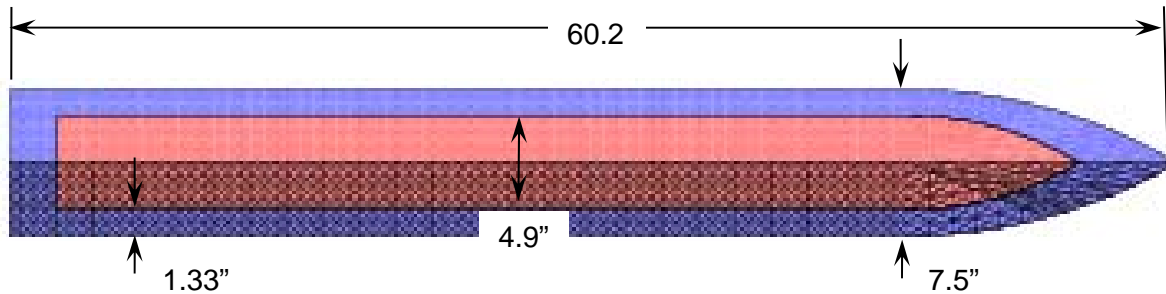
Fig. 8-3. Notional 500-lb RMS-cased bomb penetrator to replace the BLU-109/B.

8.3.2 A 7,000-lb-class Bomb to Replace MOP

A notional 7,000-lb-class bomb penetrator was conceived based on the dimensions of the 30,000-lb-class Massive Ordnance Penetrator (MOP), as summarized in Table 8-2. First, a "Scaled MOP" design was developed by simple geometric scaling of the MOP down to a 7,000-lb size. Based on a mass of the MOP of 27,500 lb, the scale factor is equal to the cube-root of (7000/27500), or 0.6338. All bomb dimensions as well as the penetration depth are scaled by this factor. Penetrations listed in the table are as predicted by Forrestal's model for an impact at 1000 ft/s into 5-ksi concrete.

Table 8-2. Development of a notional 7,000-lb-class RMS-cased bomb penetrator.

	MOP	Scaled MOP	RMS
Total mass (lb)	27500	7000	7000
Diameter	80 cm (31.5")	50.7 cm (20.0")	45.0 cm (17.74")
Effective *M/C*	2.83	2.83	6.0
Penetration into 5-ksi concrete (Forrestal's model)	3.365 m (132.5")	2.13 m (84.0")	2.48 m (97.5")
Explosive mass (lb)	5300	1349	733 (+ 6267 RMS)
Theoretical energy (GJ)	14.4	3.66	19.8
Effective energy (GJ)	7.9	2.0	15.2

Second, a 7,000-lb RMS-cased bomb design was developed from the Scaled MOP by reducing its diameter and increasing its casing thickness (while maintaining the same length) so that it would have a greater cross-sectional density, thereby increasing its penetration, while replacing its inert steel casing with RMS at the density of steel (7.8 g/cc) in order to enhance blast. As discussed above, an Effective *M/C* (ratio of casing mass to explosive charge mass) is computed. For the MOP and Scaled MOP, the Effective *M/C* is 2.83. For the RMS-cased penetrator, it was arbitrarily decided to increase the Effective *M/C* to 6.

This results in a smaller diameter and greater casing thickness (3.13 in., vs. 2.22 in. for the Scaled MOP). Its greater cross-sectional density increases the penetration over the Scaled MOP, but not to the same level as the actual MOP. An EPIC-PENCRV computation of this bomb penetrating 5-ksi concrete at 1000 ft/s predicts very low levels of plastic strain, less than 2%, as shown in the contour plot in Fig. 8-4. The RMS-cased bomb's theoretical total energy of its 733 lb of explosive (at 1430 cal/g) and 6267 lb of RMS (at 1494 cal/g) is 19.8 GJ, significantly greater than the 14.4 GJ of the MOP's 5300 lb of explosive. Total theoretical energy is computed from Eq. (8-1) above. Effective energy, calculated from Eq. (8-2), is 15.2 GJ for the RMS-cased bomb, nearly double the MOP's 7.9 GJ.
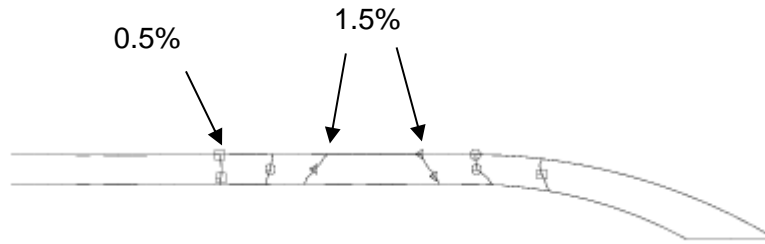
Fig. 8-4. Contours of effective plastic strain in 7,000-lb RMS bomb penetrator.

Further design changes were explored to determine whether an RMS-cased bomb in a 7,000-lb size could deliver penetration performance equal to the MOP. It was desired to investigate the possibility that RMS's lower strength (compared to steel) results in significant deformation or failure. Since Forrestal's model is limited to non-deforming penetrators, the EPIC code with PENCRV link was used to predict penetration performance. Larger values of Effective *M/C* were considered to boost predicted penetration back to the full-scale MOP level. Simple scaling indicated that MOP performance would be achieved with *M/C* of 19. Indeed, an EPIC-PENCRV computation for *M/C* = 19.47 predicted penetration slightly greater than the MOP. After some trial-and-error computations at slightly smaller *M/C* ratios, it was found that MOP performance can nearly be duplicated with a 7,000-lb-class penetrator having *M/C* about 12, shown in Fig. 8-5. The results of this study are summarized in Table 8-3.
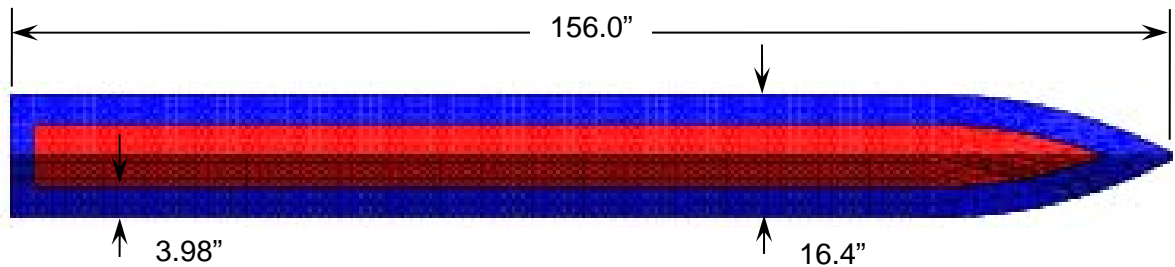
Fig. 8-5. Notional 7,000-lb RMS-cased bomb penetrator to replace the MOP (effective *M/C* = 12).

Table 8-3. Further design changes to RMS-cased bomb and penetration performance.

Effective *M/C*	OD (in.)	T_{wall} (in.)	EPIC-PENCRV	Relative Penetration	Actual mass (lb)
2.83 (MOP)	31.50	3.50	199.8"	≡1	27473
2.83 (Scaled MOP)	19.965	2.218	126.1"	0.631	7000
6.0	17.74	3.13	161.0"	0.806	6943
19.47	15.75	4.515	204.9"	1.026	6862
16.09	15.98	4.31	198.8"	0.995	6887
11.99	16.42	3.98	194.9"	0.975	6876
∞ (*C* = 0)	14.75	--	214.6"	1.074	6886

8.4 Conclusions

The above studies illustrate how the application of Reactive Material Structures can increase penetration and blast to the extent that a smaller-class bomb can perform at the level of a larger-class bomb. This has involved the use of large values of the ratio of casing to explosive mass, based on the assumption that RMS energy output in enhancing blast is not affected by this ratio. Experiments have been planned to test this hypothesis.

Section IX

Material Properties Improvement and Testing

The section reports efforts to improve the mechanical properties of the Reactive Material Structure. This involved modifying the braiding layup to increase the ultimate strength and modulus of a cylindrical specimen in compression.

Previous mechanical testing of the RMS specimens measured an ultimate tensile strength of 73.3 ± 4.5 ksi and an ultimate compressive strength of 34.3 ± 0.3 ksi. These specimens were cylindrical tubes with an outside diameter of 1.215 inches and a wall thickness of 0.105 inch.

The tensile strength exceeded the Phase I requirement of 50 ksi but the compressive strength fell short. The structural analysis of bomb casings during penetration discussed above shows that somewhat greater compressive strength is needed, and an effort was made to improve it.

9.1 Mechanical Testing

The RMS composite being developed in this program consists of multiple layers of braided tungsten wires in an aluminum-epoxy matrix. As with any composite, the fabrication process must be tailored to the size of the component. In our previous work with 250-gram 1.0-inch-inside-diameter tubes, the tungsten reinforcement was limited to the smallest-diameter tungsten wire that is commercially available, 0.004-inch. In larger specimens, the greater volume allows more options in the size of the reinforcement. To explore these options a strength study was conducted using a nominal 1-kg specimen with an OD of 2.0 inches.

To get a first baseline strength value in this larger scale, a compression test was performed on a 1.0-kg specimen, as fabricated for the ARA blast tests, which was an M/C = 3 hollow cylinder with dimensions of 1.534" ID × 2.002" OD × 7.125" length. The specimen was fabricated by braiding multiple layers of tungsten wire over a mandrel until the desired thickness and reinforcement volume were reached. The matrix material, aluminum-powder-filled epoxy, was manually applied over each braided layer. A braided layer in this case consisted of braiding wires with orientations of ±θ (bias) and 0˚ (longitudinal). The braiding machine was a maypole-type two-dimensional braider with 72 braiding carriers (bias wire dispensers) and 36 stationary carriers (longitudinal wire dispensers).

For a wire reinforcement of 30% by volume, with 40% aluminum powder and 30% epoxy, 17 braid layers were needed to meet the desired dimensions. The number of tungsten wires per carrier (or "yarn") was 7 for braiding and 30 for longitudinal. These numbers were maintained from layer to layer. To compensate for the greater diameter of each subsequent layer while maintaining uniform coverage of reinforcement, the braid angle (wire orientation) was gradually increased in succeeding layers, ranging from 45˚ in the innermost layer to 70˚ in the outermost. However, this increase in angle was insufficient to fully compensate for the growth in braid-layer diameter, resulting in decreasing wire volume fractions in successive layers, from about 57% in the innermost layer to 30% in the outermost.

The finished cylinder (Fig. 9-1a) was cut to length, and steel end caps (Fig. 9-1b) were attached to prevent the ends from mushrooming during testing. Testing was performed on a Forney compressive testing system with 600,000-lb load capacity (Fig. 9-2). The loading rate was set at 200 lbf/sec.

Failure occurred at 47,383 psi and 1.38% strain (Fig. 9-3). The right side of Fig. 9-2 shows that fracture occurred about 0.5" from the end caps, while the mid-section remained intact. It also appears that fracture occurred in the surface layers, specifically at the seams of the outer layers. The braid was seamless, but in molding the two outer layers were pinched between the mold halves, leaving small flanges along

the sides of the cylinder. These were trimmed after unmolding, which left a discontinuity of these layers, introducing a stress concentration that resulted in premature failure there, as shown in Fig. 9-4.
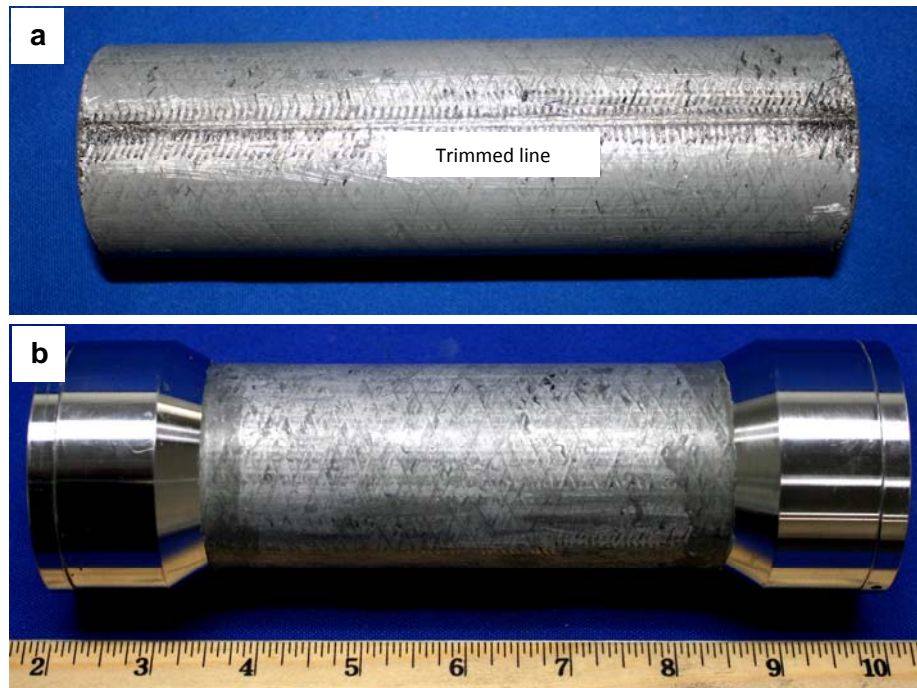
Fig. 9-1. RMS cylinder for compression test, 2" OD, *M/C* = 3: a) cylinder after trimming; and b) with end caps attached.
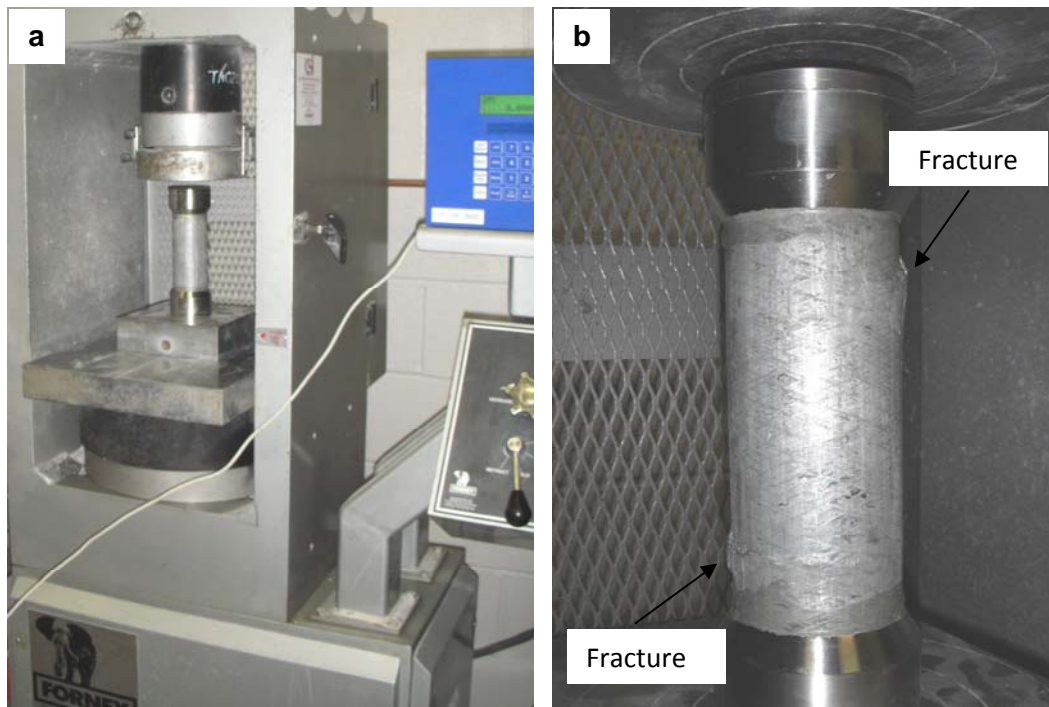
Fig. 9-2. a) Forney compressive tester with 600,000-lb load capacity; and b) fractured specimen.
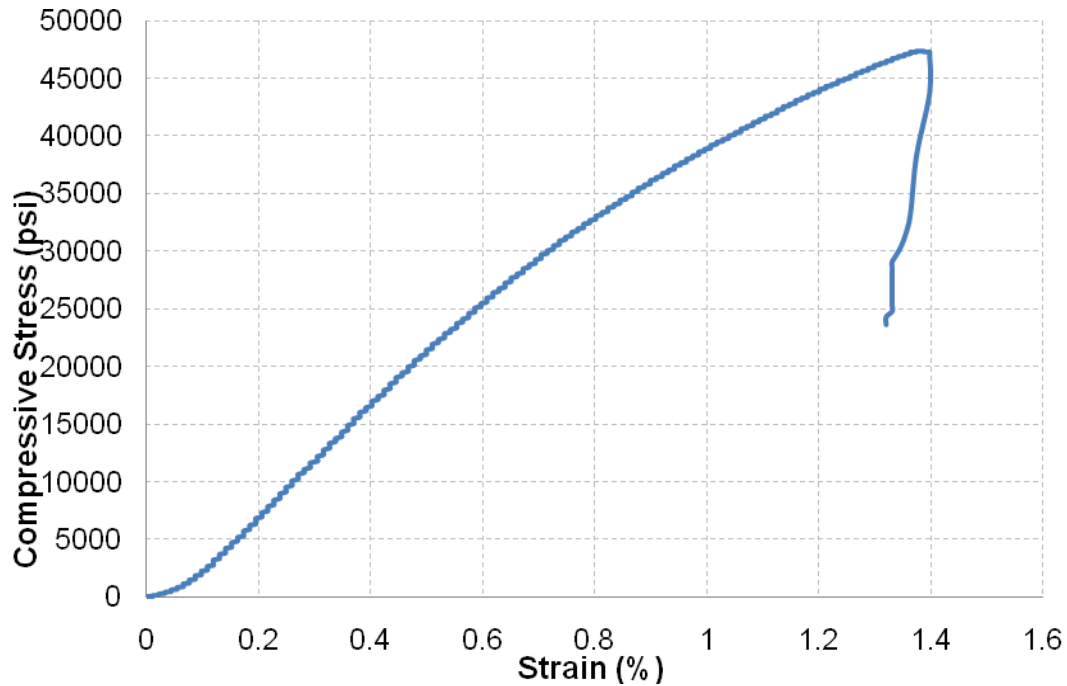
Fig. 9-3. Recorded compressive stress vs. strain for RMS cylinder.
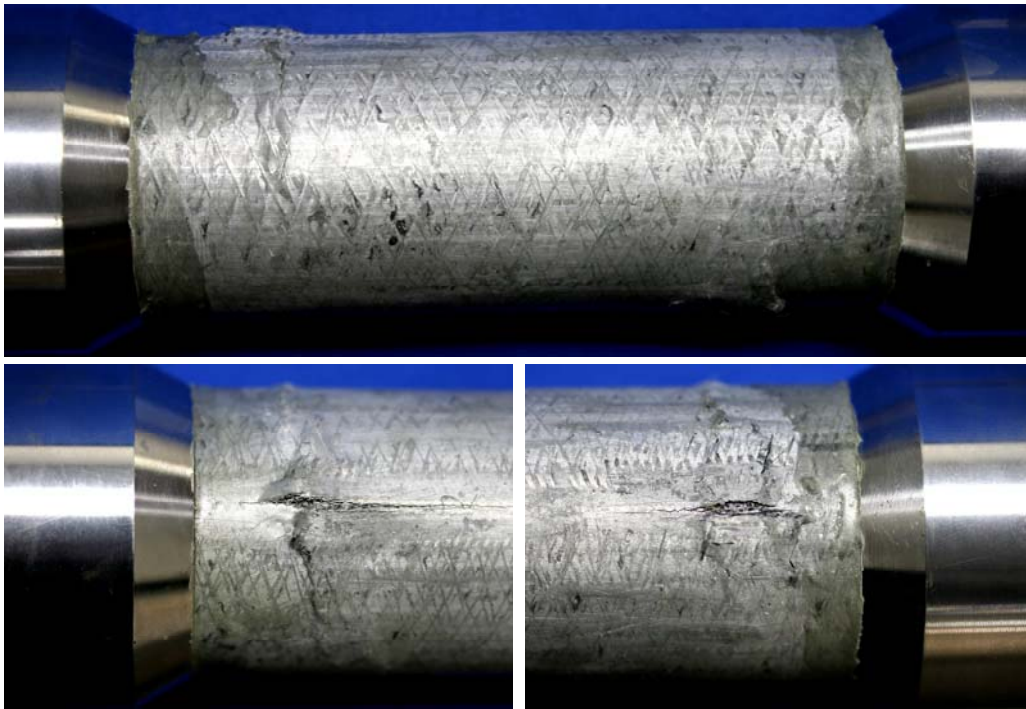
Fig. 9-4. Fracture occurred on the trimmed lines and near the end caps (opposite ends and sides) initiated by wire discontinuity arising from trimming the pinched wire layers.

Besides the stress concentration created by trimming, the gradual increase in layer diameter caused a reduction in wire volume in each successive layer. These factors adversely affected the mechanical properties of the composite. The trimming effect can be addressed by increasing the number of wires per carrier or by using thicker wires for the longitudinal reinforcement. This modification will reduce the number of layers, thereby eliminating or reducing layer pinching during the consolidation process. Main-

taining constant wire content from layer to layer by adding wires is impractical during braiding, as this would require repeated changes in machine configuration.

Based on the theoretical prediction of compressive properties, yielding occurred in the longitudinal wires in the outer layer (ANSYS simulation below) because of lower wire content there. In order to maintain high wire volume in this layer without reconfiguring the braiding process, a layer of the braid (0˚±θ) near the surface of the cylinder can be removed and replaced by a longitudinal layer. This layer can be prefabricated by weaving, with thick wires arranged in the axial (warp) direction held together by finer wires in the circumferential (weft) direction. The spacing between the warp and weft wires can be controlled to achieve proper volume and flexibility for wrapping around the cylinder. This allows additional reinforcement without altering the braiding configuration. Once this layer is in place, the braid angles on subsequent layers can be reduced to gain additional strain before failure occurs.

The preliminary compressive properties provide a guideline for further improving RMS performance. The above discrepancies were addressed in the next set of specimens, fabricated in August 2011. Different RMS configurations with various wire diameters, lay-ups, braid angles, local reinforcement, and reinforcement content were fabricated and tested to study their effects on compressive properties. Aluminum powder was omitted since our previous studies showed its negligible influence on mechanical properties of the composite.

9.2 Finite-Element Analysis

A finite-element model of the RMS specimen undergoing the compression testing described above was developed with the ANSYS structural analysis software. This model allows a parametric study of the composite structure to identify trends in composite stiffness and strength at first ply failure.

The first step in model development was to determine the matrix and fiber material properties. The composite formulation contains approximately 30% volume fraction (vf) of fibers and 40% vf of aluminum powder imbedded in the balance of 30% vf of epoxy.

The material properties of the tungsten fibers are known, as provided by the manufacturer. For the stiffness of the matrix material, estimates had to be made since the matrix is a combination of epoxy and aluminum powder. Mechanical properties for the matrix material were based on both analytical evaluations and experimental data.

The model of the braided cylinder consisted of 16 braided layers, each containing longitudinal and biased tungsten wires. The outermost 17th braid is not modeled since it was severed after unmolding as described above. Each layer is a textile composite in that the fibers are braided into a cloth-like structure. Modeling the mechanical properties of textile composites is a current topic of research, and few suitable commercial modeling packages are available. Those that exist are limited to flat-woven composites of fiberglass or carbon fiber; these models are unsuitable for tungsten wire or braids.

Our approach was to use models developed for tape composites, in which the layers are not braided or woven, but are simply layered one upon another. These models, which have been available for years, capture at least the primary parameters of the braid: braid angle and the ratio between braided and longitudinal wires. Each braid layer consists of yarns at two angles and longitudinal yarns, which in our tape model translates into three fiber layers: one at the plus braid angle, another at the minus braid angle, and the longitudinal layer; hence our final model has 48 fiber layers (3 directions times 16 braid layers). Each layer is modeled individually with a single braid angle and wire quantity and can be used to assess the effects of these parameters on stiffness and strength.

Two analytical software packages were used, CompositePro and ANSYS. CompositePro was used to determine uniaxial composite properties of each layer for the varying volume fractions. The composite

properties can then be fed into ANSYS for an overall FEA analysis. In addition, CompositePro can also perform simple beam and plate analyses of composite structures and hence can supplement ANSYS as a simple verification of results.

The compression test discussed above was modeled using the combined CompositePro-ANSYS approach. A plot of the final ANSYS model is shown in Fig. 9-5.
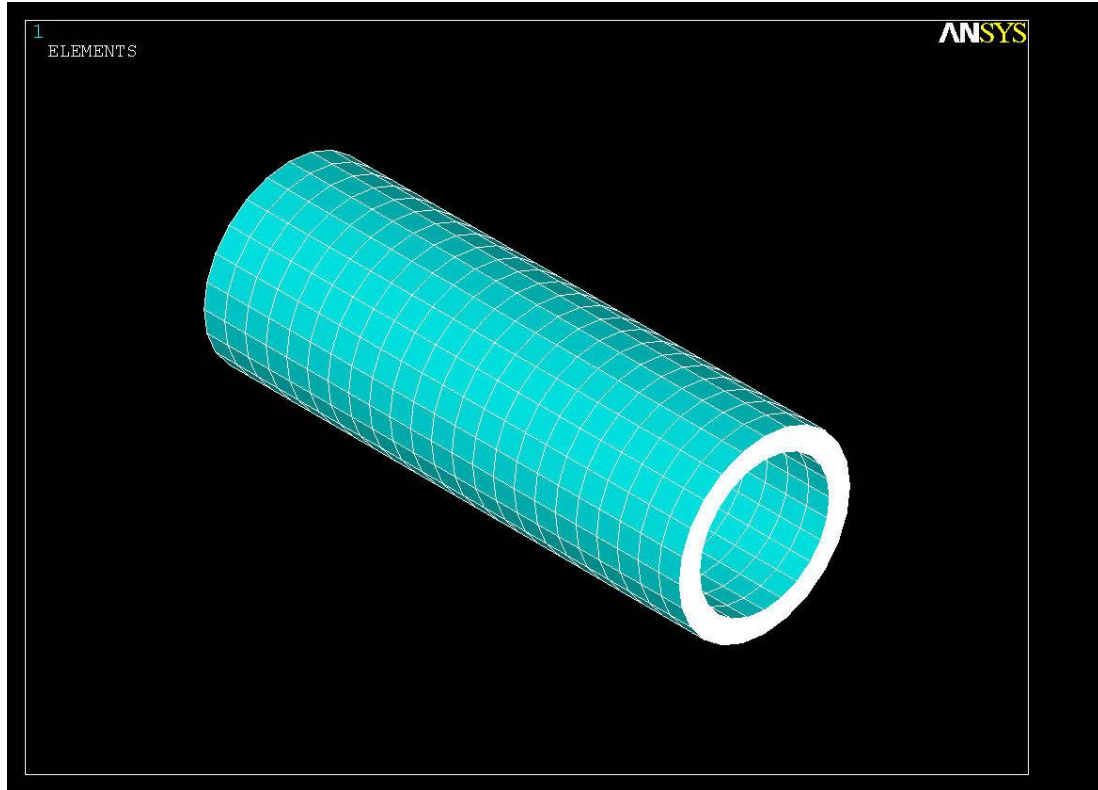
Fig. 9-5. ANSYS model of compression test of RMS cylinder.

The compression test was modeled in ANSYS by applying a fixed displacement in the axial direction. The first ply to exceed the failure strain was the outermost layer of longitudinal wire (layer 46 in our model), which occurred at a reaction force of 32,000 lb. For a cross-sectional area of 1.312 in^2, this corresponds to a first-ply-failure strength of 24,374 psi. This result agrees with the experimental results, which displayed apparent yielding at about the same stress level (see Fig. 9-4 above).

The CompositePro-ANSYS modeling approach appears to be a useful tool for at least performing trade studies of braid angle and longitudinal-to-braid wire ratio. Since the model does not reflect the braiding aspect of the actual material, it will be used only on a comparative basis to assess various fiber lay-ups. The models will be used to guide the experimental strengthening study that will commence within the coming months.

9.3 Improved Strength

The baseline RMS (W-Al-Ep) consists of 30% (by volume) tungsten wire, 40% aluminum powder, and 30% epoxy. In previous iterations, the RMS cylinders were built up of layers of 2-dimensionally braided wire. Each layer consisted of longitudinal (0˚) and biased (±θ) wire orientations, to make a triaxial braid. Both the longitudinal and bias wires were of 0.004" diameter. The longitudinal/bias ratio L/B of the baseline RMS is about 1.03. This layup demonstrated a compressive strength of ~47 ksi and modulus of ~4.2 Msi.

The approach was to layer the 2-dimensional braids to form a hollow cylinder with the desired thickness. Each layer had the same number of wires. As successive layers were added, the volume fraction of wire decreased since the volume of each layer increased with the increasing diameter. While the wire volume averaged 30% over the part, it varied from 35% in the inner layers to 25% in the outer layers.

FEA predictions of the compressive loading showed that yielding initiates in the longitudinal wires of the outer layers due to the reduction in wire volume fraction. A means of improving the compressive properties is to increase the tungsten volume fraction of the outer layers. However, adding more wires to the braiding machine during part fabrication is impractical since restringing the machine is time-consuming and cannot be completed before the epoxy cures. Of course, two braiding machines could be used but we are currently limited to one braider.

Instead, layers of unidirectional wires were introduced. These layers used thicker wires at volumes upwards of 45%. These layers were applied between the braided layers, with at least one layer near the outer surface. Each two layers of longitudinal wires is equivalent to three layers of braid.

The unidirectional layers were produced with a conventional loom by arranging a parallel series of either 0.010"- or 0.015"-diameter wires in the warp (axial) direction. These were held in place by seven ends of 0.004"-diameter wires inserted in the weft (perpendicular) direction. Finer wires were used in the weft direction at low insertions per inch to reduce crimping of the unidirectional wires. The woven unidirectional wires were produced in 1"- and 2.5"-wide ribbons, of thickness about 0.016". These ribbons were then wrapped around the braid as described below.

Figure 9-6 shows the difference between the triaxial braided and the woven ribbons. The braids consisted of longitudinal (0˚) and biased (±θ) wire orientations, to make a triaxial braid (Fig. 9-6a). Both the longitudinal and bias wires were of 0.004" diameter. The woven ribbon consisted of either 0.010"- or 0.015"-diameter unidirectional wires in the warp direction with 0.004"-diameter wires in the weft direction (Fig. 9-6b). The ribbons were then wrapped around the part (Fig. 9-6c).
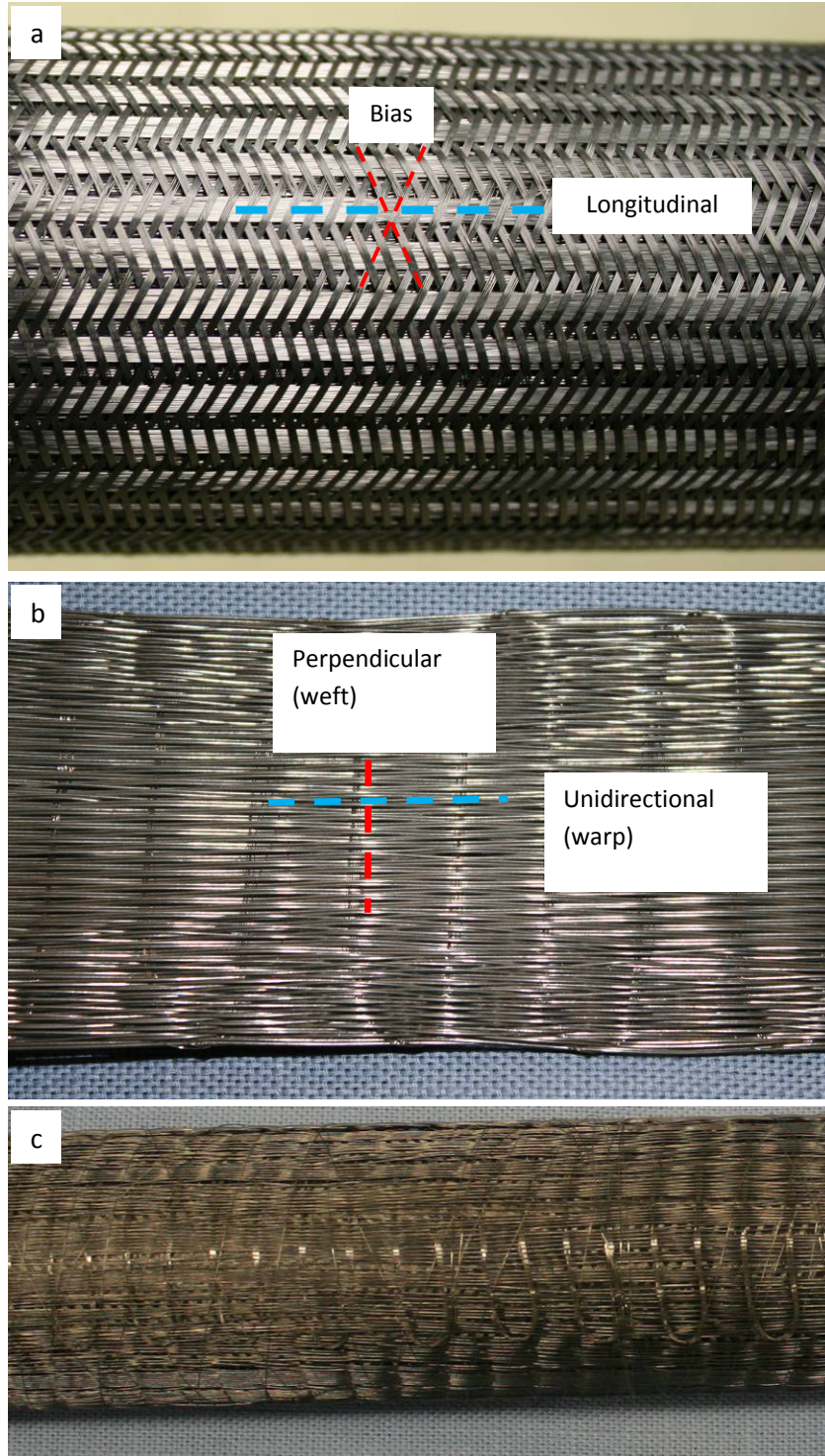
Fig. 9-6. Compressive cylinder layer layup: a) triaxially braided layer; b) woven unidirectional ribbon; c) wrapping of unidirectional ribbon around the cylinder.

9.4 Cylinder Fabrication

Tungsten-wire-reinforced epoxy hollow cylinders with a 2" OD and a 1.527" ID (M/C = 3 configuration) were fabricated for compression testing. For ease of processing and safety, the aluminum powder was

omitted. Since the wires provide the strength and load-bearing capability, the absence of the aluminum should not significantly affect the mechanical properties.

An aluminum mandrel of 1.527" diameter and 15" length was used to form the inner diameter of the cylinder. A first thin layer of braided glass fiber (Fig. 9-7) was placed over the mandrel to facilitate its later removal. For the first specimen, six layers of triaxially braided tungsten wires (0.004" diameter) were then applied (Fig. 9-8). The wire placement speed was adjusted at each layer to achieve proper coverage and wire orientation. Layer #7 consisted of 400 unidirectional wires of 0.010" diameter, shown in Fig. 9-9. Six more layers of triaxially braided wires (0.004" diameter) were then added, followed by a second layer (#14) of 552 unidirectional 0.010"-diameter wires, again wrapped around the cylinder in similar fashion to Layer #7. The outermost triaxially braided layer (#15) was then applied.
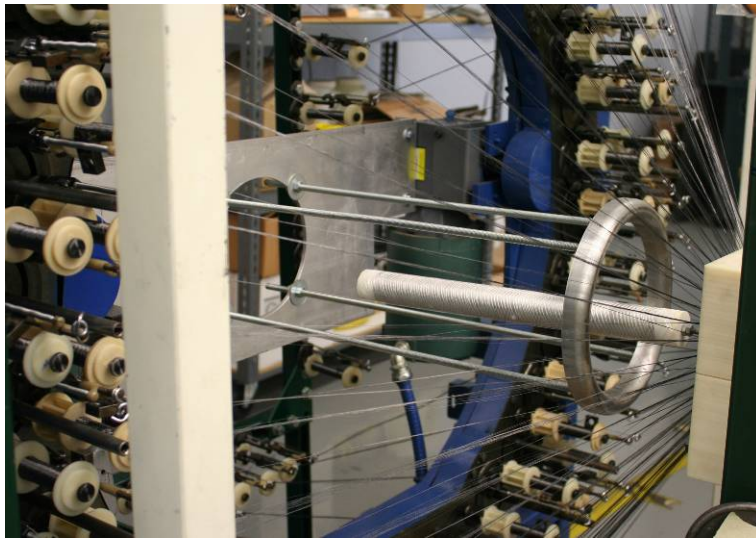
Fig. 9-7. The aluminum mandrel is wrapped in a thin layer of glass fiber braid before the tungsten wire is braided over it.
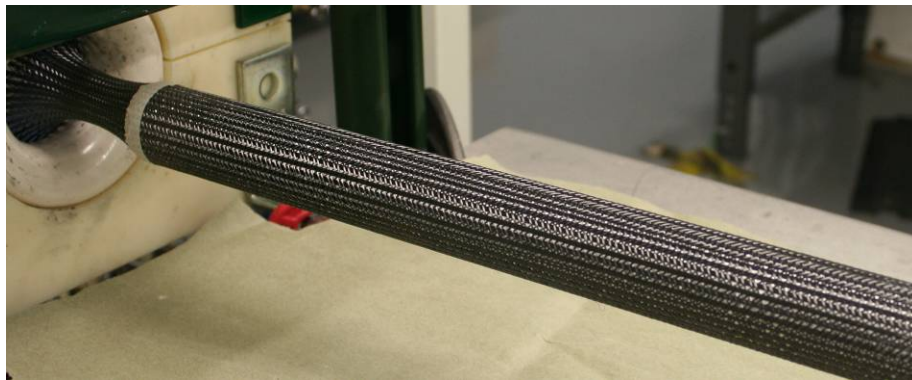
Fig. 9-8. Triaxially braided layer.

Fig. 9-9. Longitudinal layer wrap.

For the second specimen, three layers of triaxially braided tungsten wires (0.004" diameter) were braided over the initial fiberglass braid. Layer #4 consisted of 384 unidirectional wires of 0.015" diameter. Five more layers of triaxially braided wires (0.004" diameter) were then added, followed by a second layer (#10) of 408 unidirectional 0.015"-diameter wires, again wrapped around the cylinder in similar fashion to Layer #4. Two more layers of triaxially braided wires (0.004" diameter) were then added, followed by a third layer (#13) of 468 unidirectional 0.015"-diameter wires. A final triaxially braided layer (#14) was then applied.

For both specimens, the finished preform was placed in an aluminum mold (Fig. 9-10) and injected with epoxy resin. The infiltrated preform was left to cure at room temperature overnight, followed by a final curing at 140˚F for 2 hours.
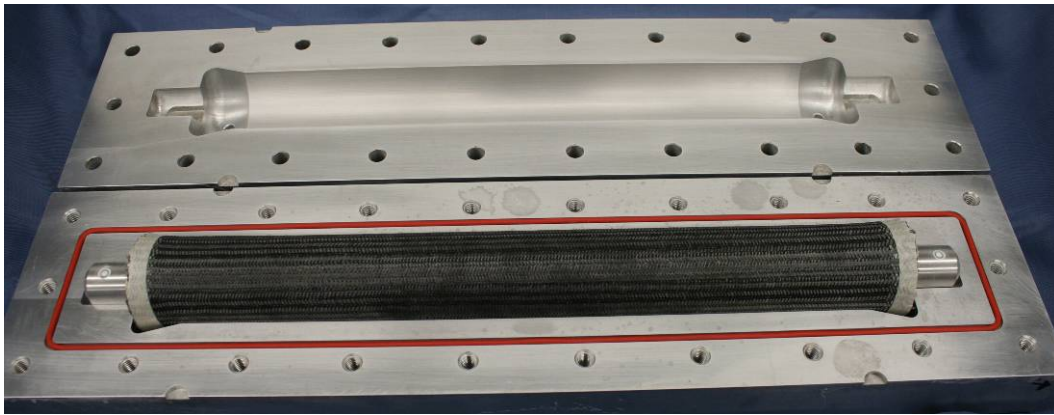
Fig. 9-10. Braided preform in mold cavity ready for infiltration with epoxy.

After curing, the part was removed from the mold, and the mandrel was withdrawn (Fig. 9-11). The tube was then cut on a diamond wheel to 7" lengths, and end fixtures were attached by bonding with epoxy (Fig. 9-12).
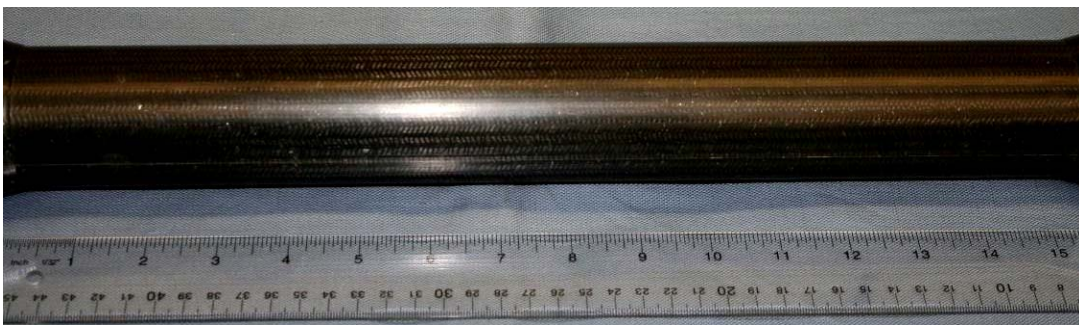
Fig. 9-11. Braided tungsten-wire-reinforced epoxy cylinder.

Fig. 9-12. Assembled compression test specimens.

9.5 Compression Tests

Two wire layup designs were tested in compression. The changes made in this iteration include:

1. Increased longitudinal wire content by adding unidirectional wire of larger diameter, 0.010" and 0.015", wrapped between the braided layers.

2. Altered fiber braid angle of braided layers.

3. Varied the longitudinal/bias (L/B) wire volumetric ratio of the wire layers. Since this is a volumetric ratio, the braid angle affects the ratio by altering the volume of biased wires. As braid angle is increased, the biased wires form a tighter spiral, thereby increasing their length and their overall volume. Therefore, larger braid angles reduce the L/B ratio. Conversely, small braid angles result in a more open braid, thereby shortening the lengths of the biased wires, which decreases their volume to result in a larger L/B ratio.

Note:

1. The longitudinal (0° relative to the axis of the cylinder) wires are 0.004" in diameter and are integrated within the triaxially braided layer.

2. The unidirectional (0°) wires are 0.010" in diameter (Specimen #1) and 0.015" in diameter (Specimen #2) woven into 3" wide ribbon. The ribbon was woven with low picks per inch (~3 ppi) and fine tungsten wire (0.004" diameter) in the weft direction (90°) to minimize crimping of the 0° wires.

3. The baseline RMS (W-Al-Ep) consists of 30% tungsten wire, 40% aluminum powder, and 30% epoxy by volume. Aluminum powder was omitted in these compressive test specimens, which were 30% tungsten wire and 70% epoxy. Since the strength properties of the material are provided mainly by the tungsten wire, omitting the aluminum powder is not expected to have significant effect on mechanical properties, other than a lower mass density. However, the purpose of these tests was to quickly study the effects of L/B ratio, unidirectional wire diameter, and wire orientation on the compressive properties. Once the compressive properties are optimized, then Al powder will be added to achieve the density and reactivity as the baseline RMS.

The overall goal was to improve the compressive properties without sacrificing tensile properties, density, or reactivity. The options are to increase the L/B ratio by increasing the number of longitudinal wires

and varying the braid angle. Wire of 0.004" diameter was used in both directions with the number of wires per bobbin at 30 longitudinal and 7 bias, respectively, yielding L/B = 1.03. Further increasing the number of longitudinals per bobbin is not preferred because it complicates the braiding process. Thus, the number of wires in each braided layer was kept the same, and layers of unidirectional wires were added between braided layers. Adding the volume of the unidirectional wires to that of the longitudinal wires in the braided layers results in a higher L/B ratio. Table 9-1 lists details of the cylinder construc-tions. Compressive tests were run on the two specimens, and their ultimate compressive strengths and strains are included in the table. In the tests, the load was applied at a rate of 200 lbf/s. Figure 9-13 shows the compressive stress-strain plot for the RMS baseline and the two revised designs.

Table 9-1. Layer constructions and compressive properties of the three specimen designs.

Specimen ID	Description	Wire diameters (in)			No. uni-layers	L/B ratio	Braid angle	Wire vol. %	Compressive modulus (Msi)	Ultimate compressive	
		Long.	Bias	Uni.						Strength (psi)	Strain (%)
W-Al-Ep	W wire braid reinforced Al-filled epoxy	0.004	0.004	NA	0	1.03	50° - 70°	29	4.2	47,383	1.38
W-Ep-1	W wire braid & unidirectional reinforced epoxy	0.004	0.004	0.010	2	1.67	45° - 68°	31	8.3	68,756	1.47
W-Ep-2	W wire braid & unidirectional reinforced epoxy	0.004	0.004	0.015	3	3.40	40° - 60°	33	3.3	97,128	6.66
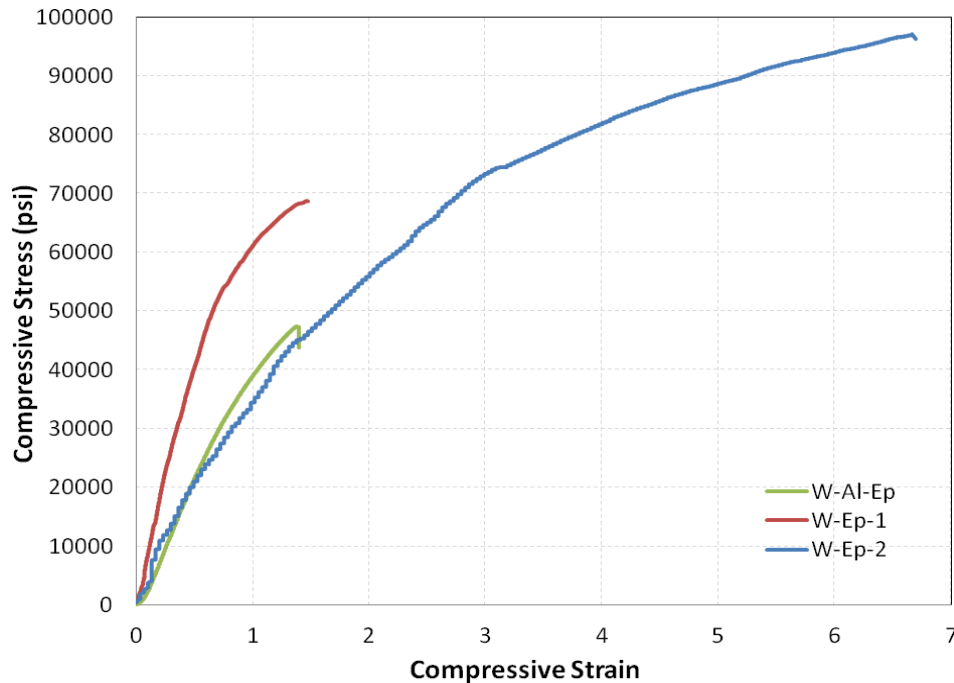
Fig. 9-13. Compressive properties of the composite cylinders.

Figure 9-13 shows that the baseline W-Al-Ep has the lowest ultimate compressive stress (47,383 psi). W-Ep-1 is about 30% higher (68,756 psi) and W-Ep-2 is double (97,128 psi) that of W-Al-Ep. It is expected that the absence of the Al powder has little effect on strength. The total wire content varies a couple of percent among designs and is expected to have only a small effect on compressive properties. The ratio

of longitudinal to bias wires (L/B) is the major factor in doubling the ultimate compressive stress in specimen W-Ep-2 (L/B = 3.4); however, its modulus is lowest of the three designs. The low modulus was attributed to the higher strain to failure (6.66%), more than four times that of the other designs. From Table 9-1, it is apparent that wire content, larger diameter of unidirectional wire, braid angle, and most significantly L/B ratio contributed to the greater compressive strength.

The lower modulus was attributed to a much larger deformation to failure that arose mainly from the crimping of the unidirectional wire in the woven tape. As can be seen in Fig. 9-6b above, the crimping is significant because the unidirectional wires are sometimes twisted around or atop each other. Under compressive loads, wires that are twisted and bunched together will be less stiff and result in a lower compressive modulus, similar to a bent column versus a straight one. Tensile loads will tend to straighten these wires, which will allow excessive displacement to occur (as in a slack rope being pulled taut), thereby lowering the effective tensile modulus of the material system.

The crimping effect can be minimized by reducing the number of wires per heddle. The unidirectional wire in specimen W-Al-2 is 0.015" in diameter. Therefore the crimping is more pronounced than in specimen W-Al-1. In addition, the lower braid angle allows radial expansion of the cylinder under compression, contributing to larger strain to failure.

Based on these observations, we conclude that the compressive properties can be optimized by adjusting the L/B ratio and fiber orientation. The construction in specimen W-EP-1 yields a higher compressive modulus of 8.3 Msi, while specimen W-Al-2 reaches 100 ksi in compressive strength. The following adjustments will be made in the next iteration to obtain compressive modulus and strength expected to be close to 10 Msi and 100 ksi:

1. Bring the total wire content to 30% to maintain density and reactivity as previously achieved;
2. For specimen W-Ep-1, maintain the same fiber orientation but double the L/B ratio to the same value as specimen W-Ep-2. This will increase the compressive strength beyond 68,756 psi while maintaining the 8.3-Msi modulus;
3. For specimen W-Ep-2, the compressive strength is close to the 100-ksi goal. However, the modulus needs significant improvement. For specimen W-Ep-1, it can be seen that it is possible to obtain a modulus close to 10 Msi. This can be done by increasing the braid angle to 45° to 68° and decreasing the number of wires per heddle in the unidirectional woven tape. This will minimize the chance of wires crossing, thus lowering the crimping effect. Increase in braid angle provides higher resistance to radial deformation, thereby increasing the modulus.

The above adjustments will improve the compressive properties of the RMS without affecting its tensile properties previously obtained. Since the axial wire contents are significantly higher than the original design, the tensile properties are expected to be better as well. Two designs with the above modifications will be produced without Al powder and tested in the next iteration to select the best design for further investigation.

This section describes mechanical tests of the surrogate RMS composite material. This non-reactive material, which is mechanically representative of the actual RMS, was used in all tests to avoid any potential hazard due to combustion of the material.

9.6 Instrumented Compression Tests

Three series of instrumented compression tests were performed on the surrogate RMS material. Specimens were tested in two diameters, 2.0 and 2.5 inches. The tests were performed by Southern Research Institute (SoRI) and Westmoreland Mechanical Testing and Research Corporation (WMTR). SoRI performed the first compression tests of the 2.0-inch-diameter specimens in October 2012. SoRI had no

testing machine with sufficient load capacity to fail the 2.5-inch-diameter specimens, so WMTR was engaged to test these in February 2013. In addition, WMTR performed tests of a set of improved-strength 2.0-inch-diameter specimens.

In the first year of the program, DET prepared material up to one inch in diameter, a size chosen to satisfy the program requirements for a 250-gram specimen with a thickness corresponding to a Metal-to-Charge ratio (*M/C*, where the "Metal" is the RMS casing material) of 3. Subsequently, DARPA requested scaling up to a 1.0-kg size, still with *M/C* = 3. This larger specimen with a 2.0-inch outer diameter is the basis for the 2.0-inch-diameter specimens discussed here. Later, DARPA directed that a 20-lb penetrating munition incorporating the RMS be designed, fabricated, and tested. Trade studies determined that an RMS casing of a 20-lb munition would have an outside diameter of 2.5 inches with a thickness corresponding to *M/C* of 9. The 2.5-inch-diameter specimens discussed here represent such an RMS casing.

The reactive material is a composite of 30% tungsten wire, 30% epoxy, and 40% aluminum powder, by volume. All specimens that were mechanically tested were of the inert surrogate material, which does not contain the aluminum powder. The inert surrogate contains only tungsten wire and epoxy, with volume fractions of 30% and 70%, respectively. This material is easier to fabricate and safer to test than the reactive material. The layup of the wire is identical in both the reactive material and inert surrogate. Since the wire provides the mechanical strength of the material, the surrogate is a realistic mechanical representative of the RMS. However, the substitution of epoxy for the denser aluminum results in the surrogate having a slightly lower mass density than the RMS.

9.6.1 2.0-inch-diameter Specimen Tests

Figure 9-14, a drawing of the 2.0-inch-outer-diameter specimen, shows also its inner diameter of 1.526 inches, wall thickness of 0.37 inch, and gauge length of 3.5 inches. If the internal cavity is filled with a typical blast explosive, this configuration represents *M/C* equal to 3.0 for the denser actual RMS. Steel end caps were glued to the specimens to provide hard, flat surfaces to bear the compressive load. Figure 10-15 is a photograph of the specimens.

Notes:
1. End caps and support rings a glued onto tube.
2. Nominal gauge length of specimen is 3.5-inches.
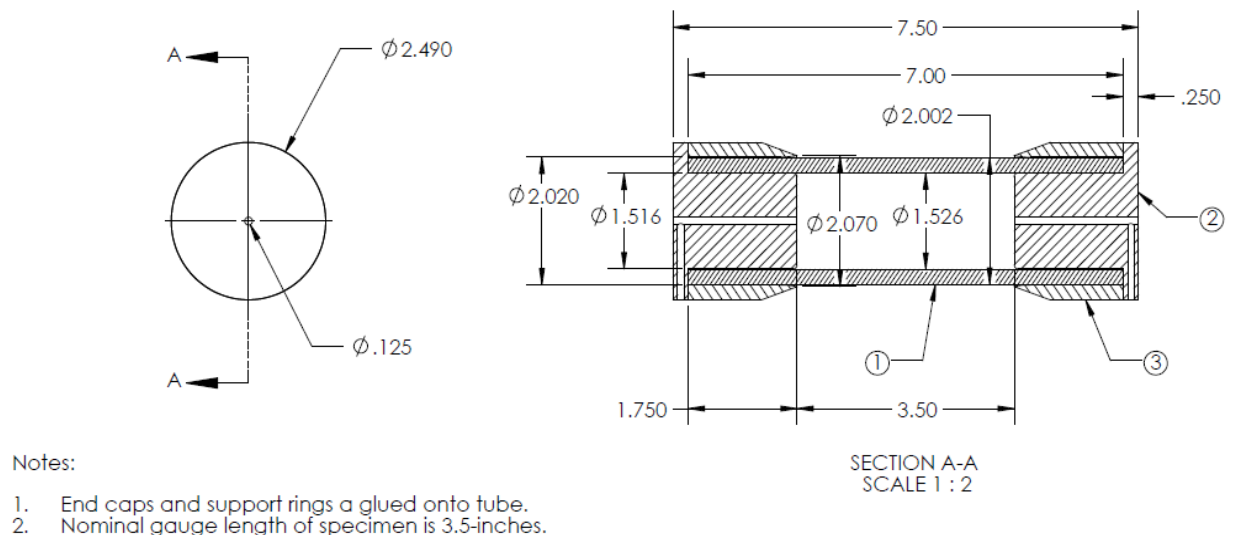
SECTION A-A
SCALE 1 : 2

Fig. 9-14. Drawing of 2.0-inch-diameter compression specimen.

Fig. 9-15. The 2.0-inch-diameter compression specimens.

Two material layups were tested, each consisting of different arrangements of unidirectional layers, composed mainly of longitudinal reinforcing wires loosely woven with thinner non-reinforcing weft wires, and triaxially braided layers, composed of wires at orientation angles that varied through the thickness of the specimen. Specimen #1 (Table 9-2) had unidirectional layers of 0.010-inch-diameter wire, while Specimen #2 (Table 9-3) had unidirectional layers of 0.015-inch-diameter wire and one less braid layer (to maintain the same total thickness). Specimens were prepared in 15-inch lengths, one of each layup, which were cut into two 7-inch-long test specimens.

Table 9-2. Braid layup for 2.0-inch-diameter Specimen #1.

Layer #	Layer type	Wire diam. (in.)	Wire orientation	Number of wires per layer		
				Bias	Longitudinal	Unidirectional
1	Triaxial braid	0.004	0° ± 45°	504	1080	0
2	Triaxial braid	0.004	0° ± 45°	504	1080	0
3	Triaxial braid	0.004	0° ± 45°	504	1080	0
4	Unidirectional	0.010	0°	0	0	900
5	Triaxial braid	0.004	0° ± 55°	504	1080	0
6	Triaxial braid	0.004	0° ± 61°	504	1080	0
7	Triaxial braid	0.004	0° ± 63°	504	1080	0
8	Unidirectional	0.010	0°	0	0	900
9	Triaxial braid	0.004	0° ± 64°	504	1080	0
10	Triaxial braid	0.004	0° ± 66°	504	1080	0
11	Triaxial braid	0.004	0° ± 68°	504	1080	0
12	Unidirectional	0.010	0°	0	0	775
13	Triaxial braid	0.004	0° ± 70°	504	1080	0

Table 9-3. Braid layup for 2.0-inch-diameter Specimen #2.

Layer #	Layer type	Wire diam. (in.)	Wire orientation	Number of wires per layer		
				Bias	Longitudinal	Unidirectional
1	Triaxial Braid	0.004	0° ± 50°	504	1080	0
2	Triaxial Braid	0.004	0° ± 55°	504	1080	0
3	Triaxial Braid	0.004	0° ± 60°	504	1080	0
4	Unidirectional	0.015	0°	0	0	500
5	Triaxial Braid	0.004	0° ± 62°	504	1080	0
6	Triaxial Braid	0.004	0° ± 63°	504	1080	0
7	Triaxial Braid	0.004	0° ± 66°	504	1080	0
8	Unidirectional	0.015	0°	0	0	400
9	Triaxial Braid	0.004	0° ± 67°	504	1080	0
10	Triaxial Braid	0.004	0° ± 67°	504	1080	0
11	Unidirectional	0.015	0°	0	0	468
12	Triaxial Braid	0.004	0° ± 70°	504	1080	0

One specimen of each layup was tested by SoRI in October 2012 and by WMTR in February 2013. Stress versus strain plots from these tests are presented in Fig. 9-16. In each test three biaxial strain gauges were affixed at 120° intervals around the specimen's circumference at the mid-plane of the gauge length. The load was applied at a rate of 30,000 lbf/minute.
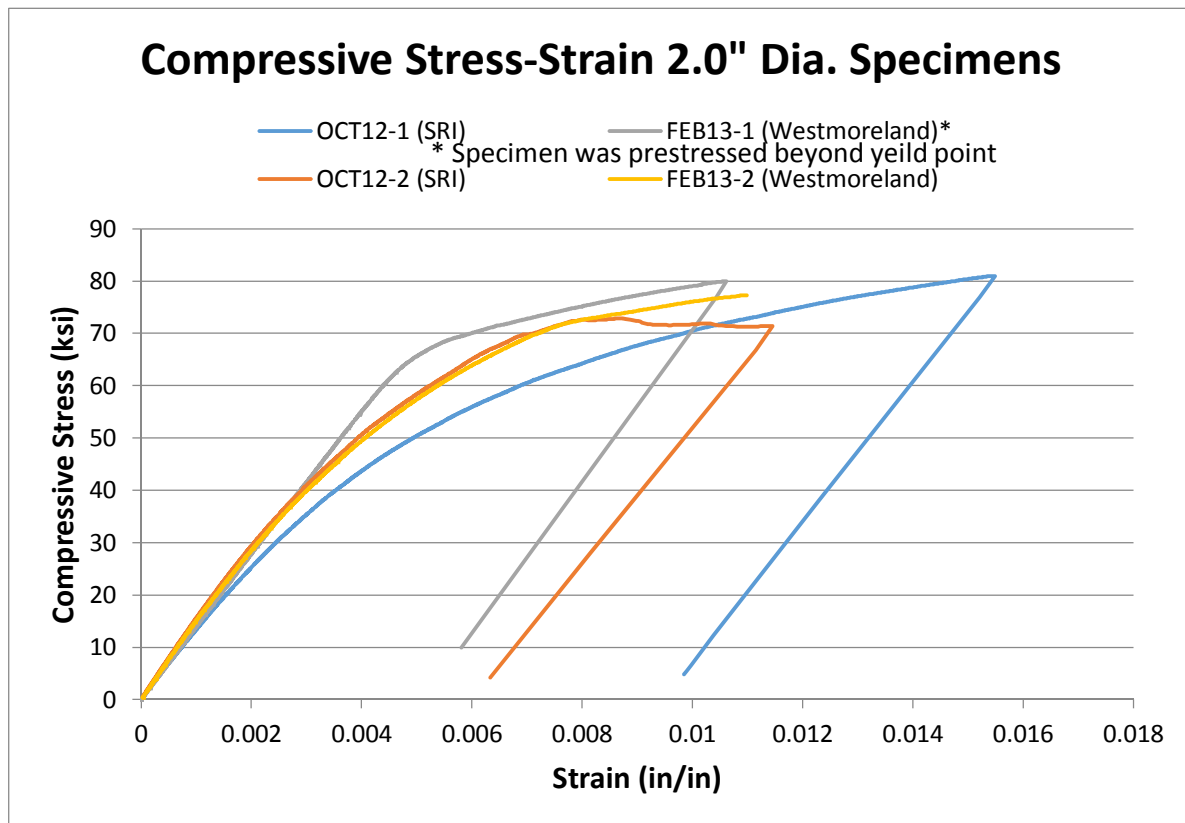
Fig. 9-16. Measured stress versus strain for the two composite configurations.

The three strain gauges were first used to align the load along the specimen axis. Before the tests the specimens were loaded to low levels, and the outputs of the three strain gages were compared. Differences in output would indicate misalignment of the specimen relative to the applied load, which was corrected with shims. In the pre-test setup of specimen FEB13-1, too large a load was applied during this step, which caused the specimen to yield, altering the resulting stress-strain curve for this specimen, as seen in Fig. 9-16 above.

The compressive mechanical properties of the 2.0-inch-diameter specimens are summarized in Table 9-4. Data for the FEB13-1 specimen have been omitted because of the excessive pre-stressing during the alignment step. Compressive yield strengths in excess of 72,000 psi were achieved. Elastic moduli ranged from 12.7 to 15.9 Msi. These values were much greater than those achieved in our previous tests. Part of this improvement is attributed to of the incorporation of the strain gauges, which resulted in more accurate strain measurements.

Table 9-4. Measured compressive mechanical properties for the 2.0-inch-diameter specimens.

Sample #	Max. load (lb)	Compressive failure strength (psi)	Average compressive elastic modulus (Msi)		Average strain to failure (in/in)	Poisson's ratio
			0-10 ksi	0-25 ksi		
OCT12-1	105,523	80,982	13.60	12.74	0.01548	0.280
FEB13-1*	104,914	----	----	----	----	----
OCT12-2	94,976	72,887	15.90	15.16	0.00868	0.300
FEB13-2	102,387	77,284	15.21	14.42	0.01099	0.308

*Specimen was pre-stressed beyond yield point.

Post-test photographs of the specimens are shown in Fig. 9-17. Specimen FEB13-1 was completely crushed, because of an improper limit setting on the testing machine, which allowed the load to go well beyond the material's failure limit. Each of the other three specimens acquired a bulge. Specimen OCT12-1 was bulged at the interface with the steel collar, which is the site of greatest stress due to a stress concentration from the confining effect of the collar. Specimen OCT12-2 had a bulge about a quarter of the gauge length away from the steel collar. Specimen FEB13-2 had a bulge near the midpoint of its gauge length.

OCT12-1 OCT12-2

FEB13-1 FEB13-2

Fig. 9-17. Post-test photographs of 2.0-inch-diameter compression specimens.

The 2.0-inch-diameter specimens were sectioned to examine their interiors. Specimen OCT12-1 (Fig. 9-18) showed no additional damage inside it. However, specimens OCT12-2 and FEB13-2 (Figs. 9-19 and 9-20) showed significant buckling and delamination along their insides. A major difference among the specimens is the wire diameter in the unidirectional layers, 0.010" for specimen OCT12-1, and 0.015" for specimens OCT12-2 and FEB13-2. On weaving, heavier wires undergo more crimping, yielding an undulating layer (Figs. 9-19 and 9-20), which makes the unidirectional layer more prone to buckling and delamination.
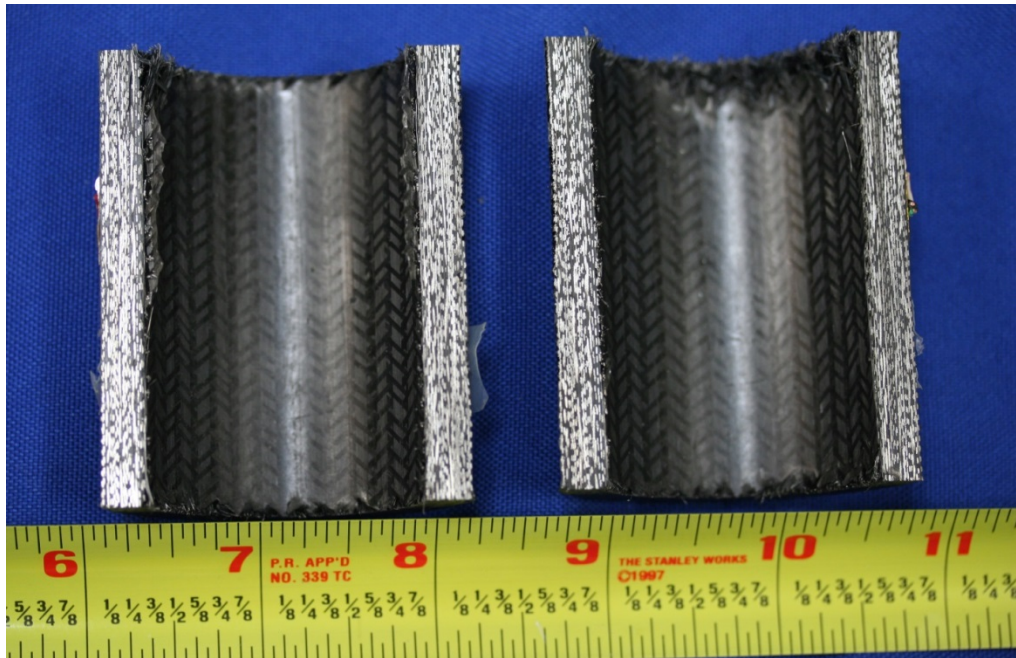
Fig. 9-18. Photograph of sectioned 2.0-inch-diameter specimen OCT12-1.

Undulating unidirectional layer
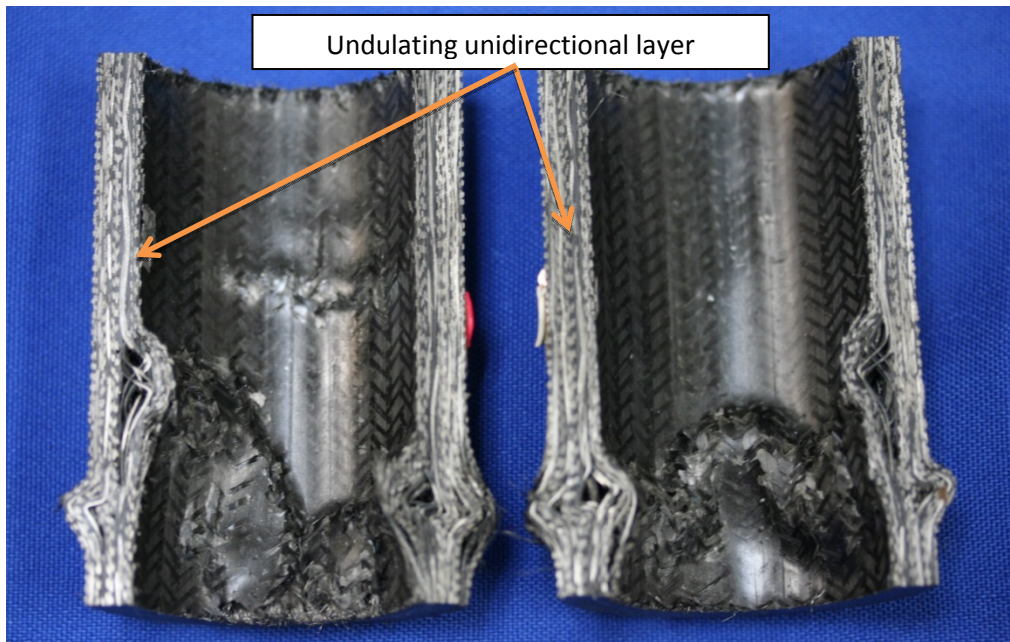
Fig. 9-19. Photograph of sectioned 2.0-inch-diameter specimen OCT12-2.

Fig. 9-20. Photograph of sectioned 2.0-inch-diameter specimen FEB13-2.

Figure 9-21, a photograph of a woven unidirectional layer, shows how the unidirectional warp wires, on being woven between the transverse weft wires, undergo some degree of undulation.

Warp Wire Diameters 0.010" or 0.015"

Weft Wire Spacing ~ 1"
Wire Diameter = 0.004"
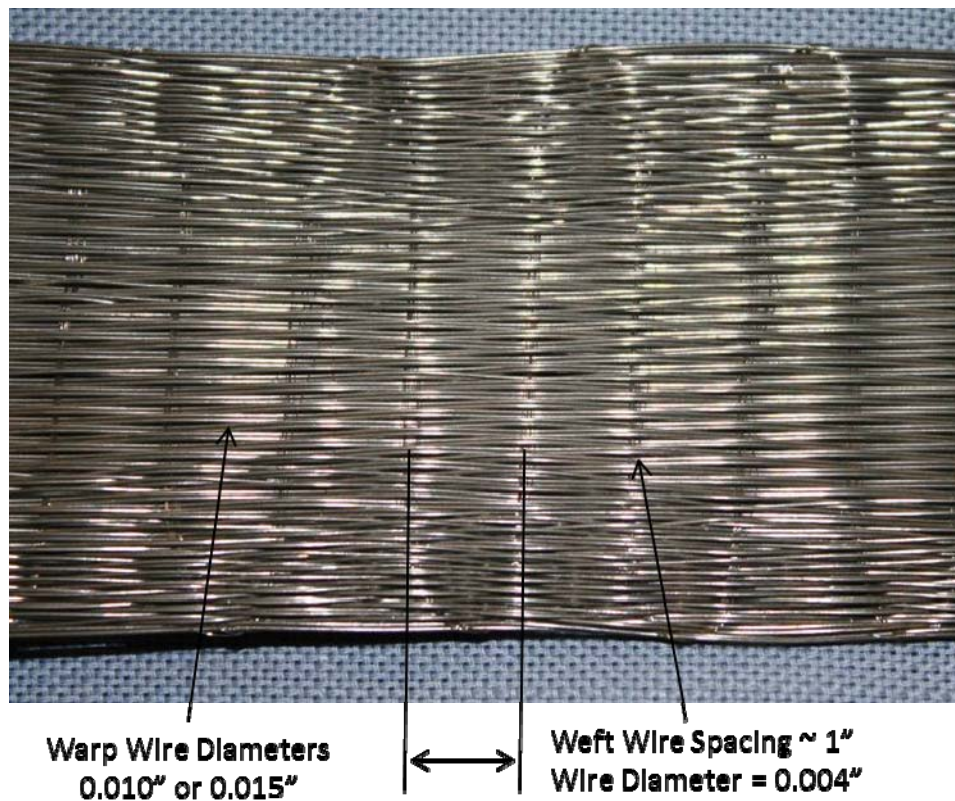
Fig. 9-21. Photograph of unidirectional layer of woven tungsten wire.

Materials Research & Design, Inc. (MR&D), who have been working with DET on the design and analysis of the RMS, analyzed the effect of this undulation on material strength. They applied beam theory to estimate the pre-stress imparted to the wires by weaving. Figure 9-22 is a diagram of a longitudinal warp wire represented as a simply supported beam undergoing a finite displacement between weft wires. The degree of displacement equals half the sum of the diameters of the warp and weft wires. The displacement generates a bending moment that results in a stress within the warp wire, which reduces the stress the braid can bear. The model predicts an 8% decrease in strength for the 0.010" warp wire and a 16% decrease for the 0.015" wire.

$$y(x) = \delta \sin\left(\frac{\pi x}{l}\right)$$

$$\frac{d^2 y}{dx^2} = -\frac{\delta \pi^2}{l^2} \sin\left(\frac{\pi x}{l}\right)$$

$$\frac{d^2 y}{dx^2} = -\frac{M}{E\,I}$$

$$\sigma = \frac{M\,c}{I}$$
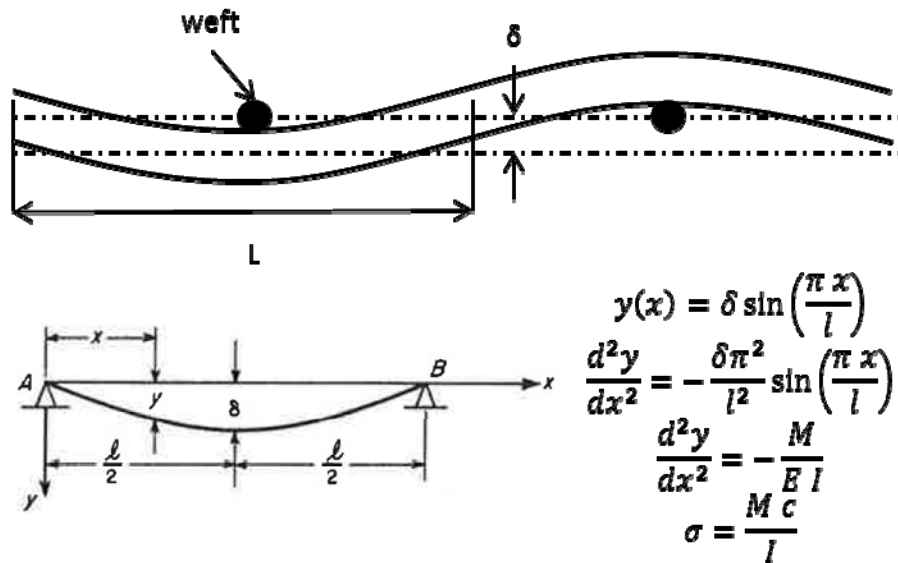
Fig. 9-22. Diagram of woven unidirectional layer where warp wire is represented as a simply supported beam undergoing a displacement equal to half the sum of the wire diameters.

Based on the test results and associated analysis, the first layup (specimens OCT12-1 and FEB13-1) was chosen as the baseline for scaling to 2.5-inch diameter. This layup uses 0.010-inch-diameter warp wires in the unidirectional layers. The finer wires experience less undulation, resulting in flatter unidirectional layers that appeared to buckle less under compression than in the specimens with the thicker warp wire (OCT12-2 and FEB13-2).

9.6.2 2.5-inch-Diameter Specimen Tests

Figure 9-23, a drawing of the 2.5-inch-diameter compression specimen, shows its inside diameter of 1.375 inches and thickness of 0.5565 inch, which correspond to $M/C = 9.0$. Again, steel caps were affixed to the ends of each specimen for testing. Each specimen had a gauge length of 5.25 inches. Figure 9-24 shows the specimens before testing.
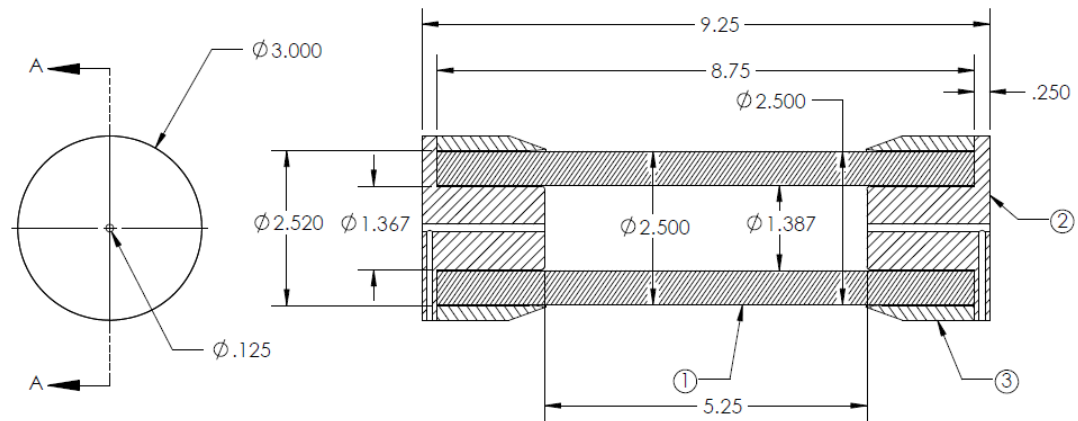
Fig. 9-23. Drawing of the 2.5-inch-diameter compression specimen.

Fig. 9-24. Photograph of 2.5-inch-diameter compression specimens.

Two layups of the tungsten reinforcement were evaluated in the 2.5-inch-diameter size, summarized in Tables 9-5 and 9-6. The layups differed in the total number of layers and the distribution of layers between triaxially braided and unidirectional layers.

Table 9-5. Braid layup for 2.5-inch-diameter specimen #3.

Layer #	Layer type	Wire diam. (in)	Wire orientation	Number of wires per layer		
				Bias	Longitudinal	Unidirectional
1	Triaxial braid	0.004	0° ± 45°	504	1080	0
2	Triaxial braid	0.004	0° ± 45°	504	1080	0
3	Triaxial braid	0.004	0° ± 46°	504	1080	0
4	Unidirectional	0.010	0°	0	0	720
5	Triaxial braid	0.004	0° ± 50°	504	1080	0
6	Triaxial braid	0.004	0° ± 54°	504	1080	0
7	Triaxial braid	0.004	0° ± 57°	504	1080	0
8	Unidirectional	0.010	0°	0	0	880
9	Triaxial braid	0.004	0° ± 58°	504	1080	0
10	Triaxial braid	0.004	0° ± 60°	504	1080	0
11	Triaxial braid	0.004	0° ± 61°	504	1080	0
12	Unidirectional	0.010	0°	0	0	960
13	Triaxial braid	0.004	0° ± 63°	504	1080	0
14	Triaxial braid	0.004	0° ± 65°	504	1080	0
15	Triaxial braid	0.004	0° ± 65°	504	1080	0
16	Unidirectional	0.010	0°	0	0	1060
17	Triaxial braid	0.004	0° ± 67°	504	1080	0
18	Triaxial braid	0.004	0° ± 68°	504	1080	0
19	Triaxial braid	0.004	0° ± 68°	504	1080	0
20	Unidirectional	0.010	0°	0	0	1200
21	Triaxial braid	0.004	0° ± 70°	504	1080	0
22	Triaxial braid	0.004	0° ± 70°	504	1080	0
23	Triaxial braid	0.004	0° ± 70°	504	1080	0
24	Unidirectional	0.010	0°	0	0	1300
25	Triaxial braid	0.004	0° ± 72°	504	1080	0
26	Triaxial braid	0.004	0° ± 72°	504	1080	0

Table 9-6. Braid layup for 2.5-inch-diameter specimen #4.

Layer #	Layer type	Wire diam. (in.)	Wire orientation	Number of wires per layer		
				Bias	Longitudinal	Unidirectional
1	Triaxial braid	0.004	0° ± 45°	504	1080	0
2	Triaxial braid	0.004	0° ± 48°	504	1080	0
3	Unidirectional	0.010	0°	0	0	864
4	Triaxial braid	0.004	0° ± 50°	504	1080	0
5	Triaxial braid	0.004	0° ± 53°	504	1080	0
6	Unidirectional	0.010	0°	0	0	960
7	Triaxial braid	0.004	0° ± 56°	504	1080	0
8	Triaxial braid	0.004	0° ± 58°	504	1080	0
9	Unidirectional	0.010	0°	0	0	1026
10	Triaxial braid	0.004	0° ± 60°	504	1080	0
11	Triaxial braid	0.004	0° ± 62°	504	1080	0
12	Unidirectional	0.010	0°	0	0	1135
13	Triaxial braid	0.004	0° ± 65°	504	1080	0
14	Triaxial braid	0.004	0° ± 67°	504	1080	0
15	Unidirectional	0.010	0°	0	0	1200
16	Triaxial braid	0.004	0° ± 68°	504	0	0
17	Triaxial braid	0.004	0° ± 68°	504	1080	0
18	Unidirectional	0.010	0°	0	0	1245
19	Triaxial braid	0.004	0° ± 69°	504	1080	0
20	Triaxial braid	0.004	0° ± 71°	504	1080	0
21	Unidirectional	0.010	0°	0	0	1368
22	Triaxial braid	0.004	0° ± 74°	504	1080	0
23	Triaxial braid	0.004	0° ± 73°	504	1080	0

WMTR performed the compression tests on these specimens. These tests again used three biaxial strain gauges affixed 120° apart around the specimen's circumference at the mid-plane of its gauge length. The load was applied at a rate of 30,000 lbf/minute. Specimens 3A and 3B had the same layup whereas Specimens 4A and 4B had a second layup. Figure 9-25 presents post-test photographs of specimens 3A and 3B. Specimen 3A failed about a third of the way into the gauge length. Specimen 3B failed along the interface with the steel support collar, the region of highest stress. Figure 9-26 presents post-test photographs of specimens 4A and 4B. Both of these failed along the interface of the steel support collar.

(a) Specimen 3A (b) Specimen 3B

Fig. 9-25. Post-test photographs of 2.5-inch-diameter compression specimens 3a and 3b.
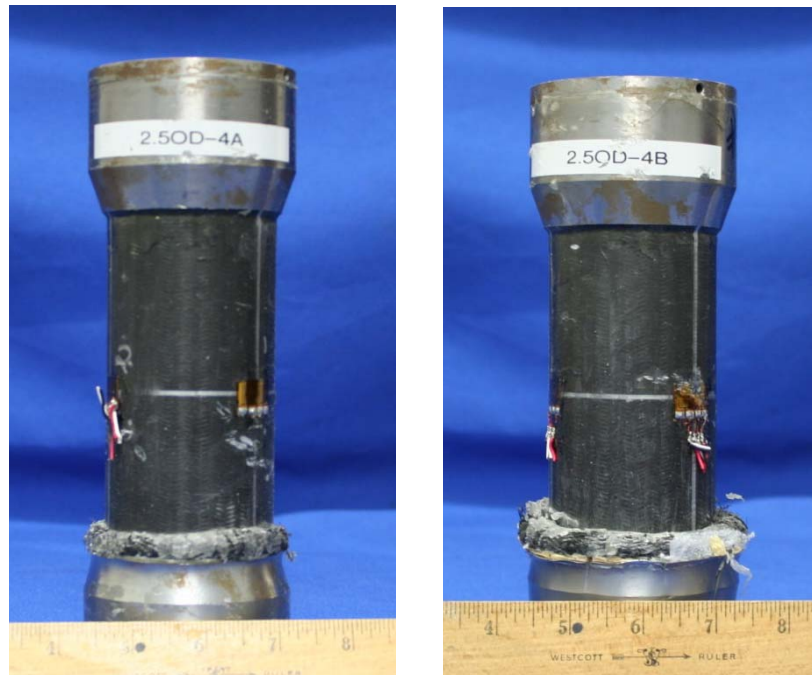
(a) Specimen 4A   (b) Specimen 4B

Fig. 9-26. Post-test photographs of 2.5-inch-diameter compression specimens 4A and 4B.

Figure 9-27 is a plot of the compression stress versus strain data for these specimens. Measured mechanical properties are summarized in Table 9-7. The data shows the specimens have nearly identical response up to a compressive stress of about 85 ksi. Specimen 3A fails at 89 ksi, while Specimen 3B fails

at just under 87 ksi. Specimens 4A and 4B both failed at 91 ksi. Specimens 4A and 4B exhibited larger failure strains of 2.42% and 2.31% than specimens 3A and 3B with 1.93% and 1.80%. The elastic moduli of 4A and 4B (14.27 and 15.07 Msi) were also greater than 3A and 3B (13.81 and 12.60 Msi). Yield stresses ranged from 18.45 to over 23.70 ksi for all specimens.
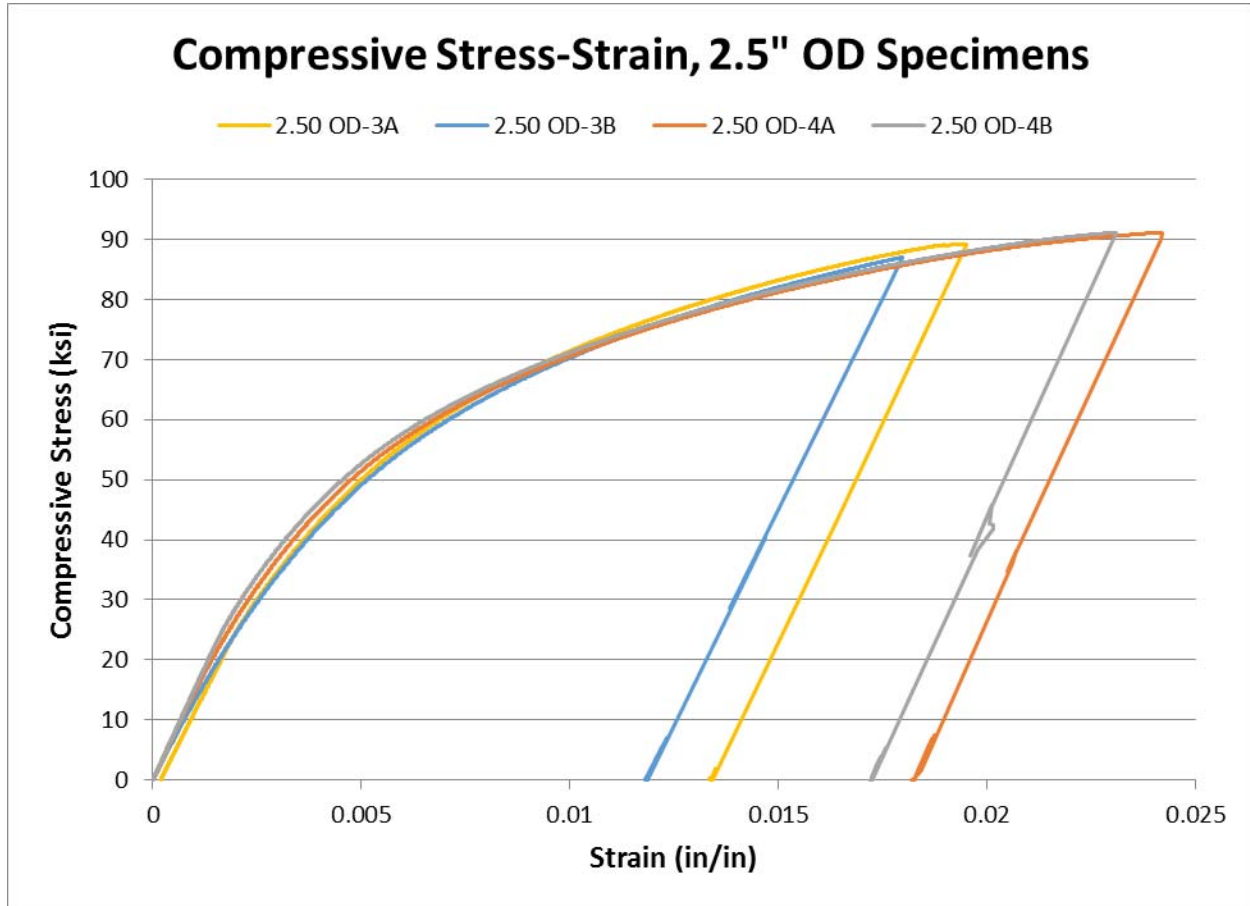
Fig. 9-27. Compressive stress versus strain for 2.5-inch-diameter specimens 3 and 4.

Table 9-7. Summary of measured mechanical properties of the 2.5-inch-diameter specimens.

Specimen	Elastic modulus (0 to 20 ksi) (Msi)	Yield stress* (ksi)	Ultimate stress (ksi)	Ultimate strain (%)
3A	13.81	23.7	89.21	1.93
3B	12.60	20.7	87.03	1.80
4A	14.27	18.45	91.17	2.42
4B	15.07	22.06	91.17	2.31

*An offset in strain of 0.0002 was used.

The specimens were sectioned to examine their interiors, shown in Fig. 9-28. No hidden damage or failure mode is evident along the interiors of the specimens.

The compression test data confirm the successful scale-up of the material from a 1.0-inch size to a 2.5-inch-diameter size. The baseline material for the penetrator design is lay-up number 4.

Fig. 9-28. Post-test photograph of sectioned 2.5-inch-diameter compression specimens.

9.7 Flexural Bending Testing

Flexural bending ("flex-bend") tests were performed on the surrogate material. Test specimens were 2.5 inches in outside diameter by 26 inches long. The test configuration was designed by MR&D, and the tests were performed by SoRI.

The purpose of these tests was to measure tensile properties, specifically elastic modulus and yield strength. Tensile testing of this material poses numerous difficulties, so most of the mechanical testing to date has been compression testing. Since the material is braided, cutting a dog-bone test coupon from it would destroy its integrity and therefore not yield representative results. Tensile testing of the 2.5-inch-diameter specimens is not practical, since loading a specimen to failure would require a force of 310,000 lb. Metal fixtures must be attached to the ends of the specimen in order to mount it in a testing machine, and the joint would have to withstand the large load. In previous tensile tests attempted on 1.0-inch-diameter specimens, to which the end fixtures were glued and pinned, failure occurred at the pinned joint in all tests.

9.7.1 Flexural Bending Test Setup

The flexural bending test setup was designed according to ASTM Standard *ASTM-C-1341-06*, "Standard Test Method for Flexural Properties of Continuous Fiber-Reinforced Advanced Ceramic Composites." Four-point loading with one-third load spacing was chosen, which corresponds to Geometry IIB de-scribed in the standard. The setup is shown in Fig. 9-29, in which *P* is the total applied load and *L* is the distance between supports, and the spacing between load points is *L*/3.
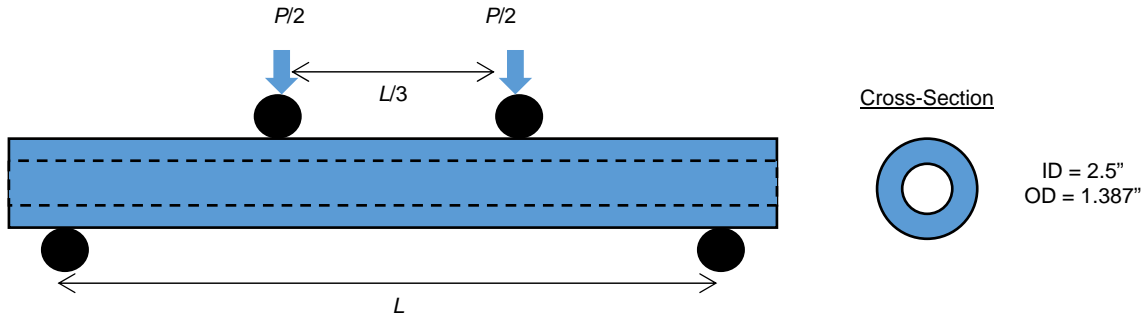
Fig. 9-29. Four-point bend test using the IIB geometry defined in ASTM-C-1431-06.

An advantage of the four-point loading is that the specimen is subjected to pure bending between the load points. For a linearly elastic material in pure bending a normal stress is produced within the beam's cross-section that varies linearly from a tensile maximum at the bottom to a compressive maximum at the top according to the equation

$$\sigma_x = \frac{My}{I}$$

where σ_x is the normal stress, M is the applied moment, y is the distance from the neutral axis (positive in the downward direction), and I is the cross-sectional moment of inertia. For materials having equal compressive and tensile moduli, the neutral axis (the vertical location where the normal stress is zero) passes through the centroid of the cross-section. Beam cross-sections that are symmetric about the neutral axis will have equal magnitudes of strains at the top and bottom of the beam (albeit positive tensile strain at the bottom and negative compressive strain at the top), provided the material has equal compressive and tensile moduli.

The flex-bend test can be used to compare the tensile and compressive moduli of the material by re-cording strain on the top and bottom of the beam with strain gauges. The strain versus load plot for the top and bottom of a neutral-axis-symmetric beam should be identical for a material that has equal com-pressive and tensile moduli. Deviations in the strain values indicate unequal moduli. Hooke's law can be applied to calculate the modulus as

$$E = \frac{Mh}{2I\varepsilon}$$

where E is the modulus (compressive for the top and tensile for the bottom), M is the applied moment, h is the total height of the beam, I is the moment of inertia, and ε is the strain.

If the strains at the top and bottom of the beam are not equal, then the material may have different compressive and tensile moduli. The normal stresses and strains still vary linearly from top to bottom, but the location of the neutral axis changes. The following equation can be used to find the location of the neutral axis in the case the strains are not equal[2]:

$$\frac{h_1}{h_2} = \left| \frac{\varepsilon_1}{\varepsilon_2} \right|$$

where h_1 and h_2 are the distances from the neutral axis to the bottom and top of the beam, respectively, and ε_1 and ε_2 are the strains at the bottom and top of the beam, respectively. The above equation for determining the modulus can then be used with the $h/2$ term replaced by h_1 for the tensile modulus and h_2 for the compressive modulus.

---

[2] S. P. Timoshenko and J. M. Gere, *Mechanics of Materials,* Brooks/Cole, 1972, p. 310.

The flex-bend test can also be used to measure yield strength. Ideally the material should reach the yield stress within the middle section of the beam. While the portion of the beam between the load points is in pure bending, the outer sections experience both bending and shear. Increasing the applied load increases the resulting moment and the corresponding normal stress within the middle section, but also increases the shear load in the outer sections. For too short a specimen, the material could fail in shear in the outer sections before the middle section reaches yield. The moment can be increased by increasing the specimen length L, which does not increase the shear stress.

Figure 9-30 is a drawing of the test specimen. Its flared ends are an artifact of the fabrication process. The wires are braided in layers, and the wires are cut from one layer to the next. Cutting the wires releases the circumferential tension in the braid, allowing the wires to expand, resulting in the flared ends. The flared ends are normally cut off but in these tests they were left on, as they do not affect the test results, and they help keep the specimen from rolling off the supports in testing.

Notes:
1. Material is a Tungsten-Wire Epoxy Composite.
2. Mass is 9682 grams (21.3 lbs).
3. Actual Outer Diameter may be from 2.42 to 2.50 inches.
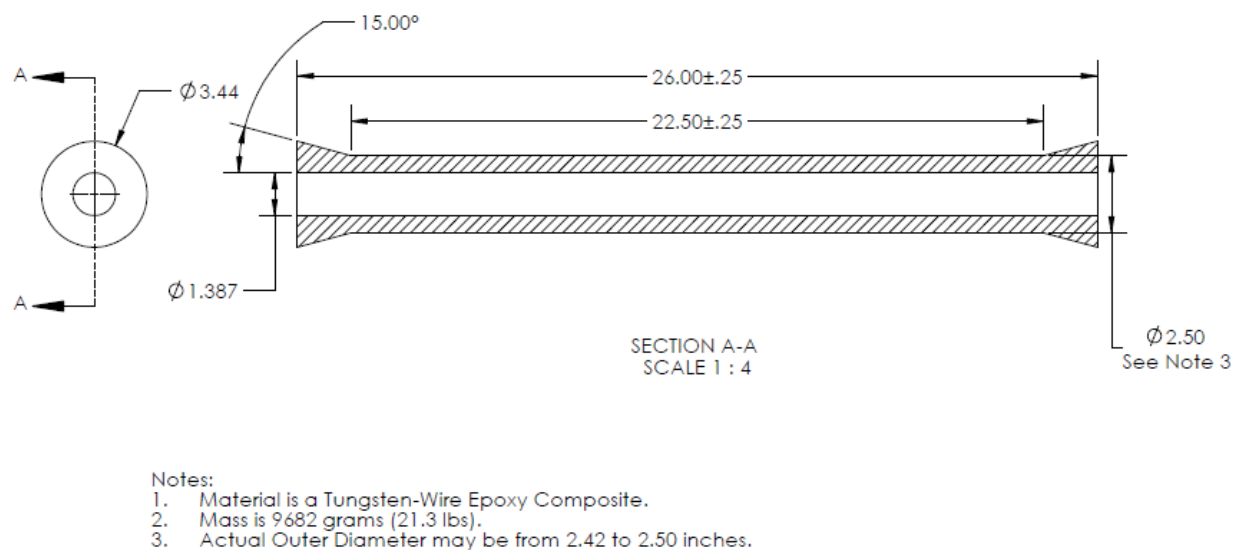
Fig. 9-30. Drawing of the tungsten-wire/epoxy flex-bend test specimen.

The span between supports was chosen as 18 inches, and the spacing between load points as 6 inches. While the shear strength of the material is unknown, MR&D estimated it to be 17 ksi, based on known values for carbon-fiber-based composites. To avoid shear failure, the load was limited to 40,000 lb, which would produce a maximum shear stress of 6.6 ksi, assuming no stress concentrations at the supports or load points. A 40,000-lb load produces a 120,000 in-lb moment along the middle section of the specimen. Assuming equal tensile and compressive moduli, the resulting normal stress is 96.6 ksi, slightly greater than the measured compressive strength of 91 ksi.

9.7.2 Flexural Bending Test Performance

Southern Research Institute (SoRI) performed three flexural bending tests. Figure 9-31 shows the specimens before testing, and Fig. 9-32 shows the test set-up. As described above, the supports were 18 inches apart, and the load points 6 inches apart. The supports and load applicators were 2.5-inch-diameter steel cylinders with saddles cut in the sides to accommodate the cylindrical specimens. The contact area of each load pin was 3.72 in². Biaxial strain gauges were affixed to the top and bottom of the specimen within the middle section. In addition a displacement transducer was placed under the specimen at its midpoint.

- 173 -
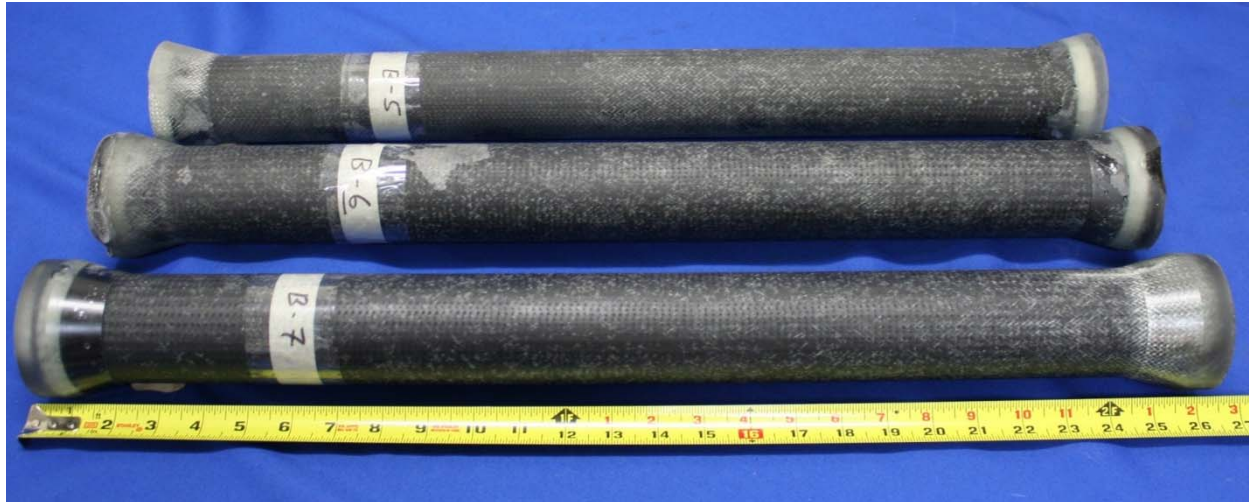
Fig. 9-31. Specimens for the flex-bend tests.
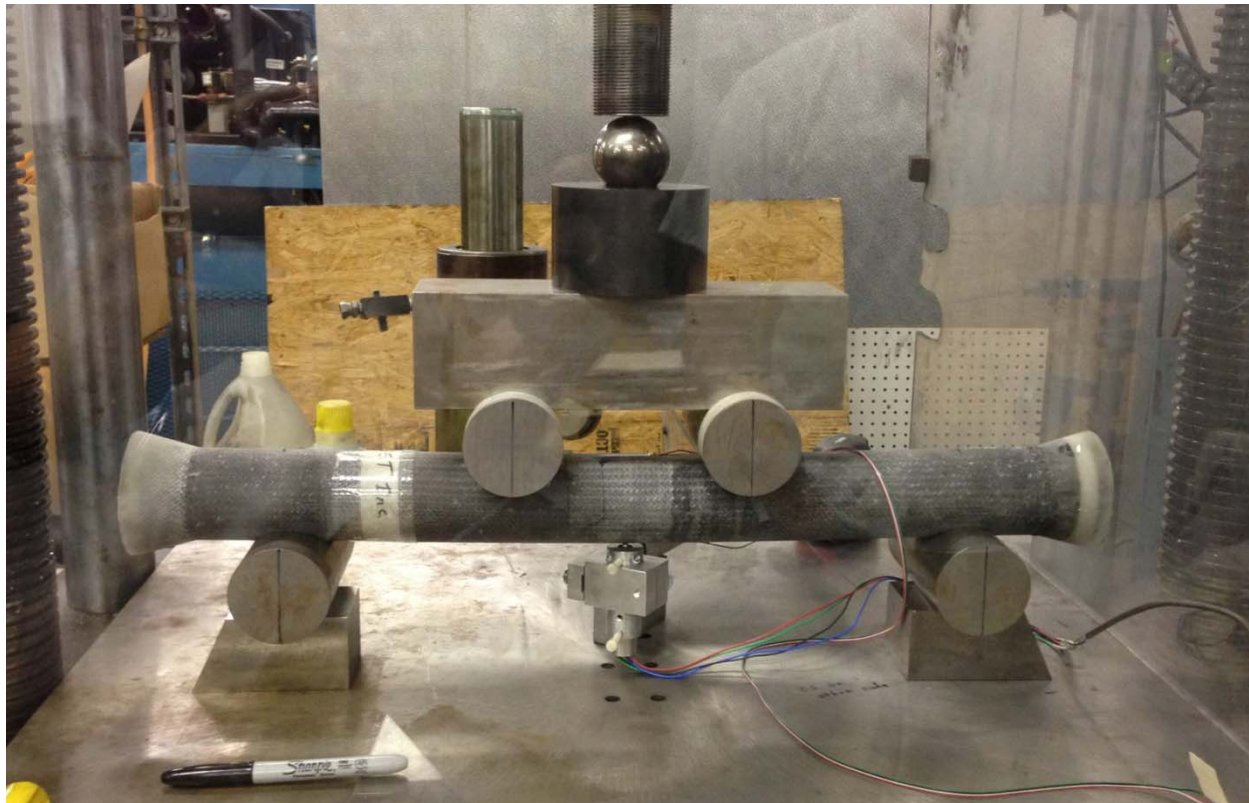
Fig. 9-32. Flex-bend test arrangement.

Flex-Bend Test Number 1

The first test was run to a load of 42,000 lb, at which point a shear band or crack appeared beneath one of the load applicator pins and the test was terminated. Figure 9-33 shows the test during loading. Observations indicated the pin under which the shear band formed was not rotating as the specimen bent under the applied load. Figure 9-34 shows the specimen after the test.

Fig. 9-33. Flex test during loading.
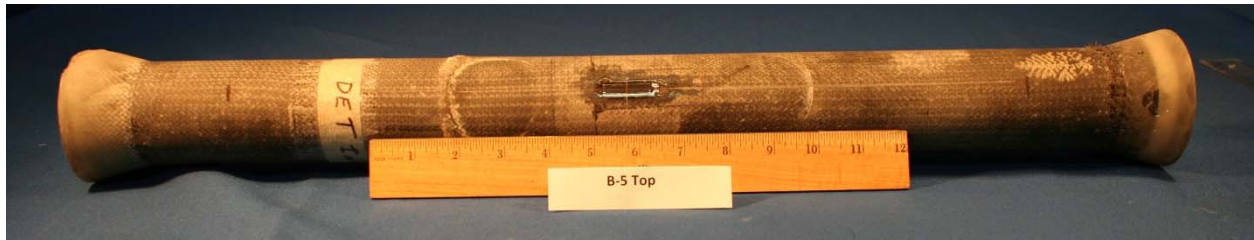
Post flex test number 1, specimen B-5, top (load) view
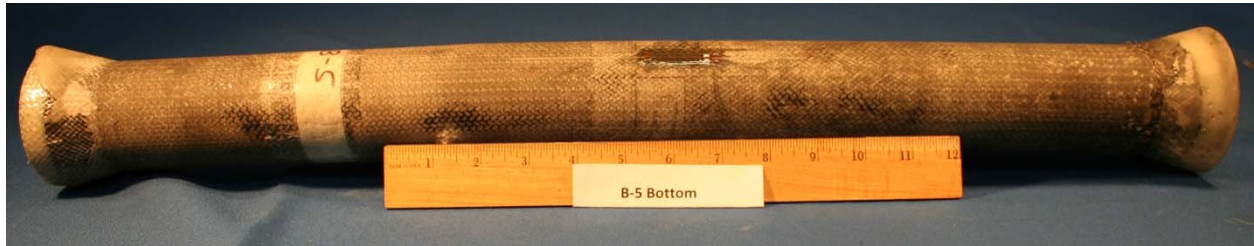
Post flex test number 1, specimen B-5, bottom (support) view

Post flex test number 1, specimen B-5, shear band from load applicator

Fig. 9-34. Post-test photographs of flex test number 1, specimen B-5.

Figure 9-35 is a plot of the measured strain versus load, which shows that the strain in the bottom gauge increases significantly more with load than in the top gauge. As discussed above, the strains should be equal in a symmetric beam of material with equal tensile and compressive moduli. The differences seen in this plot are either a consequence of material asymmetry or an aspect of the test that caused the actual loads to deviate from the assumed values. As mentioned above, during this test it was noticed that one of the load pins was not rotating as the beam bent under load, as evidenced by the shear band or crack shown in Fig. 9-34. The lack of rotation may have resulted in a load distribution that resulted in the deviations in the strain plot of Fig. 9-35. In later tests, measures were taken to facilitate the pin rotation.
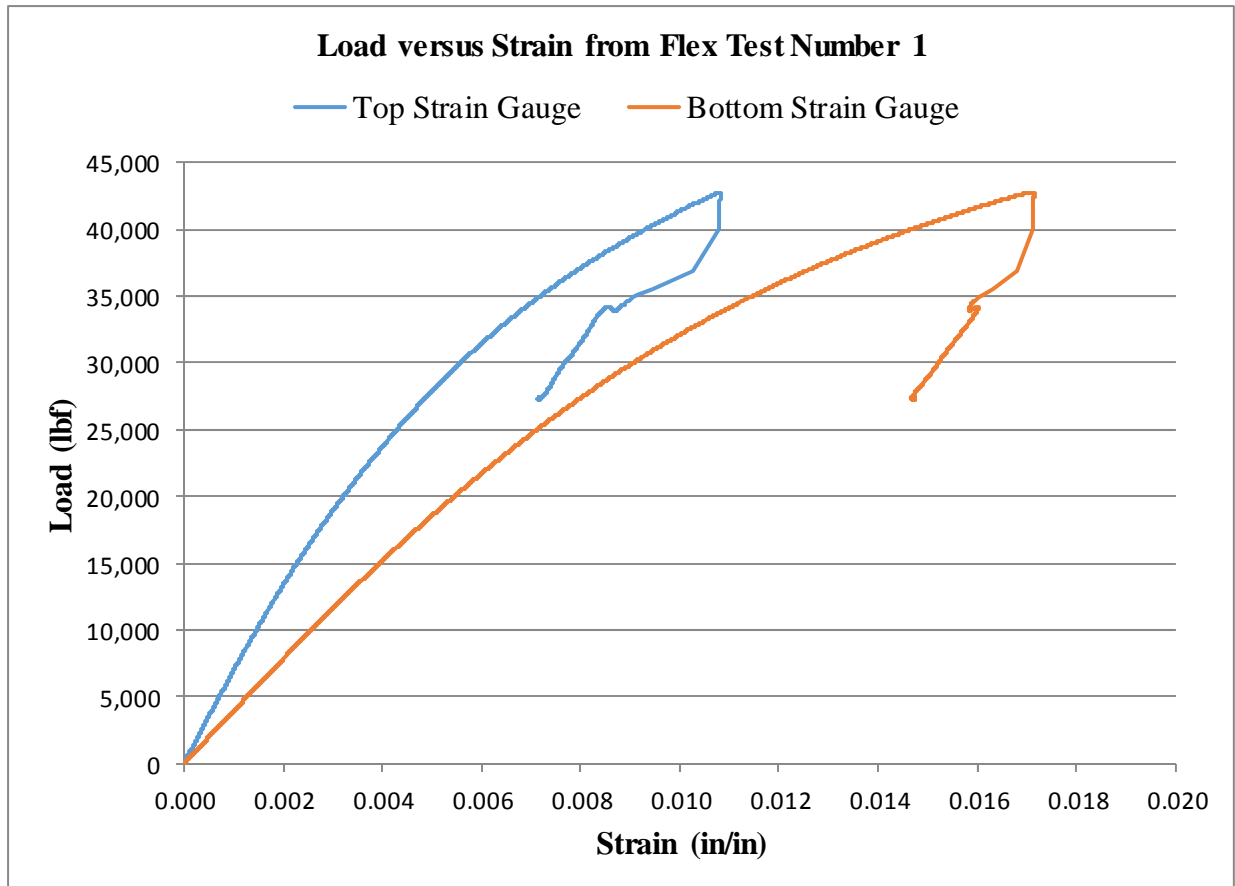
Fig. 9-35. Measured load versus top and bottom strain from flex test number 1.

Flex Test Number 2

For the second flex test, the setup was modified to improve the rotation of the pins. The changes included changing the bearing surfaces and applying grease. The test was run up to a load of about 30,000 lb, at which time the setup became unstable, resulting in the specimen being projected from the testing table. No damage was observed, and after changes were made to secure the setup the test was re-run. Figure 9-36 shows photographs of the specimen after the test. Note that a shear band or crack formed under one of the load pins in the same manner as the previous test. However, the length of the shear band was shorter in this test.

Post flex test number 2, specimen B-6, top (load) view

Post flex test number 2, specimen B-6, bottom (support) view
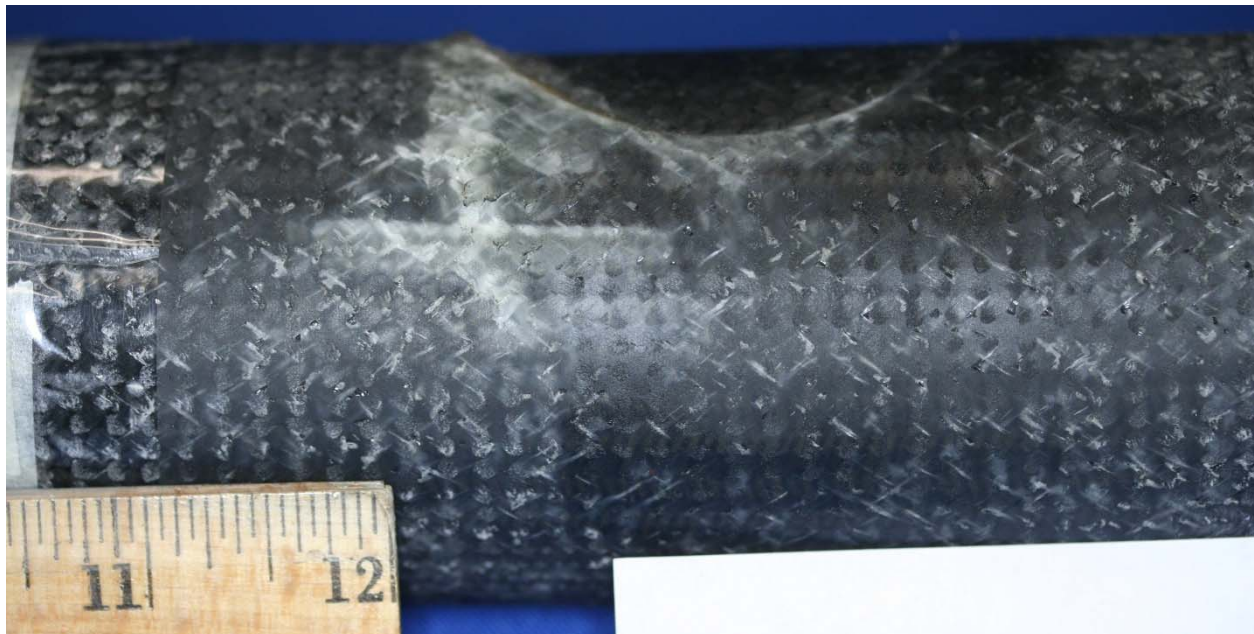
Post flex test number 2, specimen B-6, shear band from load applicator

Fig. 9-36. Post-test photographs of flex test number 2, specimen B-6.

Figure 9-37 is a plot of the measured strain versus load, which shows the strain from the top and bottom gauges are in close agreement. This indicates the material has similar tensile and compressive moduli.
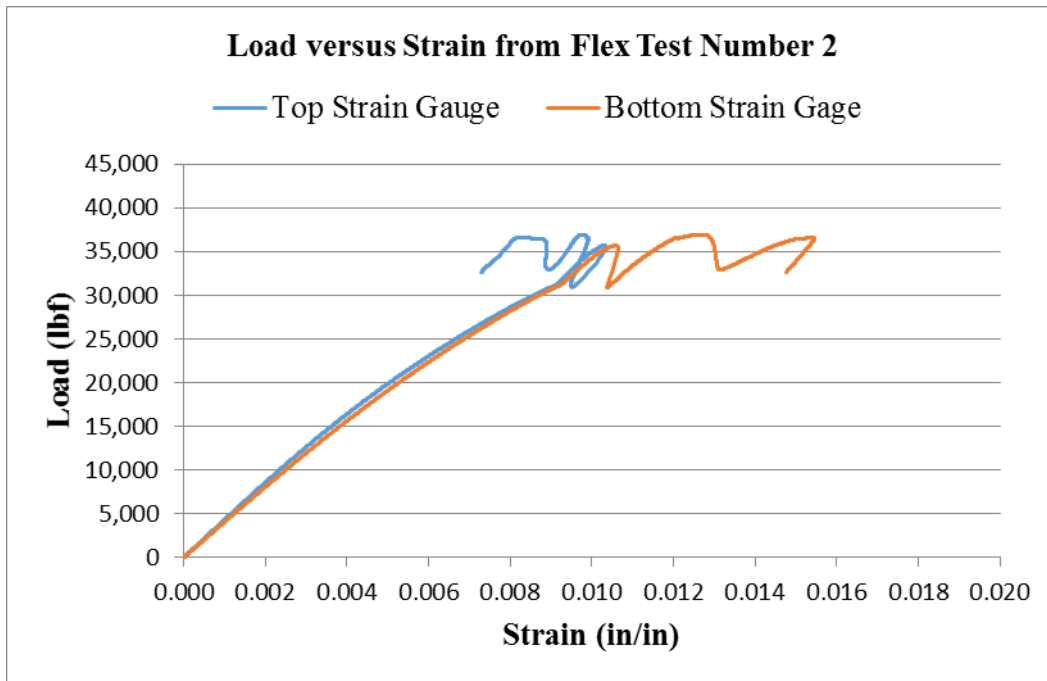
Fig. 9-37. Measured load versus top and bottom strain from flex test number 2.

Flex Test Number 3

The third test proceeded without incident. Figure 9-38 shows the specimen after the test. As in the previous test, a shear band appeared under one of the load application pins, but it was not as long as in the first test. Figure 9-39 is a plot of the load versus the top and bottom strains from the test. The top and bottom strains show a slight offset of about 0.0005 in/in as the load nears the peak. This offset is larger than that observed in test 2, but significantly smaller than observed in test 1.

Post flex test number 3, specimen B-7, top (load) view

Post flex test number 3, specimen B-7, bottom (support) view

Post flex test number 3, specimen B-7, shear band from load applicator

Fig. 9-38. Post-test photographs of flex test number 3, specimen B-7.
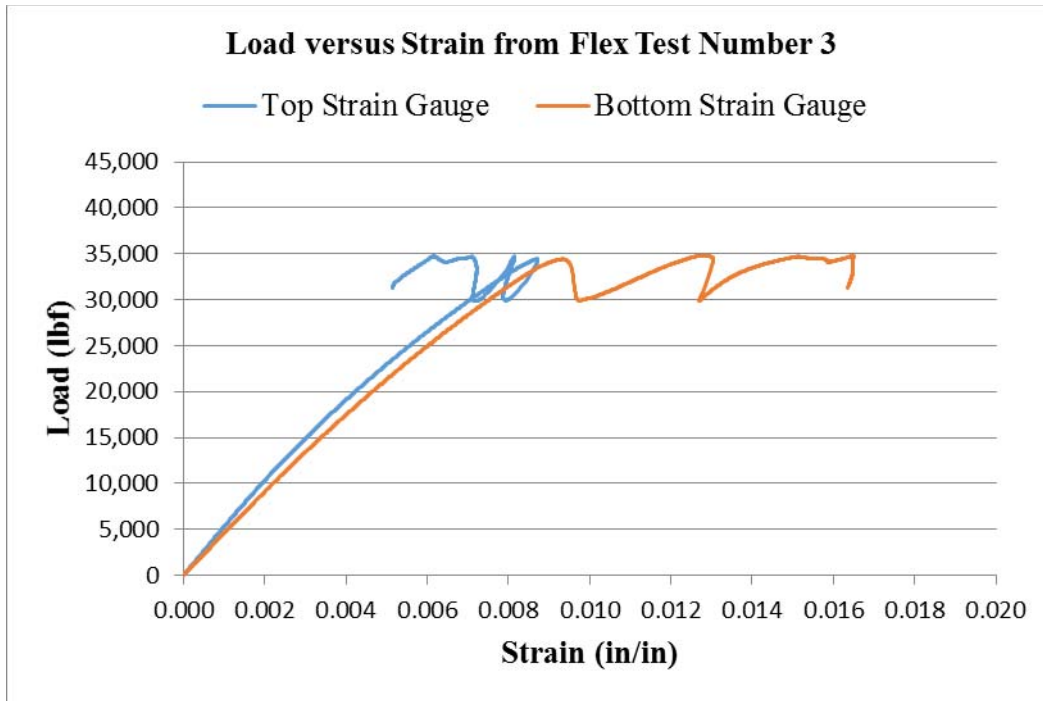
Fig. 9-39. Measured load versus top and bottom strain from flex test number 3.

9.7.3 Data Analysis

From beam bending theory, the maximum stress within the specimens can be calculated from the applied loads. Thus, stress-versus-strain curves can be developed; these are plotted in Figs. 9-40, 9-41, and 9-42. These plots show the curves for the top and bottom strain gauges as well as the average of the top and bottom. From the stress-strain data, the flexural modulus and strength can be determined, as summarized in Table 9-8. Included in the table are the estimated shear strengths from the bend tests. The shear strengths were calculated based on the maximum applied load using the thin circular tube assumption where the maximum shear stress is twice the average shear stress.
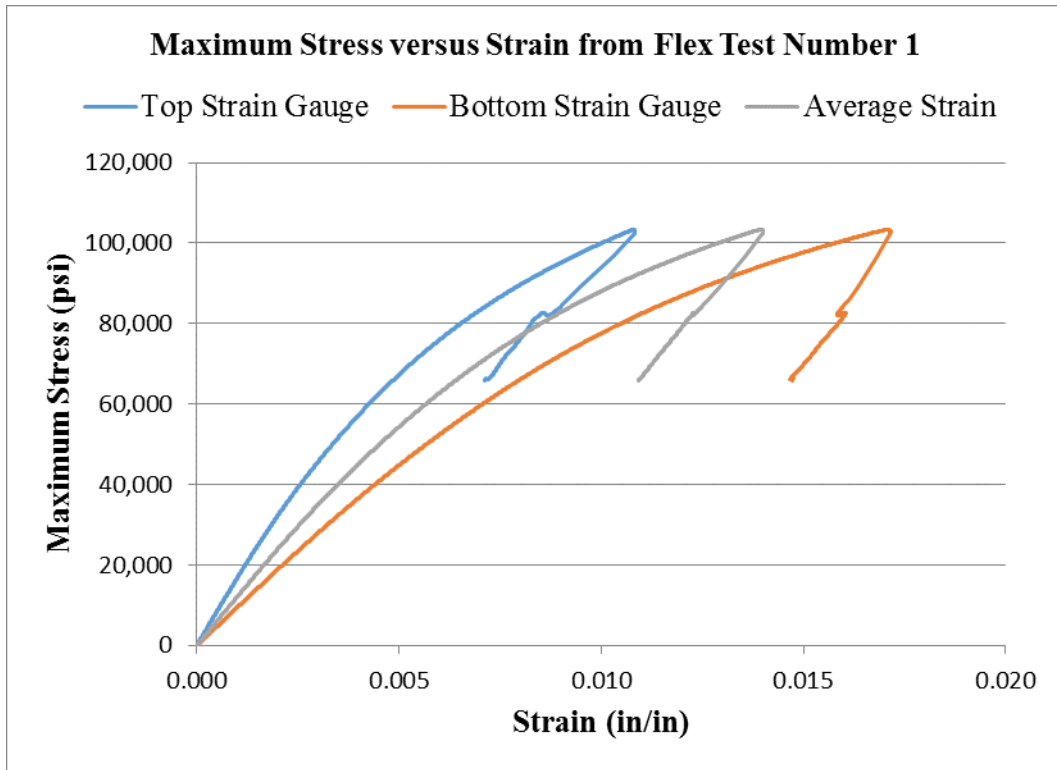
Fig. 9-40. Calculated maximum stress versus top, bottom, and average measured strain from flex test number 1.
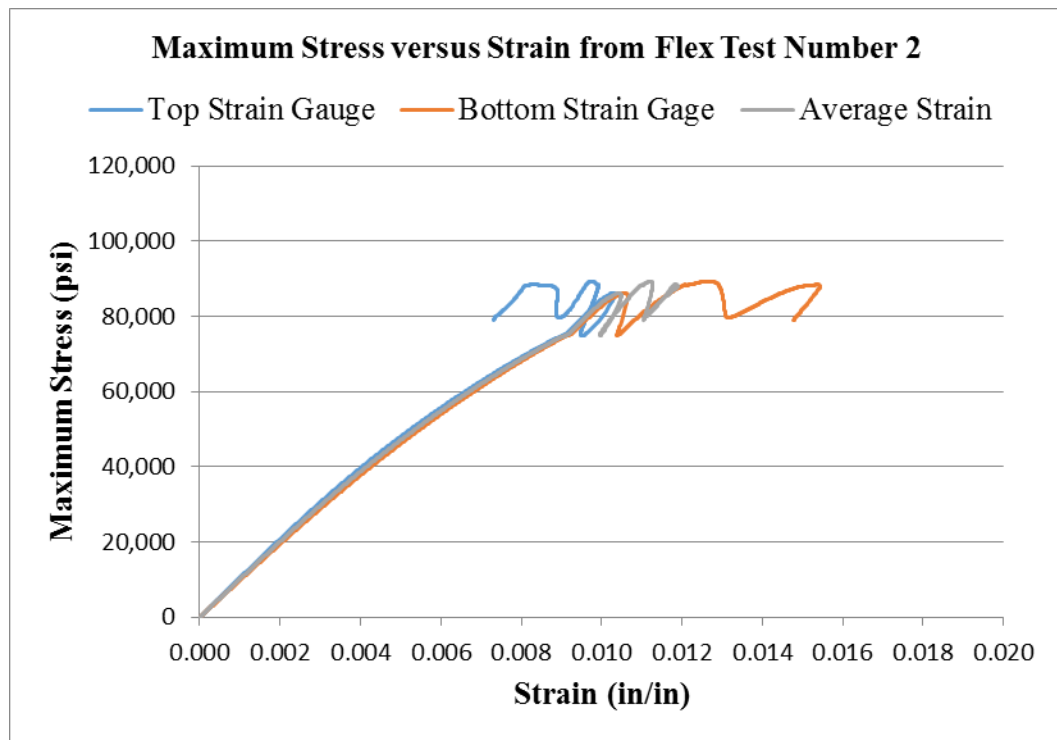
Fig. 9-41. Calculated maximum stress versus top, bottom, and average measured strain from flex test number 2.
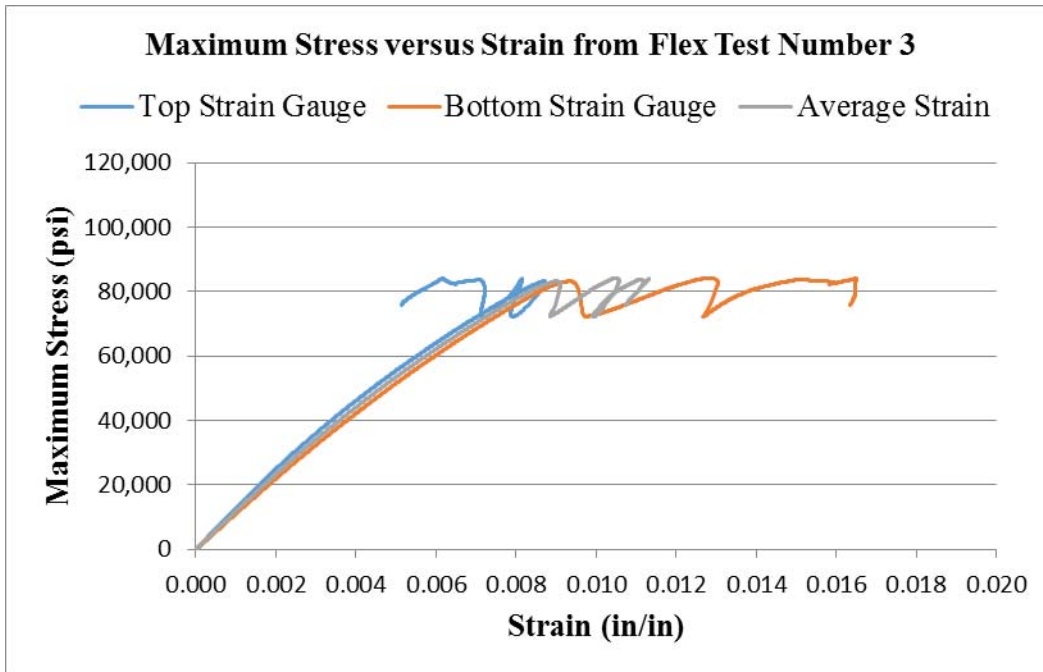
Fig. 9-42. Calculated maximum stress versus top, bottom, and average measured strain from flex test number 3.

Table 9-8. Summary of flexural properties of RMS surrogate material.

Test/Specimen	Flexural modulus (Msi)	Flexural strength (ksi)	Shear strength* (ksi)
1, B-5	12.2	103.0	13.8
2, B-6	10.2	89.3	12.0
3, B-7	12.0	84.1	11.3
Average	11.5	92.2	12.4

*Calculated based on the ultimate load at failure using the thin circular tube assumption where the maximum shear stress is twice the average shear stress.

The average stress-strain plots from all three tests are presented in Fig. 9-43. The plot shows that test numbers 1 and 3 are in good agreement, whereas the curve from test number 2 falls underneath. In test number 2 the specimen was ejected from the test apparatus and the reported data is from the second test of that specimen. The deviation in Fig. 9-43 could indicate the specimen was strained beyond its yield in the first test attempt.
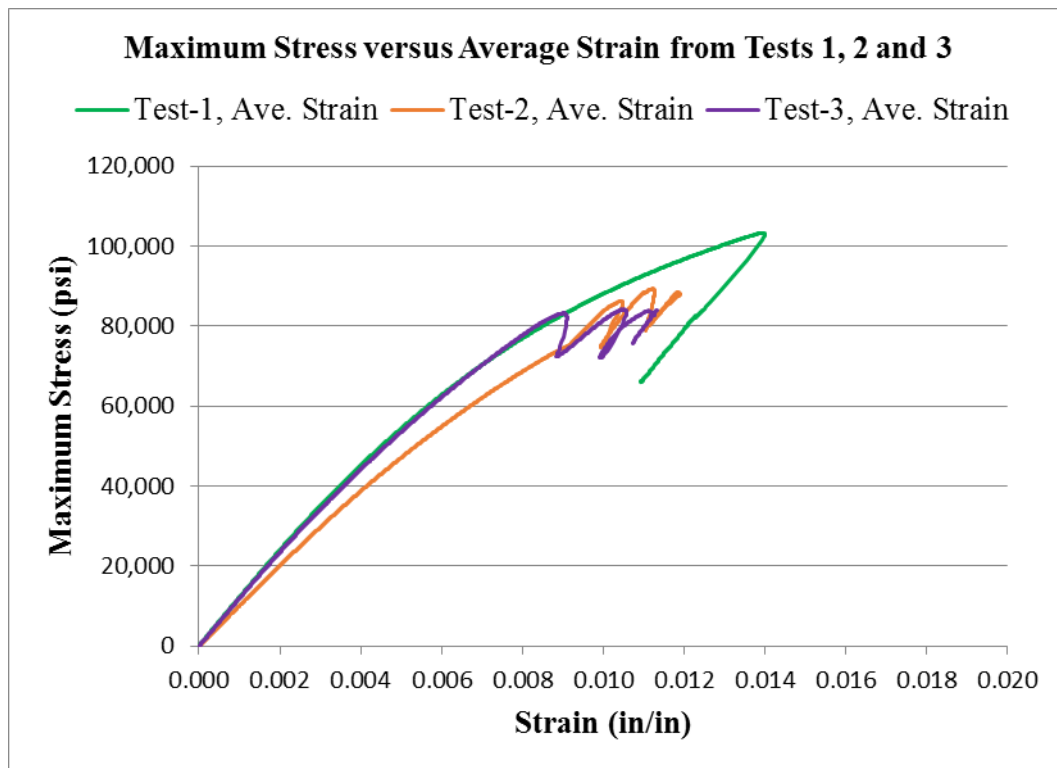
Fig. 9-43. Calculated maximum stress versus average measured strain in flex tests 1, 2, and 3.

Section X

Blast Testing

The section reports the results of Alliant Techsystems' (ATK) blast tests of the Reactive Material Structures within an enclosed chamber. These tests involved RMS-cased explosive charges configured to have various ratios of casing mass to explosive mass, *M/C*, as well as steel-encased and bare explosive charges for comparison. Recorded pressure histories were averaged over finite time periods to establish values of quasi-static pressure (QSP), which were used to evaluate the casing's effect on blast in each test.

10.1 Test Goals

The main goal of the test series was to determine the blast performance of RMS-cased charges over a wide range of *M/C* ratios. Following the notation of conventional metal-cased charges, the *M* stands for the mass of the case and *C* for the mass of the explosive charge. In the previous chamber tests, the *M/C* ratio was held constant at 3, with a variety of reactive materials and a steel case for a baseline. The *M/C* values used here are 1, 3, 6, 9, and 12. A secondary goal was to determine at what *M/C* level the blast performance starts to drop off. As in the previous tests, results will be compared to a steel-cased baseline with *M/C* = 3.

10.2 Specimen Fabrication

Various RMS specimens were fabricated for blast testing. These include the Metal-to-Charge Mass Ratio *M/C* = 3 specimens for ARA's fully enclosed and partially enclosed chamber tests, and specimens with various *M/C* ratios for blast tests at ATK. Conventionally, *M/C* refers to the mass ratio of a munition's metal casing (*M*) to its explosive charge (*C*); as used here, *M/C* refers to the mass ratio of the RMS casing to the explosive charge.

These RMS specimens were as large as 1.1 kg, compared to our previous specimens of up to 250 g. Based on this, it is projected that current equipment and techniques can produce specimens as large as about 10 kg. To produce specimens more massive than that or having outer diameter greater than about 3 inches, a larger braiding machine will be required.

10.2.1 First Group of Specimens

RMS cylinders with *M/C* = 3, shown in Fig. 10-1, were fabricated for blast tests at ARA. Each had a nominal mass of 1 kg and dimensions of 1.534" ID × 2" OD × 3.6" L. Four specimens were fabricated with average densities of 7.41 to 7.45 g/cc. Three were shipped to ARA in late March 2011 for blast testing. The fourth specimen was used for preliminary mechanical properties evaluation, as discussed above in Section IX.

Fig. 10-1. ARA blast test specimens (M/C = 3).

10.2.2 Second Group of Specimens

The second group of RMS specimens were fabricated for blast testing in the M/C study. In order that the blast delivered in each tests would be similar, the total mass of each set of charge and casing was held constant at 1200 g. In order to be able to fabricate all the specimens on the existing braiding machine and to use the same external mold, the casing's outside diameter was held constant at 2.0". Within these constraints, variations in M/C ratio were achieved by varying the specimen length and charge diameter (RMS casing inner diameter). Table 10-1 lists the planned dimensions and masses of the five different configurations that were fabricated.

Table 10-1. Planned dimensions of RMS Specimens used in the M/C Blast Tests.

M/C	ID (in)	OD (in)	L (in)	L/D	Mass (g)
1	1.792	2.00	7.996	4.00	600.0
3	1.518	2.00	5.573	2.79	900.0
6	1.272	2.00	4.535	2.27	1028.6
9	1.117	2.00	4.119	2.06	1080.0
12	1.007	2.00	3.896	1.95	1107.7

Three specimens of each configuration were fabricated, for a total of fifteen. Figure 10-2 shows one specimen of each configuration, before they were cut to their final lengths, and Table 10-2 lists the measured dimensions and densities of the M/C specimens. Densities range from 7.16 to 7.34 g/cc, with an average of 7.25 g/cc and a standard deviation of 0.7 g/cc.
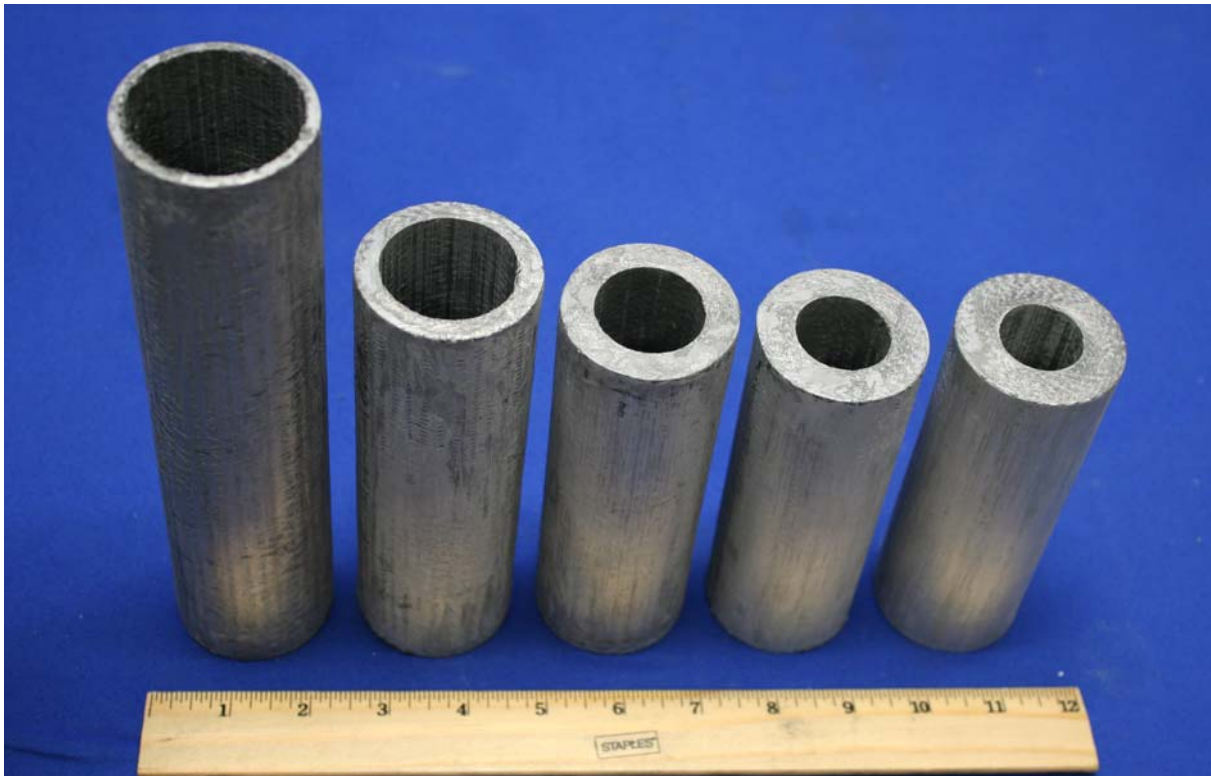
Fig. 10-2. RMS specimens for the *M/C* blast study, with *M/C*'s (from left to right) of 1, 3, 6, 9, and 12.

Table 10-2. Measured dimensions and densities of the *M/C* specimens.

M/C	ID (in)	OD* (in.)			Density (g/cc)		
		Specimen			Specimen		
		#1	#2	#3	#1	#2	#3
1	1.800 + 0.002	2.01	2.02	2.02	7.27	7.32	7.29
3	1.526 + 0.002	2.03	2.03	2.03	7.30	7.19	7.10
6	1.280 + 0.002	2.02	2.02	2.01	7.20	7.18	7.34
9	1.125 + 0.002	2.02	2.02	2.02	7.30	7.16	7.29
12	1.015 + 0.002	2.02	2.01	2.01	7.21	7.33	7.24

*Average of six readings/measurements

The charge configurations, expected fragment velocity, and expected QSP values for a chamber volume of 15 m^3 are listed in Table 10-3. The largest mass of explosive was 600 g of LX-14. The total charge will be built up from a series of L/D ~ 1 pellets pressed by ATK.

The last column in Table 10-3 lists the quantity of explosive charges required for each configuration. Three (3) units are required for each of the RM tests: one for the initial test; one for a contingency test such as instrument failure or initiation study; and one for a repeatability test.

Table 10-3. Charge configuration, calculated fragment velocity, and QSP values.

LX-14 Charge Geometry				Mass (g)			Avg. Vel.[1]	QSP[2,3,4,5]	Units of Each
M/C	OD (in)	L (in)	L/D	LX-14	Case	Total	(fps)	(psi)	#
Bare	1.518	5.573	3.67	300.0	0.0	300.0	NA	9.3 - 11.6	2
3 (Steel)	1.518	5.573	2.79	300.0	900.0	1200.0	4500	4.0 - 6.4	2
1 (RM)	1.792	7.996	4.00	600.0	600.0	1200.0	7200	24.8 - 33.5	3
3 (RM)	1.518	5.573	2.79	300.0	900.0	1200.0	4500	22.6 - 27.0	3
6 (RM)	1.272	4.535	2.27	171.4	1028.6	1200.0	3200	21.7 - 24.2	3
9 (RM)	1.117	4.119	2.06	120.0	1080.0	1200.0	2500	21.3 - 23.1	3
12 (RM)	1.007	3.896	1.95	92.3	1107.7	1200.0	2200	21.1 - 22.5	3

1. FWAC calculations
2. P=(γ-1)*E/V
3. Chamber Volume: 15-m^3
4. Value on left is based on heats of detonation while value
on right is based on heats of combustion.
5. Assumes 70% combustion of RM.

In order to reduce end effects and increase the projection velocity of the case, the ends of the unit were heavily confined with thick steel endplates. The endplates featured a boss to be inserted into the case approximately 3/16" to make contact with the explosive. Most charges were initiated at one end with a Reynolds RP-81 exploding-bridgewire (EBW) detonator inserted in a through-hole of one endplate. In a few tests, the charge was initiated by detonators at both ends. Each charge was positioned with its axis on the primary axis of the chamber. A schematic of the charge configurations is shown in Fig. 10-3.
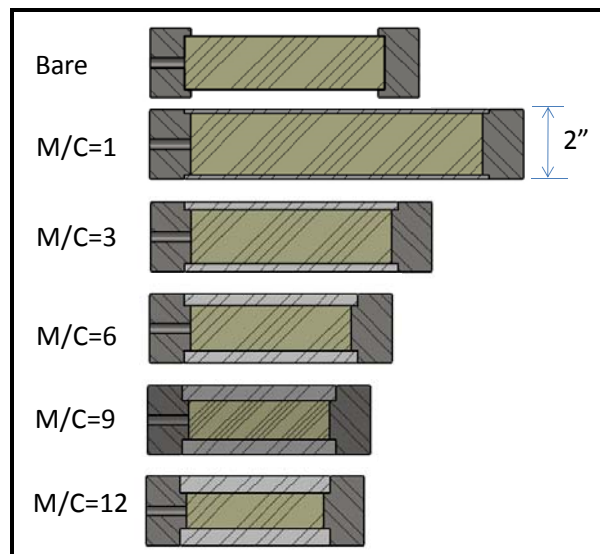
Figure 10-3. Schematic of the charge configurations in the *M/C* blast tests.

Code calculations predicted the maximum and minimum expected projection angles of the casing fragments to be +20° and −18° at the right and left (initiated) ends, respectively. Figure 10-4 shows the definition of the projection angles. To protect the cylindrical walls of the chamber from casing fragments, a belt of steel plates should be mounted around the interior wall. In determining the length of the protection plates, it is advisable to use ±25° for projection angles.
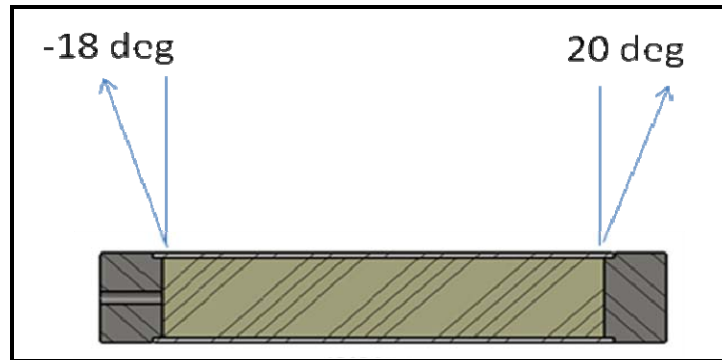
Figure 10-4. Minimum and maximum fragment projection angles for all *M/C*'s.

10.3 Test Chamber

A test site incorporating an enclosed chamber was prepared by ATK. The chamber, formerly an auto-clave, was moved to ATK's Test Range T-75, where it was modified to suit the requirements of the blast tests. The chamber is cylindrical (Fig. 10-5) with semi-elliptical domed ends, internally 8 feet in diameter by about 29 feet long, with an interior volume of about 40 m^3.

Fig. 10-5. ATK test site showing emplaced blast chamber to be used for *M/C* tests.

Preparing the chamber involved first identifying a method to reduce its volume to the ~15 m^3 required for the tests. It was desired that the method be adaptable to future testing in increasingly larger scales by enabling the volume to be adjusted accordingly. It was decided to fill the extra volume with concrete, with the intention that it would be durable enough to survive blast testing, but could later be removed when a larger volume becomes necessary.

The concrete consisted of an 8-bag, 3/8"-pea gravel mix with a 28-day strength of 5000 psi. The final layer of the Shotcrete fill was finished smooth (Fig. 10-6). A ¼"-thick steel plate was then placed atop this layer and fully welded to the autoclave wall (Fig. 10-7). The bulkhead provides an airtight seal between the test side and the concrete fill and serves as a structure to attach one end of the test fixture (Fig. 10-8). The final measured volume of the chamber is 16.0 m^3. Figure 10-9 shows as-built sketches of the chamber and stand with major dimensions. A retaining wall, concrete work pad, hydraulics shed and final earthwork completed the site (Fig. 10-10). The result is a permanent chamber capable of testing a variety of reactive and non-reactive detonation articles of various sizes and configurations.

Fig. 10-6. Application of Shotcrete (left); completed concrete volume fill (right).

Fig. 10-7. Steel bulkhead and armor plating.

The chamber's quick-opening door, driven by hydraulics powered by a small electric motor, allows easy access, resulting in reduced cost per test and faster turnaround. The chamber is mounted above ground and covered with an earthen berm to reduce wall ringing.

All internal test fixtures, instrumentation, and armor plating were installed. Three Endevco Model 8530B-500 piezoresistive pressure transducers were installed as channels P001, P002 and P003. ATK also installed a fourth redundant diaphragm-type pressure transducer, Taber Model 217 (100 psig), designated channel P004. All required safety and operational checkouts were completed. Vessel integrity and seal checks were performed through static leak testing at 15 psig, 30 psig, and 100 psig.

Fig. 10-8. Test stand construction consisted of a steel tripod and bracket on bulkhead.
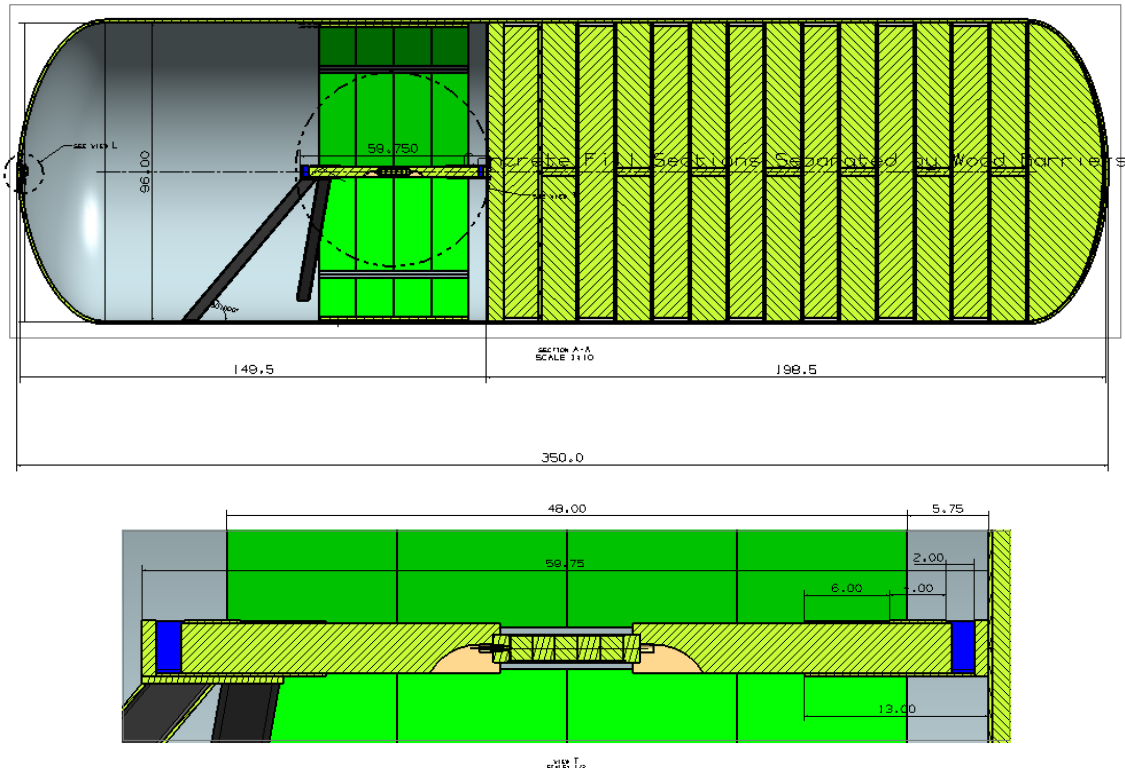
Fig. 10-9. As-built dimensions of test chamber.

Fig. 10-10. Finished installation with hydraulics shed.

10.4 Calibration Tests

The first calibration test of the chamber, conducted in late November 2012, of a bare LX-14 charge (Fig. 10-11), was a checkout of the pressure gauges. Preliminary analysis of the gauge data indicated the instrumentation was functioning correctly.

The test chamber, fixtures, instrumentation and data acquisition were validated utilizing bare LX-14 pellets. No modifications were identified as necessary as a result of these tests, as all design features functioned as intended.
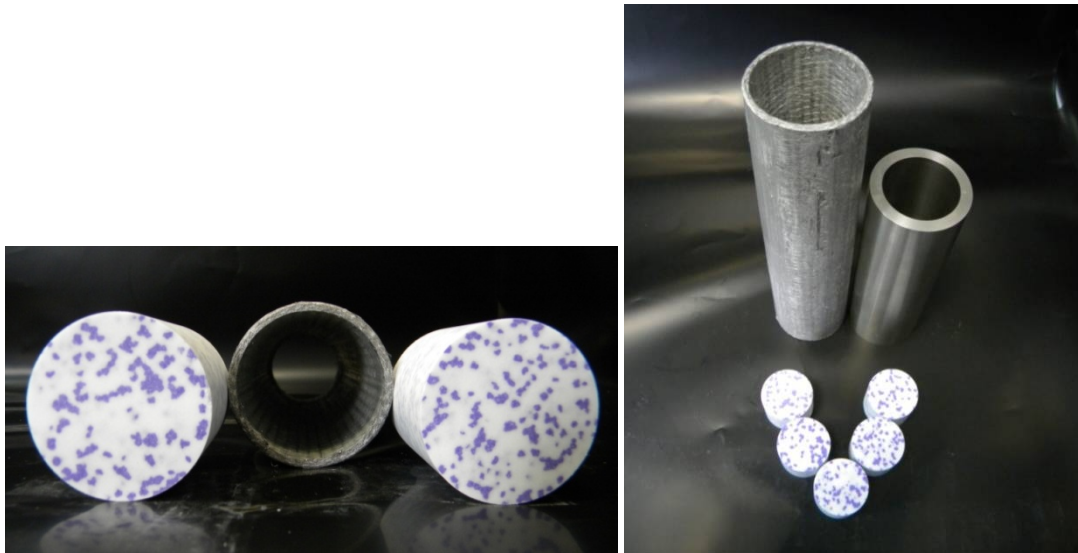
Fig. 10-11. Machined LX-14 explosive pellets with RMS and steel casings.

10.5 M/C Blast Tests

Mr. David Jann of DET traveled to ATK in order to witness and direct the Phase 1 test matrix. Testing ran from December 5 through 8, 2012.

In the first few tests, several pressure transducer cables were damaged with resulting data loss. Cables were re-routed within heavy wall conduits. An additional modification was made to the mount for transducer P003 to provide greater protection.

Figure 10-12 shows the modification to the dome-end pressure transducer mount. This modification was performed to provide better protection of the transducer cabling from fragments. The transducer mount was changed from an off-axis mount relative to the chamber (left photos) to an on-axis mount (right photos). Originally the cables (not shown) exited the right side of the mount and were routed un-protected to a port on the straight section of the chamber. The new mount utilizes a shroud for full pro-tection of the cabling. The transducer cables now pass through a port directly behind the front plate.
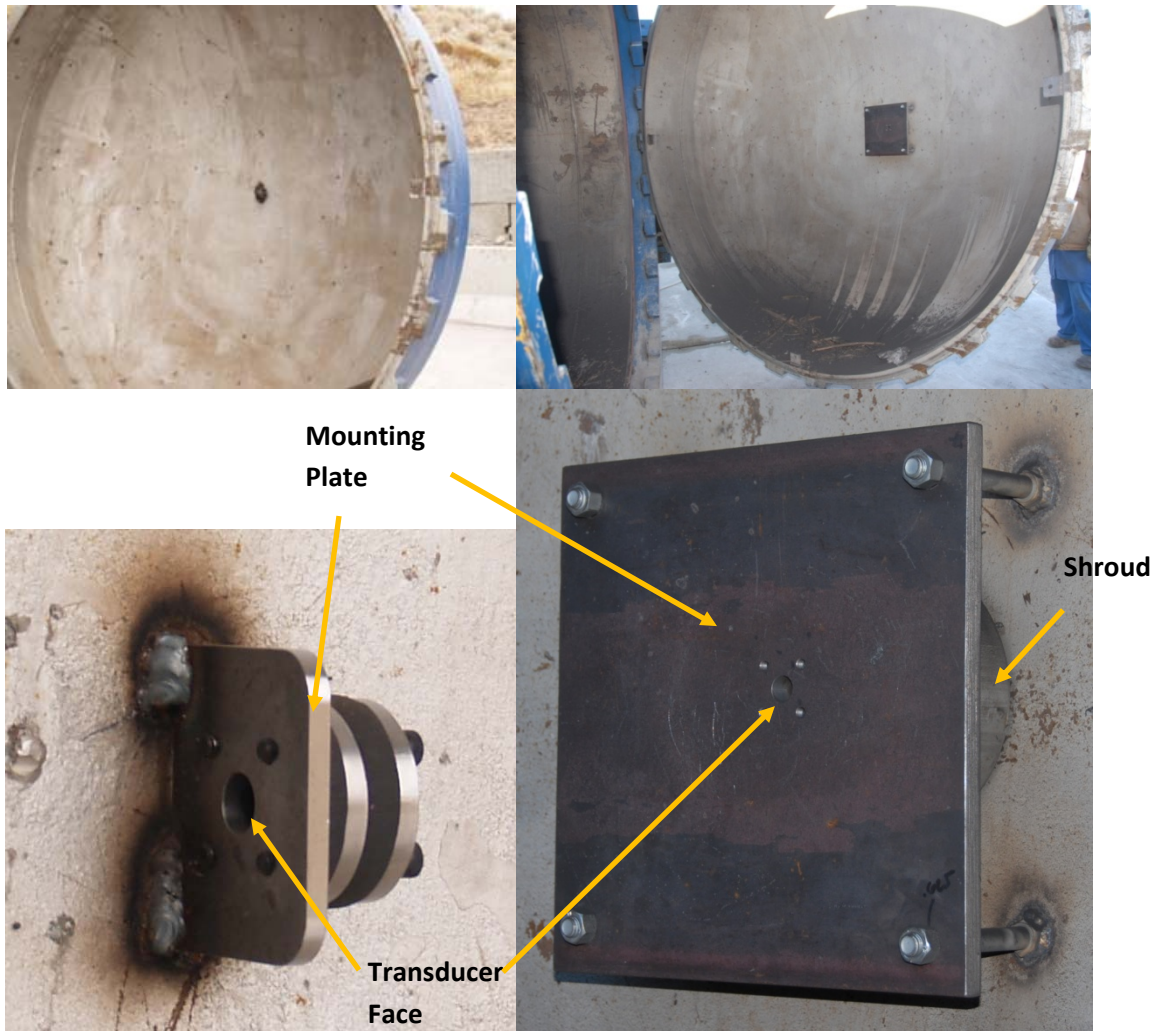
Fig. 10-12. Transducer mount P003 before (left) and after (right) modification.

Due to this modification, all tests after Test #7 used the modified mount in which the transducer face was positioned coaxially with the chamber. This results in higher peak pressures in the data after test #7. The remaining tests were conducted with minimal cable damage. Eighteen tests were completed in all.

At the conclusion of the testing, discussions were held on relocating the pressure transducer mounts to provide more additional cable/transducer protection. This modification will be completed prior to the next series of tests.

The armor plating for vessel fragment protection worked very well. Half-inch thick plate was used so the plates could be easily slid out and replaced when needed. Photos of one of the steel case tests are included to show test setup (Figs. 10-13 and 10-14), results (Fig. 10-15), armor plate fragment patterns (Fig. 10-16), and recovered metal fragments (Fig. 10-17).
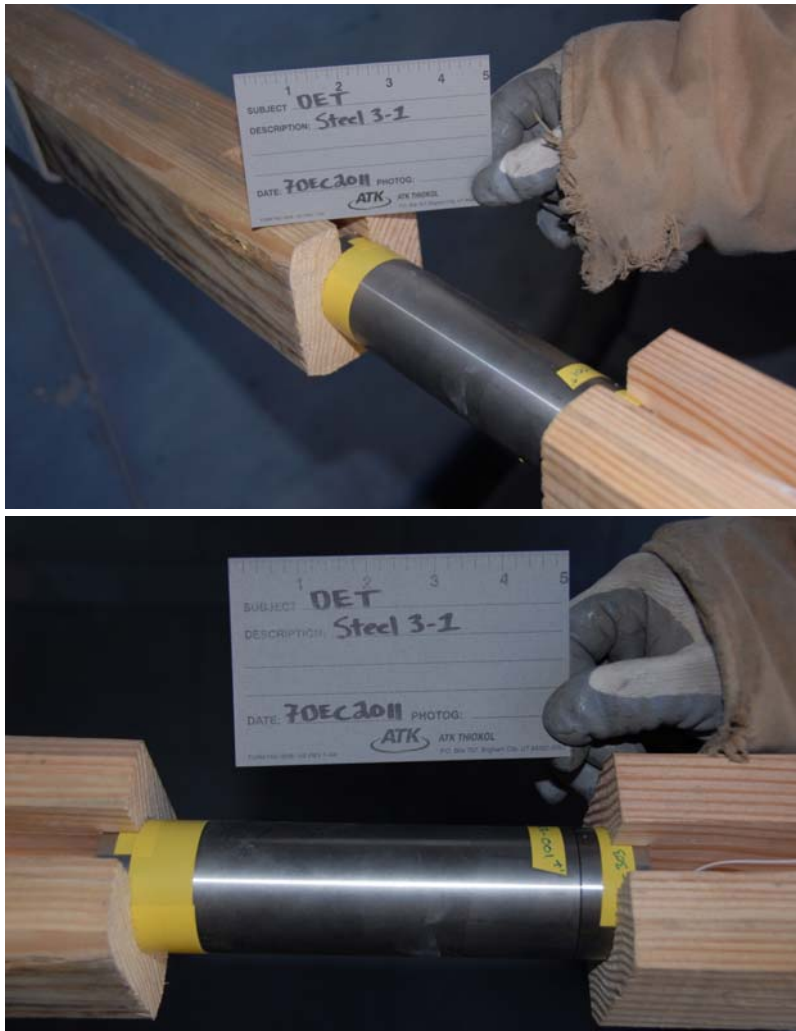
Fig. 10-13. Steel-cased explosive charge mounted between wooden supports.

Fig. 10-14. Steel tripod mounting the test charge between wooden supports oriented coaxially within the chamber.

Fig. 10-15. Post-test powdery residue/ash on chamber floor.

Fig. 10-16. Fragment damage to armor plating.

Fig. 10-17. Recovered metal fragments from end caps and casing.

The blast test parameters are summarized in Table 10-4.

Table 10-4. Test Parameters.

Test no.	Case material	M/C	Initia-tion	DAQ recording number	Test tempera-ture (°F)	Hu-midity (%)	Barom. pressure (psi)	Comments
C1	Bare-2	Bare	RP-81	051	42	56	12.43	P001 QSP high; replace & repeat checkout shot
1	Bare-1	Bare	RP-81	053	25	15	12.463	P002, P003 cables fragged, need better protection
2	RM MC3-1	3	RP-81	055	22	18	12.461	P002 has a DC shift
3	RM MC6-1	6	RP-81	060	24	18	12.46	All 3 traces bad, need to provide more protection
4	RM MC1-2	1	RP-81	062	22	56	12.486	P003 cable got hit
5	RM MC12-1	12	RP-81	063	25	58	12.487	Tested w/o P003 per David Jann. All worked
6	RM MC9-1	9	RP-81	065	28	51	12.471	Tested w/o P003. All worked
7	Steel MC3-1	3	RP-81	066	28	54	12.462	Tested w/o P003. P001 got hit. Ok?
8	Steel MC1-1	1	RP-81	067	29	51	12.447	P003 back in. S/N 12160. P001 is dead, needs re-placement
9	RM MC1-3	1	2x RP-81	068	25	53	12.43	New P001. S/N 25358. P002 cable got hit, need to repair
10	RM MC3-2	3	2x RP-81	071	21	68	12.43	P002 cable repaired. All OK
11	RM MC6-2	6	2x RP-81	072	26	58	12.43	All good
12	RM MC9-2	9	2x RP-81	073	26	53	12.43	All good
13	RM MC12-2	12	2x RP-81	074	29	55	12.447	All good
14	RM MC6-3	6	RP-81	075	30	54	12.446	All good
15	RM MC3-3	3	RP-81	076	32	50	12.436	All good. P001 over-ranged. OK?
16	RM MC1-4	3	RP-81	077	33	48	12.433	All good
17	Steel MC3-2	3	RP-81	078	35	48	12.43	P001 got hit, need to look at cable & gage.

10.6 Analysis

The raw data were reduced, filtered where required, and exported to MS Excel spreadsheets. Several parameters were identified for reporting: peak pressures on all transducers, quasi-static pressures (QSP) in the time ranges of 40-100 ms, 40-200 ms, and 200-300 ms after initiation.

The test designator uses the format ## MC*x-y*, where ## = "RM" designates a reactive material casing or "Steel" indicates a steel casing, *x* is the casing-to-charge mass ratio *M/C*, and *y* is the specimen number. "Bare" indicates no containment where the LX-14 pellets are taped end to end.

Figure 10-18 shows a typical pressure versus time trace, including both the raw and filtered data. The filter is a Butterworth, 2nd-order 30-Hz low-band-pass type. Filtered pressure histories for all of the 1,200-gram (total mass) configurations are shown in Fig. 10-19. The data show the RMS-encased charges produced significantly higher pressures than the steel-encased charges.
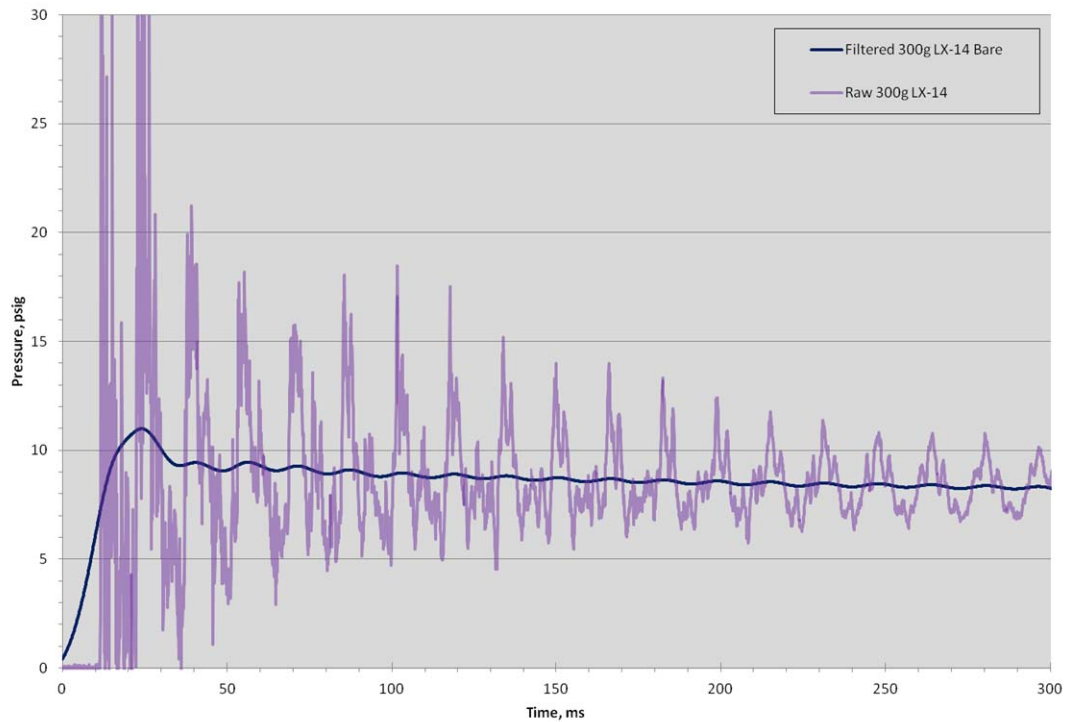
Fig. 10-18. Experimental pressure histories (filtered and non-filtered) for a bare 300-g LX-14 charge.
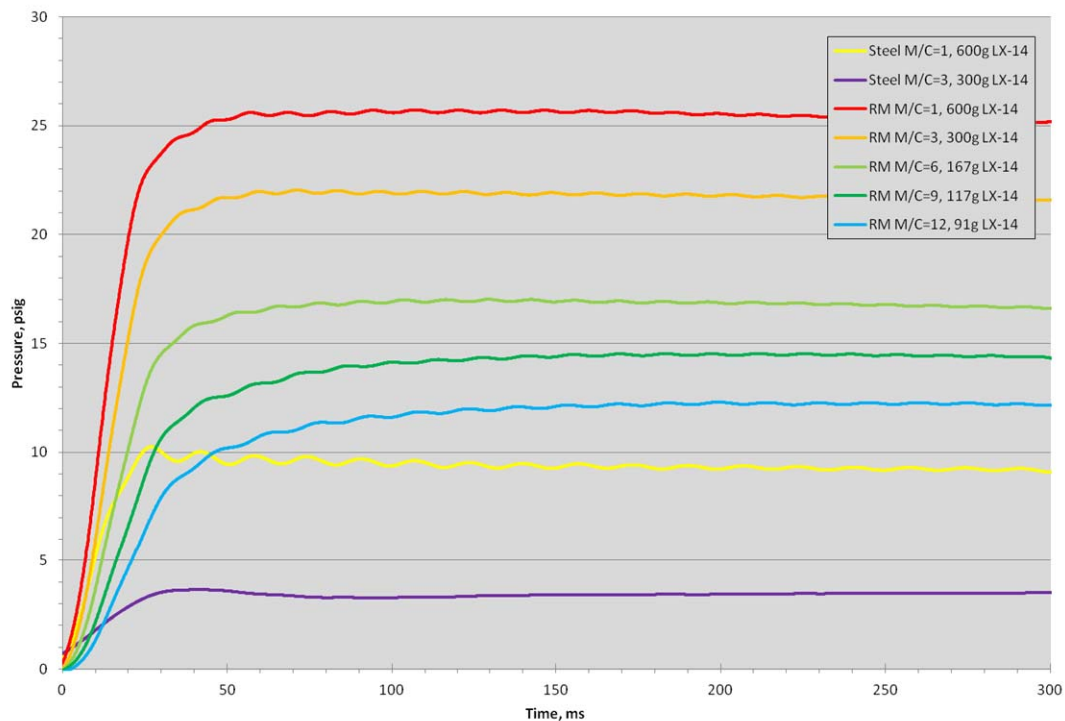
Fig. 10-19. Filtered experimental pressure histories for the 1,200-g (total mass) charges.

The Quasi-Static pressures (QSP) were determined by performing a linear regression on the filtered pressure-history data over three time intervals: 40 to 100 ms; 40 to 200 ms; and 200 to 300 ms. QSPs from these data are presented in Figs. 10-20 through 10-22. The data in all cases show a decrease in QSP as M/C increases. However, the QSPs of the RM casings are all significantly higher than the steel casings.
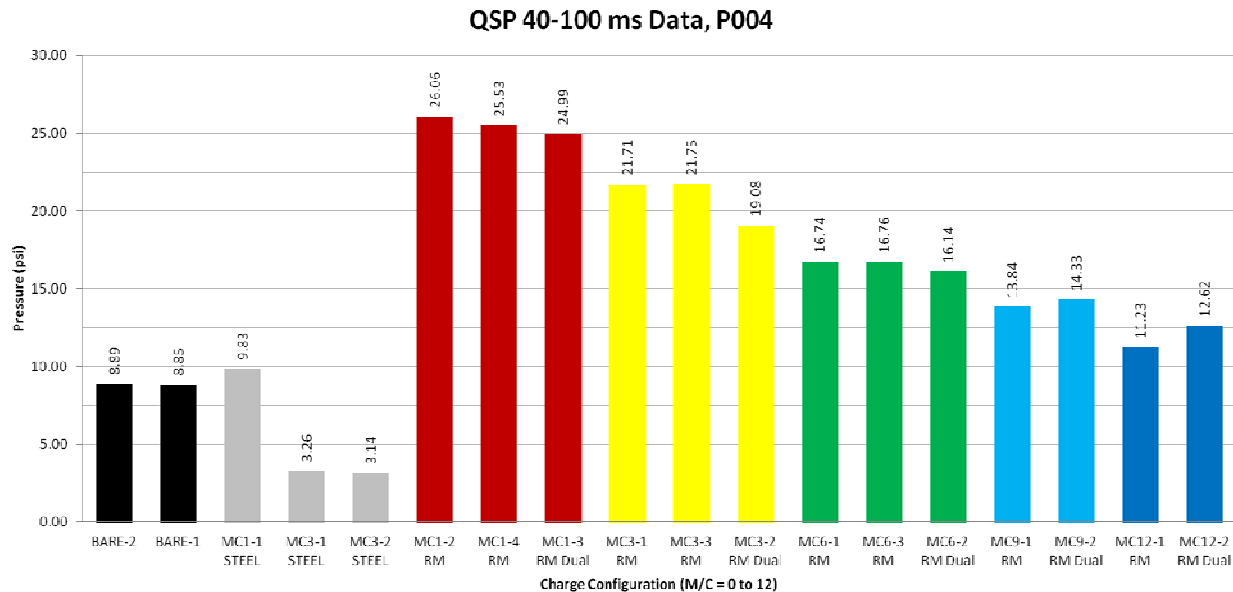
Fig. 10-20. Experimental QSPs from the early-time pressure data, 40 to 100 ms.
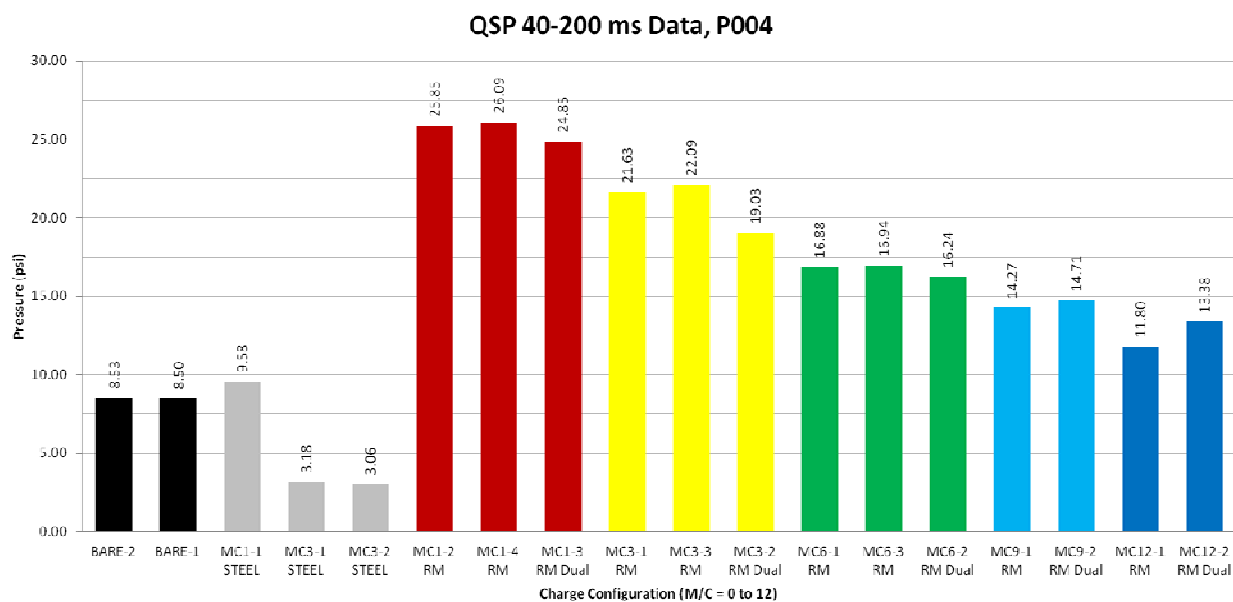
Fig. 10-21. Experimental QSPs from the medium-time pressure data, 40 to 200 ms.
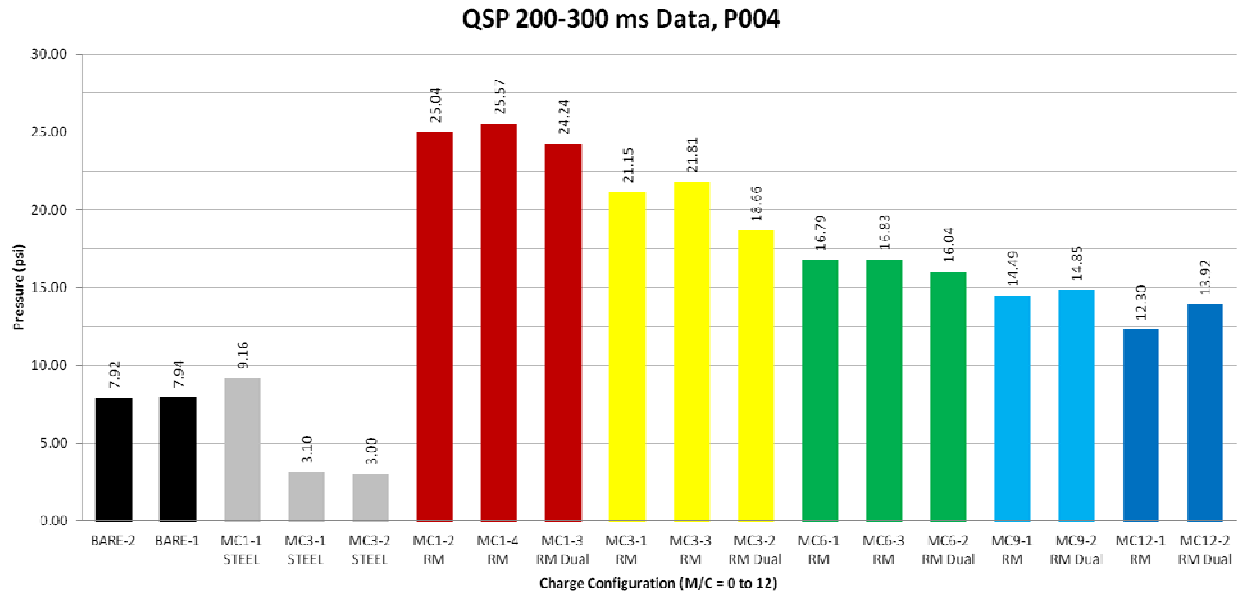
Fig. 10-22. Experimental QSPs from the late-time pressure data, 200 to 300 ms.
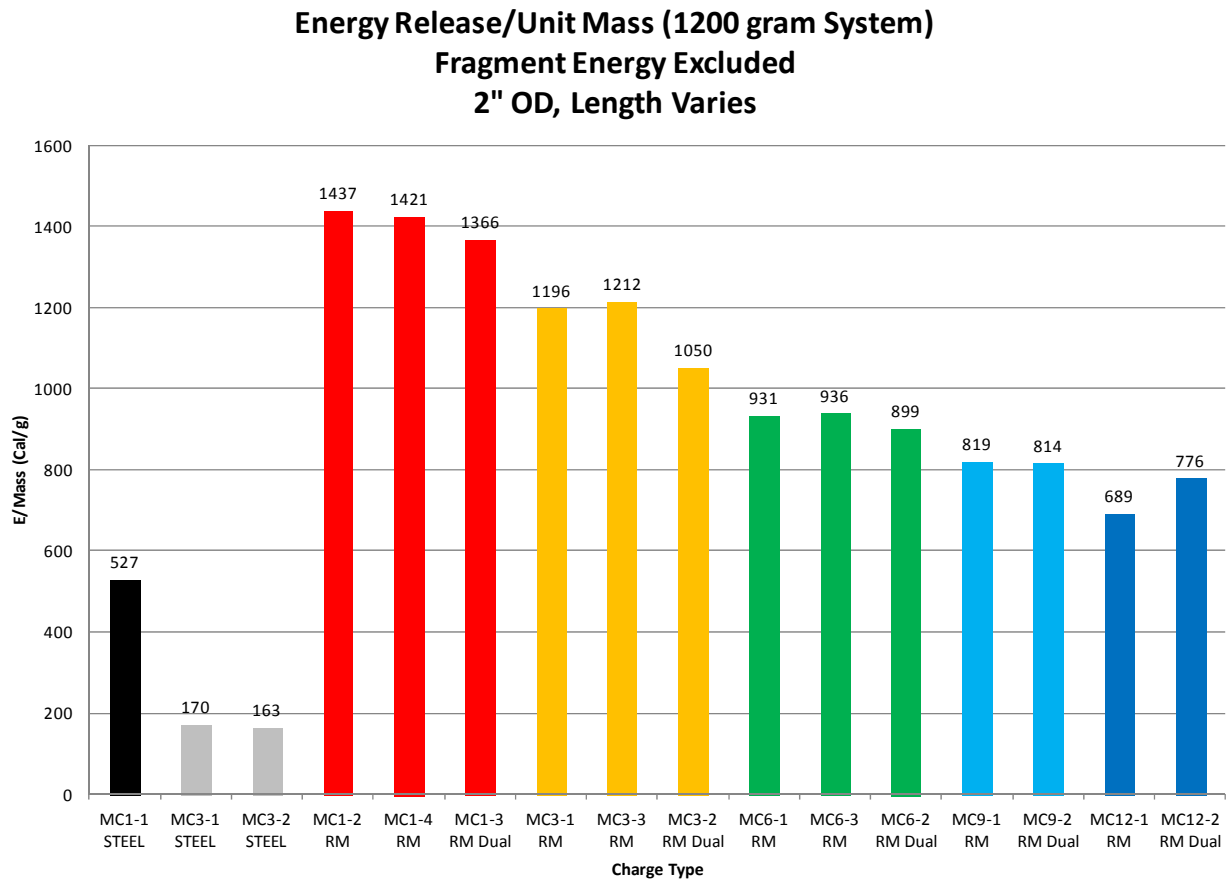
Fig. 10-23. Estimated energy released per unit of combined explosive and reactive mass.

10.7 Blast Modeling

We exercised our previously developed simple model of closed-chamber blast enhancement to analyze the results of the blast tests performed at ARA and ATK. This is contrasted with existing formulas of blast reduction due to an inert casing.

For a chamber of fixed volume V, the change in internal energy E is related to the change in pressure P by the ideal-gas law,

$$\Delta E = \frac{\Delta PV}{\gamma - 1}$$

(10-1)

The energy per unit explosive mass C, which we shall call the *specific energy*, is then

$$\Delta e = \frac{\Delta E}{C} = \frac{1}{C}\frac{\Delta PV}{\gamma - 1}$$

(10-2)

The specific energy relative to a bare explosive charge having a mass C_{bare} is then

$$\frac{\Delta e}{\Delta e_{bare}} = \frac{\Delta E}{C}\frac{C_{bare}}{\Delta E_{bare}} = \frac{C_{bare}}{C}\frac{\Delta P}{\Delta P_{bare}}$$

(10-3)

This formula was used to analyze all of the data from the ARA and ATK closed-chamber blast tests. In the latter, the casing-to-explosive-charge mass ratio M/C was varied over a range from 0 to 12 in such a way that the total mass $M + C$ would remain constant. Also, for each test series, the energies in Eq. (10-3) were normalized by the bare-charge ($M = 0$) tests in that same series.

Various formulas have been proposed in the literature to predict the effect of an inert casing in reducing blast. These include the Fano (1945) equation,

$$\frac{W'}{W} = 0.2 + \frac{0.8}{1 + 2\dfrac{m_c}{W}}$$

(10-4)

where W is the explosive mass (or weight), m_c is the mass of the (inert) casing, and W' is the equivalent bare-charge mass (i.e., the mass of a bare explosive charge that yields the same blast effect as the cased charge); the modified Fano equation (Fisher, 1953),

$$\frac{W'}{W} = 0.2 + \frac{0.8}{1 + \dfrac{m_c}{W}};$$

(10-5)

Fisher's (1953) "best-fit" formula,

$$\frac{W'}{W} = \frac{1 + \dfrac{m_c}{W}(1 - M')}{1 + \dfrac{m_c}{W}}$$

(10-6)

where

$$M' = \begin{cases} \dfrac{m_c}{W}, & \text{for } \dfrac{m_c}{W} < 1 \\ 1, & \text{for } \dfrac{m_c}{W} \geq 1 \end{cases};$$

(10-7)

and Hutchinson's (2009) formula,

$$\frac{W'}{W} = \frac{1}{\sqrt{1 + 2\dfrac{m_c}{W}}}$$

(10-8)

All of these formulas predict that the equivalent charge mass is monotonically decreasing with increasing (inert) casing mass. These formulas were compared to the inert-casing data from each test series.

10.8 Data Analysis

The test data include the ARA tests (M/C = 0 and 3) and the ATK tests (M/C = 0, 1, 3, 6, 9, and 12), both of which included bare, steel-encased, and RMS-encased charges. For the ATK tests, the recorded dynamic pressure histories were averaged to obtain quasi-static pressures (QSP) over three time regimes: 40-100 ms, 40-200 ms and 200-300 ms. For each dataset, the best (largest) bare-charge energy (computed from Eq. (10-1)) was taken as the baseline ($E_{rel} \equiv 1$), to which the other energies were normalized. Since the ARA and ATK chambers had different volumes (~2 m^3 and 16 m^3, respectively), each test set is reckoned relative to its own best bare-charge test.

Figures 10-24 to 10-26 present the results of our analysis, in terms of relative energy versus casing-to-explosive mass ratio M/C. In each figure, the ATK data are based on QSP values determined over a different time range; the ARA data are repeated on each of these figures.
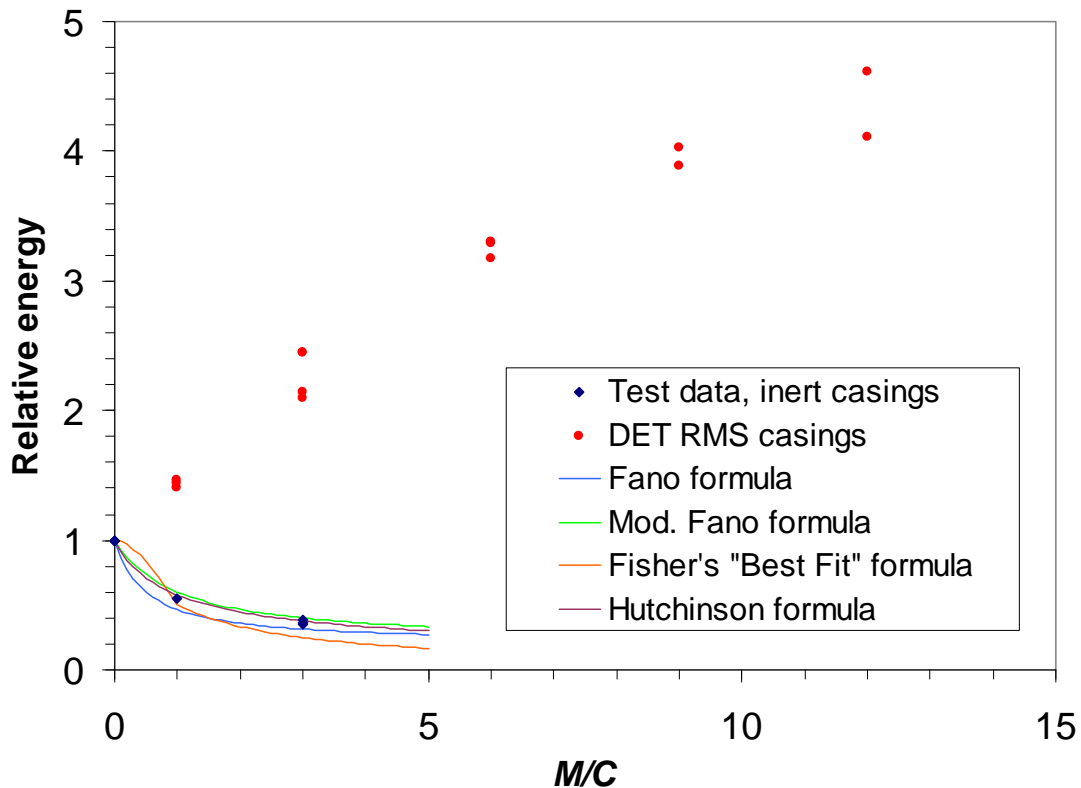
Fig. 10-24. Relative energies versus casing-to-explosive mass ratio M/C for the ARA tests and the ATK tests for the 40-100 ms range.
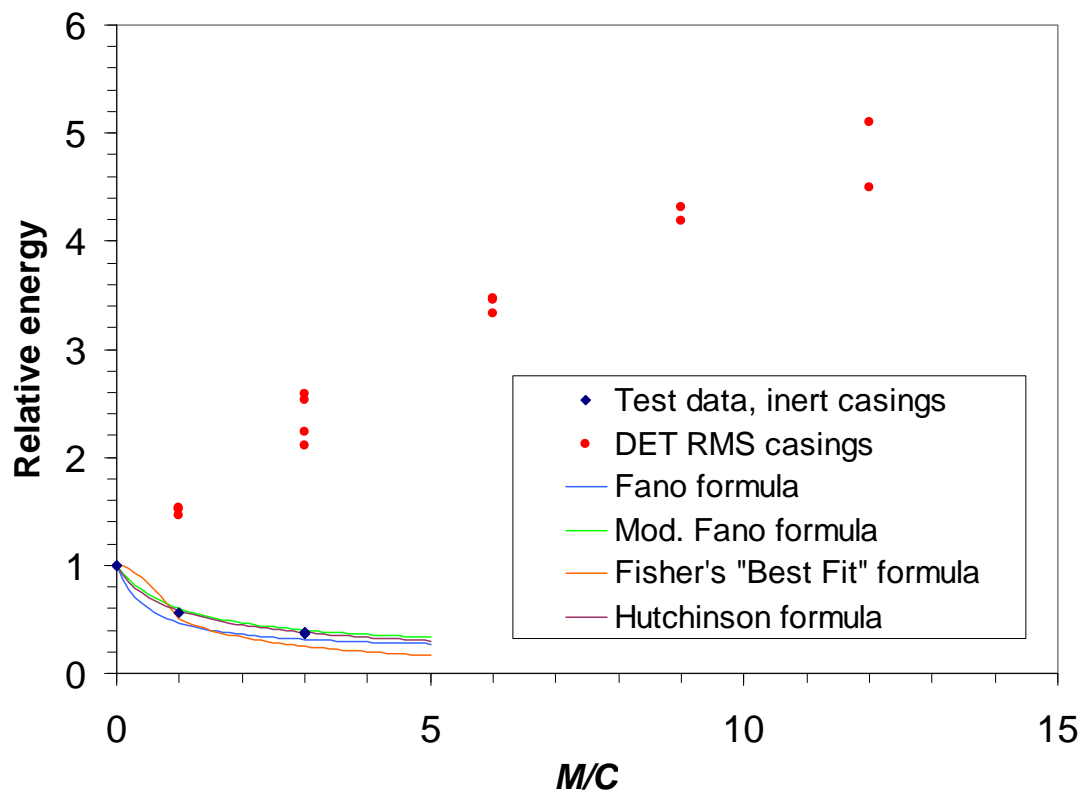
Fig. 10-25. Relative energies versus casing-to-explosive mass ratio *M/C* for the ARA tests and the ATK tests for the 40-200 ms range.
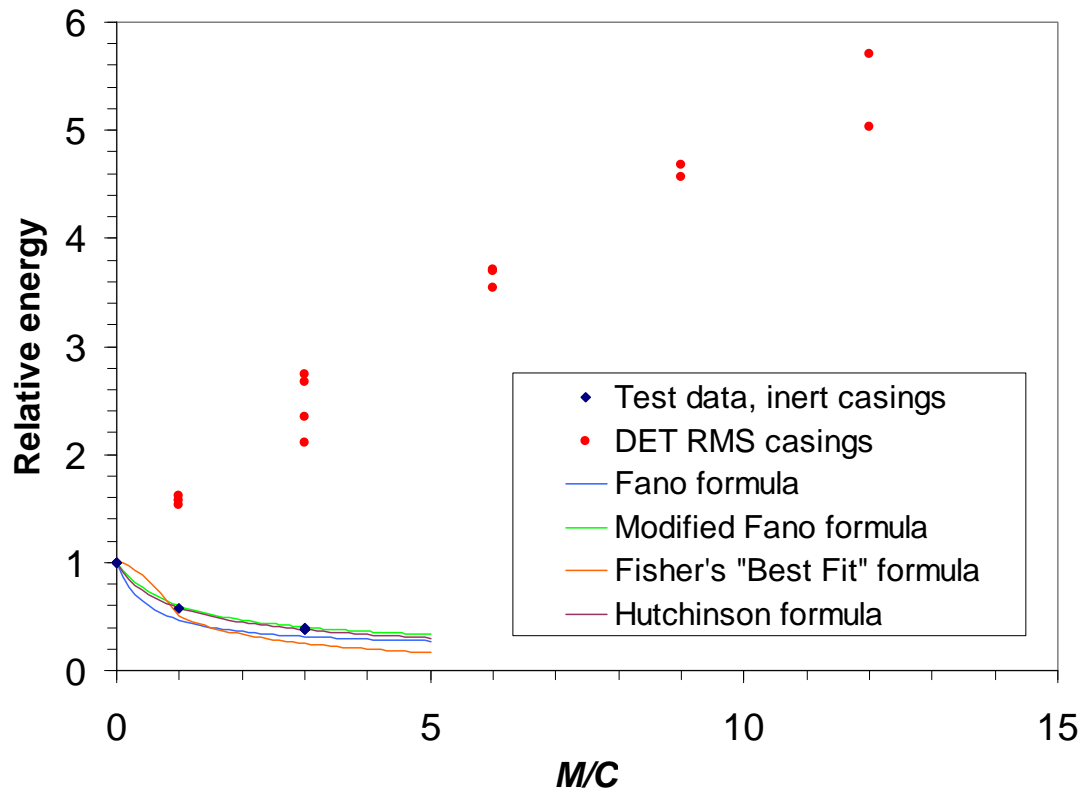
Fig. 10-26. Relative energies versus casing-to-explosive mass ratio *M/C* for the ARA tests and the ATK tests for the 200-300 ms range.

We observe that, where the two sets of data (ARA and ATK) overlap (at M/C = 3), they jibe. Moreover, collectively, the two sets of data form a smooth curve with a narrow dispersion. We conclude that the two sets of data are fairly consistent with each other.

The measured quasi-static pressures (QSP) show a steadily larger advantage for increasing the M/C ratio. Measured QSPs averaged over longer or later periods show a slight progressively greater increase of blast enhancement by the RMS, especially for larger M/C values (6 to 12).

The formulas for the inert casings, Eqs. (10-4) through (10-8), are plotted on the same coordinates, since the explosive energy is proportional to its mass. Of these, Hutchinson's formula, Eq. (10-8), gives the best overall fit to the data, followed closely by the modified Fano formula, Eq. (10-5).

Dual-end explosive initiation (detonators at both ends of the explosive charge, initiated simultaneously) was used in some of the ATK tests. This had a small and inconsistent effect on blast output compared to the standard single initiation, so the associated data are included in the plot without discrimination. Dual-end initiation slightly reduced QSP for low-M/C devices and increased QSP for large M/C.

Section XI

Process Scale-Up

At the conclusion of Phase I, the fabrication process was capable of making RMS specimens as large as about 1.0 kg. It was desired to scale up the process to fabricate 10-kg specimens. Preliminary planning has begun to address the various issues associated with the scale-up.

The geometry envelope of the 10-kg specimens should relate to the penetrator designs that were discussed below in Section VIII. A notional sketch of the 7000-lb RMS bomb is shown in Fig. 11-1. The specific *M/C* for the bomb has yet to be determined, but is currently thought to be between 6 and 12. Table 11-1 summarizes the full-scale dimensions of the RMS-encased penetrating bombs for *M/C* ratios of 6 and 12 along with the corresponding length and mass of the cylindrical sections of the RM casings.
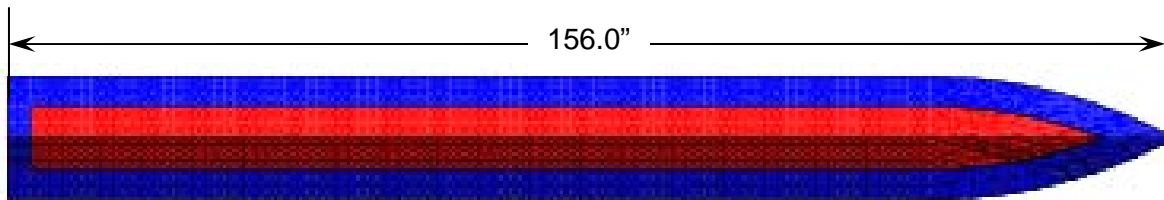
Fig. 11-1. Notional sketch of 7000-lb RMS penetrating bomb.

Table 11-1. Dimensions and mass of RMS casings for the 7000-lb bombs with *M/C* of 6 and 12.

Effective *M/C*	OD (in.)	T_{wall} (in.)	RM case mass (kg)	Total length (in)	Cylinder length (in)	L_{cyl}/D
6.0	17.74	3.13	2540	156.0	138.3	7.8
11.99	16.42	3.98	2774	156.0	139.6	8.5

Table 11-2 below summarizes the dimensions for 10-kg scaled hollow cylinders for both the *M/C* = 6 and *M/C* = 12 configurations. Of course a 10-kg mass can be achieved by infinite combinations of OD, ID and length; the table below represents the geometries that are most suitable for an RMS penetrating bomb based on our current knowledge.

Table 11-2. Dimensions and mass of RMS casings for the scaled bombs with *M/C* of 6 and 12.

Effective *M/C*	OD (in.)	T_{wall} (in.)	RM case mass (kg)	Cylinder length (in)	L_{cyl}/D
6.0	2.76	0.48	10	21.6	7.8
11.99	2.51	0.61	10	21.4	8.5

Two main issues arise with scaling the current fabrication process up to 10 kg. The first involves the size of braiding machine used to make the tungsten reinforcement structure. The quantity of tungsten increases with the size of the specimen. The amount of tungsten can be increased by using larger-diameter wire, and/or increasing the quantity of the wire. However, for the braided wires the diameter is limited to 0.008 inch. Any thicker and the wire is difficult to spool onto the carriers. Thicker wire can be used for the longitudinal yarns as they do not need to be spooled. To maintain the strength of the specimen, the ratio of braided to longitudinal yarns must be maintained. Therefore using thicker wire for the longitudinal yarns would require an increase in the quantity of braided wire.

Currently DET uses a 72-carrier braiding machine. As specimen diameter grows, more carriers are needed to keep the volume fraction of wire at the desired 30%. The upper diameter limit for braiding on this

machine is thought to be 2.5 inches, with 2.75 inches perhaps possible. Therefore, a 10-kg specimen is probably the machine's limit. The next larger size of commercially available braiding machine is a 144-carrier model, which should be able to handle specimens up to 4.0 inches in diameter.

The capabilities and limits of the current braider will be better understood once the strength studies are completed and the specific tungsten wire layup is defined. A change in either the length or ID of the specimen will enable the fabrication of a 10-kg specimen with the existing braider, albeit the specimen geometry will deviate somewhat from what is proposed in Table 11-2 above. While the use of the existing braider may not yield the most ideal 10-kg specimen, it would conserve resources, reduce time, and enable a quicker assessment of the technology before an investment is made in a larger machine.

The second issue with scaling up is the safe handling of the aluminum-epoxy matrix. A 10-kg RMS specimen contains 2 kg of this mixture. The epoxy is of a thermoset type that generates heat during curing. It is well known that mixing large quantities of epoxy can result in a fire hazard. DET contracted Exponent Corporation to investigate the hazards associated with handling large batches of the aluminum-epoxy mixture. Exponent began performing Differential Scanning Calorimetry and Thermogravimetric Analyzer testing of both the epoxy and epoxy/aluminum/tungsten mixtures to ascertain the magnitude of the self-heating. Early results indicated that the aluminum and tungsten act as heat sinks and tend to keep the mixture's temperature below combustion levels.

In anticipation of fabricating 10-kg RMS specimens, studies were conducted to ascertain the risks involved in processing large quantities of the aluminum-epoxy mixture. Curing of the epoxy is an exothermic reaction. The current material processing approach limits the batch size of the aluminum-epoxy mixture during mixing to eliminate the possibility of bulk heating and resulting combustion of the aluminum and epoxy. The current size limit is suitable for fabricating RMS specimens with a net mass of about 1.0 kg. In order to fabricate larger RMS specimens, larger aluminum-epoxy batches will be needed.

Exponent Corporation was contracted to perform safety tests of mixing large batches of the aluminum-epoxy mixture. Exponent performed three types of tests: Differential Scanning Calorimetry (DSC); Thermogravimetric Analysis (TGA); and Accelerating Rate Calorimetry (ARC). Tests were performed on neat epoxy and the aluminum-epoxy-tungsten mixture.

The DCS/TGA tests were conducted over a temperature range up to 300 °C. The rate of temperature increase was 10 °C/min, and the samples were held at 300 °C for one hour. The mass of the neat epoxy specimen was 25 mg and 120 mg for the epoxy-metal specimen. A plot of the heat generated by the sample versus temperature from the DSC test is shown in Fig. 11-2, which shows how the metal in the mixture greatly reduces the heat generated by the specimen.
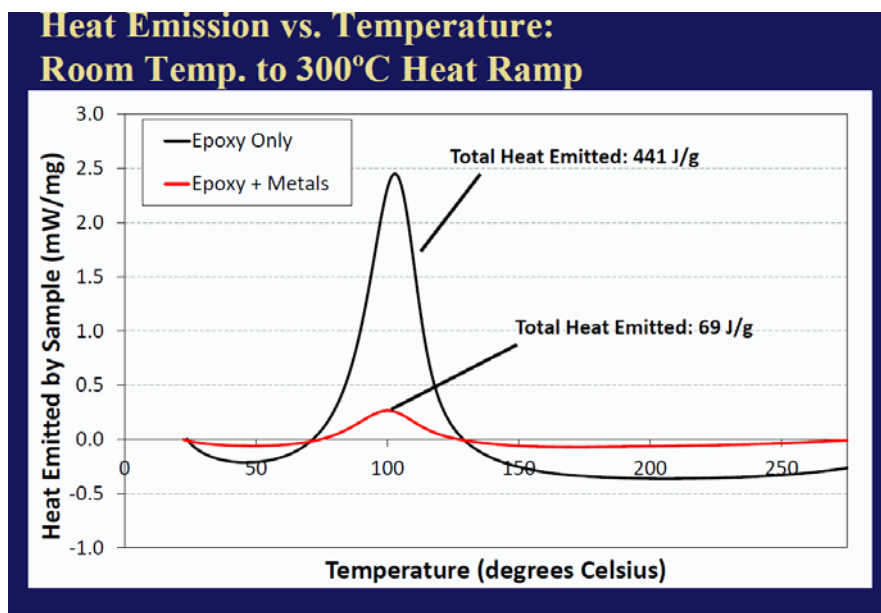
Fig. 11-2. Experimental heat emission versus temperature for neat epoxy and epoxy-aluminum-tungsten mixture.

Results of the TGA testing are listed in Table 11-3. According to the TGA data, the epoxy-metal mixture experienced a 3% mass reduction during the temperature hold at 300 °C versus an 18% mass reduction for the neat epoxy. Large reductions in mass can indicate reaction and/or combustion of the specimen. A 3% reduction in mass indicates that combustion is not occurring in the epoxy-metal specimen.

Table 11-3. TGA results for neat epoxy and epoxy-aluminum-tungsten mixture.

	Point of maximum temperature change (°C)	Heat of curing exotherm (J/g)	Sample Weight Loss during Temperature Ramp (%)	Sample Weight Loss during Isothermal Hold (%)
Epoxy Only	103	441	1.5	18
Epoxy + Metals	100	69	0.5	3

For the ARC tests, three different cure temperatures were used: room temperature, 100 °F, and 200 °F. The sample size was 10.2 grams for the neat epoxy and 34.3 grams for the epoxy-metal specimen. The head space in the calorimetric bomb consisted of 2.5 ml of air. The results of these tests are listed in Table 11-4 below. In general the tests showed that the tungsten and aluminum act as a heat sink within the mixture, thereby reducing the bulk heating effect associated with curing large batches of epoxy. The resulting temperatures of the epoxy-metal mixture at all three cure temperatures are well below the combustion temperature of the aluminum-epoxy mixture. Therefore processing larger batches of the RM should not pose a significant fire/combustion hazard.

Table 11-4. Summary of ARC test results for neat epoxy and a mixture of epoxy-aluminum-tungsten.

ARC Results

ROOM TEMPERATURE CURE	Cure Temperature (ºC)	End Temperature (ºC)	Difference (Adjusted) (ºC)	Maximum Rate (ºC/min)	Time to Maximum Rate (Adjusted) (min)
Epoxy Only	20.0	122.6	154.7	104.3	21.9
Epoxy + Al + W	20.0	39.3	36.5	0.10	32.2

38ºC (~100ºF) CURE	Cure Temperature (ºC)	End Temperature (ºC)	Difference (Adjusted) (ºC)	Maximum Rate (ºC/min)	Time to Maximum Rate (Adjusted) (min)
Epoxy Only	38.0	102.6	97.5	64.2	19.3
Epoxy + Al + W	38.0	43.4	10.0	0.26	3.6

93ºC (~200ºF) CURE	Cure Temperature (ºC)	End Temperature (ºC)	Difference (Adjusted) (ºC)	Maximum Rate (ºC/min)	Time to Maximum Rate (Adjusted) (min)
Epoxy Only	93.0	161.7	103.3	66.0	12.4
Epoxy + Al + W	93.0	92.1	N/A	N/A	N/A

While it appears that processing larger batch sizes of baseline formulation will not pose a significant safety risk, concern remained as to the stability of the mixtures where the proportions of aluminum and/or hardener deviate significantly from the nominal values; as a consequence of operator error or equipment malfunction. The specific concern was that mixtures with reduced aluminum or increased hardener would experience sufficient heating during curing to cause an unstable condition. Specifically the mixtures with decreased aluminum would experience a larger temperature increase since the aluminum acts as a heat sink. Also, additional harder may cause a greater temperature increase since the hardener is the agent that causes the exothermic reaction in the curing of the epoxy.

To investigate these situations, Exponent conducted tests to investigate the resulting temperature during curing of the RMS with half the nominal ratio of aluminum, and double the amount of hardener. The results indicate that the increased hardener formulation exhibited the same cure temperature as the nominal mixture, 80 °C, which has been deemed stable for processing. The reduced aluminum formulation resulted in a cure temperature of 100 to 115 °C, higher than the nominal mixture but still below the level for stability concerns.

As a final step, Exponent will perform curing tests of the RMS mixture with the tungsten wires in a closed volume of a nominally 1-lb specimen of RMS to simulate the molding step used when fabricating specimens. If temperatures in these tests remain under the critical limits, then work will begin on finalizing the SOP for larger-batch processing.

Section XII

Design of RMS-Cased Penetrating Bombs

This section reports the assessment of the survivability of an RMS-cased penetrating bomb. The EPIC hydrocode was used to simulate RMS-cased bombs penetrating 5-ksi concrete over a range of impact velocities, obliquities, and angle of attacks.

12.1 EPIC Model Calibration and Verification

Section VIII above reviews three computer codes for analyzing bomb penetration into concrete, CTH, ALE-3D and EPIC. While it was noted that each code has advantages and disadvantages regarding concrete penetration, it was determined that EPIC is best suited for modeling penetration depth and casing survivability of RMS-cased penetrators.

To verify the EPIC code model, several calibration simulations were performed. EPIC was used to simulate two existing designs of penetrating bombs impacting concrete at obliquity. One design was a "small"-size penetrating bomb while the second was a large-size bomb. The impact conditions for both bombs were a velocity of 1,350 ft/s with 3° angle of attack (AoA) and 20° obliquity.

The EPIC simulations used a 3D geometry in half-symmetry. The target was modeled using two different computational schemes. The first was the EPIC PENCRV algorithm, where the resistance of the target is determined from an analytical model. The second scheme consisted of modeling the target with a finite-element mesh using element erosion. For both schemes the strength of the concrete was set to 5 ksi.

The initial geometry of the small-sized bomb using the PENCRV algorithm is shown in Fig. 12-1(a) and a plot of the casing strain contours at the final time is presented in Fig. 12-1(b). It can be seen EPIC predicted some bending of the casing with a maximum strain level of about 6%. The calculated penetration depth was 73% of the bomb length.
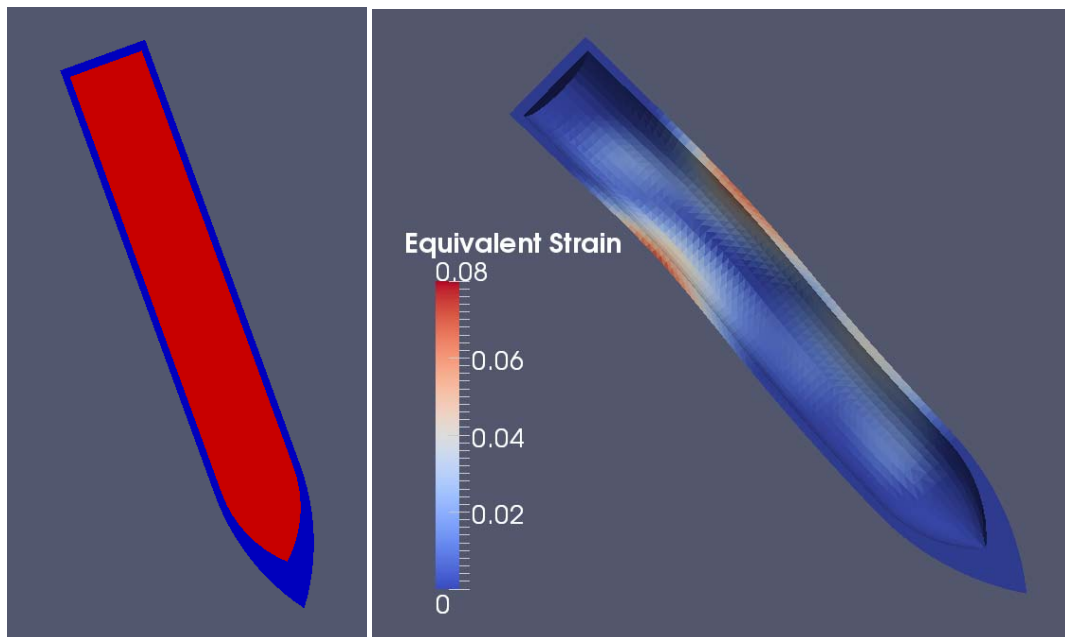
Fig. 12-1. EPIC-PENCRV simulation of small-sized penetrating bomb into concrete: (a) initial geometry plot and (b) final plot of strain contours in casing.

The initial and final plots for the simulation of the large sized bomb using the PENCRV algorithm are presented in Fig. 12-2, which shows more deformation and higher strains than seen in the small-sized bomb. The calculated penetration depth was 86% of the bomb length.
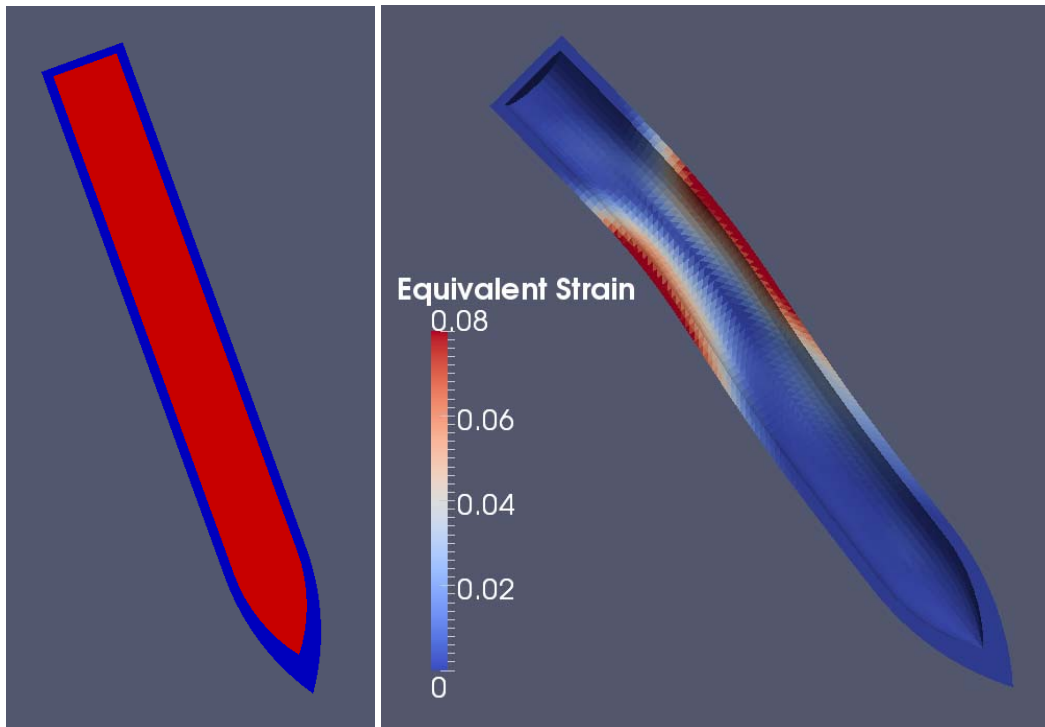
Fig. 12-2. EPIC-PENCRV simulation of large-sized penetrating bomb into concrete: (a) initial geometry plot and (b) final plot of strain contours in casing.

The same configurations were simulated with the finite-element concrete target. Figure 12-3 shows the results for the small-sized bomb. The predicted strain levels were 3-4%, lower than in the PENCRV simulation. The calculated penetration depth was 87% of the penetrator length. Figure 12-4 shows the simulation of the large-sized bomb with the finite element target. The strain levels are 4-5%, again lower than the PENCRV simulation. The calculated penetration depth was 97% of the penetrator length.
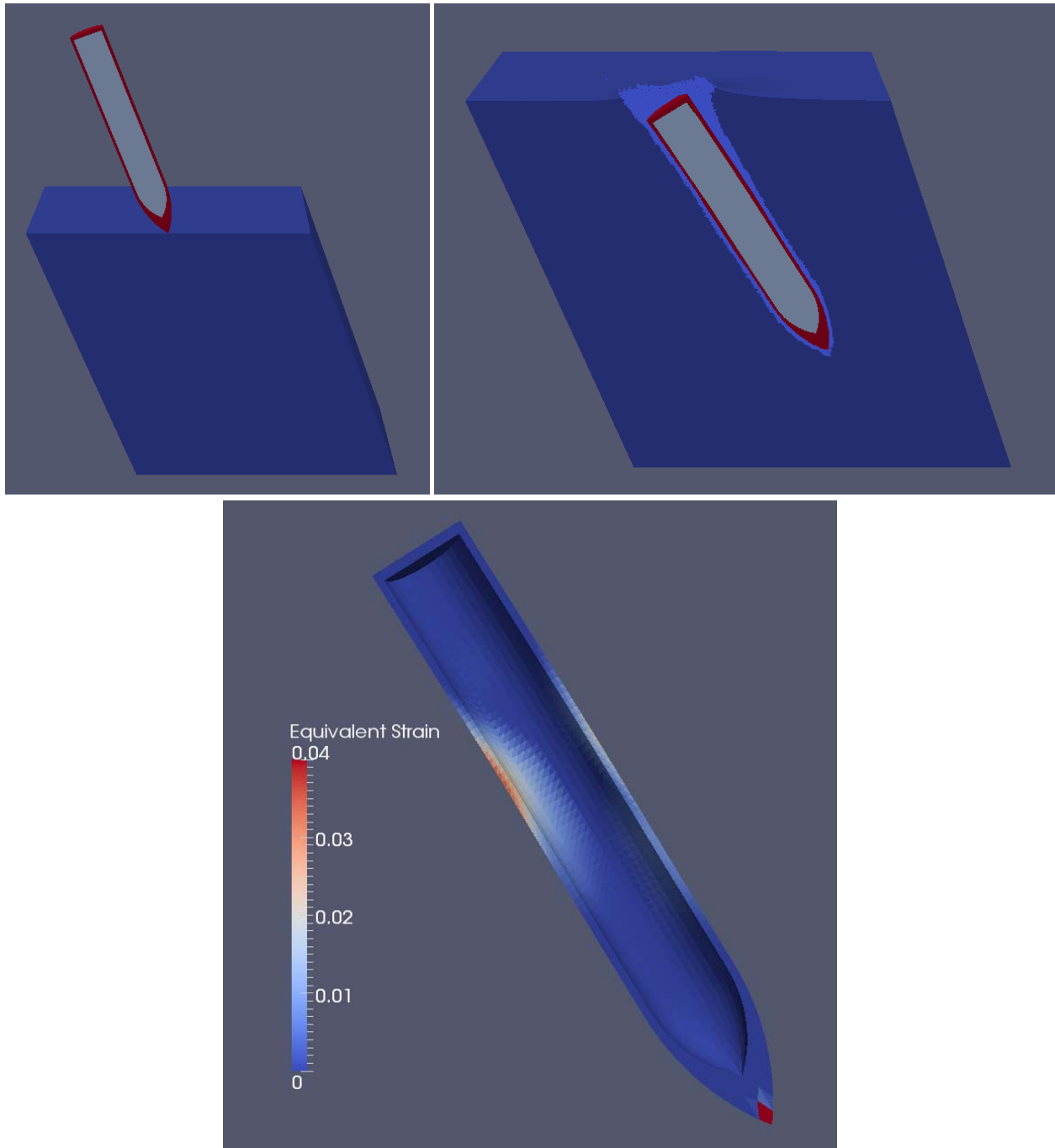
Fig. 12-3. EPIC simulation with finite-element target of small-sized penetrating bomb into concrete: (a) initial geometry, (b) final geometry, and (c) final plot of strain contours in casing.
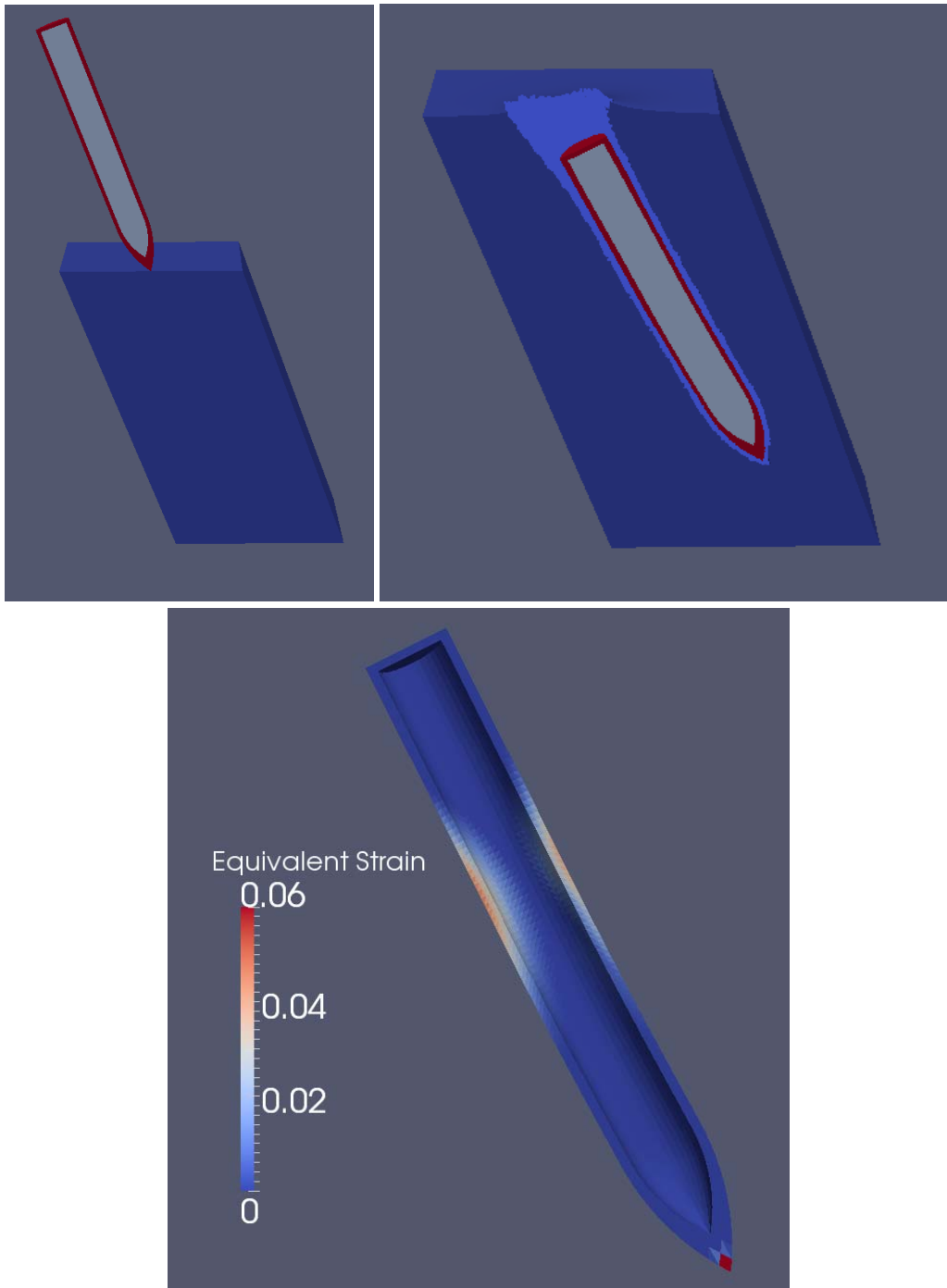
Fig. 12-4. EPIC simulation with finite-element target of large-sized penetrating bomb into concrete: (a) initial geometry, (b) final geometry, and (c) final plot of strain contours in casing.

Of the two approaches, the PENCRV method appears to be a stiffer model of the target than the finite-element target, as evidenced by the larger casing strains. Both models appear to give reasonable results. PENCRV required less computer memory and ran faster than the finite-element model. PENCRV will thus be beneficial in conducting trade studies that involve numerous runs.

12.2 Penetration Trade Studies

12.2.1 Low-velocity Impact

A trade study was conducted to ascertain the survivability of an RMS-encased penetrating bomb. The RMS material has a nominal tensile and compressive strength of 70 ksi, considerably lower strength than the alloy steels currently used for penetrating bomb casings, whose strengths run to 170 ksi and greater.

The RMS bomb designs considered in this study were versions of a scaled 7,000-lb RMS design. The length and outer diameter of the RMS bomb design was reduced but the casing thickness was increased. The high-density RMS enables a more compact bomb design that contains the same amount of chemical energy as larger non-RMS bombs. The mass per unit cross-sectional area of the bomb is increased by reducing the outside diameter while increasing the casing thickness. This results in greater penetration efficiency and enables a lower-mass bomb to achieve the same penetration depth as a larger one. However, the smaller diameter decreases the moment of inertia of the casing, which combined with the lower strength of the RMS material means the RMS casings could be more prone to bending failure.

The RMS bomb designs considered in the trade study are presented in Fig. 12-5 and Table 12-1 in addition to the large bomb design. The relative penetration is from a 2-D EPIC computer code simulation with a velocity of 1,000 ft/s at normal impact. All designs have the same theoretical blast energy and achieved penetration depths within 13% of the large bomb.

Large Bomb

M/C 6

M/C 9

M/C 12
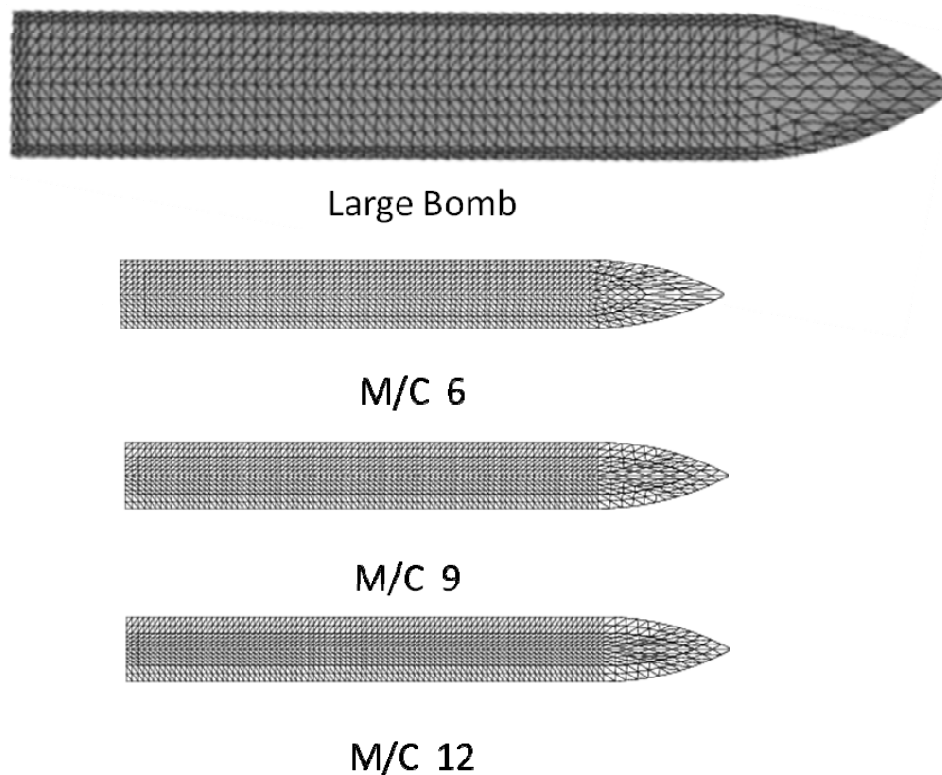
Fig. 12-5. EPIC finite-element models of the large bomb and the 7,000-lb RMS designs with M/C of 6, 9, and 12.

Table 12-1. Bomb Designs and Penetration Depths for a Velocity of 1,000 ft/s at Normal Impact.

Effective M/C	OD (in)	T$_{wall}$ (in)	Relative penetration	Mass (lb)
Bomb B	31.50	3.50	$\equiv 1$	--
6	17.74	3.13	0.872	6943
9	16.91	3.64	*0.930*	6868
12	16.42	3.98	0.975	6876

EPIC was used to simulate the penetration and casing response of the RMS bombs. Since this study included impact conditions with obliquity, the simulations were done using a 3-D model. The concrete target was modeled using the fast-running PENCRV3D algorithm. The concrete's strength was set to 5 ksi.

The RMS material was modeled using the Johnson-Cook (J-C) strength model for 1006 steel. A comparison of tensile strength between the J-C strength model and the RMS measured tensile strength is shown in Fig. 12-6. Maximum tensile strength of the J-C model is 68 ksi, slightly less than the nominal 70-ksi tensile/compressive strength of the RMS material.
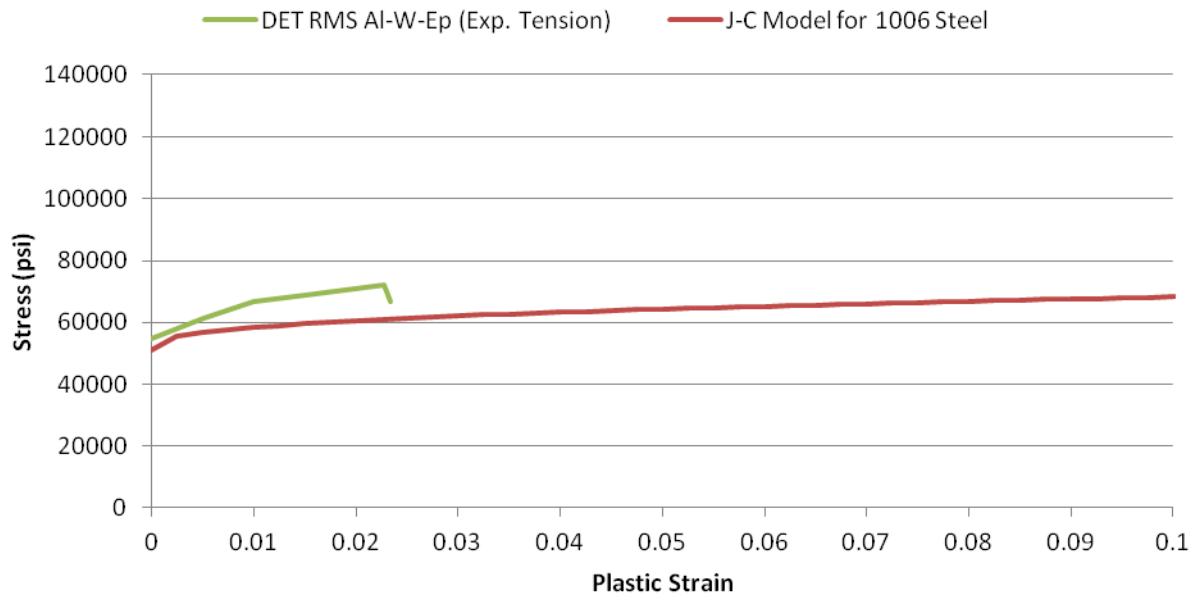
Fig. 12-6. Comparison between Johnson-Cook strength model for 1006 steel used in EPIC and measured tensile behavior of the RMS.

EPIC-PENCRV3D was used to simulate penetration into concrete of the 7,000-lb RMS configurations with M/C of 6, 9, and 12. Simulations covered a range of impact velocities, obliquities, and angles of attack (AoA). Velocities ranged from 1,000 to 1,400 ft/s in 100-ft/s increments; obliquity ranged from 0° to 20° in 5° increments; and AoA ranged from 0° to 3° in 1° increments. Each casing configuration was simulated at 5 velocities, 5 obliquities, and 4 AoA's, for a total of 100 simulations for each of the three configurations.

The RMS configurations were modeled using the finite-element grids shown in Fig. 12-5 above. For all three designs, the length of the ogival nose was twice the diameter of the cylindrical section. The simulation of each configuration was terminated when the maximum penetration depth was reached. Predicted strains in the casing were then assessed in addition to the degree of bending that occurred during penetration. It was found that excessive bending occurred when a significant amount of the casing experienced strains larger than 6%.

Figure 12-7 is a plot of the percentage of the M/C 6 casing with strain greater than 6% versus impact velocity for obliquities from 0° to 20°, with 0° AoA. The data show the percentage of the casing with strain greater than 6% remains low for obliquities from 0° to 10° across the velocity range. The strain is significantly higher for the 15° and 20° obliquities. Figure 12-8 is a plot of the same data for the M/C 6 configuration with 3° AoA. The data show a large increase in strain for the 3° AoA.
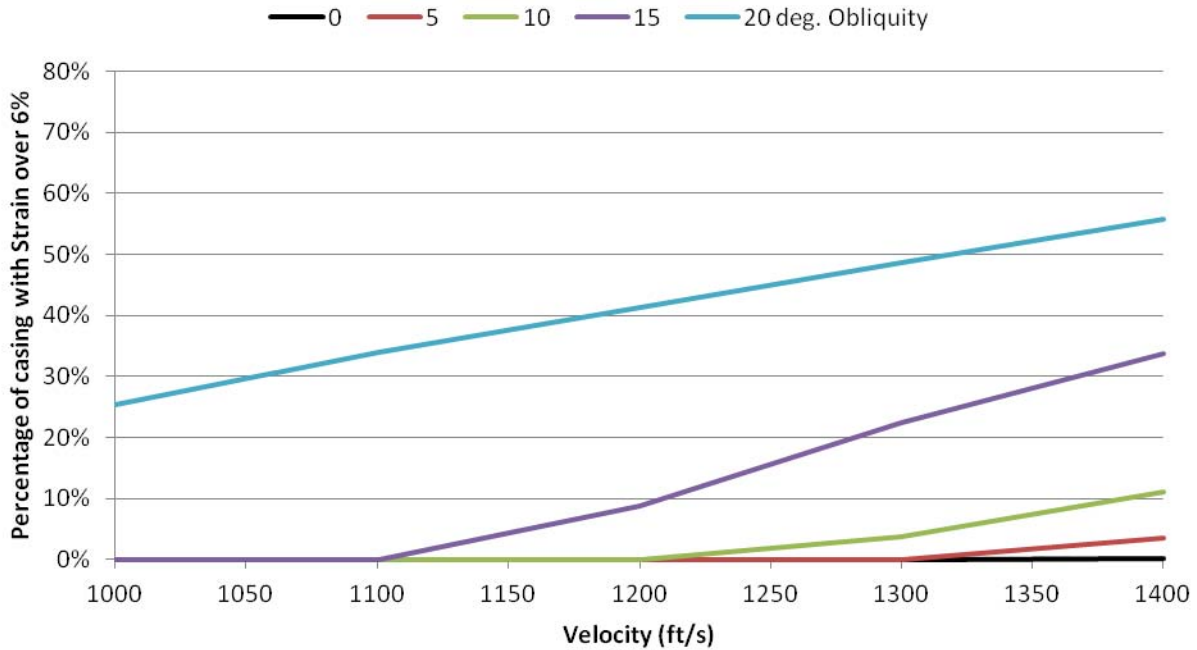
Fig. 12-7. Plot of percentage of casing with strain greater than 6% versus impact velocity for the M/C = 6 configuration at obliquities of 0° to 20° and 0° AoA.
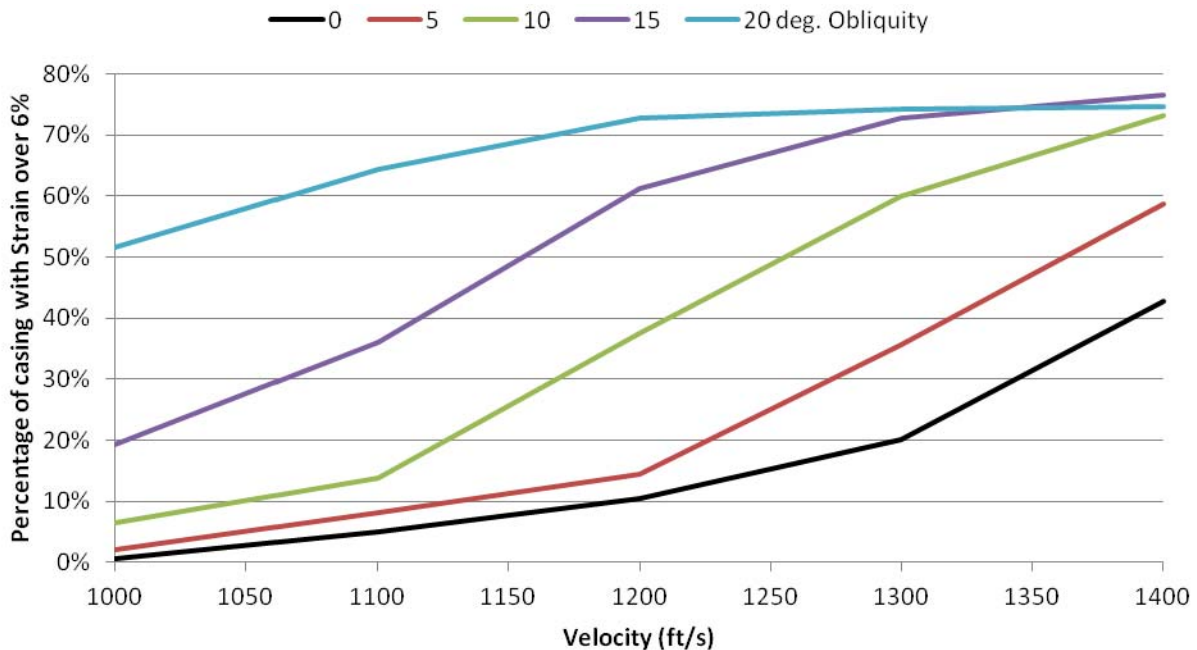
Fig. 12-8. Plot of percentage of casing with strain greater than 6% versus impact velocity for the M/C = 6 configuration at obliquities of 0° to 20° and 3° AoA.

Similar plots were generated for each AoA and M/C configuration. To assist in assessing casing survivability, a simple strain-based criterion was employed where survivability is defined if 95% of the total casing volume experiences less than 6% plastic strain. That is, a casing does not survive if more than 5% of its total volume experiences strain greater than 6%.

Applying the above survivability data to the EPIC-calculated strains enables the definition of impact conditions for survivability. These regions are depicted graphically for each M/C configuration in Figs. 12-9, 12-10, and 12-11. The graphs show a general increase in survivability as M/C increases from 6 to 12. However, none of the configurations survive the 20° obliquity at any velocity or AoA. In addition, all three configurations survive 3° AoA only at the lowest velocity of 1,000 ft/s.
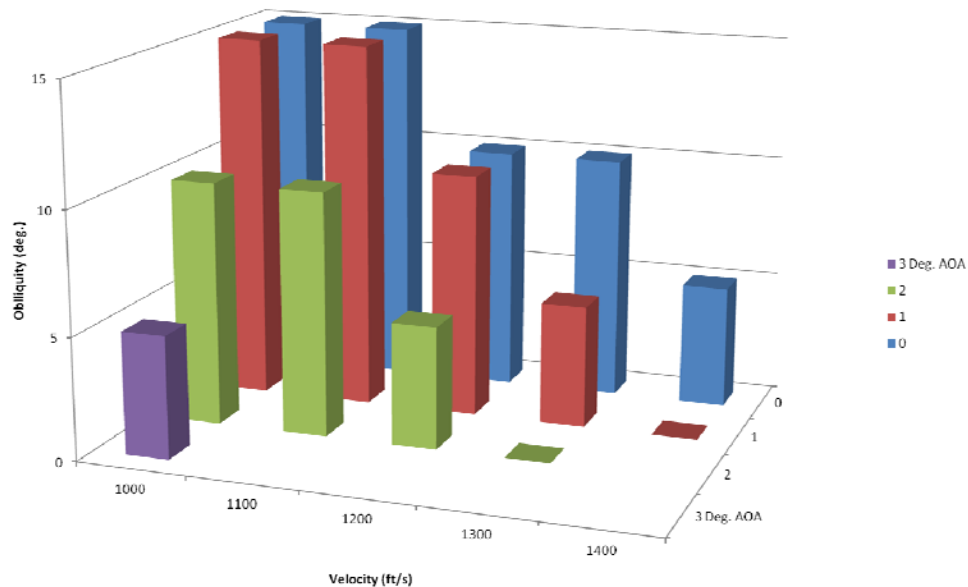
Fig. 12-9. Predicted survivable impact conditions for M/C = 6 RMS casing.
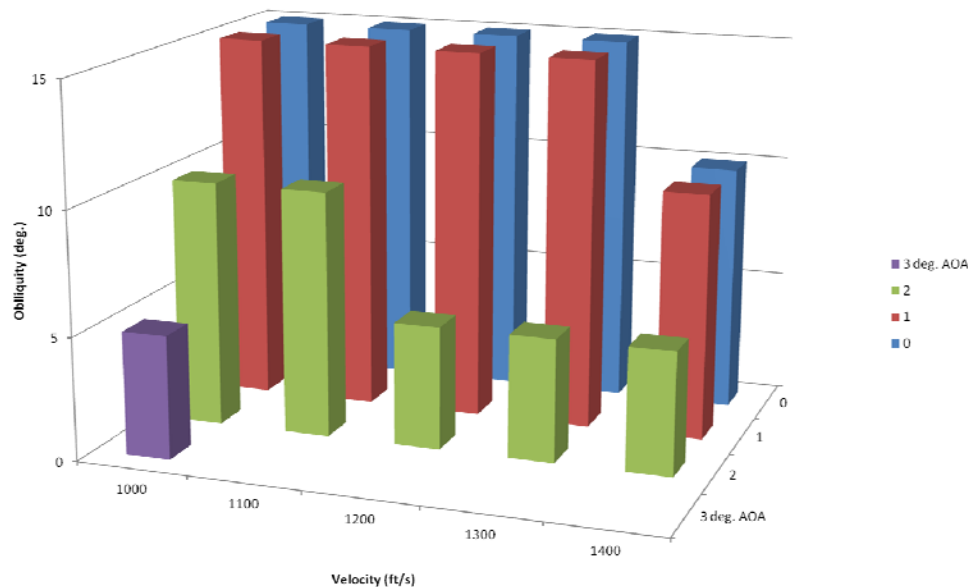
Fig. 12-10. Predicted survivable impact conditions for M/C = 9 RMS casing.
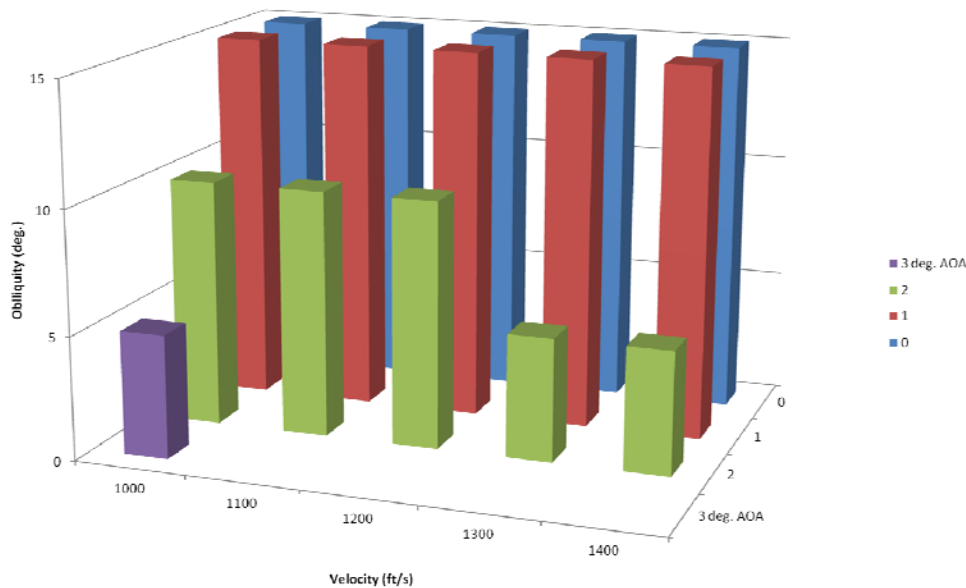
Fig. 12-11. Predicted survivable impact conditions for M/C 12 = RMS casing.

The above analysis shows an RMS bomb casing can survive over a reasonable range of impact conditions consisting of: impact velocity up to 1,200 ft/s; obliquities of 0° to 15°; and AoA of 0° to 2°. While the above plots indicate that at 1,000 ft/s and obliquities less than 5° the RMS casings survive 3° AoA, there appears to be excessive bending of the rear of the projectile under these conditions and therefore survivability is deemed marginal. This is true also for velocities greater than 1,200 ft/s.

12.2.2 High-Velocity Impact

The application of RMS in high-speed penetrating bombs was analyzed with EPIC. Simulations were performed of RMS-cased bombs penetrating concrete at speeds of 1,400 to 2,400 ft/s. The bomb configurations simulated were 2,000-lb RMS configurations with L/D of 10 and M/C of 6, 9, and 12. The simulations were performed for normal impact (0° obliquity and 0° angle of attack). EPIC-PENCRV-calculated plastic strains are shown for the three configurations over a range of velocities in Figs. 12-12, 12-13, and 12-14. High levels of strain occur in all three configurations at velocities above 1,600 ft/s. Generally the M/C 9 and M/C 12 configurations experienced lower strains; however, the simulations indicate these configurations would also fail. Consequently the RMS casings will need to be strengthened in order to survive these higher velocities.
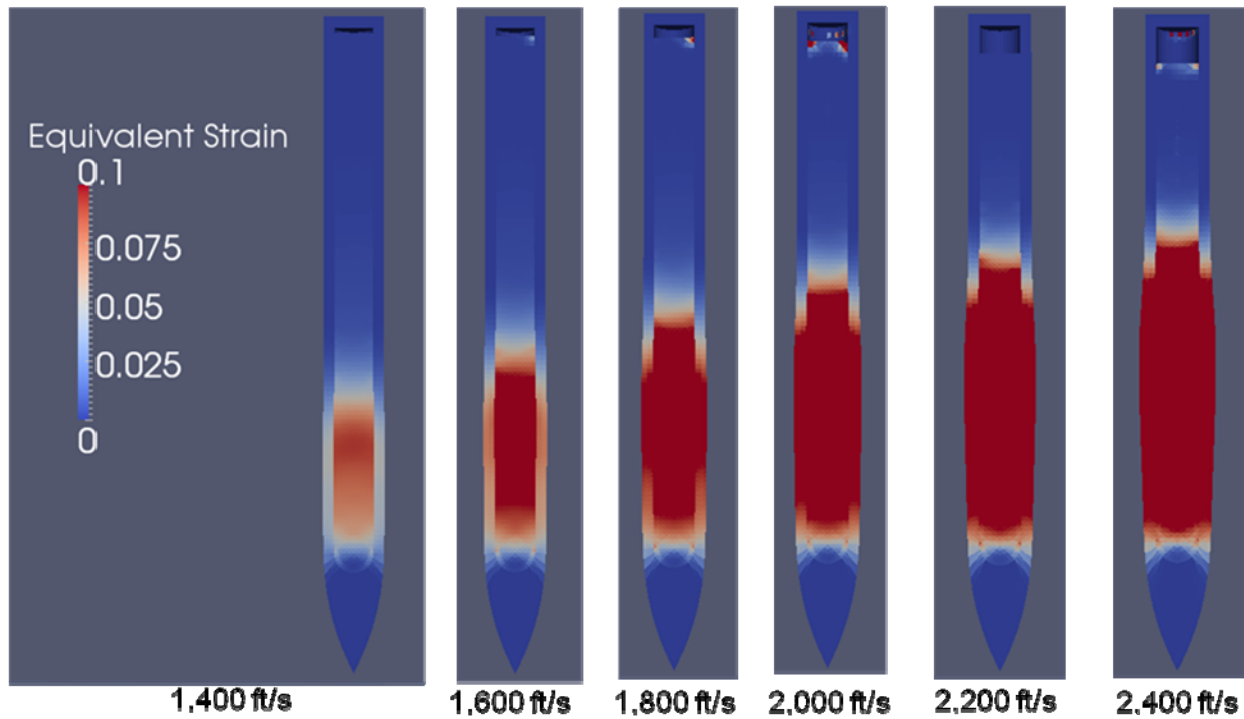
Fig. 12-12. Contours of equivalent plastic strain calculated by EPIC of an M/C = 6 RMS-cased bomb pene-
trating concrete at velocities from 1,400 to 2,400 ft/s.
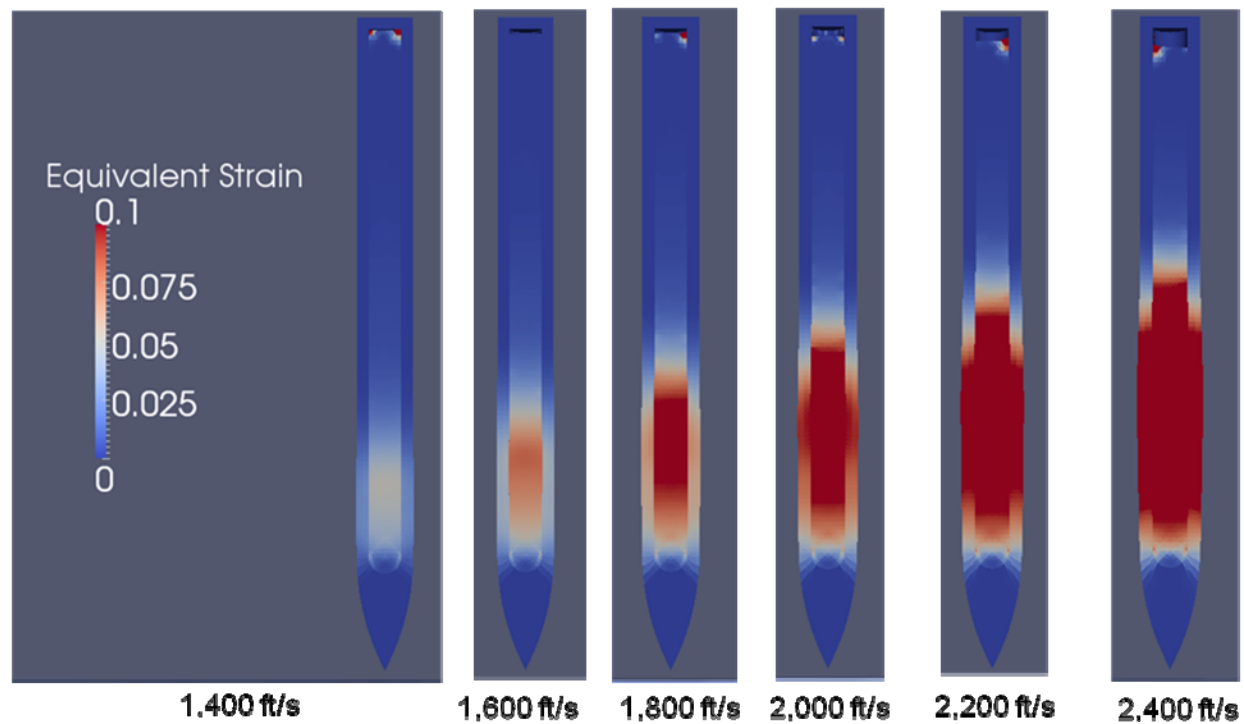
Fig. 12-13. Contours of equivalent plastic strain calculated by EPIC of an M/C = 9 RMS-cased bomb pene-
trating concrete at velocities from 1,400 to 2,400 ft/s.
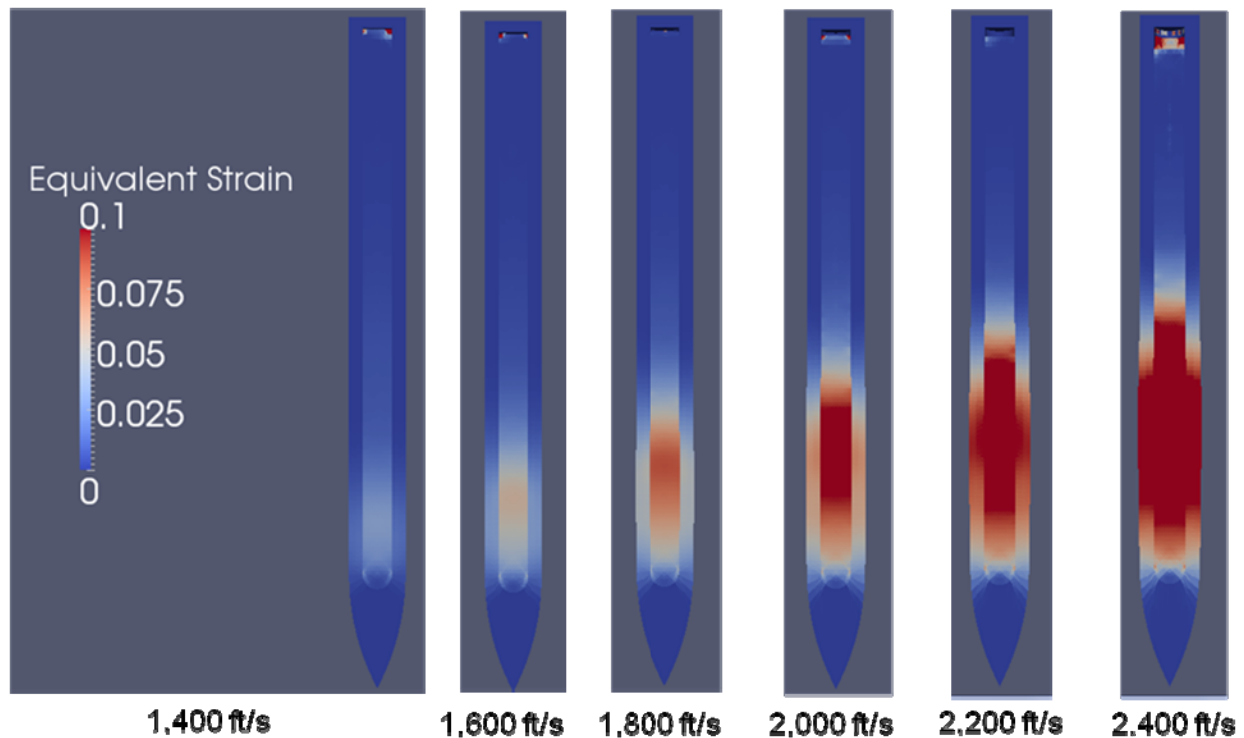
Fig. 12-14. Contours of equivalent plastic strain calculated by EPIC of an M/C = 12 RMS-cased bomb penetrating concrete at velocities from 1,400 to 2,400 ft/s.

The inclusion of an external steel sleeve around the RMS bomb was analyzed for improving the high-speed survivability of the RMS penetrating bomb. A series of EPIC simulations of the RMS penetrating bomb with an external steel sleeve were performed. Figure 12-15 is a drawing of this design, which incorporates a 1/2-inch-thick steel sleeve with an M/C 9 RM casing. (M is the mass of the RM casing not including the steel sleeve) The sleeve covers the full length of the cylindrical section of the bomb.
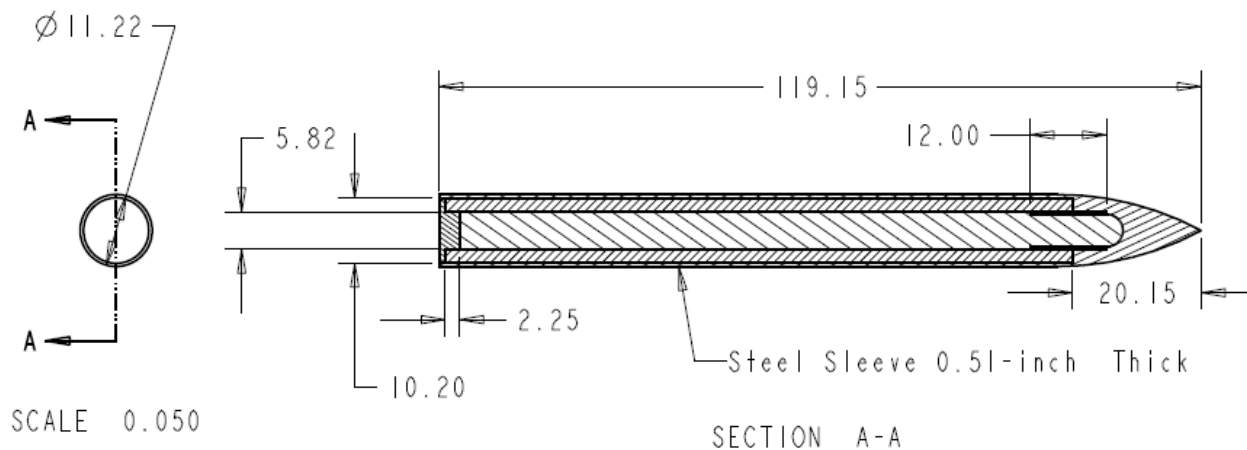
Fig. 12-15. Penetrating bomb design with external steel sleeve.

EPIC was used to simulate the new internal sleeve design for velocities ranging from 1,400 to 2,400 ft/s for obliquities of 0°, 5°, and 10° and AoA of 0° and 1°. Plots of calculated plastic strain are presented in Figs. 12-16 through 12-21. Figures 12-16, 12-17, and 12-18 are from simulations at obliquities of 0°, 5°, and 10° respectively, all at 0° AoA. The contour plots show the external sleeve experiences minimal

strain, although the RMS casing does exhibit significant strain. Very little deformation is observed in the bomb over the velocity and obliquity ranges at 0° AoA.
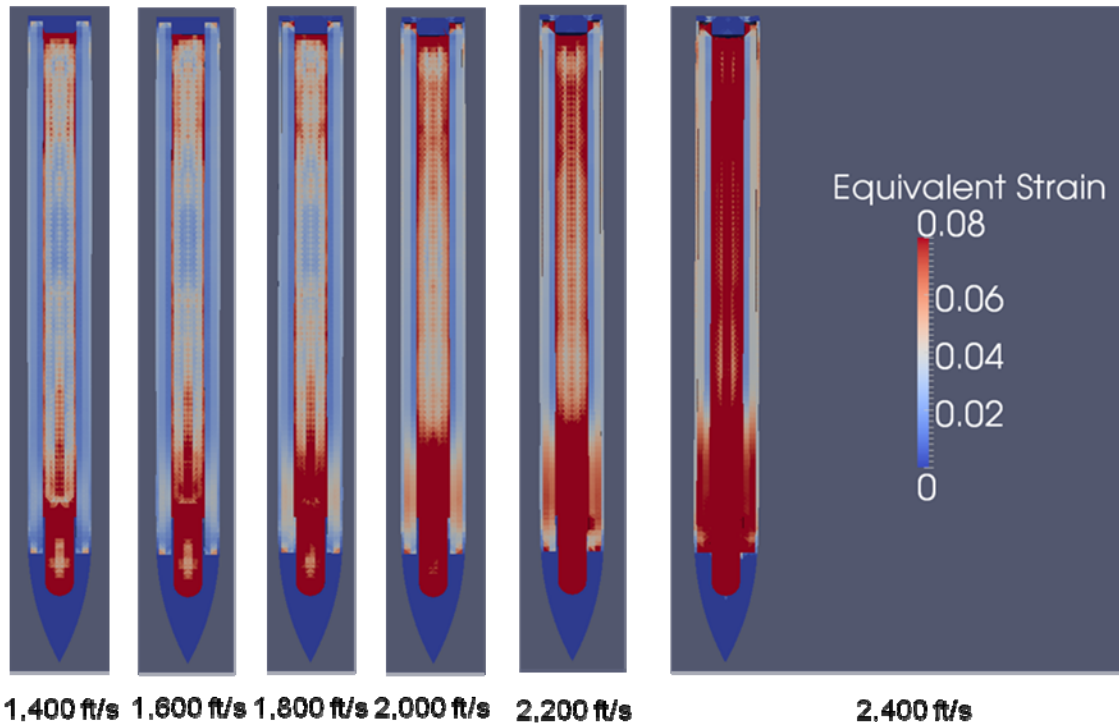
Fig. 12-16. Contours of equivalent plastic strain calculated by EPIC of an M/C = 9 RMS-cased bomb with external steel sleeve penetrating concrete at 1,400 to 2,400 ft/s, 0° obliquity, 0° AoA.
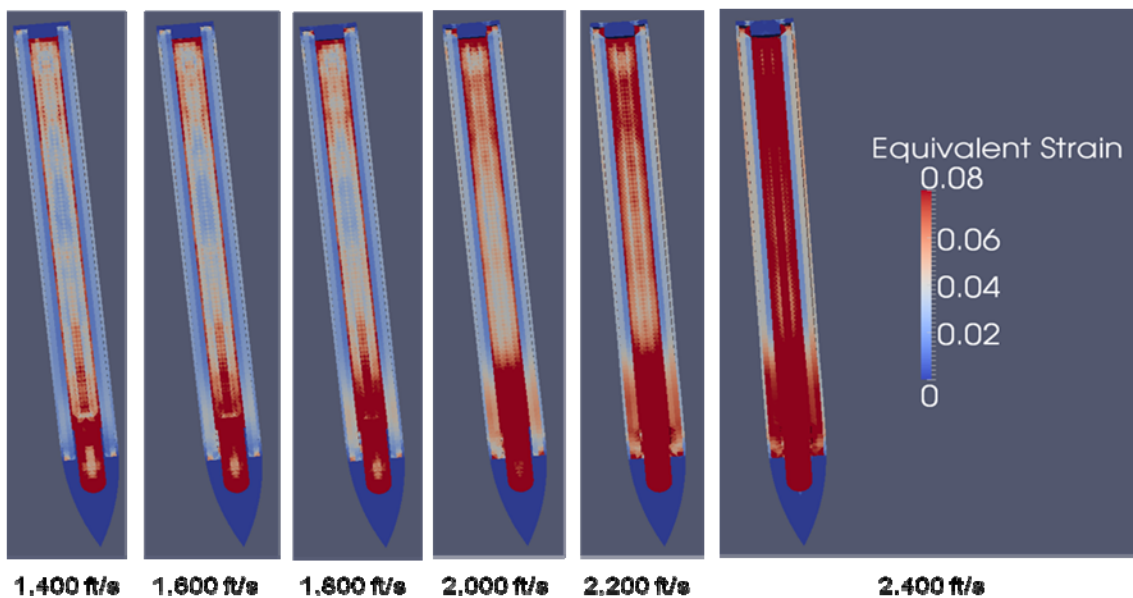
Fig. 12-17. Contours of equivalent plastic strain calculated by EPIC of an M/C = 9 RMS-cased bomb with external steel sleeve penetrating concrete at 1,400 to 2,400 ft/s, 5° obliquity, 0° AoA.
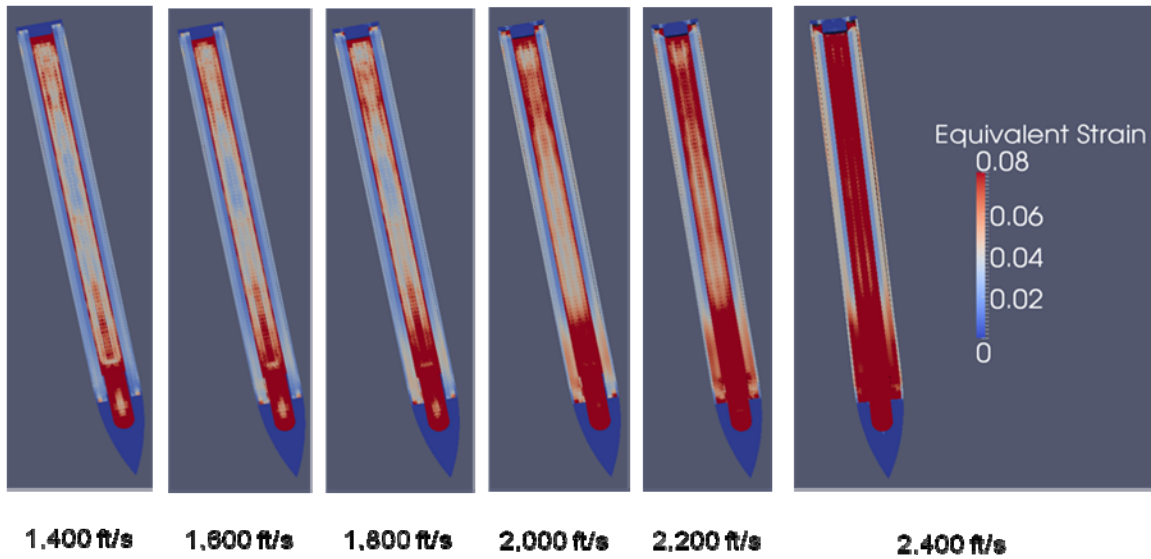
Fig. 12-18. Contours of equivalent plastic strain calculated by EPIC of an M/C = 9 RMS-cased bomb with external steel sleeve penetrating concrete at 1,400 to 2,400 ft/s, 10° obliquity, 0° AoA.

Figures 12-19, 12-20, and 12-21 show simulations with 1° AoA at obliquities of 0°, 5°, and 10°, respectively. These plots show high levels of strain in the external sleeve near the tail of the bomb. In addition the tail is bending in a typical tail-whip fashion. The external sleeve improved the survivability of the RMS bomb at 0° AoA. However, at 1° AoA, significant tail whip is observed. Efforts will continue to analyze reinforcement options.
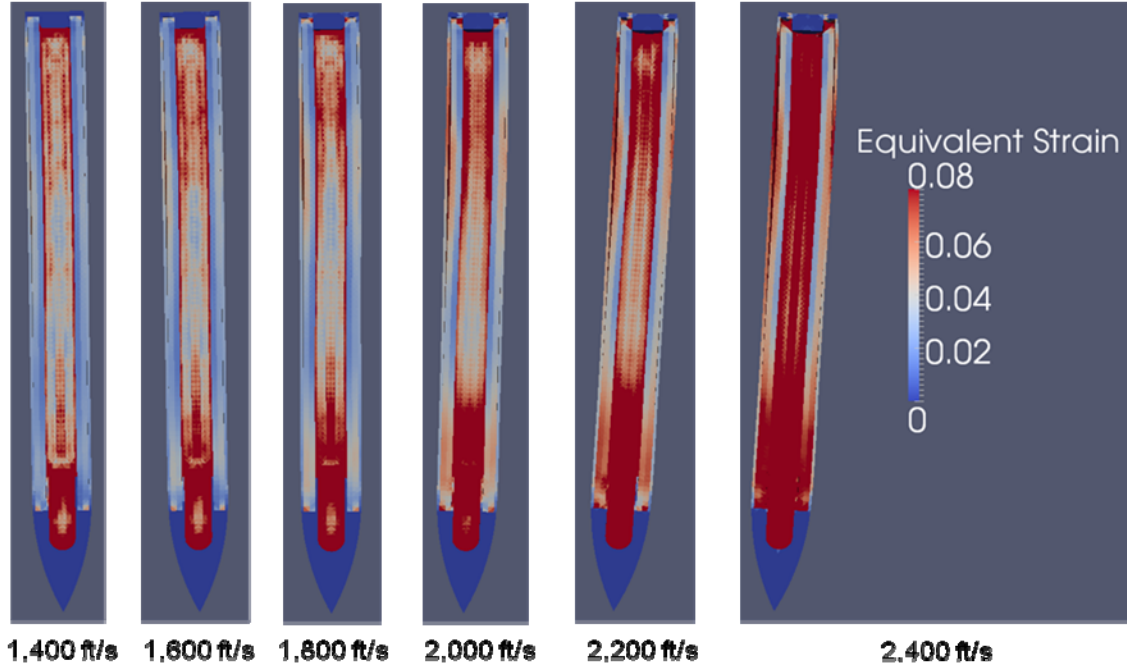
Fig. 12-19. Contours of equivalent plastic strain calculated by EPIC of an M/C = 9 RMS-cased bomb with external steel sleeve penetrating concrete at 1,400 to 2,400 ft/s, 0° obliquity, 1° AoA.
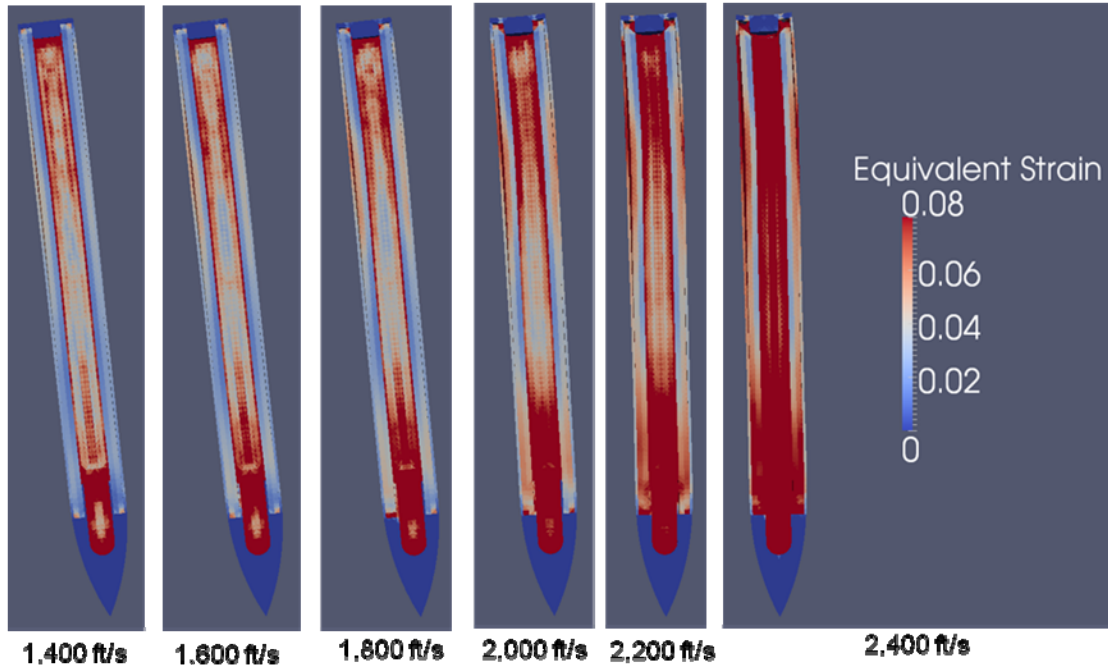
Fig. 12-20. Contours of equivalent plastic strain calculated by EPIC of an M/C = 9 RMS-cased bomb with external steel sleeve penetrating concrete at 1,400 to 2,400 ft/s, 5° obliquity, 1° AoA.
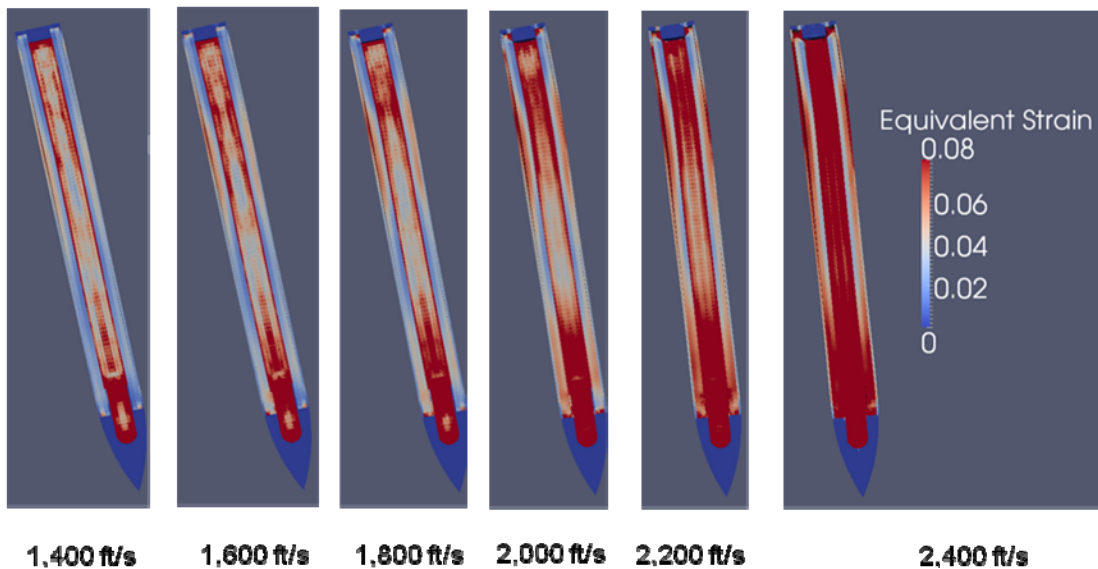
Fig. 12-21. Contours of equivalent plastic strain calculated by EPIC of an M/C = 9 RMS-cased bomb with external steel sleeve penetrating concrete at 1,400 to 2,400 ft/s, 10° obliquity, 1° AoA.

12.2.3 Summary

The analysis shows the RMS bomb has the potential to survive concrete penetration. At velocities under 1,400 ft/s, the RMS bomb can survive over a range of obliquities and AoA. At velocities above 1,400 ft/s, the RM casing experiences significant swelling even at 0° obliquity and 0° AoA. The addition of an external, ½-inch-thick, steel sleeve improves the survivability of the RMS significantly. The EPIC simulations show that the RMS bomb can survive at velocities up 2,400 ft/s and obliquities up to 10°. However the RMS bomb experiences significant tail whip at all velocities at an AoA of only 1°.

12.3 Interface Design and Compression/Tension Testing

This section describes the design and testing of the interface configurations for the RMS penetrator to be used in the concrete penetration tests. The RMS has a strength of about 90 ksi, stronger than mild steel, but it lacks the hardness to withstand the erosion that occurs at the nose of a penetrator impacting concrete. Therefore, an RMS penetrator will need a nose or protective covering of a hard, erosion-resistant material. Moreover, penetrating munitions have fuses and guidance-and-control packages that must be attached to the casing. These attachments require threaded interfaces and lugs that are impractical to fabricate in composites. Therefore the RMS penetrator design will most likely require metallic attachment points on the aft end as well.

The notional penetrator design, shown in Fig. 12-22, consists of a steel nose, RMS body, and steel aft closure. The steel is 4340 grade hardened to Rockwell C42 with a 175-ksi yield strength and 190-ksi ultimate strength. Computer simulations shown in Section VIII predict the penetrator should survive concrete impact at velocities up to 1,400 ft/s. These simulations focused on survival of the RMS casing, and the behavior of the interfaces between the nose, aft closure, and RMS casing was not analyzed. Instead these interfaces were modeled using non-physical numerical schemes that treat the interfaces as inseparably tied together. This simplified treatment allowed the computer simulations to assess the overall response of the RMS.
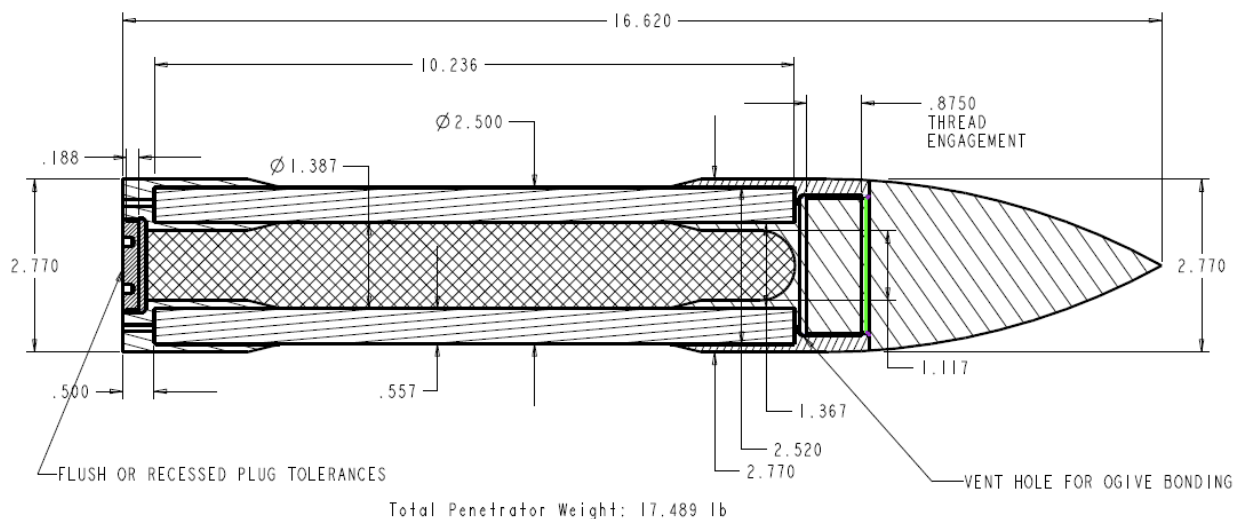
Fig. 12-22. Notional RMS penetrator design.

Simulating the detailed interface response would require a high-fidelity computational mesh with sufficient resolution to capture the details of the complicated stress and strain fields around the various features such as threaded holes, fasteners, and adhesive joints. Such simulations are useful in the last stage of design optimization where test data and material models have been obtained and verified. This is not the case in this program as it is the first dynamic test of the material. Material models and test data do not yet exist for this type of analysis.

In lieu of the high-fidelity FEA simulations, the interface was designed through basic engineering principles, drawing on the team's experience and background. Computer simulations were used to provide estimates of loading levels. These loads were then applied to the joint design using material-mechanics principles. The final designs were then statically tested to verify their predicted strengths. The design and testing results are described below.

12.3.1 Interface Design and Supporting Analysis

The first step in designing the interfaces was to estimate the expected loads. Current performance goals are to penetrate concrete at velocities of 1,000 to 1,400 ft/s, with no angle of attack or obliquity. Eliminating angle of attack and obliquity allows the simplification that the loads are axial. In the tests the penetrators will be gun-launched. Therefore each test imparts four phases of loading: 1) a compressive acceleration during gun launch, 2) a tensile unloading on exit from the barrel, 3) a compressive deceleration during impact with the concrete, 4) a tensile unloading after penetration.

Of the compressive loads, the impact load is expected to be much larger than the gun-launch load. Analytical models and FEA simulations predict a 25,000-G peak deceleration from impact. From the load curves for the gun, the peak acceleration is estimated as 5,000 G. Both loads result in compression of the penetrator, but they have opposite senses. In penetration, the decelerative force acts on the front of the penetrator, and the compressive load is generated by its inertia and is maximum near the front interface between the nose and RMS casing. The force of the launch acts on the rear of the penetrator, and the inertia of the penetrator results in a maximum force at the rear interface.

Given the above acceleration and deceleration, the compressive loads can be estimated. For gun launch, the 5,000-G acceleration results in an inertia load of 87,000 lb at the aft interface. This force is due to the inertia of the nose, RMS casing, and explosive fill (total mass of 17.4 lb). During penetration, the peak 25,000-G deceleration results in an inertial force at the forward interface of 293,500 lb. This force is due to the inertia of the casing, explosive fill, and aft closure (total mass of 11.74 lb).

The forward and aft interface designs shown in Fig. 12-22 above are based on interfaces that had been used to attach the steel end caps to the RMS tubes for compression testing. The test interfaces consisted of a butt joint between the end of the RMS casing and a steel shoulder in addition to an inner steel plug and outer steel collar. The steel parts were glued to the tube. The butt joint between the tube and the steel shoulder bore most of the compressive load, with the inner and outer steel supports preventing mushrooming of the tube. The interfaces withstood compressive loads over 300,000 lb in the tests.

Estimating the tensile loads is a bit more complex. The tensile loads arise within the penetrator on the release of the compressive loads. Their magnitudes depend on the magnitudes of the compressive loads and the dynamics of their release. Since the compressive forces from impact are greater than from the gun launch, only the tensile loads arising from impact were considered in the analysis.

Tensile loads arise at the end of the penetration event. In elastic impact without penetrating the target, all the projectile's kinetic energy is returned back into the projectile by the target, resulting in the projectile bouncing off the target at a velocity equal to the impact velocity. In this case the tensile forces have the same magnitude as the compressive forces. When an elastic projectile penetrates a target, the target consumes much of the penetrator energy, but the elastic projectile also stores some of the impact energy like a compressed spring. Once the compressive loads are removed, the penetrator decompresses and the stored energy converts to kinetic energy resulting in accelerations and inertial loads.

Materials Research & Design, Inc. (MR&D) performed a series of ABAQUS simulations of penetration events in order to estimate the tensile loads. Three targets were modeled: semi-infinite concrete; a 25-inch-thick concrete slab; and a 10-inch-thick concrete slab.

For a semi-infinite target, velocities of 900, 1,200, and 1,600 ft/s were modeled. The 900 and 1,200 ft/s simulations were based on a 25-lb penetrator (an early design) at 0° angle of attack. The 1,200-ft/s simulation was done with an 18-lb penetrator (a more recent design) at 2° angle of attack. The axial normal stresses in the penetrator were recorded at the forward, mid, and aft locations along the penetrator body, shown in Fig. 12-23. The plots show a maximum tensile stress of 4 ksi, which translates to a 13,600-lb tensile force across the interfaces.
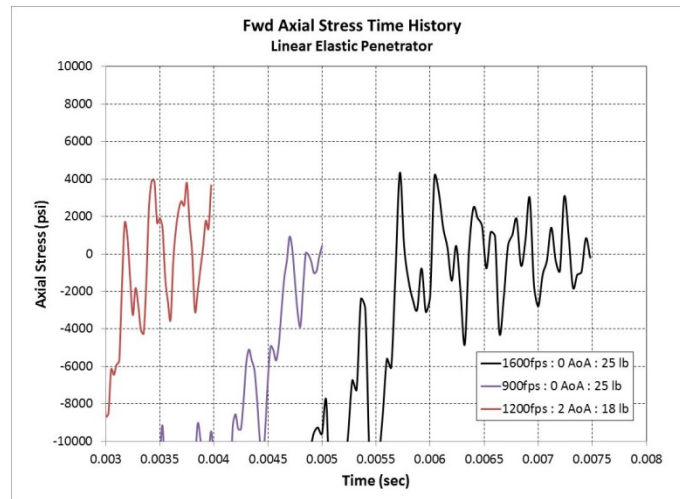
a) Forward location
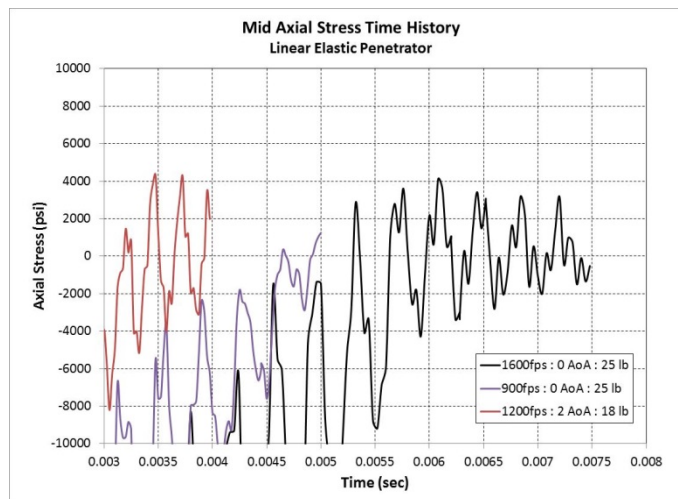
b) Middle location
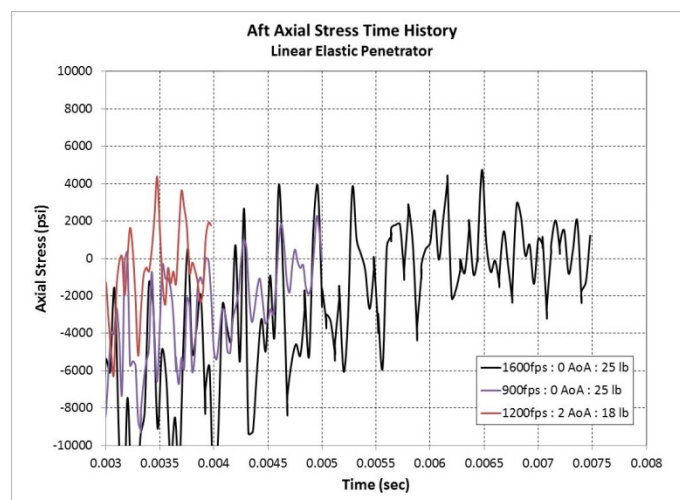
c) Aft location

Fig. 12-23. ABAQUS-calculated axial stress histories for the RMS penetrator penetrating semi-infinite concrete.

ABAQUS was also used to simulate penetration into a 25-inch-thick target. The impact was at 1,500 ft/s with zero angle of attack. ABAQUS predicted the acceleration histories at the forward and aft interfaces, which are plotted in Fig. 12-24. In this plot deceleration is positive (compression) and acceleration is negative (tension). The plot shows the minimum acceleration of −1,000 G occurs at the aft interface at 0.0022 sec. If this acceleration is assumed to occur at both the nose and aft interface, given the nose mass of 7.5 lb and aft closure mass of 2.14 lb, the resulting tensile forces are 7,500 and 2,140 lb, respectively.
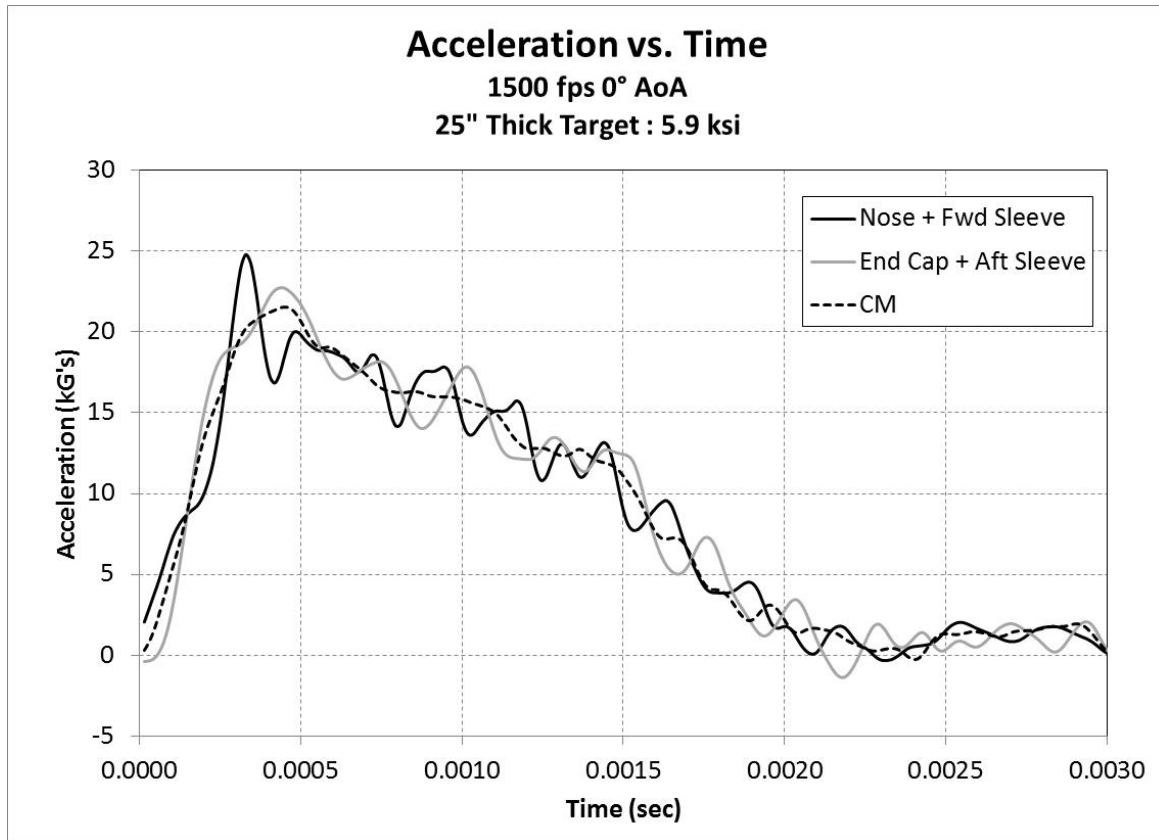
Fig. 12-24. ABAQUS-calculated acceleration history of RMS penetrator impacting a 25-inch-thick concrete target at 1,500 ft/s.

A similar ABAQUS analysis was done for a 10-inch-thick concrete target. The acceleration history is shown in Fig. 12-25. As above, deceleration is positive (compression) and acceleration is negative (tension). The minimum acceleration at the forward interface is 4,000 G and occurs at 0.012 sec. The minimum acceleration at the aft interface is −5,000 G at 0.00109 sec. These accelerations produce a 30,000-lb force at the nose and a 10,700-lb force at the aft interface.
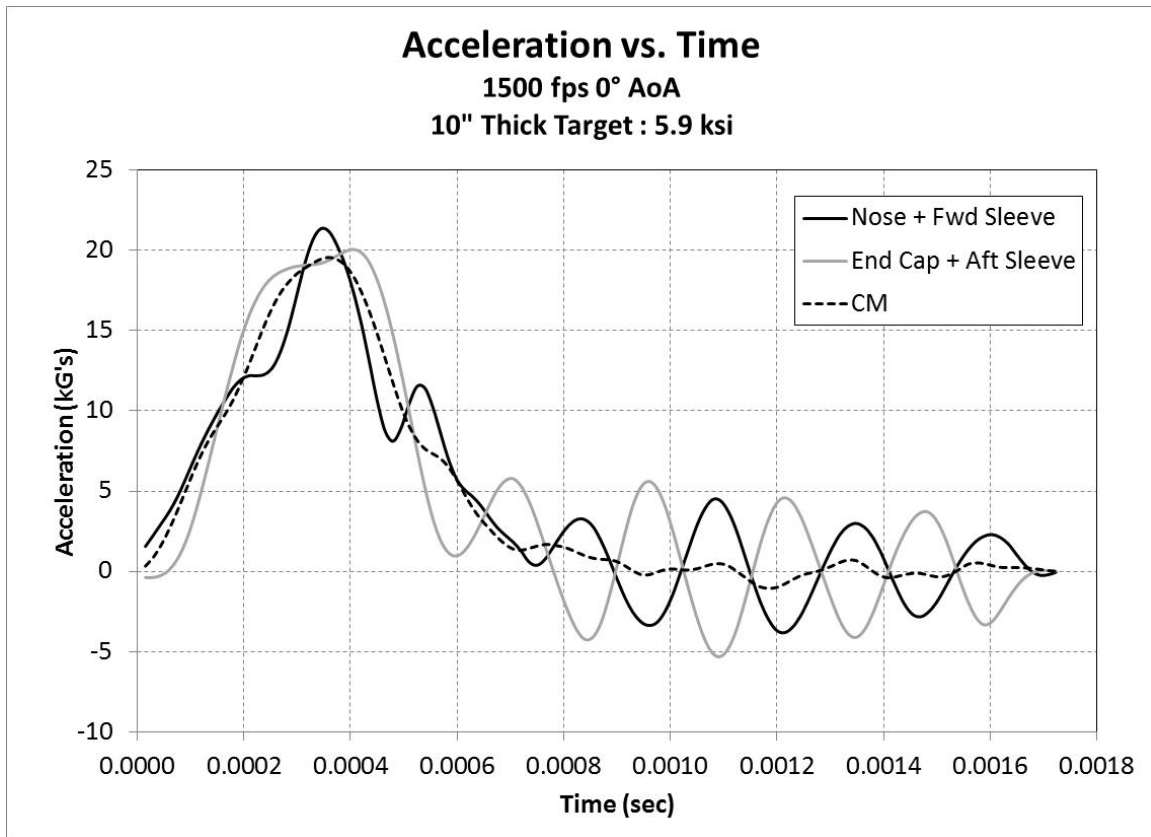
Fig. 12-25. ABAQUS-calculated acceleration history of RMS penetrator impacting a 10-inch-thick concrete target at 1,500 ft/s.

The calculated tensile forces are summarized in Table 12-2. The maximum estimated tensile load is 30,000 lb. The largest tensile load occurs when impacting the thinnest of the three targets. This load was taken as the minimum requirement for the interface design.

Table 12-2. Summary of calculated tensile loads along front and aft interfaces.

Analysis	Forward tensile load (lb)	Aft tensile load (lb)
Semi-Infinite Concrete Target	13,600	13,600
Finite Concrete Target 25-inch Thickness	7,500	2,140
Finite Concrete Target 10-inch Thickness	30,000	10,700

The baseline interface designs shown above in Fig. 12-22 were bonded with adhesive. As discussed above, since the interfaces are basically butt joints, the adhesive do not contribute to their compressive strength but is relied on only for tensile strength. Given the adhesive's shear strength of 5,000 psi and the surface area of the bond, the total strength of the adhesive-only joint would be over 78,000 lb, well above the design minimum of 30,000 lb. However, even though the adhesive does not directly support the compressive load, it is still subjected to loading during compression, because of the different elastic moduli of the steel, 30 Msi, and RMS, 15 Msi. Under compression, the RMS displaces more than the steel, which generates a large shearing in the adhesive that precipitates failure in the bond. This happens on launch and again during penetration, with the result that the adhesive is not at full strength for the tensile loads.

Based on the above, it was decided to incorporate a mechanical connection into the interface. Since the RMS is a composite, cutting threads into it is not feasible. Instead, a pattern of eight steel pins was adopted, shown in Fig. 12-26. The interface consists of eight 5/16-inch-diameter threaded studs, arranged in two rows offset by 45°. The holes in the RMS to accommodate the studs are slotted to prevent the studs from being subjected to compressive loads. The slots provide clearance to allow the RMS to compress without contacting the studs. This ensures the studs retain full strength for the tensile loads.
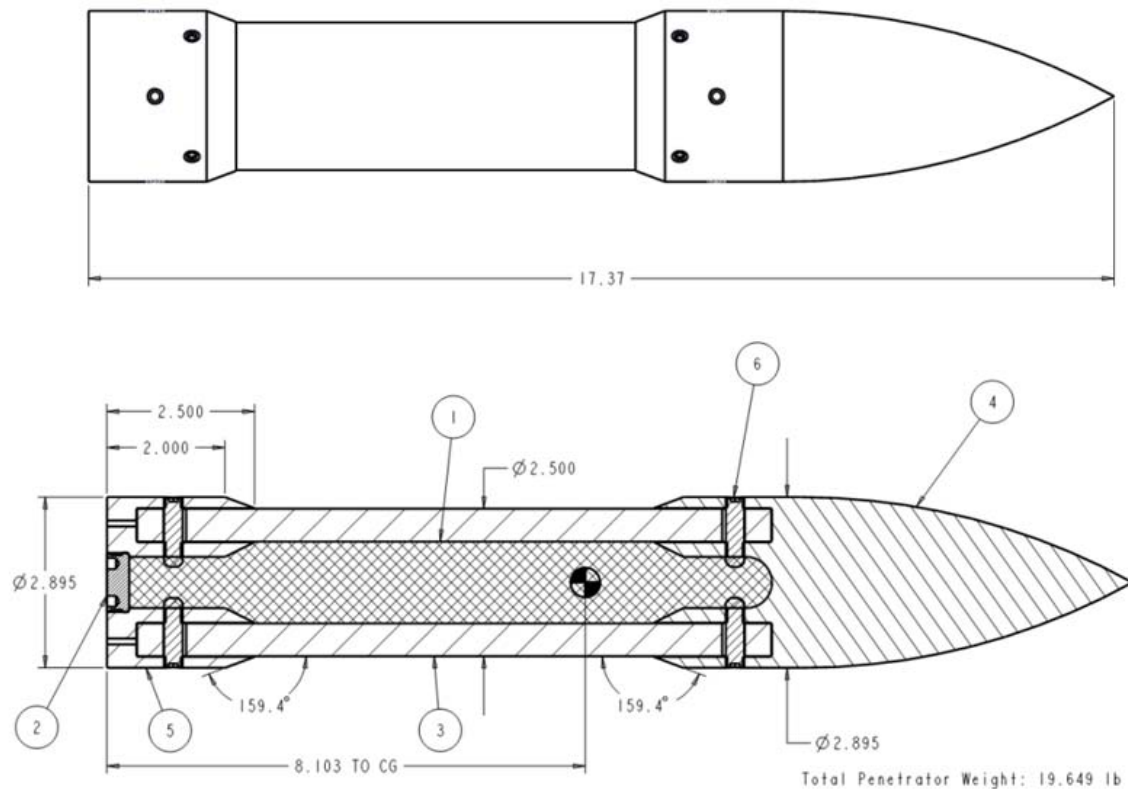
Fig. 12-26. RMS penetrator design showing bolted interfaces.

MR&D estimated the loads and failure strengths of the bolted interface under tension. The analysis started with assessing the loads on the studs as they transfer the tensile load from the composite body to the steel ends. It was calculated that the inboard studs bear 53.5% of the load of 16,050 lb, while the outboard pins bear 46.5% or 13,950 lb. The load balance along the inner and outer sleeves is summarized in Fig. 12-27.

Outer Sleeve ↑ **21,400**

Inner Sleeve ↑ **8,600**

Composite

9,940

13,94

4,000

11,460

16,060

4,600
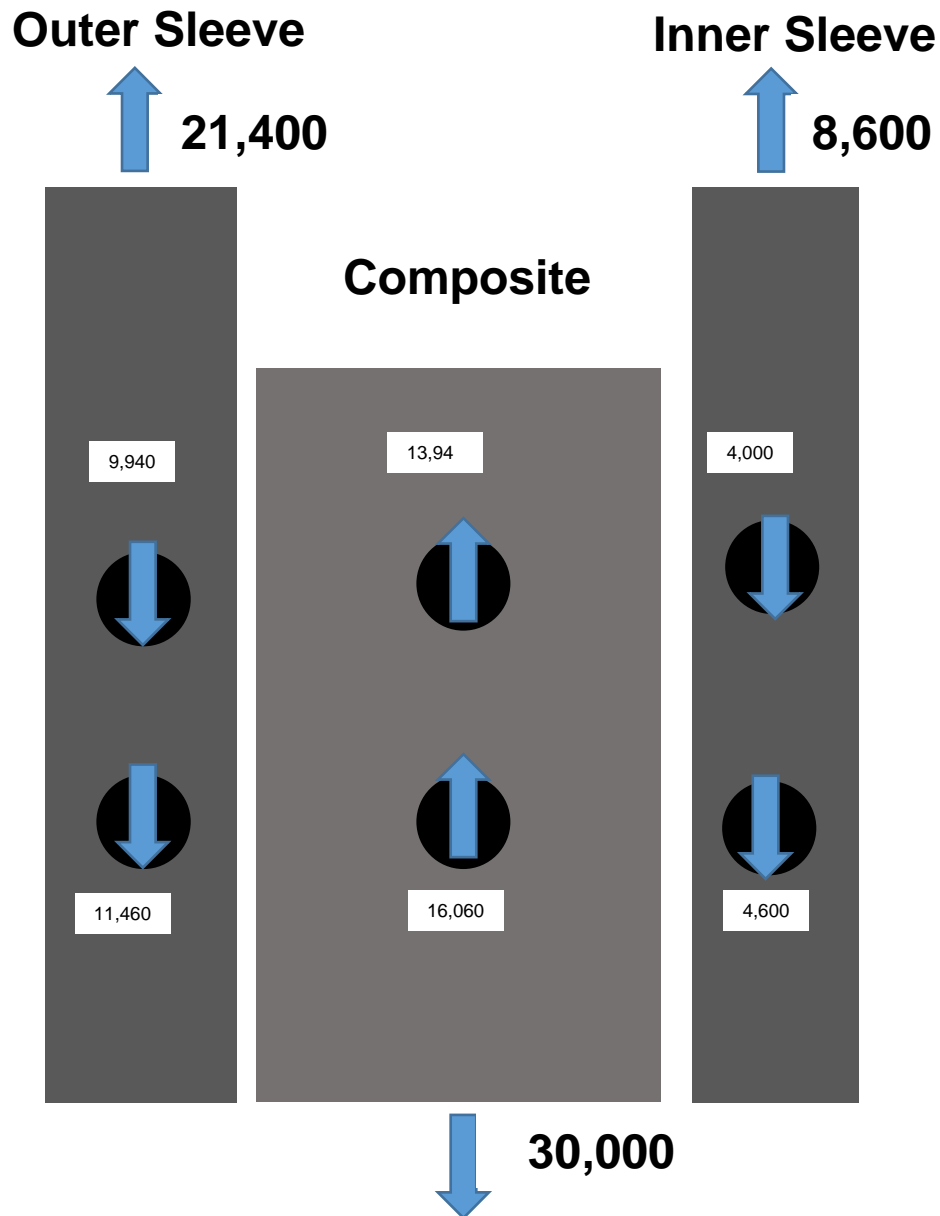
↓ **30,000**

Fig. 12-27. Calculated forces in RMS interface design under a 30,000-lb tensile load.

Given the load distributions, a failure analysis of the interface was done on a component basis. The failure modes considered were: shear of the inboard pins, compressive failure of the RMS and steel sleeves directly under the pins, tensile failure of the RMS and steel sleeves, and shear tear-out of the RMS and steel sleeves. The shear strength of the steel was taken as 66 ksi, and its tensile and compressive strengths were assumed to be a conservatively low value of 115 ksi. For the RMS, the compressive strength was assumed to be 91.2 ksi, and the tensile strength, 55 ksi; the shear strength was estimated as 115 ksi, a value measured in graphite-epoxy materials.

Table 12-3 summarizes the failure analysis. A margin value of 1.0 corresponds to failure. The table shows the largest margin is 0.615 for the shear failure of the inboard studs. Based on this analysis, the interface should withstand at least a 48,780-lb tensile load. Failure would occur on shearing of the inboard stud.

Table 12-3. Summary of calculated component loads of the RMS interface at 30,000 lb tension.

Component	Load @ 30,000 lb (lb)	Failure load (lb)	Margin
In-board Pin Shear	16,050	26,100	0.615
Composite Bearing	16,050	50,800	0.316
Composite Shear	16,050	33,400	0.481
Composite Net Tensile	16,050	157,000	0.102
Inner Sleeve Shear	4,600	28,700	0.160
Inner Sleeve Bearing	4,600	83,000	0.055
Inner Sleeve Net Tensile	4,600	36,000	0.128
Outer Sleeve Shear	11,450	21,500	0.533
Outer Sleeve Bearing	11,450	62,200	0.184
Outer Sleeve Net Tensile	11,450	80,900	0.142

12.3.2 Compression and Tensile Testing of Interface Design

A static test series was conducted to evaluate the strength of the interface design. Figure 12-28 is a drawing of the test specimen, which consists of the RMS surrogate body attached to steel end fixtures. The specimen incorporates the same interface as the penetrator design. The testing consisted of compressing the specimens to a load value and then subjecting them to a tensile load, thereby replicating the gun launch and penetration events.
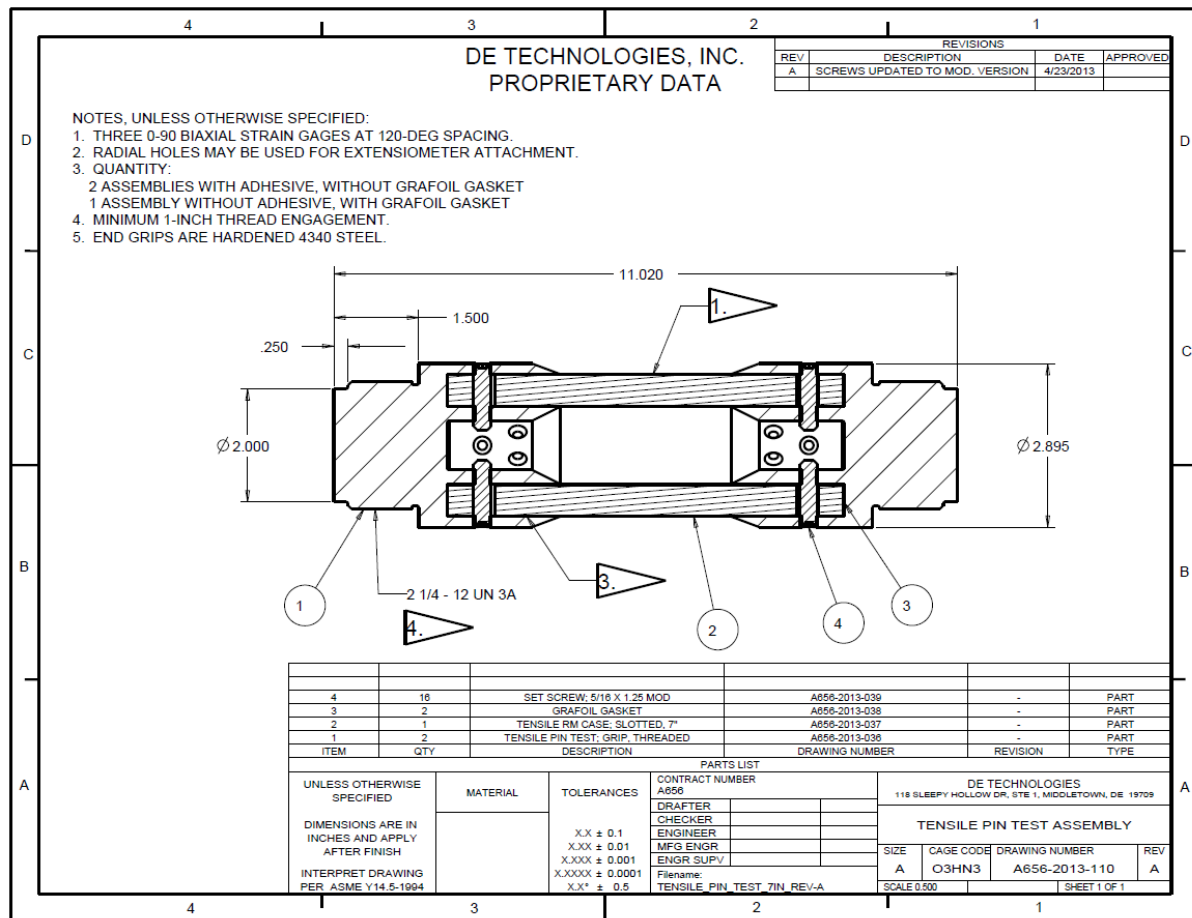
Fig. 12-28. Compression/tension specimen for evaluating joint strength.

Three testing specimens were fabricated. Figures 12-29 and 12-30 show the specimen hardware and the assembled specimens. Glue was used to assemble two of the specimens, while the third specimen was left unglued, which was used to assess the tensile strength of the bolted joint only.

Fig. 12-29. Compression/tension specimen hardware.

Fig. 12-30. Assembled compression/tension specimen.

Southern Research Institute (SoRI) performed the testing. Figure 12-31 shows the test setup for both compression and tension. A total of three tests were performed. The first was of the specimen assembled without glue and consisted only of a tensile test. The second and third tests were combinations of compression and tensile testing.
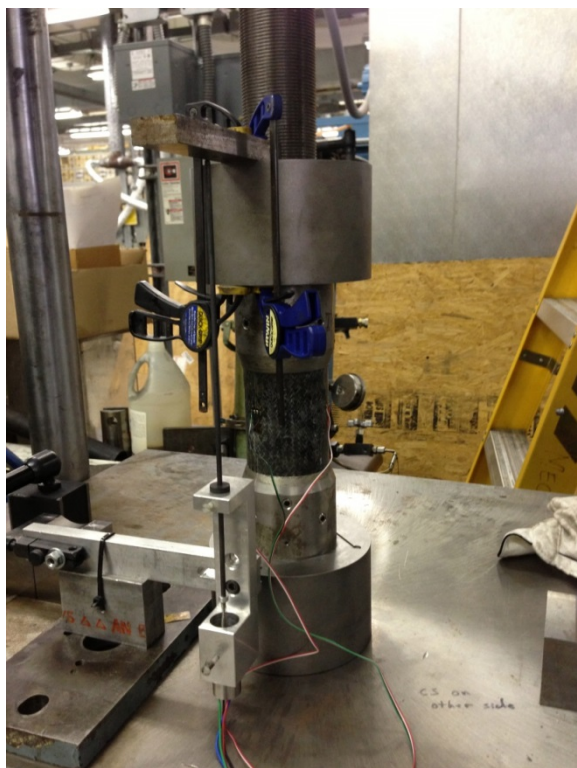
Compression   Tension

Fig. 12-31. Southern Research Institute test setups for testing of interface design.

The force versus time data from the first test is presented in Fig. 12-32. The peak load reached during this test was 74,666 lb, well above the 3000-lb design requirement and the 48,780-lb estimate.
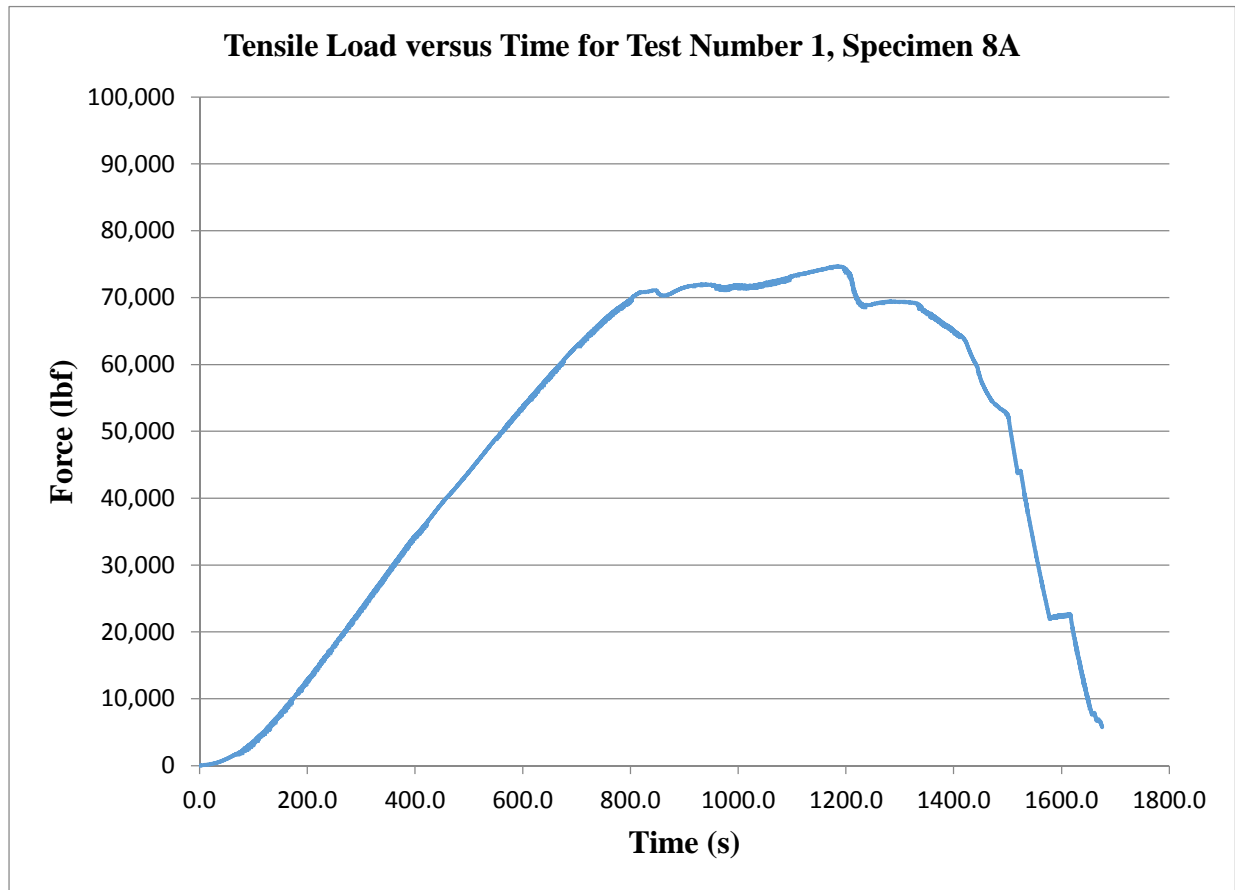
Fig. 12-32. Tensile load versus time for specimen 8A, test number 1.

In the next two tests, the specimens were first loaded in compression. For these specimens the interfaces included adhesive between the composite body and the steel end fixtures. The objective of the tests was to verify that the integrity of the joint was maintained in tension after being subjected to a compressive load. The compressive load versus time plot from test number 2 is presented in Fig. 12-33. The early data (before 38 sec) in the test were not captured. Test number 2 was run up to a 100,000-lb load.
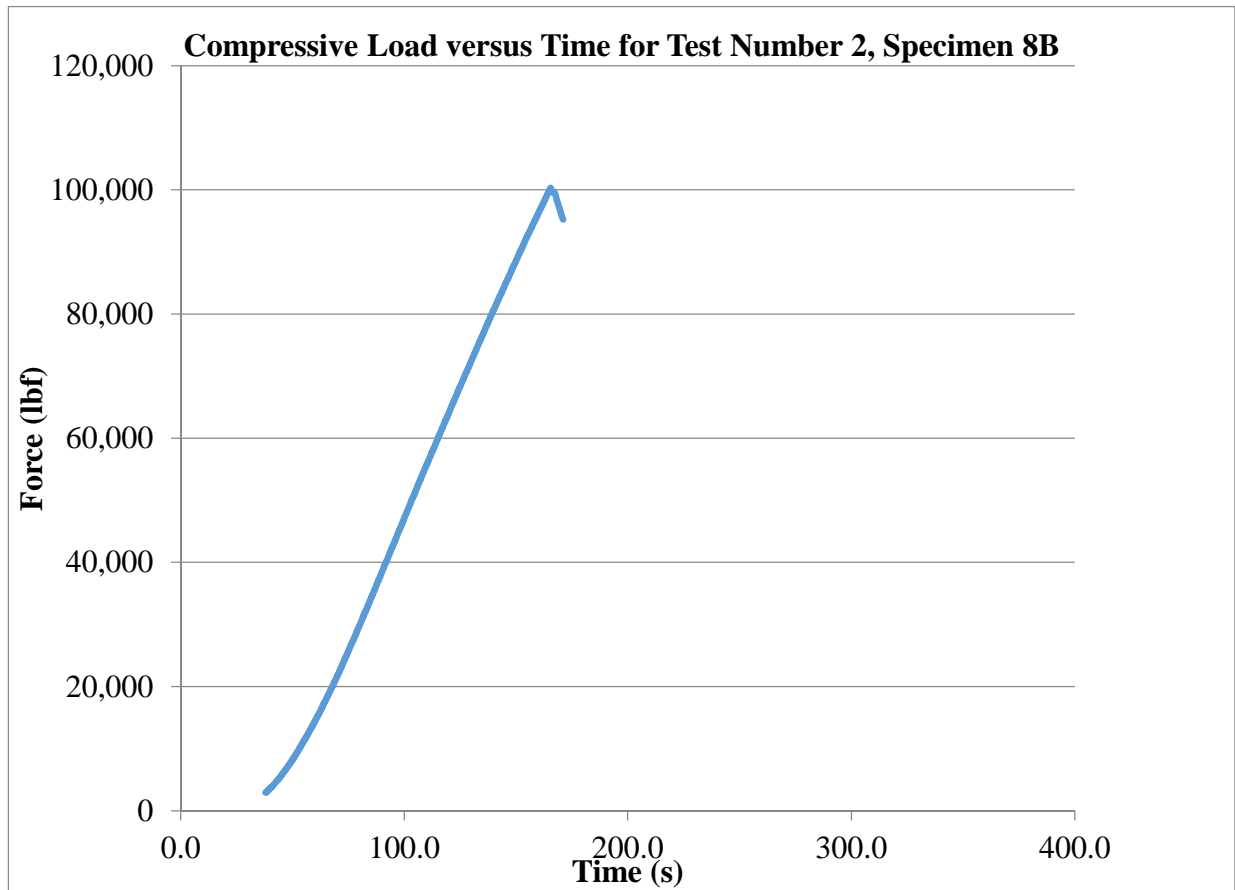
Fig. 12-33. Compressive load versus time for specimen 8B, test number 2.

In test 3, the final compressive load was increased to 110,000 lb. The plot of load versus time is shown in Fig. 12-34. The load rate was decreased from that of test 2.
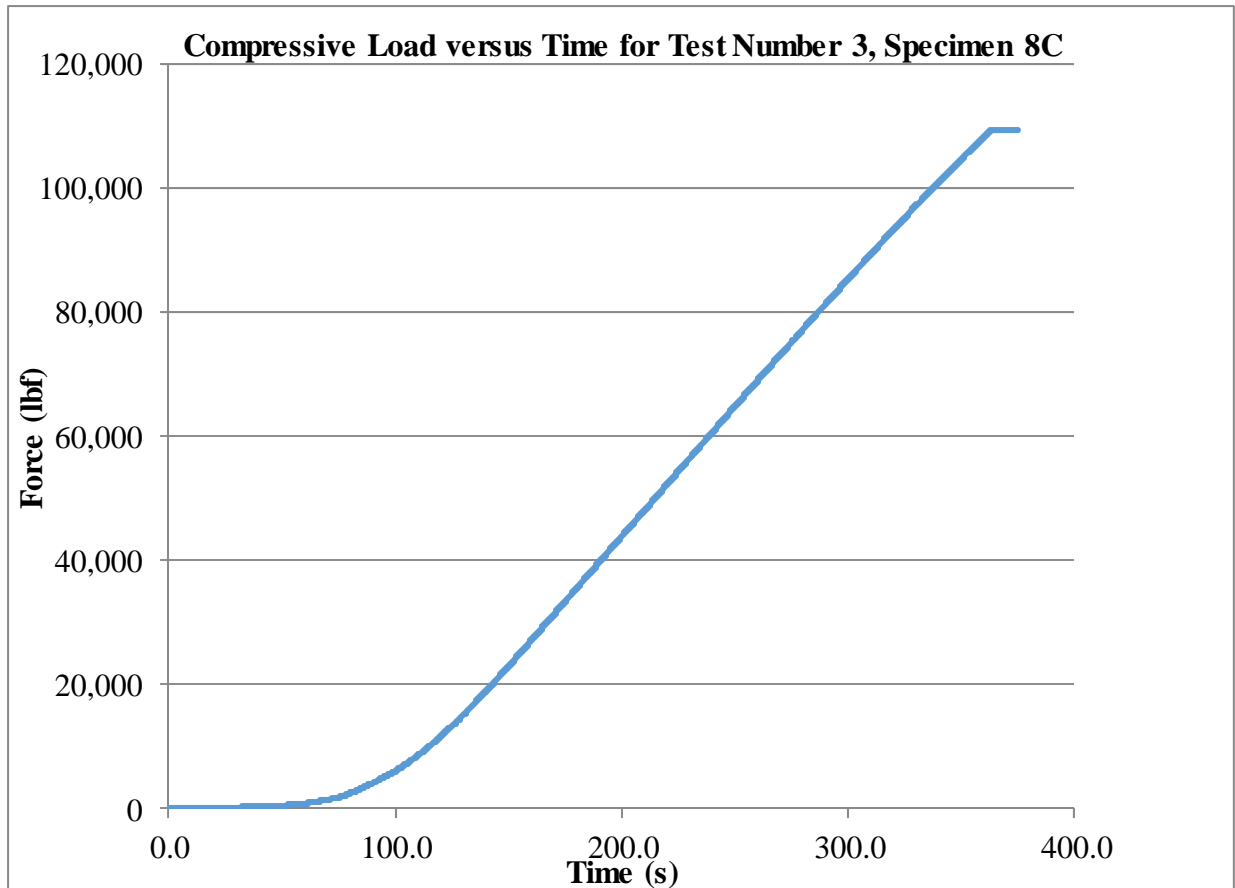
Fig. 12-34. Compressive load versus time for specimen 8C, test number 3.

Specimens 8B and 8C were subjected to tensile loads. The tensile load versus time plots for these two tests are presented in Fig. 12-35. Also included on this plot is the tension data from the first tests. The plot shows the peak tensile loads from tests 2 and 3 were over 90,000 lb, much greater than test 1. Since the specimen in test 1 had no adhesive, it seems that adhesive is contributing tensile strength to the interface despite the prior compressive load.
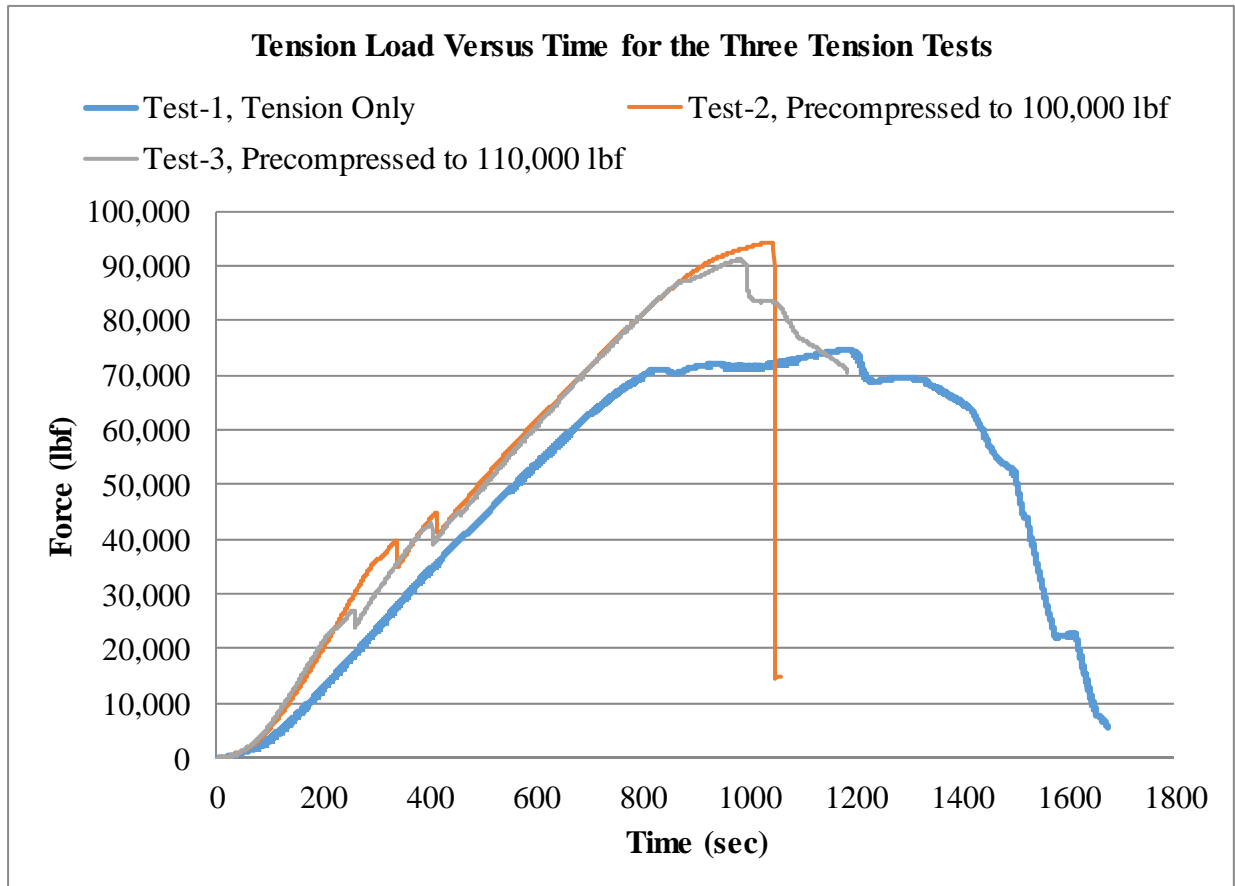
Fig. 12-35. Tensile load versus time for all three tensile tests, specimens 8A, 8B, and 8C.

In all of the tests strain gauges were used on the specimens. This enabled the derivation of stress versus strain curves. Figure 12-36 is a plot of stress versus strain in both compression and tension, compared to the compression tests discussed above. Figure 12-37 shows the same data but plotted with smaller axis scales. The plots of the curves represent the elastic moduli of the material.
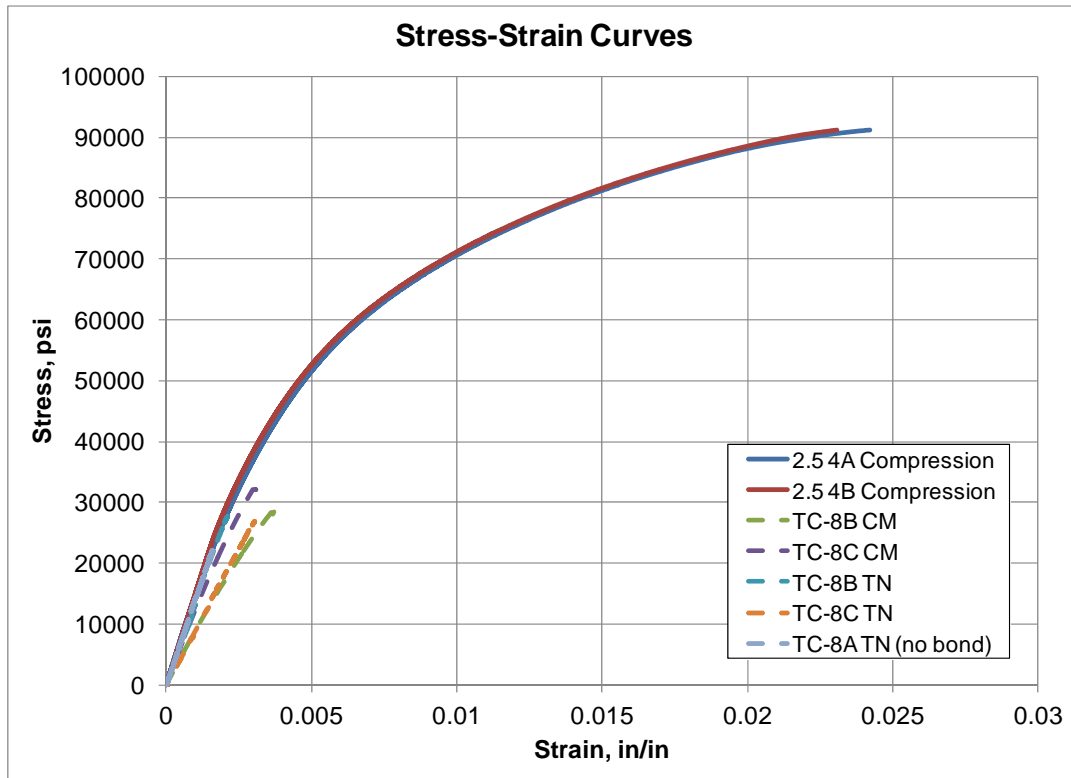
Fig. 12-36. Measured stress versus strain for the compression and tension tests.
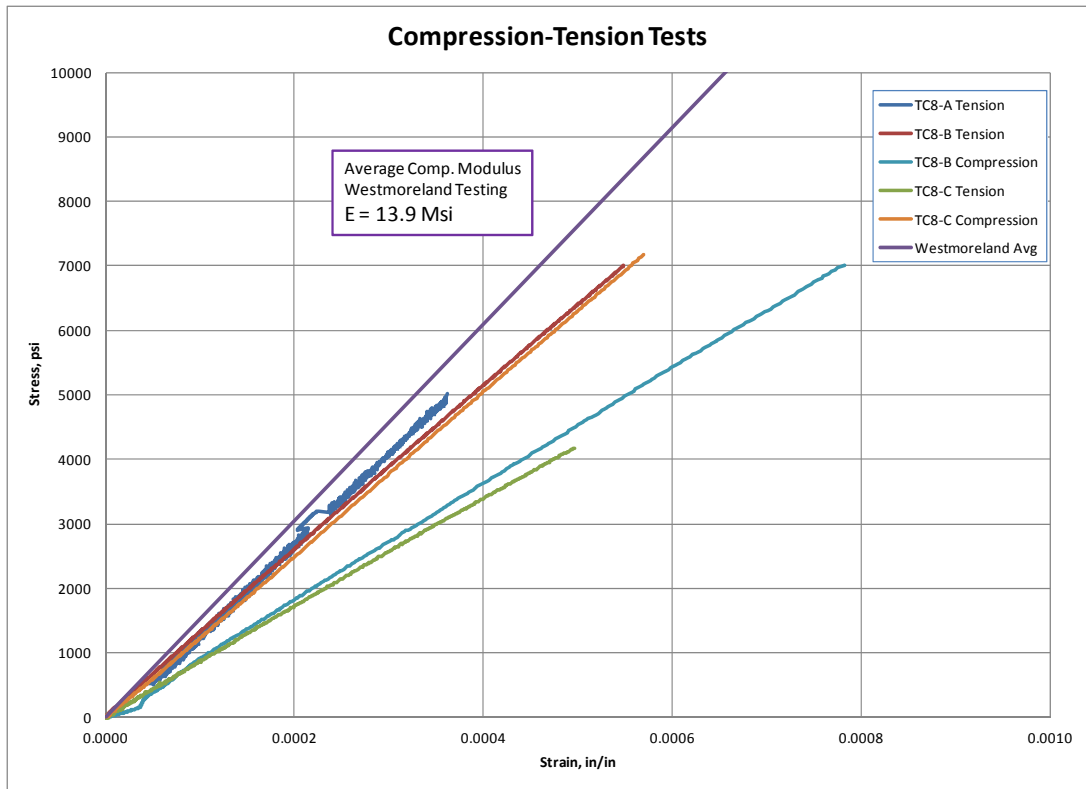
Fig. 12-37. Measured stress versus strain using smaller axes for the compression and tension tests.

Section XIII

Penetration Trade Studies and Penetrator Design

This section describes the development of an improved material model for the RMS and its application in trade studies aimed at the development of designs for test penetrators incorporating the RMS.

13.1 Material Properties

Previous work concerning the survivability of the RMS material in penetrating bomb casings used the EPIC computer code. The RMS was modeled as mild 1006 steel using the Johnson-Cook plasticity model. This model's yield stress is about the same as measured compression test values for the RMS. While this approximation is suitable for simple trade studies concerning material strength, it does not accurately represent the compressibility and elastic response. Since current activities are focused on designing an RMS penetrator for the upcoming concrete penetration tests, a better model for the RMS material was developed. The development is not complete and will continue as additional data are obtained.

A material model for the EPIC code must include at least three components: an equation of state, elastic properties, and plastic properties. As do many hydrocodes, EPIC incorporates the Mie-Gruneisen equation of state to model compressibility. Mie-Gruneisen parameters have been determined for many materials, including the components of tungsten, epoxy, and aluminum that make up the RMS.

The rule of mixtures[3] was applied to determine Mie-Gruneisen parameters for both the tungsten-aluminum-epoxy RMS and the tungsten-epoxy simulant based on established values of the component properties. A model for the tungsten-epoxy formulation is needed because the first round of penetration tests will use it instead of the aluminum-loaded RMS in order to simplify fabrication and to avoid gun-launching a reactive material.

The mass density ρ_a, Gruneisen parameter γ_a, and specific heat C_v at ambient conditions were computed directly from the appropriate rule-of-mixture equations:

$$\frac{1}{\rho_a} = \sum_i \frac{m_i}{\rho_{a,i}} \tag{13-1}$$

$$\frac{1}{\rho_a \gamma_a} = \sum_i \frac{m_i}{\rho_{a,i} \gamma_{a,i}} \tag{13-2}$$

$$C_V = \sum_i m_i C_{V,i} \tag{13-3}$$

where subscript i denotes each component, and m_i is the mass fraction of the ith component. (Absence of subscript i denotes values for the mixture.) Parameters for the component materials, taken from Kinslow[4], are listed in Table 13-1.

Table 13-1. Parameters for the Component Materials.

	W	Al	Epoxy
Density, ρ_a (g/cm^3)	19.224	2.785	1.198
Gruneisen parameter, γ_a	1.54	2.00	1.13
Specific heat, C_v (10^6 ergs/(g-K))	1.31	8.38	10.42

---

[3] R.G. McQueen, S.P. Marsh, J.W. Taylor, J.N. Fritz, and W.J. Carter, "The Equation of State of Solids from Shock Wave Studies," Ch. VII in *High-Velocity Impact Phemonena*, R. Kinslow, ed., Academic Press, N.Y. 1970.

[4] R. Kinslow, ed., *High-Velocity Impact Phenomena*, Academic Press, N.Y., 1970.

The equation-of-state parameters were developed using the following procedure.

1) Murnaghan's expression

$$V_i(T = 0, p) = \frac{V_{0,i}}{\left(1 + \dfrac{n_i p}{B_{0,i}}\right)^{1/n_i}}$$

(13-4)

where B_0 is bulk modulus, was fit to the cold-compression (0-Kelvin) curve of each of the component materials by adjusting the values of the fitting parameters $B_{0,i}$ and n_i. Note that $V_{0,i}$ is the specific volume of the ith component at zero pressure and absolute-zero temperature (and not the reciprocal of ρ_a, the mass density at ambient conditions). Points along each cold-compression curve were taken from computed values given in Appendix E of Kinslow. In each case, the maximum relative error between the fit and data, in terms of specific volume, was less than 0.5% over the entire range of pressures covered by the data.

Table 13-2. Murnaghan parameters for the cold-compression
curves of the component materials.

	W	Al	Epoxy
Volume, V_0 (cm^3/g)	0.05188	0.35499	0.80645
Density, ρ_0 (g/cm^3)	19.276	2.817	1.240
Bulk modulus, B_0 (Mbar)	3.152	0.825	0.0966
Murnaghan exponent, n	3.70	3.76	5.02

2) Points along the cold-compression curve of the mixture were computed from the components' cold-compression curves using the rule of mixture (equivalent to Amagat's law for gases):

$$V(T = 0, p) = \sum_i m_i V_i(T = 0, p)$$

(13-5)

3) Murnaghan's expression (13-4) was fit to the computed cold-compression points of the mixture. The value of the 0-Kelvin, zero-pressure volume of the mixture $V_{0,mix}$ was required to follow (15-5) exactly,

$$V_{0,mix} = \sum_i m_i V_{0,i}$$

(13-6)

but B_0 and n were adjusted to yield the best overall "eyeball" fit in each case. The value of B_0 for the mixture may be estimated by differentiating Eq. (15-5) and evaluating at zero pressure to yield

$$\frac{V_0}{B_0} = \sum_i m_i \frac{V_{0,i}}{B_{0,i}}$$

(13-7)

In every case, however, a slightly different value was found to give the best overall fit. In each case, the maximum relative error between the points and computed curve, again in terms of specific volume, was less than 0.7% over the entire range of pressures covered by the data.

4) The shock-velocity–particle-velocity Hugoniot (U_s vs. U_p) of the mixture was constructed using the shock equations:

$$p_h = \frac{p_0(V_h) + \dfrac{\gamma_a}{V_a}\left[E_a - \dfrac{1}{2}p_a(V_a - V_h) - E_0(V_h)\right]}{1 - \dfrac{\gamma_a}{2V_a}(V_a - V_h)}$$

(13-8)

where the quantity (γ/V) is assumed constant, and

$$U_s = V_a \sqrt{\frac{p_h - p_a}{V_a - V_h}}$$
(13-9)

$$U_p = \sqrt{(p_h - p_a)(V_a - V_h)}$$
(13-10)

where $p_0(V)$ is given by the Murnaghan expression of the cold-compression curve. The energy E_0 along this curve is given by

$$E_0(V) = \frac{B_0 V_0}{n(n-1)} \left[\left(\frac{V_0}{V}\right)^{n-1} - (n-1)\left(1 - \frac{V}{V_0}\right) - 1 \right]$$
(13-11)

and the energy E_a at ambient conditions by

$$E_a = \frac{V_a}{\gamma_a} \left[p_a - p_0(V_a) \right] + E_0$$
(13-12)

In these equations, the subscript 0 denotes the 0-Kelvin values, and subscript a denotes ambient conditions ahead of the shock. To use these equations, the volume behind the shock V_h is varied parametrically to give pairs of U_s and U_p values.

5) The quadratic function

$$U_s = C_s + S_1 U_p + \frac{S_2}{C_s} U_p^2$$
(13-13)

was then fit to the computed shock-velocity–particle-velocity Hugoniot points of the mixture. The constants C_s, S_1, and S_2 so obtained may be used directly in the input to the CTH code.

The mixtures included the reactive material, composed by volume of 30% tungsten, 40% aluminum, and 30% epoxy, and its inert structural simulant, composed of 30% tungsten and 70% epoxy.

The CTH input parameters for the mixtures are listed in Tables 13-3 and 13-4.

Table 13-3. EOS parameters for mixture of tungsten/epoxy
(30/70 by volume, 87.31/12.69 by mass)

	Value in cm-g-μs units	CTH name	Value in CTH units
Ambient mass density, ρ_a	6.6058 g/cm^3	R0	6.6058 g/cm^3
Bulk sound speed, C_s	0.13688 cm/μs	CS	136880. cm/s
U_s vs. u_p Hugoniot term, S_1	2.040 (dimensionless)	S1	2.040
U_s vs. u_p Hugoniot term, S_2	−0.114 (dimensionless)	S2	−0.114
Gruneisen parameter, γ_a	1.2281 (dimensionless)	G0	1.2281
Specific heat, C_v	2.467 × 10^6 ergs/(g-K)	CV	2.863 × 10^{10} ergs/(g-eV)

Table 13-4. EOS parameters for mixture of tungsten/epoxy/aluminum
(30/30/40 by volume, 79.65/4.96/15.39 by mass)

	Value in cm-g-μs units	CTH name	Value in CTH units
Ambient mass density, ρ_a	7.2406 g/cm^3	R0	7.2406 g/cm^3
Bulk sound speed, C_s	0.20507 cm/μs	CS	205070. cm/s
U_s vs. u_p Hugoniot term, S_1	2.165 (dimensionless)	S1	2.165
U_s vs. u_p Hugoniot term, S_2	−0.178 (dimensionless)	S2	−0.178
Gruneisen parameter, γ_a	0.5704 (dimensionless)	G0	0.5704
Specific heat, C_v	2.853 × 10^6 ergs/(g-K)	CV	3.311 × 10^{10} ergs/(g-eV)

13.2 20-lb RMS Dynamic Test Vehicle Design

13.2.1 Test Conditions and Requirements

RMS-cased projectiles will be ballistically tested at New Mexico Tech's Energetic Materials Research and Testing Center (EMRTC). The projectiles will be gun-launched for impact into unreinforced concrete targets. The concrete's unconfined compressive strength was planned to be 5 ksi, but after casting and testing crush cylinders, the strength appears to be closer to 6 ksi. The smoothbore gun is of caliber about 5 inches. Since the RMS case under development is about 2.5 inches in diameter, a sabot will be used. The anticipated impact velocities will range from 1000 ft/s to 1500 ft/s at zero angle of attack. The nominal mass of the projectile is 20 lb, which will result in accelerations of up to 4,000 G.

13.2.2 Computational Tools

Several software packages are used designing the RMS projectile. Pro/Engineer[5] was used for solid modeling and detailed drawings. Cubit[6] was used to convert solid models to finite-element Exodus models for use in dynamic and structural evaluation codes. SAMPLL[7] and EPIC-PENCRV[8] are used for impact simulations. SAMPLL, a fast-running empirical code based on Young's equations of penetration[9], allows simple penetrator geometries to be quickly evaluated. EPIC is an explicit finite-element hydrocode with the PENCRV link for discrete modeling of the penetrator during impact with an empirically based model of the target. EPIC was modified under this program to add the capability of modeling AFX-757 Explosive Simulant[10] to represent the explosive fill. EPIC does not have a non-linear orthotropic model available, so bilinear isotropic properties were used to model the RMS case. Library values for 4340 steel were used for steel components. Post-processing is done with Paraview[11]. Simulations of gun launch survivability are done with LS-Dyna[12].

13.2.3 Configuration A

The first geometry concept is shown in Fig. 13-1. The projectile is 25.6 inches long with a maximum diameter of 2.89 inches and weighs approximately 24.6 lb. Overall L/D is 8.85.

Fig. 13-1. Dynamic test vehicle configuration A.

Several important design features are incorporated in this configuration. In order to avoid drilling, threading, or pinning of the RMS case, the case may be shaped around matching steel components that lock the case in place. In the nose section, the case could be braided over an end cap with a protruding,

---

[5] http://www.ptc.com

[6] http://cubit.sandia.gov

[7] C.W. Young, "Simplified Analytical Model of Penetration with Lateral Loading; Users Guide", Applied Research Associates, Inc., SAND98-0978, May 1998.

[8] G.R. Johnson et al., "User Instructions for the 2011 Version of the EPIC Code", Southwest Research Institute, November 2011.

[9] C.W. Young, "Penetration Equations," Applied Research Associates, Inc., SAND97-2426, October 1997.

[10] B. Plunkett and M. Green, "Constitutive Behavior of AFX-757 Simulant During Penetration," AFRL-RW-EG-TR-2009-07074, January 2009.

[11] http://www.paraview.org

[12] "LS-Dyna Keyword User's Manual; Nonlinear Dynamic Analysis of Structures," Version 950, Livermore Software Technology Corp., May 1999.

threaded stud that would allow a nose cap to lock onto the front. The rear section could be braided over a tapered sleeve that would allow an end cap to be threaded on. These features would have each end attachment mechanically interlocked with the composite case. Unfortunately, the constant volume of braided material over each unit length of the case makes the case thicker near the tapering nose, and thinner near the aft interface. Since quasi-static material properties will only be available for the nominal thickness along the center section of the case, any change in composite stiffness and strength will be poorly validated. In addition, the challenges of controlling the thickness of the braided structure in the varying-thickness regions would be very difficult at the current level of maturity for the composite system.

13.2.4 Configuration B

Configuration B simplified the end connections of the nose and end cap, as shown in Fig. 13-2. The projectile is now 27 inches long with a maximum diameter of 2.7 inches for an overall L/D = 10. The weight is approximately 24.1 lb. The primary change is to a uniform-thickness composite case, which simplifies fabrication to allow increased uniformity, repeatability, and decreased fabrication time. The nose, as in configuration A, has a drag-optimized shape.

Fig. 13-2. Dynamic test vehicle configuration B.

EPIC-PENCRV was used to simulate impact of this projectile into a semi-infinite 5-ksi concrete target at 1200 ft/s. Initial 2D axisymmetric simulations indicate that the projectile survives normal impact by a wide margin, but 3D simulations at an angle of attack (AoA) show that the projectile fails. Figure 13-3 shows the setup of five simulations for 0° to 2° AoA, and Fig. 13-4 shows the subsequent results. Damage contours indicate the percent of plastic strain from yield to ultimate failure; red contours indicate material failure. The 0° AoA result agrees with the 2D axisymmetric simulation that the projectile survives impact at 1200 ft/s. Damage increases with increasing AoA, from the 0.5°-AoA case that may survive, to the 2.0°-AoA case where the case is completely destroyed. The primary damage mechanism is tail-whip against the target surface. This effect may be reduced by reducing the angle of attack and by reducing the projectile length. Angle of attack in the gun tests cannot be completely controlled but is not expected to exceed 2°, with most instances under 1° (according to EMRTC staff). The next projectile configuration will reduce the L/D.
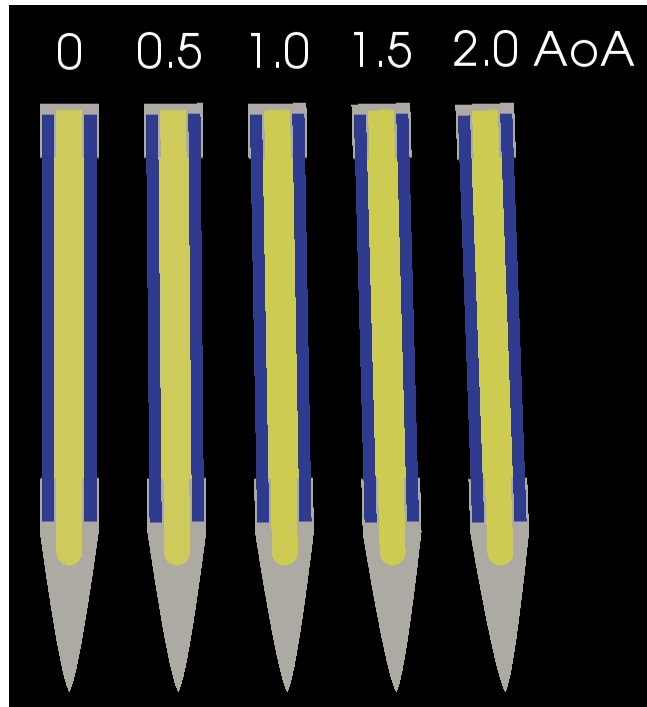
Fig. 13-3. Configuration B PENCRV simulation setup.
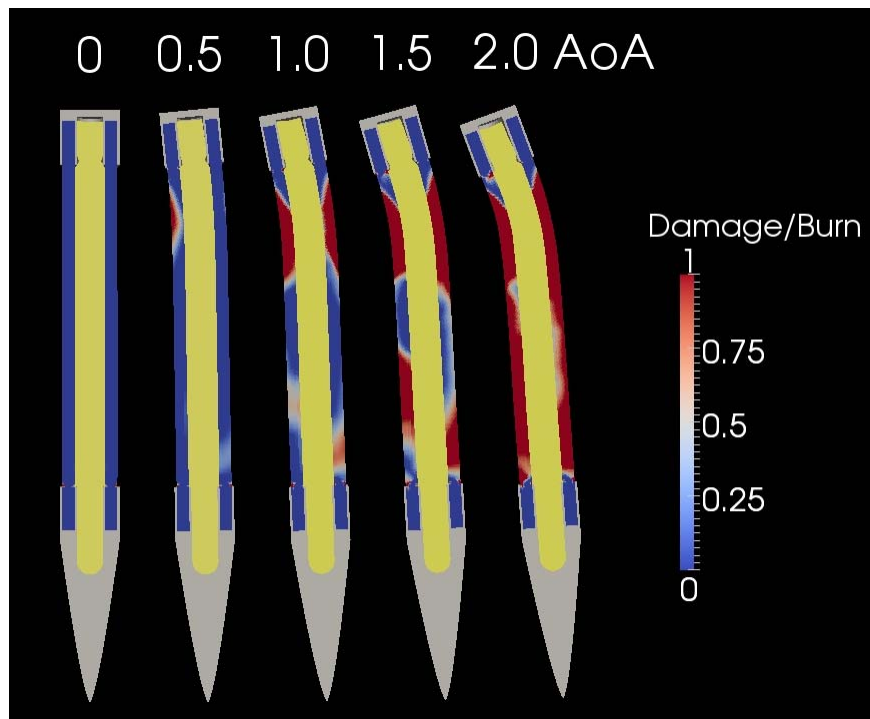
Fig. 13-4. Configuration B PENCRV simulation results.

13.2.5 Configuration C

Configuration C reduces the L/D to 7, as shown in Fig. 13-5. The projectile length is 18.9 inches with a maximum diameter maintained at 2.7 inches. Its nominal weight is 20.3 lb. The change in projectile length was implemented by shortening the composite case, as well as replacing the nose with a shorter ogive, with 4.0 CRH (Caliber Radius Head).

Fig. 13-5. Dynamic test vehicle configuration C.

To reduce the L/D, the nose was changed from a drag-optimized nose to a shorter ogive. The drag-optimized nose was intended to reduce the impact loading on the case. To compare the differences in strains for the different nose shapes, a simulation was done along with a hemispherical nose, all with equivalent overall lengths. Figure 13-6 shows that very little difference between the ogive and drag-optimized noses, while the hemispherical nose fared very poorly. The ogive will be carried forward for all subsequent designs for this test series.
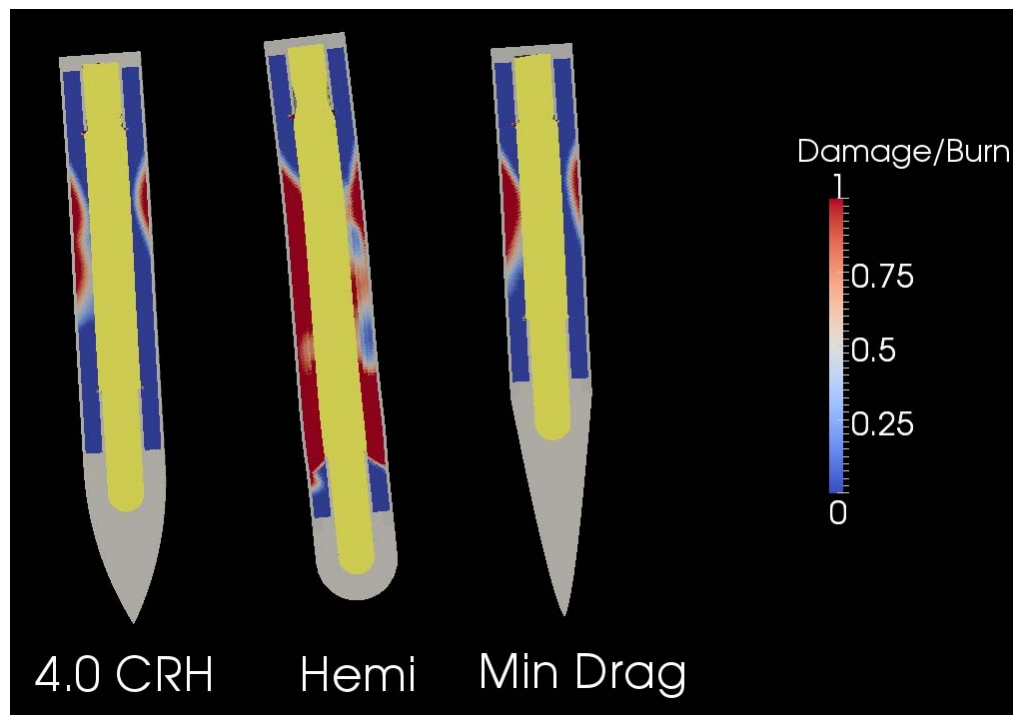
Fig. 13-6. Configuration C nose comparison at 2° AoA at 1500 ft/s.

Figure 13-7 shows the simulation results for 1200 ft/s impact at 1° and 2° AoA. Three versions of the projectile are shown: no sleeve, a partial sleeve, and a full-length sleeve. The exterior sleeves add local reinforcement around the RMS case to reduce the strains within the case. Even at 2° AoA, the full sleeve version shows little damage in the case. In Fig. 13-8, impacts with the same AoA are simulated at 1500 ft/s with similar results. Again, the full-sleeve design shows a high chance of surviving impact at 1° AoA and only moderate damage at 2°.
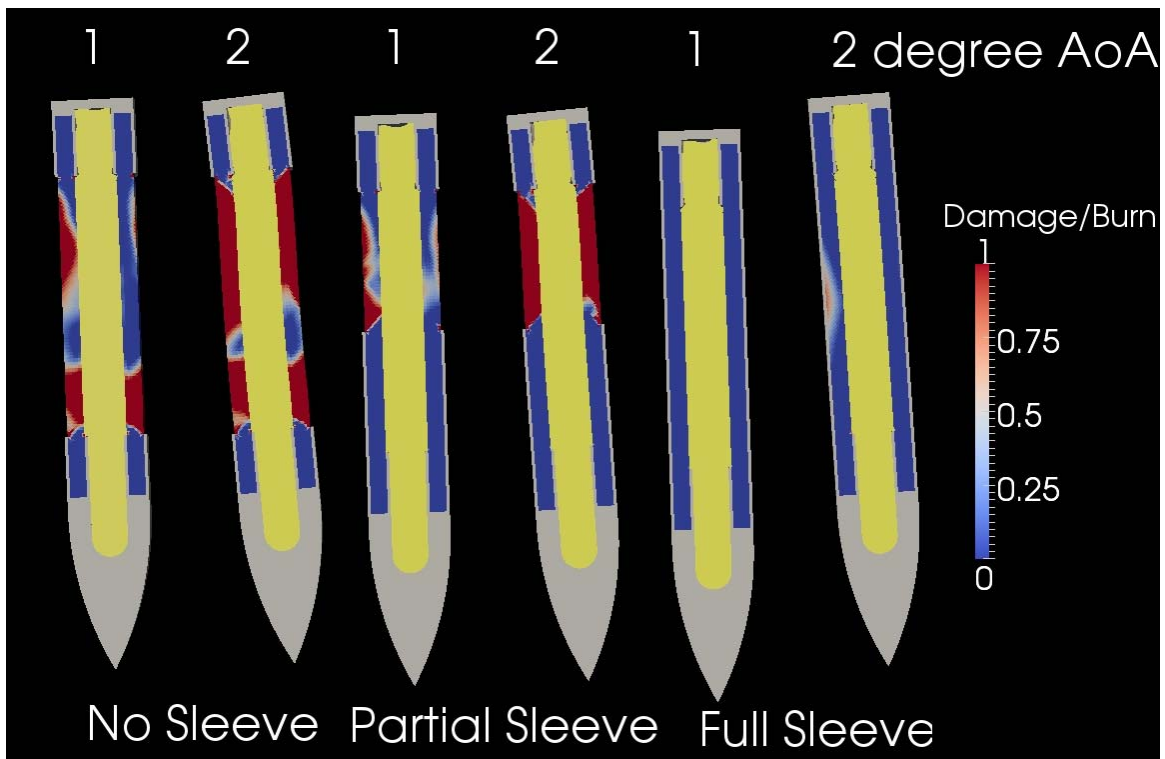
Fig. 13-7. Configuration C sleeve and AoA parametric simulations at 1200 ft/s.
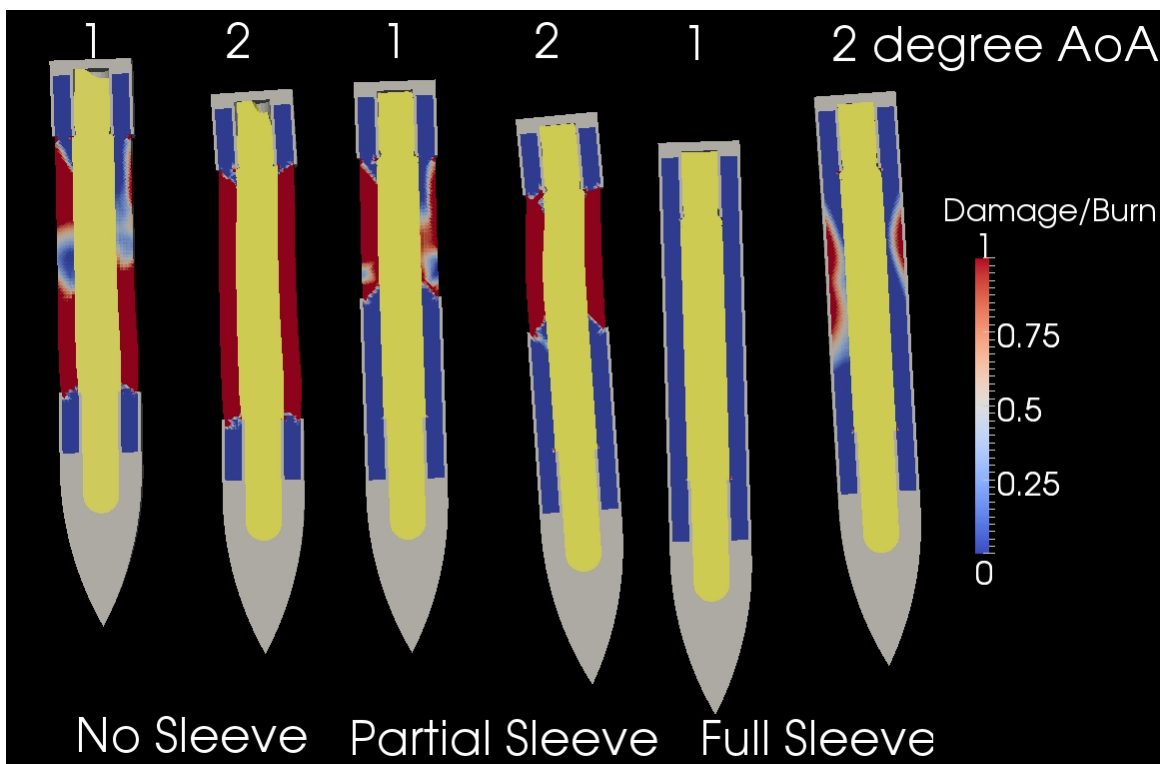
Fig. 13-8. Configuration C sleeve and AoA parametric simulations at 1500 ft/s.

Since the full-sleeve design of L/D = 7 survives impact at 1° AoA and marginally at 2°, a simulation was done to determine how much shortening to L/D = 6 would improve survivability. Figure 13-9 shows the

results for a full sleeve design for L/D=6 and 7, and indicates the reduced damage in the shortened projectile. This modification was further investigated as Configuration D.
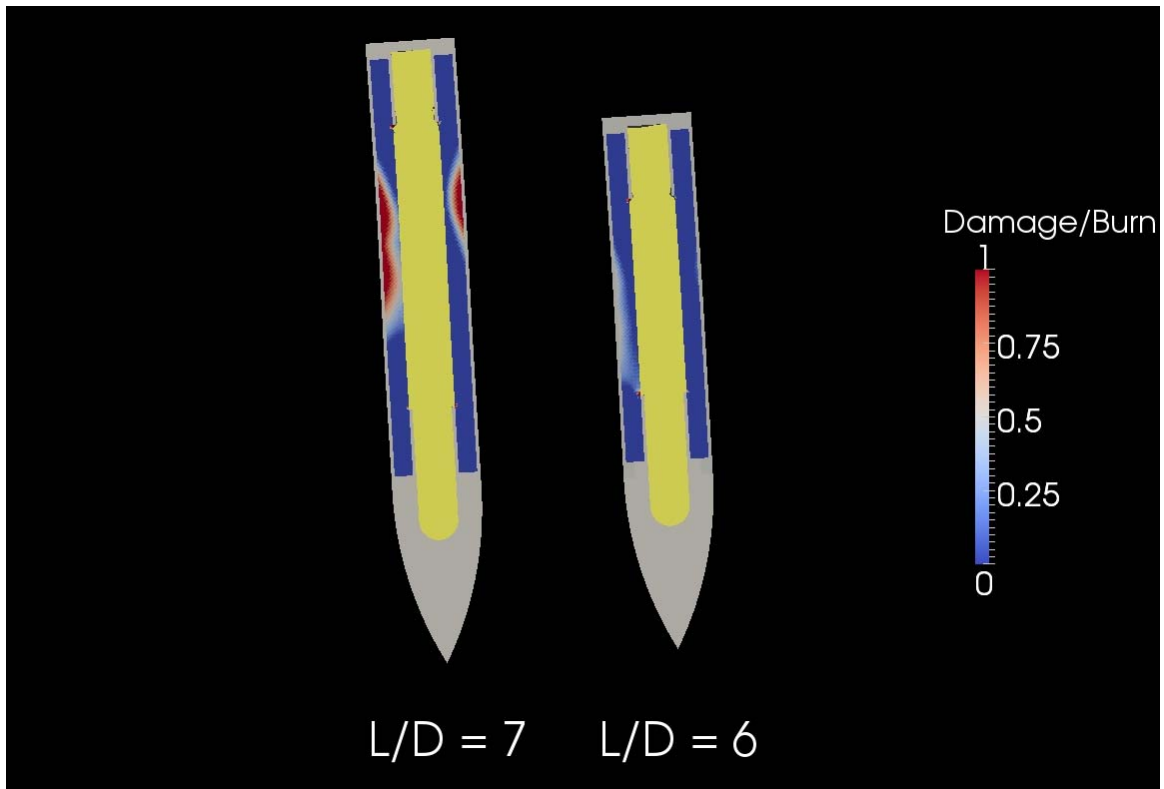
Fig. 13-9. Configuration C L/D = 6 and 7 impacts at 2° AoA and 1500 ft/s.

13.2.6 Configuration D

The projectile was shortened to 16.2 inches and the maximum diameter was kept at 2.7 inches, as shown in Fig. 13-10. With L/D = 6, total mass is 17.3 lb. This is the minimum L/D ratio in order to have a test that has a substantial length of RMS case. Any shorter, and the nose and aft steel components begin to dominate the design.

Fig. 13-10. Dynamic test vehicle configuration D.

Figure 13-11 shows the damage contours for 1200 and 1500 ft/s impacts at 2° AoA. The full-sleeve design survives impact at both velocities, however the designs with partial and with no sleeves have significant damage. For impacts at 1200 ft/s at 1° AoA, shown in Fig. 13-12, the projectile has only limited regions of damage in the case, indicating it may survive impact, whereas at 2°, total failure is anticipated.
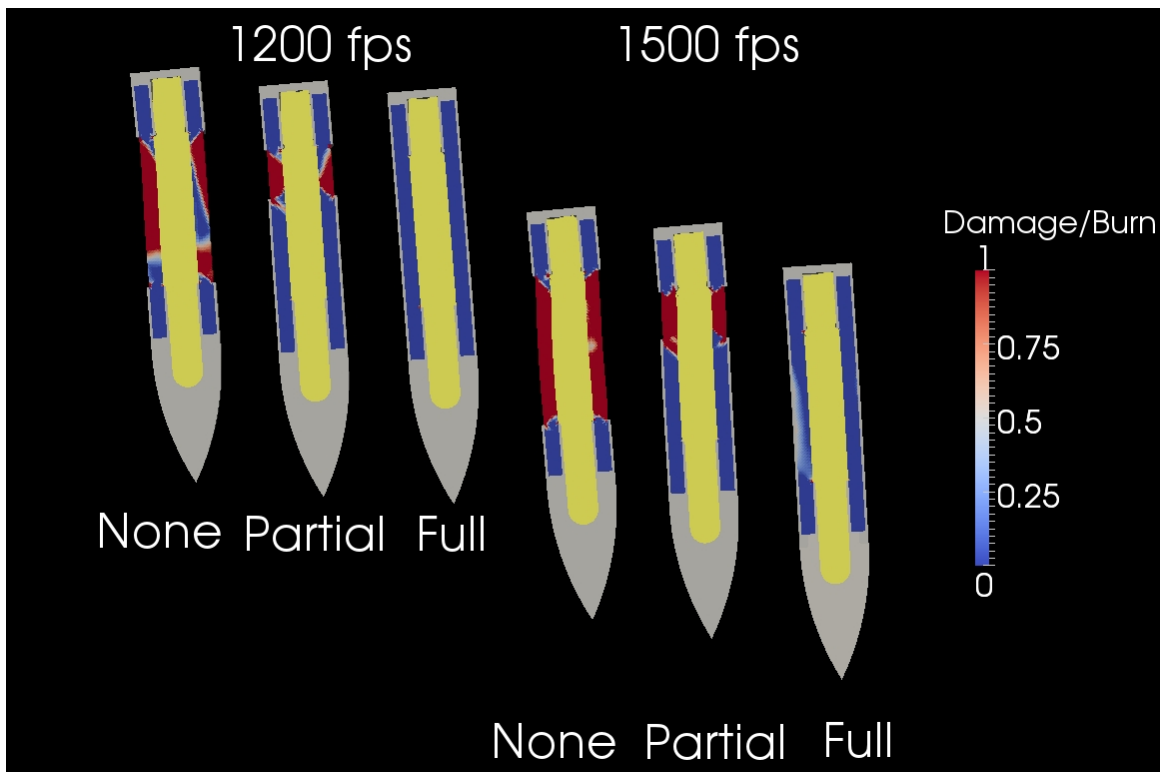
Fig. 13-11. Configuration D sleeve parametric results at 2° AoA.
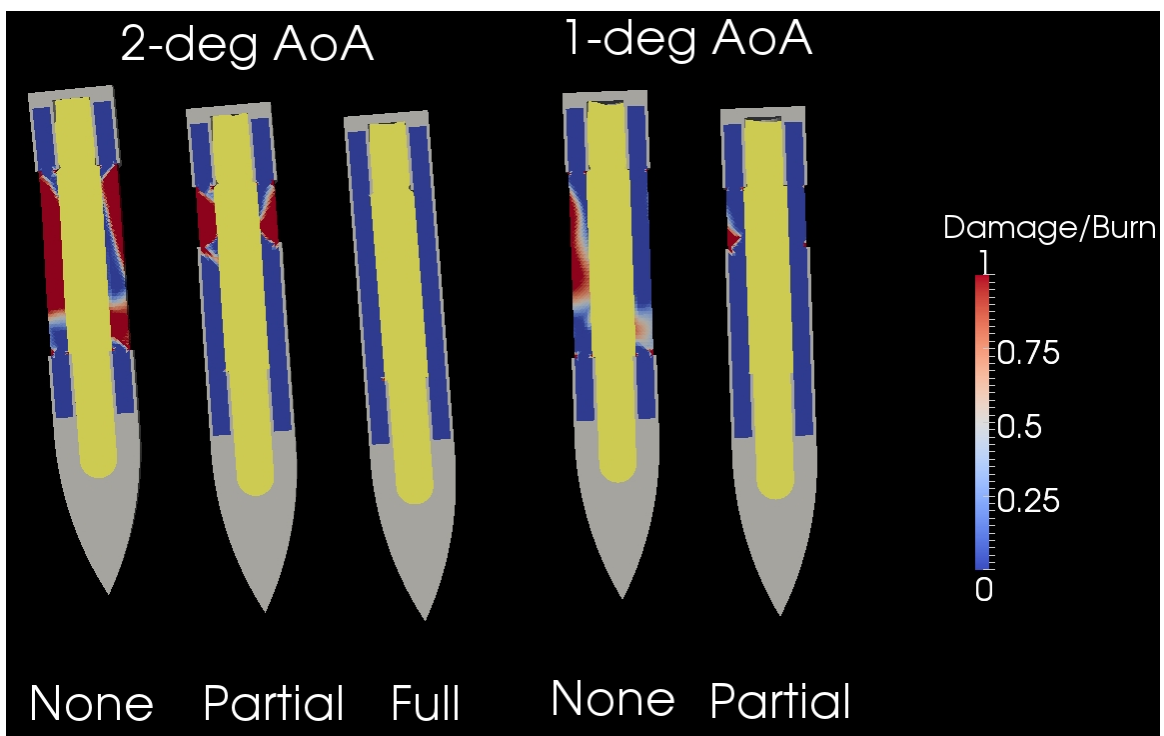
Fig. 13-12. Configuration D sleeve parametric results at 1200 ft/s.

Now that the projectile has the potential to survive impact at 1200 ft/s at 1° AoA without implementing a full sleeve, the impact test plan was considered. Earlier, EMRTC had indicated that most test launches would be under 1° AoA with a maximum of 2° possible. DET personnel consulted with Ron Lundgren at

his penetration short course about our test setup, and he indicated that even smaller angle of attack is possible. Based on his experience[13], if the projectile is shot through layered plywood, any angle of attack would be converted to a small angle of obliquity, which has a relatively insignificant effect on penetrator survivability. A simulation of impact into a thickness of plywood equal to one penetrator length at 2° AoA was done to verify this effect. As the histories of AoA and obliquity in Fig. 13-13 show, AoA decreases from 2° to about 0°, while obliquity increases from 0° to about 3°, an insignificant level. With this, simulations at 0° AoA (normal impact) can be used to design the projectile.
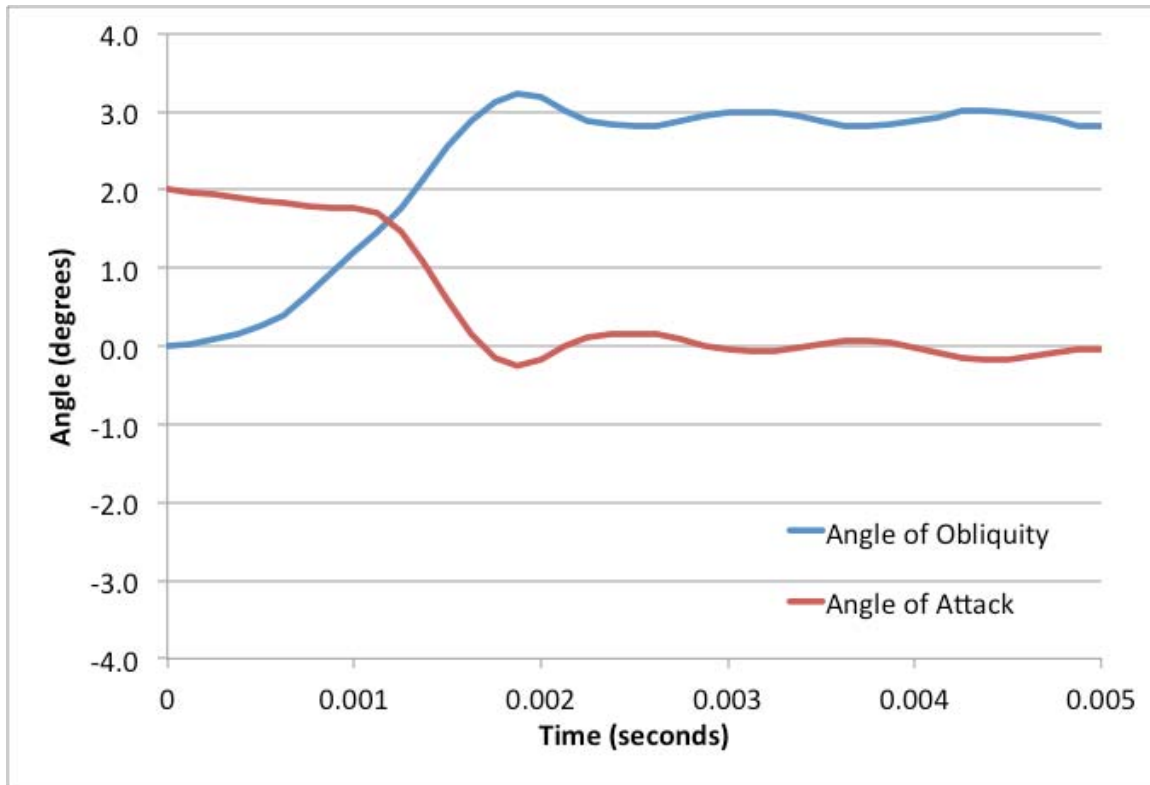
Fig. 13-13. 1200 ft/s impact with 2° AoA against plywood target.

To verify that the projectile survives gun launch, a simulation was done with LS-Dyna. Figure 13-14 shows the plastic strains in the case due to an 8,000-G launch acceleration. Since the only part in the case that experiences any plastic strain is the aft section (at the very end of the case), and the actual launch loads should be around 4,000 G, the projectile easily survives.

[13] R. Lundgren, HA Consulting, personal communication, February - March 2013.
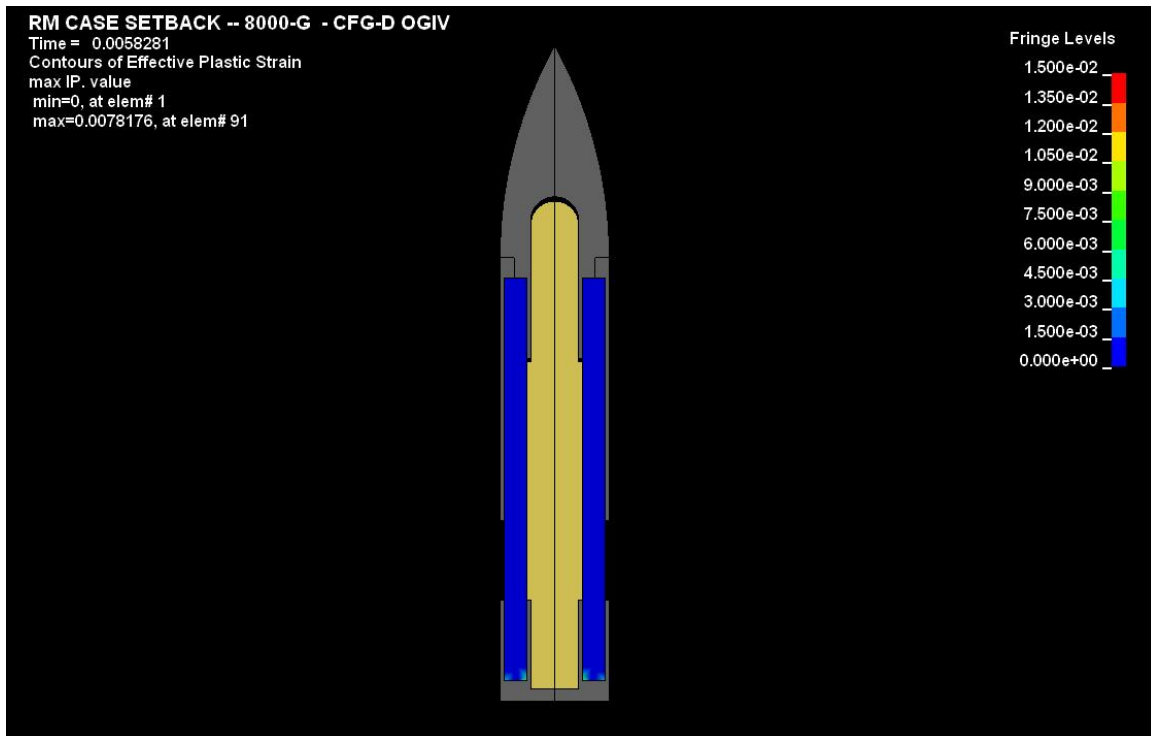
Fig. 13-14. Configuration D LS-Dyna launch simulation plastic strain results.

13.2.7 Configuration E

On completion of the simulations of Configuration D, design efforts were focused on the steel hardware that mates with the RMS case material for Configuration E, shown in Fig. 13-15. Concrete test cylinders poured at the same time as the concrete targets to be used in our tests showed the estimated unconfined compressive strength to be about 6 ksi. Simulation results of an impact at 1500 ft/s against 6-ksi concrete are shown in Fig. 13-16.

Fig. 13-15. Dynamic test vehicle configuration E.
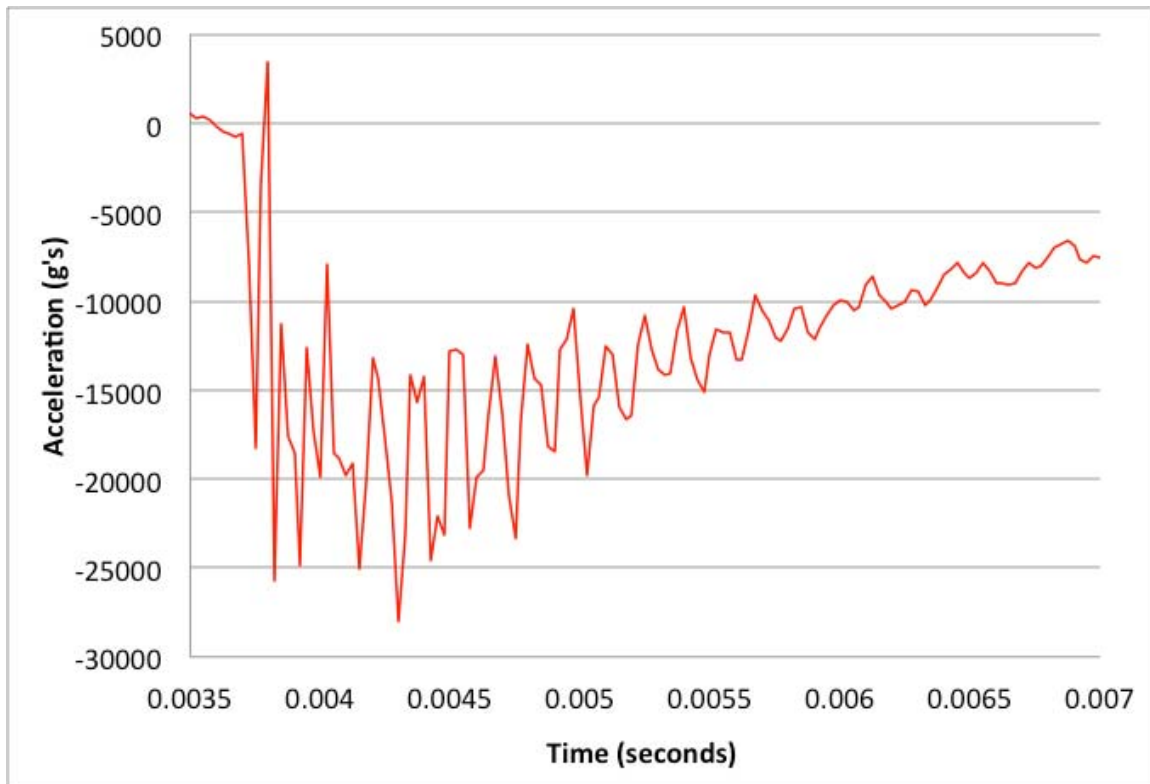
Fig. 13-16. Deceleration history for 1500 ft/s impact.

The steel hardware must survive the estimated impact acceleration on the order of 30,000 G. One concept under consideration is to use screw threads to join the nose to the flanges that are bonded to the RMS case. At 30,000 G, these threads will experience axial loads of almost 365,000 lb. The thread diameter, length, and pitch were selected to provide a minimum strength of 414,000 lb. A two-inch flange is maintained for the nose and aft bond lines. This length was confirmed as sufficient by MR&D, based on case diameter and expected adhesive strength. The changes implemented for configuration E result in the diameter increasing to 2.77 inches. To maintain L/D = 6, length is increased to 16.62 inches, with a projectile weight of 17.4 lb. Figure 13-17 shows a simulation of configuration E impacting 6-ksi concrete at 1200 ft/s and 0° AoA, for which the case fails above the nose bonding sleeves. The sleeves need to be modified to survive impact at 1200 ft/s.
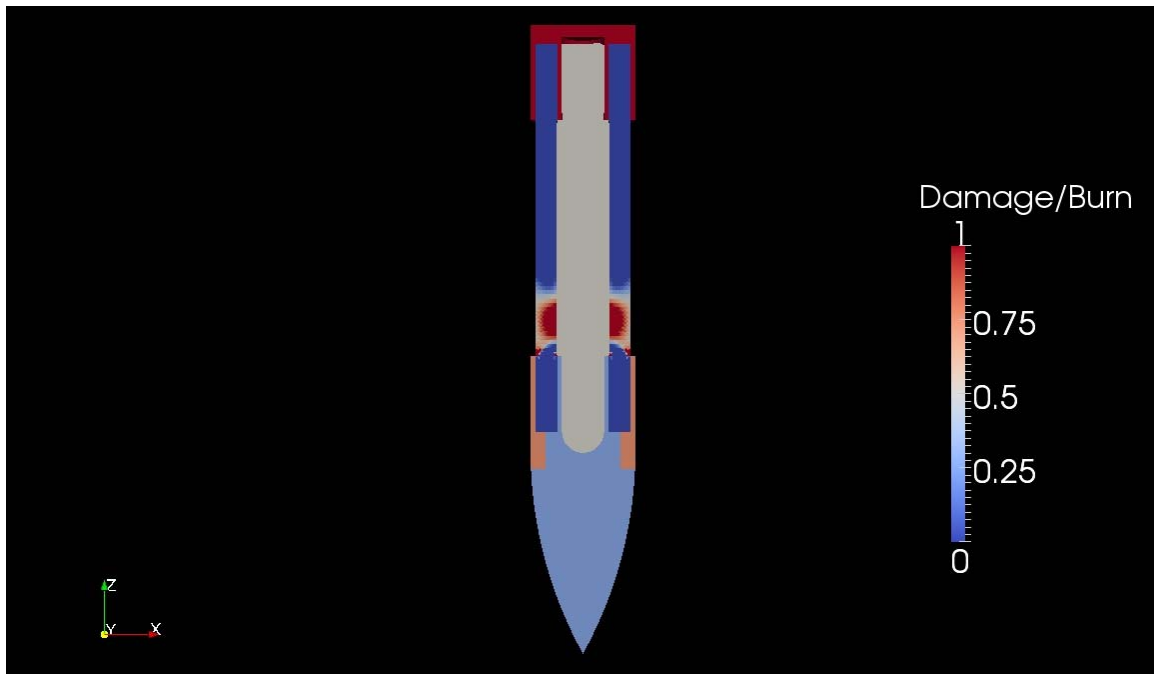
Fig. 13-17. Configuration E impact at 1200 ft/s against 6-ksi concrete.

13.2.8 Configuration F

Configuration F, shown in Fig. 13-18, shows the modification to the explosive cavity in the nose. The prior configurations with the cavity submerged in the nose only have a tensile strength on the flanges of 282,000 lb. By moving the forward edge of the explosive cavity back to a position in line with the end of the composite case, the new flange strength goes up to 464,000 lb and exceeds the 30,000-G load of 365,000 lb. Overall dimensions are the same as Configuration E. The projectile is 16.62 inches long with a 2.77-inch maximum outside diameter, with L/D = 6 and a weight of 17.5 lb.
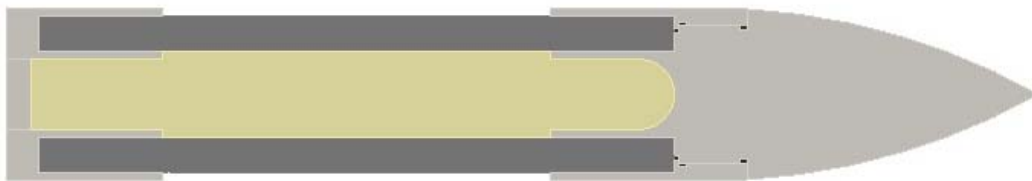
Fig. 13-18. Dynamic test vehicle configuration F.

When performing a simulation of the new geometry, the material properties for the RMS were included in the simulation. The most distinctive change is an increase in failure strain from a total strain of 1.5% to 2.5%. Figure 13-19 shows configuration F impacting 6-ksi concrete at 1200 ft/s and 0° AoA. The result is very similar to the Configuration E result, except for the lower damage value due to the increased plastic strain capacity of the RMS.
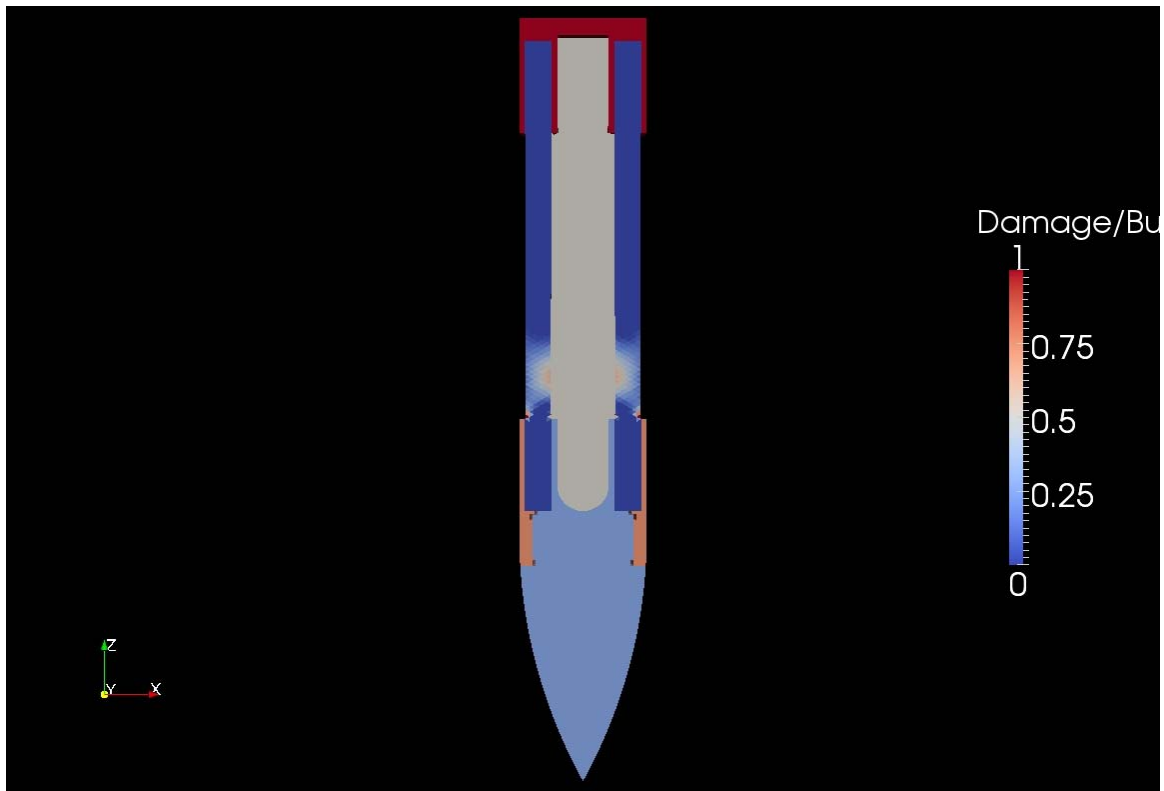
Fig. 13-19. Configuration F simulation of impact at 1200 ft/sec and 0° AoA.

13.2.9 Configuration G

Configuration G, shown in Fig. 13-20, has the flange thicknesses increased for support of pin fasteners to the hold the case in the event of adhesive failure. The outside diameter is 2.895 inches with a length of 17.37 inches to maintain L/D = 6.
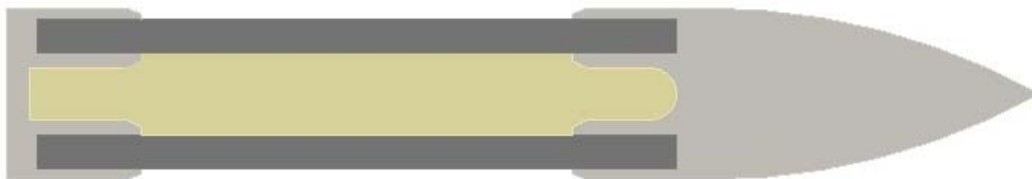
Fig. 13-20. Dynamic test vehicle configuration G.

Details of the joint design were finalized using the lessons learned from the Very High Velocity Penetrator test series[14]. The holes in the RMS are slotted to prevent preloading of the pins on initial impact, which creates very high compressive loads in the projectile. The slots are sized so deflection of the case does not preload the pins, so they retain full strength to bear the tensile stresses that occur during target breakout and axial vibration of the projectile. The pins are hardened setscrews with a modified tool socket. The as-manufactured depth of the socket is over 0.150 inch, which equals almost the entire thickness of the sleeves. The sockets are modified to only 0.062-inch deep, leaving the pin with a solid cross section for over 0.100 inch of the flange thickness. The design of these slots and pins was tested in compression and tension at Southern Research Institute (SoRI) as described in Section IX. Testing

---

[14] Feltz, L. V., "Structural Design of Very High Velocity Penetrators," Sandia Laboratories, presented at the *Conference on Rapid Penetration of Terrestrial Materials*, February 1973.

showed that the adhesive bond strength exceeds 30,000 lb, so it was decided to include some bond-only designs in the impact tests.

Figure 13-21 shows the five projectile designs selected for impact testing. The penetrators weigh from 19.6 to 23 lb, depending on sleeve length. The predicted damage of each design, shown in Fig. 13-22, indicates the expected performance at the different velocities. All penetrators are expected to survive at all impact velocities, except the sleeveless baseline at the higher velocities; we plan on testing these anyway in order to investigate failure criteria and damage modes.
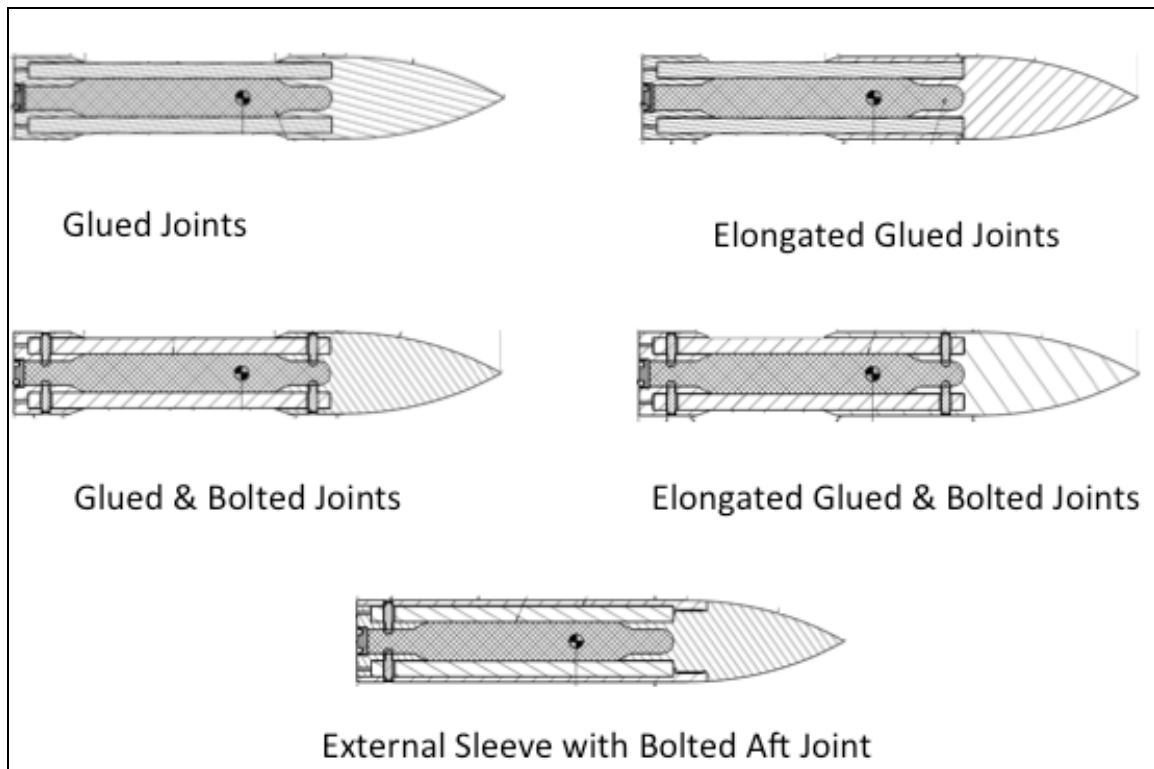
Fig. 13-21. Projectile designs.
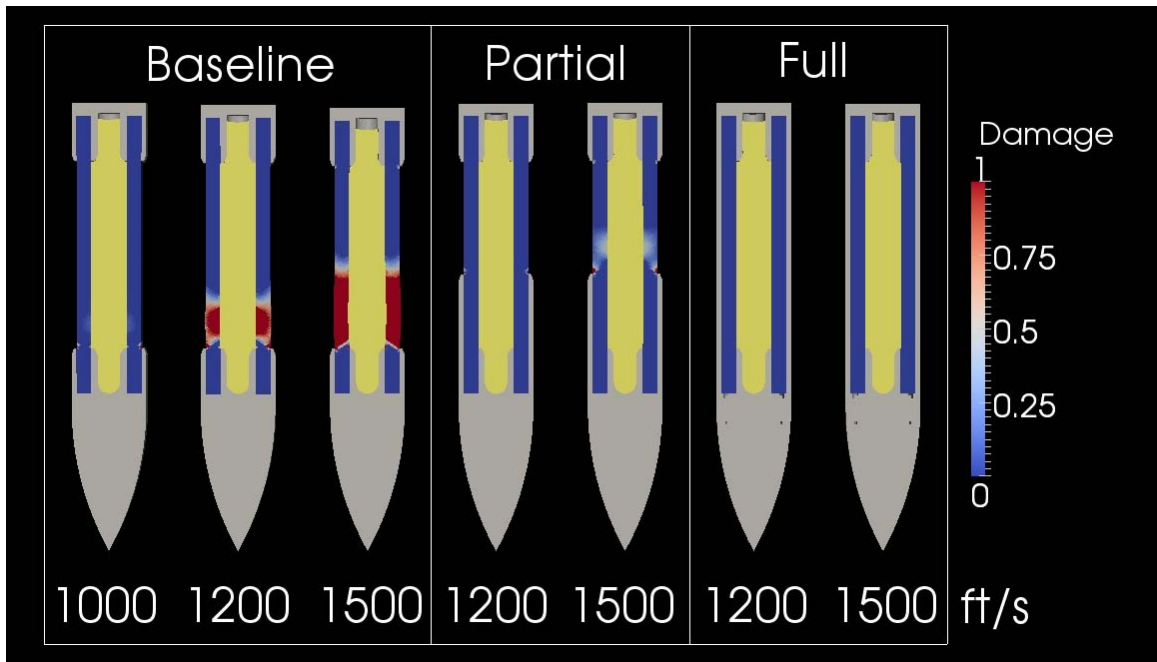
Fig. 13-22. Predicted damage of projectile designs at different impact velocities.

Section XIV

Ballistic Penetration Tests

This section describes the Ballistic Penetration Tests performed of the Dynamic Test Vehicle (DTV) configurations discussed in Section XIII above. A total of thirteen (13) tests were performed during the period from December 2 through 13, 2013. The tests were performed by the Energetic Materials Research and Testing Center (EMRTC), in Socorro, New Mexico.

Five (5) different DTV configurations were tested over a range of velocities. The primary objective of the test series was to ascertain the response of the composite bodies and associated joint designs to the penetration loads. The velocity of the penetrated was adjusted from test to test depending on the casing response from previous tests.

14.1 DTV Test Configurations

A total of five (5) configurations of the DTV were tested. Drawings of the five configurations are presented in Figs. 14-1 through 14-5, and a photograph of the completed specimens is shown in Fig. 14-6. All five configurations had the same overall length of 17.370 inches, and the same maximum outer diameter of 2.895 inches. The length-to-diameter (L/D) ratio for all configurations was 6. The nose and aft closure were made from 4340 steel, hardened to Rockwell C41. The nose was an ogive with a CRH of 4. The main body of the penetrators was made of a Tungsten-Epoxy composite, the inert surrogate of the RMS. The composite bodies had an average density of 6.274 g/cc. All of the penetrators were filled with an inert simulant of the Air Force Explosive AFX-757. The inert fills were loaded by McAlester Army Ammunition Plant. This fill was developed and characterized by Plunkett (2009). The density of the inert loads was measured to be 1.82 g/cc and the hardness was a 27 durometer, Shore A scale. The nominal masses of the configurations are summarized in Table 14-1.

ITEM	QTY	DESCRIPTION	DRAWING NUMBER	REVISION	TYPE
5	1	DTV RM CASE; BONDED	A656-2013-031	-	PART
4	1	DTV AFT CLOSURE PLUG	A656-2013-029	-	PART
3	1	DTV AFT END; PARTIAL EXT SLEEVE	A656-2013-027	-	PART
2	1	DTV OGIVE; SOLID, BONDED, 2" SLV	A656-2013-024	-	PART
1	1	CAST AFX-757 SIMULANT	-	-	PART

PARTS LIST
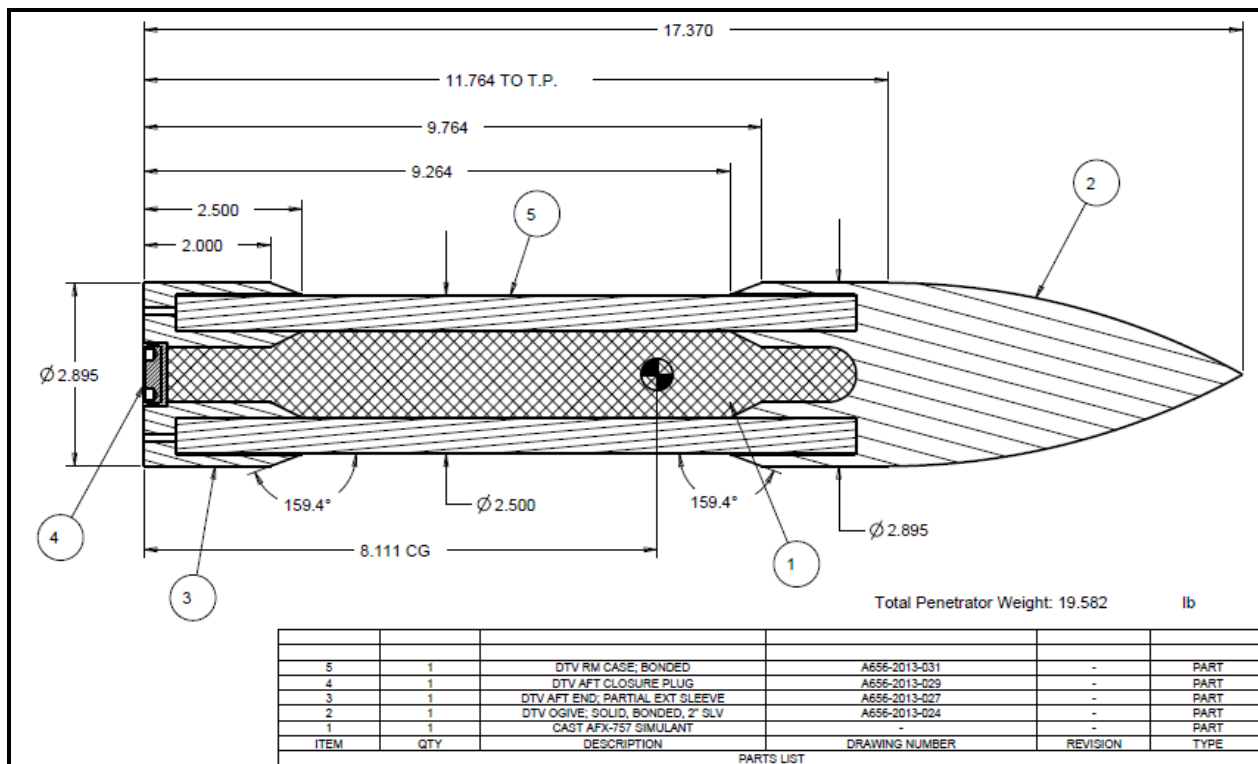
Fig. 14-1. DTV Configuration A.
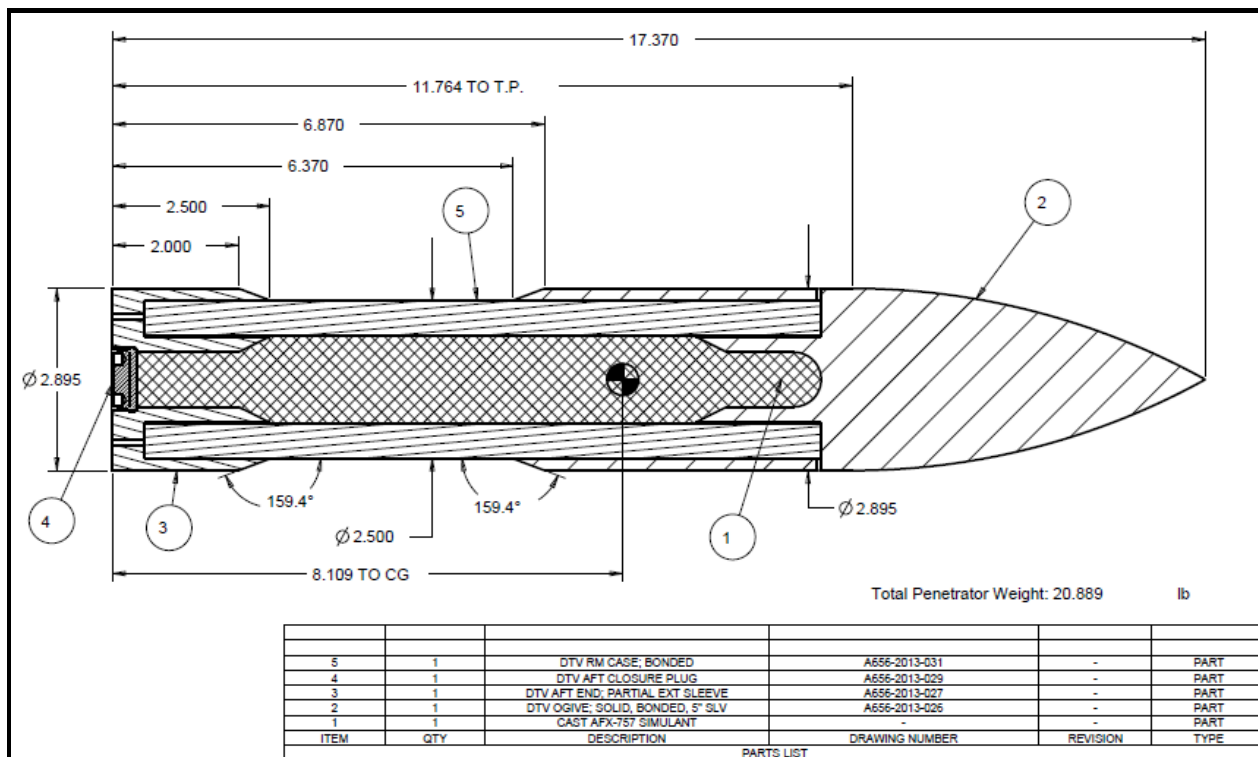
Fig. 14-2. DTV Configuration B.

5	1	DTV RM CASE; BONDED	A656-2013-031	-	PART
4	1	DTV AFT CLOSURE PLUG	A656-2013-029	-	PART
3	1	DTV AFT END; PARTIAL EXT SLEEVE	A656-2013-027	-	PART
2	1	DTV OGIVE; SOLID, BONDED, 5" SLV	A656-2013-026	-	PART
1	1	CAST AFX-757 SIMULANT	-	-	PART
ITEM	QTY	DESCRIPTION	DRAWING NUMBER	REVISION	TYPE
		PARTS LIST			
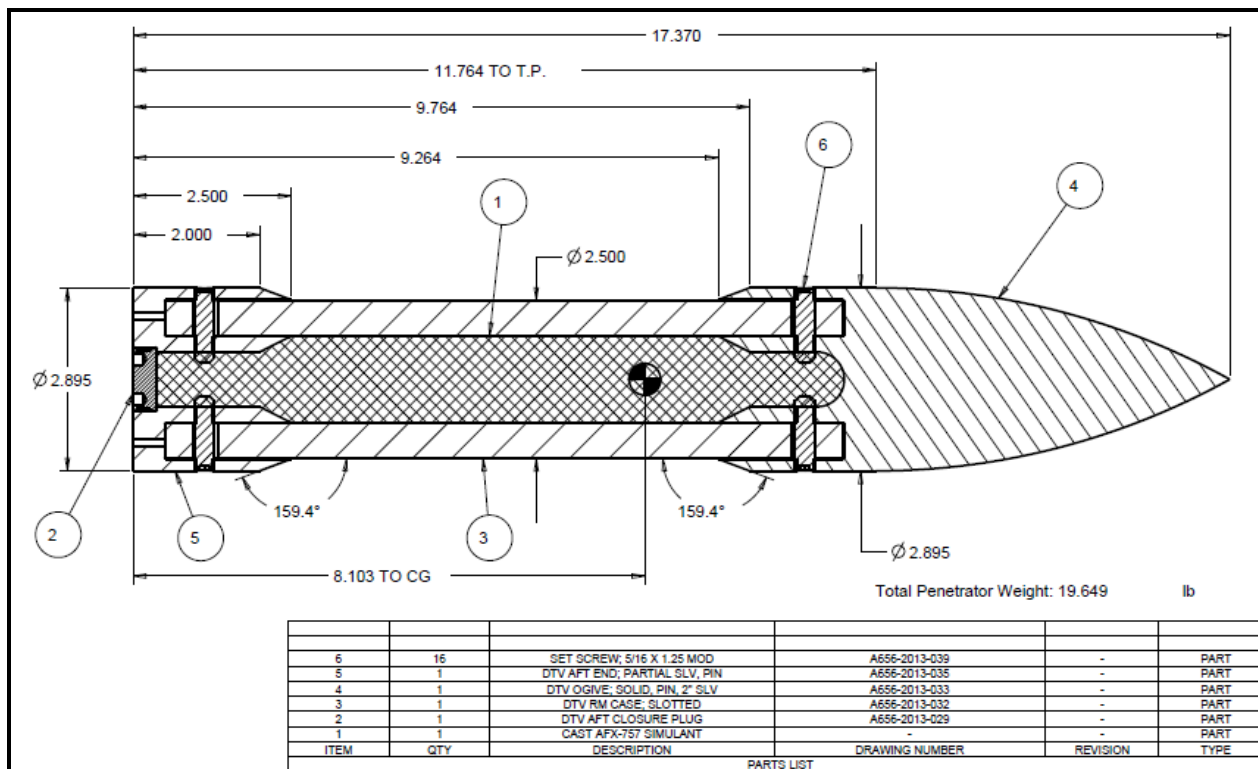
Fig. 14-3. DTV Configuration D.

6	16	SET SCREW; 5/16 X 1.25 MOD	A656-2013-039	-	PART
5	1	DTV AFT END; PARTIAL SLV, PIN	A656-2013-035	-	PART
4	1	DTV OGIVE; SOLID, PIN, 2" SLV	A656-2013-033	-	PART
3	1	DTV RM CASE; SLOTTED	A656-2013-032	-	PART
2	1	DTV AFT CLOSURE PLUG	A656-2013-029	-	PART
1	1	CAST AFX-757 SIMULANT	-	-	PART
ITEM	QTY	DESCRIPTION	DRAWING NUMBER	REVISION	TYPE
		PARTS LIST			

Fig. 14-4. DTV Configuration E.

ITEM	QTY	DESCRIPTION	DRAWING NUMBER	REVISION	TYPE
6	16	SET SCREW; 5/16 X 1.25 MOD	A656-2013-039	-	PART
5	1	DTV AFT END; PARTIAL SLV, PIN	A656-2013-035	-	PART
4	1	DTV OGIVE; SOLID, PIN, 5" SLV	A656-2013-034	-	PART
3	1	DTV RM CASE; SLOTTED	A656-2013-032	-	PART
2	1	DTV AFT CLOSURE PLUG	A656-2013-029	-	PART
1	1	CAST AFX-757 SIMULANT	-	-	PART

PARTS LIST

Total Penetrator Weight: 20.955 lb

Fig. 14-5. DTV Configuration F.

ITEM	QTY	DESCRIPTION	DRAWING NUMBER	REVISION	TYPE
7	1	DTV RM CASE; TAIL SLOTTED	A656-2013-040	-	PART
6	8	SET SCREW; 5/16 X 1.25 MOD	A656-2013-039	-	PART
5	1	DTV AFT CLOSURE PLUG	A656-2013-029	-	PART
4	1	DTV AFT END; FULL EXT SLEEVE	A656-2013-028	-	PART
3	1	DTV FWD SLEEVE; FULL	A656-2013-025	-	PART
2	1	DTV OGIVE; THREADED, NO PIN	A656-2013-023	-	PART
1	1	CAST AFX-757 SIMULANT	-	-	PART

PARTS LIST

Total Penetrator Weight: 22.947 lb

Fig. 14-6. The five DTV Configurations.

Table 14-1. Masses of the DTV Configurations.

Configuration	Joint Connection	Nominal Mass
A. 2-inch sleeve	Bonded	19.9 lb
B. 5-inch sleeve	Bonded	21.2 lb
D. 2-inch sleeve	Bonded & Pinned	19.8 lb
E. 5-inch sleeve	Bonded & Pinned	21.1 lb
F. Full Sleeve	Bonded & Rear Pinned	23.1 lb

The main differences between the configurations were the length of the steel sleeve and the interface attachment method of the fore and aft steel components. Configurations A and D have the shortest sleeve with a 2-inch length. The fore and aft interfaces of configuration A were only bonded, while the interfaces of configuration D were both bonded and screwed each with eight (8) 5/16-inch-diameter screws. Configurations B and E had 5-inch-long forward steel sleeves, with B having the bonded-only joints and E being both bonded and screwed as in Configuration D. Configuration F had a full-length steel sleeve. The forward interface of Configuration F was threaded onto the ogive while the aft interface was bonded and screwed in the same fashion as configurations D and E.

14.2 Test Setup

The tests were conducted at EMRTC's 1K West Range. EMRTC test engineers were Mr. Kent Harvey and Mr. Tony Zimmerly. A schematic of the test setup is shown in Fig. 14-7, and a photograph in Fig. 14-8. A 5-inch-diameter smoothbore powder gun, shown in Fig. 14-9, was used to launch the penetrators. The gun was converted from two 120-mm rifled naval guns with their barrels joined end to end to get a 50-ft muzzle length. The long barrel allows slower acceleration and softer launches. A 120-mm brass cartridge was used to contain the propellant, of type HC-33-FS, with grains about 1/8-inch diameter by 3/16-inch long with seven perforations. The primer was 28E01A.
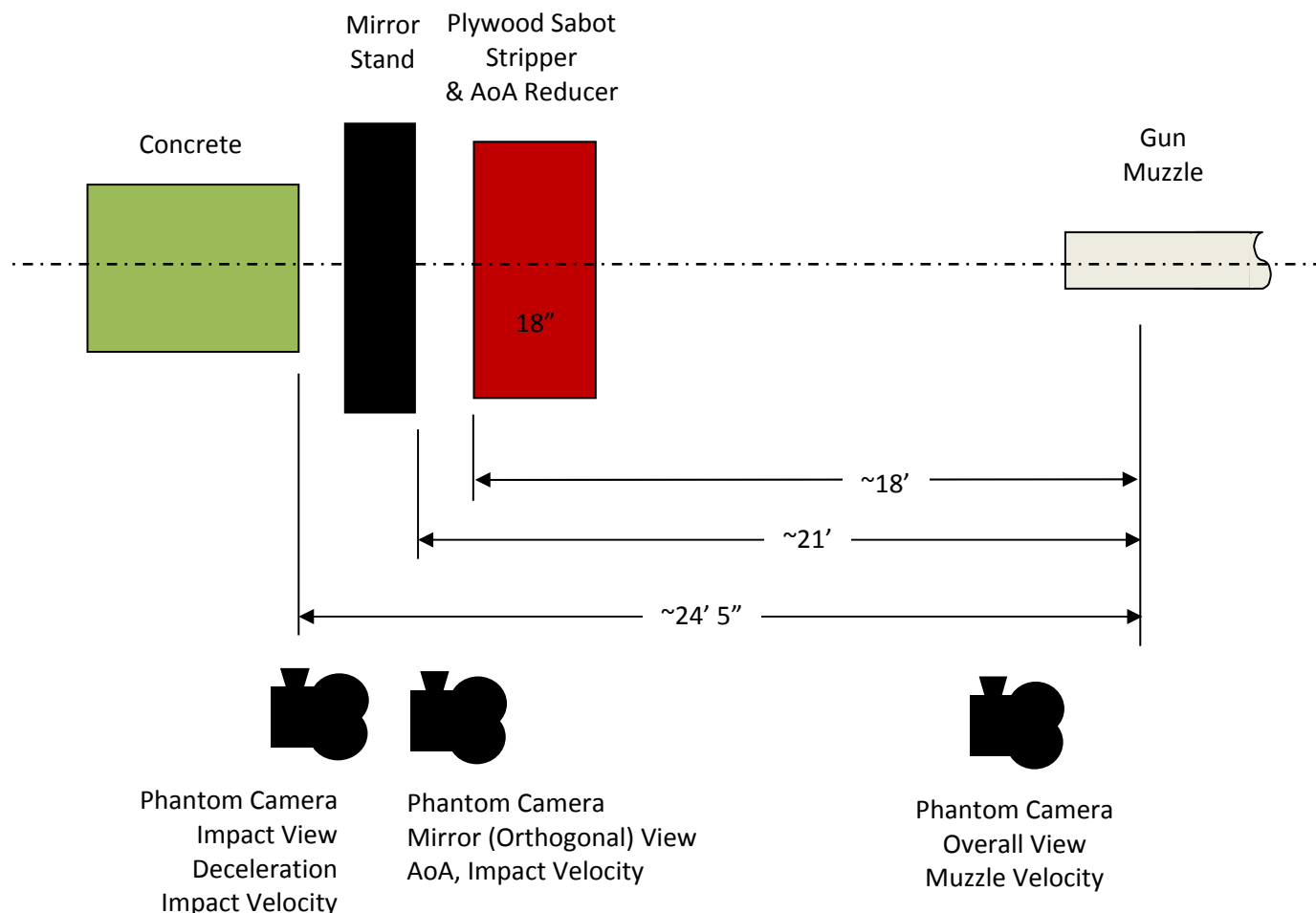
Fig. 14-7. Sketch of EMRTC 1K West Test Setup, plan view.

The launch package consisted of the DTV penetrator, a four-petal HDPE sabot, a steel or aluminum pusher plate, and a HDPE gas-sealing obturator. The sabot design underwent several changes during the testing. Photographs of the three sabot designs are presented in Fig. 14-10. The first sabot design (Fig. 14-10 (a)) had an internal step that mated with the composite body of the DTV penetrator. It was originally thought this step was needed to provide support to the penetrator during gun launch. In the first few shots, the sabot pedals were not separating from the penetrator quick enough, most probably due to the relatively low launch velocities. To promote separation a cylindrical, 5/8-inch-wide channel was machined along the internal surface of the sabot (Fig. 14-10(b)). The reasoning behind this modification was that during acceleration the air trapped in this channel gets compressed from the forward acceleration of the projectile. Once the launch package leaves the muzzle, this compressed air acts like a spring and pushes the sabot petals from the penetrator. The channels did help separation, but another problem was encountered. In some tests it seemed the penetrator was getting tipped in the plywood sabot stripper. It was proposed the internal step on the sabot has interacting with the aft steel fixture of the penetrator. This step was removed resulting in the third sabot modification shown in Fig. 14-10 (c).
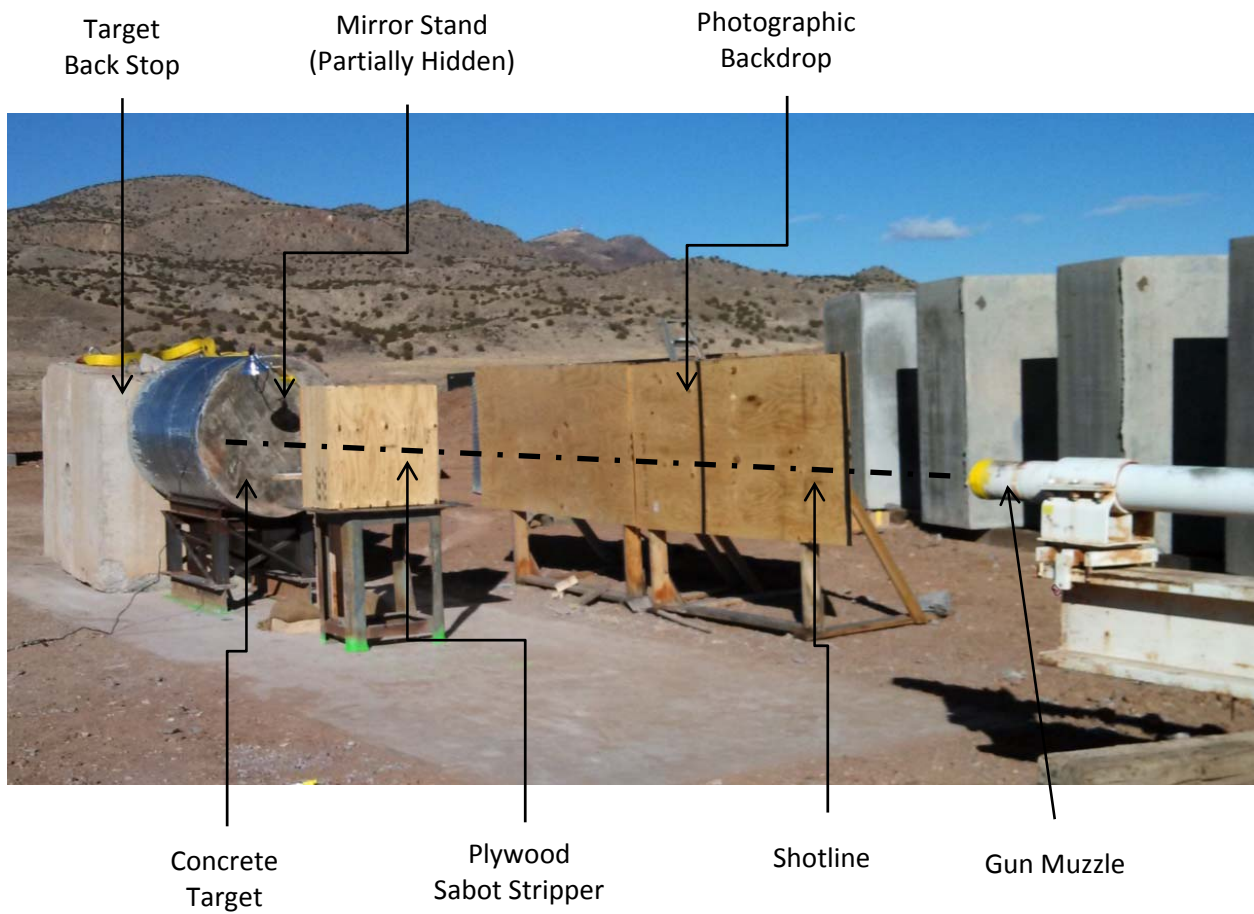
Fig. 14-8. EMRTC 1K West Test Setup.

Fig. 14-9. EMRTC 5-inch-Diameter Smoothbore Powder Gun.

(a) Design-1, stepped internal surface matching outside diameter of composite case

(b) Design-2, stepped internal surface matching outside diameter of composite case with cylindrical channels along the length

(c) Design-3, internal step removed with cylindrical channels along the length

Fig. 14-10. The three sabot designs used in the test series.

The sabot stripper was a 32-inch square by 18-inch-thick bundle of ½-inch-thick, 3-ply plywood sheets glued together. Besides stripping the sabot, it also helped to reduce the Angle of Attack (AoA) of the penetrator. AoA as used here refers to the angle between the penetrator's velocity vector and its centerline. An AoA of even only a couple of degrees can cause failure of a penetrator impacting concrete. EMRTC has used plywood bundles in the past to reduce the AoA of a penetrator prior to target impact.

Instrumentation included three Phantom video cameras. Recorded videos were used to measure muzzle velocity, impact velocity, AoA, and the deceleration of the penetrator while it was entering the target. One camera provided an overall view of the flight line from the gun muzzle to the target. Since this view covered a large area, the image resolution was much lower than the other two cameras. For the overall camera, the interval between frames was 100 microseconds, and the exposure time varied from 4 to 30 microseconds, depending on lighting conditions. This view was used primarily to measure the muzzle velocity of the penetrator and also recorded the sabot separation.

A second camera was trained on a mirror placed downrange of the sabot stripper. Its field of view was much smaller than the overall view, so its resolution was much finer. The interval between frames was 20 μs, and the exposure time was generally 0.43 μs. A flash bulb was used to illuminate the view area. The mirror provided an orthogonal view of the penetrator, thereby enabling an AoA measurement. This camera view was also used to measure the impact velocity of the penetrator.

A third camera was trained across the front face of the concrete target. As with the orthogonal view camera, the field of view was much smaller than the overall view, and consequently the image resolution was much finer. The interval between frames was 17.85 μs and the exposure time was generally 0.72 μs. The same flash bulb used to illuminate this view and the orthogonal view. This camera recorded the aft end of the penetrator during the penetration event. The data from this recording was primarily used to calculate the deceleration of the penetrator during impact with the concrete.

14.3 Targets

For all of the tests but two (Tests 12 and 13) the target was a concrete cylinder with a diameter of 48 inches and a length of 72 inches cast in corrugated steel tubes, as shown in Fig. 14-11. In Tests 12 and 13, the targets were two concrete cylinders butted one in on front of the other.

Fig. 14-11. Concrete target, 48 inches in diameter by 72 inches.

Five batches of concrete were required to fill fifteen targets. During the casting, seven crush cylinders (4 inches in diameter by 8 inches) were cast from each batch for strength testing. The measured density of the concrete was 134 lb/ft^3 (2.15 g/cc).

The specification for the concrete was 5,000 psi compressive strength. Crush tests were done on the crush cylinders at cure times of 14, 28, and 311 (time of testing) days. Table 14-2 summarizes the measured strengths. As the data shows, the average concrete strength during the tests was 9,900 psi. IN the discussion of each test below, the specific concrete strength is reported.

Table 14-2. Measured Compressive Strengths of Concrete Crush Cylinders.

Cure Time (days)	Average Strength (ksi)
14	5.9
28	7.3
311 (Test condition)	9.9*

* Batch 1 strength was 9.4 ksi. Average w/o batch 1 is 10.0 ksi.
Batch 1 was only used in 1 test (#13)

14.4 Test Results

A total of thirteen tests were performed of the various DTV configurations discussed above. The primary objective of the test series was to ascertain the maximum velocity that each DTV configuration survived the impact and penetration of the concrete. During the test series, the velocities were adjusted based on the state of the recovered DTV penetrator from previous tests. Hence not all of the DTV configurations were tested over the same velocity range.

The results from each test are discussed below. Table 14-3 summarizes the tests according to DTV configuration, impact velocity, Angle of Attack (AoA), and penetration. Included are images taken from the high-speed videos from the three cameras. The velocity, AoA, and deceleration were calculated from the high-speed videos. Also included are photographs of the recovered post-test DTV penetrators.

Table 14-3. Summary of Experimental Data from Tests of the DTV Configurations.

Test	Design	Impact Velocity		Angle of Attack		Deceleration		Penetration (inches)
		Nominal (ft/sec)	± Error (ft/sec)	Nominal	± Error	Peak (kG)	Average (kG)	
1	E-1	1327	16	0.28°	0.71°	21.9	19.5	21
2	B-1	1319	26	0.80°	0.88°	21.2	15.6	21.3
3	D-1	1287	6	0.48°	0.95°	20.0	18.6	17*
4	A-1	954	7	0.52°	0.49°	17.4	14.4	14
5	D-2	910	4	0.48°	0.13°	20.7	17.8	12
6	D-3	1090	8	0.57°	0.56°	20.7	17.5	21
7	D-4	983	13	0.02°	0.63°	23.0	18.3	14.5
8	E-2	1523	11	1.35°	0.48°	25.8	22.1	27
9	E-3	1652	7	0.41°	0.75°	23.9	20.4	31.3
10	E-4	1946	24	7.46°	0.49°	N/A	N/A	36*
11	B-2	1809	13	0.72°	0.65°	22.0	17.5	38.5
12	F-1	2086	9	0.48°	0.43°	21.3	16.5	54.9
13	F-2	2494	11	0.53°	0.16°	17.1	14.0	76

*Penetrator completely failed.

Test Number 1

Test Number 1 was of the DTV-E-1 configuration. A summary of the test parameters is presented in Table 14-4. Two still images taken from each of the overall and orthogonal videos are presented in Figures 14-12 and 14-13. Three still images taken from the impact view video are presented in Fig. 14-14.

Table 14-4. Summary of Test Number 1.

Test	1
Date	12/3/2013
Design	DTV-E-1
Muzzle Velocity (ft/s)	1,426 ± 5
Impact Velocity (ft/s)	1,327 ± 16
Angle of Attack	0.28° ± 0.71°
Peak Deceleration (kG)	21.9
Average Deceleration (kG)	19.5
Penetration (in)	21.0
Concrete Lot #	3
Concrete Strength (ksi)	Tests 1, 2, 3: 10.27; 9.88; 9.70; Average: 9.95
Comment	Undamaged

Early

Late

Fig. 14-12. Images from overall video of Test Number 1, Design DTV-E-1.

Early

Late

Fig. 14-13. Images from orthogonal video of Test Number 1, Design DTV-E-1.
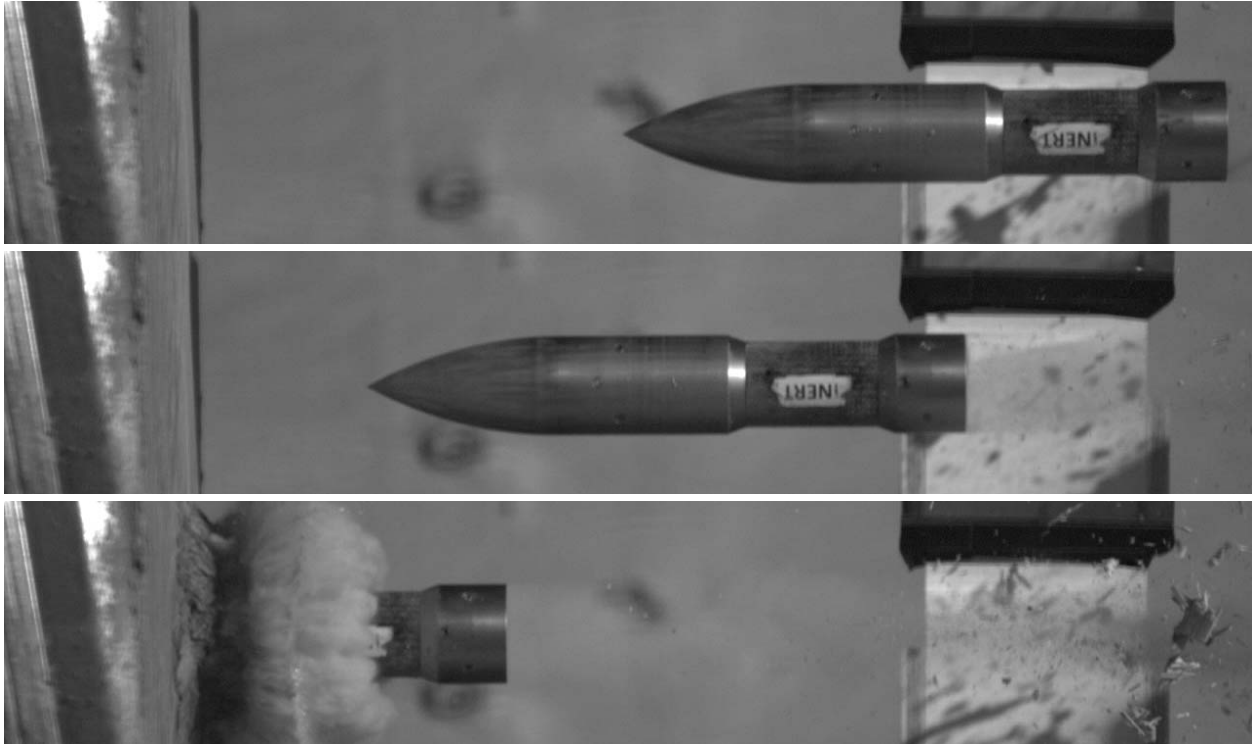
Fig. 14-14. Images from impact video of Test Number 1, Design DTV-E-1.

The DTV-E-1 penetrated 21.0 inches into the concrete target. A photograph of the target after the test is presented in Fig. 14-15. A post-test analysis of the penetrator indicated no significant damage to the composite body nor the attachment interfaces. Photographs of the post-test penetrator are presented in Fig. 14-16.

Fig. 14-15. Concrete target from Test 1, Design DTV-E-1, EMRTC technician for size reference.

0°

90°

180°

270°

Fig. 14-16. Views of DTV-E-1 Penetrator from Test 1 at 0°, 90°, 180°, and 270°.

Test Number 2

Test Number 2 was of the DTV-B-1 configuration. Since the DTV-E-1 design survived at 1,327 ft/s in Test 1 above, this test was conducted at the same velocity to determine if the bonded-only interfaces would survive. A summary of the test parameters is presented in Table 14-5. Two still images taken from each of the overall and orthogonal videos are presented in Figs. 14-17 and 14-18. Three still images taken from the impact view video are presented in Fig. 14-19. These images were somewhat overexposed.

Table 14-5. Summary of Test Number 2.

Test	2
Date	12/4/2013
Design	DTV-B-1
Muzzle Velocity (ft/s)	1,422 ± 5
Impact Velocity (ft/s)	1,319 ± 26
Angle of Attack	0.80° ± 0.88°
Peak Deceleration (kG)	21.2
Average Deceleration (kG)	15.6
Penetration (in)	21.3
Concrete Lot #	5
Concrete Strength (ksi)	Tests 1, 2, 3: 9.92; 10.10; 10.02; Average: 10.01
Comment	Undamaged

Early

Late

Fig. 14-17. Images from overall video of Test Number 2, Design DTV-B-1.

Fig. 14-18. Images from orthogonal video of Test Number 2, Design DTV-B-1.
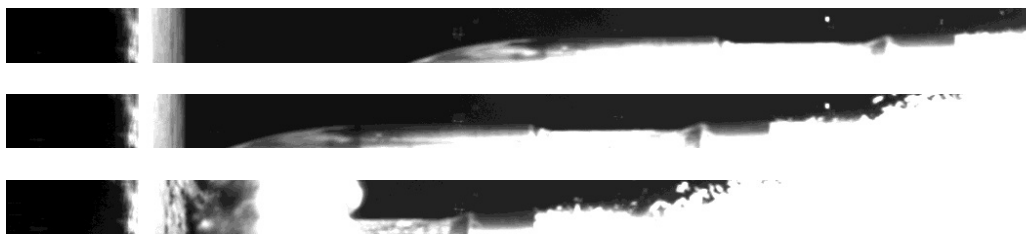
Fig. 14-19. Images from impact video of Test Number 2, Design DTV-B-1.

The DTV-B-1 penetrated 21.3 inches into the concrete target. A photograph of the target after the test is presented in Fig. 14-20. A post-test analysis of the penetrator indicated no significant damage to the composite body nor the attachment interfaces. Both the forward and aft bonded only interfaces survived. Photographs of the post-test penetrator are presented in Fig. 14-21.

Fig. 14-20. Concrete target from Test 2, Design DTV-B-1.

0°   90°

180°   270°

Fig. 14-21. Photographs of DTV-B-1 Penetrator from Test 2 at 0°, 90°, 180°, and 270°.

Test Number 3

Test Number 3 was of the DTV-D-1 configuration. This was the first test of the 2-inch-sleeve configuration. It was decided to test the short sleeve design at the same velocity as the previous two tests of the 5-inch sleeve configuration. A summary of the test parameters is presented in Table 14-6. Two still images taken from each of the overall and orthogonal videos are presented in Figs. 14-22 and 14-23. Three still images taken from the impact view video are presented in Fig. 14-24.

Table 14-6. Summary of Test Number 3.

Test	3
Date	12/9/2013
Design	DTV-D-1
Muzzle Velocity (ft/s)	1,427 ± 4
Impact Velocity (ft/s)	1,287 ± 6
Angle of Attack	0.48° ± 0.95°
Peak Deceleration (kG)	20.0
Average Deceleration (kG)	18.6
Penetration (in)	17.0
Concrete Lot Number	4
Concrete Strength (ksi)	Tests 1, 2, 3: 9.99, 10.07; 10.16; Average: 10.07
Comment	Failed

Early

Late

Fig. 14-22. Images from overall video of Test Number 3, Design DTV-D-1.

Fig. 14-23. Images from orthogonal video of Test Number 3, Design DTV-D-1.

Fig. 14-24. Images from impact video of Test Number 3, Design DTV-D-1.

The composite body of the penetrator completely failed just aft of the forward interface. The DTV-D-1 penetrated 17.0 inches into the concrete target. Photographs of the post-test penetrator are presented in Fig. 14-25.

Fig. 14-25. Photographs of DTV-D-1 Penetrator from Test 3.

Test Number 4

Test Number 4 was of the DTV-A-1 configuration. Based on the structural failure of the short sleeve design in Test 3, the velocity was lowered in this test. A summary of the test parameters is presented in Table 14-7. Two still images taken from each of the overall and orthogonal videos are presented in Figs. 14-26 and 14-27. Three still images taken from the impact view video are presented in Fig. 14-28.

Table 14-7. Summary of Test Number 4.

Test	4
Date	12/9/2013
Design	DTV-A-1
Muzzle Velocity (ft/s)	1,091 ± 3
Impact Velocity (ft/s)	954 ± 7
Angle of Attack	0.52° ± 0.49°
Peak Deceleration (kG)	17.4
Average Deceleration (kG)	14.4
Penetration (in)	14.0
Concrete Lot #	4
Concrete Strength (ksi)	Tests 1, 2, 3: 9.99; 10.07; 10.16; Average: 10.07
Comment	Undamaged

Early

Late

Fig. 14-26. Images from overall video of Test Number 4, Design DTV-A-1.

Fig. 14-27. Images from orthogonal video of Test Number 4, Design DTV-A-1.
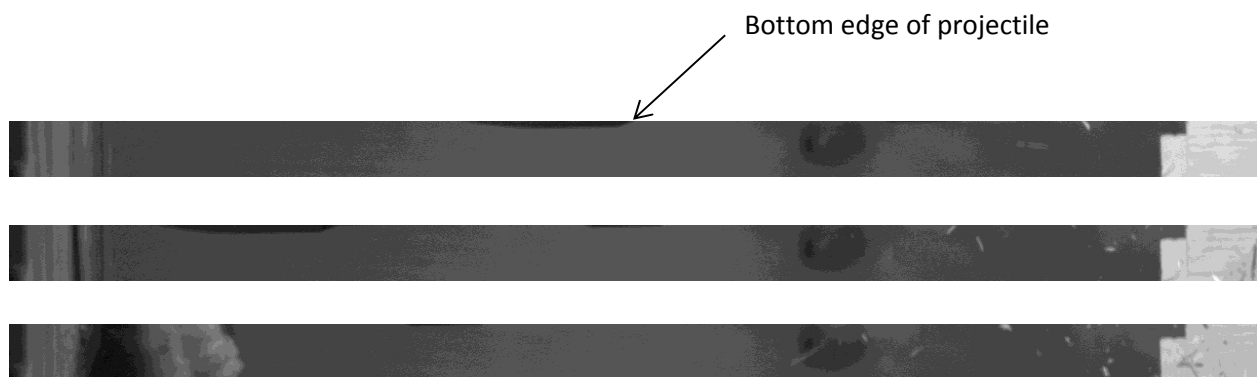
Fig. 14-28. Images from impact video of Test Number 4, Design DTV-A-1.

The DTV-A-1 penetrated 14.0 inches into the concrete target. A photograph of the target after the test is presented in Fig. 14-29. A post-test analysis of the penetrator indicated no significant damage to the composite body nor the attachment interfaces. Photographs of the post-test penetrator are presented in Fig. 14-30.

Fig. 14-29. Concrete target from Test 4, Design DTV-A-1.

0°

90°

180°

270°

Fig. 14-30. Photographs of DTV-A-1 Penetrator from Test 4 at 0°, 90°, 180°, and 270°.

Test Number 5

Test Number 5 was of the DTV-D-2 configuration at the same nominal velocity as Test 4. A summary of the test parameters is presented in Table 14-8. Two still images taken from each of the overall and orthogonal videos are presented in Figs. 14-31 and 14-32. Three still images taken from the impact view video are presented in Fig. 14-33. There was some interference with these images.

Table 14-8. Summary of Test Number 5.

Test	5
Date	12/10/2013
Design	DTV-D-2
Muzzle Velocity (ft/s)	1,055 ± 3
Impact Velocity (ft/s)	910 ± 4
Angle of Attack	0.48° ± 0.13°
Peak Deceleration (kG)	20.7
Average Deceleration (kG)	17.8
Penetration (in)	12.0
Concrete Lot #	4 (front 1-foot of target), Lot 5 in rear
Concrete Strength (lot 4) (ksi)	Tests 1, 2, 3: 9.99; 10.07; 10.16; Average: 10.07
Comment	Undamaged

Early

Late

Fig. 14-31. Images from overall video of Test Number 5, Design DTV-D-2.

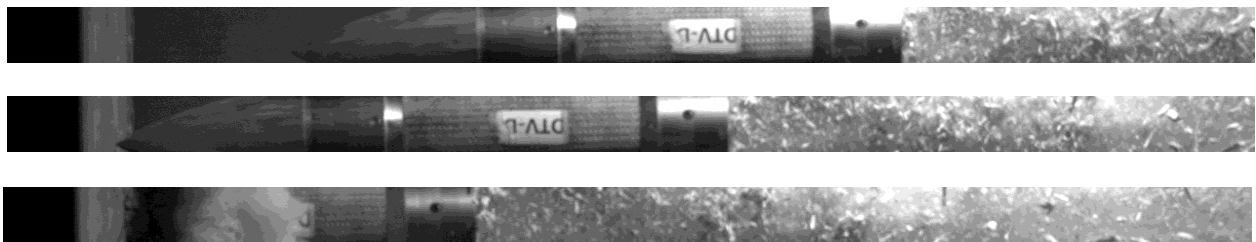Fig. 14-32. Images from orthogonal video of Test Number 5, Design DTV-D-2.

Fig. 14-33. Images from impact video of Test Number 5, Design DTV-D-2.

The DTV-D-2 penetrated 12.0 inches into the concrete target. A photograph of the target after the test is presented in Fig. 14-34. A post-test analysis of the penetrator indicated no significant damage to the composite body nor the attachment interfaces. Photographs of the post-test penetrator are presented in Fig. 14-35.

Fig. 14-34. Concrete target from Test 5, Design DTV-D-2.

0°

90°

180°

270°

Fig. 14-35. Photographs of DTV-D-2 Penetrator from Test 5 at 0°, 90°, 180°, and 270°.

Test Number 6

Test Number 6 was of the DTV-D-3 configuration. Since the short sleeve design survived the last two tests, the velocity was increased about 200 ft/s for this tests. A summary of the test parameters is presented in Table 14-9. Two still images taken from each of the overall and orthogonal videos are presented in Figs. 14-36 and 14-37. Three still images taken from the impact view video are shown in Fig. 14-38.

Table 14-9. Summary of Test Number 6.

Test	6
Date	12/10/2013
Design	DTV-D-3
Muzzle Velocity (ft/s)	1,224 ± 3
Impact Velocity (ft/s)	1,090 ± 8
Angle of Attack	0.57° ± 0.56°
Peak Deceleration (kG)	20.7
Average Deceleration (kG)	17.5
Penetration (in)	20.0
Concrete Lot #	3 (front 3-feet of target), Lot 4 in rear
Concrete Strength (lot 3) (ksi)	Tests 1, 2, 3: 10.27; 9.88; 9.70; Average: 9.95
Comment	Failed

Early

Late

Fig. 14-36. Images from overall video of Test Number 6, Design DTV-D-3.

Fig. 14-37. Images from orthogonal video of Test Number 6, Design DTV-D-3.

Fig. 14-38. Images from impact video of Test Number 6, Design DTV-D-3.

The DTV-D-3 penetrated 20.0 inches into the concrete target. A photograph of the target after the test is presented in Fig. 14-39. The penetrator was severely bent aft of the forward steel sleeve. Post-test photographs of the penetrator are presented in Fig. 14-40.

Fig. 14-39. Concrete target from Test 6, Design DTV-D-3.

0°

90°

180°

270°

Fig. 14-40. Photographs of DTV-D-3 Penetrator from Test 6 at 0°, 90°, 180°, and 270°.

Test Number 7

Test Number 7 was of the DTV-D-4 configuration. Since the short sleeve design failed in the previous test, the velocity was lowered about 100 ft/s in this test. A summary of the test parameters is presented in Table 14-10. Two still images taken from each of the overall and orthogonal videos are presented in Figs. 14-41 and 14-42. Three still images taken from the impact view video are presented in Fig. 14-43.

Table 14-10. Summary of Test Number 7.

Test	7
Date	12/11/2013
Design	DTV-D-4
Muzzle Velocity (ft/s)	1,124 ± 4
Impact Velocity (ft/s)	983 ± 13
Angle of Attack	0.02° ± 0.63°
Peak Deceleration (kG)	23.0
Average Deceleration (kG)	18.3
Penetration (in)	14.5
Concrete Lot #	4
Concrete Strength (ksi)	Tests 1, 2, 3: 9.99; 10.07; 10.16; Average: 10.07
Comment	Slight Damage

Early

Late

Fig. 14-41. Images from overall video of Test Number 7, Design DTV-D-4.

Fig. 14-42. Images from orthogonal video of Test Number 7, Design DTV-D-4.
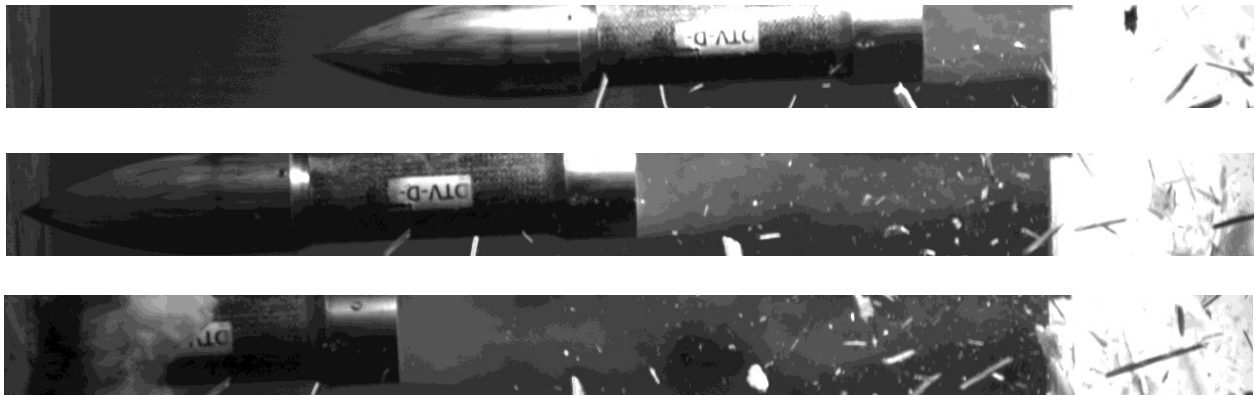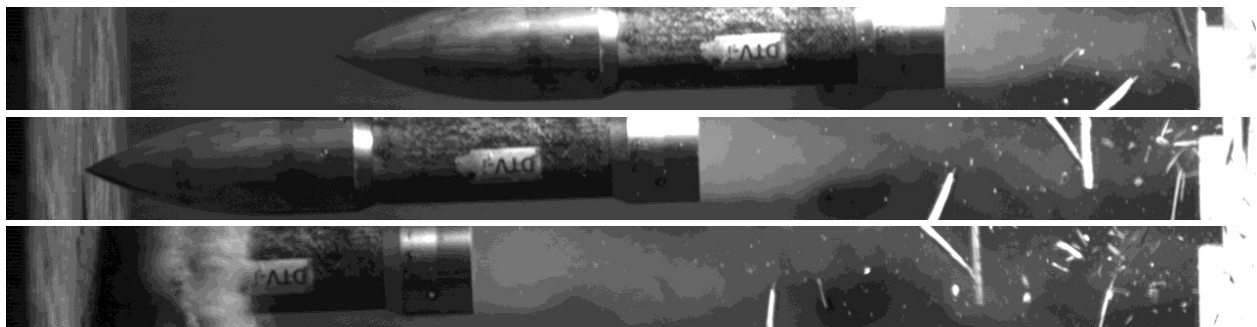

Fig. 14-43. Images from impact video of Test Number 7, Design DTV-D-4.

The DTV-D-4 penetrated 14.5 inches into the concrete target. A photograph of the target after the test is presented in Fig. 14-44. The penetrator exhibited some slight damage just aft of the forward steel sleeve. Photographs of the post-test penetrator are presented in Figs. 14-45 and 14-46.

Fig. 14-44. Concrete target from Test 7, Design DTV-D-4.

0°

90°

180°

270°

Figure 14-45. Photographs of DTV-D-4 Penetrator from Test 7 at 0°, 90°, 180°, and 270°.
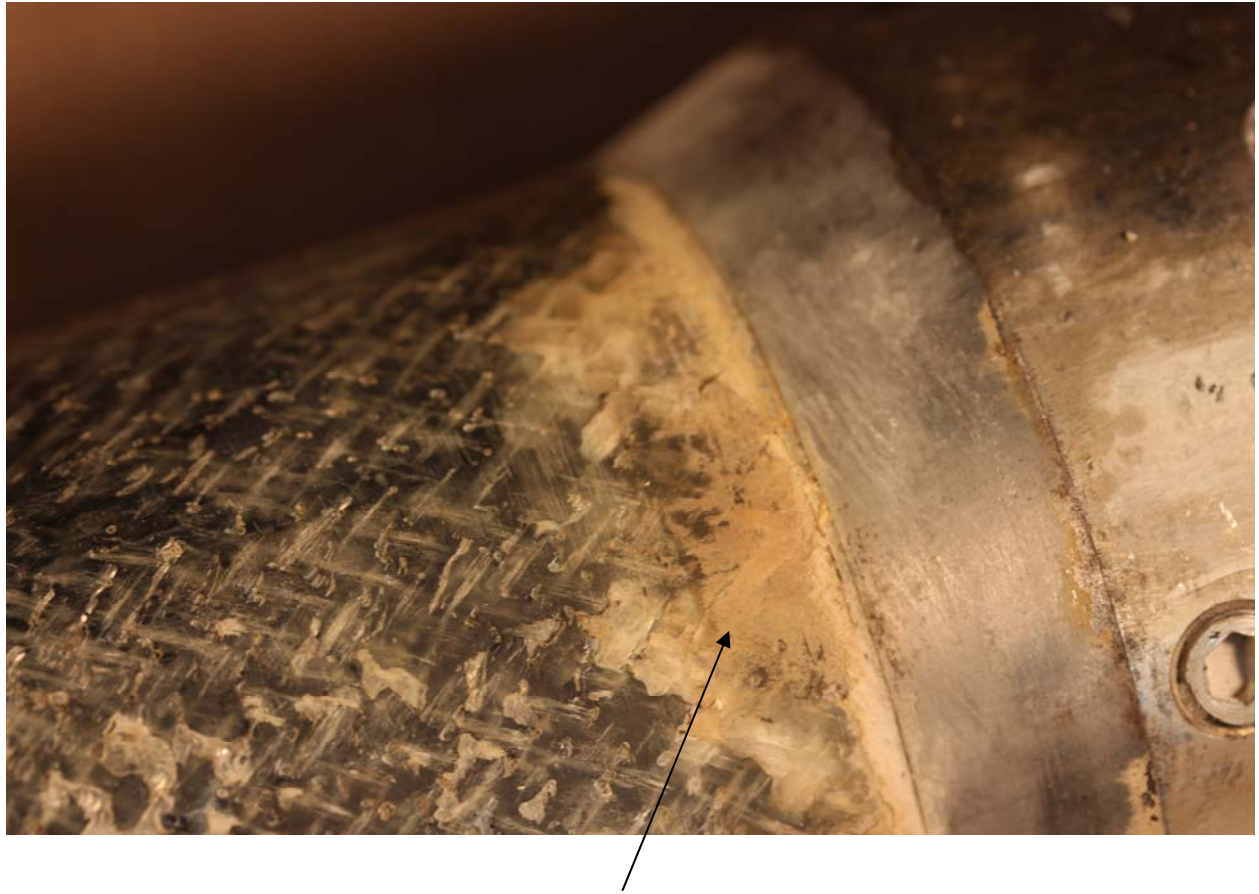
Onset of damage just aft of the
forward steel sleeve

Fig. 14-46. Damage to the DTV-D-4 Penetrator from Test 7.

Test Number 8

At this point in the series it was decided to cease testing the short-sleeve designs (Configurations A and D) as the apparent velocity for the onset of failure was determined in the previous two tests. Efforts focused on the 5-inch-long sleeve designs (Configurations B and E). Test Number 8 was of the DTV-E-2 configuration but at a faster velocity than the previous two tests of the 5-inch design. A summary of the test parameters is presented in Table 14-11. Two still images taken from each of the overall and orthogonal videos are presented in Figs. 14-47 and 14-48. Three still images taken from the impact view video are presented in Fig. 14-49.

Table 14-11. Summary of Test Number 8.

Test	8
Date	12/11/2013
Design	DTV-E-2
Muzzle Velocity (ft/s)	1,637 ± 4
Impact Velocity (ft/s)	1,523 ± 11
Angle of Attack	1.35° ± 0.48°
Peak Deceleration (kG)	25.8
Average Deceleration (kG)	22.1
Penetration (in)	27.0
Concrete Lot #	2
Concrete Strength (ksi)	Tests 1, 2, 3: 10.05; 10.02; 9.71; Average: 9.93
Comment	Undamaged

Early

Late

Fig. 14-47. Images from overall video of Test Number 8, Design DTV-E-2.
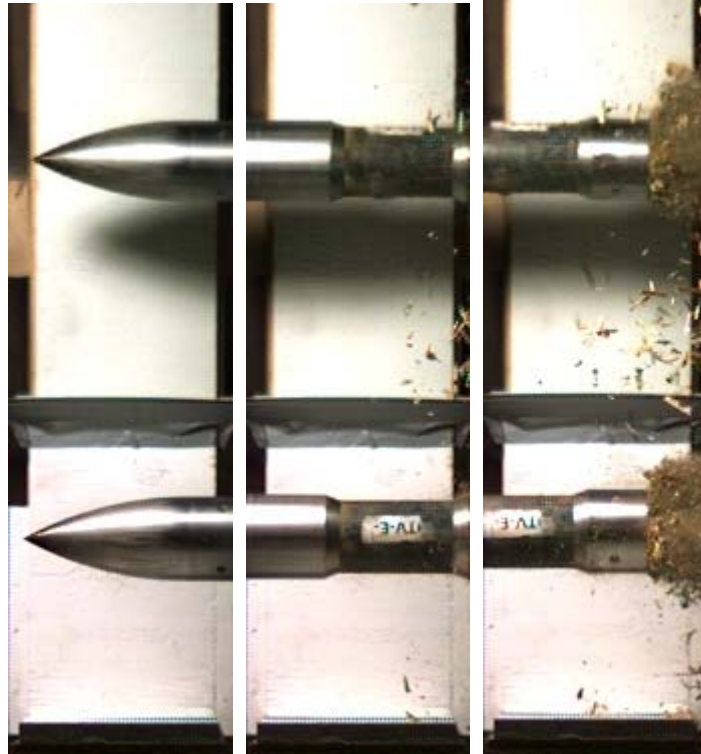
Fig. 14-48. Images from orthogonal video of Test Number 8, Design DTV-E-2.
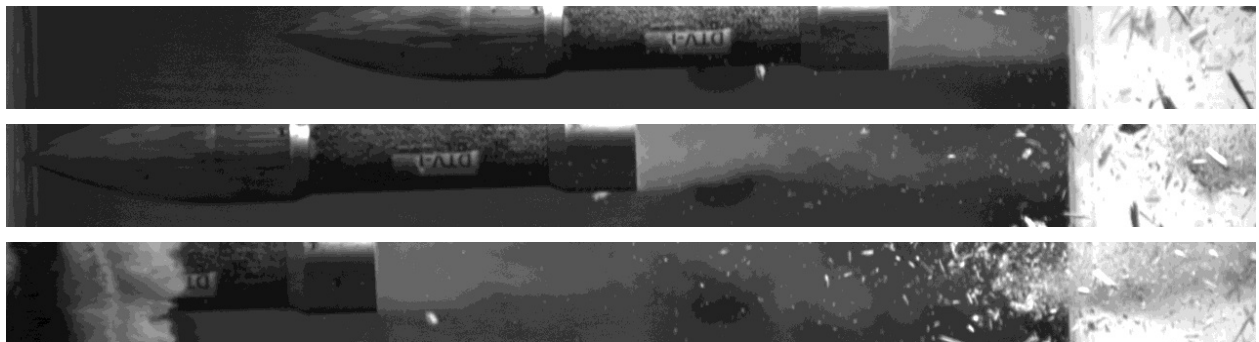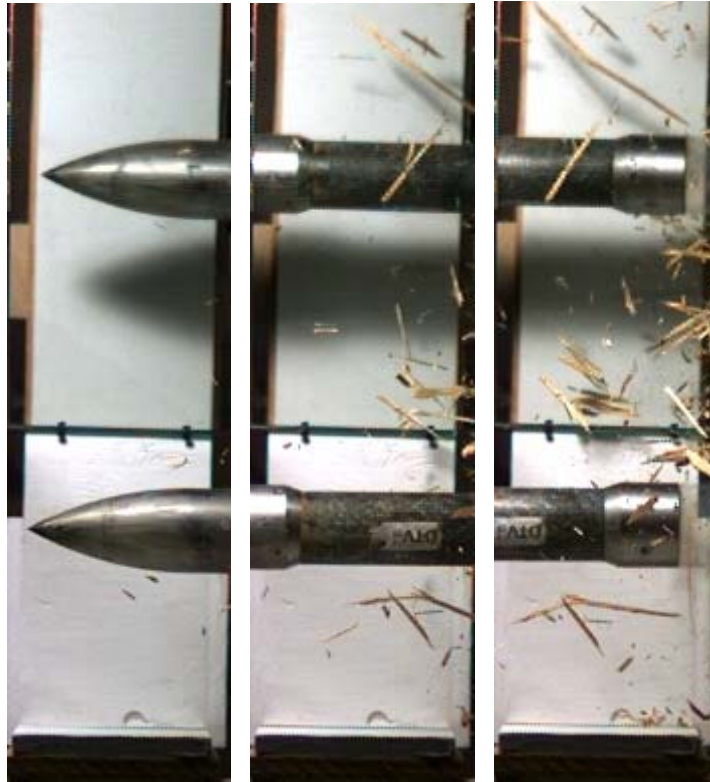

Fig. 14-49. Images from orthogonal impact video of Test Number 8, Design DTV-E-2.

The DTV-E-2 penetrated 27.0 inches into the concrete target. A photograph of the target after the test is presented in Fig. 14-50. The composite body exhibited some slight damage just aft of the forward steel sleeve. In addition the aft steel end fixture exhibited minor damage. Photographs of the post-test penetrator are presented in Figs. 14-51 and 14-52.

Fig. 14-50. Concrete target from Test 8, Design DTV-E-2.

0°

90°

180°

270°

Fig. 14-51. Photographs of DTV-E-2 Penetrator from Test 8 at 0, 90, 180, and 270°.

(a) Mark indicating axial compression of case within forward sleeve

(b) Slight damage to end cap taper due to target interaction

Fig. 14-52. Damage to the DTV-E-2 Penetrator from Test 8.

Test Number 9

Test Number 9 was of the DTV-E-3 configuration, but the velocity was increased given the success of the previous test. A summary of the test parameters is presented in Table 14-12. Two still images taken from each of the overall and orthogonal videos are presented in Figs. 14-53 and 14-54. Three still images taken from the impact view video are presented in Fig. 14-55.

Table 14-12. Summary of Test Number 9.

Test	9
Date	12/11/2013
Design	DTV-E-3
Muzzle Velocity (ft/s)	1,758 ± 5
Impact Velocity (ft/s)	1,652 ± 7
Angle of Attack	0.41° ± 0.75°
Peak Deceleration (kG)	23.9
Average Deceleration (kG)	20.4
Penetration (in)	31.3
Concrete Lot #	2 (front 3.25-feet of target), Lot 3 in rear
Concrete Strength (Lot 2) (ksi)	Tests 1, 2, 3: 10.05; 10.02; 9.71; Average: 9.93
Comment	Undamaged

Early

Late

Fig. 14-53. Images from overall video of Test Number 9, Design DTV-E-3.

Fig. 14-54. Images from orthogonal video of Test Number 9, Design DTV-E-3.

Fig. 14-55. Images from orthogonal impact video of Test Number 9, Design DTV-E-3.

The DTV-E-3 penetrated 31.3 inches into the concrete target. A photograph of the target after the test is presented in Fig. 14-56. The aft steel closure exhibited minor damage. Photographs of the post-test penetrator are presented in Figs. 14-57 and 14-58.

Fig. 14-56. Concrete target from Test 9, Design DTV-E-3.

0°

90°

180°

270°

Fig. 14-57. Photographs of DTV-E-3 Penetrator from Test 9 at 0°, 90°, 180°, and 270°.

Damage to aft steel closure.

Fig. 14-58. Damage to the DTV-E-3 Penetrator from Test 9.

Test Number 10

Test Number 10 was of the DTV-E-4 configuration. The velocity for this test was increased based on the success of the previous test. The test parameters are summarized in Table 14-13. Two still images taken from each of the overall and orthogonal videos are presented in Figs. 14-59 and 14-60. The images from the orthogonal video in Fig. 14-58 show a steel fragment that appears to have fractured from the aft fixture while the penetrator was interacting with the sabot stripper. This interaction caused significant rotation of the penetrator resulting in an AoA of over 7°. Three still images taken from the impact view video are presented in Fig. 14-61. The large AoA can be seen in the images of Fig. 14-61.

Table 14-13. Summary of Test Number 10.

Test	10
Date	12/12/2013
Design	DTV-E-4
Muzzle Velocity (ft/s)	2,133 ± 6
Impact Velocity (ft/s)	1,946 ± 24
Angle of Attack	7.46° ± 0.49°
Peak Deceleration (kG)	*
Average Deceleration (kG)	*
Penetration (in)	36.0†
Concrete Lot #	3
Concrete Strength (ksi)	Tests 1, 2, 3: 10.27; 9.88; 9.70; Average: 9.95
Comment	Failure

*Insufficient data

† Penetrator exited side of target

Early

Late

Fig. 14-59. Images from Overall Video of Test Number 10, Design DTV-E-4.

Steel fragment
from tail end cap

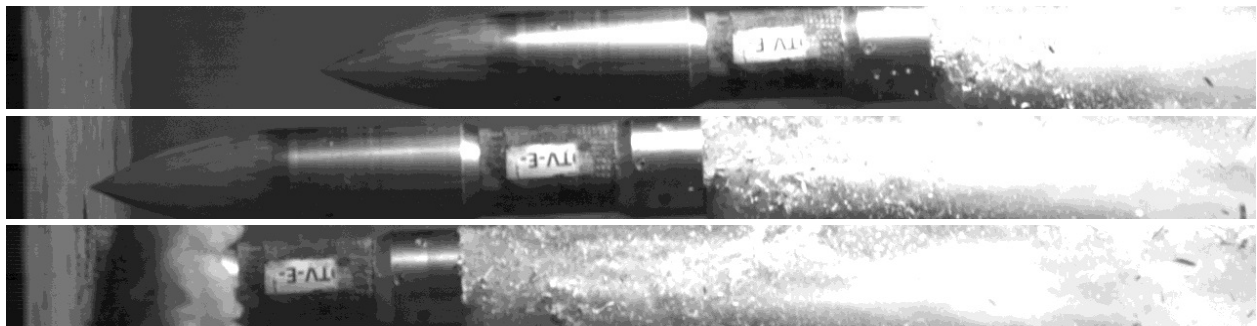Fig. 14-60. Images from orthogonal video of Test Number 10, Design DTV-E-4.

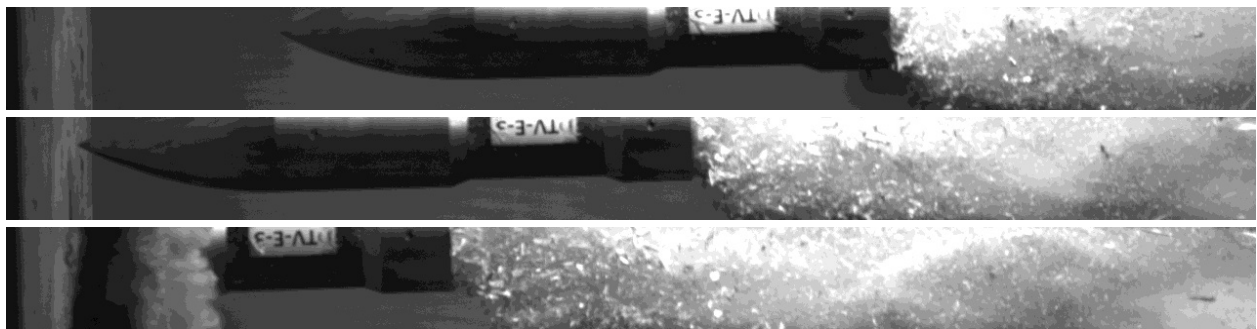

Fig. 14-61. Images from orthogonal impact video of Test Number 10, Design DTV-E-4.

The DTV-E-4 penetrated 36.0 inches into the concrete target before it exited out the side of the concrete target. A photograph of the target after the test is presented in Fig. 14-62. As shown in the figure, the steel nose of the projectile was found about 120 feet behind and to the right of the target. The steel aft closure was found a few feet in front of the target. A photograph of the post-test penetrator is presented in Fig. 14-63.

Projectile nose found ~120 feet away from target in ditch behind this concrete slab.

Broom handle indicating projectile path through target to exit point approximately 36 inches from front face.

Fig. 14-62. Concrete target from Test 10, Design DTV-E-4.

Fig. 14-63. Photograph of DTV-E-4 Penetrator from Test 10.

Test Number 11

Test Number 11 was of the DTV-B-2 configuration. This test was basically a repeat of the previous test. A summary of the test parameters is presented in Table 14-14. Two still images taken from each of the overall and orthogonal videos are presented in Figs. 14-64 and 14-65. Three still images taken from the impact view video are presented in Fig. 14-66.

Table 14-14. Summary of Test Number 11.

Test	11
Date	12/12/2013
Design	DTV-B-2
Muzzle Velocity (ft/s)	1,917 ± 15
Impact Velocity (ft/s)	1,809 ± 13
Angle of Attack	0.72° ± 0.65°
Peak Deceleration (kG)	22.0
Average Deceleration (kG)	17.5
Penetration (in)	38.5
Concrete Lot #	2
Concrete Strength (ksi)	Tests 1, 2, 3: 10.05; 10.02; 9.71; Average: 9.93
Comment	Aft Fixture Failure

Early

Late

Fig. 14-64. Images from overall video of Test Number 11, Design DTV-B-2.

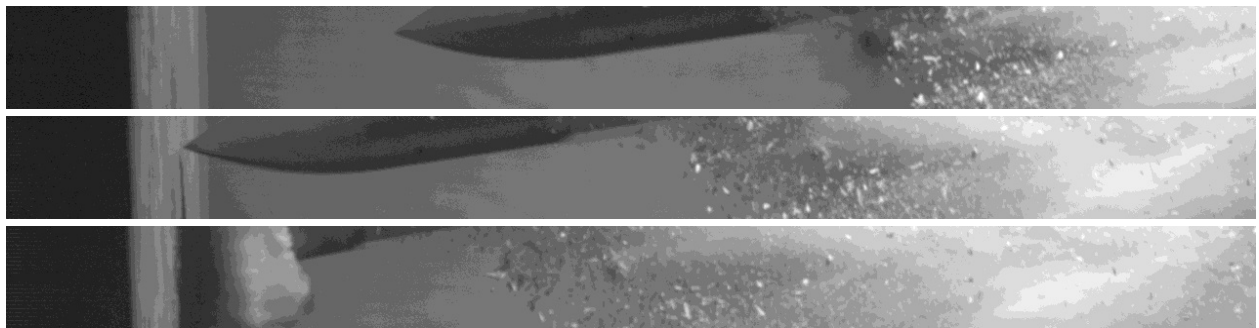Fig. 14-65. Images from orthogonal video of Test Number 11, Design DTV-B-2.

Fig. 14-66. Images from orthogonal impact video of Test Number 11, Design DTV-B-2.

The DTV-B-2 penetrated 38.5 inches into the concrete target. A post-test photograph of the target is presented in Fig. 14-67. The aft steel end closure fractured and partially debonded from the composite body. Photographs of the post-test penetrator are presented in Figs. 14-68 and 14-69.

Fig. 14-67. Concrete target from Test 11, Design DTV-B-2.

0°

90°

180°

270°

Fig. 14-68. Photographs of DTV-B-2 Penetrator from Test 11 at 0°, 90°, 180°, and 270°.

Fig. 14-69. Damage to the DTV-B-2 Penetrator from Test 11.

Test Number 12

The last two tests were of the full sleeve designs. Test Number 12 was of the DTV-F-1 configuration. The test parameters are summarized in Table 14-15. Two still images taken from each of the overall and orthogonal videos are presented in Figs. 14-70 and 14-71, respectively. Three still images from the impact view video are presented in Fig. 14-72.

Table 14-15. Summary of Test Number 12.

Test	12
Date	12/13/2013
Design	DTV-F-1
Muzzle Velocity (ft/s)	2,159 ± 20
Impact Velocity (ft/s)	2,086 ± 9
Angle of Attack	0.48° ± 0.43°
Peak Deceleration (kG)	21.3
Average Deceleration (kG)	16.5
Penetration (in)	54.9
Concrete Lot # (Two cylinders used)	Front: 2, Back: 1
Concrete Strength (Lot 2) (ksi)	Tests 1, 2, 3: 10.05; 10.02; 9.71; Average: 9.93
Comment	Undamaged

Early

Late

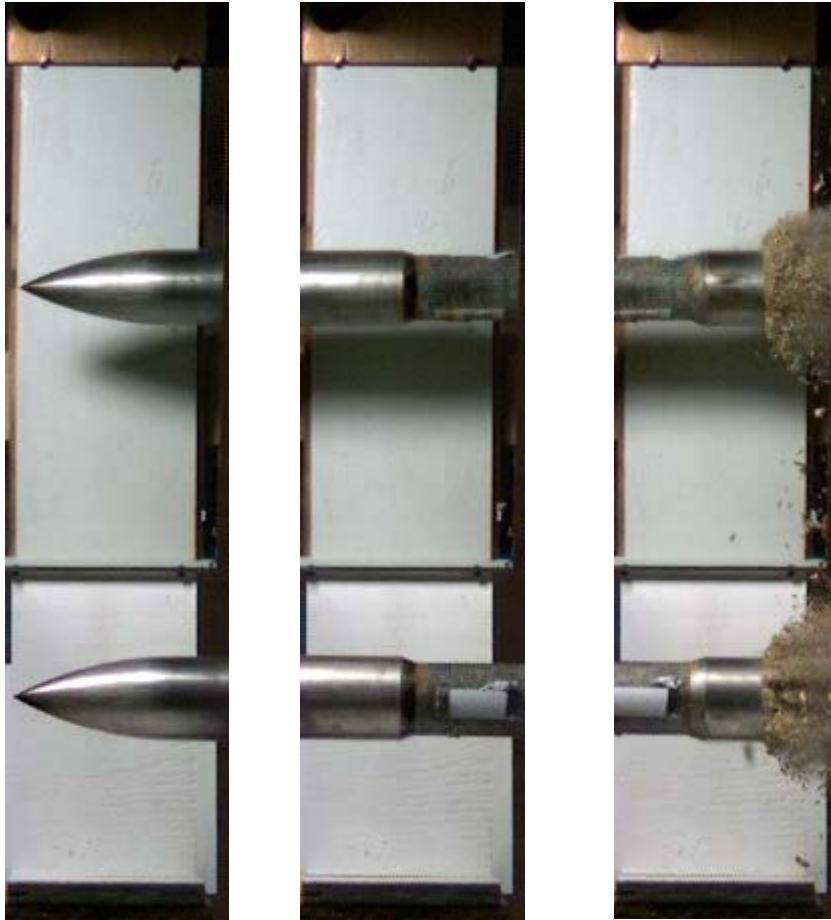Fig. 14-70. Images from overall video of Test Number 12, Design DTV-F-1.
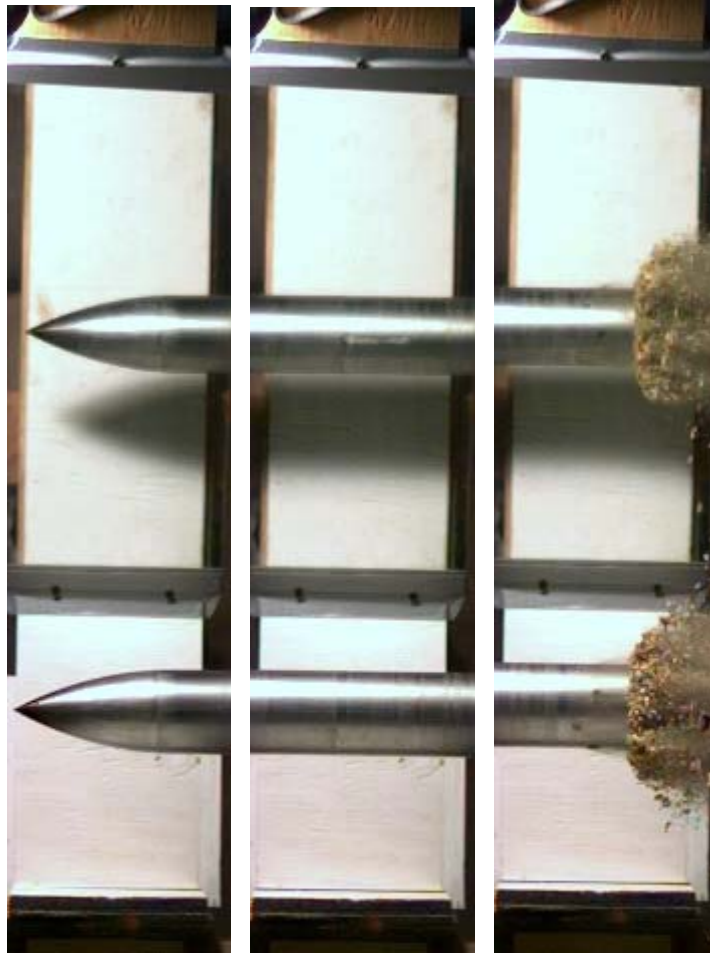
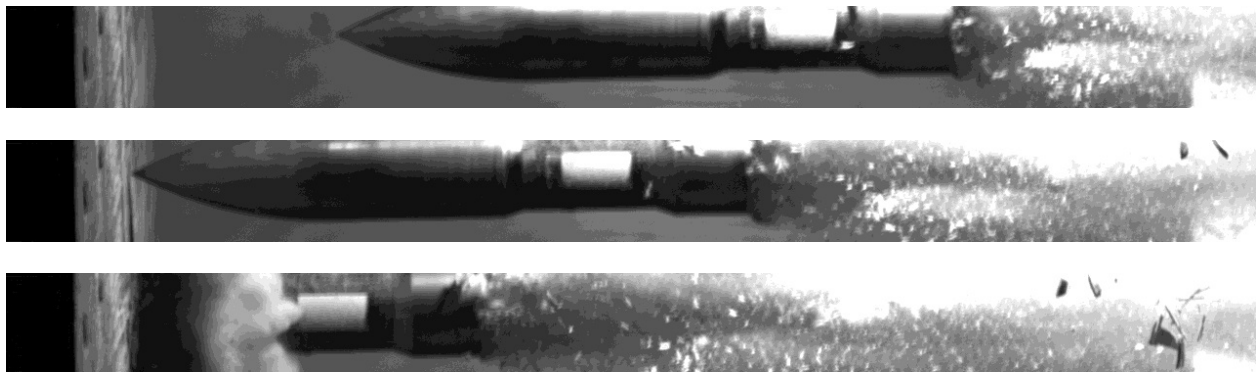Fig. 14-71. Images from orthogonal video of Test Number 12, Design DTV-F-1.

Fig. 14-72. Images from impact video of Test Number 12, Design DTV-F-1.

The DTV-F-1 penetrated 54.9 inches into the concrete target. A photograph of the target after the test is presented in Fig. 14-73. The penetrator was undamaged. Photographs of the post-test penetrator are presented in Fig. 14-74.

Fig. 14-73. Concrete target from Test 12, Design DTV-F-1.

0°

90°

180°

270°

Fig. 14-74. Photographs of DTV-F-1 Penetrator from Test 12 at 0°, 90°, 180°, and 270°.
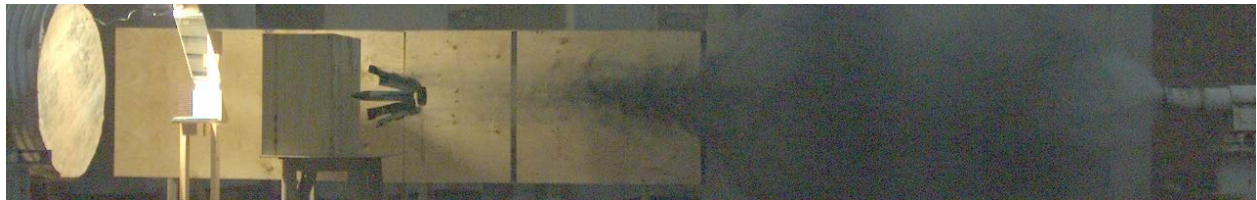
Test Number 13

Test Number 13 was of the DTV-F-2 configuration. The test parameters are listed in Table 14-16. Based on the success of the previous test, the velocity was increased in this test. Two still images taken from the overall video are presented in Fig. 14-75. Because of a malfunction, orthogonal videos were not recorded. Three still images taken from the impact view video are shown in Fig. 14-76.

Table 14-16. Summary of Test Number 13.

| Test	13
Date	12/13/2013
Design	DTV-F-2
Muzzle Velocity (ft/s)	2,581 ± 7
Impact Velocity (ft/s)	2,494 ± 11
Angle of Attack	0.53° ± 0.16°
Peak Deceleration (kG)	17.1
Average Deceleration (kG)	14.0
Penetration (in)	76.0
Concrete Lot # (Two cylinders were used)	Front: 1, Back: 1
Concrete Strength (ksi)	Tests 1, 2, 3: 9.28; 9.21; 9.63; Average: 9.37
Comment	Undamaged

Early

Late
Fig. 14-75. Images from overall video of Test Number 13, Design DTV-F-2.

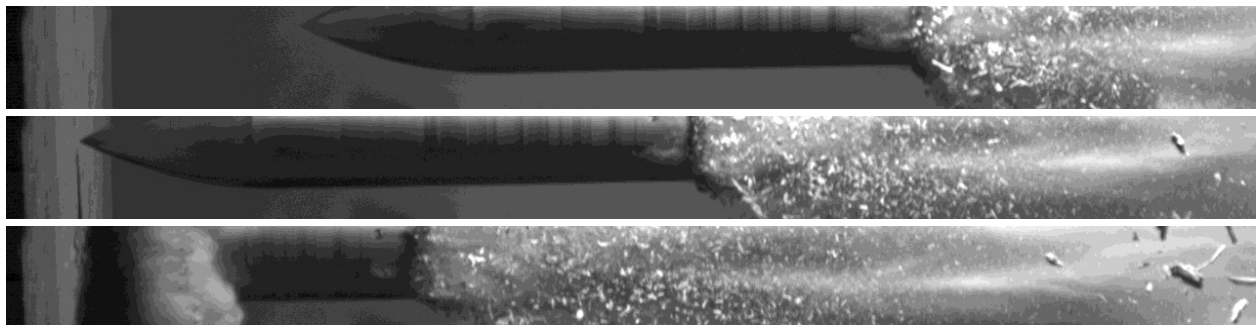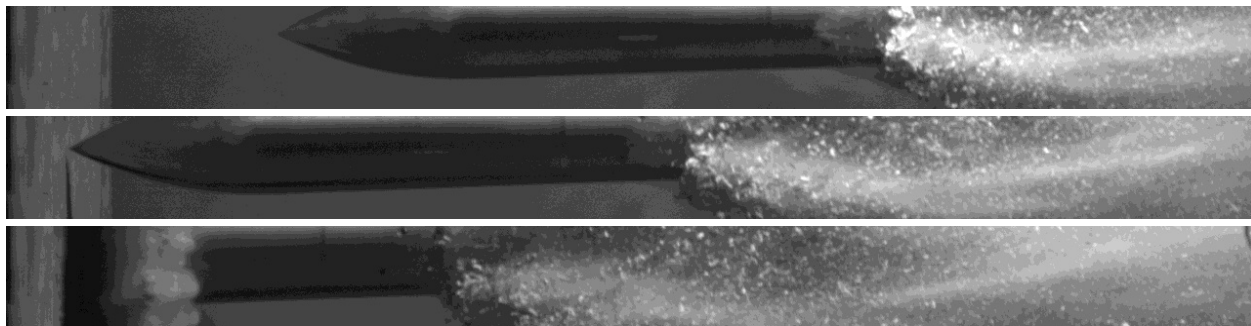Fig. 14-76. Images from impact video of Test Number 13, Design DTV-F-2.

The DTV-F-2 penetrated 76.0 inches into the target. It completely perforated the first 72-inch-thick cylinder and left a 4-inch-deep crater in the second. A post-test photograph of the target is presented in Fig. 14-77. Post-test photographs of the penetrator in Fig. 14-78 show that it was undamaged.

Fig. 14-77. Concrete target from Test 13, Design DTV-F-2.

0°   90°

180°   270°

Fig. 14-78. Photographs of DTV-F-2 Penetrator from Test 13 at 0°, 90°, 180°, and 270°.

14.5 Summary of Results

The overall objective of the test series was achieved in that the response of the composite material as a function of penetration velocity was determined for the design configurations. Figure 14-78 presents the survivability of the three designs versus velocity and AoA. Except for Test Number 10, all of the tests exhibited AoA's of less than 2°. The short-sleeve design survived only at the lower velocities of 900 to 1,000 ft/s. The five-inch-sleeve design survived at velocities of 1,600 ft/s, but indications are that this design could have survived even higher velocities. Finally, the full-sleeve designs demonstrated survivability at velocities up to almost 2,500 ft/s.
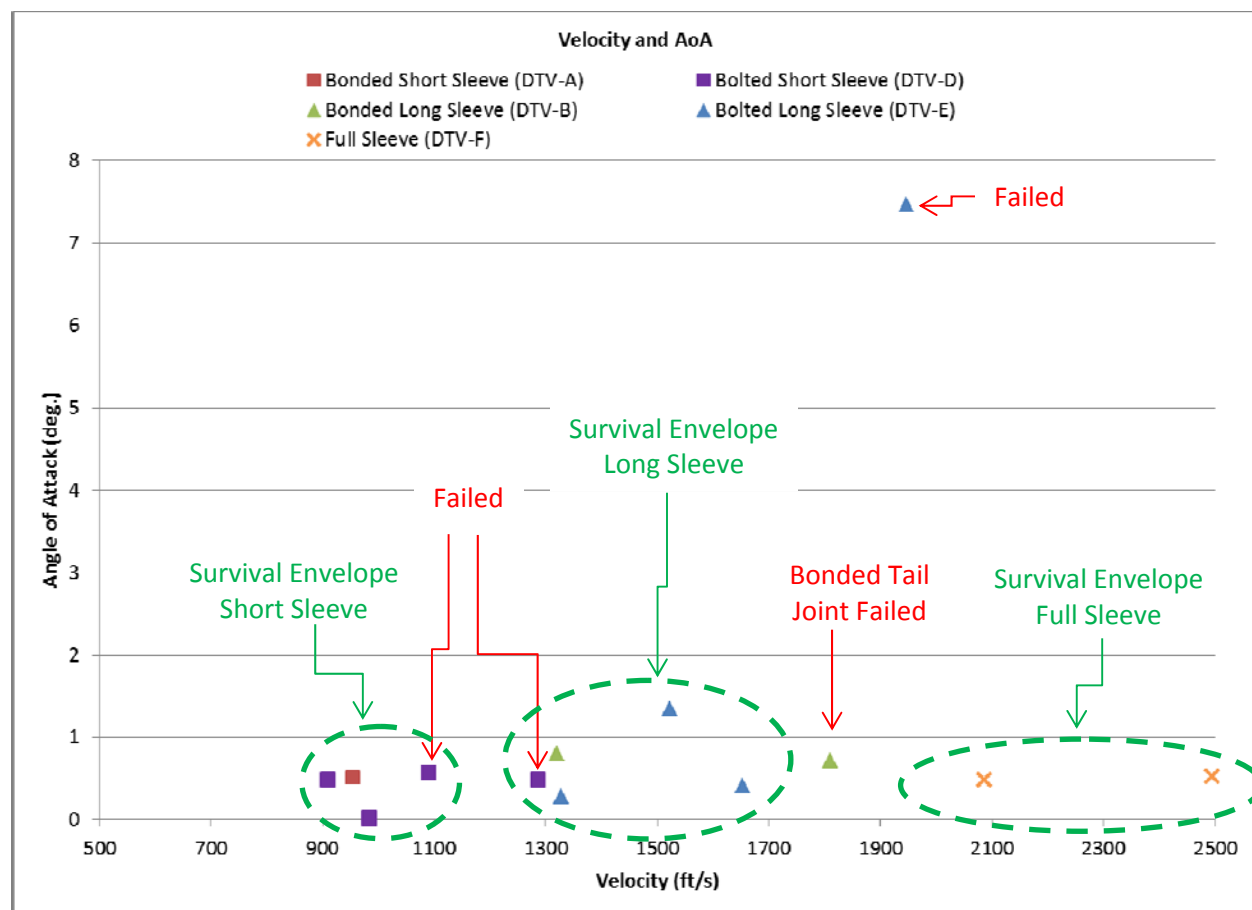
Fig. 14-78. Survivability as a Function of Impact Velocity and AoA for the Three Penetrator Designs.

The penetration data from the test series is summarized graphically in Fig. 14-79. Also included is the PENCRV computer model predictions. The data show the penetration increases with increasing velocity. In general the experimental data falls somewhat in between the PENCRV predictions with the target strengths of 5 and 10 ksi. However, for the two tests of the full sleeve configurations the PENCRV values for the 10-ksi target strength are significantly lower than the experimental values. This deviation can be attributed to the fact that the target diameter was somewhat undersized for the penetrators. An accepted rule of thumb is the diameter of a concrete target should be 20 times the penetrator diameter.

Fig. 14-79. Summary of experimental penetration data and PENCRV computer model predictions.

Finally the integrity of the interface design was verified in this test series. The interfaces incorporating the screws survived in all test cases. Most of the tests with the bonded interfaces also survived with the exception of one test where the tail piece fractured and debonded.

Section XV

Summary of Accomplishments

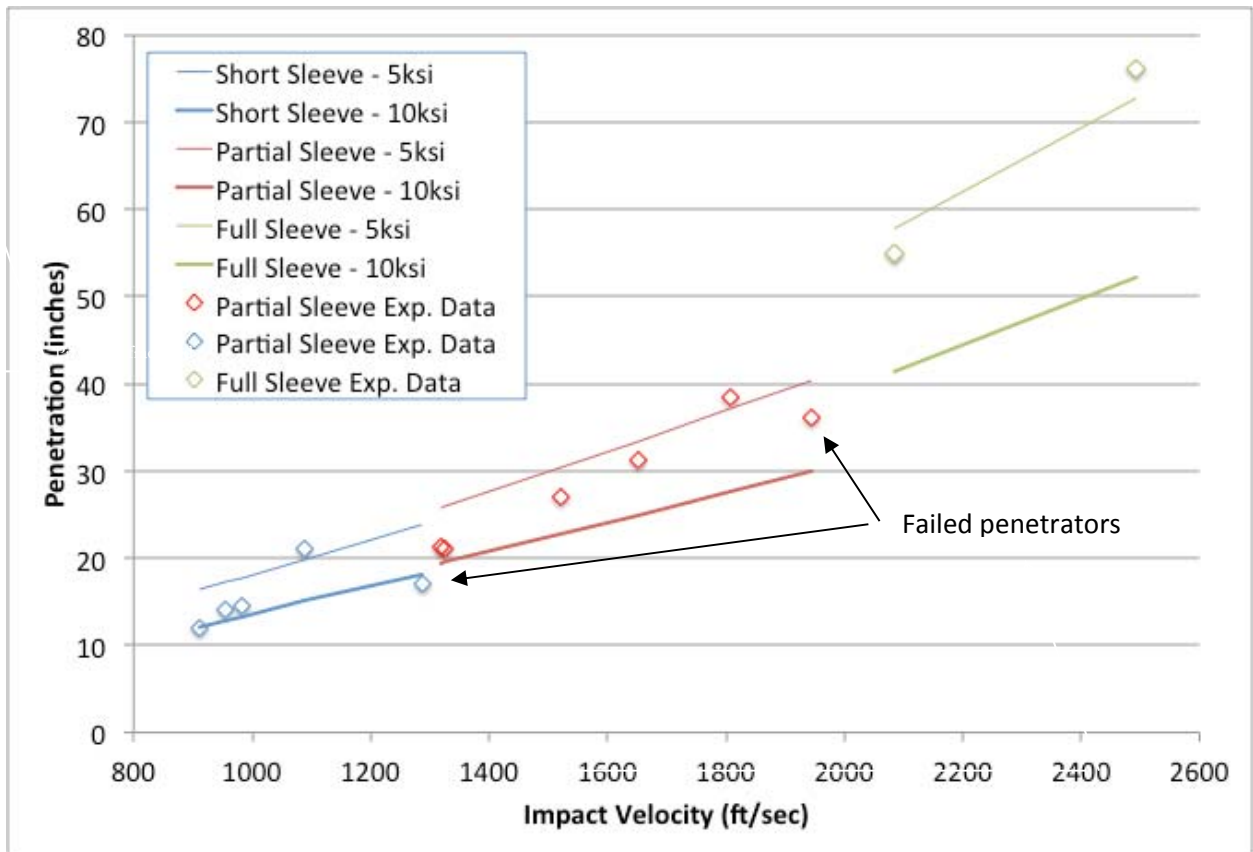This program involved three major types of activities, material development, blast testing, and penetrator development and testing. Material development consisted of downselecting among several material candidates, scaling up the fabrication process, and improvement in mechanical properties. The downselection involved assessment of the properties of each material and its demonstrated ability or potential to achieve the required performance. We quickly arrived at the material system—tungsten wire, mostly braided, in an epoxy matrix doped with aluminum powder—which we believed to have the greatest potential to achieve the program goals of strength, reaction energy, and blast enhancement.

Fabrication scale-up consisted of a stepwise progression from small flat dog-bone coupons through hollow cylindrical specimens of increasing diameters, culminating in 2.5"-outside-diameter specimens weighing as much as 20 pounds. Producing larger specimens sometimes required acquisition of a larger braiding machine to accommodate the larger diameter while maintaining similar densities and orientations of reinforcement; machines having 24 and 48 yarn carriers were used, with a 72-carrier device planned for the next phase. Attention was continuously paid to shop safety, with special testing to assess potential hazards of working with reactive materials at each stage.

Improvements in material properties were achieved by modifying the reinforcement layup (braid angles) according to analysis using standard lamination theory, performed by team member Materials Research & Design, Inc. This included augmenting the braided reinforcement with woven wires, which provided additional axial wires for greater strength in that direction, important for a penetrating weapon. Incremental improvements in fabrication technique were also gained through practical experience with the material.

Blast testing began early in the program with very small-scale enclosed-chamber tests at University of Illinois at Urbana-Champaign to screen candidate materials. Larger-scale chamber tests at Alliant Techsystems investigated the degree of blast enhancement as a function of reactive-casing mass.

Penetrator development began with the implementation of a capability to model penetration into unreinforced conventional concrete to predict loads on a projectile up to several thousand feet per second. The finite-element code EPIC, exercised with and without its PENCRV link, was used for predicting penetration capability and axial failure modes. The ALE-3D code was used to predict trajectory stability and bending and complex failure modes.

We prepared designs for RMS-cased penetrators to investigate their ability to survive concrete penetration over a range of velocities. Steel sleeves of various lengths (short, long, full) were added to several designs to improve their survivability. Several means of securing the steel noses and aft closures to the RMS bodies, including pins and adhesive bonding, were designed, tested, and implemented. Several specimens of each design combination, including the variations in sleeve length and attachment method, were fabricated. Subsequent ballistic tests demonstrated projectile survivability in impacts into 10-ksi-compressive-strength concrete at velocities up to 2500 feet per second.

References

G. Ben-Dor, A. Dubinsky, & T. Elperin, "Shape optimization of impactor penetrating into concrete or limestone targets," *Intl. J. Solids Structures*, Vol. 40, pp. 4487-4500, 2003.

J.A. Canfield & I.G. Clator, "Development of a scaling law and techniques to investigate penetration in concrete," U.S. Naval Weapons Laboratory Report No. 2057, Dahlgren, VA, 1966.

X.W. Chen, "On Penetration/Perforation of Concretes Struck by Rigid Projectiles," *Proc. 24th International Symp. on Ballistics*, New Orleans, LA, 22-26 Sep. 2008.

A.J. Eggers, Jr., M.M. Resnikoff, & D.H. Dennis, "Bodies of Revolution having Minimum Drag at High Supersonic Airspeeds," National Advisory Committee for Aeronautics, Report No. 1306, 1954.

U. Fano, "Methods for Computing Data on the Terminal Ballistics of Bombs – Estimation of the Air Blast," Ballistic Research Laboratories Report 524, 1945.

S.H. Fischer & M.C. Grubelich, "A Survey of Combustible Metals, Thermites, and Intermetallics for Pyrotechnic Applications," pres. *32nd AIAA/ASME/SAE/ASEE Joint Propulsion Conf.*, Lake Buena Vista, FL, July 1-3, 1996.

S.H. Fischer & M.C. Grubelich, "Theoretical Energy Release of Thermites, Intermetallics, and Combustible Metals," pres. *24th International Pyrotechnics Seminar*, Monterey, CA, July 1998.

E.M. Fisher, "The effect of the steel case on the air blast from high explosives," NAVORD report 2753, 1953. AD 009708.

W.J. Flis, L. Shan, and D. Jann, "Improved Trajectory Control for Penetration into Soils at 3000 to 4000 ft/sec", AFRL-RW-EG-TR-2008-xxxx, Contract No. FA8651-05-C-0114, 2008.

M.J. Forrestal, B.S. Altman, J.D. Cargile, & S.J. Hanchak, "An empirical equation for penetration depth of ogive-nose projectiles into concrete targets," *Intl. J. Impact Engrg.*, 15(4):395-405, Aug. 1994.

Carl Gotzmer & Steve Kim, "Reactive Materials," undated briefing.

M.D. Hutchinson, "The Escape of Blast from Fragmenting Munitions Casings," *Int. J. Impact Eng.*, Vol. 36, p. 185, 2009.

S.E. Jones & W.K. Rule, "On the optimal nose geometry for a rigid penetrator, including the effects of pressure-dependent friction," *Intl. J. Impact Engrg.*, Vol. 24, pp. 403–415, 2000.

S.E. Jones, W.K. Rule, D.M. Jerome, & R.T. Klug, "On the optimal nose geometry for a rigid penetrator," *Proc. Intl. Symp. Impact and Penetration Problems*, Atlanta, GA, Oct. 1998. Also, *Computational Mechanics*, 1998:22/413.

Brian J. Kohn, "Compilation of Hugoniot Equations of State," Air Force Weapons Laboratory, Report No. AFWL-TR-69-38, April 1969. AD 852300.

Q.M. Li & X.W. Chen, "Dimensionless formulae for penetration depth of concrete target impacted by a non-deformable projectile," *Intl. J. Impact Engrg.*, 28(1):93-116, 2003.

Rayment E. Moxley & Toney K. Cummins, "ERDC Cor-Tuf Ultra High Performance Concrete Walls," U.S. Army Engineer Research and Development Center, pres. to Standardized MOUT Target Testing Board, Fort Benning, GA, 21 Feb. 2008.

I. Newton, *Philosophiæ Naturalis Principia Mathematica*, 1687. Motte's Translation Revised, Univ. Cal. Press, 1946.

B. Plunkett & M. Green, "Constituent Behavior of AFX-757 Simulant During Penetration," AFRL-RW-EG-TR-2009-7074, Interim report, Air Force Research Laboratory, Munitions Directorate, AFRL-RWAC, Eglin, AFB, January 2009.

S. A. Silling, "CTH Reference Manual: BFK Model for Concrete," Sandia National Laboratories, Albuquerque, NM, Rev. 3, 2/21/2001.

Daniel J. Steinberg, "Equation of State and Strength Properties of Selected Materials," Lawrence Livermore National Laboratory, UCRL-MA-106439, rev. Feb. 13, 1996.

M. Unosson, "Numerical Simulations of Penetration and Perforation of High Performance Concrete with 75mm Steel Projectile," FOA-R-00-01634-311-SE, FOA, Tumba, Sweden, Nov. 2000.

Robert C. Weast, ed., *Handbook of Chemistry and Physics*, 58th edition, CRC Press, Cleveland, OH, 1977.

C.W. Young, "Penetration equations," Sandia Natl. Lab., Albuquerque, NM, Report No. SAND97-2426; 1997.